Forschungsbericht 2024-20

The Earth Explorer Mission Aeolus for atmospheric wind observations – Final Report from the Aeolus Data Innovation and Science Cluster DISC of Phase E

Aeolus DISC
Data Innovation and Science Cluster

Deutsches Zentrum für Luft- und Raumfahrt
Institut für Physik der Atmosphäre
Oberpfaffenhofen

Deutsches Zentrum
DLR für Luft- und Raumfahrt

Forschungsbericht 2024-20

The Earth Explorer Mission Aeolus for atmospheric wind observations – Final Report from the Aeolus Data Innovation and Science Cluster DISC of Phase E

Aeolus DISC
Data Innovation and Science Cluster

Deutsches Zentrum für Luft- und Raumfahrt
Institut für Physik der Atmosphäre
Oberpfaffenhofen

333 Seiten
162 Bilder
21 Tabellen
243 Literaturstellen

Deutsches Zentrum
DLR für Luft- und Raumfahrt

Herausgeber:

Deutsches Zentrum
für Luft- und Raumfahrt e. V.
Wissenschaftliche Information
Linder Höhe
D-51147 Köln

ISSN 1434-8454
ISRN DLR-FB-2024-20
DOI: 10.57676/93c3-n766

Erdbeobachtung, Atmosphäre, Wind, ESA, Aeolus, DISC, Doppler-Wind-Lidar

Dr. Oliver Reitebuch (auf Englisch veröffentlicht)
DLR, Institut für Physik der Atmosphäre, Oberpfaffenhofen, Deutschland

Die Earth Explorer Mission Aeolus für atmosphärische Windbeobachtung – Abschlussbericht des Aeolus „Data Innovation and Science Cluster" DISC der Phase E

Die im August 2018 gestartete Earth Explorer Mission Aeolus der ESA hat zum ersten Mal atmosphärische Windprofile global vermessen. Als erstes Doppler-Wind-Lidar-Instrument im Weltraum trug Aeolus durch die Messung einer Komponente des horizontalen Windvektors erheblich zur Verbesserung der numerischen Wettervorhersage (NWV) bei. Die operative Phase der Mission endete im April 2023, gefolgt von einer ausgedehnten Testphase des Instruments bis Juli 2023. Aeolus hat alle Missionsziele erreicht und eine deutliche Verbesserung auf die Wettervorhersage in mehreren Wettervorhersage-Modellen erzielt.

Diese Errungenschaften wurden durch die entscheidenden Beiträge des Aeolus Data Innovation and Science Cluster (DISC) ermöglicht. Das DISC unterstützte die Mission mit einer Vielzahl von Aktivitäten, darunter die Überwachung der Instrumenten- und Produktqualität, die Verbesserung der Auswertealgorithmen und operationellen Prozessoren, sowie die Bewertung des Einflusses von Wind- und Aerosolprodukten von Aeolus auf die Wettervorhersage. Unter der Koordination des DLR brachte das Aeolus DISC das Fachwissen von ECMWF, KNMI, Météo-France, TROPOS, DoRIT, ABB, S&T, Serco, OLA, Physics Solutions, IB Reissig und Les Myriades zusammen, wobei mehr als 40 Wissenschaftler und Ingenieure im DISC beteiligt waren.

Dieser Abschlussbericht fasst die Beiträge des Aeolus DISC während der operationellen Phase der Aeolus-Mission von 2018 bis 2023 zusammen. Er enthält zudem ein Kapitel über die „Lessons Learnt" für zukünftige Erdbeobachtungsmissionen, mit besonderem Fokus auf die kürzlich gestartete EarthCARE-Mission und die Entwicklung der zukünftigen Aeolus-2-Mission.

Earth Observation, Atmosphere, Wind, ESA, Aeolus, DISC, Doppler-Wind-Lidar

Dr. Oliver Reitebuch (Published in English)
German Aerospace Center (DLR), Institute of Atmospheric Physics, Oberpfaffenhofen, Germany

The Earth Explorer Mission Aeolus for atmospheric wind observations – Final Report from the Aeolus Data Innovation and Science Cluster DISC of Phase E

Launched in August 2018, ESA's Earth Explorer mission Aeolus was the first to measure atmospheric wind profiles on a global scale. As the first-ever Doppler Wind Lidar instrument in space, Aeolus significantly contributed to the improvement in numerical weather prediction (NWP) by measuring one component of the horizontal wind vector. The operational phase of the mission concluded in April 2023, followed by an extended instrument testing phase until July 2023. Aeolus successfully achieved its mission objectives, demonstrating a clear positive impact on weather forecasts across several NWP models.

These accomplishments were made possible through the critical contributions from the Aeolus Data Innovation and Science Cluster (DISC). The DISC supported the mission with a wide range of activities, including instrument and product quality monitoring, retrieval algorithm and operational processor enhancements, and NWP impact assessments using wind and aerosol products from Aeolus. Coordinated by DLR, the Aeolus DISC brought together expertise from ECMWF, KNMI, Météo-France, TROPOS, DoRIT, ABB, S&T, Serco, OLA, Physics Solutions, IB Reissig and Les Myriades, involving more than 40 scientists and engineers within the DISC.

This Final Report summarizes the contributions from the Aeolus DISC during the operational phase of the Aeolus mission from 2018 to 2023. It also includes a chapter on lessons learnt for future Earth observation missions, with a particular focus on the recently launched EarthCARE mission and the development of the upcoming Aeolus-2 mission.

Beteiligte Autoren:

Oliver Reitebuch, Isabell Krisch, Christian Lemmerz, Oliver Lux, Karsten Schmidt, Benjamin Witschas, Uwe Marksteiner, Michael Rennie, Ines Nikolaus, Frédéric Fabre, Dimitri Trapon, Alain Dabas, Dave Donovan, Gerd-Jan van Zadelhoff, Ping Wang, Gert-Jan Marseille, Arie Kuijt, Filippo Tagliacarne, Gaetan Perron, Dorit Huber, Markus Meringer, Katja Reissig, Jos de Kloe, Massimo Cardaci, Giacomo Gostinicchi, Will McLean, Karen Henry, Angela Benedetti, Sebastian Bley, Ad Stoffelen, Paola Sabbatini, Jean-François Mahfouf, Vivien Pourret

Aeolus Data Innovation Science Cluster DISC

The Earth Explorer Mission Aeolus for atmospheric wind observations – Final Report from the Aeolus Data Innovation and Science Cluster DISC of Phase E

DISC-Ref.: AED-PR-DLR-GEN-013

Issue: V 3.0

Date: 28/10/2024

Document Change Log

Issue	Date	New pages	Modified pages (after introducing new pages)	Observations	Name
V 1.0	29 February 2024	All	-	Version 1.0 prepared	Oliver Reitebuch with support from Oliver Lux, Isabell Krisch based on input from DISC team
V 2.0	14 June 2024			Revised Version 1.1 prepared including new chapter on IRC/IRONIC (3.5) and L2B bias correction (4.7) Revision of LL chapter after Aeolus LL workshop on May 22-23, 2024, Frascati	Oliver Reitebuch with support from Oliver Lux based on input from DISC team
V 3.0	28 October 2024			Integration of Annex and change of style sheet for publication	Oliver Reitebuch with support from Stefanie Knobloch

Table of Contents

0 General Remarks

0.1 Compliance Statement

The Earth Explorer Mission Aeolus for atmospheric wind observations – Final Report from the Aeolus Data Innovation and Science Cluster DISC of Phase E is fully compliant with the management requirements of the DISC contract.

0.2 Applicable and Reference Documents

All references are found in an Annex of this report. The references are structured for each chapter and section and a complete list of Technical Notes delivered by the DISC.

0.3 Acronyms & Abbreviations

An up-to-date list of abbreviations used within DISC and in this document can be found in the Annex of this Report.

1 Introduction and objectives of the Aeolus DISC

Oliver Reitebuch and Isabell Krisch, DLR

The Data Innovation and Science Cluster (DISC) is a core element of ESA's data quality strategy for the Aeolus mission. The DISC is a consortium of partners from science institutes (DLR, TROPOS), weather forecasting centres (KNMI, ECMWF, Météo-France/CNRM/CNRS) and industry (DoRIT, Serco, ABB, S&T). The main tasks of the DISC are shown in Figure 1.

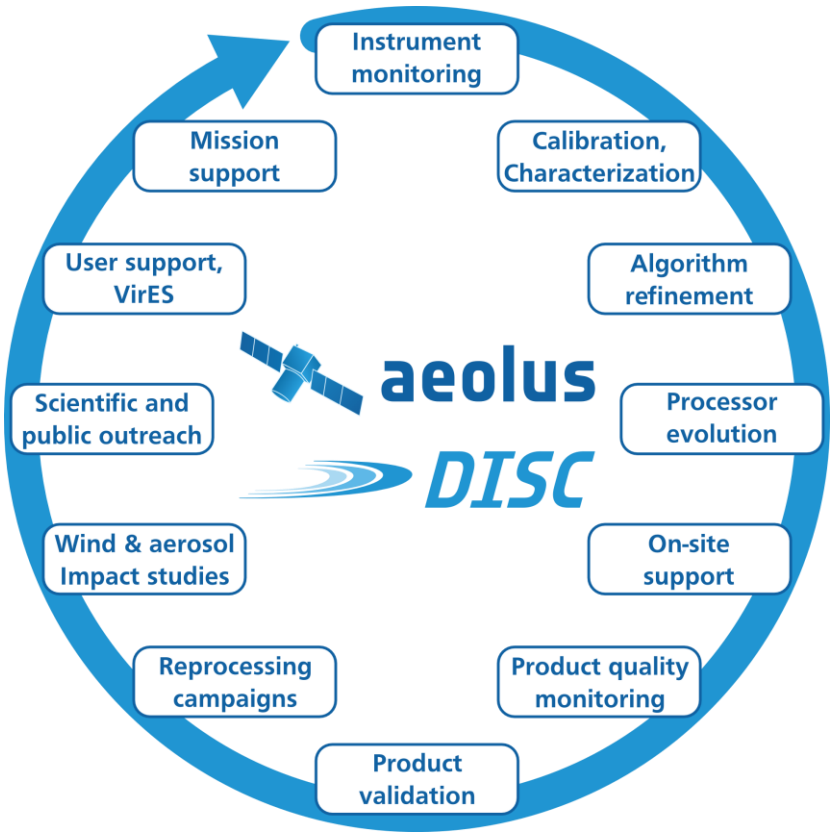

Figure 1: The Aeolus DISC tasks.

Among the responsibilities of the Aeolus DISC in Phase E2 was the daily monitoring of the ALADIN instrument performance, which included for example the surveillance of the laser energy, the optical signal throughput or the detector performance (see Chapter 3). Additionally, the Aeolus DISC supported ESA in the detection, investigation and correction of systematic errors and the instrument calibration (see chapter 3). The correction of such systematic errors often goes along with processor algorithm refinements and upgrades of the operational data processors (see Chapter 4), which is also part of the Aeolus DISC. All operational software processors (L0, L1A, L1B, L2A and L2B) were updated on a half-yearly basis. These updates played a significant role for data quality improvements and gave the opportunity to frequently introduce new data products.

When new processors were introduced, older Aeolus observations needed to be reprocessed to ensure a homogeneous stream of data products. Reprocessing of Aeolus data requires detailed knowledge of the underlying data processing algorithms and calibration concepts. This knowledge is only available within the Aeolus DISC due to the 2 decades of preparation in the Aeolus mission before launch. Thus, all pre-preparations necessary for reprocessing, e.g. generation of all necessary auxiliary files and documentation, are performed by the Aeolus DISC (see section 5.1).

Another important task of the Aeolus DISC is the validation of the Aeolus data products (atmospheric wind and optical properties of aerosols and clouds) and their quality monitoring and documentation. The Aeolus DISC team members at ECMWF prepared and used monitoring tools to automatically compare the Aeolus L2B winds with the ECMWF model data immediately after instrument switch-on, producing statistical comparisons on a regular basis (section 5.3). This unique concept helped to identify many systematic errors shortly after launch and still is a prerequisite to evaluate the Aeolus data quality of reprocessed datasets.

Besides this daily data quality monitoring, ECMWF was also tasked to study the impact of Aeolus wind data for numerical weather prediction starting directly after launch (see section 6.1). Due to this, ECMWF was the first weather centre to use Aeolus data for their daily weather prediction already on 9 January 2020 – less than 1.5 years after launch.

The optical products of aerosols and clouds were constantly monitored by the teams at Météo-France/CNRM, TROPOS and KNMI and weekly data quality reports were provided (see section 5.2). In addition, a team at ECMWF set up a tool to compare the Aeolus optical products of aerosols to data from the CAMS (Copernicus Atmosphere Monitoring Service) model (see section 5.4). Also, a conversion tool for the native Aeolus data in Earth Explorer Format to BUFR (Binary Universal Form for the Representation of meteorological data) was developed, which was a prerequisite for the impact analysis studies of Aeolus aerosol products also performed at ECMWF (see section 6.2).

The Aeolus Monitoring and Calibration Facility (ACMF) was maintained by S&T and ABB during the DISC phase. The ACMF hosts both the calibration processors and also performs and automatic quality-monitoring of the products. In addition, the codadef-tools for reading the Aeolus products were updated regularly by S&T (see section 0 and 4.9)

An important element was the DISC on-site support (DOS by serco), which acted as an interface between the DISC and ESA´s Payload Data Ground Segment (PDGS). The DOS was responsible for configuration and processor release management, anomaly management and daily support for PDGS activities (see section 4.14)

The Aeolus DISC also supported the external and registered Cal/Val teams by providing guidance of using and validating the products and maintaining a Wiki-page specifically for those teams (see section 5.5). Also, the half-yearly to yearly reports of the Cal/Val teams were reviewed and synthesized in a summary report, where also recommendations for algorithm updates and quality improvements were compiled. In addition, the DISC supported ESA in answering any user requests, which were communicated via several functional e-mail accounts.

The Aeolus DISC activities were regularly reported during the regular Aeolus Science and Validation Conferences, the half-yearly Aeolus Science Advisory Groups (SAG). Under the lead of the DISC also special Aeolus issues were established for the EGU on-line journals AMT, ACP and WCD and the Quarterly Journal of the Royal Meteorological Society (QJRMS), where also a significant amount of publications was placed by authors from the DISC. In addition, DISC supported ESA in organizing the Aeolus conferences and provided support for content management of the Aeolus ESA-Websites (see section 5.7).

The final report is concluded with a list of Lessons Learnt (LL) and recommendations for future missions with a special focus on Aeolus 2 (see section 7).

2 DISC management approach

Isabell Krisch and Oliver Reitebuch, DLR

The DISC consortium organization is shown in Figure 2. The prime contractor and main contact point for ESA is DLR. In Phase E2, DLR was supported by 8 subcontractors (DoRIT, TROPOS, CNRS-CNRM/Météo-France, ABB, ECMWF, S&T, KNMI, and Serco) and 5 consultants (Physics Solutions, IB Reissig, Optical & Lidar Associates, Les Myriades, and LMU Munich). Most of them throughout the whole project duration, others only for a shorter period. Many of the consortium members have been involved in the Aeolus mission long before launch and some even before the selection of the Atmospheric Dynamics Mission (ADM) at the workshop in Granada in 1999.

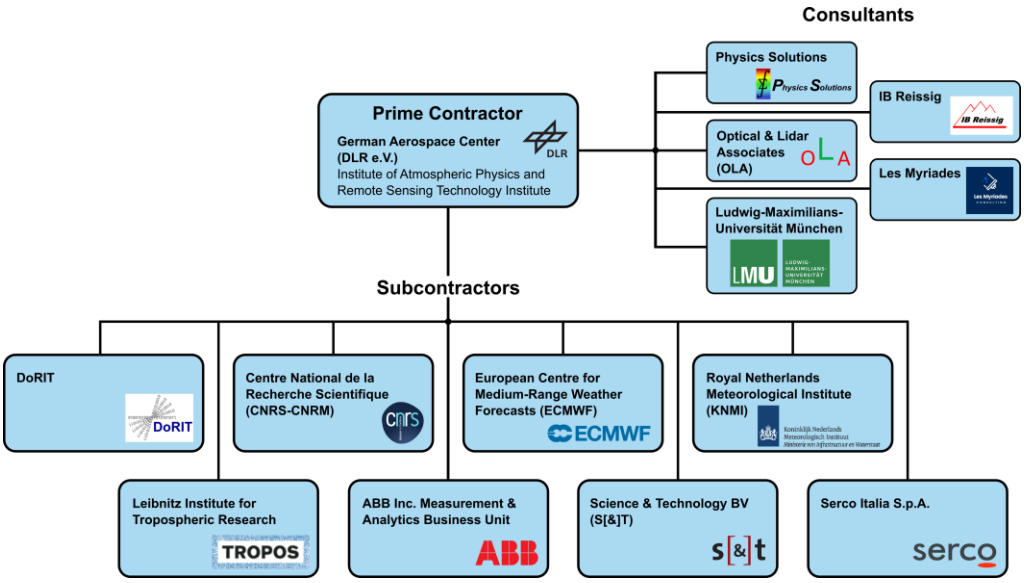

Figure 2: Organigram of the DISC consortium.

Most of the team members cooperated closely during the algorithm/processor studies for L1B, L2A and L2B, which started in 2004. In parallel to this also the development of the ALADIN airborne demonstrator A2D started at DLR in 2003. This involvement was mainly through different development and research contracts with ESA-ESTEC until the end of the Aeolus commissioning phase E1 in January 2019. Even though the contracts were usually independent from one another, the various partners were all working for the same goal and have established efficient ways of communication and collaboration, e.g. by common progress meetings and common definitions of the functionalities and interfaces among the different processors. After launch on 22 August 2018 and finalization of phase E1 in January 2019, with the establishment of the DISC, all these different contracts were bundled into one. This facilitated the collaboration and data exchange among the consortium members, but also created new challenges in managing such a diverse team from industry, science and weather forecasting centres.

To tackle these new challenges, a project management team was assembled by DLR with clear roles. The study manager on DLR side, with the role of a scientific coordinator, has been supported by a project manager for organizational matters and a contracts officer for contractual matters. In addition, a Processor Release Manager and Coordinator and a Quality Control Scientist were assigned.

For efficient communication and information exchange, regular online meetings with all DISC partners and ESA were performed. These online meetings took place weekly in the beginning of the project (first half year), then reduced to bi-weekly during the course of the project and further reduced to monthly after the decommissioning of the satellite. For the online status meetings all partners prepared short status reports one day in advance, which were uploaded to a shared ftp server.

To discuss technical topics in more detail, topical online meetings were organized from time to time. In addition, yearly face-to-face working meetings were organized. These meetings were usually split into wind and aerosol/cloud related topics. ESA assessed the progress of the project every half year in progress review meetings. A list of all meetings within the DISC is provided in the Annex.

An important tool for communication, discussion and documentation of the achievements is the Aeolus DISC wiki; this was complemented by an ftp-server for delivery of regular status reports, deliverables as Technical Notes TN´s or progress reports, software, processors, and archiving presentation and minutes of meetings. The structure and the content of the WIKI were already laid in the preparation phase with the EDAFECS (ESA Data Analysis From Expert Core Teams) approach initiated by ESA. The main topics and objectives of the WIKI were:

- Announcement and agenda of weekly, bi-weekly and then monthly DISC status meetings including report from ESA about mission performance; the DISC consortium partners status report for each meeting were collected on the ftp-server.
- A major part of the WIKI activities is related to data product and algorithm discussions for each processing level as well as instrument topics. Each discussion items contains the relevant information, figures and presentation about this topic. The item is considered as closed, if the respective item is implemented in the processors and verified, or if the relevant discussion on instrument topics is concluded. It contains 96 items for L0/L1A/1B processing, 33 items for L2A, 12 items for L2B, and a number of 50 items for instrument discussions, and items for other topics (status 29 February 2024). More recently a collection of items started related to reprocessing campaigns. Team members were encouraged to summarize discussions on special topics (e.g. via e-mail) on WIKI items for documentation.
- Collection of all delivered TN´s, proposals, progress reports or software documentation.
- Collection of different configuration management topics.
- Aeolus activity timeline compiled by ESA, which provides a detailed list of instrument activities, changes in operating parameters, and test sequences.
- Monitoring pages for the DISC performance indicators
- List of acronyms, conferences, tools, planned or published papers, outreach activities, and other list of interest for information

It can be stated that a significant part of the knowledge and experience gained from the Aeolus DISC is made available and archived in the DISC wiki items (in addition to the TN´s and meeting presentations), and is of invaluable benefit for future work in phase F and Aeolus 2. It can be also stated that it provides a very good knowledge base for cooperation among a large team distributed over several institutes, although it is certainly a continuous effort for all to keep it up-to-date. The DISC wiki is hosted on a Confluence page, which turned out to be a good and flexible solution. In addition to the DISC wiki, which is only accessible to the DISC team members, also the information for the Aeolus Cal/Val teams was collected on a separate WIKI page.

The tasks of the DISC Consortium can be arranged into 11 major topics:

- Project Management
- Ramping up the Project
- Corrective Maintenance of Processors and Tools
- Perfective Maintenance of Processors and Tools

- Anomaly and Configuration Management
- Validation, Testing, Configuration Parameters, Reprocessing and Tools
- Calibration/Validation (Cal/Val) Support, Quality Control and Monitoring
- User, Quality Working Group and Outreach Support
- Numerical Weather Prediction (NWP) Monitoring and Impact Assessment
- Aeolus Calibration and Monitoring Facility (ACMF) Analysis and Processor Release Coordination
- ACMF Maintenance and Evolution

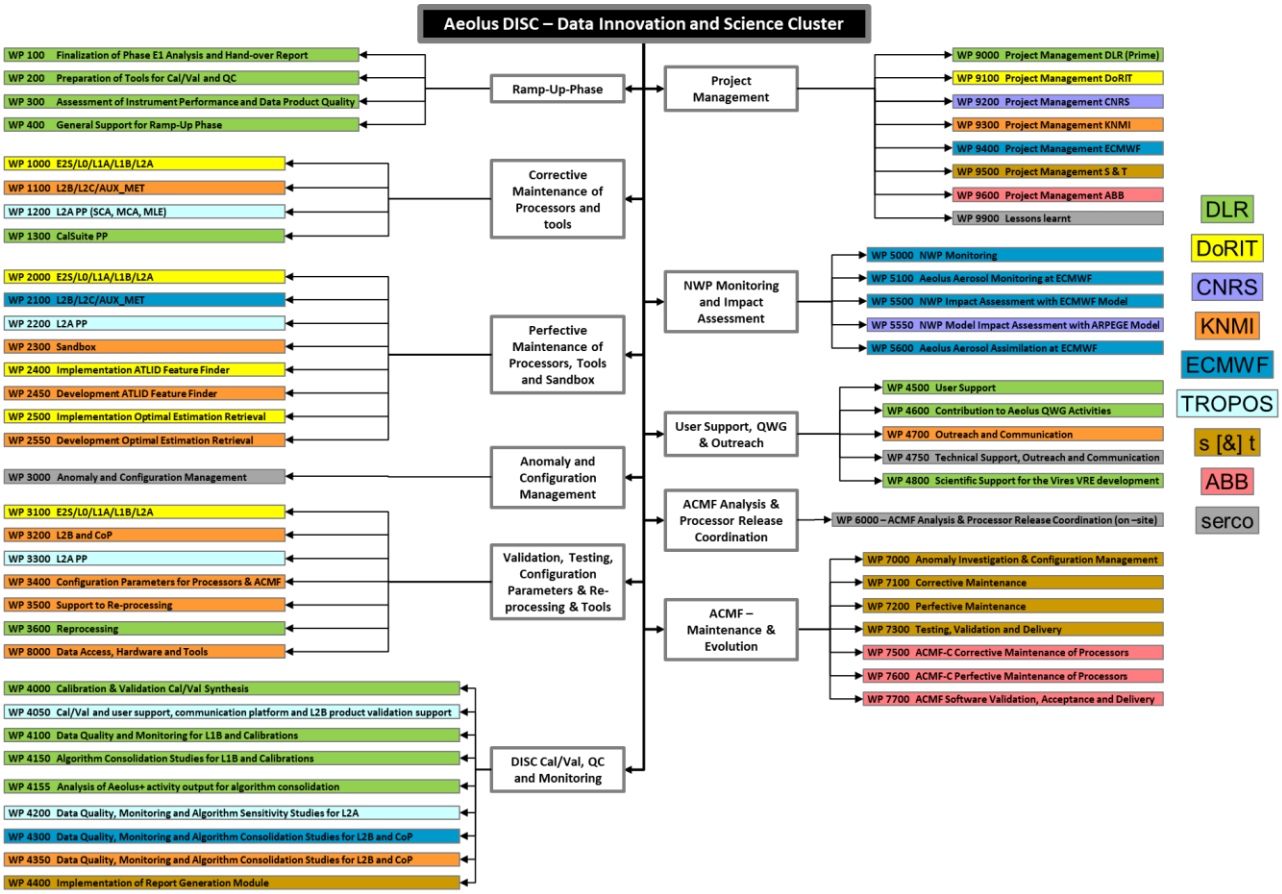

Figure 3: The Aeolus DISC Work Breakdown Structure (WBS).

In each topic, work packages were defined to tackle the tasks. Some work packages were present over the whole project lifetime, others were only necessary over a limited period of time (see Figure 4). Among these short-term work packages were the work packages related to the project ramp-up, the development of the Python Report Generator and the VirES VRE (VirES: Virtual Workspace for Earth Observation Scientists, VRE: Virtual Research Environment).

Due to the experimental nature of the mission and many unexpected instrument anomalies, a high flexibility was required by all DISC partners. For an optimal support of ESA and the mission goals, frequent project management meetings between ESA and DLR took place to constantly reassess the project priorities and reschedule the upcoming tasks. Throughout the project 9 work orders and 5 contract-change-notices were signed expanding existing tasks or assigning new ones.

ID	Task Name	WP Manager	Start	Finish
0	**DISC_Workpackages**		**Fri 01.02.19**	**Sun 31.03.24**
1	**Specific WPs for Ramp-Up Phase**		**Fri 01.02.19**	**Fri 07.06.19**
2	WP ID 100 - Preparation of Hand-Over Report & Analysis	**OR**	Fri 01.02.19	Tue 07.05.19
3	WP ID 200 - Preparation of Tools for Optimization Phase: Cal/Val & QC	**UM**	Wed 08.05.19	Thu 06.06.19
4	WP ID 300 - Assessment Instrument Performance and Product Quality	**OR**	Fri 01.02.19	Thu 06.06.19
5	WP ID 400 - General Support RUP	**OR**	Fri 01.02.19	Thu 06.06.19
6	**Corrective Maintenance of processors and tools**		**Fri 01.02.19**	**Sun 31.03.24**
7	WP ID 1000 - E2S/L0/L1A/L1B/L2A	**DH**	Fri 01.02.19	Sun 31.03.24
8	WP ID 1100 - L2B/L2C/AUX_MET	**JdK**	Fri 01.02.19	Sun 31.03.24
9	WP ID 1200 - Cal-Suite PP and L2A PP	**AD**	Fri 01.02.19	Sat 31.12.22
10	WP ID 1200 - L2A PP	**DT**	Sun 01.01.23	Sun 31.12.23
11	WP ID 1300 - Cal_Suite PP	**BW**	Sun 01.01.23	Sun 31.03.24
12	**Perfective Maintenance of processors and tools**		**Fri 01.02.19**	**Sun 31.03.24**
13	WP ID 2000 - E2S/L0/L1A/L1B/L2A	**DH**	Fri 07.06.19	Sun 31.03.24
14	WP ID 2100 - L2B/L2C/AUX_MET	**MR**	Fri 01.02.19	Sun 31.03.24
15	WP ID 2200 - Cal-Suite PP and L2A PP	**AD**	Fri 01.02.19	Sat 31.12.22
16	WP ID 2200 - L2A PP	**DT**	Sun 01.01.23	Sun 31.03.24
17	WP ID 2300 - Sandbox	**JdK**	Fri 01.02.19	Sun 31.03.24
18	WP ID 2400 - Implementation ATLID Feature Finder	**DH**	Tue 01.09.20	Fri 29.01.21
19	WP ID 2450 - Development ATLID Feature Finder	**GJvZ**	Tue 01.09.20	Sun 31.03.24
20	WP ID 2500 - Implementation Optimal Estimation Retrieval	**DH**	Fri 01.01.21	Sat 31.07.21
21	WP ID 2550 - Development Optimal Estimation Retrieval	**DD**	Tue 01.09.20	Sun 31.03.24
22	**Anomaly & Configuration Management**		**Fri 01.02.19**	**Sun 31.03.24**
23	WP ID 3000 - Anomaly & Configuration Management	**FB**	Fri 01.02.19	Tue 30.11.21
24	WP ID 3000 - Anomaly & Configuration Management	**GG**	Wed 01.12.21	Sun 31.03.24
25	**Validation, Testing, Configuration Parameters & Reprocessing & Tools**		**Fri 01.02.19**	**Sun 31.03.24**
26	WP ID 3100 - E2S/L0/L1A/L1B/L2A	**DH**	Fri 01.02.19	Sun 31.12.23
27	WP ID 3200 - L2B / L2C / AUX_MET + CoP	**JdK**	Fri 01.02.19	Sun 31.12.23
28	WP ID 3300 - Cal-Suite PP and L2A PP	**AD**	Fri 01.02.19	Sat 31.12.22
29	WP ID 3300 - L2A PP	**DT**	Sun 01.01.23	Sun 31.12.23
30	WP ID 3400 - Configuration Parameters for Processors and ACMF	**JdK**	Fri 01.02.19	Sun 31.03.24
31	WP ID 3500 - Support to Re-processing	**JdK**	Fri 07.06.19	Tue 31.12.19
32	WP ID 3600 - Preparation of L2A and L2B datasets with improved quality	**OR**	Fri 01.11.19	Sun 31.03.24
33	WP ID 8000 - Data access, hardware and Tools	**JdK**	Fri 01.02.19	Sun 31.12.23
34	**DISC Cal/Val, QC and Monitoring**		**Fri 01.02.19**	**Sun 31.03.24**
35	WP ID 4000 - Cal/Val Synthesis	**OR**	Wed 08.05.19	Sun 31.12.23
36	WP ID 4050 - Cal/Val support, communication platform and L2B product validation suppc	**SBI**	Thu 01.04.21	Sun 31.03.24
37	WP ID 4100 - Data Quality and algorithm sensitivity studies for L1B and Calibrations	**UM**	Wed 08.05.19	Sun 31.03.24
38	WP ID 4150 - Algorithm Consolidation Studies for L1B and Calibrations	**UM**	Wed 08.05.19	Sun 31.03.24
39	WP ID 4155 - Aeolus+ activity output for algorithm consolidation	**OR**	Sun 01.01.23	Sun 31.03.24
40	WP ID 4200 - Data Quality and algorithm sensitivity studies for L2A and calibrations	**AD**	Fri 01.02.19	Sat 31.12.22
41	WP ID 4200 - Data Quality and algorithm sensitivity studies for L2A and calibrations	**DT**	Sun 01.01.23	Sun 31.03.24
42	WP ID 4300 - Data Quality and algorithm sensitivity studies for L2B and CoP	**MR**	Fri 01.02.19	Sun 31.03.24
43	WP ID 4350 - Data Quality and algorithm sensitivity studies for L2B and CoP	**GJM**	Fri 01.02.19	Sun 31.03.24
44	WP ID 4400 - Implementation of report generator module	**MV**	Mon 01.06.20	Sun 15.08.21
45	**User Support, QWG & Outreach**		**Fri 01.02.19**	**Sun 31.03.24**
46	WP ID 4500 - User Support	**FW**	Fri 01.02.19	Sat 31.12.22
47	WP ID 4600 - QWG Support	**OR**	Tue 07.05.19	Sun 31.12.23
48	WP ID 4700 - Outreach and Communication	**AS**	Fri 01.02.19	Sun 31.03.24
49	WP ID 4750 - Technical Support, Outreach and Communication	**CdV**	Fri 01.02.19	Sun 31.03.24
50	WP ID 4800 - Scientific Support for the Vires VRE development	**IK**	Sat 01.05.21	Wed 30.03.22
51	**NWP Monitoring and Impact Assessment**		**Fri 01.02.19**	**Sun 31.03.24**
52	WP ID 5000 - NWP Monitoring	**MR**	Fri 01.02.19	Sun 31.12.23
53	WP ID 5100 - Aeolus Aerosol Monitoring at ECMWF	**AB/MR**	Sun 01.08.21	Sun 31.12.23
54	WP ID 5500 - NWP Impact Assessment	**MR**	Fri 01.02.19	Sun 31.03.24
55	WP ID 5550 - NWP Impact Assessment with ARPEGE model	**JFM**	Fri 01.02.19	Sat 31.12.22
56	WP ID 5600 - Aeolus Aerosol Assimilation at ECMWF	**AB/MR**	Sun 01.08.21	Sun 31.03.24
57	**ACMF Analysis & Processor Release**		**Fri 01.02.19**	**Sun 31.03.24**
58	WP ID 6000 - ACMF Analysis and Processor Release (on-site)	**Sbu/GG**	Fri 01.02.19	Sun 31.03.24
59	**ACMF - Maintenance & Evolution**		**Fri 01.02.19**	**Sun 31.03.24**
60	WP ID 7000 - Anomaly Investigation & Configuration Maintenance	**MV/AK**	Fri 01.02.19	Sun 31.03.24
61	WP ID 7100 - ACMF corrective maintenance excluding ACMF-C	**MV/AK**	Fri 01.02.19	Sun 31.12.23
62	WP ID 7200 - ACMF perfective maintenance excluding ACMF-C	**MV/AK**	Fri 01.02.19	Sun 31.12.23
63	WP ID 7300 - ACMF testing, validation, and delivery	**MV/AK**	Fri 01.02.19	Sun 31.12.23
64	WP ID 7500 - ACMF-C corrective maintenance	**GP/PB**	Fri 01.02.19	Sat 31.12.22
65	WP ID 7600 - ACMF-C perfective maintenance	**GP/PB**	Fri 01.02.19	Sat 31.12.22
66	WP ID 7700 - ACMF-C testing, validation, and delivery	**GP/PB**	Fri 01.02.19	Sat 31.12.22
67	**Project Management**		**Fri 01.02.19**	**Sun 31.03.24**
68	WP ID 9000 - Project Management DLR (Prime)	**IK**	Fri 01.02.19	Sun 31.03.24
69	WP ID 9100 - Project Management DoRIT	**DH**	Fri 01.02.19	Sun 31.03.24
70	WP ID 9200 - Project Management CNRS	**AD**	Fri 01.02.19	Sat 31.12.22
71	WP ID 9300 - Project Management KNMI	**AS**	Fri 01.02.19	Sun 31.03.24
72	WP ID 9400 - Project Management ECMWF	**MR**	Fri 01.02.19	Sun 31.03.24
73	WP ID 9500 - Project Management S+T	**MV/AK**	Fri 01.02.19	Sun 31.03.24
74	WP ID 9600 - Project Management ABB	**GP/PB**	Fri 01.02.19	Sat 31.12.22
75	WP ID 9700 - Project Management TROPOS	**SBI**	Sun 01.01.23	Sun 31.03.24
76	WP ID 9900 - Lessons Learnt	**MC**	Wed 01.12.21	Sun 31.03.24

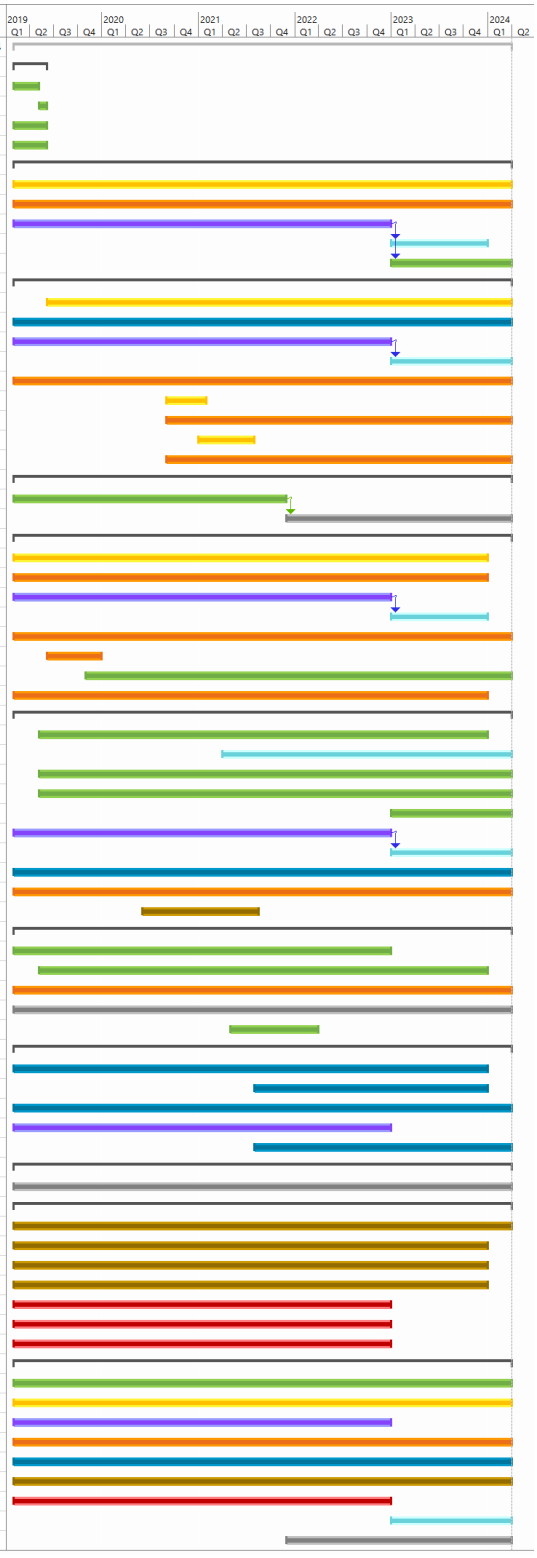

Figure 4: Gantt Chart of the Aeolus DISC work packages.

Some of the DISC tasks and work packages took a considerable larger effort than originally foreseen in the proposal. This was either solved by reprioritization of these tasks in agreement with ESA on the cost of other tasks, which then resulted in less activities or slower progress as planned. Or it was solved by additional resources via a work-order or contract change process, where the additional effort was outlined by the DISC in new proposals. The setup of the DISC and its relation to ESA was flexible enough to accommodate such changes successfully. The workload for management of these additional activities with more than 10 proposals during 5 years was also higher than originally anticipated. The main reasons for the larger effort were mainly related to in-orbit performance of ALADIN, but also to the new setup of such a DISC activity for an Earth Explorer mission. It is important to anticipate such surprises and built on the willingness of flexible, agile project management on DISC and on ESA side. The work packages with significantly more resources than originally foreseen in the proposal were for example:

- Instrument monitoring and analysis of instrument performance and anomalies including support to instrument anomaly boards, root cause analysis and instrument operation during test campaigns and laser switch-on periods
- Analysis of calibration procedures and analysis of wind, but also aerosol product biases and their correction with ground-processing
- Definition and implementation of new retrieval algorithms for the L2A aerosol product, which was originally considered as a spin-off product for Aeolus, but where significant resources were spent in the DISC phase on improvements
- Reprocessing campaigns, which includes a rather complex and iterative flow of different activities with a significant larger effort to correct for instrument anomalies and biases

The work of the Aeolus DISC was organised in four phases, the Ramp-Up Phase (Feb. – Jun. 2019), the Optimization Phase (Jun. 2019 – Sep. 2020), the Exploitation Phase (Sep. 2020 – Apr. 2023), and the Transition Phase (May 2023 – Mar 2024). A timeline with the major highlights of the DISC and the different phases is shown in Figure 5.

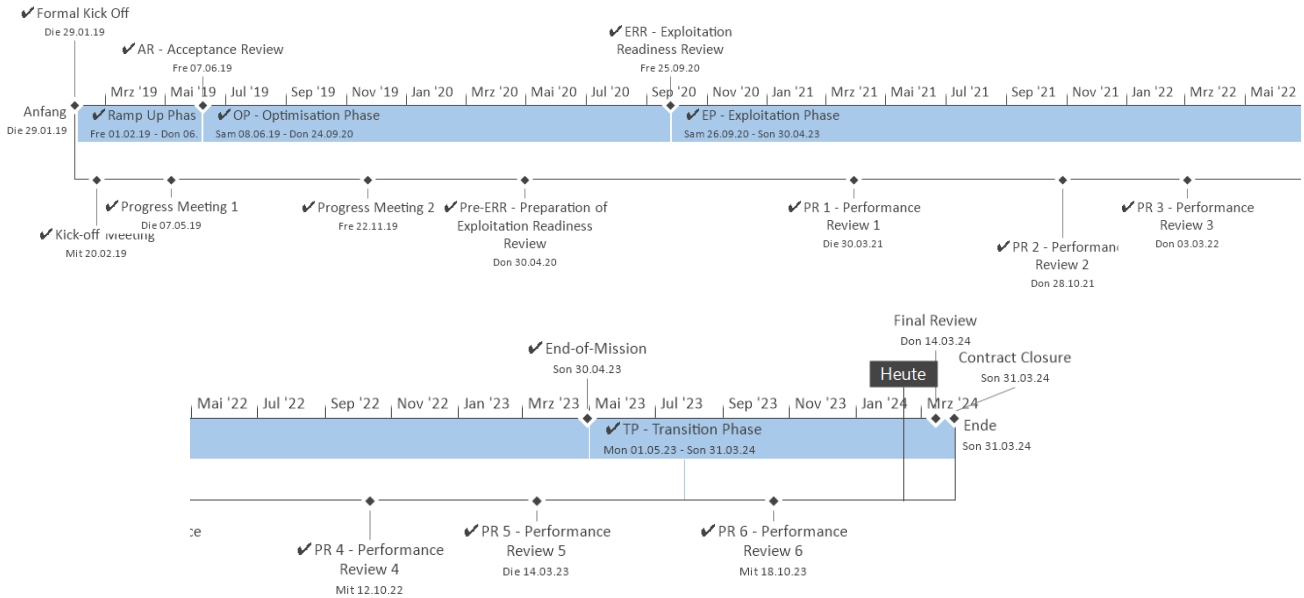

Figure 5: Timeline of the DISC project showing the different project phases.

The Ramp-Up Phase was dedicated to ramping up the project and creating all the necessary structures and tools for the DISC activities. The activities of this phase were summarized in a ramp-up plan and were concluded with the successful Acceptance Review taking place on 06/07 June 2019 in ESRIN.

During the Optimization Phase, the focus was laid on the swift improvement of the Aeolus NRT products. This included improving the ground processors, optimising the ALADIN operations, setting-up automated NWP monitoring routines and developing bias-correction algorithms. Once the Aeolus data quality became sufficiently stable, first NWP impact experiments were conducted and L2C data disseminated. At the Preparation for Exploitation Review (pre-ERR) in April 2020, it could be demonstrated that the product quality reached a quality level sufficient for routine dissemination to NWP users and a positive impact of the data in NWP could be shown. ECMWF started to use the Aeolus data in their operational assimilation in January 2020. In May 2020, the Aeolus data was made available to the public and other NWP centres followed ECMWF with operationally assimilating the Aeolus data (e.g. DWD, Météo-France, UK Met-Office). The Optimization Phase was concluded by the Exploitation Readiness Review (ERR) in September 2020.

The focus in the Exploitation Phase was to assure a long-term consistent data quality, corresponding to the needs of NWP centres assimilating the wind products and scientific users of the Aeolus products. During this phase the optimization of the processors and the monitoring of the data quality continued to be important, but with the reprocessing of older data a new focus appeared. Also, the interaction with and engagement of data users became more important in this phase.

At the start of the Exploitation Phase, ~30 performance indicators were defined to monitor the performance of the DISC. Each performance indicator belonged to one of the following major tasks of the Aeolus DISC:

- Ensure optimal ALADIN instrument performance
- Ensure optimal / continuous NRT data processing
- Constantly improve the Aeolus data quality
- Support Aeolus data usage
- Assure project success and keep ESA informed about DISC activities

The status of each performance indicator was reported on a monthly basis on the Aeolus DISC wiki. At each performance review meeting, the status of the performance indicators was assessed by ESA.

With the end of the operational mission in April 2023, the Transition Phase started. This phase was dedicated to a smooth transition from Phase E2 to Phase F1. It started with dedicated end-of-life test on board the satellite to gain a better understanding of the behaviour of the instrument in space (May and June 2023). With the re-entry of the satellite in July 2023, consolidation and reprocessing activities became the main focus of the DISC Consortium. All the acquired data and results were collected and first lessons-learnt derived.

3 Instrument Performance and Monitoring

Christian Lemmerz and Oliver Lux, DLR

This section reports on the ALADIN instrument monitoring of its behaviour and performance in space from IOCV to the final laser shots. The knowledge and experience gained from developing and operating the sub-orbital avatar of ALADIN on Aeolus, the ALADIN Airborne Demonstrator (A2D), led to establish a comprehensive instrument performance monitoring within DISC. From 2004 onward, the A2D was deployed for numerous measurement campaigns on ground and airborne, as well as during four airborne Aeolus validation campaigns in 2018 – 2021 after launch (Lemmerz et al., 2023a). Based on the resulting lessons learnt, technological and operational expertise, the scientific and housekeeping (HK) data provided by Aeolus was screened, including results from ground tests (IFP and TVac) to prepare the in-orbit performance monitoring prior to launch (Lemmerz et al., 2018) and during in-orbit commissioning and validation (IOCV) phase (Lemmerz et al., 2019). Over the course of the mission, the tools and analysis methods evolved considerably, as documented in more than 150 performance analysis reports generated for the weekly/bi-weekly DISC reporting (Lemmerz and Lux, 2018-2023) as well as additional meetings with ESA and industry on special measurement periods and actions like instrument recoveries, laser and telescope tests or the end-of-life activities (Lemmerz et al., 2023b). As the wind measurement performance of the instrument is driven by both the radiometric budget and the spectral stability of the laser and the two receiver channels, the monitoring focused on the following topics:

- Performance of both lasers (section 3.1)
- Evolution of the internal and atmospheric path signals (section 3.2) in both lidar and imaging acquisition modes, incl. their alignment dependency (section 3.9) and the monitoring of the transmit-receive optics
- Regular characterization of the spectrometers and their spectral responses from ISR (section 3.4), IRC and IRONIC measurements (section 3.5)
- Opto-electronic performance of the detection chain based on solar background evolution (section 3.8) and the monitoring of the ADDC detectors in imaging and memory zone (section 3.3)
- Instrumental bias verification from ground returns (section 3.7)

In addition to HK-data and detector signals, monitoring results from the L2A processing chain (section 5.2), that characterize the lidar efficiency as well as random and systematic errors detected with the NWP monitoring (section 5.3) were used for correlative analysis. A synthesis of different performance topics is summarized in section 3.10. In addition to the efforts of the Cal/Val-community on assessing the wind measurement performance of Aeolus (section 5.5), the airborne validation with the A2D and 2-µm reference lidar was contributing to a detailed performance monitoring of the wind products in different regions on the globe and during four mission phases in strong cooperation with ESA, campaign partner and the DISC (Lemmerz et al., 2023a).

3.1 Laser performance

Oliver Lux and Christian Lemmerz, DLR

The laser performance was monitored based on HK-data providing the IR section energies (master oscillator – MO; pre-amplifier – PreAMP; amplifier – AMP), the residual green and UV energies. The laser temperatures turned out to be important parameters, as both lasers showed a significant energy variation during frequency scans, with the energy maximum being very sensitive to laser temperature. The root cause for the strongly varying energy with frequency lies in the MO gain modulation with frequency and is not fully understood so far. But managing the energy maxima with temperature tuning was key to keep and increase the laser performance as performed from March 2020 on and reported in sections 3.1.1 and 3.1.2. The laser frequency stability and single frequency operation was evaluated based on the cavity control housekeeping data as well as the Mie channel fringe position and shape. A strong dependency on vibration levels was revealed which caused varying patterns of enhanced frequency noise over the orbits, whenever the reaction wheels operated at certain critical speeds (see section 3.1.3).

Both laser energy and frequency stability performance could be significantly improved during the End-of-life (EOL) activities (section 3.6), demonstrating new records for a single frequency UV laser in space. To compensate for the loss in atmospheric return signal during the first operational time of FM-B from July 2020 to October 2022, several laser parameter tunings of pump currents, pump and Q-switch phasings with compensating laser temperatures were performed up to a level of 100 mJ. Similar activities led to a stable, high UV output for the second FM-A phase (Dec. 2022 – May 2023). To manage the risk of these complex procedures, laser sensitivity tests were performed in space, and with FM-C on ground. Decisions were based on monitoring results of the laser HK-parameters as well as internal and atmospheric path HK and ACCD-signals contributed by the DISC team. The ACCD results in imaging and lidar modes were especially important to characterize effects on the laser beam profile, divergence and pointing, because these parameters could not be derived from HK-data. An overview of the most relevant laser parameters is provided in Table 1.

Table 1: Selected parameters of the ALADIN lasers. See also Cosentino (2012) and Mondin et al. (2017a,b).

Parameter	Value
Type	Frequency-tripled Nd:YAG
Laser wavelength	354.8 nm
Pulse repetition rate	50.5 Hz
Pulse energy	FM-A: 40 to 70 mJ; FM-B: 60 to 100 mJ (182 mJ over 1 day)
Pulse energy correction factors for PD74	FM-A: 0.7663; FM-B: 0.9409
Pulse width (FWHM)	20 ns
Spectral width (FWHM)	< 50 MHz
Frequency stability (rms over 540 pulses)	< 12 MHz (< 7 MHz at optimized cavity control setting)
Beam diameter	< 6.2 mm
Beam divergence (full angle)	< 600 µrad
Operation time in space	FM-A: 15 months; FM-B: 41 months

Total number of pulses	FM-A: 1.9 Gigashots; FM-B: 5.3 Gigashots

3.1.1 Energy evolution and influence of cold-plate temperature

Soon after the beginning of operation, a decreasing trend in the first flight model laser (FM-A) output energies, particularly the UV emit energy, was observed from internal photodiodes (PDs) placed at different stages of the laser. The temporal evolution of the UV energy (PD74) over the full mission lifetime is depicted in Figure 6. Note that the different scaling factors for the PD74 readings in both lasers that were determined on-ground were not considered due to their high uncertainty. Aside from the fact that the initial UV energy of 65 mJ was lower than the expected level of 80 mJ which was reached on-ground, this parameter dropped by an average of –0.4 mJ per day during the first 14 days after power-on. Consequently, several adjustments to the laser parameters were carried out to alleviate the energy loss. In mid-September 2018, thermal adjustments were made to the two amplifiers, leading to a better temperature distribution of the laser optical bench. As a result, the UV energy increased by 3 mJ, while its decrease rate was considerably reduced to –0.14 mJ/day, or -1 mJ/week, which was comparable to that observed on-ground for the FM-A laser.

Several temporary adjustments of the amplifier currents (laser tests) were made to check the impact on the laser energy and fluence, and a permanent adjustment was made on 15 December 2018, elevating the UV energy by 12% to 57 mJ from which it dropped by the same rate of –1 mJ/week until the end of the four-month commission phase (Lux et al., 2020).

A similar decrease rate was observed after the re-switch-on of FM-A following a Failure Detection Isolation and Recovery (FDIR) event that was caused by a GPS reboot error in January 2019. It is interesting to note that the energy degradation trend continued during the one-month period when the laser was off (the amplifiers were operating during the majority of this non-lasing period), suggesting that the degradation was not due to the presence of the laser beam, i.e., not due to LID or LIC.

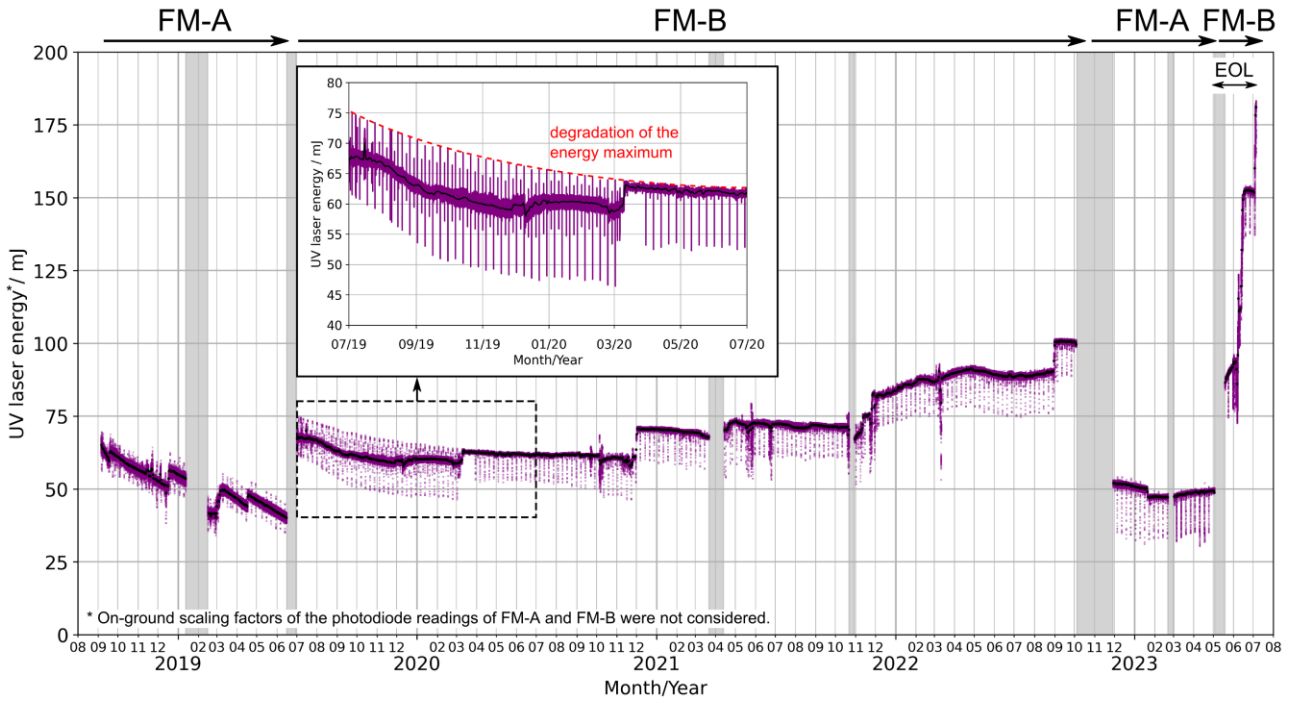

Figure 6: Timeline of the UV output energy of the two ALADIN laser transmitters FM-A and FM-B over the mission period. On-ground scaling factors of the PD74 readings of FM-A and FM-B were not considered. Periods when the laser was temporarily switched off are indicated by grey-shaded areas. The purple dots show the reading of the laser-internal photodiode with a temporal resolution of about 1 minute, while the black dots represent the daily

means. The pulse energy was increased up to 182 mJ during the last days of operations in July 2023 in the frame of the end-of-life (EOL) activities. The frequency-dependence of the laser energy results in an energy modulation during the weekly calibrations as seen in the periodic oscillations (see text).

The FM-A laser continued to be operated up until June 2019 when the energy had reached 40 mJ, and it was decided to switch to the second flight laser (FM-B) which, from on-ground tests, was known to be the better performing laser. The switch between the two lasers was realized by a so-called flip-flop mechanism (FFM) which enabled two stable configurations to direct either FM-A or FM-B onto the optical path of the ALADIN instrument. The FFM consisted of several optics (mirrors and an optical invariant cube) that were mounted on quasi-isostatic mounts and could be mechanically translated by a binary paraffin actuator that could be latched either to an extended or a retracted position corresponding to the two configurations to operate either FM-A or FM-B (Székely and Henzelin, 2005).

In accordance with the on-ground tests, the FM-B reached a higher initial energy than FM-A (67 mJ) and a much slower decrease rate in the first months of operations. However, like for the FM-A laser, the output energy of the FM-B laser was found to vary by more than 10% during frequency scans, whereby this frequency-dependence of the laser energy was sensitive to temperature changes of the cold-plate of the laser bench that carried all active components of the laser (master oscillator, amplifiers). The components were conductively cooled through the cold-plate with the heat being transferred to a radiator on the side of the satellite via heat pipes.

The investigation of the temperature sensitivity opened up a path to improve and stabilize the laser performance, albeit the root cause for the strong frequency dependence remained an open issue. Hence, in March 2020, the cold-plate temperature was adjusted such that the laser was operating at the energy maximum during wind velocity mode, i.e., at the nominal laser frequency. As a result, the energy degradation rate followed the trend that was expected from the slow ageing process of the pump laser diodes with a loss in UV energy of about -25% over three years of operation. This optimization of the laser's operating point in March 2020 is illustrated in the inset of Figure 6 where the dashed red line indicates the gradual decrease of the energy maximum during the first year of FM-B operations, while the purple curve represents the measured UV energy which was modulated by frequency scans during Instrument Spectral Registration (ISR) modes on a weekly basis.

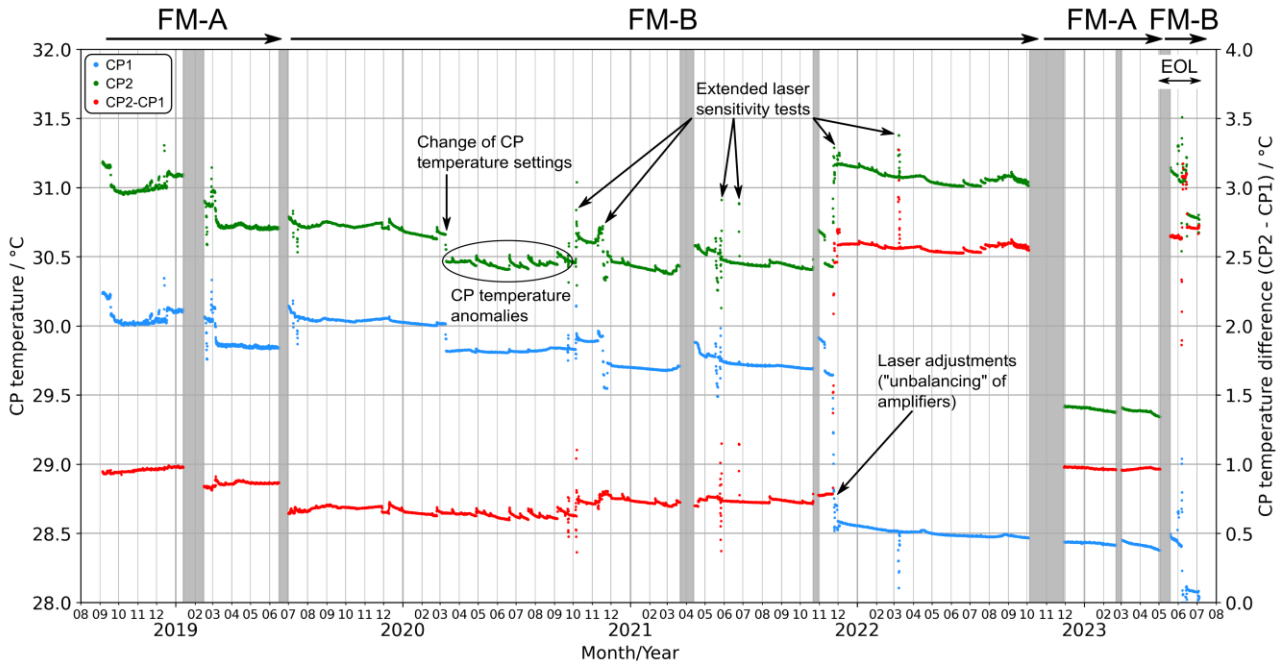

Figure 7: Timeline of the cold-plate temperatures CP1 (blue) and CP2 (green) of the two ALADIN laser transmitters FM-A and FMB over the mission period. The temperature difference CP2 minus CP1 is plotted in red. Periods when the laser was temporarily switched off are indicated by grey-shaded areas.

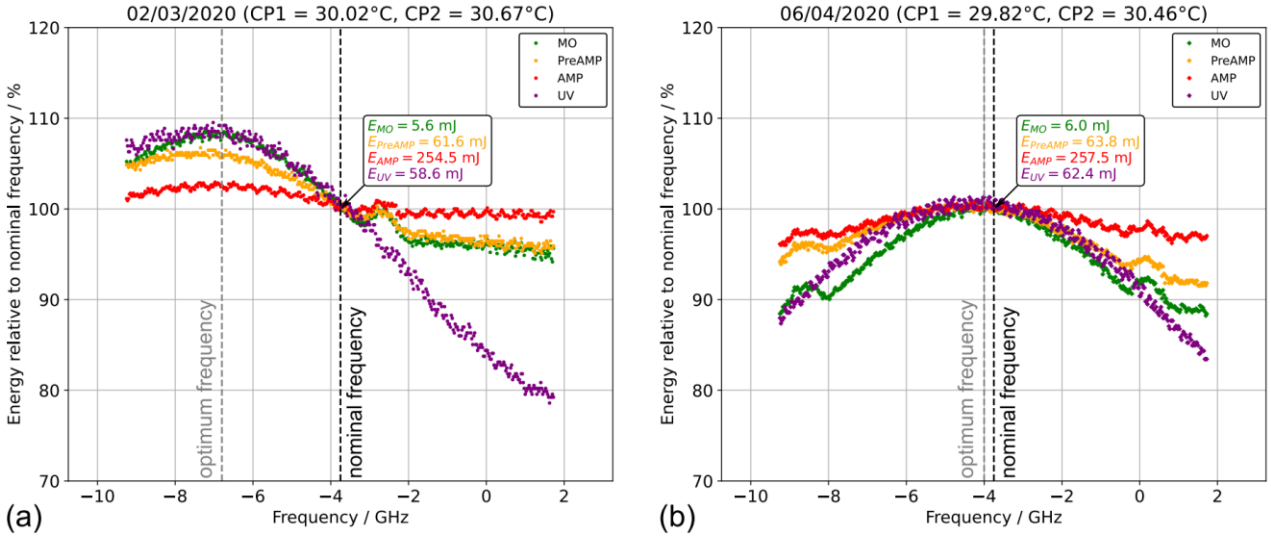

Figure 8: Frequency-dependence of the FM-B laser energies measured at the output of the master oscillator (MO, green), the preamplifier (PreAMP, orange), the power amplifier (AMP, red) and the UV conversion stage (UV, purple) derived from the Instrument Spectral Registration (ISR) on (a) 02/03/2020 and (b) 06/04/2020 at different CP temperatures. The nominal frequency at -3.75 GHz is indicated by a vertical dashed line while the optimum frequency where the energies are highest is marked by a grey vertical line.

The setpoint change is also marked in Figure 7 which shows the timeline of the temperatures that were measured on two sensors attached to the laser cold-plate CP1 and CP2. As depicted in Figure 8, the CP temperature reduction by about 0.2 K involved a spectral shift of the frequency-dependent energy curve by about -2.8 GHz such that the spectral location of the energy maximum nearly coincided with the nominal frequency at -3.75 GHz. This was also true for the laser energies that were measured at the preceding stages of the laser system (MO, PreAMP, AMP) which underlines that the laser was operated at a more stable working point after the CP temperature adjustment in March 2020. The root cause for the frequency-dependence of the laser energies has still to be found, but a parasitic etalon effect inside the MO is one of the most likely candidates to explain the high temperature sensitivity of about -14 GHz/K in the UV or -4.7 GHz/K in the IR correspondingly.

3.1.2 Laser activities

Thanks to the optimization of the cold-plate temperature in March 2020, stable laser operation of the FM-B was achieved over 40 months until the switch-back to the FM-A laser in October/November 2023, only interrupted by two additional FDIR events in March and October 2021. Both FDIRs were triggered by a failed consistency check by the on-board software on the operational mode of the instrument. It is worth noting that the time for the recovery of the instrument including the ramp-up of FM-B took not more than ten days in March and even less than six days in October in comparison to the re-switch-on of the FM-A laser in January which took about one month. The FDIR in March involved a change in the emitted frequency of the reference laser head which necessitated an adaptation of the nominal frequency and Rayleigh cover temperature to optimize the spectral working point of the instrument (see also Table 5 in section 3.2.4).

Over the course of FM-B operations, a strong signal decrease was suffered on the emit path behind the laser at a nearly constant rate of -1%/week (see section 3.2.1). Consequently, in order to compensate

for the signal loss, the laser energy was increased several times up to more than 100 mJ, mostly by increasing the (pre-)amplifier pump currents and/or by reducing the delay between the MO pulse emission and the amplifier pumping phase in combination with a shortening of the MO Q-switch duration.

Moreover, the alignment of the FM-B laser beam along the instrument path, which was worse compared to that of the FM-A laser, was optimized by multiple laser adjustments where the heating currents of the PreAMP and AMP were oppositely changed ("unbalancing") which, to some extent, allowed to steer the laser beam along the horizontal axis. However, this procedure had an impact on the cold-plate temperatures, especially due to the fact that the MO arrangement was located in the middle between the two amplifier blocks on the laser bench. Therefore, a subsequent tuning of the CP temperatures was necessary to keep the maximum of the laser energy at the spectral position of the nominal frequency, as shown in Figure 3 (b). This was achieved, most notably, in end of November 2021 when CP1 was reduced by 1.0 K while CP2 was increased by 0.8 K, thereby altering the temperature gradient (CP2 – CP1) from 0.8 K to 2.6 K.

As shown in Figure 7, this temperature change was very large compared to occasional CP temperature anomalies of typically less than 0.1 K, which, nevertheless, affected the laser energies by a few percent, depending on the spectral distance to the gain maximum. The anomalies were mostly triggered by orbit correction manoeuvres, but became much less frequent after an adjustment of the top floor heaters located outside the laser assembly in May 2021 which significantly reduced seasonal temperature variations, particularly during the eclipse season, as well as during platform manoeuvres.

Despite the excellent performance of the FM-B laser, the drastic signal loss on the emit path of more than 70% by mid-2022 (Lux et al., 2022) led to the decision to switch back to the FM-A laser. As elaborated in section 3.2.1, the loss occurred solely on the optics along the FM-B path, resulting in a full recovery of the emit path transmission upon the switch-over to the FM-A laser. Based on the knowledge gained during the FM-B period, particularly with regard to the interplay of CP temperatures, frequency and laser energy, the FM-A was optimized according to the procedures developed in the preceding years. This approach resulted in a stable performance of the FM-A laser at its gain maximum of around 50 mJ over five months until the end of the operational mission on 30 April 2023. During the second FM-A period, another FDIR was triggered on 21 February 2023 when a spurious energy spike was detected on the MO photodiode, thereby exceeding a set energy threshold and ultimately causing the instrument to go into Survival mode. The recovery took again a bit less than one week.

Following the end of nominal operations of ALADIN, a series of special tests, referred to as end-of-life activities (EOLAs), was performed to address a number of instrument-related and scientific questions (see section 3.6). After a final switchover to the more powerful FM-B laser in mid-May 2023, its output energy was successively increased by boosting the MO and amplifier pump currents, by reducing the amplifier phasings and Q-switch duration as well as by optimizing the heating currents while adapting the CP temperatures as described above. During its final 33 hours of operations on 4 and 5 July 2023, the ALADIN FM-B laser transmitter delivered more than 182 mJ of output energy without any sign of degradation inside the laser which set a new record for a UV laser operated in space.

Table 2 lists all interruptions of the laser operations both commanded and related to FDIRs. An overview of the most relevant laser activities and switch-on procedures performed during the Aeolus mission including the EOLA phase is provided in Table 3. The laser activities can be classified into extended sensitivity tests (13, indicated by red vertical bars in Figure 9), cold-plate temperature tests (7, yellow) and laser optimizations with permanent changes (12, green). Figure 9 shows that the frequency of laser tests varied a lot during the mission. While there were many tests in the first half year aiming at the

optimization and stabilization of FM-A, there were only few tests in the early FM-B phase. As the signal loss in the emit path progressed (see section 3.2.1), several tests were carried out to improve the laser beam alignment along the instrument path. In addition, the laser energy was increased multiple times in order to counteract the degrading transmission through the optics behind the laser output.

Table 2: Interruptions of the laser operation (commanded and related to FDIRs) during the mission.

Date and time of laser switch-off	*Commanded or FDIR*	*Reason for interruption*	*Date and time of continuation at nominal laser settings*
14/01/2019, 01:41 UTC	FDIR (system level)	GPS error	15/02/2019, 20:10 UTC
16/06/2019, 19:00 UTC	Commanded	Switchover to FM-B	28/06/2019, 15:22 UTC
22/03/2021, 02:57 UTC	FDIR (instrument level)	Failed consistency check by the on-board software (wrong mode error during ISR)	01/04/2021, 10:41 UTC
22/10/2021, 14:18 UTC	FDIR (instrument level)	Failed consistency check by the on-board software (wrong mode error during LBM)	28/10/2021, 10:36 UTC
04/10/2022, 14:34 UTC	Commanded	Switchover to FM-A	28/11/2022, 22:33 UTC
21/02/2023, 03:27 UTC	FDIR (laser level)	Energy spike in master oscillator	28/02/2023, 08:55 UTC
03/05/2023, 13:20 UTC	FDIR (laser level)	Failure of amplifier pump module; switchover to FM-B	17/05/2023, 16:00 UTC
05/07/2023, 14:30 UTC	Commanded	Final switch-down before re-entry	-

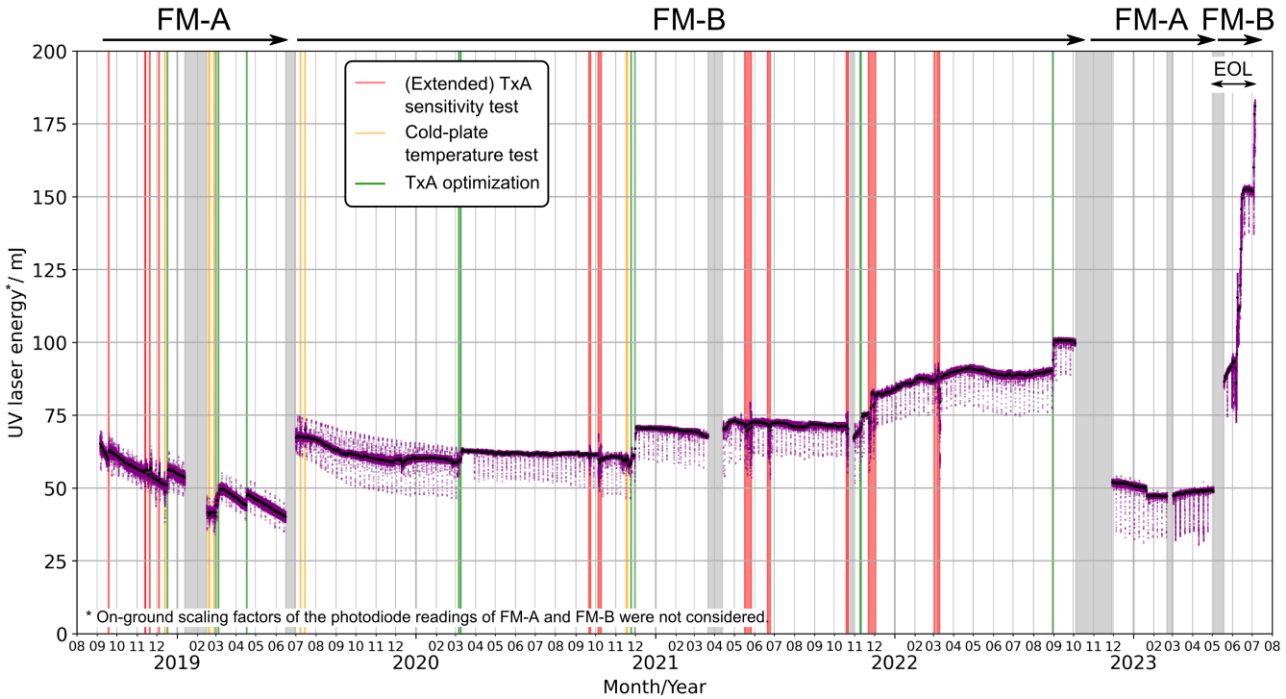

Figure 9: Same as Figure 6, but with additional vertical bars indicating periods of laser activities: red – (extended) sensitivity test, yellow – cold-plate temperature test, green – laser optimizations with permanent settings changes. Laser tests that were carried out in the frame of the EOL phase are not illustrated.

Table 3: List of laser activities during the Aeolus mission and the resulting UV output energy (MO: master oscillator; PreAMP: pre-amplifier; AMP: amplifier, SHG/THG: second/third harmonic generation).

Date	*UTC Time*	*Activity*	*Applied changes to instrument*	*UV energy after activity*	*Comments*
03/09/2018	10:38	Start of operations with FM-A		50.8 mJ	Initial pump and heating currents: PreAMP pump: 63.25 A, AMP pump: 58.80 A, PreAMP heating current: 3.0 A, AMP heating current: 1.9 A
04/09/2018	08:24	Finalization of FM-A laser settings	Increase of PreAMP pump current from 63.25 A to 65.75 A; increase of AMP pump current from 58.80 A to 60.80 A	Increase of UV energy from 50.8 mJ to 64.5 mJ	
18/09/2018	20:56	TxA optimization	Decrease in PreAMP heating currents from 3.0 A to 2.4 A; decrease in AMP heating currents from 1.9 A to 1.2 A	Increase of UV energy from 59.8 mJ to 63.6 mJ	Energy decrease rate was reduced
13/11/2018	08:30	TxA optimization (temporary)	Increase of PreAMP pump current from 65.75 A to 66.00 A; increase of AMP pump current from 60.80 A to 61.05 A	Increase of UV energy from 55.4 mJ to 57.0 mJ	Settings were restored on 16/11/2018 at 20:00 UTC.
20/11/2018	09:00	TxA optimization (temporary)	Increase of PreAMP pump current from 65.75 A to 66.25 A; increase of AMP pump current from 60.80 A to 61.30 A	Increase of UV energy from 54.5 mJ to 57.2 mJ	Settings were restored on 23/11/2018 at 10:40 UTC.
04/12/2018	08:38	TxA sensitivity test	Increase of PreAMP pump current from 65.75 A to 66.50 A; increase of AMP pump current from 60.80 A to 61.55 A	Increase of UV energy from 52.4 mJ to 56.4 mJ	
05/12/2018	06:42	TxA sensitivity test	Increase of PreAMP pump current from 65.75 A to 66.75 A; increase of AMP pump current from 60.80 A to 61.80 A	Increase of UV energy from 56.4 mJ to 58.7 mJ	Settings from before 04/12/2018 were restored on 05/12/2018 at 08:50 UTC.
13/12/2018	02:53	CP temperature sensitivity test	Increase of CP temperature (TC-15) by 0.3°C	Decrease of UV energy from 51.5 mJ to 46.4 mJ	Settings were restored on 13/12/2018 at 15:20 UTC
17/12/2018	10:30	TxA optimization	Increase of PreAMP pump current from 65.75 A to 66.50 A; increase of AMP pump current from 60.80 A to 61.55 A	Increase of UV energy from 51.1 mJ to 55.0 mJ	
18/12/2018	07:05	TxA optimization	Increase of PreAMP pump current from 66.50 A to 66.75 A; increase of AMP pump current from 61.55 A to 61.80 A	Increase of UV energy from 55.0 mJ to 56.8 mJ	
14/01/2019	01:41	Stop of operations (GPS error)			

15/02/2019	20:10	Continuation of operations with FM-A		42.1 mJ	Initial pump and heating currents: PreAMP pump: 65.75 A, AMP pump: 60.80 A, PreAMP heating current: 2.4 A, AMP heating current: 1.2 A
18/02/2019 to 20/02/2019		CP temperature sensitivity test	Decrease of CP temperature (TC-15) by 0.3°C in steps of 0.1°C	Decrease of UV energy from 41.7 mJ to 40.5 mJ	Settings were restored on 20/02/2019 at 09:14 UTC.
26/02/2019 to 27/02/2019		CP temperature sensitivity test	Increase of CP temperature (TC-15) by 0.3°C in steps of 0.1°C	Decrease of UV energy from 41.5 mJ to 37.6 mJ	Settings were restored on 27/02/2019 at 16:36 UTC.
01/03/2019	09:40	TxA optimization	Increase of PreAMP pump current from 65.75 A to 66.75 A; increase of AMP pump current from 60.80 A to 61.80 A	Increase of UV energy from 41.4 mJ to 46.0 mJ	
05/03/2019	05:33	TxA optimization	Decrease in PreAMP heating currents from 2.4 A to 1.9 A; decrease in AMP heating currents from 1.2 A to 0.2 A	Increase of UV energy from 46.0 mJ to 48.9 mJ	
06/03/2019	04:50	TxA optimization	Decrease in PreAMP heating currents from 1.9 A to 1.2 A	Increase of UV energy from 48.9 mJ to 49.8 mJ	
17/04/2019	05:55	TxA optimization	Reduction of Q-switch duration from 235 µs to 230 µs	Increase of UV energy from 44.1 mJ to 48.3 mJ	
16/06/2019	19:00	Stop of operations for switchover to FM-B			
28/06/2019	15:22	Start of operations with FM-B		66.2 mJ	Initial pump and heating currents: PreAMP pump: 65.85 A, AMP pump: 63.75 A, PreAMP heating current: 4.4 A, AMP heating current: 1.9 A
08/07/2019	4:00	CP temperature sensitivity test	CP temperature +0.1°C	Decrease of UV energy from 67.6 mJ to 65.5 mJ	Settings were restored at 10:45 UTC.
08/07/2019	17:00	CP temperature sensitivity test	CP temperature -0.1°C	Increase of UV energy from 67.6 mJ to 70.4 mJ	Settings were restored at 23:45 UTC.
15/07/2019	11:00	CP temperature sensitivity test	CP temperature -0.2°C	Increase of UV energy from 67.5 mJ to 70.9 mJ	Settings were restored on 16/07/2019 at 01:00 UTC.
06/03/2020	07:30	TxA optimization	Decrease of THG temperature from 33.6°C to 33.5°C	Increase of UV energy from 59.0 mJ to 59.8 mJ	
09/03/2020	21:00	TxA optimization	CP temperature -0.1°C	Increase of UV energy from 59.8 mJ to 62.3 mJ	
10/03/2020	20:00	TxA optimization	CP temperature -0.2°C	Increase of UV energy from 62.3 mJ to 63.2 mJ	Influence of ICS pressure cycle was largely reduced by this adjustment.
21/09/2020 to 24/09/2020		Extended TxA sensitivity test	Variation of SHG and THG temperatures; PreAMP and AMP heating and pump currents; Q-switch duration	Variation of UV energy between 59.3 mJ and 64.0 mJ	Settings were restored on 24/09/2020 at 05:00 UTC.
05/10/2020 to 10/10/2020		Extended TxA sensitivity test	Variation of PreAMP and AMP heating and pump currents; Q-switch duration	Variation of UV energy between 55.5 mJ and 68.1 mJ	Settings were restored on 10/10/2020 at 01:00 UTC.
17/11/2020 to 19/11/2020		CP temperature sensitivity test	Variation of CP temperature (TC-15) between 24.65°C and 24.25°C	Variation of UV energy between 57.9 mJ and 61.3 mJ	
24/11/2020	19:00	TxA optimization	Increase of CP temperature (TC-15) to 24.45°C	Increase of UV energy from 59.2 mJ to 60.9 mJ	
30/11/2020	16:00	TxA optimization	Decrease of amplifier phasing from 75 µs to 65 µs	Increase of UV energy from 61.1 mJ to 67.7 mJ	
01/12/2020	16:00	TxA optimization	Decrease of amplifier phasing from 65 µs to 60 µs	Increase of UV energy from 67.7 mJ to 70.6 mJ	
22/03/2021	02:57	Stop of operations (wrong mode error)			
01/04/2021	10:41	Continuation of operations with FM-B		72.8 mJ	Initial pump and heating currents: PreAMP pump: 65.85 A, AMP pump: 63.75 A, PreAMP heating current: 4.4 A, AMP heating current: 1.9 A
17/05/2021 to 27/05/2021		Extended TxA sensitivity test	Variation of CP temperatures, PreAMP and AMP heating and pump currents	Variation of UV energy between 65.2 mJ and 78.5 mJ	Settings were restored on 27/05/2021 at 20:00 UTC.
21/06/2021 to 25/06/2021		Extended TxA sensitivity test	Variation of SHG and THG temperatures; AMP heating and heating current	Decrease of UV energy from 72.6 mJ to 65.5 mJ	Settings were restored on 25/06/2021 at 08:25 UTC.
19/10/2021 to 22/10/2021		MO sensitivity test	Variation of Q-switch duration, amplifier phasings; MO heating and pump currents	Variation of UV energy between 66.0 mJ and 75.5 mJ	Settings were restored on 22/10/2021 at 02:24 UTC.
22/10/2021	14:18	Stop of operations (wrong mode error)			
28/10/2021	10:36	Continuation of operations with FM-B		66.8 mJ	Initial pump and heating currents: PreAMP pump: 65.85 A, AMP pump: 63.75 A, PreAMP heating current: 4.4 A, AMP heating current: 1.9 A

09/11/2021	16:00	TxA optimization	Decrease of CP temperature (TC-15) from 24.45°C to 24.25°C	Increase of UV energy from 69.8 mJ to 70.9 mJ	
11/11/2021	15:30	TxA optimization	Increase of MO pump current from 60.3 A to 62.3 A	Increase of UV energy from 70.9 mJ to 75.0 mJ	
22/11/2021 to 03/12/2021		Extended TxA sensitivity test and TxA optimization	Variation of PreAMP and AMP heating and pump currents; CP temperatures; SHG and THC temperatures; amplifier phasings; final changes used for optimization: decrease of PreAMP heating current from 4.4 A to 1.9 A; increase of AMP heating current from 1.9 A to 4.4 A; decrease of amplifier phasings from 60 µs to 50 µs; increase of THG temperature from 33.5°C to 33.6°C	Increase of UV energy from 75.8 mJ to 82.1 mJ	CP temperatures were adjusted (CP1: -1 K, CP2: +0.8 K) in order to keep the nominal frequency at the E(f) maximum; optimization was completed on 03/12/2021 at 14:15 UTC.
03/03/2022	17:00	Standard TxA sensitivity test		Variation of UV energy between 78.0 mJ and 92.6 mJ	
07/03/2022 to 11/03/2022		Extended TxA sensitivity test	Variation of amplifier currents; PreAMP and AMP heating and pump currents; CP temperatures; THC temperature	Variation of UV energy between 59.4 mJ and 92.3 mJ	Settings were restored on 11/03/2022 at 14:52 UTC.
30/08/2022	10:30	TxA optimization	Increase of MO pump current from 62.3 A to 64.3 A	Increase of UV energy from 90.2 mJ to 96.0 mJ	
31/08/2022	08:00	TxA optimization	Increase of MO pump current from 64.3 A to 66.3 A	Increase of UV energy from 96.0 mJ to 100.7 mJ	
04/10/2022	14:34	Stop of operations for switchover to FM-A			
28/11/2022	22:33	Start of operations with FM-A		52.2 mJ	Initial pump and heating currents: PreAMP pump: 67.75 A, AMP pump: 59.75 A, PreAMP heating current: 0.25 A, AMP heating current: 0.25 A
21/02/2023	03:27	Stop of operations due to MO energy spike			
28/02/2023	08:55	Continuation of operations with FM-A		47.4 mJ	Initial pump and heating currents: PreAMP pump: 67.75 A, AMP pump: 59.75 A, PreAMP heating current: 0.25 A, AMP heating current: 0.25 A
30/04/2023	23:59	Stop of nominal operations			
01/05/2023	00:00	Start of end-of-life activities with FM-A		49.5 mJ	Initial pump and heating currents: PreAMP pump: 67.75 A, AMP pump: 59.75 A, PreAMP heating current: 0.25 A, AMP heating current: 0.25 A
03/05/2023	13:20	Stop of operations (AMP pump module failure)			
17/05/2023	16:00	Continuation of end-of-life activities with FM-B		84.5 mJ	Initial pump and heating currents: PreAMP pump: 65.85 A, AMP pump: 63.75 A, PreAMP heating current: 4.4 A, AMP heating current: 1.9 A
06/06/2023 to 09/06/2023		Extended TxA sensitivity test and TxA optimization as part of the end-of-life activities	Variation of PreAMP and AMP heating and pump currents; CP temperatures; final changes used for optimization: decrease of PreAMP heating current from 1.9 A to 0.2 A, decrease of CP temperatures from 23.35°C to 22.65°C, decrease of amplifier phasings from 50 µs to 30 µs	Increase of UV energy from 93.2 mJ to 110.5 mJ	CP temperatures decreased by 0.7°C in order to keep the nominal frequency at the E(f) maximum; optimization was completed on 09/06/2023 at 02:00 UTC.
12/06/2023 to 15/06/2023		Extended TxA sensitivity test and TxA optimization as part of the end-of-life activities	Variation of HHC temperatures, CP temperatures; final changes used for optimization: decrease of AMP heating current from 4.4 A to 3.4 A, increase of PreAMP pump current from 65.85 A to 67.85 A, increase of AMP pump current from 63.75 A to 65.75 A, decrease of amplifier phasings from 30 µs to 18 µs, reduction of Q-switch duration from 230 to 215 µs	Increase of UV energy from 111.2 mJ to 150.8 mJ	Optimization was completed on 15/06/2023 at 08:00 UTC.
03/07/2023 to 05/07/2023		TxA optimization as part of the end-of-life activities	Increase of the MO, PreAMP and AMP pump currents by 2 A to 69 A, 69.85 A and 67.75 A, decrease of CP temperatures from 22.65°C to 22.45°C	Increase of UV energy from 151.5 mJ to 180.2 mJ	The UV energy increased up to 182.7 mJ for 33 hours until the laser was switched off.
05/07/2023	14:30	Final shutdown of FM-B			

3.1.3 Frequency stability

The frequency stability of the ALADIN lasers was assessed based on internal path Mie channel data during wind velocity mode (WVM) from the L1A product, which is available on single pulse level. As the laser frequency is represented by the centroid position of the interference fringe that is imaged onto the Mie detector, the temporal variations of the Mie response can be interpreted as laser frequency fluctuations. Previous studies have shown that the influence of alignment variations on the Mie response are negligible (Lux et al., 2021). However, it was found that the amplitude of the response variations depends on the location of the Mie fringe pixel position on the detector due to the nonlinearity of the Mie response with respect to frequency. This is important when comparing the results for various phases of FM-A and FM-B lasers, as the instrument was operated at different fringe positions during the mission. Conversion of the Mie response into relative laser frequency is based on response calibration data from which a sensitivity of ≈100 MHz per detector pixel was determined. The accuracy of the relative laser frequency determination is estimated to be 1 MHz and is mainly limited by the shot-noise-limited SNR of the Mie signal and the FWHM of the interference fringe (≈ 1.3 pixel).

The assessment of the frequency stability revealed pulse-to-pulse fluctuations of less than 12 MHz root-mean-square (rms) during the entire mission lifetime and even less than 9 MHz when considering the nonlinearity of the Mie response. The excellent frequency stability was achieved despite the regular occurrence of short periods with significantly enhanced frequency noise (>30 MHz) which were found to coincide with specific rotation speeds of the satellite's reaction wheels (Figure 12). This result suggested that the root cause were micro-vibrations that deteriorated the laser stability on timescales of a few tens of seconds. The existence of "critical" reaction wheel speeds entailed a clustering of observations with enhanced frequency variations in specific regions of the Earth, forming linear and circular structures around the globe. The identified detrimental frequencies of the reaction wheels ranged between 14 and 28 rotations per second and were consistent among the three active wheels, although the relative impact on the two lasers was different. Refer to Lux et al. (2021) for more details.

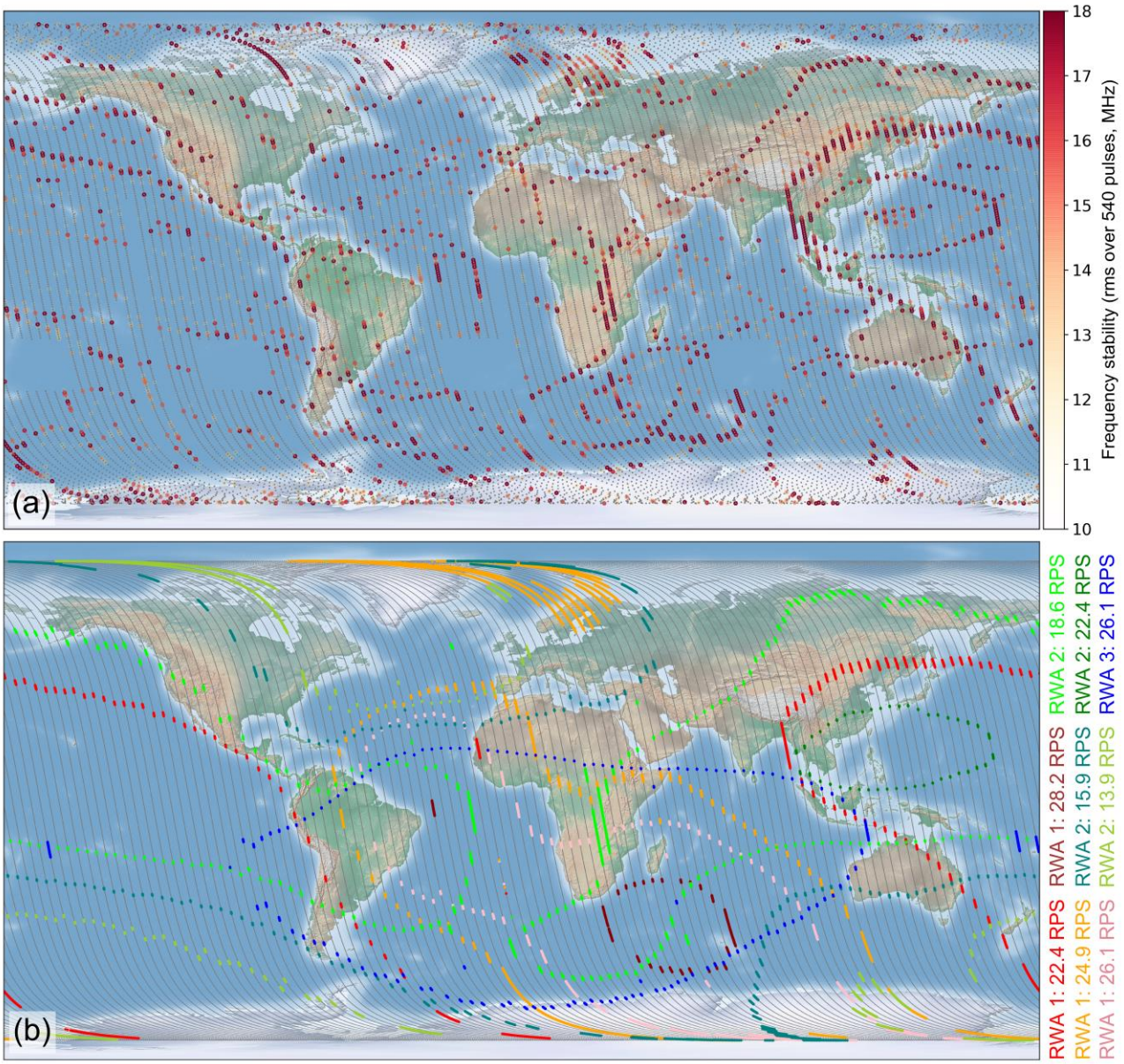

Figure 10: (a) Geolocation of wind observations with enhanced frequency noise for ascending orbits from the week between 14 and 21 October 2019. Each dot corresponds to one observation (12 s), whereby the colour coding describes the frequency stability. (b) Geolocation of the most critical frequencies of the three active reaction wheels (as listed on the bottom right) for the same orbits. Each dot corresponds to one observation in which one of the reaction wheels operates at one of the critical wheel speeds. Figure modified from Lux et al. (2021).

Analysis of the Aeolus wind error with respect to ECMWF model winds showed that the temporally degraded frequency stability of the ALADIN laser transmitter had only a minor influence on the wind data quality on a global scale, which was primarily due to the small percentage of wind measurements for which the frequency fluctuations were considerably enhanced. Hence, although the Mie wind bias was increased by 0.3 m/s at times when the frequency stability was worse than 20 MHz, the small contribution of 4% from all Mie wind results rendered this effect insignificant (<0.1 m/s) when all winds are considered during the operational phase. The impact on the Rayleigh wind bias was negligible even at high frequency noise. Similar results were demonstrated for the apparent speed of the ground returns that were measured with the Mie and Rayleigh channel of the ALADIN receiver. Here, the application of a frequency stability threshold that filters out wind observations with variations larger than 20 MHz improves the accuracy of the Mie and Rayleigh ground velocities by only 0.1 m/s at the expense of useful ground data. The influence will be re-evaluated with newer baselines in Phase-F.

One of the end-of-life activities (EOLA#05, see section 3.4) aimed at the improvement of the laser frequency stability by changing the laser cavity control parameter which defines the locking of the seed laser with the MO cavity resonance. The test was performed for both lasers on 19 April and 29 May 2023, respectively, and could improve the frequency stability in both cases by a factor of two, reaching a values of 4 to 6 MHz rms (see Table 4). Moreover, the portion of observations with large frequency fluctuations ($\sigma > 15$ MHz) was considerably reduced from 9% (FM-A) and 20% (FM-B) to only 1%, indicating that the lasers were less susceptible to micro-vibrations that were caused by the two reaction wheels at their critical rotational speeds. The outcome of this EOL activity was a big success and demonstrated the capability of both lasers to generate highly-stable laser emission even after almost five years in orbit.

Table 4: Laser frequency stability of the two lasers and percentage of wind observations with degraded stability before and after the CLCL ramp set point changes on 19/04/2023 (FM-A) and 29/05/2023 (FM-B), respectively.

Laser	FM-A		FM-B	
Parameter	**CLCL ramp set point 5/8**	**CLCL ramp set point 7/8**	**CLCL ramp set point 5/8**	**CLCL ramp set point 7/8**
Frequency stability (shot-to-shot rms)	(8.2 ± 3.2) MHz	(4.5 ± 1.5) MHz	(11.6 ± 3.5) MHz	(6.3 ± 1.3) MHz
Percentage of obs with $\sigma > 10$ MHz	24.9%	5.6%	45.1%	5.6%
Percentage of obs with $\sigma > 15$ MHz	9.1%	1.0%	20.3%	0.9%
Percentage of obs with $\sigma > 25$ MHz	1.2%	0.01%	4.3%	0.07%

3.1.4 Lessons learnt from the laser performance monitoring

- The sensitivity of the laser to laser bench temperature (gradients) should be characterized on ground and validated during commissioning. For Aeolus lasers once the temperature sensitivity was managed, the tunability of the lasers was crucial to optimize the send-receive co-alignment for improved atmospheric signal and wind error performance.
- Science data from the detector signals and wind performance need to be an integral part of the laser performance monitoring on top of the instrument HK-data. This has to be considered already during mission preparation and rehearsed during ground tests prior to launch.
- The build-up of a strong collaboration with ESA, DISC and laser-industry already before launch is the basis for an efficient and effective performance management.
- Thanks to its high technological commonality with ALADIN, the ALADIN Airborne Demonstrator (A2D) provided insights into technical and optical issues as well as the operation of the full instrument chain. Moreover, it delivered atmospheric return signals to test and develop the processing chain already before launch. All these mission preparation aspects were vital for the fast commissioning of Aeolus and the quick solutions to unforeseen issues that rendered the mission successful over almost 5 years. In order to reduce risks from remaining uncertainties, the same approach of complementing instrument tests by ESA and space industry with atmospheric measurements taken by a representative sub-orbital instrument is seen as mandatory for mission preparation and validation, especially in light of the major design changes and the fully operational mission character with two satellites over minimum 10 years.

3.2 Internal reference and atmospheric path signals

Oliver Lux and Karsten Schmidt, DLR

The wind measurement principle of ALADIN relied on detecting frequency differences between the laser pulsed that were emitted into the atmosphere and those backscattered from the atmospheric particles and molecules moving with the ambient wind. The frequency shift $\Delta f_{Doppler}$ in the backscattered signal that is introduced by virtue of the Doppler effect is proportional to the wind speed v_{LOS} along the laser beam line-of-sight (LOS) according to $\Delta f_{Doppler} = 2\ f_0\ v_{LOS}/c$, where c is the speed of light and f_0 is the frequency of the emitted light. Accordingly, a LOS wind speed of 1 m/s translates to a frequency shift of 5.63 MHz at the UV frequency of the emitted light (f_0 = 844.75 THz). Therefore, the relative accuracy of the frequency measurement is on the order of 10^{-8} which poses stringent requirements on the frequency stability of the laser transmitter as well as on the precision of the spectrometers.

The frequency of the emitted laser pulses is measured by guiding a small portion of the laser emission from the laser directly to the field stop within the sealed transmit-receive optics (STRO) from which it illuminates the receiver channels (see Figure 11). This portion is referred to as the internal reference path (INT) signal and not only served the determination of f_0, but was also essential for the calibration of the frequency-dependent transmission of the two receiver spectrometers (Mie and Rayleigh channel). The atmospheric return (ATM) signal that is collected by the telescope enters the STRO, where it passes through a laser chopper mechanism (LCM, Székely and Henzelin, 2005), realized by a moving blade, before being spatially overlapped with the INT beam by a beam splitter. Due to the long travel time of the atmospheric return of a few milliseconds, the detection is temporally separated from the INT signal which is acquired on single pulse level. Further details on the design and operating principle of ALADIN can be found in Lux et al. (2021).

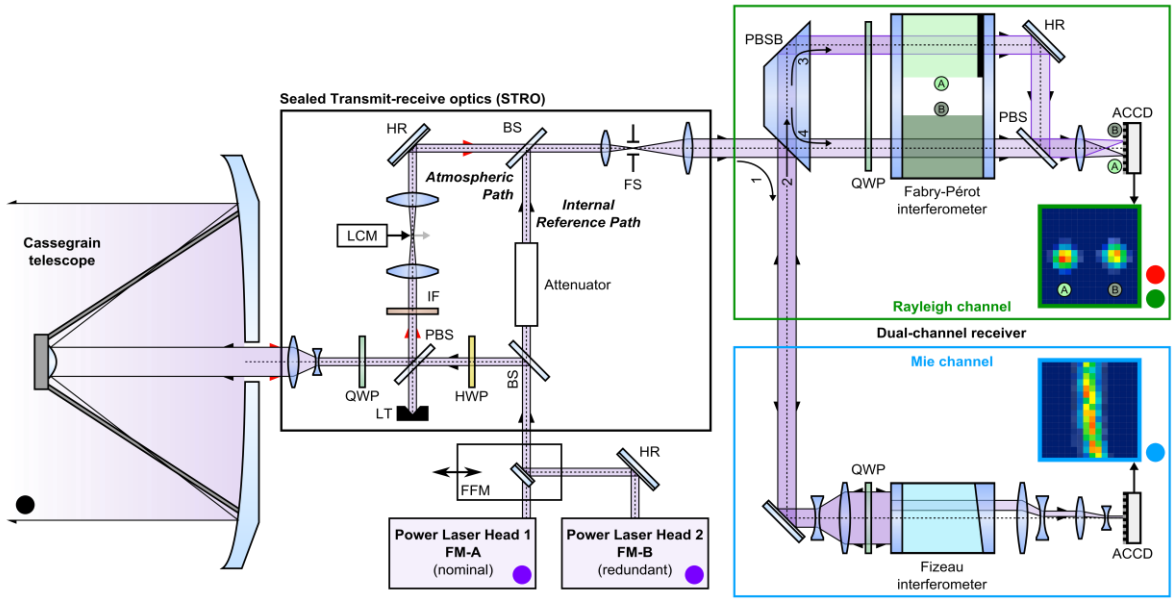

Figure 11: Schematic of the direct-detection Doppler wind lidar ALADIN on board Aeolus. The instrument consists of two fully redundant, switchable UV laser transmitters (FM-A, FM-B), a Cassegrain telescope, transmit–receive optics (TRO) and a dual-channel receiver. The latter is composed of a Fizeau interferometer and sequential Fabry–Pérot interferometers for analysing the Doppler frequency shift from particulate and molecular backscatter signals, respectively. HR: highly reflective mirror; FFM: flip-flop mechanism; BS: beam splitter; PBS: polarizing beam splitter; HWP: half-wave plate; QWP: quarter-wave plate; IF: interference filter; LT: light trap; LCM: laser chopper mechanism; FS: field stop; ACCD: accumulation charge coupled device. Numbers indicate the sequential light path in the receiver. The coloured dots refer to the signals that are measured at different locations along the optical path, as shown in Figure 12. The small insets in the two receiver channels represent exemplary images of the two Rayleigh spots corresponding to filters A and B as well as the Mie fringe recorded in imaging mode.

3.2.1 Signal evolution

The performance of the ALADIN instrument and the quality of the Aeolus wind and aerosol products was largely determined by the atmospheric signal levels that were directed to the two receiver channels and then incident on the detectors. This is especially true for the precision of the Rayleigh wind data where the random error was dominated by Poisson noise. Therefore, the signal levels were carefully monitored during the mission, whereby several tools were applied to measure the signal levels at different locations along the instrument's optical path. The top panel of Figure 12 depicts the temporal evolution of the signal levels during the mission lifetime after normalization to the respective value from 26 July 2019. The colours of the curves are in accordance with those of the large dots in Figure 11 marking the locations of the signal detection as follows: violet – pulse energy measured on a photodiode (PD74) at the output of the laser transmitter (FM-A or FM-B); green/light blue – signal level on the Rayleigh/Mie ACCD (sum over all 16 pixels) obtained from the internal path acquisition; red – signal level on the Rayleigh ACCD (sum over all 16 pixels) obtained from the atmospheric backscatter at ≈10 km altitude under clear-sky conditions (see section 3.2.5). The latter signal is additionally provided after normalization to the emitted laser energy (ATM/PD74), representing the ATM path transmission (dark red curve). Finally, the yearly energy measurement provided by the Pierre Auger Observatory (PAO) between 2019 and 2021 (section 3.2.2) is plotted as black dots with the error bars denoting the statistical error.

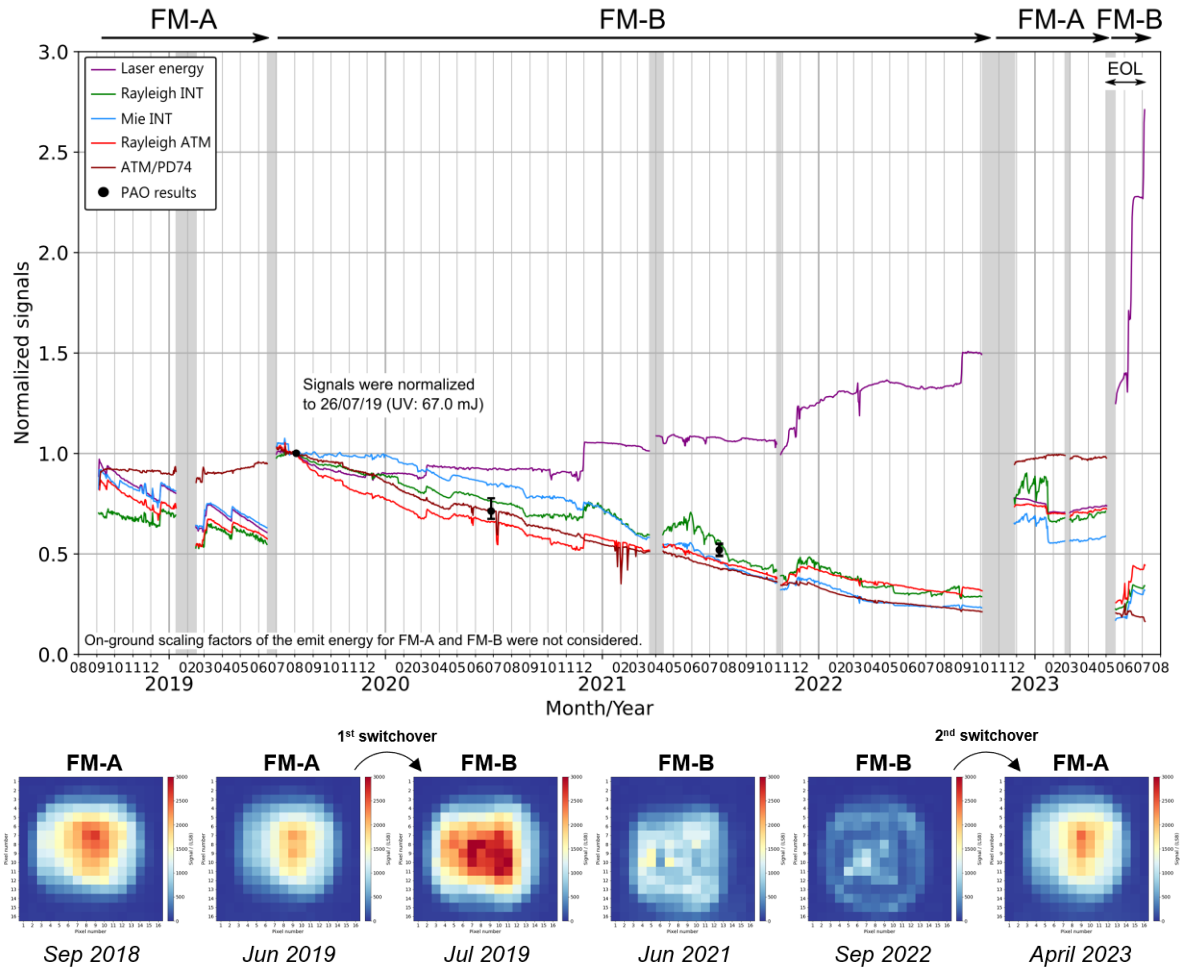

Figure 12: Top: Timeline of the ALADIN signal levels measured at different locations in the instrument over the mission period. The signal levels are normalized to the respective value from 26 July 2019 shortly after the switchover to the FM-B laser. Periods when the laser was temporarily switched off are indicated by grey-shaded areas. The energy measurements from the Pierre Auger Observatory (black dots) are normalized to the value from

3 August 2019 with the error bars indicating the respective statistical error. Bottom: Laser beam monitoring images over the mission lifetime derived from internal path Mie channel data.

Shortly after the start of FM-A operations in autumn 2018, the UV laser energy showed a linear decrease at a rate of about -1 mJ/week, leading to less than 40 mJ by June 2019 despite several laser adjustments. The energy degradation was at the time traced back to a gradual misalignment of the MO caused by a thermal drift of the laser bench. Since the energy loss occurred already inside the laser, the signal levels measured at the subsequent stages of the instrument (INT and ATM path) followed this trend. In June 2019, a switchover to the redundant laser FM-B was performed which delivered an initial energy of 67 mJ and significantly slower power degradation, ensuring a higher signal-to-noise ratio (SNR) of the atmospheric backscatter return and, hence, lower random error for the wind observations. However, despite the stable laser energy, which was even increased to more than 100 mJ by several laser adjustments, the INT and ATM path signal levels decreased by more than 70% over the three years until October 2022 following the switchover in June 2019.

The root-cause analysis which was supported by the measurements at the PAO (section 3.2.2) ultimately led to the decision to switch back to the FM-A laser in November 2022. Despite the much lower output energy compared to FM-B at the end of its operation (101 mJ), the switchover to FM-A increased the atmospheric signal by a factor of 2.2, to a level comparable to early 2019 (Lux et al., 2023). The FM-A laser performance could be optimized based on the knowledge gained with the second laser during the nearly 40 months of its operation. As a result, stable output energy above 50 mJ was achieved until the end of the nominal Aeolus operations on 30 April 2023. Subsequently, dedicated instrument tests, referred to as end-of-life (EOL) activities (see section 3.4), were carried out over a period of seven weeks including another switch to the FM-B laser. The laser adjustments at the end of the EOL phase led to an output energy of 182 mJ over 33 hours before the instrument was finally switched off on 5 July 2023.

One of the main questions regarding the instrument performance concerned the root cause of the signal degradation during the FM-B period between 2019 and 2022. In contrast to the first FM-A phase, the signal loss did not occur inside the laser, but along the optical path that is unique to the FM-B, most likely within the relay optics, including the FFM (section 3.1.1), which guide the redundant FM-B laser beam onto the nominal optical path (see Figure 11). The actual loss mechanism is subject of ongoing studies as of writing of this report. Laser-induced contamination (LIC) and laser-induced damage (LID) of the affected optics are currently assessed to be the most probable causes. Since the loss is suffered before the beam splitter that separates the internal and the emit path, it was observed on all detectors behind the laser output. The discrepancies between the normalized INT and ATM path signal levels in Figure 12 can be explained by signal anomalies affecting the INT path, as elaborated in section 3.2.3.

The degraded transmission of the laser beam through the optics of the FM-B-only emit path behind the laser is visualized by the laser beam monitoring (LBM) images that were acquired on a weekly basis during the mission through a specific operation mode, where the ACCD is used in imaging mode as a camera, by utilizing the INT path signal on the Mie channel ACCD. Selected LBM images are shown in the bottom panel of Figure 12. The signal decrease during the first FM-A period between September 2018 and June 2019 was more of less homogeneous across the beam profile, whereas a flattening of the signal intensity distribution, followed by the formation of a ring pattern was observed over the course of the FM-B period between July 2019 and September 2022.

The switch-back to the FM-A laser restored the conditions from June 2019, but at a higher and more stable UV laser energy, thereby providing a consistent performance until April 2023 when the nominal operations ended. The nearly constant decrease rate of the ATM path transmission by about -1% per week (dark red curve in Figure 12) and the ring structure in the LBM images point to LIC as the major

root cause for the signal loss on optics specific for the emission path of FM-B inside the TRO. There were no signs of LIC and LID detectable with the laser internal HK-sensors.

3.2.2 Measurements at the Pierre Auger Observatory

The Pierre Auger Observatory, located in Argentina, is designed to detect ultra-high energy cosmic rays in the Earth's atmosphere. One measurement method used for this purpose is fluorescence detection in the wavelength range between 280 and 430 nanometres. Since the ALADIN laser emitted within this range, the observatory could detect ALADIN's laser beam when it passed the observatory. Due to its dawn-dusk orbit with 6 am/pm equator crossing times, accurate reconstruction of the laser beam was only possible during a few months in the southern-hemisphere winters and only at nights without clouds or significant amount of aerosol in the atmosphere. The data from the best overpasses in 2019, 2020 and 2021 were used to determine the laser energy at the exit of the telescope which allowed for an independent assessment of the in-orbit instrument performance of ALADIN during the FM-B period (Figure 13). In particular, the Auger measurements confirmed that the signal loss observed between 2019 and 2021 already occurred on the emit path between the laser output and the telescope, thereby driving the efforts to switch back to the FM-A laser. As an additional outcome of the unique collaboration between the Auger and Aeolus teams, a satellite ground track error in the L1A processor was corrected, reducing the horizontal offset between the ground track reported in the product and the actual ground track from 6.8 km to 0.8 km.

It is interesting to note that the energy decrease observed by the PAO in 2020 (–28%) and 2021 (–48%) with respect to the reference measurement in 2019 is smaller than the signal loss registered on the ALADIN detectors (–34% and –53%, see Figure 12). This points to an additional loss mechanism in the receive path, most likely clipping of the atmospheric return signal at the field stop. It is also notable that the absolute laser energy in 2019 reconstructed by the Auger Observatory (≈33 mJ, right panel of Figure 13) is lower than what would be expected at the Aeolus telescope output (44 mJ) when considering the specified emit-path transmission of around 0.704 and correction factors for the laser energy. This points to additional transmission loss in the emit path of ALADIN. An initial loss of about a factor of two compared to pre-launch simulations was already observed after launch for the atmospheric-backscatter signals of the Rayleigh channel. The root cause is assumed to be a combination of telescope aberrations, stress-induced phase shifts of the wave plates in the TRO (see also Figure 11) as well as roughness and scattering losses of the primary telescope mirror.

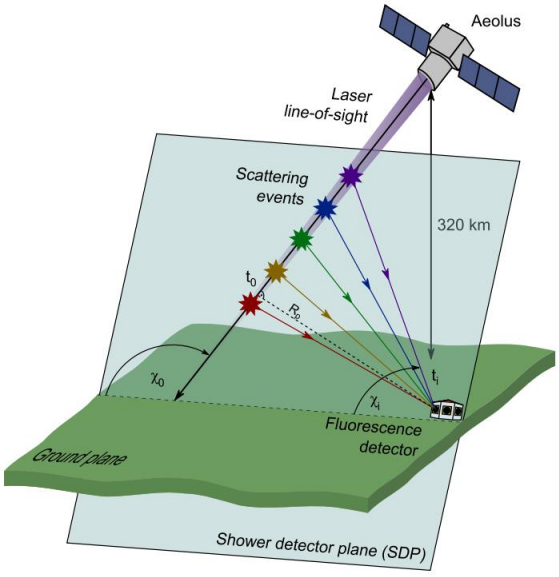

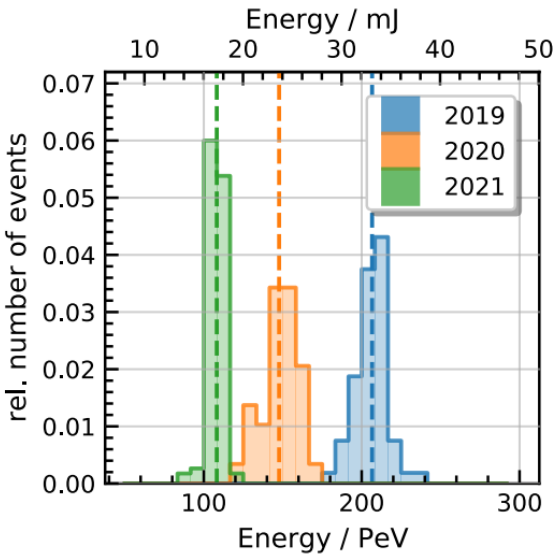

Figure 13: Left: Geometry of the Aeolus laser beam being detected by one of the four fluorescence detectors of the Pierre Auger Observatory. Right: Reconstructed energies for three sample Aeolus overpasses in 2019, 2020 and 2021. The average energy per overpass is marked by the dashed line. The energy is given in mJ by the top axis and in PeV (10^{15} eV) by the bottom axis. Figs taken from Pierre Auger Collaboration et al. (2024).

3.2.3 Internal reference anomalies

Starting from July 2020 several anomalies occurred on the internal path affecting the signal levels and associated parameters like spectrometer responses and Rayleigh spot parameters over a broad range of time scales from the sub-second regime up to several weeks. The first anomaly was the appearance of random signal jumps when the INT path Rayleigh signal level was increased by up to 80% on pulse level and up to 15% on observation level, respectively. This phenomenon is depicted in Figure 14 (a). The effect was about 2 to 3 times smaller on the Mie channel, while a pixel-wise analysis revealed that the gained signal was concentrated within the Mie fringe at the same location of the ACCD as the nominal signal.

On the Rayleigh detector the two-dimensional signal distribution, obtained by comparing LBM images without and with signal jumps, resembled that of a homogeneously illuminated field stop (Figure 14 (b)). These observations pointed to a narrowband parasitic signal such as straylight that was over-illuminating the field stop. The frequency of the signal jumps decreased during the second half of 2020 and stopped in early 2021. However, the variability of the INT path signal levels was still higher than before the onset of the jump events. This was found to be related to the pressure cycle of the oxygen that is injected into the sealed transmit-receive optics (STRO) arrangement in order to mitigate LIC.

The modulation of the Rayleigh signal level with the STRO pressure cycle is depicted in Figure 14 (c), while the signal distribution across the ACCD in the low- and high-pressure regime is shown in panel (d). The Rayleigh signal was modulated by about ±5% over the 15 Pa-range of the STRO pressure cycle which had a period of 2 to 3 hours. Subtracting the low signal at high pressure from the high signal at low pressure yields a one-dimensional distribution (blue curve) that agrees with the horizontal cut of the LBM difference of panel (b), suggesting a common root cause of both signal anomalies. After the INT path signal had started to be influenced by the STRO pressure cycle in mid-2020, the amplitude of the signal modulation (or pressure sensitivity) has varied over the mission ranging from about 0.1%/Pa to about 0.4%/Pa without any obvious link to other instrument parameters or operational settings. Changes in the signal variability were most pronounced in 2022 when the noise periodically increased over several weeks and then rapidly decreased within a few days or even hours.

This third phenomenon is illustrated in panel (d) of Figure 14. Between March and September 2022, there were four instances when the INT path Rayleigh signal dropped by more than 10%, while the signal noise, which was predominantly related to the STRO pressure cycle, was significantly reduced. In the weeks following each drop, the signal levels remained constant or even increased, despite the continuous signal loss on the emit path, and the noise was building up again. Hence, instead of a monotonic signal decrease by about -1%/week, as observed for the ATM path signal, the INT path signal decreased in a step-wise manner during this phase of the mission which explains the discrepancies in the signal evolutions plotted in Figure 12. The difference of the LBM images just before and after a signal drop, presented in panel (e) of Figure 14, again agrees with a signal distribution that is expected from a uniformly illuminated field stop.

As a conclusion, although the three phenomena described above occurred on very different time scales, their spatial and spectral characteristics were very similar. This suggested that they represented three different manifestations of the same anomaly. Extensive analysis of the INT path data from different operation modes (WVM, LBM, IRC) led to the assumption that a parasitic signal with varying intensity,

which was originated before the instrument field stop in the STRO or at the secondary mirror of the telescope, was incident on the ACCDs at the time of the internal path signal acquisition.

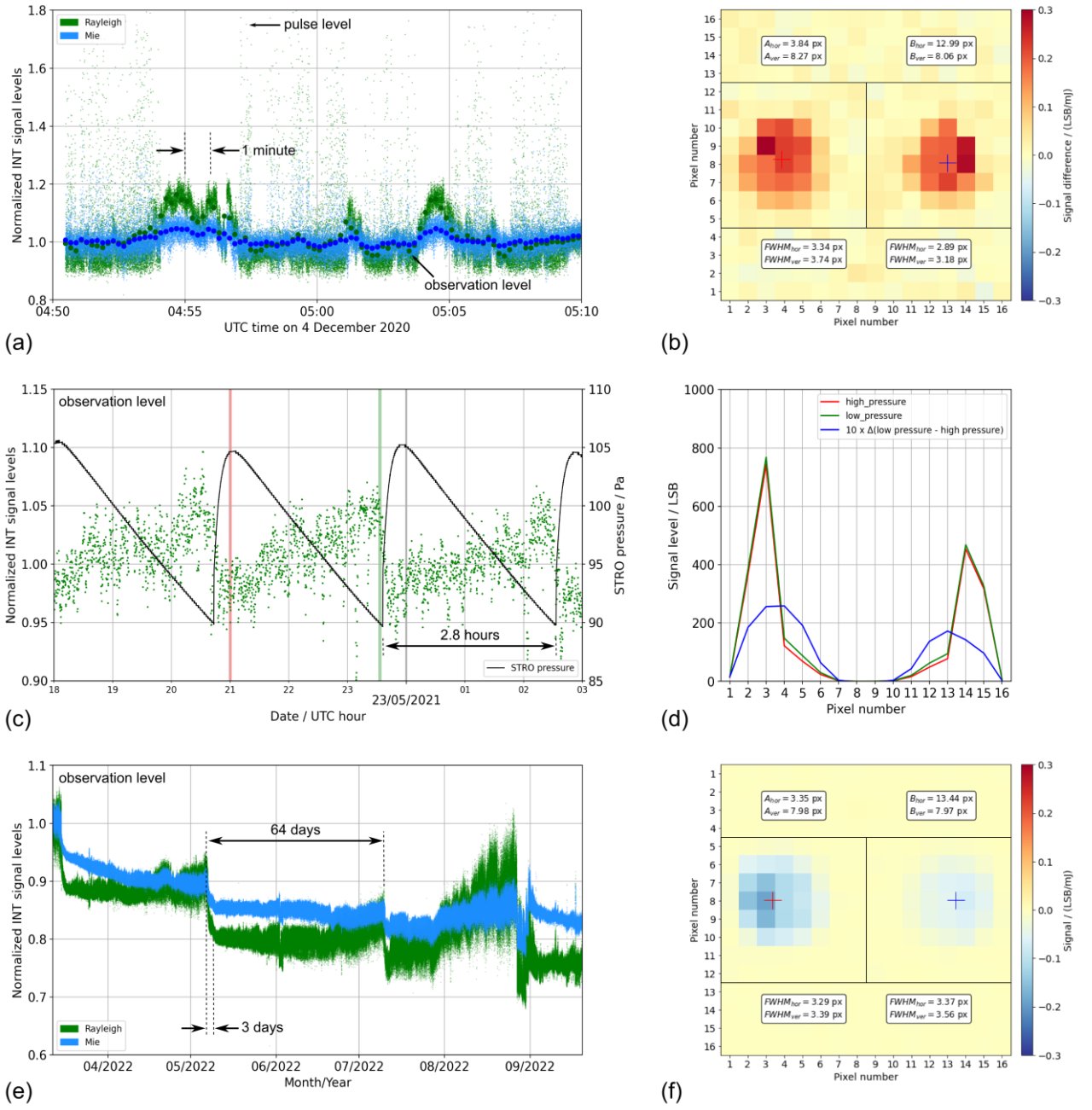

Figure 14: Internal path signal anomalies: (a) Time series of the normalized internal path Rayleigh (green) and Mie (light blue) signal levels over a 15-minute period on 04/12/2020 with the occurrence of signal jumps. The data is shown on pulse level (small dots) and on observation level (large dots). (b) Distribution of the Rayleigh signal difference between LBM images with (04/12/2020) and without a signal jump (18/12/2020). The markers and insets denote the horizontal and vertical positions and widths (FWHM) of a Gaussian fit applied to the left (A) and right spot (B). (c) Time series of the normalized internal path Rayleigh signal level (green dots) and the STRO pressure level (black line) over a 9-hour period on 22-23/05/2021. The observations falling into the red- and green-shaded 2-minute periods were averaged to obtain the two signal distributions (red and green line) depicted in panel (d). The difference between the two distributions, scaled by a factor of 10, is plotted in blue. (e) Time series of the normalized internal path Rayleigh (green) and Mie (light blue) signal levels over a 6-month period between March and September 2022. (f) Distribution of the Rayleigh signal difference between LBM images before (26/08/2022) and after (30/08/2022) the signal drop on 27/08/2022. The markers and insets denote the horizontal and vertical positions and widths (FWHM) of a Gaussian fit applied to the left (A) and right spot (B).

Imperfect synchronization between the laser pulse emission and the LCM blade motion was suspected as the root cause for the INT path anomalies and a dedicated test was carried out as one of the EOL activities (section 3.6). The test aimed at varying the LCM phase via the delay parameters dt1 and dt2 while checking the INT path parameters. Since a wrong synchronization of the LCM could have also impacted the ATM path signal levels due to a partially closed chopper blade, they were analysed as well. The timing sequence of the LCM with respect to the laser emission and the ATM path signals is illustrated in Figure 15.

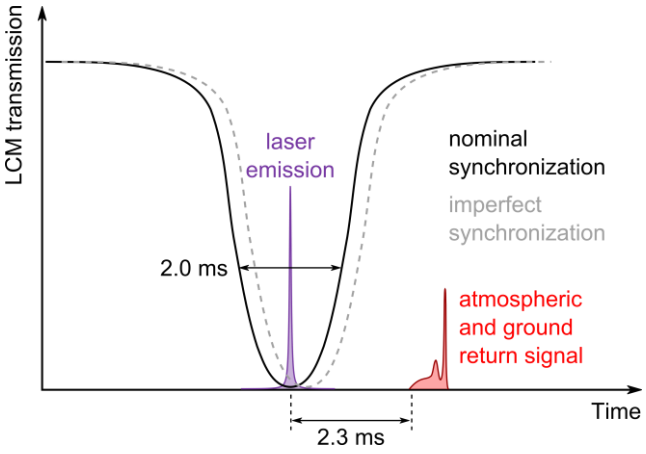

Figure 15: Timing sequence of the LCM with nominal and imperfect synchronization of the laser pulse emission with respect to laser pulse emission (purple) and the atmospheric signals including strong ground return (red).

After a first test sequence in May 2023, an extended test was performed in early June 2023 when the delay parameters were varied in steps of 0.125 ms. After identifying the setting with the lowest INT signal noise, it was kept for 24 hours on 3 June 2023 to study the longer-term behaviour at this LCM phasing setting. For assessing the influence of the LCM phasing settings on the internal path stability, the variability of the Rayleigh and Mie signal levels was determined as the root mean square (rms) over all observations in 5-minute intervals. For comparison the same was done for the laser-internal reading of the UV output energy, as shown in Figure 16.

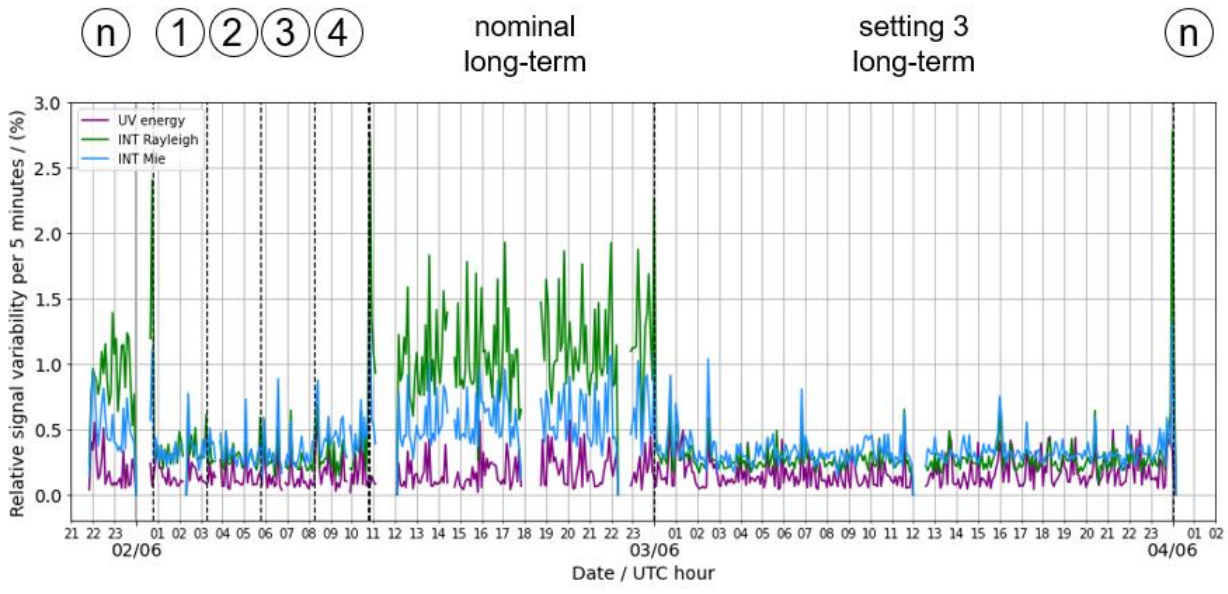

Figure 16: Time series of the temporal variability (standard deviation over 5 minutes) of the UV energy (purple) and the Rayleigh (green) and Mie (blue) internal path signal levels during the extended LCM timing test on 2 to 4 June 2023. The dashed lines indicate changes in the LCM delay parameters (see text).

When reducing the dt1 and dt2 values by 0.375 ms (setting 3), the Rayleigh signal variability decreased by a factor of 4 from 1.1% rms to 0.27% rms. The effect was less pronounced on the Mie channel where the reduction was about 40% from 0.57% rms to 0.33% rms. Since the UV energy variations were on the order of 0.2% rms over the 5-minute-intervals, this means that the INT path signal variability was almost limited by that of the laser energy. This observation was strengthened by a Fast Fourier Transform analysis which revealed that the influence of the STRO pressure cycle had disappeared so that the orbital cycle had become the dominant source of signal and response variations, particular for the Mie channel. Moreover, a movement of the Rayleigh spots toward the ACCD periphery and a reduction in spot size was evident, pointing to an elimination of the parasitic signal contribution that had caused the various INT path anomalies observed during the mission. The atmospheric path was not affected by the setting changes which suggested that the LCM was still fully open when the atmospheric backscatter signal arrived despite the small phasing change. The optimized LCM phasing setting was permanently applied from 10/06/2023, 12:30 UTC onwards until the final switch-off of ALADIN on 5 July 2023, in addition to the optimization of the FM-B laser cavity control which had been applied on 29 May 2023.

3.2.4 Internal reference responses

The accuracy and precision of the Aeolus wind results were directly connected to those of the INT path spectrometer responses, as the latter were used for the calculation of the outgoing laser frequency and thus of the Doppler frequency shift. Therefore, changes that were introduced only to the INT path but not on the ATM path responses resulted in systematic wind errors. The response of the Rayleigh channel, which relies on the double-edge technique, is defined by the contrast between the signal levels I_A and I_B that are transmitted through the two filters of the Rayleigh spectrometer (RSP): $(I_A - I_B) / (I_A + I_B)$. For the Mie channel, the response is represented by the centroid position of the interference fringe that is produced by the Mie Fizeau spectrometer (MSP) and imaged onto the ACCD.

The temporal evolution of the INT path Rayleigh and Mie responses is presented in Figure 17. Both parameters were altered by commanded laser frequency adjustments (LFAs) which were in some cases accompanied by changes of the Rayleigh cover temperature (RCT). The nominal frequency setting was changed six times between September 2018 and April 2023, as indicated by the red dots in Figure 17. An overview of the different frequency and RCT set points in provided in Table 5.

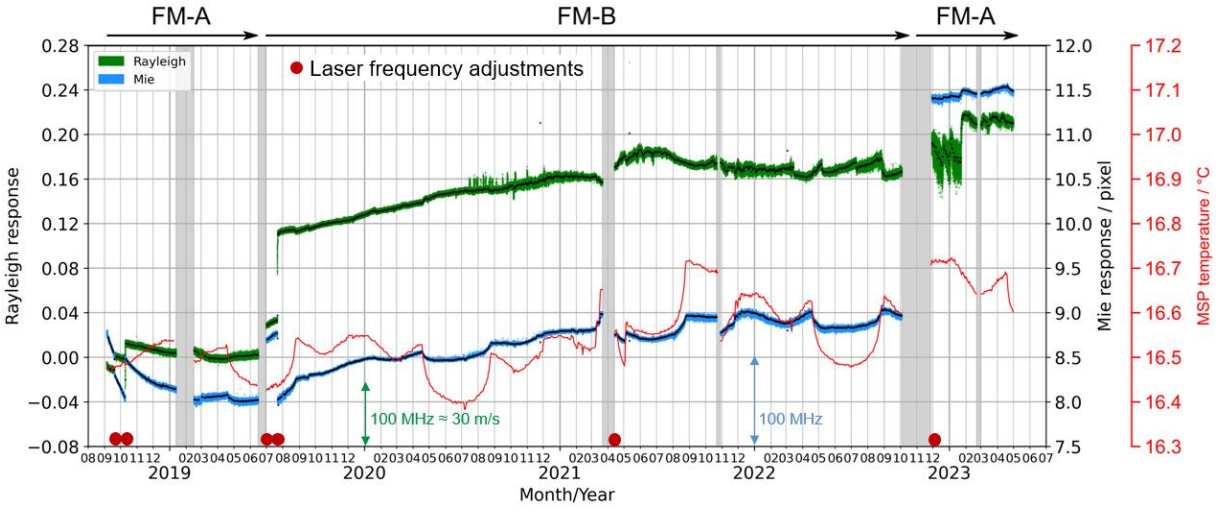

Figure 17: Timeline of the internal path responses for the Rayleigh (green) and the Mie channel (light blue) over the mission period. The Mie spectrometer (MSP) temperature is additionally plotted as red line. Changes in the nominal frequency setpoint are indicated as red dots (see also Table 5); the blue and green arrows indicate the magnitude of a change in response by 100 MHz corresponding to about 30 m/s HLOS.

Table 5: Nominal frequency settings during the Aeolus mission. The Rayleigh cross point (CP) location refers to the spectral position of the transmission peaks for the direct (A) and reflected (B) Fabry-Pérot filter of the Rayleigh spectrometer with respect to the intersection of the two transmission curves (= cross point frequency).

Period of setting (start/stop)	03/09/18, 13 UTC / 19/09/18, 7 UTC	19/09/18, 7 UTC / 09/10/18, 15 UTC	09/10/18, 15 UTC / 18/06/19, 4 UTC	27/06/19, 13 UTC / 22/07/19, 0 UTC	22/07/19, 0 UTC / 22/03/21, 3 UTC	13/04/21, 12 UTC / 05/10/22, 16 UTC	27/11/22, 0 UTC / 01/05/23, 0 UTC
Laser transmitter	FM-A	FM-A	FM-A	FM-B	FM-B	FM-B	FM-A
Nominal frequency (GHz)	1.700	1.675	1.725	-3.675	-3.750	-2.225	6.425
RSP temp. (AHT-11) (°C)	19.05	19.05	18.90	18.90	18.75	18.75	20.45
Rayleigh CP location	filter A left, filter B right	filter A left, filter B right	filter A left, filter B right	filter A left, filter B right	filter A left, filter B right	filter A left, filter B right	filter A right, filter B left
Range of Mie fringe centroid position (pixel)	8.5 to 8.8	8.0 to 8.3	8.0 to 8.5	8.7 to 8.8	8.0 to 9.0	8.7 to 9.0	11.4 to 11.5

Aside from the LFAs, the responses were influenced by drifts of the emitted laser frequency, especially during the first one and a half years of FM-B operations when both the Mie and Rayleigh response increased by about 80 MHz. The Mie response was additionally modulated by the MSP temperature (plotted as red curve in Figure 17) which was mainly influenced by the eclipse phases between April and August of each year, which influenced a majority of the satellite and instrument thermal environment, as well as by the applied modifications of the instrument's top floor temperature in March and May 2021. After the switch back to the FM-A laser in November 2022, the Mie fringe was located off-centre on the ACCD between pixels 11 and 12 to test an operating frequency on the RSP-response, less sensitive to atmospheric temperature.

On short time scales relevant for the wind processing, the Mie response was sufficiently stable over the mission with variations of typically less than 1 MHz rms on observation level and less than 10 MHz on pulse-to-pulse level limited by the laser frequency stability (section 3.1.3). The Rayleigh response, however, showed large fluctuations starting from July 2020 which were dominated by the anomalies described in the previous section. Since the signal variations were inhomogeneous across the ACCD, sudden signal jumps, drops and the signal modulations driven by the STRO pressure cycle resulted in corresponding Rayleigh response variations. The variability on observation level reached more than 5 MHz in the second half of 2020 which led to the decision to use a fixed INT response value in the Rayleigh wind retrieval starting from 5 December 2020 in order to eliminate the wind error that was caused by the INT path anomalies.

3.2.5 Atmospheric path signal evolution

The intensity of laser signals that are backscattered from air molecules in the atmosphere and directed to the ALADIN detectors along the atmospheric path of the instrument was one of the most crucial system parameters as it determined the quality of the L2B Rayleigh wind data which is dominated by Poisson noise (see also section 3.2.1). Consequently, the atmospheric path signal levels were continuously monitored during the mission to assess the performance of the ALADIN instrument including its two redundant lasers FM-A and FM-B. To avoid interfering signals coming from cloud particles and aerosols, the latter had to be suppressed by rejection of all atmospheric L1B Rayleigh useful signals in and below height bins with a refined scattering ratio (RSR) larger than 1.3 on observation level. In this manner, about 45% of all Rayleigh useful signals were rejected and only so-called clear sky normalised valid Rayleigh useful signals (CSNVRUS) were considered in the analysis. The corresponding scheme to do so has been presented by Schmidt et al. (2019, 2022, 2023). The cyan dots in Figure 18 represent the sum of CSNVRUS of the Rayleigh channels A and B in the altitude range between 9.5 km and 10.5 km. Additionally, a quality control had been applied to reject large signal outliers (grey line in Figure 18). The quality controlled and daily averaged CSNVRUS in this altitude range are shown as red line in Figure 18 and as Rayleigh ATM (red line) in the top panel of Figure 12. Note that CSNVRUS had been also regularly monitored in the altitude range between 14.5 km and 15.5 km. Other altitudes were only considered in special investigations.

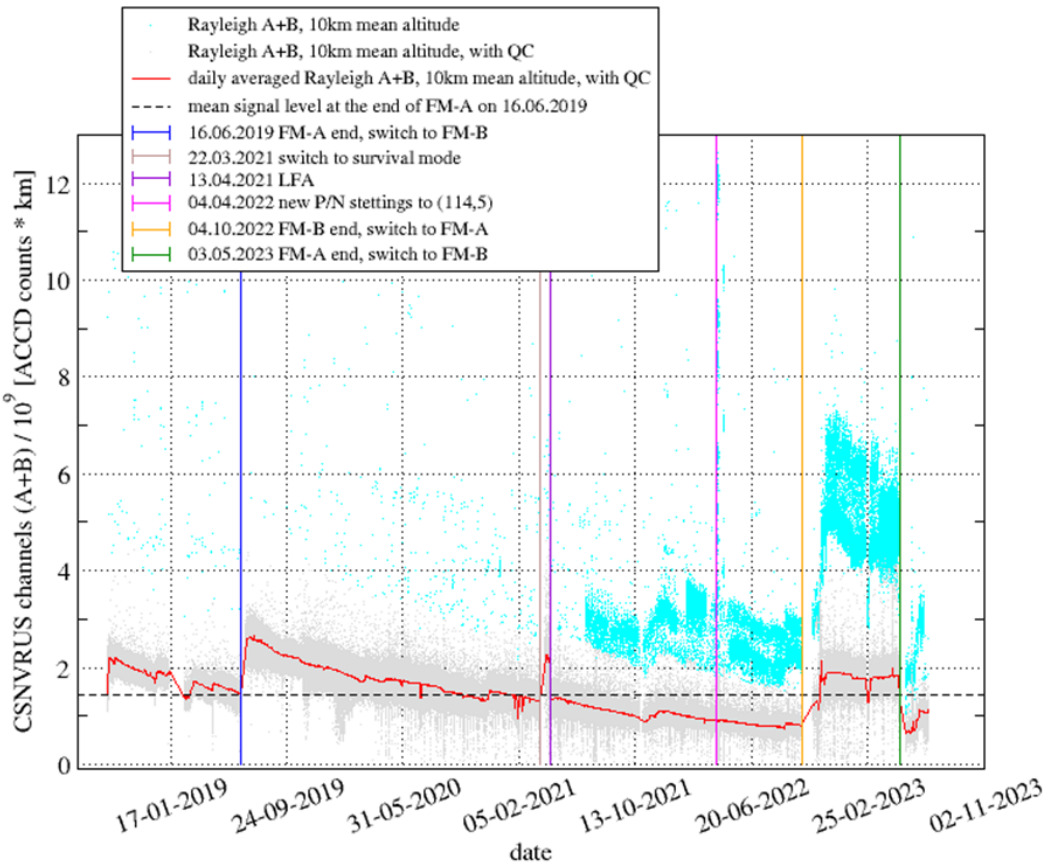

Figure 18: Sum of Aeolus in orbit atmospheric L1B Rayleigh useful signals of channels A and B on observation level for clear sky conditions (CSNVRUS) during the complete mission from 03/09/2018 to 05/07/2023 at 10km mean altitude, i.e. in the range (9.5, 10.5) km (cyan line, partly covered by the grey line). Only valid useful signals have been considered. A normalization w.r.t. the bin thicknesses and satellite ranges have been also applied. Grey line – same as cyan line but with an additional quality control to reject large signal outliers. Red line – daily averaged signals of grey line. Some important dates are plotted as coloured bars.

In the first half of the first FM-A period from 09/2018 – 01/2019, the Rayleigh ATM signals have decreased, following the laser energy. This is seen by the relatively constant efficiency (ATM/PD74, dark red line in Figure 12) over time. In the second half of the first FM-A period from 01/2019 – 06/2019, the general trend of a decreasing ATM signal level has continued, but slightly weaker than the laser energy decrease, which has resulted in a slight efficiency increase. In general, the Rayleigh ATM signal decrease in the first FM-A period was caused by the decrease of the laser energy, which in turn, is assumed to be due to a misalignment of the FM-A master oscillator (Krisna et al., 2022). Several adjustments have been performed to increase the UV laser energy (see Table 3), leading to short-term ATM signal increases, but the overall decreasing trend could not be stopped.

The switch from laser FM-A to FM-B in 06/2019 involved a large Rayleigh ATM signal increase by about 77%, due to a better laser performance. After a thermalization phase of the FM-B laser in summer 2019, its output energy was stable over more than three years of operations. Moreover, several measures to increase the laser energy output have succeeded. The atmospheric Rayleigh signals, however, decreased at a nearly constant rate of -1% per week, resulting in a decreasing efficiency. Only short-term improvements have been obtained after the UV laser energy adjustments. The most likely cause for this were damages and/or laser-induced contaminations (LIC) of a few optical elements which are only present in the emit path of the FM-B laser, as described in section 3.2.1.

Noticeably large Rayleigh ATM signals were obtained in the beginning of April 2021 after the switch of ALADIN from the measurement to the survival mode on 22/03/2021 (red line in Figure 18, masked in Figure 12). A too short background integration time caused too small Rayleigh and Mie useful signals for solar background which, in turn, led to a wrong background correction of the atmospheric signals (see section 3.8). The issue was corrected during the LFA on 13/04/2021 by choosing the right integration time.

Artificially large atmospheric Rayleigh useful signals were also observed after the P/N setting change on 04/04/2022 (magenta line in Figure 18). They were caused by saturated Rayleigh solar background pixels leading to erroneous background corrections of the atmospheric signals. Two subsequent decreases of the background integration time on 11/04 and 22/04/2022 corrected these artefacts. In contrast to the previous case in the beginning of April 2021, these large Rayleigh signals were rejected by the quality control so that they are no longer to be seen in the grey and red lines of Figure 18.

The switch-back from laser FM-B to FM-A in 11/2022 decreased the UV laser energy as expected, but resulted in a large Rayleigh ATM signal increase by about 50%. This has led in turn to the largest stable efficiency ATM/PD74 over the longest period from 11/2022 to the beginning of 05/2023, when ALADIN was switched down to standby. The reason for this has been the choice of more optimal set points in the laser FM-A operation, compared to the first FM-A period from 09/2018 – 06/2019.

After the switch down of FM-A and the change back to FM-B in the beginning of 05/2023, the atmospheric Rayleigh signal level decreased again to about that one at the end of the first FM-B period in 10/2022. The stepwise increase of the FM-B laser energy during the EOLA, finally up to the record value of 182 mJ, has also resulted in a corresponding ATM signal increase by about 41% compared to the end of the first FM-B period in 10/2022. This increase is, however, much smaller than the laser energy increase so that the corresponding efficiency has continued to decrease, again at the same level as that one at the end of the first FM-B period in 10/2022.

3.2.6 Lessons learnt from the signal performance monitoring

- Different optical and spectral characteristics of the internal and atmospheric path have to be well characterized on ground and in orbit to be considered for the monitoring analysis. These differences hindered the use of the internal signals for its intended purpose as Doppler frequency reference for the wind measurement.
- Special performance activities like laser and telescope optimizations require dedicated signal analysis on the relevant time-scales. Orbital variations of the atmospheric signal caused by air density variations along a fixed altitude can be of a similar magnitude as effects caused by laser or telescope parameter changes. The radiometric calibration coefficients K_{ray} and K_{mie} (see section 4.3.2) were important reference parameters for quantifying the atmospheric path signal levels.
- The availability of internal signals on shot-to-shot basis is crucial for the assessment of the laser frequency stability and other phenomena acting on short time scales like the parasitic signal from the LCM.

3.3 ACCD hot pixels and other detector anomalies

Oliver Lux, DLR

Already during the commissioning phase of the Aeolus mission in end of 2018, it turned out that dark current signal anomalies of single pixels (so-called "hot pixels") of the Aeolus detectors detrimentally impacted the quality of the wind and aerosol data products. A steadily increasing number of hot pixels in the memory zone of the accumulation charge-coupled devices (ACCDs) was observed, leading to wind errors of up to several meters per second. Consequently, a dedicated dark current calibration technique was introduced and performed throughout the mission on a regular basis in order to mitigate the systematic errors. Additional anomalies became also evident in the image zone of the ACCDs.

This section recapitulates the in-orbit performance of the Aeolus detectors during the mission lifetime. The various dark current anomalies are classified into categories. The categorization forms the basis for discussing the impact of these anomalies on the wind measurements and its correction in the wind retrieval. A detailed description of the detector design and its operating principle is found in Weiler et al. (2021), while a general overview of CCDs is provided by Janesick (2001). Table 6 summarizes some specifications of the ALADIN ACCDs including values describing the in-orbit performance.

Table 6: Specifications and in-orbit performance of the ALADIN ACCDs.

Parameter	Value
Type	Thinned backside-illuminated accumulation Si-CCD
Area	Image zone: 0.43 mm × 0.43 mm – 16 × 16 pixels Memory zone: 0.43 mm × 0.75 mm – 32 × 25 pixels
Pixel size	Image zone: 27 µm × 27 µm Memory zone: 13.5 µm × 30 µm
Operating temperature	-30°C
Temporal resolution	2.1 to 16.8 µs / 250 to 2000 m for atmospheric layers (#1–#24) 625 µs / 1250 µs / 3750 µs for solar background (layer #25)
Radiometric gain	Mie: 0.684 LSB/e-; Rayleigh:0.434 LSB/e-
Dark current signal rate (rms, in-orbit)	Mie: (0.72 ± 0.31) e- s^{-1}; Rayleigh: (0.64 ± 0.31) e- s^{-1}
Dark current signal noise (rms, in-orbit)	0.78 to 0.89 e-
Readout noise (rms, in-orbit)	(5.6 ± 0.2) e-

3.3.1 Overview of hot pixels and classification

Hot pixels are typically described as pixels with a permanent increase of the dark current. This increase is mostly caused by radiation-induced effects which can be categorized into three groups: ionization damage, displacement damage, and transient effects. Ionization damage involves an increase of trapped charges in the dielectric materials of the CCD and thus an increased dark current as well as a shift in the optimum operating voltages of the CCD. However, this effect is largely avoided by efficient shielding of the optical sensors from ionization radiation. Displacement damage is caused by higher-energetic particles, mainly protons, that can pass through the shielding and the detectors. This may displace atoms from their lattice and create vacancy–interstitial pairs some of which form stable displacement damages in the lattice, thereby increasing the dark current. In addition, displacement damage may also introduce random telegraph signal (RTS) noise which is characterized by sudden step-like transitions between two or more discrete dark current levels at random and unpredictable times.

Transient effects occur due to ionization-induced generation of charges within the detectors and do not cause permanent damage. Nevertheless, since transient effects might be visible as spurious signal spikes on one or more pixels, the affected measurements must also be rejected in the quality control of the lidar signals analysis. Apart from radiation-induced effects, so-called clock-induced charges (CICs) can cause an increase of the dark signal. Here, a spurious signal is generated by transferring measurement signals through the CCD and contributes to the dark signal. When clocking the charges through a register, there is a small probability that additional charges are created, which eventually manifest as additional dark signals.

After the first identification of hot pixels in the nominal Aeolus wind lidar measurements, the so-called DUDE (down under dark experiment) was established as a new procedure to characterize the dark signal levels on the memory zone during continuous laser operation. During DUDE measurements, which were regularly performed starting from 26 November 2018, the range gate timing settings are adjusted such that the theoretical return signal is acquired from below the Earth's surface. In this manner, dark current signals of all pixels of the memory zone can be measured without lidar signal contributions and negligible solar background signals provided that the DUDE is conducted at geolocations with a sun elevation angle below -4°. The frequency of the DUDEs was increased over the course of the mission to two per day from 17 December 2018 onwards, to four per day from 22 January 2019 onwards, to seven per day from 6 September 2021 and finally to eight per day from 30 October 2021 onwards.

The DUDE data was used to analyse the dark current levels on the 24 x 16 pixels in each of the memory zones of the Mie and Rayleigh ACCD and their evolution during the mission period. To this end, the measured signal was corrected for the detection chain offset (DCO) and the solar background. The fact that the number of detector signal accumulations per observation (P/N settings) was changed several times during the mission lifetime was considered when summing up the dark current levels. Quality checks were performed to ensure negligible influence of solar background and to filter out measurements when the detection range was accidentally not completely below the Earth's surface leading to contamination of the upper range bins (= memory zone rows) with return signal.

Based on the time series of the dark current, a segmentation was performed according to a definable cost function that was minimized. The segmentation approach described in Weiler et al. (2021) was further refined by Reichert (2023) using a Monte Carlo simulation to achieve a more robust identification of the discrete RTS levels. As result of the dark current analysis, the individual hot pixels were classified and several parameters that are relevant for the Aeolus data quality were derived. The outcome of the analysis is exemplarily shown in Figure 19 for Mie pixel [06,03] (counting starts from 1) which became hot on 3 June 2021 with an activation level of 149 least significant bits (LSB, equivalent to digitizer numbers DN or counts).

About one month after its onset, the pixel showed a two-level RTS behaviour, as indicated by two distinct peaks in the distribution of dark currents at 43 LSB and 169 LSB (panel (b)). As the dark current almost only fluctuated between these two levels, there is a pronounced peak at 126 LSB in the transition energy (or jump size) distribution (panel (c)). The average lifetime of the RTS levels is 3.1 days (75 hours). It is obtained from a sigmoid function fit which describes the relationship between segment length and jump size. The treatment of two-level RTS hot pixels like Mie [06,03] during the data reprocessing is comparatively easy, as the jump size is foreseeable which facilitates the differentiation of RTS noise from other noise sources, e.g. due to atmospheric signal variations. Other hot pixels that show two-level RTS noise behaviour are for the Mie ACCD: [02,10], [02,15], [05,11], [07,02], [08,07], [09,13], [09,14], [13,05], [20,02] and for the Rayleigh ACCD: [14,02], [24,04] and [24,06].

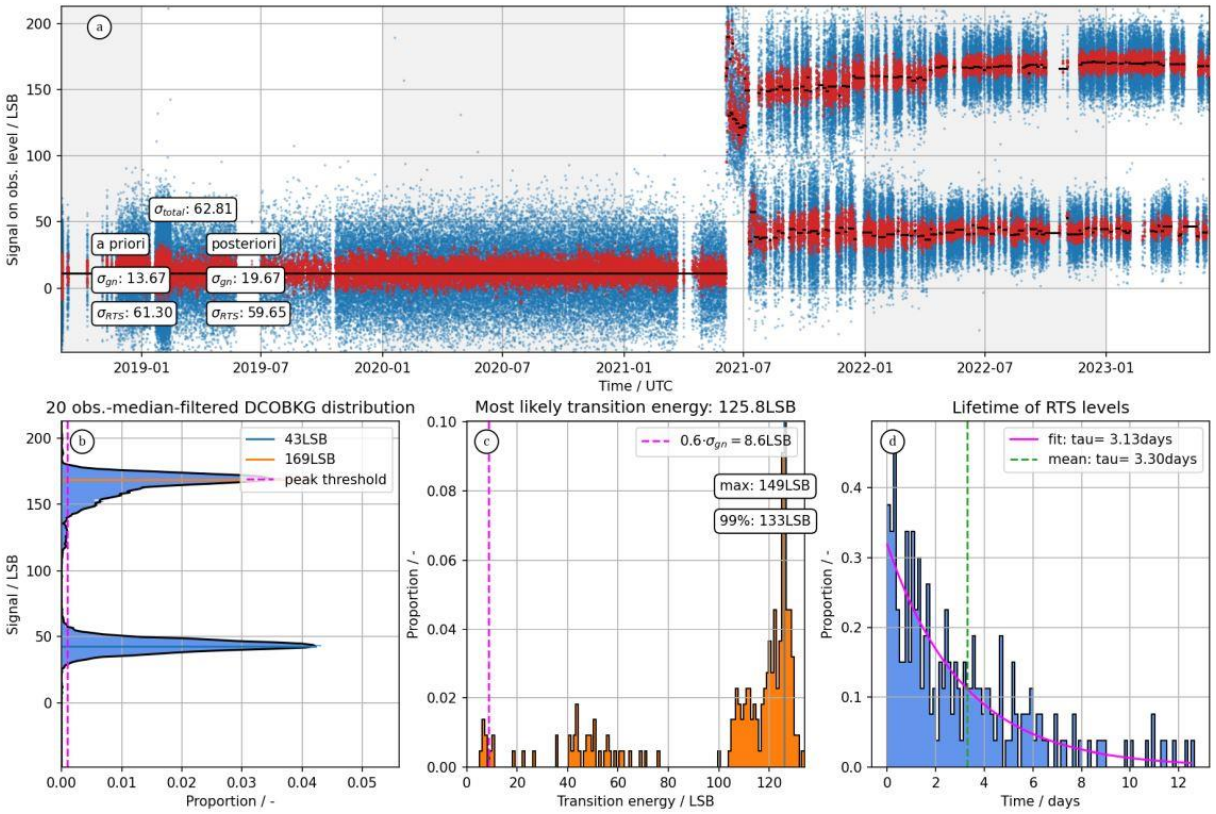

Figure 19: Characterization of Mie hot pixel [06,03]: (a) Time series of the dark current on observation level. The blue dots represent the original resolution, while the red dots are obtained after applying a median filter over 20 observations. The black dots indicate the identified segments. (b) Distribution of the median filtered data. The peaks indicated by the horizontal line were retrieved by a Gaussian kernel density estimation (KDE) in combination with a peak finding algorithm (threshold marked by the magenta dashed line). (c) Distribution of transition energies (or step sizes). The step sizes corresponding to the identified RTS levels in panel (b) are additionally drawn as vertical blue lines. The magenta dashed line marks the sensitivity limit. (d) Distribution of segment lengths (or RTS lifetimes). The magenta curve is the result from a sigmoid function fit. The corresponding average lifetime is given in the legend. The dashed green vertical line marks the arithmetic average lifetime which is more meaningful for hot pixels that show less than 100 transitions (here: 219 transitions).

A different behaviour was observed for Mie hot pixel [03,15] (see Figure 20). Its activation occurred on 12 October 2020 with a jump of the dark current by 64 LSB. In contrast to the example above, there were only sporadic shifts of the mean dark current level, but no RTS noise. The frequency of these shifts even decreased over the mission. This behaviour was also evident for most of the other hot pixels of this class, namely for the Mie ACCD: [01,02], [03,04], [04,01], [04,03], [08,13], [12,13], [13,07], [14,14], [15,08], [24,03], [24,13] and for the Rayleigh ACCD: [05,02], [08,10], [15,04], [17,10], [20,10] and [20,16]. Thanks to their low activity, these hot pixels have rather small detrimental impact on the Aeolus data products.

Some hot pixels show a combination of RTS noise and shifts of the mean dark current. One extreme example is Mie hot pixel [13,09] which shows a superposition of multi-level RTS noise with sporadic mean shifts. This pixel became hot on 2 November 2018 with an activation value of 320 LSB. The peak finding algorithm reveals 7 RTS levels (Figure 21 b). The distribution of transition differences shows two major peaks at 47 LSB and close to 200 LSB (Figure 21 c). It appears that interaction between RTS levels takes place in three-level clusters. In 2020, there was a lower level cluster of three RTS levels at 194 LSB, 251 LSB, and 312 LSB and an upper level cluster of RTS levels at 448 LSB, 481 LSB and 526 LSB. Intra-cluster transitions result in the peak at transition differences of 47 LSB, while the second peak close to 200 LSB is related to inter-cluster transitions. After 2020, two superimposed sporadic mean shifts in March 2021 and October 2021 led to an even more complicated RTS level system.

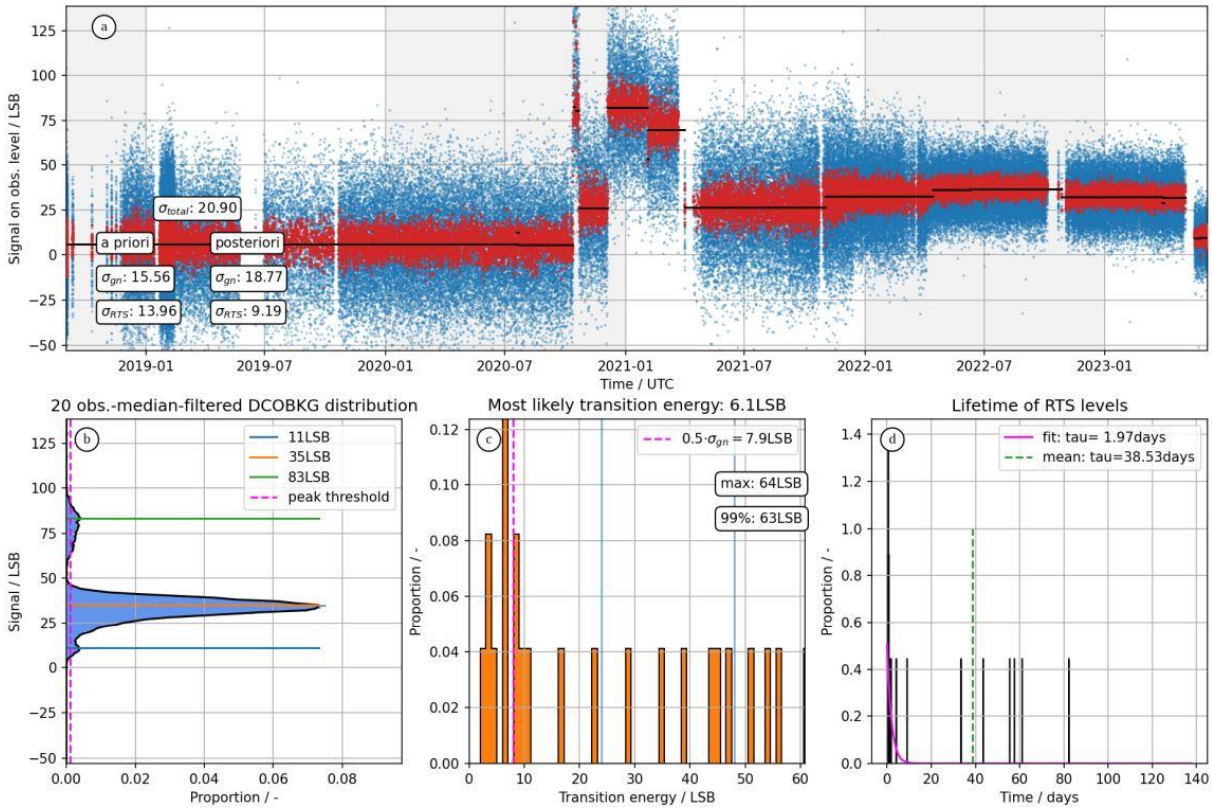

Figure 20: Characterization of Mie hot pixel [03,15]. Description of the panels see Figure 19.

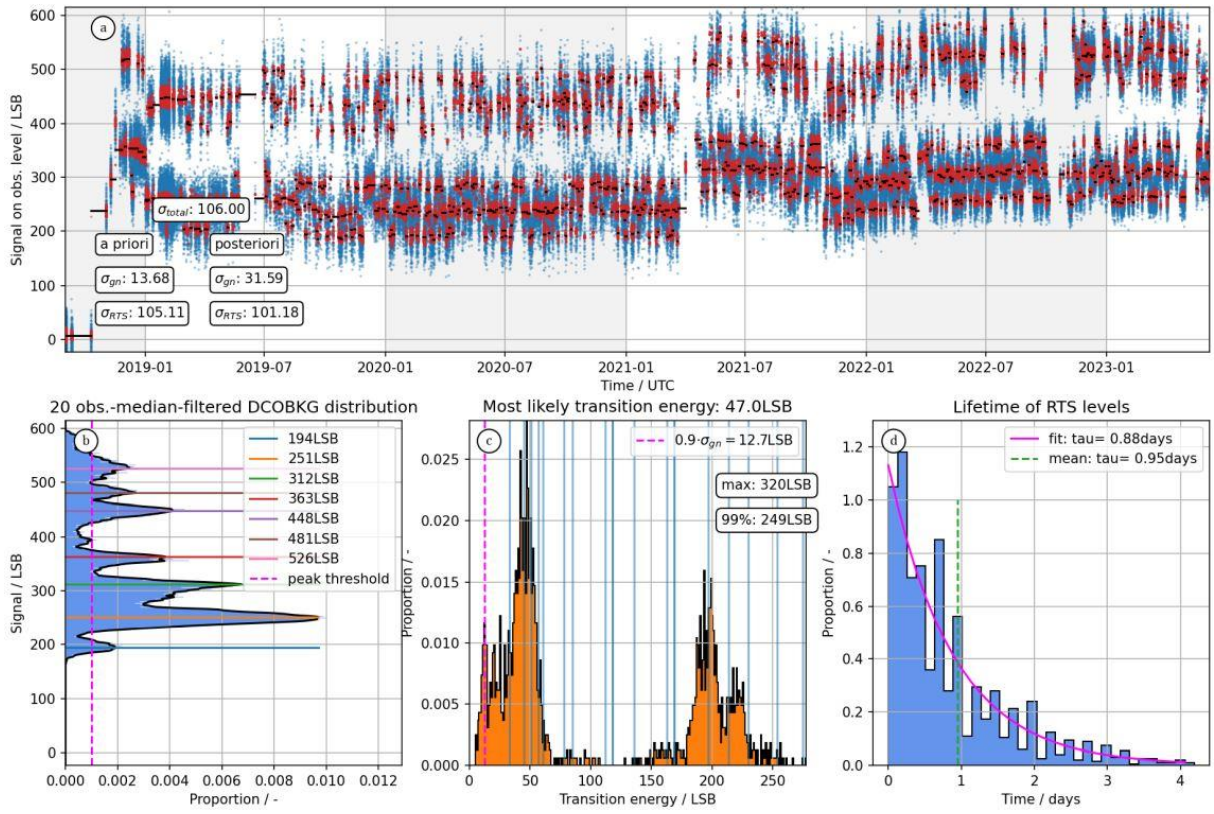

Figure 21: Characterization of Mie hot pixel [13,09]. Description of the panels see Figure 19.

Apart from the three categories of hot pixels shown above (mean shifts, RTS, combination of both), there are also some special cases which exhibit additional characteristics. For instance, Rayleigh hot pixel [03,02], activated on 8 May 2019, showed RTS noise and two mean shifts in the dark current level in February and October 2022. In addition, the dark current levels were slowly drifting to lower values between July 2020 and the first mean shift in February. Consequently, the distribution of dark current levels is strongly broadened.

The two Rayleigh hot pixels [13,15] and [16,04] stand out from all the others, as they introduced large wind biases in the corresponding range bins despite the dark current in memory zone (DCMZ) correction applied during the wind retrieval. The reason was traced back to a strongly reduced memory zone efficiency which will be discussed in section 3.3.3.

Lists with all Mie and Rayleigh hot pixels are given in Table 7 and Table 8, respectively. Besides the introduced classification and activation date and time, the lists provide the most likely step size between RTS levels and the average lifetime of the dark current levels. These parameters facilitate the detection of hot pixel steps despite large atmospheric signal variations using a change point detection tool which was developed for the reprocessing of the Aeolus data products (Weiler et al., 2022).

The classification of the hot pixels is also visible in Figure 20 which additionally illustrates their location on the memory zones of the Mie and Rayleigh ACCDs as well as the order of their onset. The maps reveal that the hot pixels are not randomly distributed, but show a certain clustering both locally and temporally. For instance, Mie hot pixels [17,05], [16,05], [17,07] and [18,04] are very close together and were activated within one year between June 2021 and June 2022. Conversely, there are no Mie hot pixels in the ACCD rows 21 through 23. The same holds for rows 2, 4, 12, 19 and 21 of the Rayleigh ACCD, whereas there were even four hot pixels in row 24.

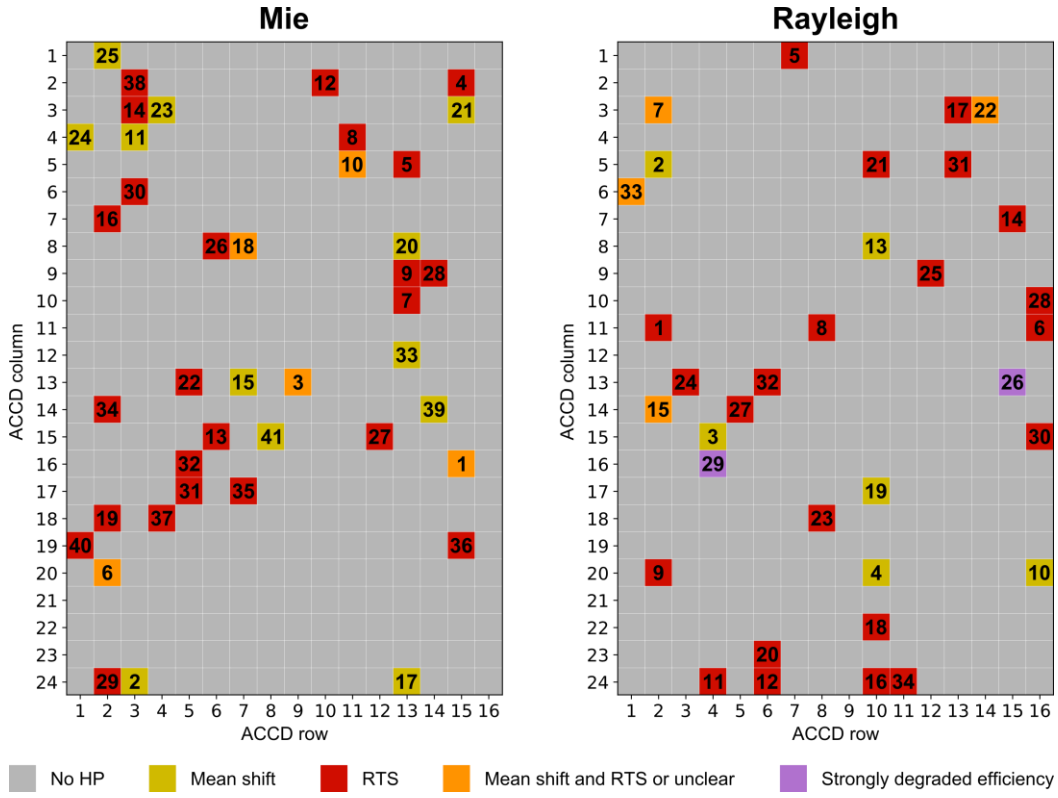

Figure 22: Overview of hot pixels on the Mie ACCD (left) and the Rayleigh ACCD (right). The colour coding refers to the classification of the individual hot pixel characteristics (see text), while the number indicates the order of the activation on the respective detector.

Table 7: Selected parameters of the hot pixels on the Mie ACCD. The pixel counting start from 1. The colour coding refers to the classification (see also Figure 22).

Hot pixel	Activation date, UTC time (if available)	Classification	Most likely step / LSB	Lifetime / hours
[01,02]	2021-03-03, 02:01:40	mean shifts	-	944
[02,03]	2022-06-11, 14:25:46	RTS	56	13
[02,10]	2020-02-28, 20:35:40	RTS	167	38
[02,15]	2018-10-24, 07:00:43	RTS	41	80
[03,03]	2020-05-10, 13:31:28	RTS	75	19
[03,04]	2021-02-21, 00:35:52	mean shifts	-	837
[03,15]	2020-10-12, 06:17:16	mean shifts	-	925
[04,01]	2021-03-02, 06:30:04	mean shifts	-	1355
[04,03]	2019-10-03, 22:21:52	mean shifts	-	2097
[04,11]	2019-07-19, 20:07:04	RTS	13	28
[05,11]	2019-10-03, 05:16:16	mean shifts, later RTS	51	108
[05,13]	2019-01-09, 14:22:55	RTS	11	51
[06,03]	2021-06-03, 13:07:49	RTS	126	75
[07,02]	2020-07-17, 03:22:16	RTS	247	33
[08,06]	2021-08-25, 06:38:37	RTS	48	14
[08,07]	2020-08-17, 19:04:52	mean shifts, later RTS	98	62
[08,13]	2020-09-17, 06:20:52	mean shifts	-	2240
[09,13]	2019-08-08, 05:04:28	RTS	26	15
[09,14]	2021-05-24, 22:40:49	RTS	67	64
[10,13]	2019-04-26, 00:27:22	RTS	23	72
[12,13]	2021-12-30, 20:28:58	mean shifts	-	895
[13,05]	2020-11-26, 21:10:04	RTS	69	89
[13,07]	2020-06-28, 00:33:16	mean shifts	-	155
[13,09]	2018-10-21, 17:19:07	mean shifts and RTS	47	21
[14,02]	2022-03-23, 12:06:22	RTS	56	25
[14,14]	2022-06-23, 15:53:34	mean shifts	-	277
[15,06]	2020-03-14, 09:02:40	RTS	14	87
[15,08]	2023-04-03, 15:58:50	mean shifts	-	37
[15,12]	2021-04-19, 04:00:13	RTS	51	11
[16,05]	2021-11-23, 09:11:58	RTS	47	17
[16,15]	Pre-launch	mean shifts, later RTS	11	108
[17,05]	2021-06-17, 05:05:25	RTS	45	14
[17,07]	2022-04-13, 11:29:22	RTS	12	24
[18,02]	2020-09-13, 04:36:52	RTS	12	19
[18,04]	2022-06-03, 12:22:46	RTS	62	34
[19,01]	2022-07-23, 07:49:46	RTS	17	13
[19,15]	2022-05-01, 08:25:22	RTS	49	34
[20,02]	2019-03-31, 03:39:34	mean shifts and RTS	65	72
[24,02]	2021-05-25, 23:40:01	RTS	17	43
[24,03]	Pre-launch	mean shifts	-	13
[24,13]	2020-07-24, 23:31:16	mean shifts	-	864

Table 8: Selected parameters of the hot pixels on the Rayleigh ACCD. The pixel counting start from 1. The colour coding refers to the classification (see also Figure 22).

Hot pixel	Activation date, UTC time (if available)	Classification	Most likely step / LSB	Lifetime / hours
[01,07]	2019-02-20, 07:57:22	RTS	19	76
[03,02]	2019-05-08, 21:01:22	mean shifts, slow drift, RTS	20	17
[03,13]	2020-08-22, 21:04:28	RTS	64	47
[03,14]	2021-04-07, 15:47:25	mean shifts, later RTS	68	17
[05,02]	2018-11-04	mean shifts	-	1560
[05,10]	2021-01-25, 12:32:16	RTS	25	16
[05,13]	2023-01-23, 13:19:31	RTS	33	22
[06,01]	2023-02-22	mean shifts and RTS	-	87
[07,15]	2020-04-18, 22:26:28	RTS	5	39
[08,10]	2020-01-28, 21:55:28	mean shifts	-	1822
[09,12]	2022-02-06, 21:20:34	RTS	11	24
[10,16]	2022-12-07, 16:55:19	RTS	18	16
[11,02]	2018-09-07	RTS	16	66
[11,08]	2019-06-15, 18:40:34	RTS	19	73
[11,16]	2019-03-17, 06:50:34	RTS	32	10
[13,03]	2021-07-03, 15:41:25	RTS	33	41
[13,06]	2023-01-23, 23:32:19	RTS	19	14
[13,15]	2022-06-26, 21:49:22	RTS and strongly reduced efficiency	13	9
[14,02]	2020-05-07	mean shifts and RTS	25	75
[14,05]	2022-11-25, 06:13:31	RTS	38	5
[15,04]	2018-11-24	mean shifts	-	662
[15,16]	2023-01-07, 21:05:07	RTS	14	25
[16,04]	2022-12-22, 09:33:19	RTS and strongly reduced efficiency	5	70
[17,10]	2020-12-03, 04:35:04	mean shifts	-	934
[18,08]	2021-05-11, 05:01:37	RTS	27	12
[20,02]	2019-08-01, 03:54:16	RTS	31	16
[20,10]	2019-01-27	mean shifts	-	187
[20,16]	2019-08-17, 08:37:04	mean shifts	-	972
[22,10]	2020-11-27, 20:53:28	RTS	9	18
[23,06]	2020-12-10	RTS	9	24
[24,04]	2019-08-29, 08:13:16	RTS	33	55
[24,06]	2019-12-21, 17:06:04	RTS	114	48
[24,10]	2020-07-06, 21:41:16	RTS	10	59
[24,11]	2023-05-17	RTS	2	36

The total number of hot pixels is 75 (Mie: 41, Rayleigh: 34) which corresponds to about 10% of all pixels of the two memory zones (768). Their activation followed a nearly linear trend with a time difference between successive hot pixel emergences of (23 ± 21) days. The left panel of Figure 23 shows that larger departures from linearity were present during the mission, e.g. in summer/autumn 2021 or between July and November 2022 when there was no new hot pixel for 124 days. However, no correlation was found between the hot pixel onset rate and space weather activity, nor with any platform or instrument parameters. In particular, the hot pixel activation could not be correlated with the K index, which is a measure of the disturbances of the horizontal component of the Earth's magnetic field, i.e., no threshold of activity could be identified (Weiler et al., 2021). It is also noticeable that, after the long gap in 2022, seven Rayleigh hot pixels became hot before another Mie hot pixel emerged.

The geolocation of the satellite during the onset of the individual hot pixels is depicted in the right panel of Figure 23, indicating a preponderance around the poles and the South Atlantic Anomaly (SAA) region. The latter is characterized by a reduced intensity of the Earth's magnetic field at altitudes between 200 and 800 km, resulting in a strong exposure of the Aeolus satellite (about 320 km altitude) to cosmic radiation. It was also found that transient events are accumulated around the SAA region, occurring about three times more frequently in the box between 40° to 60°S latitude and 60° to 30°W longitude compared to the rest of the globe. Nevertheless, the relative frequency of such events is very low with only 0.24% of all measurements being affected, equally distributed among all pixels on both detectors. Further studies revealed that in about half of the events, more than one pixel showed a spurious peak at the same time. In some cases, even more than 10 pixels are simultaneously affected, resulting in stripes on the memory zone which display the propagation of the cosmic ray across the detector.

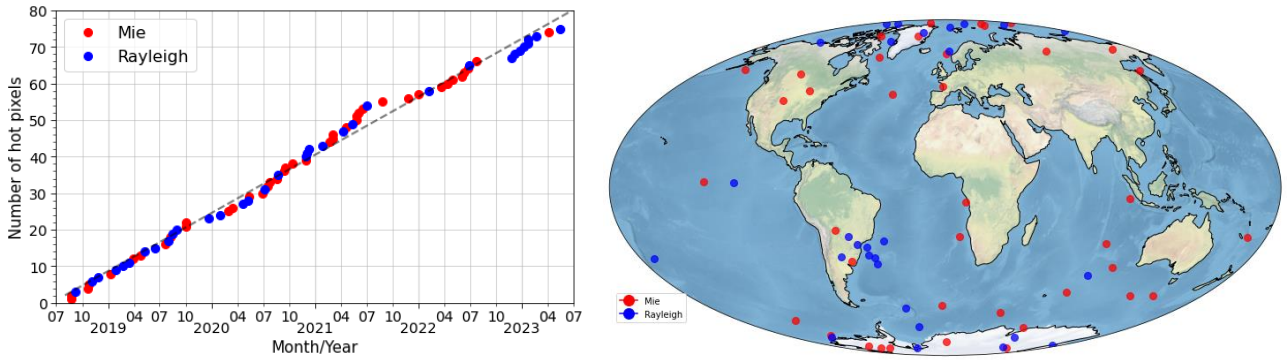

Figure 23: Left: Temporal evolution of the number of hot pixels over the mission timeline. Mie hot pixels [16,15] and [24,03] were already present before launch. Right: Geolocation of the satellite during the activation of each hot pixel on global map with Mollweide projection (only if data of the exact activation time is available). Mie and Rayleigh hot pixels are indicated as red and blue dots, respectively.

3.3.2 Temperature dependence of the dark current levels

Following a pre-test with the A2D ACCDs on ground in 2020, the temperature dependence of the dark current levels was investigated in the framework of the EOL activities (see also section 3.4). For this purpose, the ACCD temperature was increased from the nominal value of -30°C to -15°C in step of 5 K. The three non-nominal temperature settings at -25°C, -20°C and -15°C were kept for 4.5 hours (about three orbits) each which enabled a precise determination of the dark current levels on all pixels of the memory zone. However, the periods were too short to investigate the influence of temperature on the RTS noise on the hot pixels, let alone the probability of their activation.

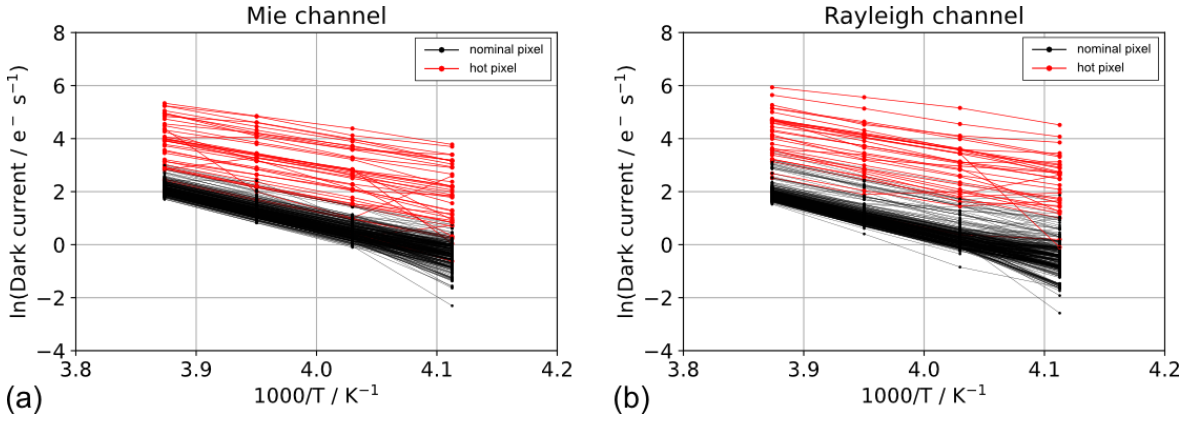

Figure 24: Arrhenius plots for all pixels of the Mie (a) and Rayleigh ACCD (b). Hot pixels are indicated in red.

Based on the test data, the median dark current level was calculated for all individual pixels at the four temperature settings. The temperature dependence was found to follow the Arrhenius law (Widenhorn et al., 2002), so that the temperature coefficient could be determined for each pixel from a linear fit of the respective Arrhenius plot (Figure 24). This procedure yielded maps of the temperature coefficients which are depicted in Figure 25 together with the corresponding histograms for the two ACCDs.

The temperature coefficients, which are related to the activation energies for the dark current on the individual pixels (Widenhorn et al., 2002), are relatively consistent across both ACCDs with median values of $E_{a,Mie}$ = (0.87 ± 0.09) eV and $E_{a,Ray}$ = (0.87 ± 0.13) eV, respectively. The energies are systematically smaller by about 25% for the hot pixels: $E_{a,Mie,hot}$ = (0.67 ± 0.13) eV and $E_{a,Ray,hot}$ = (0.65 ± 0.16) eV. This result is expected for surface dark currents that are caused by radiation-induced displacement damages which strongly supports the assumption that the dark current anomalies were "conventional" hot pixels and not caused by CICs.

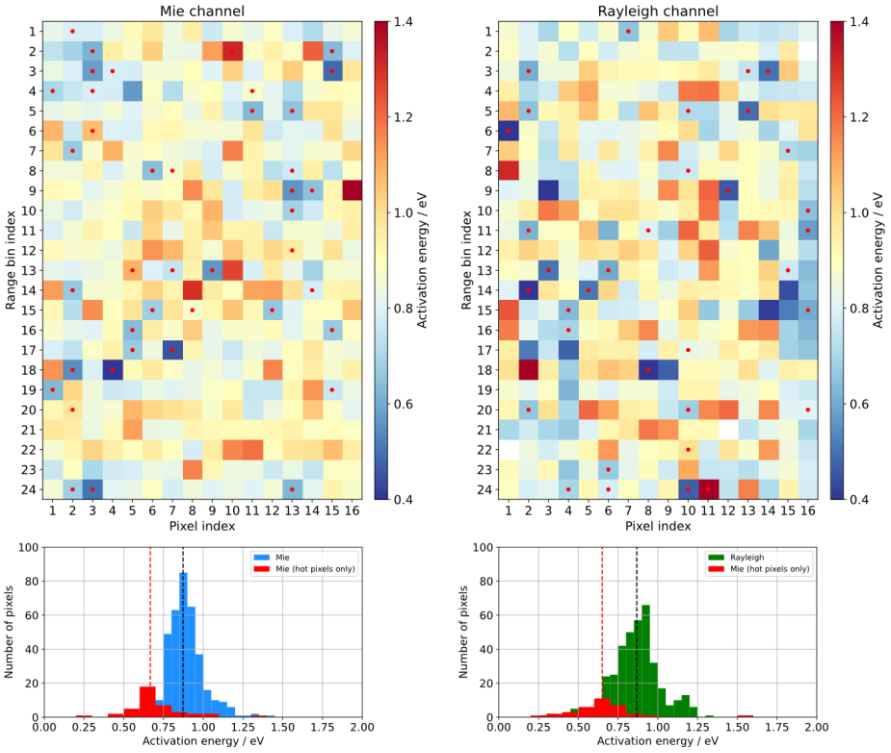

Figure 25: Activation energies of the pixels from the memory zone of the Mie (left) and Rayleigh ACCD (right). Hot pixels are indicated by a red dot. The corresponding histograms are shown in the bottom panels.

When excluding the hot pixels, the dark current rates at the nominal ACCD temperature of -30°C were DC_{Mie} = (0.72 ± 0.31) e- s^{-1} and DC_{Ray} = (0.64 ± 0.31) e- s^{-1} (Figure 26), i.e., similar for both detectors when considering the spread among all pixels. Note that the radiometric gain factors of g_{Mie} = 0.684 LSB/e- and g_{Ray} = 0.434 LSB/e- were used for conversion from LSB to e- (see Table 6). In addition, the number of pulses P = 114 and the pulse repetition frequency (50.5 Hz) had to be considered.

The derived temperature-dependence allowed for the extrapolation of the dark current rates to -50°C, which is the temperature specified for the Aeolus-2 detectors, yielding DC_{Mie} = (0.017 ± 0.012) e- s^{-1} and DC_{Ray} = (0.015 ± 0.012) e- s^{-1}. This corresponds to a reduction by a factor of ≈40 compared to -30°C for the nominal pixels. Due to the smaller activation energies, i.e., temperature sensitivities, of the hot pixels, their dark current rates are only reduced by a factor of ≈17. Nevertheless, 47 of the 75 hot pixels at -50°C (63%) would have dark current rates <0.8 e- s^{-1} and are thus comparable to the dark current levels of normal pixels at -30°C during the Aeolus mission. However, they would still stand out with similarly increased rates compared to that of normal pixels.

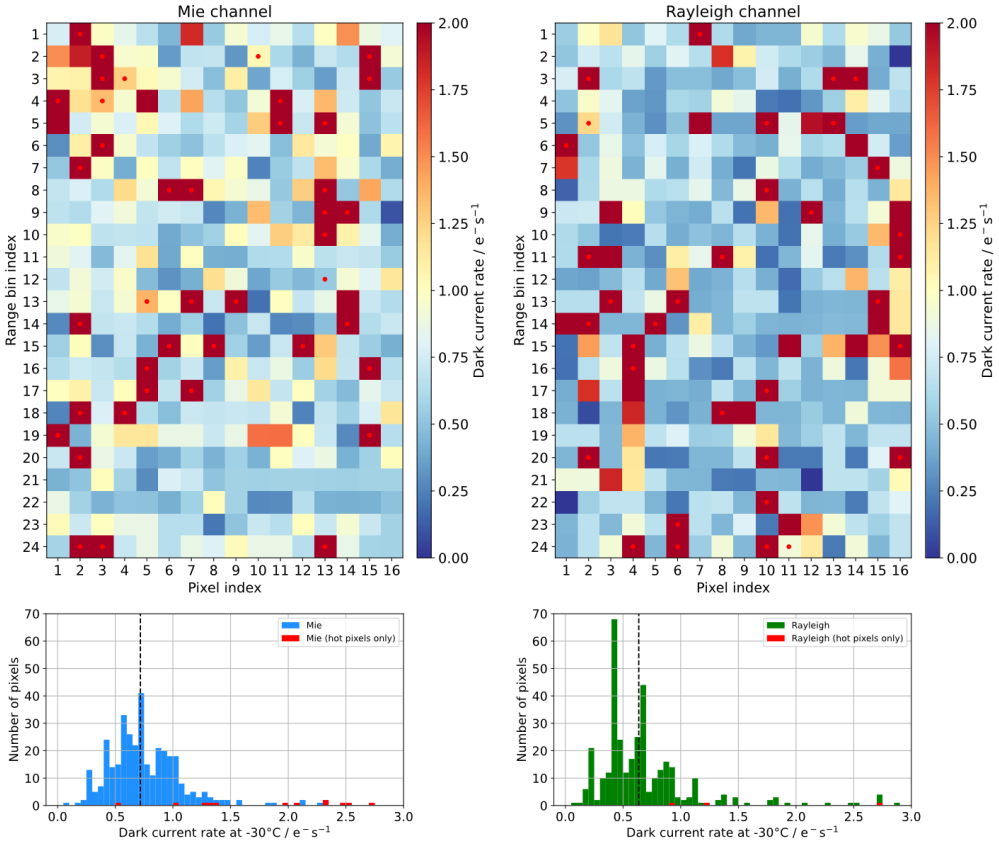

Figure 26: Dark current rates at -30°C of the pixels from the memory zone of the Mie (left) and Rayleigh ACCD (right), as determined from the Arrhenius law. Hot pixels are indicated by a red dot. The corresponding histograms are shown in the bottom panels.

3.3.3 Memory zone efficiency

The implementation of the regular DCMZ measurements, i.e. DUDEs, in early 2019 largely eliminated the systematic errors that were introduced by the dark current fluctuations on the steadily increasing number of hot pixels. Remaining biases were only present in periods between an RTS transition and the following dark current calibration that was then used for the processing of the next orbits. In early 2023, however, a large persistent Rayleigh wind bias of 8 m/s was noticed in range bin 16 which was traced back to hot pixel [16,04] which was activated on 22 December 2022. In contrast to the other hot pixels, its onset involved a signal saturation not only on the pixel itself, but also on the three pixels below in the same ACCD column, suggesting a particularly strong exposure to cosmic radiation. Following this event, pixel [16,04] exhibited a reduced memory zone efficiency (MZE), meaning that the measured solar background levels were about 15% lower than those measured on other pixels of the same column 4 but other rows (=range bins) after normalization to the respective integration time. Consequently, the underestimation of the signal levels led to a systematic error of the Rayleigh useful signal in range bin 16, and thus to a wind bias, which could only be partly compensated for by switching off the DCMZ correction for this pixel, thereby increasing the signal levels by the amount of the dark current offset.

Subsequent investigations of this anomaly revealed that Rayleigh hot pixel [13,15], which had become hot already on 26 June 2022 also showed a significantly reduced MZE, albeit to a lesser extent (-4%), which is why this was only discovered afterwards. The analysis of a dedicated test, performed in the period between the laser switchover in May 2023, allowed for the determination of the efficiency of all illuminated pixels on the Rayleigh ACCD, i.e., those on columns 2 through 6 and columns 11 through 15. The resulting MZE map is shown in the right panel of Figure 27 together with the maps obtained

from earlier data. Since the calculation of the MZE requires sufficient signal intensity on the respective pixels and the absence of atmospheric backscatter signals, i.e., only strong solar background, the maps could only be derived on a few occasions during the mission lifetime when the laser was switched off. The maps illustrate in the inhomogeneity of the MZE across the Rayleigh ACCD of about ±3% which has an impact on the Rayleigh useful signal, and ultimately on the Rayleigh wind bias in the respective range bins. Extreme cases are the aforementioned pixels [13,15] and [16,04] which appeared in 2022. As a lesson learnt for Aeolus-2, extended measurements of this kind should be performed on a regular basis in order to characterize the MZE of the detectors and to potentially correct for its non-uniformity. Due to the low sensitivity of the Mie channel to broadband solar background and the correspondingly low signal levels on the Mie ACCD, a corresponding MZE map could not be derived for the Mie channel.

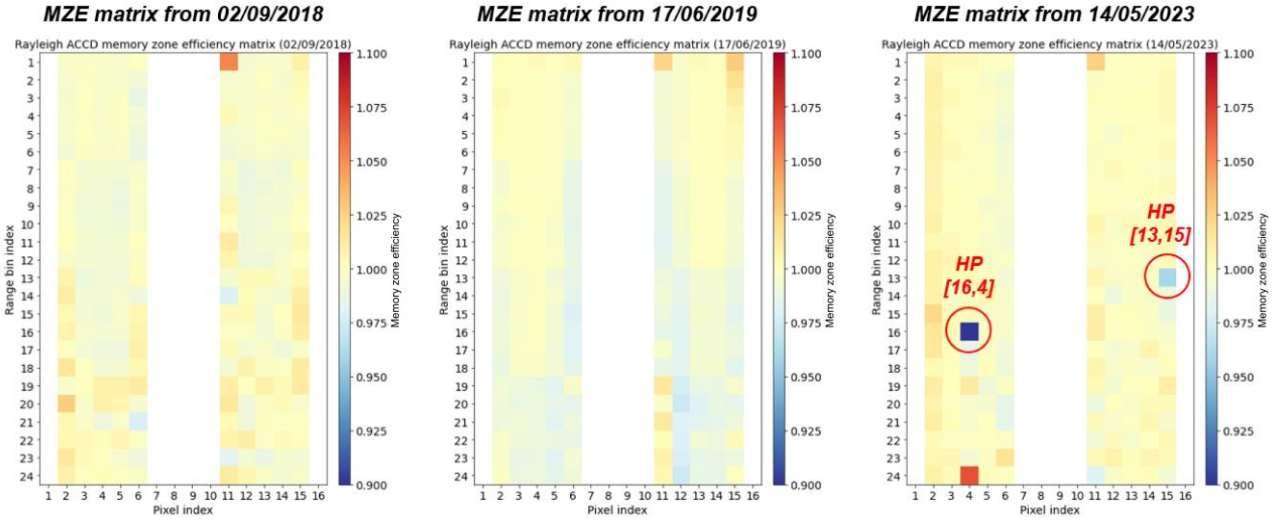

Figure 27: Memory zone efficiency (MZE) matrix for the Rayleigh ACCD obtained on three occasions during the mission on 02/09/2018 (left), 17/06/2019 (middle) and 14/05/2023 (right). Determination of the efficiency requires sufficient signal intensity on the respective pixels. Therefore, data is only available on illuminated pixels, i.e., in columns 2 through 6 and columns 11 through 15.

3.3.4 Dark current calibrations and anomalies in the image zone

The dark current levels and rates were also assessed in imaging mode at times when the instrument was in laser burst warm-up (LBWU) mode, i.e., at the very beginning of the mission, during laser switchovers and in the frame of the EOL activities (section 3.6). Figure 28 depicts an example of an in-orbit Dark Current Calibration (DCC) measurement on 31/08/2018, i.e. only nine days after launch. It represents the raw dark signals averaged over all measurements on the 16 x 16 pixels image zone of the ACCD. Both detectors exhibit a vertical gradient of about 2e- from top to bottom. The gradient is also present on the two pixels at both edges of the ACCD (not shown) which represent the DCO, so that it is removed when applying DCO correction on the raw dark signals. This gradient was found to be stable over the mission lifetime, although the DCO increased by about 2% on both detectors over the nearly five years.

Apart from the vertical DCO gradient, a horizontal gradient from left to right was evident in the raw DCC signals, especially on the Mie channel. As the DCO correction was applied per row, the horizontal gradient was still present in the DCO-corrected signals. However, it was smaller (<0.3 e- on both ACCDs) than the vertical gradient and also stable over the mission lifetime. The same holds true for the dark signal non-uniformity (DSNU) and the mean dark signal of the two detectors which were <0.2 e- in accordance with on-ground tests (Masoumzadeh et al., 2022).

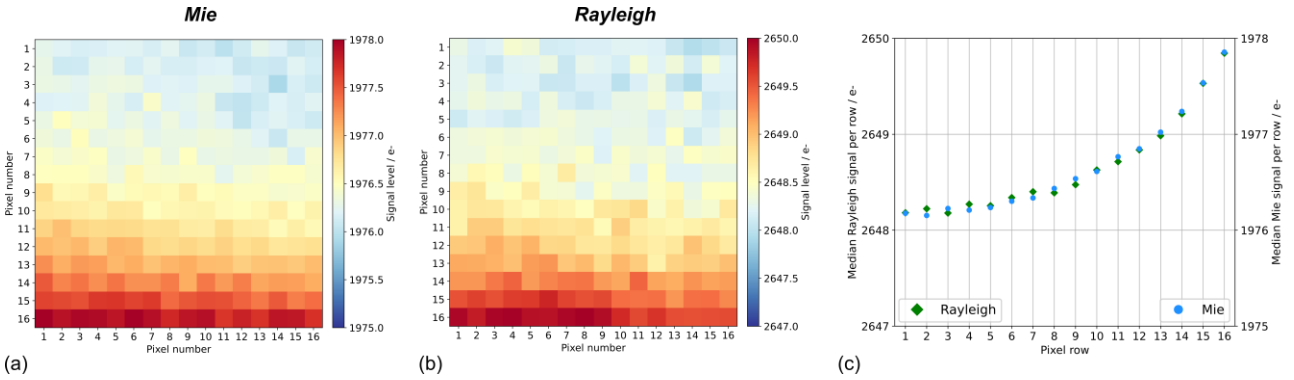

Figure 28: Dark current calibration at the beginning of the mission on 31/08/2018: The raw signals including the detection chain offset on the Mie (a) and Rayleigh ACCD image zone (b) exhibit a vertical gradient of about 2e-. The median signals per row are shown in panel (c).

Like on the ACCD memory zones, pixel anomalies were also identified on the respective image zones of the two detectors. Most notably, enhanced signal levels appeared along certain columns of the image zone with decreasing intensity from the bottom to the top of the image (vertical smearing), which pointed to a charge transfer inefficiency (CTI) effect during the read-out process when the charges are shifted to the memory transfer section row by row, starting from row 16 toward row 1. This anomaly was strongest in column 14 of the Rayleigh ACCD and was first observed in November 2018.

Starting from early May 2022, the neighbouring column 15 was affected as well (Figure 29). Further analysis showed that the signal intensity on the anomalous pixels was correlated with that on the right hemisphere of the Rayleigh image, i.e. it was fed by both solar background and atmospheric backscatter signals. As the additional signal levels accounted for only about 1% of the total signal levels when the laser was switched-on and atmospheric backscatter was present, this effect is assumed to have had no significant impact on the Aeolus data products. It would have had a detrimental effect on the response stability, if the intensities had been higher, because a post-processing correction would have been difficult without a regular monitoring of the imaging mode DCO. More results on the nature and root-cause of the anomalous pixels was revealed during special tests, as described for EOLA#16 in section 3.6.2.

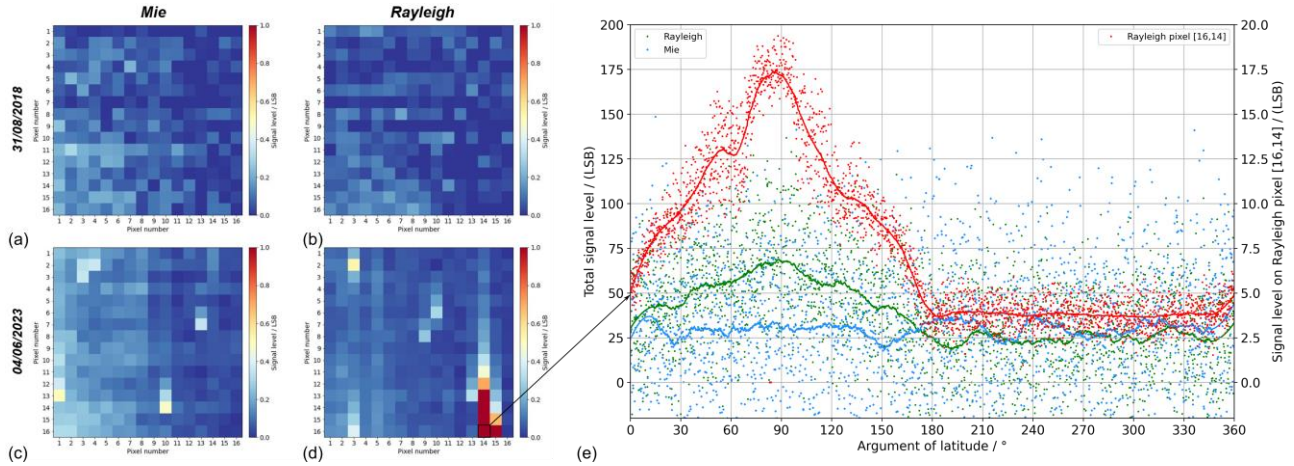

Figure 29: Signal anomalies in the image zone: The left and middle panels depict the signal levels on the Mie (a,c) and Rayleigh ACCD (b,d) after subtraction of the DCO measured in dark current calibration (DCC) mode at the beginning (31/08/2018) and the end of the mission (04/06/2023), respectively. Panel (e) shows the orbital variation

of the Rayleigh (green) and Mie signal levels (light blue) together with those on Rayleigh pixel [16,14] (red), measured over multiple orbits with the laser being switched-off.

3.3.5 Lessons learnt from the detector performance monitoring

- A root cause analysis regarding the activation of hot pixels should be performed during the preparation of future missions in order to define strategies for their mitigation. Extensive on-ground tests should be performed to characterize nominal and hot pixels over longer time scales and at different temperatures. Moreover, it is recommended to explore possibilities for the reduction or even elimination of RTS noise on activated hot pixels, e.g. annealing procedures.
- The determination of the MZE map should be performed on a regular basis, e.g. two times per year, in order to monitor its temporal variability to potentially correct for its non-uniformity.
- Regular monitoring of the dark current in the image zone, e.g. by Hi-DCC measurements (see section 3.6.2) is recommended for future missions, to properly characterize anomalies like CTI or defect pixels and to develop corresponding correction schemes. This is not possible based on lidar mode data only.

3.4 Characterization of the ALADIN spectrometers

Benjamin Witschas, DLR

An instrument spectral registration (ISR) is an Aeolus measurement mode which is useful to characterizing the Rayleigh (RSP) and Mie (MSP) spectrometers, and thus, the ALADIN receiver alignment in detail. The data obtained from an ISR measurement within the AUX_ISR file contains 147 observations in Lidar mode from the internal reference path, and each observation itself contains three different frequency steps which are spectrally separated by 25 MHz (similar as for IRC measurements). Hence, the ISR frequency range is (3 × 147 – 1) × 25 MHz = 11 GHz and thus, covers one free spectral range (FSR) of the Fabry-Perot interferometers (FPIs) of the RSP and five FSRs of the Fizeau interferometer of the MSP. During the mission, ISR measurements were performed on a weekly basis, and more frequently during particular test phases. In total, 335 ISRs were performed between September 2018 and April 2023 and provide a unique data set for characterizing the ALADIN spectrometer performance during the mission.

Usually, the results of ISR measurements are used to generate AUX_RBC files used to perform the "Rayleigh-Brillouin" correction (RBC) in the L2B processor (see also Section 4.5). Additionally, by a detailed analysis of the acquired interferometer transmission curves, conclusions regarding the instrumental alignment and ongoing drifts can be drawn. To do so, respective mathematical model functions are derived and used in non-linear fit procedures. The tools used in this study were pre-developed already before the launch of Aeolus based on measurements performed with the ALADIN airborne demonstrator (A2D) and have been adapted accordingly within the last years. In this section, the main outcomes from ISR measurements are discussed. Further details about the analysis procedure and the ISR data raw processing can be found in Witschas et al. (2019, 2020a, 2020b, 2022).

3.4.1 Model functions for the FPI and the Fizeau interferometers

The spectral shape of the light transmitted through the direct-channel FPI $\mathcal{T}_{\mathrm{dir}}(f)$ is described by

$$\mathcal{T}_{\mathrm{dir}}(f) = \mathcal{I}_{\mathrm{dir}} \cdot \left(1 + 2\sum_{k=1}^{\infty} R_{\mathrm{dir}}^{k} \cos\left(\frac{2\pi k}{\Gamma_{\mathrm{FSR_{dir}}}}(f - f_{0_{\mathrm{dir}}})\right) \exp\left(-2\left(\frac{\pi k \sigma_{g_{\mathrm{dir}}}}{\Gamma_{\mathrm{FSR_{dir}}}}\right)^{2}\right)\right) \cdot \mathcal{R}_{\mathrm{Fiz}}(f),$$

where $\mathcal{I}_{\mathrm{dir}}$ is the mean intensity per FSR, R is the mean FPI plate reflectivity, f_0 it the centre frequency, Γ_{FSRdir} is the FSR, σ_{gdir} is the defect parameter and $\mathcal{R}_{\mathrm{Fiz}}(f)$ depicts the frequency dependent reflection on the Fizeau interferometer, which is described by an empirically derived formula according to

$$\mathcal{R}_{\mathrm{Fiz}}(f) = \left(1 - \mathcal{I}_{\mathrm{Fiz}}\left(\cos\left(\frac{\pi}{\Gamma_{\mathrm{FSR_{Fiz}}}}(f - f_{0_{\mathrm{Fiz}}})\right)^{4} - d_{\mathrm{Fiz}}\right)\right),$$

where $\mathcal{I}_{\mathrm{Fiz}}$ is the modulation depth (peak to peak), Γ_{FSRFiz} is the FSR of the Fizeau interferometer, $f_{0\mathrm{Fiz}}$ is the centre frequency (valley of the cosine function), and d_{Fiz} is the y-axis shift from zero and is set to be constant (d_{Fiz} = 0.5). To describe the transmission through the reflected-channel FPI, one additionally has to consider the reflection on the direct-channel FPI, which makes it more complicated as discussed in Witschas et al. (2022). To investigate the ALADIN instrumental alignment and ongoing spectral drifts, a downhill simplex fit of the FPI model functions is applied to ISR data. Except for Γ_{FSR} = 10946 MHz and d_{Fiz} = 0.5, all parameters are not constrained and thus a result of the fit routine.

The narrowband signal that is transmitted through the Fizeau interferometer is forming a fringe on the ACCD detector, where the fringe position is depending on the frequency of the illuminating light. Due

to the small wedge angle and the low finesse of the ALADIN Fizeau interferometer, the originating fringe can be described by a Lorentzian peak function according to

$$\mathcal{T}_{\mathrm{Fiz}}(x) = \mathcal{I}_{\mathrm{Peak_{height}}}\left(\frac{\Delta f_{\mathrm{FWHM_{Fiz}}}^{\,2}}{4(x-x_0)^2 + \Delta f_{\mathrm{FWHM_{Fiz}}}^{\,2}}\right),$$

where $\mathcal{I}_{\mathrm{Peakheight}}$ is the peak amplitude, $\Delta f_{\mathrm{FWHMFiz}}$ the FWHM, and x_0 the position of the fringe, which is called the Mie response. Recent investigations have revealed that the actual spectral shape of the Fizeau fringe is following a Voigt profile, which is so far not considered for the ISR data analyses.

An exemplary plot of ISR data is shown in Figure 30, for a measurement performed on 7 September 2020. Panel a) shows the FPI transmission curves for the direct (blue crosses) and the reflected channel (orange crosses) as well as the corresponding best fits indicated by the light blue and yellow line, respectively. Panel b) shows the corresponding relative residual of the data to the fit, illustrating the very good accordance for all signal levels and frequencies. The small, but distinct modulations are remaining from an imperfect representation of the Fizeau reflection as it is also obvious from panel d), which shows the integrated Mie peak height, and hence, a quantity that is proportional to the frequency dependent transmission through the Fizeau interferometer. Panel c) depicts the Mie response which is also varying with laser frequency.

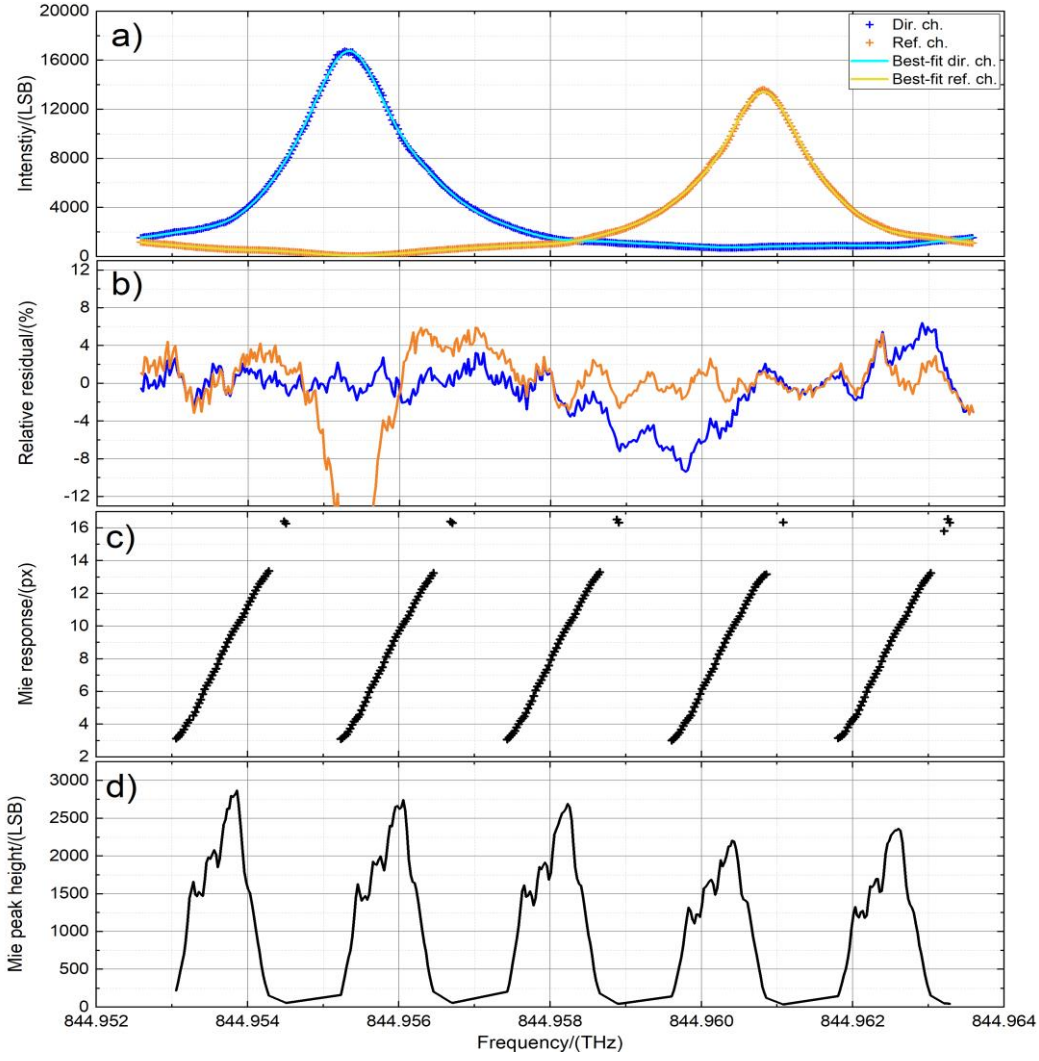

Figure 30: (a): FPI transmission curves for the direct channel (orange crosses) and the reflected channel (blue crosses) measured during the ISR performed on 7 September 2020. The light blue and yellow lines indicate the respective best fits. (b): Corresponding relative residuals. (c): Mie response. (d) Mie peak height.

All 335 ISR measurements were analyzed during the DISC phase E2. A few selected main results as well as the "lessons learnt" for Aeolus and other space missions are summarized below.

3.4.2 Laser energy drift correction

Already at the beginning of the mission, it was realized during an ISR measurement, that the UV output laser energy varies during the frequency scan. Hence, the intensity detected per frequency scan needs to be corrected accordingly by a photo diode signal (PD-74) in the UV section of the respective laser transmitter. A detailed analysis of the measured FPI transmission curves measured during ISRs revealed that the energy correction of the short-wave modulations works reasonably well, but the correction of the overall trend seems to be insufficient. This is especially obvious from the skewness that is visible in the relative residuals of the analyzed FPI transmission curves. Such a tilt is not explainable by incorrectness caused by the fit model as only symmetrical functions are used for the analysis. Thus, it is likely that the energy drift detected by PD-74 is not completely representative of the internal Rayleigh channel signal. For that reason, ISR data was used to determine an additional Energy Drift Correction Factor (EDCF), that accounts for linear drifts in the energy monitoring by PD-74 during scans over a large frequency range. After this additional correction, the relative residuals of the FPI fits are not skewed anymore (see also panel b) in Figure 30. It is worth mentioning that the EDCFs vary over time and are slightly different for the direct and the reflected channel FPIs. For the reprocessed Aeolus data, the EDCFs are provided on a weekly basis for both FPI channels.

In addition, as the frequency dependency of the laser energy also changes with the laser cold plate temperature, ISR measurements were used to optimize the laser output energy for the frequency set point where the wind measurements were performed. Although it is not known if the ATLID laser on EarthCARE may behave similarly, it should be kept in mind that a frequency scan (as performed during ISR measurements) may help to significantly optimize the laser and overall instrument performance.

3.4.3 FPI centre frequencies and spectral spacing

The quality of Aeolus Rayleigh winds is among others depending on the stability of the Rayleigh spectrometer which is composed of two sequentially illuminated FPIs which are spectrally separated by about 5.4 GHz to measure the frequency shift of molecular scattered light by means of the double-edge technique. A quantity that is representative for the Rayleigh spectrometer stability is the FPI spectral spacing, which is defined as the spectral distance between the centre frequencies of the direct channel and the reflected channel with the direct channel being placed at the lower frequencies. The spacing evolution derived from ISR data is shown in Figure 31 (black crosses). The red line indicates an exponential fit to the data to visualize the settlement of the spectral spacing evolution.

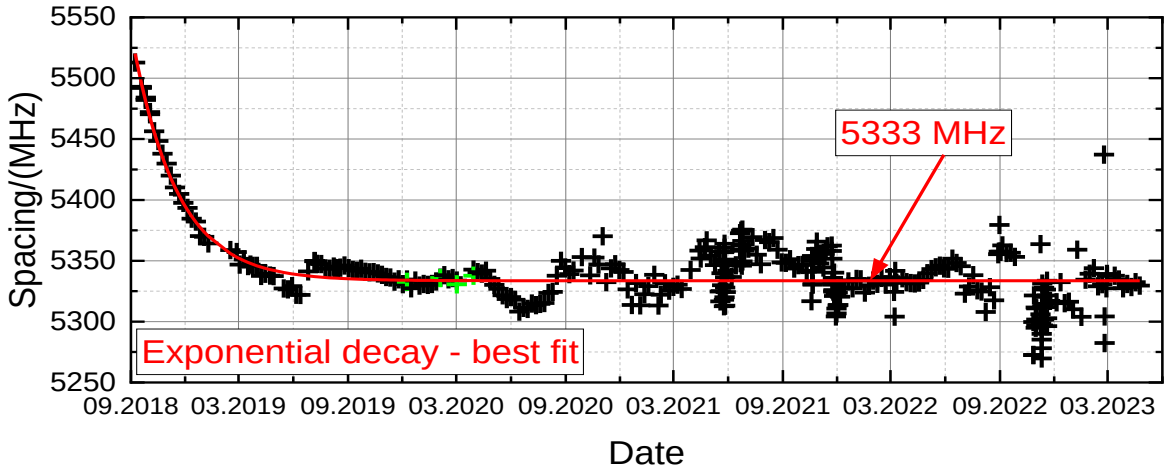

Figure 31: Spectral spacing between the direct channel and the reflected channel of the FPIs (black crosses) and an exponential decay fit (red) to illustrate the settlement of the spacing drift.

The spectral spacing is an important measure, as a significant spacing drift would lead to systematic errors in the retrieved wind speeds, if not considered in the response calibrations, whereas an equal centre frequency drift for both the direct and the reflected channel would not affect the wind retrieval. At the beginning of the mission, the spacing was determined to be about 5550 MHz and then decreased rapidly to smaller values. This is a result of the centre frequency drift of the direct and the reflected channel occurring towards different spectral directions and with a different rate in this period (not shown). Although the root-cause for this behaviour is not known yet, it could be explained by an outgassing process of air happening inside the cavity of the FPIs. This is affirmed considering the spacing of about 5450 MHz as determined during the thermal vacuum test before launch.

The drift of the spacing shows a settlement which is even independent of the switch to the FM-B laser in June 2019. The settlement continues/remains until the end of the mission asymptotically reaching a spacing of 5333 MHz. During the course of the mission, the spacing shows modulations of ±30 MHz which are caused by the temperature changes in the instrument that happened during the eclipse phases. Thus, it can be summarized that the overall Rayleigh channel performance and alignment was very stable during this mission after a settling phase of about 9 months, but on the other hand also very sensitive even to small temperature changes of a few 10 mK happening during the eclipse phases.

Except for the FPI centre frequencies and the resulting spectral spacing, other FPI parameters and their evolution in the course of the mission have been analyzed as discussed in detail in Witschas et al. (2022). For instance, the mean intensity showed a clear signal decrease as it was also observed from other analyses. The benefit of using ISR data is, that they are independent of the frequency set point, as the entire frequency range is analyzed. Furthermore, the FWHM of the FPI filter curves was analyzed, showing a rather stable width of about 1.6 GHz, in case that only the reflectivity and the defect finesse is considered, but the Fizeau reflection is excluded. When including the Fizeau reflection (as it is in reality), the width of the FPIs can vary by up to 150 MHz, depending on the spectral location of the Fizeau reflection with respect to the FPIs.

Another important investigation performed by Michael Vaughan (OLA) was also triggered by ISR and IRC measurements as it was realized that the centre frequencies derived from the INT signal seem to differ by up to more than 100 MHz compared to the one derived from the ATM path. Careful analysis (see also Witschas et al., 2022) revealed that the different field of views (FOV) of the INT and the ATM

path, together with an off-axis illumination of the spectrometers can explain the observed centre frequency difference. This finding also improved the derived AUX_CAL and AUX_RBC files.

3.4.4 Fizeau illumination function

Before the light is illuminating the FPIs, it is reflected on the Fizeau interferometer. Hence, any changes in the spectral transmission and reflection of the Fizeau interferometer, should have an impact on the Rayleigh channel. In the Fizeau interferometer, light is successively reflected between the surface coatings of the two plates set at the required wedge angle. Multiple interference occurs, ideally leading to straight-line fringes parallel to the wedge vertex. The integrated fringes can be approximated to be Lorentzian shaped and appear at different positions on the detector depending on the light's frequency. Hence, the fringe peak height acquired during an ISR measurement at different frequencies is a representation of the illumination function of the Fizeau interferometer. Based on the illumination function, alignment changes or potential damages in the optical path and the laser beam profile can be observed and investigated in lidar mode, similar to what is done in imaging mode with the LBM procedure.

In Figure 32, the Mie peak height of the central USR (Useful spectral range: part of the frequency range, which is imaged onto the 16 pixels of the ACCD of about 1.6 GHz) is shown for all ISR measurements performed with FM-A (left) and FM-B (right). To better emphasize the evolution over time, the curves are normalized to unit area. Brownish colours correspond to the early time of the respective laser period and blueish colours to the later times.

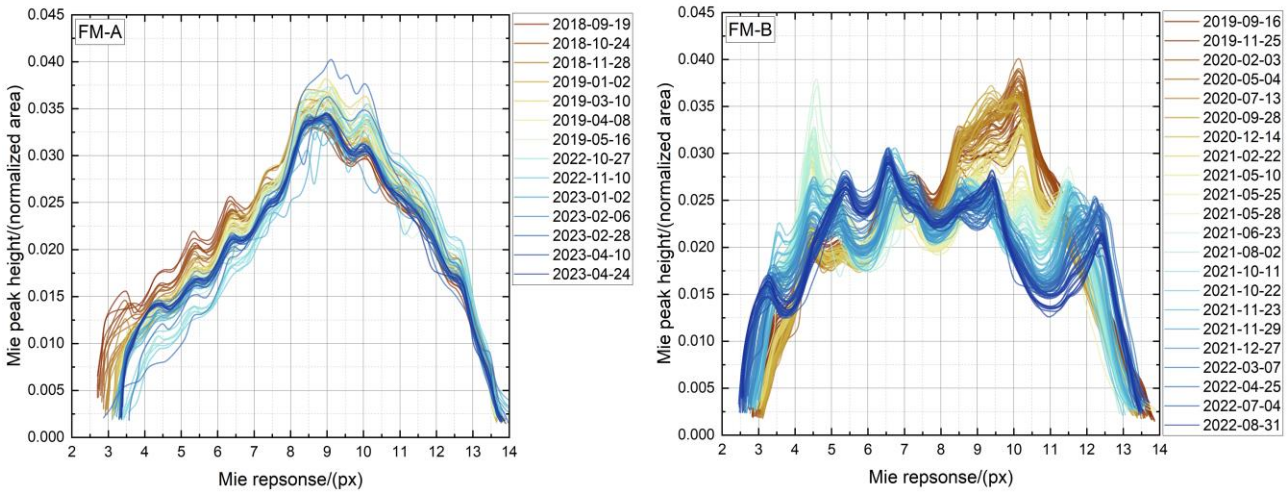

Figure 32: Mie peak height versus Mie response obtained during ISR measurements normalized to unit area for the FM-A (left) and the FM-B (right) as a representation of the evolution of the Fizeau interferometer spectral illumination.

What immediately can be seen is that the Fizeau transmission looks different for FM-A and FM-B and that it evolves with time. Although the pronounced maximum around the Mie response of 9 px is similar for FM-A and FM-B, the distribution for smaller Mie responses looks different, which points to a different intensity distribution of the illuminating beam or rather different illumination conditions as for instance clipping on other optical elements. Additionally, it can be recognized that for FM-A, the width of the Fizeau transmission is decreasing with time, which could be explained by a shrinking beam diameter or

a change in the divergence of the illuminating beam. For FM-B, the width is first decreasing until end of 2020, and then increasing again. Furthermore, it is obvious that not only the width but also the overall spectral features are evolving, especially for the FM-B period. The pronounced feature around pixel 10 vanishes until the end of operation which is likely to be due to LIC or LID.

These results demonstrate that a characterization of the Fizeau illumination function on a regular basis is needed (see also Section 4.3). The detailed fringe analysis also led to a novel Mie fringe analysis algorithm – the R_4 algorithm, developed by Michael Vaughan (OLA), that shows a similar accuracy than the Mie Core 3, but with a factor of 100 and more faster computation time, as it is based on an intensity ratio approach but not on an iterative fit procedure. Details about this algorithm are summarized in Witschas et al. (2023).

3.4.5 Summary, conclusion and lessons learnt from ISR measurements

- Data resulting from internal path measurements over a large frequency range (e.g. 11 GHz or rather at least over one entire FSR of the spectrometer) are valuable to characterize the spectrometer and laser performance
- The repetition cycle of one week is suitable to monitor instrumental alignment changes.
- A frequency step size of 25 MHz was helpful to investigate features as the imprint of the Fizeau reflection. If there are time constraints, larger frequency steps of e.g. 50 MHz could also be of interest.
- ISR measurements revealed the large frequency dependency of the laser energy and the uncertainty of the laser energy measurement over the entire frequency range. This fact should be considered for Aeolus 2. A better laser energy measurement characterization has to be performed on ground for the entire frequency range.
- ISR measurements were very useful to optimize the laser cold plate temperature to achieve maximum laser output energy at the frequency of the wind measurements. Such an approach might also be useful for the ATLID laser on-board EarthCARE and the Aeolus-2 lasers.
- The spectral spacing drift in the beginning of the mission is not yet understood by might be explained by an outgassing process. After that, the Rayleigh spectrometer performance was very stable throughout the mission. Still, the small temperature fluctuations during the eclipse phase were obvious.
- ISR measurements together with the imaging Fizeau interferometer revealed a 1-D information of the illumination function which contains information of the laser beam profile and the optical path. The evolution of the illumination function indicated LIC/LID in the optical path in the course of the mission.

3.5 IRC and IRONICS

Uwe Marksteiner, DLR and Michael Rennie, ECMWF

3.5.1 Instrument Response Calibrations

The Instrument Response Calibration (IRC) constitutes a fundamental part of the Aeolus processing chain and the basis for accurate and precise wind information provided to the global user community. The IRC is a crucial instrument mode for the wind measurement and has, hence, been extensively investigated with the ALADIN Airborne Demonstrator already before launch of the Aeolus satellite (Marksteiner et al., 2018). IRCs are used to determine the relationship between the Doppler frequency shift on the backscattered light, i.e. the wind speed, and the response of the Rayleigh and Mie spectrometers. This is achieved by sampling a frequency range of 1 GHz in steps of 25 MHz around the nominal laser frequency for the wind measurement. Whereas Aeolus wind measurements are obtained under an off-nadir viewing angle of 35° (satellite attitude), IRCs are performed in nadir viewing mode, thereby avoiding potential additional frequency shifts due to the horizontal wind component.

The special importance of the IRC mode has changed with the detection of unexpected and varying wind speed biases after the launch of Aeolus. These biases could neither be addressed by an IRC nor by the HBE, but instead required the introduction of a new correction method which considered the temperature gradients across Aeolus' primary telescope mirror. Regarding L2B winds this effective new bias correction method considerably reduced the need for regular updates of the operational IRC during the mission lifetime. The initial idea of a weekly update of the IRC as part of the ACMF and the Cal-Suite for L2B was found to be unfavourable because of the impact of the large variations of IRC characteristics and the obvious lack of representativeness of an IRC (performed while nadir pointing) as calibration for winds measured under off-nadir viewing conditions.

Furthermore, the monitoring of Aeolus winds against winds from the European Centre for Medium-Range Weather Forecasts revealed systematic errors in the Mie channel winds as well as imperfections in the calibration data that is used as input to the wind retrieval. It was found that, by making use of winds from the numerical weather prediction model, these systematic errors could be reduced as part of the Level 2B wind processing since July 2021 (Marseille et al., 2022).

Throughout the mission the characteristics of the IRCs were monitored to support the general assessment of the stability and performance of the Aeolus instrument. The quality assessment of Mie and Rayleigh channel response curves for the Internal Reference path, the atmosphere and the ground return was continuously extended, optimized and adapted to the operating conditions of the flight-model lasers FM-A and FM-B. The influence of different instrument parameters (laser frequency stability, alignment) on the IRC results was studied.

As presented in Figure 33 a total of 133 IRCs were performed during the Aeolus mission over three different locations: the Arctic, Antarctica and Africa. The dataset used for the below plots comprises:

- IRCs #001 - #036 (FM-A-1) from the 3rd reprocessing campaign with Baseline 14
- IRCs #037 - #061 (FM-B) from the 2nd reprocessing campaign with Baseline 11
- IRCs #062 - #063 (FM-B) from manual reprocessing with Baseline 12
- IRCs #064 - #121 (FM-B) taken as NRT versions with Baseline 11 – 15
- IRCs #122 - #133 (FM-A-2) from manual reprocessing with Baseline 15

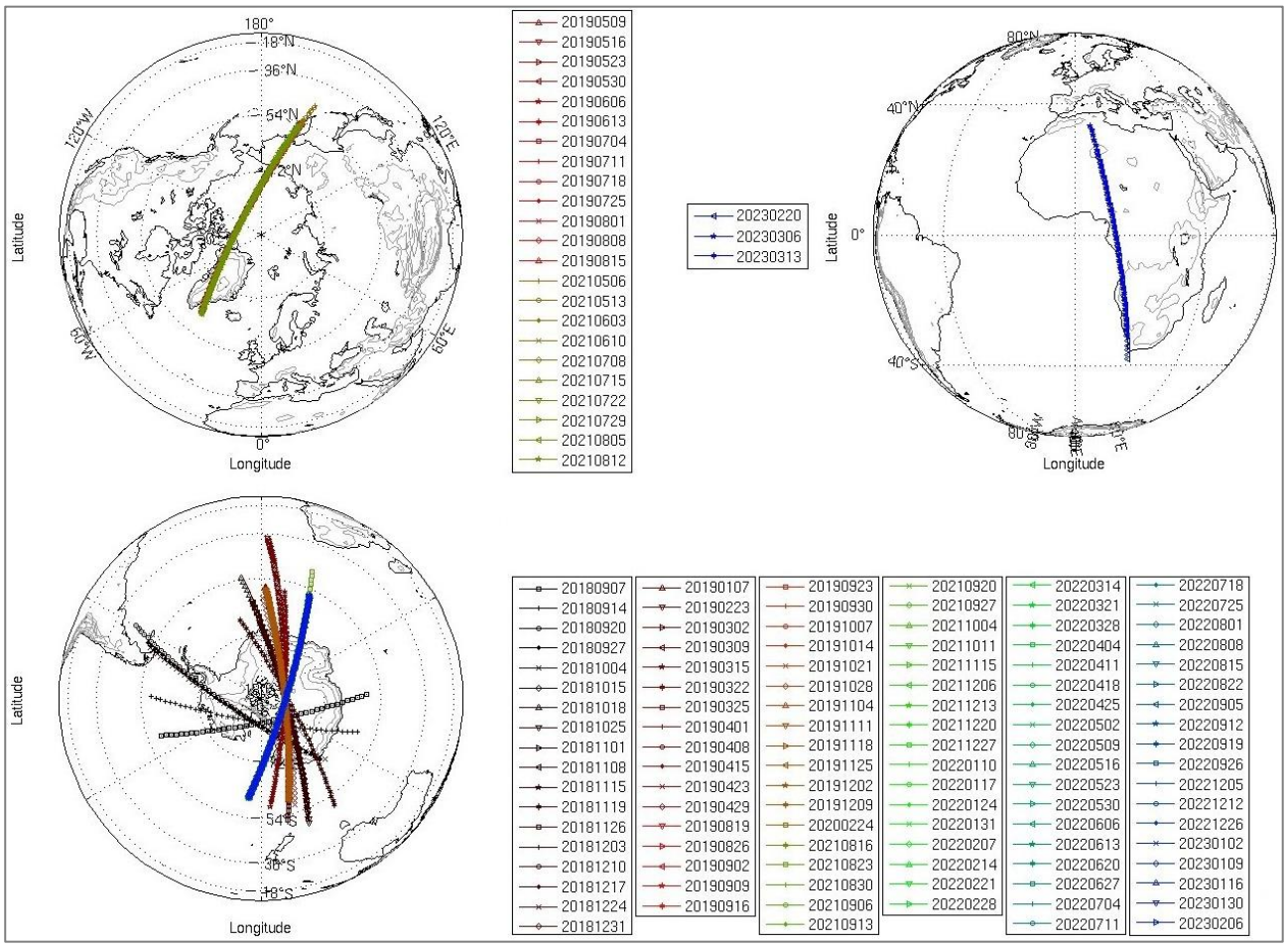

Figure 33: Ground tracks of all 133 IRCs of the Aeolus mission located over the Arctic (top left), the Saharan Desert (top right) and Antarctica (bottom left). The timeline of the legends is coded from black (2018) via red to green and finally blue (2023).

Figure 34 shows the response calibration curves for the Rayleigh channel, derived from three signal sources: the internal reference, the atmospheric broadband molecular backscatter and the narrowband ground return reflection. The atmospheric responses are derived from signals between 6 and 21 km altitude, the quality of which is controlled, among other things, by a threshold value of 1.164 for the scattering ratio. For the derivation of valid ground response curves several quality control parameters are considered, for example the number of valid measurements per frequency step, a maximum bin thickness above DEM and a maximum altitude offset of the detected signal with respect to the DEM. The 133 curves in each plot are basically separated into four chunks caused by the operation of the laser on four different base frequencies during the mission related to three of the switch-offs of the instrument:

1. on 2019-06-24 for the switch from laser FM-A to FM-B
2. on 2021-03-22 due to a switch to survival mode (*frequency step error*)
3. on 2022-10-11 for the switch back from laser FM-B to FM-A

A striking feature is the opposite orientation of the blue set of Rayleigh response curves in the top row. This inversion of the slope is related to ALADIN having been operated at the other (second) cross point of the Fabry-Perot filter transmission curves during the FM-A-2 period causing a flip of the sign in the signal difference according to the definition of the Rayleigh response as $R = (A - B)/(A + B)$.

Overall, the position of the response curves of the internal reference seems to be stable, which in fact is by definition, as the cross point of the internal reference is taken as a common relative reference for the x-axis. Since this common reference is also applied to the atmosphere and the ground return response curves, relative changes between these optical paths become visible here. For example, the root-cause of the split of the blue subset of response curves (FM-A-2) by about 70 MHz is located between the IRC on 2023-01-16 and the one on 2023-01-30. This coincides with a significant signal drop in laser emit energy which in turn can be related to changing thermal conditions of the laser, finally affecting the illumination of the Fabry-Perot interferometer on the internal reference path. Eventually, the L1B HLOS Rayleigh winds experienced an uncontrolled and unexpected bias drift by about 21 m/s between 2023-01-20 and 2023-01-25.

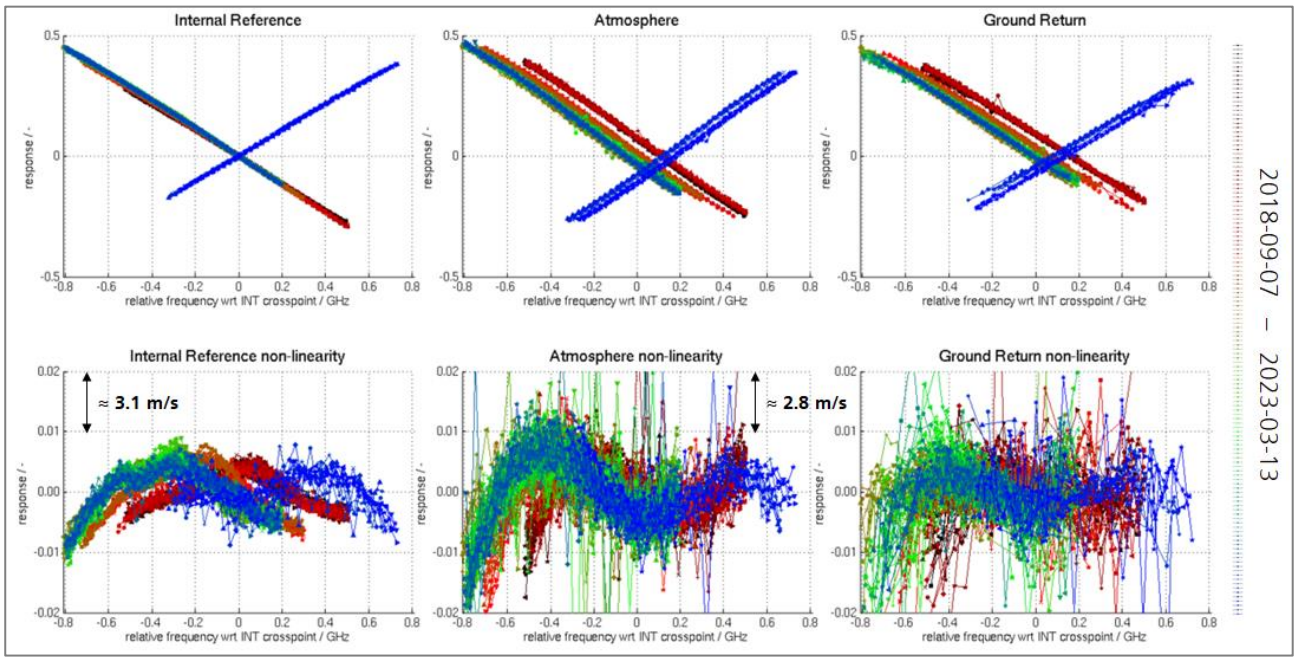

Figure 34: Response curves (top) and non-linearities (bottom) for all 133 Rayleigh response calibrations from the internal reference path (left), the atmospheric molecular return (middle) and the ground return (right). For the atmospheric and internal (similar for ground) non-linearities small arrows indicate the relation between response and LOS wind speed. During the mission the laser was operated at basically four different frequencies. To have a common reference, all curves are shown with respect their Rayleigh filter cross point frequency for the internal reference. The timeline is coded from black (2018) via red to green and finally blue (2023).

The non-linearities, shown in the second row of Figure 34, are obtained after subtracting linear fits from the Rayleigh response curve and give insight into their fine structure. As expected, the noise on the internal reference measurements is low based on the high SNR, whereas the atmospheric path is affected by an imperfect quality control with respect to signal contamination by clouds and aerosols between 6 – 21 km altitude. The ground return measurements suffer from signal contamination by the remaining atmospheric column in ground bins (broadband vs. narrowband signal), imperfections in the detection of the involved ground bins and generally low SNR over surfaces with low albedo.

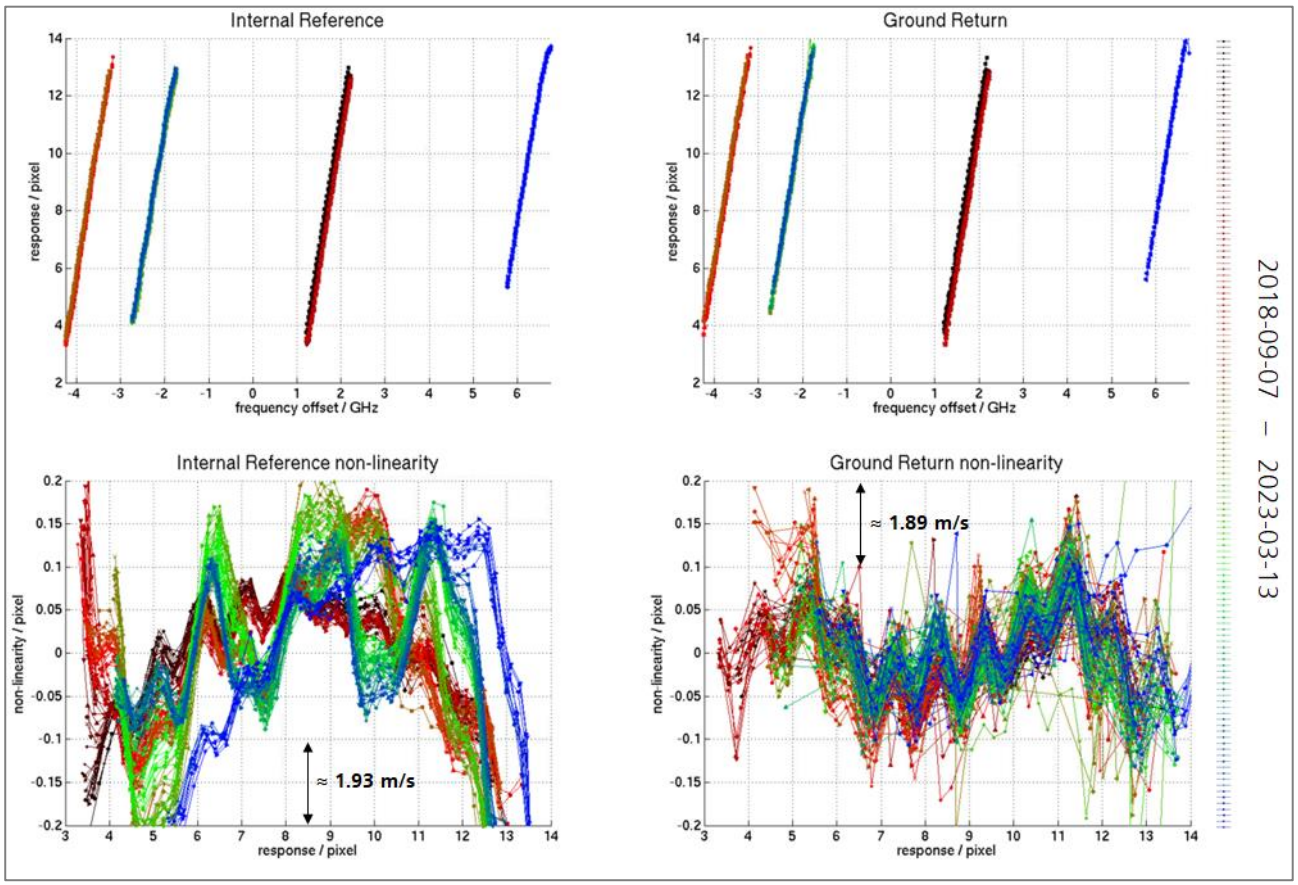

Figure 35: Response curves (top) and non-linearities (bottom) for all 133 Mie response calibration curves from the internal reference path (left column) and the ground return (right column).

In the same manner as above, Figure 35 presents the response calibration curves for the internal reference and the atmospheric path of the Mie channel. Again, the top row shows the separation of the 133 response calibrations into four chunks related to the different laser operation frequencies during the mission being apart by about 10 GHz at maximum. The non-linearities in the bottom row are given with respect to the ACCD pixel position 8.5 to have a common reference, which allows a better visualization of the drifts and jumps that occurred also on this channel. The details of the Mie non-linearities reveal a pixelation effect related to the ACCD structure which lies still on top of other remaining non-linear modulations. Whereas the non-linearity of all Mie response curves follows about the same shape for the ground return, i.e. the atmospheric optical path, the non-linearity on the internal reference path clearly exhibits several different shapes. These differences and drifts are strongly related to changes in the illumination of the Fizeau spectrometer. The shifted range of the blue part (FM-A-2 period) from about pixel 5.5 – 13.5 instead of the usual range of about 3.5 – 12.5 is related to the adapted operation point for the wind measurement mode during this period. By default, the wind speed was derived from Mie fringes located in the centre of the ACCD, which is subject to the influence of the so-called central obscuration, i.e. a shadow of the telescope secondary mirror. To overcome this drawback and to make use of more signal being transmitted on either side of the central obscuration, the laser operating frequency was tuned to the region around pixel 11. The IRC frequency scan range was then adapted accordingly to characterize also the measurement range at higher ACCD pixel values to allow for correct computation of wind speeds in this region, too.

From the Rayleigh as well as from the Mie response calibration curves three different basic parameters were derived from linear fits to characterize and monitor the state of the instrument and its changes:

1. The sensitivity (also called slope)
2. The zero frequency (also called intercept / intersection of the response curve with the y-axis)
3. The offset (intersection of the response curve with the x-axis)

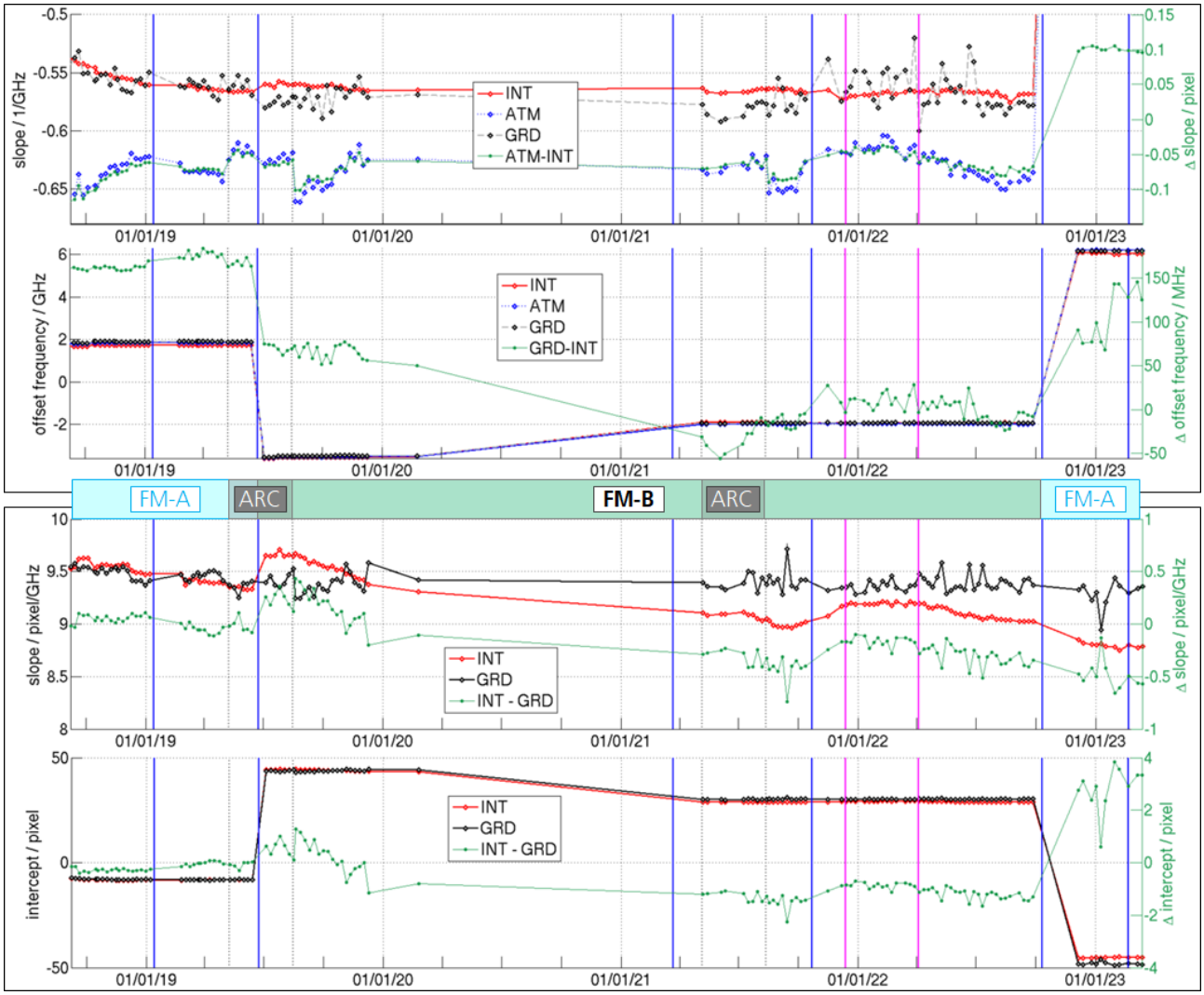

Figure 36: Slope (top-top) and offset frequency (top-bottom) of the Rayleigh response calibration curves for the internal reference path (INT, red), the atmospheric return (ATM, blue) and the ground return (GRD, black). Slope (bottom-top) and intercept (bottom-bottom) of the Mie response calibration curves for the internal reference path (INT, red) and the ground return (GRD, black). The respective differences are indicated as green lines. The two phases during which the FM-A laser was operated are marked as light blue areas. Vertical blue and pink lines indicate "switch-offs" of Aeolus and a change in P/N settings, respectively. The two periods during which the IRCs were performed over the Arctic (ARC) instead of over Antarctica are marked by vertical dotted grey lines (Marksteiner et al., 2023).

Slope and intercept, and optionally the Mie non-linearity, are input to the wind retrieval algorithm. Figure 36 presents the development of the slope for both channels as well as the offset for the Rayleigh and the intercept for the Mie channel. In particular, the different levels in the timelines of the Rayleigh offset and the Mie intercept reflect the subdivision of the response calibration curves into four chunks as mentioned above. The split of the subset of the Rayleigh response curves for the FM-A-2 period becomes visible in the jump of the Δ offset frequency (green) in the middle of January 2023. Several periods of long-term drifts can be seen, for example in the slope of the Rayleigh channel during the first 4 months of the mission (where internal reference and ground return show an opposite trend compared to the atmospheric path) or even a general trend towards smaller slope values for the internal reference

of the Mie channel over the whole mission duration. In addition, the location over which the IRCs are performed plays a role as can be seen from the jump in the slope of the Rayleigh atmospheric path between May and August 2019. Here, the differences in atmospheric temperature over the Arctic and Antarctica are assumed to be the root-cause. However, such drifts and jumps are mostly deemed to point to changes in the environment of the satellite or the conditions of the spectrometer and laser (*optics*). Marked by pink vertical lines, the change of P/N settings, i.e. the number of pulses being integrated to one measurement, was found to have no significant impact on the characteristics of the response calibration curves. For visualization purposes, the Rayleigh slopes for the FM-A-2 period are kept outside the display range as they have positive (and flatter) values due to the operation at the opposite filter cross point.

In total 12 AUX_MRC/RRC file pairs were delivered to DOS/PDGS (DISC On-site Service DOS, 2023, AeolusPDGS_AUXfileusage_timeline_v4.1.xlsx, https://csde.esa.int/confluence/display/AEOLUSDISC/PDGS+AUX+files) for application in the NRT L1B wind processing, between 2018/08/08 (artificial E2S based pre-launch version) and 2023/05/19 (for period after the official end-of-mission). These 12 pairs in turn are based on only 7 IRCs (5 pairs constitute only format updates coming along with new baseline deliveries):

1. E2S created and based on pre-launch Thermal Vacuum test results (2018-07-13)
2. IRC #002 from 2018-09-14 for FM-A-1 operation
3. IRC #006 from 2018-10-15 as update during for FM-A-1 operation
4. IRC #025 from 2019-03-25 as update during for FM-A-1 operation
5. IRC #037 from 2019-07-04 for FM-B operation
6. IRC #123 from 2022-12-05 for FM-A-2 operation
7. IRC #079 from 2021-10-04 for FM-B-2 operation (after official end-of-mission)

Mainly, the following parameters of the measured IRCs were monitored for the two channels:

a) Calibration validity indicators for the internal reference, the atmospheric molecular return (*Rayleigh only*) and the ground return
b) Ratio of valid to total number of measurements for the ground return
c) Number of invalid frequency steps on the internal reference, the atmospheric molecular return (*Rayleigh only*) and the ground return
d) Standard deviation of the residual (after subtraction of a 5th order polynomial) for the internal
e) Laser frequency stability (*Allan deviation*) on observation, measurement and pulse level
f) reference, the atmospheric molecular return and the ground return (*all Rayleigh only*)
g) Total number of invalid measurements
h) Number of corrupt measurement bins

Based on these parameters an empirical quality assessment was performed to justify the selection of the above listed IRCs 2. – 7. from the available set of IRCs at the respective time. The rough weight assigned to the parameters during this empirical assessment is reduced from top to bottom, i.e. giving the highest and lowest influence to the validity indicators and the corrupt bins, respectively. More specifically, the monitoring of these parameters assures the consideration of both, the atmospheric state, for example cloudiness and surface albedo, as well as the state of the instrument, e.g. laser emit energy, frequency stability and the internal reference path.

Before the launch of Aeolus, it was thought that the instrument would be stable enough to exhibit only long-term bias drifts (over months) or intentionally introduced bias steps which could then be corrected via the application of an updated IRC. However, after launch unexpected wind speed biases were observed that varied on timescales shorter than anticipated and which could not be addressed by the foreseen bias correction methods, neither by IRCs nor by the readily developed HBE. Instead, it required

the introduction of a new correction method which considers the temperature gradients across Aeolus' primary telescope mirror (Weiler et al., 2021). This method implicitly also performed a part of the bias correction for which the IRC mode was initially implemented for. The impossibility to disentangle the effects of an IRC and the alternative bias correction renders an analysis about the detailed impact of IRCs onto the wind speed errors along the mission very challenging and could only be answered by reprocessing activities.

Furthermore, the monitoring of Aeolus winds against winds from the European Centre for Medium-Range Weather Forecasts (ECMWF) revealed systematic errors in the Mie channel winds pointing to imperfections in the calibration data that is used as input to the wind retrieval. It was found that, by making use of winds from the numerical weather prediction model, these systematic errors could be reduced as part of the Level 2B wind processing since July 2021 (Marseille et al., 2022). Figure 37 describes the observed difference in the shape of the Mie non-linearity as derived from a measured IRC and from a NWP calibration procedure.

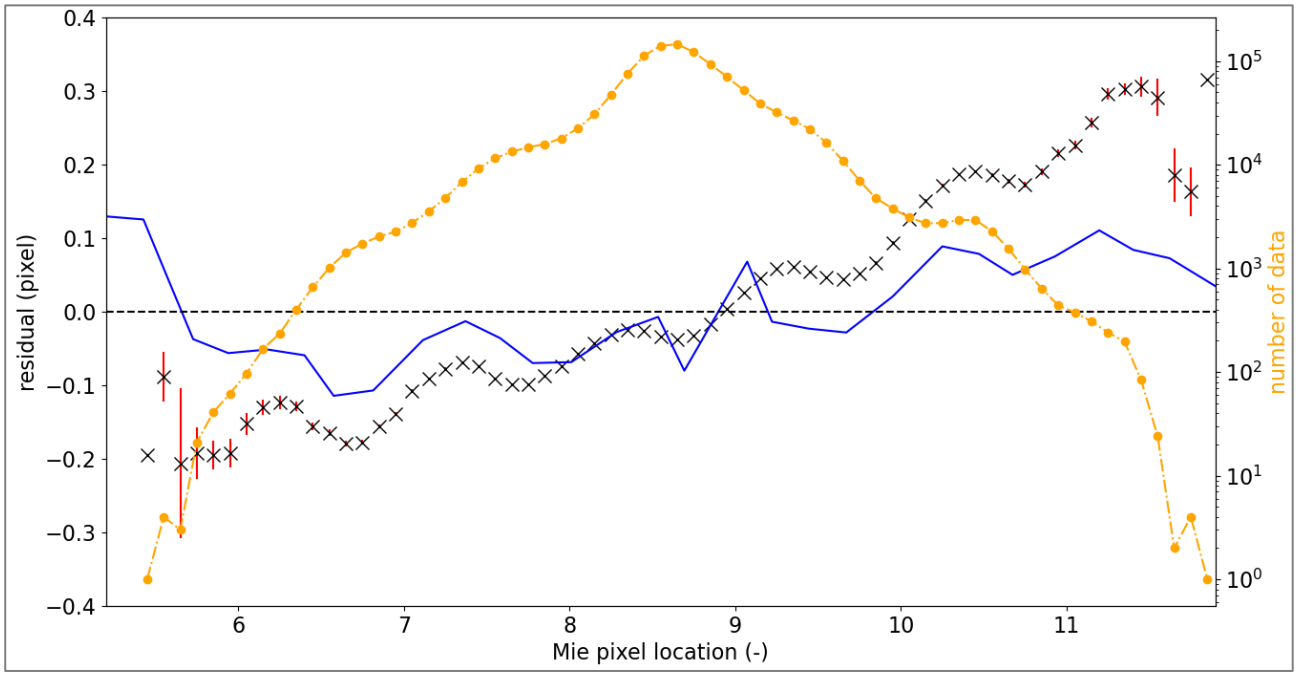

Figure 37: The solid blue line denotes the Mie non-linearity as a function of Mie centroid location derived directly from the measured IRC #48 from 2019-09-16. The black crosses denote the Mie non-linearity obtained from a NWP calibration procedure (Marseille et al., 2022) and was derived on the basis of one month (December 2019) of Aeolus L2B wind data. Orange dots indicate the number of L2B wind data points available within the 0.1 pixel sized bins. The red error bars shall reflect the standard deviation of the mean value, which is negligible for most pixel bins.

The IRC related parameters slope, intercept and offset have been compared to those of IRONICs (Instrument Response OffNadIr Calibration). Clear differences in the characteristics of the response curves between both modes can be observed for which no clear explanation was found yet, also not on the basis of test during the End-of-Life Activities. The most probable candidate would be the different temperature environment of the satellite in nadir and off-nadir mode (under which wind measurements are performed). IRC measurements cannot be corrected for alignment variations due to changes in the M1-temperatures during the IRC as, first, it is not meaningful to apply the correlation coefficients from off-nadir pointing to nadir pointing conditions and, second, the duration of an IRC is too limited to derive dedicated correlation coefficients for nadir pointing. Additionally, the fact that the motion of the Rayleigh spots along the orbit in wind mode is larger than the difference of the spot positions between

off-nadir and nadir operation supports the argument that IRCs (which were almost always performed over polar regions) are not representative for the entire orbit (MoM EOLA Workshop 2024-01-24, EOLA#17). As the IRCs had to be performed over geolocations with high albedo (snow/ice) to achieve high SNR for the ground returns, the IRCs would only be representative for an instrument alignment over this geolocation. This geolocational bias limits the applicability of IRCs for wind calibration and needs to be complemented by performing a sequence of IRONICs over the globe.

For the Reprocessing Campaigns the information from the monitoring and quality assessment was used to select the most suitable IRCs. These were then manually reprocessed with optimized and up-to-date AUX_PAR_1B and AUX_CHAR file settings. For example, versions based on IRC #016 as well as on IRCs #037, #048 and #079 were used to cover the FM-A-1 and FM-B period in the 4th reprocessing campaign, respectively (*names as delivered by DISC and with datetimes indicating the start and stop of the application period*):

- AE_OPER_AUX_R/MRC_1B_20180822T000000_20190623T235959_4001.EEF (#016 / FM-A-1)
- AE_OPER_AUX_R/MRC_1B_20190624T000000_20190722T000100_0001.EEF (#037 / FM-B)
- AE_OPER_AUX_R/MRC_1B_20190722T000100_20210322T020000_0001.EEF (#048 / FM-B)
- AE_OPER_AUX_R/MRC_1B_20210322T020000_20221006T000000_0001.EEF (#079 / FM-B)

3.5.1.1 IRCs in the L1B wind retrieval

The following information from IRCs are currently input to the L1B wind retrieval (*DPM, 2023*):

- MRC:
  - Reference_Pulse_Error_Mie_Response (non-linearity for internal path)
  - Measurement_Error_Mie_Response (non-linearity for atmospheric path)
  - Reference_Pulse_Mean_Sensitivity (slope from linear fit for intern. path)
  - Measurement_Mean_Sensitivity (slope from linear fit for atmos. path)
  - Reference_Zero_Frequency (intercept from lin. fit for int. path)
  - Measurement_Zero_Frequency (intercept from lin. fit for atm. path)
- RRC:
  - Reference_Pulse_Error_Rayleigh_Response (non-linearity for internal path)
  - Measurement_Error_Rayleigh_Response (non-linearity for atmospheric path)
  - Ground_Measurement_Error_Rayleigh_Response (non-linearity for ground ret. path)
  - Reference_Pulse_Mean_Sensitivity (slope from linear fit for intern. path)
  - Measurement_Mean_Sensitivity (slope from linear fit for atmos. path)
  - Ground_Measurement_Mean_Sensitivity (slope from lin. fit for ground path)
  - Reference_Zero_Frequency (intercept from lin. fit for int. path)
  - Measurement_Zero_Frequency (intercept from lin. fit for atm. path)
  - Ground_Measurement_Zero_Frequency (intercept from linear fit for ground)

As presented in Figure 35, the shape of the Mie non-linearity showed considerable drifts in the internal reference path and also some long-term drift for the ground return. Additionally, the noise on the non-linearity curves is obvious, in particular for the ground return. This noise can directly translate into both, wind biases and an increased wind random error. To reduce this effect, it was decided to determine averaged non-linearity curves for appropriate periods of the mission and to insert these via the AUX_PAR_1B file to the L1B wind retrieval.

The wind retrieval for the Rayleigh channel does not use directly the response calibration either. Instead 5th order polynomial fits through the response calibration curves are determined to avoid introducing

the noise of single frequency steps into the wind retrieval. Accordingly, the Rayleigh non-linearity, as the residual after subtraction of the linear fit from the 5th order polynomial, constitutes a smooth curve.

3.5.1.2 Summary and lessons learnt

- The IRC characteristics (*slope, intercept, offset frequency*) show drifts and jumps that reflect changing instrument conditions and geolocation (*Arctic vs. Antarctica*). Additionally, the curves for the atmospheric path and ground return exhibit a significant amount of noise very likely caused by imperfections in the QC (*cloud and aerosol removal*) and ground detection (*e.g. molecular contamination*). Further contributions to a reduced stability are the signal (*SNR*) decay over the mission lifetime and the varying cloud coverage which hampers the ground visibility. Thus, only a subset of the whole IRC collection was flagged valid.
- The bias of L1B winds depends strongly on the IRC selected for the wind retrieval. However, the characteristics of the IRCs that are used within the wind retrieval (*slope, intercept and Mie non-linearity*) show significant variability even in periods of expected stable instrument conditions.
- Following the pre-launch idea of applying a new IRC on an about weekly basis, would therefore translate into little artificial jumps of bias and wind speed dependent error on L1B stage. Even if IRCs of good quality were available on a weekly basis, it is questionable if a more frequent update of the IRC to the wind retrieval was beneficial.
- Outlier detection is important as a single erroneous response value among the steps of the calibration curve can have significant impact on the derived characteristics (*intercept and slope*) and, hence, the computed wind speed.
- Including further parameters, such as useful signal (*already implemented for Mie in L1B v.07.13*) and remaining atmospheric column, in the quality control scheme, in a correction scheme or as input to a weighted fit through Mie and Rayleigh ground return response curves could reduce the noise on the response curves and, hence, increase the stability of the fit parameters.
- As a Rayleigh Brillouin Correction cannot be implemented on L1B stage (*due to the missing input on actual atmospheric temperature and pressure*), the location over which the IRCs are performed can obviously affect the slope of the Rayleigh atmospheric path response calibration and consequently lead to wind speed dependent biases in the L1B winds.
- Depending on which quality requirements will be put onto L1B winds for Aeolus-2, a detailed monitoring will be needed to detect bias drifts and jumps and quickly react with the conduction of several IRCs (*to improve the chance of obtaining a high-quality one*) and the application of the best one in order to represent again the state of the instrument. An example case would be the uncontrolled and unexpected bias drift by about 21 m/s in the Rayleigh L1B HLOS winds between 2023-01-20 and 2023-01-25.
- In case that a reliance on NWP models is to be avoided for Aeolus-2, then calibrations should again preferably be performed over surfaces with high albedo in order to minimise influence of the atmospheric contamination for both channels. The high ground return signals result in a smaller random error of the responses per frequency step and more stable fit parameters of the response calibration curve, which in turn leads to more reliable ground correction velocities that can be used for zero wind correction.
- IRCs (*performed in nadir view and over limited area*) do not seem to be representative for off-nadir wind measurements along the whole orbit. Additionally, IRONICs (*performed in off-nadir view and distributed over the whole globe*) show differences to IRCs in terms of the

characteristics of the response calibration curves. Therefore, it might be worth investigating a potential merging of information obtained from IRCs and IRONICs into artificial response calibration curves. Such a procedure to be developed could be tested with the available Aeolus-1 data set in Phase-F and, if successful, could also be considered for Aeolus-2.

- There are indications that IRONICs, compared to IRCs, can provide better response calibration curves, as IRONICs are conducted under the same viewing angle as wind measurements and, hence, under very similar instrument conditions, in particular thermally. For the Aeolus-2 mission, the L1B instrument response calibration curves for the Mie and Rayleigh internal reference and the Rayleigh atmospheric path could be generated from IRONICs at L2B stage instead of being taken from dedicated IRCs. For a decent quality of the Rayleigh atmospheric path calibration curve at L2B stage, this would require several IRONICs, preferably up to 20, to be carried out in quick succession (to reflect the current state of the instrument). These measurements are then corrected for the satellite LOS-velocity, the LOS winds component and the dependence on atmospheric temperature using NWP data. The IRONICs should be geographically well distributed, i.e. cover a wide range of latitudes in order to cover as wide a temperature range as possible. Still the polar regions need to be included for strong ground return signals. Uncertainties remain regarding the accuracy of the ground return response curves due to the impact of the LOS component of wind in the atmospheric column of the ground bin. Therefore, the ability to perform IRCs in nadir viewing attitude should be retained for Aeolus-2 as a fall-back option.

3.5.2 Instrument Response Off NadIr Calibration

After anomalous behaviour (energy drop) during nadir measurements in December 2019 and February 2020 the IRCs had been suspended (although they were later found not to be the cause of the observed anomaly). To compensate for the loss of this calibration and monitoring ability, the setup of a similar activity in off-nadir mode was discussed. Considering compromises in terms of operational constraints it was decided to perform Laser Beam Monitoring procedures (LBMs), which have a similar frequency ramp as the IRC with one step every 2 BRCs ("Calibration Slow" scheme, instead of the "Calibration Fast 2" scheme applied for ISRs). However, the LBM went with frequency steps of 50 MHz instead of 25 MHz, and its execution needed to be changed from imaging to lidar mode. Additionally, the range of the frequency ramp is larger for the LBM with 68 steps over 3.3 GHz instead of the 40 steps over 1 GHz for the IRC, which resulted in an increase of the measurement time from 16 min to 26 min. This new calibration called IRONIC (Instrument Response Off NadIr Calibration) was then performed for the first time on 2020-10-19, finally ending up after its 132nd executions on 2023-04-25 (with about a weekly repeat cycle). As it was the case for the IRCs, also the IRONICs were located over the Antarctica most of the time, apart from special operation requests. The conduction of IRONICs in off-nadir mode also posed less constraints on their execution and particularly their repetition frequency. The IRONICs had never been allocated an own IFID (Instrument Function Identifier), instead they were performed in NOP (non-operational) mode. As a consequence, this data had never been evaluated in an automated processing way but could only be accessed after intensive manual preparation. A step-by-step manual of how to process IRONIC measurements in WVM and IRC mode was provided by DISC. Detailed information about the history of IRONICs along the mission are available under the Confluence wiki dSYS_033. The processing of the IRONICS is explained in Huber and Marksteiner (2021).

The Aeolus Level-2B wind calibration (Rayleigh and Mie response versus frequency) was investigated using the IRONIC procedures. 132 IRONICs were performed from 19 October 2020 to 25 April 2023.

To improve the sampling for statistics, the data (specially processed into L1B format as WVM products) from many IRONICs during which the instrument was reasonably stable was concatenated into larger datasets, since a single IRONIC was found to be too noisy to capture the calibrations well.

The investigation focused on the use of L1B measurement-scale data. A correction to the commanded laser frequency was necessary and applied per measurement-bin to remove the effect of the off-nadir horizontal wind-induced Doppler shift. This was determined from the u- and v- wind components stored in the AUX_MET data (ECMWF operational short-range forecasts) and subtracted from the commanded laser frequency as follows:

$$f_{corrected} = f_{commanded} - \frac{2}{\lambda} v_{LOS}$$

Errors in the AUX_MET winds will cause errors in this correction, however over large samples this correction appeared to work well i.e. it improved the response versus frequency compared to what is seen via other methods: IRCs, AUX_RBC_L2 (Rayleigh-Brillouin correction look-up tables).

Many factors influence the Aeolus calibration. Therefore, parameters which were thought to influence the Rayleigh or Mie atmospheric calibration could be investigated by partitioning the L1B measurement-bin data by, for example:

- The amount of Mie signal (cloudy or clear-air returns) by using thresholds on the range-bin thickness and satellite range normalized Rayleigh useful signal for the Rayleigh measurement-bins or the refined Mie SNR for the Mie measurement-bins. Appropriate values were found by inspecting lidar curtain plots and experimenting with thresholds.
- Discarding ground returns due to uncertainty in the horizontal wind correction for bins partially containing ground and atmosphere, by using the L1B DEM and altitude of the measurement-bins. For Mie calibrations, more convincing results were found using cloud backscatter compared to ground returns (due to larger samples).
- Atmospheric temperature and pressure from collocated AUX_MET data, for the Rayleigh calibration.
- M1 temperature gradient values (mean(outer) – mean(inner)) calculated from the L1B provided thermistor readings.

An aim of this research was to improve our understanding of what causes the altitude-varying bias for the L2B Rayleigh-clear winds and to try to measure the Mie calibration non-linearity in off-nadir pointing conditions (as opposed to the IRC in nadir pointing).

The most promising dataset was from a special operation of 20 IRONICs measured over a short period between 11-13 October 2021 (so the instrument is relatively stable), with good sampling of temperature and pressure conditions across the globe. The nominal weekly IRONICs tended to be restricted to Antarctica and so had a limited range of temperature and pressure, and large noise in austral summer for the Rayleigh channel.

Figure 38 shows an example of the Rayleigh response data and model fit performed with the concatenated 20 IRONICs dataset. Interestingly the internal RR (green) and atmospheric path RR from cloud returns (blue) matched very well for this period, as shown in the raw data of Figure 38a). The steepening of the RR curves with colder temperatures is evident in Figure 38b) and c), from functional fits to the raw data of Figure 38a). It is reassuring to see this behaviour, which is predicted in the forward modelling of the Calibration Suite from the ISR Rayleigh transmission functions and a priori knowledge of Rayleigh-Brillouin spectra.

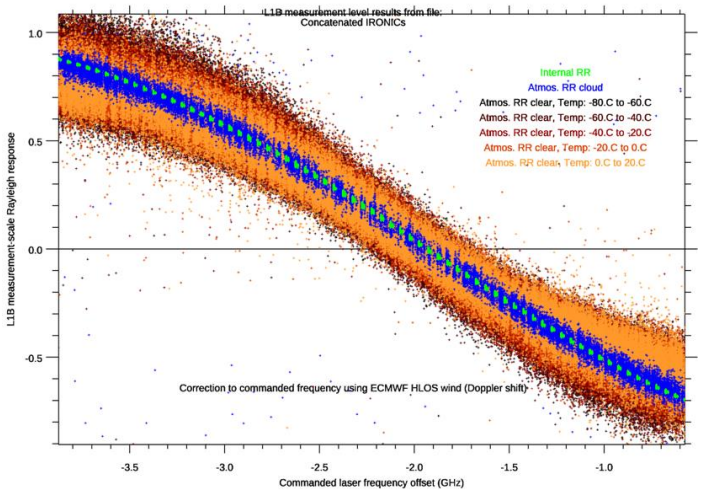

a)

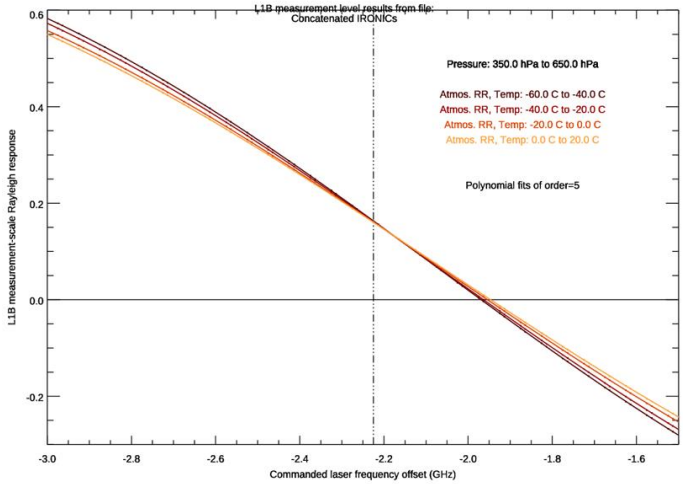

b)

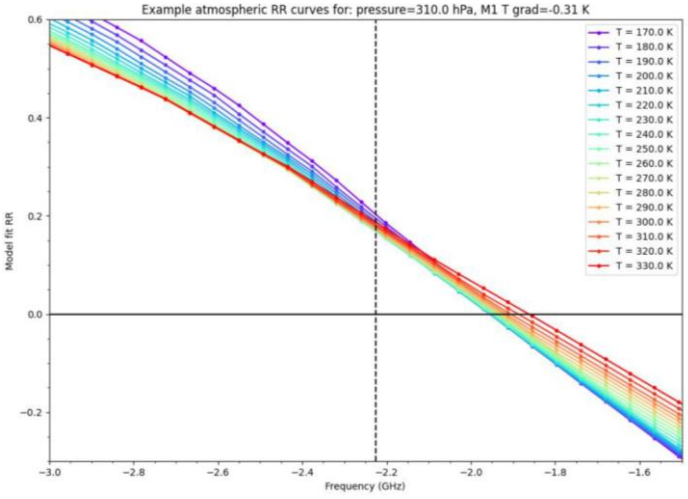

c)

Figure 38: L1B Rayleigh response data versus "corrected" commanded frequency from the "20 IRONICs" dataset (11-13 October 2021). a) Raw measurement-scale Rayleigh-response values showing the internal RR (green), the atmospheric RR from cloud returns (blue) and the atmospheric RR from clear-air in orange hues (for different atmospheric temperatures). b) A subset of the clear-air RR for a range of temperatures and a pressure range of 350-650 hPa after fifth-order polynomial fits have been made. The steeper gradients of RR for colder temperatures are seen. c) A machine learning (non-linear regression, neural network) model fit for a range of atmospheric temperatures for pressure=310 hPa and M1 T gradient=-0.31 K. The vertical dashed line in b) and c) is the nominal commanded laser frequency for the 20 IRONICs dataset (-2.25 GHz).

Quality control for outliers was necessary to get robust functional fits. The "node" position (where the Rayleigh response (RR) versus frequency curves for different temperature and pressures converge to almost a point) is evident in the fifth order polynomial fits of Figure 38b) for different temperature ranges with a fixed pressure range. The node is more diffuse in the non-linear regression via machine learning in Figure 38c), which may point to some issues with that method e.g. a lack of data in specific temperature bands at 310 hPa. For the machine learning (non-linear regression) model fit, the M1 mirror temperature gradient (outer minus inner) was used as a predictor, along with commanded frequency (wind corrected), temperature and pressure. Therefore, the ML learned how M1 T gradient affects the calibration. Figure 38c) is the output of the ML model for a fixed value of M1-T gradient of -0.31 K.

The research is not yet finalized, but here are some findings and associated further questions:

- The Mie non-linearity could be captured reasonably well by IRONICs from cloud returns compared to IRCs (not shown), but it appears that much larger samples are needed to avoid noise spoiling the non-linearity and perhaps imperfect corrections for horizontal wind in clouds from AUX_MET. The delta-frequency resolution (50 MHz) of IRONICs was not as good as for IRCs (25 MHz) which did not help.
- Findings related to L2B Rayleigh-Brillouin calibration curves (AUX_RBC_L2) and altitude varying (temperature dependent) bias:
    - The AUX_RBC_L2 RR slope was found to be too steep for low temperature, low pressure atmospheric conditions compared to empirically derived curves from concatenated IRONICs.
    - IRONICs (given good samples) are very useful at determining the atmospheric path node position.
    - The AUX_RBC_L2 node position can vary a lot from one AUX_RBC_L2 to the next. This strongly influences the altitude varying bias. With the wrong node position then for a given atmospheric RR, one ends up with a gap between each temperature, pressure RR calibration curves and hence wind bias.
- IRONICs helped in choosing the outgoing laser frequency for the switch to FM-A in November 2022 by aligning the outgoing frequency to lie at the atmospheric path "node" frequency for the Rayleigh channel, thus minimising sensitivity to temperature. This was demonstrated to reduce the altitude-varying bias, which was initially large for FM-A switch-on.
- IRONICs data show that as the centre of M1 mirror warms compared to the edge the RR vs frequency curves shift to smaller RR values (basically a delta RR effect). This has a sensitivity of ~48 m/s (HLOS) per K via IRONICs (for FM-B), which is close to what was observed when initially looking at M1 T effect via O-B statistics. The M1 T bias correction (AUX_TEL) works because similar offset in Δf occurs for different RR values (so there is hardly any wind-speed dependence).
    - It should be possible to make the AUX_RBC_L2 look-up table a function of (T, p and additionally M1 T gradient) via the IRONICs data as alternative to current AUX_TEL method.
- The machine learning modelling from concatenated IRONICs showed promise, but it should be tested if it is accurate enough to be written to e.g. AUX_RBC_L2 format and applied in the L2Bp without introducing large wind biases.

Based on its usefulness for Aeolus, a large global sampling, high frequency-step resolution IRONIC-like calibration mode is recommended for Aeolus-2. Especially if there are stronger sensitivities to Mie cross-talk on the Rayleigh channel compared to Aeolus, when using a different Rayleigh spectrometer. Given the best results were found from the dataset of 20 IRONICs performed over three days, with pseudo-random global sampling, then we would recommend something similar for Aeolus-2 but with a larger sample e.g. ~60 IRONICs, to further improve the sample. The stability of the Aeolus-2 instrument will determine how often this is required, but at the very least during the Commissioning Phase. Given the limited benefit of individual weekly IRONICs, due to limited sampling of meteorological conditions and instrument drift, then we would not recommend this for Aeolus-2. IRCs should still be considered for Aeolus-2, so the IRONIC derived calibration can be compared to the more traditional method. An advantage of IRONICs, due to being in off-nadir pointing, is that many can be performed in close succession to improve the sampling, whereas this was not possible for Aeolus IRCs due to the platform limitations in nadir duration.

3.6 End-of-life activities (EOLAs)

Christian Lemmerz and Oliver Lux, DLR

The EOLA phase at the end of the operational Aeolus mission provided a unique opportunity to perform special tests concerning instrument-related and scientific issues with regard to the Aeolus performance, re-processing input and the preparation of future space lidar instruments with a focus on Aeolus-2 and ATLID on EarthCARE. Together with inputs from ESA, the Aeolus Science Advisory Group (SAG) and industry tests were suggested by the Aeolus DISC and down-selected based on their risk assessment and relevance for the Aeolus performance, re-processing and future missions. 9 out of 12 tests proposed by DISC could be selected and three additional tests were defined during the EOLA-phase. Finally, these 12 tests from DISC formed the majority of a total of 22 different tests that could be executed once or with a few repetitions and adaptions. A chronological overview of all EOLA tests and their main results is provided in Table 9 and will be discussed in this section. The preparation and analysis of 17 tests was supported by DISC in addition to the laser switch-over activities.

3.6.1 Overview of EOL tests

The tests were mainly motivated by increasing the level of insight into instrument performance issues including optical alignment stability and other noise sources, but also served the exploring character of the mission, which was for the longest time dampened by the operational demand for NRT Aeolus wind data by NWP centres. Finally, through these tests, Aeolus has demonstrated in many ways the full performance potential of its wind lidar technology, that would have been achieved, e.g. if the results of the laser full energy (EOLA#07, #08 and #11) could have been combined with the improved frequency (EOLA#05, also see 3.1) and internal reference signal stability (EOLA#12, also see 3.2.3). An outlook to the improved Aeolus-2 like detector noise and a better characterization of the ACCD in imaging and memory zone was provided with EOLA#03 and EOLA#27 results (see also 3.3). New measurement and calibration modes with relevance for Aeolus-2 were demonstrated like Hi-DCC (EOLA#16), atmospheric temperature profiling (BIER, EOLA#18), wind measurements at 42° off-nadir, atmospheric LBM (EOLA#23), vertical wind measurements (EOLA#24) and the High-DUDE (EOLA#26). Alignment-stability specific tests confirmed the reliability of the measurements performed during nadir operations (EOLA#17 and #19) and provided a more detailed knowledge of the variation of the return signal along the orbit in both ACCD axis (EOLA#10 and #19 in imaging mode).

To prepare and perform the tests, an enormous effort had to be coordinated between ESA-ESTEC, ESA-ESRIN, ESA-ESOC, Airbus D&S and the Aeolus DISC, partly based on NRT analysis of the instrument housekeeping and scientific data. The increasing solar activity in late 2022 and early 2023 led to a start of the EOLA phase earlier than initially planned, but nonetheless the efficient collaboration of the Aeolus team allowed to perform most of the planned tests, adapt the parameters in case of a required repeat, and all this even despite a necessary switch back to the FM-B laser begin of May, earlier than planned. To our knowledge, this was the most complex space lidar operations phase and provided valuable lessons learnt for the commissioning and operation of future lidar missions. The analysis of most tests was also demanding due to the non-nominal operations, that for some cases required a special adjustment of the tools developed for data processing.

Table 9: Chronological overview of all EOLAs with DISC involvement as executed. Tests that were repeated with the same or similar settings share a common colour. Other tests are single executions or a repeat with different test parameters. Missing test numbers were not selected for execution.

Test #	Date	Goal/Activity/➔Result	Acquisition Mode		Attitude		
			Lidar	Imaging	Nadir	Nominal	
EOLA#17	03/04/2023	Alignment stability verification in two dimensions during nadir and transition. Performed by replacing one IRC slot prior to EOLA-phase ➔ Stable alignment during nadir.		x	x	x	FM-A
EOLA#18	10/04 & 17/04	Atmospheric path illuminated spectrometer response characterization and temperature profiling by BIER (Broad Instrument Response with Extended Range). Performed by replacing two IRC slots over Antarctica. Go-NoGo based on cloudiness prediction.	x		x		FM-A
EOLA#05	19/04	Improved laser frequency stability by optimized cavity control settings ➔ setting maintained after analysis showing > 40% reduction in frequency noise.	x			x	FM-A
EOLA#24	24/04	Vertical wind measurement performance - nadir West of Andes to Antarctica.	x		x		FM-A
EOLA#10	01/05	Orbital alignment variation characterization in two dimensions - 24 h duration (1st test in EOLA-phase after end of operational phase).		x		x	FM-A
EOLA#12	02/05	Internal and atmospheric signal stability dependence on Laser Chopper Mechanism (LCM) phasing ➔ improved INT stability detected.	x			x	FM-A
EOLA#20	03/05	Wind measurement performance characterization @ 42° off-nadir instead of nominal 35°. DUDE measurements partly affected by return signal.	x			42°	FM-A
FM-B switch (on 16/05)							
EOLA#27	14/05	ACCD Memory Zone characterization - different background integration times and adapted P/N - settings ➔ Integration time dependent Bkg signal overestimation and special signal response for strange hot pixel confirmed.	x			x	FM-B
EOLA#03	15/05	ACCD hot pixel temperature sensitivity -30 °C – -15°C (performend during FM-B switch).	x			x	FM-B
EOLA#16	19/05	ACCD dark current characterization (DCC) with laser on, but acq. above atm., Hi-DCC 6 h duration.		x		x	FM-B
EOLA#24	19/05	Vertical wind measurement performance - nadir West of Andes to Antarctica East of Andes to Antarctica.	x		x		FM-B
EOLA#23	19/05	Atmospheric path Mie – channel illumination composite, i.e. ATM-LBM frequency scan, acq. 6 km to below ground.		x	x		FM-B
EOLA#04	22/05+	Telecope tuning: Main mirror M1 ultimate temperature control coefficient tuning ➔ no improved setting detected.	x	x		x	FM-B
EOLA#04	24/05+	Telecope tuning incl. M1 increase (EOLA#13) with strut tuning ➔ no improved setting detected.	x	x		x	FM-B
EOLA#05	29/05	Improved laser frequency stability by optimized cavity control settings with FM-B ➔ setting maintained, > 40% reduction in frequency noise.	x			x	FM-B
EOLA#26	30 & 31/05, 01/06	Hi-DUDE above atmosphere instead of nominal below ground, necessary for the repeat of operation at 42° (EOLA#20). Mode designed during EOLA-phase	x			x	FM-B
EOLA#20	30/05	Wind measurement performance characterization @ 42° off-nadir instead of nominal 35°. Hi-DUDEs implemented (special processing required)	x			x	FM-B
EOLA#02	31/05	ATLID test and maximum transmission of Rayleigh direct channel (A) and in Mie channel MOUSR frequency, various RBS over ocean, ice, desert.	x		x	x	FM-B
EOLA#16	31/05 & 01/06	Hi-DCC with laser on and acq. above atm., in ATLID configuration at low SBkg., á 15 min. ➔ new elevated pixels on Rayleigh channel A hemisphere.		x		x	FM-B
EOLA#19	01/06	Alignment stability verification in two dimensions in ATLID configuration with high signal on Rayleigh direct channel spot.		x		x	FM-B
EOLA#18	02/06	Atmospheric path illuminated spectrometer response characterization and temperature profiling by BIER with FM-B over Greenland. Tonga-like BRC table in nadir to cover higher altitudes; 11 min. duration. ➔ Ground return and atmospheric transmission too variable for ATM ISR calibration	x		x		FM-B
EOLA#23	02/06	Repeat ATM-LBM over Antarctica and over ocean, acquisition 30 km to below ground.		x	x		FM-B
EOLA#12	02/06	LCM phasing test repeat with FM-B ➔ potential improvement confirmed.	x			x	FM-B
EOLA#12	03/06	LCM optimized phasing long term test, 24 h duration ➔ x 3 lower Rayl. INT noise; setting made permanent from 10/06 12:30 UTC.	x			x	FM-B
EOLA#16	04/06	Hi-DCC characterization, 9h duration ➔ Hi-DCC is recommended for future missions.		x		x	FM-B
EOLA#10	04/06	Orbital alignment variation characterization in two dimensions with FM-B, 9 h duration.		x		x	FM-B
EOLA#14	05 - 06/06	OBA temperature test +/- 2 K variation for alignment sensitivity and Fizeau thermal stability characterization, 19 h duration.	x	x		x	FM-B
EOLA#08	06/06+ & 13/06+	FM-B performance demonstration with on ground energy 06 - 08/06, heating currents decrease and pump increase, phasings.	x	x		x	FM-B
EOLA#07	12/06 & 14/06	FM-B master oscillator (MO) and amplifier (AMP) stages maximum energy including increase of STRO pressure part 1 & 2 ➔ high and stable MO output achieved ➔ 150 mJ UV achieved and kept as permanent setting after 14/06 incl. EOLA#08 results	x	x		x	FM-B
EOLA#11	08/06 & 13/06	Laser divergence test and influence on alignment, atmospheric signal performance	x	x		x	FM-B
EOLA#23	09/06	Repeat ATM-LBM over Antarctica and over ocean, acq. 30 km to below ground. Different acq. start times to compensate for range above GND.		x		x	FM-B
EOLA#12	10/06	Improved INT stability with optimized LCM phasing setting, permanent for rest of mission ➔ INT disturbance originated from stray light outside field stop	x			x	FM-B

3.6.2 Main conclusions of selected EOLA examples

Some tests and results have already been touched on in other sections, like state in the overview. A description of the execution and results for every test is out of scope of this document, even when limiting to the tests suggested by the DISC. For more information, please refer to the relevant publication listed in the Annex. In these publications and the references therein, a detailed description of every test can be found. As examples for EOLA results with relevance for Aeolus and following missions, condensed reports of selected tests are given below.

EOLA#14 – Fizeau temperature sensitivity and OBA alignment stability

During the operational phase two phenomena were observed that led to the formulation of the optical bench assembly (OBA) temperature test EOLA#14. During entry and exit of the eclipse phase in 2020 the atmospheric signal changed. One hypothesis for the root cause was a change in alignment of the emit – receive optics and thus the co-alignment between send and return beam. Also, the fringe position on the Mie channel changed with temperature by around 160 MHz/K which is a temperature sensitivity of the Fizeau spectrometer much higher than expected. Hence, the temperature of the OBA which changes both the temperature of the Fizeau and the Transmit-Receive Optics (TRO) was changed for this test by +/- 2 K to aim for two goals:

a) Verify instrument tunability w.r.t. alignment, atmospheric (ATM) path efficiency and AHT-19 (TRO beam dump temperature sensor) correction for emit path intensity
b) Characterize the Fizeau temperature sensitivity

The Rayleigh spectrometer is enclosed in a separate housing, temperature controlled with heating capability only, so it needs to be operated always at a higher temperature (usually ~ +2 K) as the OBA temperature.

As a result, a Fizeau sensitivity of around 120 MHz/K was derived from the test, which is much higher than the specified value for Zerodur (17 MHz/K) and the value determined for the pre-development Fizeau in the A2D (54 MHz/K). As open questions remain, how much alignment changes contribute to the Fizeau frequency drift and weather the higher sensitivity and alignment is in line with RSP alignment sensitivity. Atmospheric and internal path optical efficiencies improved by 10% only for the 2 K lower setting for the Rayleigh channel. This result is similar to what was observed during the 2020 eclipse phase for a temperature change of only around 0.1 K. Apart from alignment influences, another hypothesis for the changing and different thermal sensitivity is a pressure change from outgassing of the cavity which might have lost the vacuum during the long storage on ground, due to the non-zero glass permeability. Analysis is still ongoing by time of writing this report. But one conclusion is to test the temperature sensitivities of the receiver optical arrangement around its operating point on ground and to plan a verification in space during commission phase E1.

EOLA#16 – Hi-DCC – ACCD dark current in imaging zone measurements during operation

As described in section 3.3.4, some "anomalous" pixels in the imaging zone of the Rayleigh channel ACCD showed an abnormal behaviour. The characteristics of this behaviour and its potential contribution to bias and random error of the Rayleigh winds could not be studied in all details during the mission, because this dark current characterization (DCC) was only possible to be performed in phases where the laser-emission was switched off, i.e. in laser burst warm-up mode during switch-on operations. When preparing the EOLAs in imaging mode, a more detailed understanding of the timing commandability for the acquisition start and integration length revealed a possibility to perform DCC-measurements while the laser emission is on. For monitoring the dark current measurements in the

memory zone (DCMZ) of the ACCD as a basis for the HP correction (see section 3.3) so-called Down-Under Dark Experiments (DUDEs) were performed regularly. These were lidar mode acquisitions, but with a long delay w.r.t. the laser emission, such that the atmospheric return had already faded out (equivalent to hypothetically acquiring below ground returns). Such a long delay time was out of the parameter range for imaging mode. However, the acquisition window could be placed in the few milliseconds between the laser emission and the resulting atmospheric return, i.e. high above atmosphere. This procedure was called Hi-DCC and successfully tested within EOLA#16. It was similarly adapted for Hi-DUDEs required for EOLA#20, a test at 42° off-nadir instead of the nominal 35°, as the longer distance to ground and commanding limits made the nominal DUDEs unreliable.

Five Hi-DCCs acquired during the EOLA-phase in different conditions w.r.t. solar background, and laser frequency provided a valuable data-set that helped to reveal the characteristics of the anomalous pixels on the Rayleigh channel ACCD, when compared to nominal DCCs with laser-off (see section 3.3.4). The following conclusions could be drawn from EOLA#16 results:

1) A regular DCC monitoring is recommended for future missions, because not all effects can be monitored in lidar mode, nor be corrected in post-processing from lidar mode data only. The Hi-DCC is a recommended alternative mode for future missions, which would allow a characterization of each pixel's dark current evolution in imaging mode, if a DCC below ground can't be commanded.
2) Anomalous pixels in imaging mode:
    a) Anomalous pixel illumination on the Rayleigh ACCD depends on laser and/or solar background intensity, thus also on geolocation and season.
    b) The most prominent anomalous pixel [16,14] on the Rayleigh channel scales with spot B intensity (IDC - EOLA#23 result) and is minimal at spot B minimum (Hi-DCC at low solar background during EOLA#02 – result, when frequency was set at max. spot A/min. spot B during ATLID test).
    c) Px. [2,3] on a Rayleigh-spot-A - covered column detected → increases intensity in Hi-DCC measurements for the ATLID setting.
    d) The minimum of Rayleigh px [16,14] varies over time from 0.6 to 2 LSB, as revealed from comparing different DCCs taken in LBWU (laser burst warm up mode) when the laser emission was off. DCO gradients have not changed between BOL and EOL, but overall offsets have increased by about 2%. The anomalous pixels were not present BOL.

    Root-cause hypothesis: As a laser direct illumination of anomalous pixels can be excluded in cases where no spot is visible (like during Hi-DCCs), the intensity can be explained by a non-perfect ACCD flushing process. This leaves traces of the charges generated on spot B during the non-read-out illumination from laser emission. The vertical smearing of pixel. [16,14] along column 14 shows charge transfer inefficiency in read-out direction (line 16 read-out first, line 1 last), which supports the hypothesis of a more in-efficient flushing in this column (section 3.3.4).

Alignment Stability Tests: EOLA#17 – in Nadir, EOLA#19 in ATLID configuration, EOLA#23 – Atmospheric – Path Illumination Profile

The efficiency and stability of the laser-receiver co-alignment is a crucial aspect for lidar performance and especially for ALADIN on Aeolus, with its alignment-sensitive spectrometer response. However, in the nominal operation lidar mode for wind profiling, only the horizonal axis is available in the data, as the charges in the vertical rows from the imaging zone are binned into 1 row during the charge transfer process. To monitor the alignment in both horizontal and vertical axes, the imaging mode was set for

usually 15 min. on a weekly basis and during special operations like telescope and laser tunings during the mission. In imaging mode, nominally executed as instrument defocus characterization (IDC), the column integrated atmospheric and ground return contributes to the signal (except for the Hi-DCC setting described above). For EOLA#17, the imaging mode was for the first time used in nadir operation including during the transition to and from nadir, to observe the alignment variations. This is also relevant for the representativity of the instrument response calibrations (IRCs), which were performed regularly during most part of the mission, but showed a frequency offset causing a bias w.r.t. the model (see chapter 3.5). Some samples of imaging mode results for the Rayleigh and Mie channels acquired during EOLA#17 are shown in Figure 39. The evolution of the spot positions and size during the tests showed that the alignment changes significantly in the transition phases, but is stable in nadir and representative for the nominal wind measurements at 35°. Also fringe movements on the Mie channel were observed during the transition, which probably stem from satellite speed induced doppler shifts resulting from off-limits pointing-control while the spacecraft is turned to/from nadir.

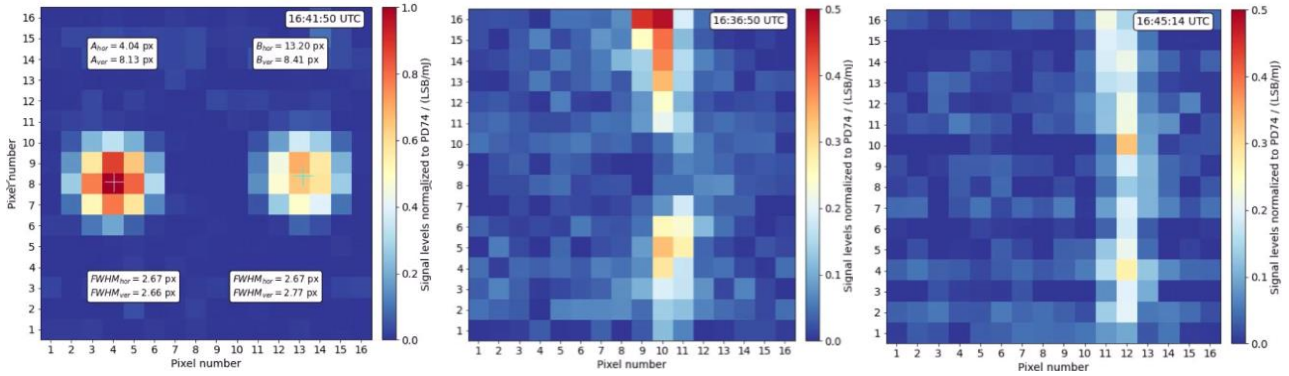

Figure 39: Atmosphere and ground return (i.e. atmospheric column integrated) imaging mode results (one observation mean, DCO-corrected) taken during the nadir operation of EOLA#17 on 03/04/2023 with FM-A. (Left) Rayleigh signals with the two spots of the direct channel (left spot A) and the reflected channel (right spot B) with their COG fit results of positions and sizes for the apparent spots incident to the spectrometers after the FS. (Middle) Mie fringe when shifted towards the centre during the sweep to nadir. The fringe interruption is due to the image of the M2 shadow and wave-front distortion around the centre of the optical axis on the ACCD. (Right) nominal fringe position during the second FM-A phase. Vertical integration to one line resembles the intensity distribution of the raw data of one range-bin in lidar mode.

The imaging mode was also applied during other EOLA tests, e.g. for EOLA#19 in ATLID frequency setting (EOLA#02) where all the backscattered intensity was accumulated in Rayleigh filter A (left spot A) and the Mie fringe was outside the useful spectral range imaged on the ACCD (MOUSR condition). However, this test was performed with FM-B which was known to have a degraded alignment w.r.t. the receiver. A horizontal spot movement of 0.1 pixel towards the centre was observed when crossing the Antarctica, i.e. the location where most of the IRCs were performed also during the first long FM-B phase. It has to be noted that the Rayleigh ACCD only can detect the apparent alignment drift result after the FS. The real alignment change before the FS is usually larger than what was simulated after fitting to the apparent spot results (see section 3.9). At the same time, with the ATLID setting in MOUSR condition, the broadband solar background and Rayleigh return allows to illuminate the full Fizeau aperture of the Mie channel. This shows the illumination profile on the Mie channel in both axis (as used for determination of the EMSR array in horizontal axis - lidar mode, see section 4.2) and was set few times during the mission for alignment characterization, as is done regularly during A2D field campaigns. However, during EOLA#02 the atmospheric return was already too weak with the degraded send-path optics for FM-B and the test was performed in low-solar-background conditions. Hence, in order to deduce MOUSR information, more repetitions of EOLA#19 would have been required.

The same is true for EOLA#23, which had the goal to resemble the MOUSR illumination profile of the Mie channel from adding up fringes of the atmospheric path for different frequency settings across the Fizeau spectral range, similar like was regularly done for the laser beam monitoring (LBM) in the internal path. Although there were three executions for EOLA#23, the required cloud-free atmospheric conditions could not be found. A higher number of executions, as e.g. for IRCs, would have been required.

The imaging mode tests confirmed the high value for alignment monitoring, and lead to the recommendation to perform these tests regularly to achieve a high number of samples under the targeted weather conditions. To allow QC e.g. for cloud detection, a mixed lidar/imaging mode for the different detector channels is highly recommended to be implemented in future missions.

3.6.3 Lessons learnt from EOLA:

- A risk-minimized testability for performance relevant topics in space shall be foreseen in the instrument and operational design.
- A transparent risk assessment including severity and likelihood shall be established already prior to launch for the IOCV – phase. For the Earth-Explorer mission Aeolus, the focus on demonstrating NWP impact was traded versus measures to increase the instrument performance for longer than the designed mission life-time. The risk assessment shall be regularly adapted to the goals of the mission to allow reaching and maintaining the optimal performance.
- Operation and commanding flexibility of the instrument are required for test designs. E.g. for Aeolus, a mixed imaging/lidar operation mode for the two ACCDs would have been beneficial to study the atmospheric path stability in both axes and with additional ranging information and QC options.
- The instrument design should give value to embedded additional information or functionality of all components and sensors. E.g. the AHT-19 thermal sensor attached to the beam-dump in the TRO could have been designed as auxiliary energy monitor. For Aeolus-2, e.g. the cross-polar detector can provide additional or back-up co-alignment monitoring in both lidar and imaging mode.
- The characterization of the instrument around its operational conditions already during tests on ground and in space during IOCV is the basis for maintaining a robust performance without the need to explore outside the tested parameter-space during the mission.
- Some tests could not be performed or repeated during the limited time of the EOLA phase. Refined test procedures or parameters are often a result of intense analysis that becomes available as late as after the EOLA phase. However, some EOLA tests lead to a significantly improved performance and all tests to a deeper understanding of instrumental effects. Thus, in addition to implementing an EOLA phase, regular time-slots for potential test executions should be foreseen already during the operational mission, to harvest and maintain the full performance. Go-NoGo decision strategies e.g. based on weather conditions or building on prior test results can increase the test efficiency.
- In addition to instrument ground tests, a ground and airborne operated sister instrument with high technological commonality for the core components is crucial for preparing a successful mission and minimizing the risk of reduced performance. Already before launch, the operational and technological details and pitfalls can be best explored with such an instrument, illuminated with real atmospheric scenes and during full human-in-the-loop control. In addition, it can provide de-risking, test preparation and independent second source information during the mission.

3.7 Ground-returns, harmonic bias estimator and range-dependent bias

Uwe Marksteiner, DLR and Ines Nikolaus, Physics Solutions

A powerful ground detection algorithm forms the basis for the determination of accurate, so-called "ground correction velocities" (GCVs). Prior to the launch of Aeolus-1, the measurement of ground return signals was seen as an integral contribution to reducing of the systematic error in the wind speed and thus the fulfillment of the strict accuracy requirements. The high satellite velocity of more than 7 km/s in combination with uncertainties in the knowledge of the platform attitude, the geometry of the instrument mounting or from unknown instrumental contributions can lead to large additional frequency deviations and thus to a bias in the wind speed (Nikolaus, 2018; Marksteiner et al., 2018). Therefore, ground returns originating from stationary targets can constitute a valuable measure for a zero-wind reference. The resulting GCVs contained in the "zero wind correction" (ZWC) files, were deemed to serve either as:

- a direct correction value applied per wind profile
- or as input to computations of a potential harmonic bias via the harmonic bias estimator (HBE) (Marksteiner et al., 2020)
- or as input to computations of a potential range dependent bias (RDB) (Marksteiner et al., 2020)

To validate, among other things, the handling and application of ground return signals, the ALADIN Airborne Demonstrator (A2D) was developed and used in several airborne campaigns before and during the Aeolus mission (Marksteiner, 2013; Weiler, 2017; Huber, 2018).

However, the Aeolus-specific dominant M1 mirror temperature dependent error, which was detected after launch and could not directly be corrected, ultimately prevented the meaningful application of the Harmonic Bias Estimator (Weiler et al., 2021). The M1 bias was found to be a function of both the orbit phase (argument-of-latitude) and the longitude, and it varies significantly from orbit to orbit. The idea of the HBE was based on much slower bias drifts. In addition, the HBE relies on a longer averaging time with an input of ground correction velocities over several days to about one week to counteract the low SNR and reduce the error in the wind. Consequently, the HBE is not capable of correcting for such fast bias variations as caused by the M1 temperature.

The M1 temperature correction also corrects for the linear term of the bias evolution associated with slow drifts in laser LOS or laser receive path alignment, that actually the HBE was designed to correct. The harmonic bias of L1B GCVs manually corrected for the M1 temperature bias shows amplitudes of < 0.75m/s for a 1st order fit and 1 m/s for a 2nd order (or higher) for most of the tested weeks. However, the lack of data in the equatorial region prevented the determination of a suitable harmonic fit order (Nikolaus, 2020).

The effect of the RDB was too small to be detected compared to other much bigger errors, such as the M1 temperature bias, which is not corrected on L1B (Weiler et al., 2021).

Nevertheless, ground return signals served as valuable input to various studies throughout the mission. Notably, a sensitivity of Aeolus ground return signals to surface characteristics was discovered and will be exploited as a new surface reflection parameter in the L2A processor (Labzovskii et al., 2023).

As foreseen, ground returns were used to derive the IRC (Instrument Response Calibration) curves for narrowband signals on the Rayleigh and Mie channel received via the atmospheric path. These curves were used as input for the L1B wind retrieval and, in a different way, also for the L2B wind retrieval (Marksteiner et al., 2023; Marseille et al., 2022).

Based on the coarse vertical resolution of Aeolus, with a minimum vertical resolution of 250 m but mostly 500 m per range-gate in off-nadir viewing modes, the accuracy of Rayleigh ground correction velocities (actually derived from a narrowband signal) suffers particularly from the atmospheric molecular (broadband) contamination within the detected ground bins (Nikolaus et al., 2019) and the atmospheric wind component within the ground bin. Additionally, ground returns from ocean surface need to be considered with caution due to the possible influence of ocean waves and currents moving relative to the instrument. Even under high albedo conditions (ice, snow), wind speed biases might be introduced by the effect of blowing snow over ice or snow surfaces.

3.7.1 Ground returns

One of the first activities after the launch of the satellite was the assessment of the radiometric performance of the instrument using, among others, the normalized Rayleigh and Mie ground useful signal from IRCs (Marksteiner, 2018; 2019). By considering the first 12 IRCs, it was found that the measured useful signals appear to be lower than the values obtained from simulations (E2S v.3.07 / L1B v.6.06 low orbit) by a factor of ≈5.0 and ≈2.75 for the Rayleigh and Mie channel, respectively. After correcting the impact of parameters influencing the radiometric budget (range, laser pulse energy, transmissions of optical path elements) known with different accuracy, the factors could be reduced to ≈3.8 and ≈2.1. This discrepancy between expected and measured signal was referred to as "initial loss", and could be explained by issues on the real instrument (e.g. clipping at the field stop), a too optimistic/ideal simulation setup (no clouds, no/homogeneous aerosol, high albedo, etc.) and/or E2S parameters deviating between characterizations obtained on-ground and in-orbit. A major uncertainty factor in this comparison using ground returns is the lack of knowledge about the actual albedo values for ice and snow, where value from the ADAM albedo map (version 3) were used in the simulations (E2S v.3.07 / L1B v.6.06 with lower orbit and patch for ground detection). Similar loss values were found in Marksteiner et al. (2020) and Nikolaus et al. (2019) which also confirms the disparity between Mie and Rayleigh channel. Detailed investigations into the causes of the initial loss can be found in section 3.10.2.

With respect to the operationally applied model-based M1 mirror temperature correction method using ECMWF model winds to determine the bias (Weiler, 2017), it could be shown that an alternative approach using measured ground correction velocities as an independent source of information can provide an almost comparable performance in reducing the variable bias in the L1B Mie and Rayleigh winds, namely by about 11% on average (with maximum deviations of up to 25.6 %). In contrast to the operational correction, the success of the independent approach is limited by the generally low availability of valid ground measurements outside the polar latitudes (Weiler, 2022). This is shown exemplarily in the Figure 40 below, which also reveals a seasonality effect in the availability based on the ice and snow coverage (Cito Filomarino et al., 2023).

For the A2D, the zero-wind correction mechanism was shown to work for the Mie channel, but with limitations for the Rayleigh channel at low albedo (Marksteiner et al., 2020), as it is hindered by the atmospheric contamination. It was shown, that the ground-return velocities can be used to determine the errors in the reported LOS pointing angles (mainly in the roll direction), which arise from uncertainty in determination of the star-tracker pointing wrt. instrument LOS. Applied to the Aeolus mission, such optimizations based on ground correction velocities led to the use of four different values for the <Roll_Error> parameter in the AUX_CHAR file during the reprocessing of the FM-A-1 phase (until the star tracker update on May 24, 2019).

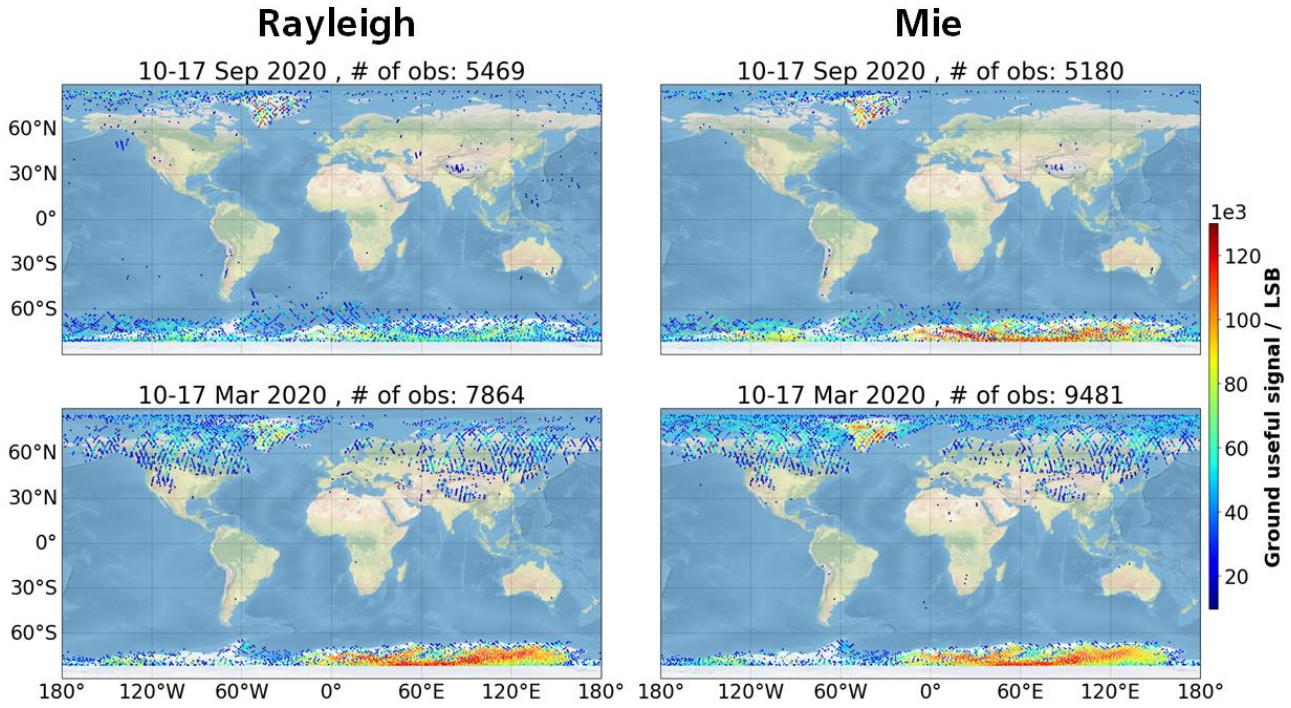

Figure 40: Geographical distribution of Rayleigh (left) and Mie (right) valid ground returns for March (bottom) and September 2020 (top) with the useful signal indicated by colour. Quality control was applied via a minimum threshold on the useful signal (> 9700 LSB) and a maximum threshold on the MAD Z-score value (< 3). The data was taken from Baseline 11 L1B products. (Cito Filomarino et al., 2023).

In general, the tuning of the ground detection algorithm, including an improved quality control (Weiler, 2019), resulted in a satisfactory ground detection performance in both channels in off-nadir mode (mainly WVM). An unresolved issue regarding a mismatch between the expected (from DEM) and the detected (from measurements) ground altitude was identified in nadir mode, i.e. for IRCs, for which a work-around could be provided.

3.7.2 Harmonic Bias Estimator

The original justification of setting up a Harmonic Bias Estimator (HBE) was the need to correct the Aeolus winds for potential harmonic contributors with orbital or suborbital periodicity, e.g. depending on the altitude (via orbital velocity) and latitude of the satellite. Due to the lack of heritage in terms of an Earth Explorer mission, the construction of the HBE was based on theoretical assumptions and simulations (Marksteiner et al., 2020).

Two independent algorithms for the reconstruction of the harmonic coefficients have been developed, one based on a harmonic fit method proposed by Airbus D&S and DLR (Marksteiner et al., 2020), and one based on a generalized Wiener filter with Bayesian statistics (Marksteiner et al., 2020; Nikolaus et al., 2019). The harmonic bias is a bias which can be expressed by harmonic functions of the argument of latitude x as

$$bias_{HBE} = \frac{A_0}{2} + A_1 \cos x + A_2 \cos 2x + \cdots + B_1 \sin x + B_2 \sin 2x + \cdots$$

, i.e. can be decomposed into Fourier series, where Ai and Bi are coefficients of order i in cosine and sine, respectively. It was found that the variation of the linear term $A_0/2$ is related to instrument drifts, that are also visible in development of the characteristics of the Mie and Rayleigh response calibration curves of IRCs and in ISRs. It was also shown that there is a correlation between IRC characteristics (drift and switch if IRC in the wind retrieval) and the linear HBE term in both the Mie and Rayleigh channels.

Part of the first-order B1 term was explained by the reported AOCS line-of-sight velocity, which is subtracted from the ground velocity in the L1b processor. Like the B1 coefficient, the v_{LOS_AOCS} also changes seasonally with a period of 1 year. It was assumed that the input for the calculation of the LOS speed (performed by the EO-CFI in the L1A) is not correctly reported by the on-board navigation filter. Therefore, the subtraction of v_{LOS_AOCS} was skipped. In the end, only the B1 coefficient showed a residual contribution to the harmonic bias with amplitudes of up to 0.145 m/s and 0.8 m/s in the Mie and Rayleigh channel respectively (Nikolaus, 2019).

Because of the strong spatial and temporal variations of the harmonic bias in the measured ground correction velocities, an estimation of harmonic bias coefficients over periods longer than approximately one week is not feasible without introducing a suitable preceding bias correction. If at all, a bias correction of 1st and 2nd harmonic order seems to be appropriate for the Mie and Rayleigh channel respectively. The root cause for the strong variations was eventually tracked down to the temperature dependence of the telescope primary mirror (M1), whose strongly non-harmonic and longitude dependent impact could only be corrected in the L2B stage using ECMWF model winds. As shown in Marksteiner et al. (2020), the correction curves provided by the HBE nevertheless largely resemble the development of the O-B bias. The fact that an end-to-end test up to L2B with HBE-corrected Mie (with satellite LOS velocity correction turned off) and Rayleigh winds showed no improvement in the winds, indicates the superiority of the operationally applied M1 temperature bias correction method (Marksteiner et al., 2020).

The HBE correction is only significant for high useful signals, approximately >30.000 LSB. For lower useful signals the Poisson noise is predominant (Marksteiner et al., 2020), but also for higher signal levels Poisson noise is relevant. At measurement (green) and observation level (violet), the standard deviation of the Rayleigh ground velocities is greater than that of the Mie ground velocities by a factor of around 10 (measurement) and 2 (observation) respectively (see Figure 41). The standard deviation of the ground velocity over all observations with useful signals >70.000 LSB (ice returns) is ≈1.0 m/s for the Rayleigh channel and ≈0.26 m/s for the Mie channel. These standard deviation values were derived from data sets from which the HBE had previously been determined and corrected.

The HBE was integrated into the Aeolus Calibration and Monitoring Facility (ACMF) with the possibility to be activated for operations. However, it was never switched on in operation (Jupin-Langlois and Perron, 2021; Marksteiner et al., 2020).

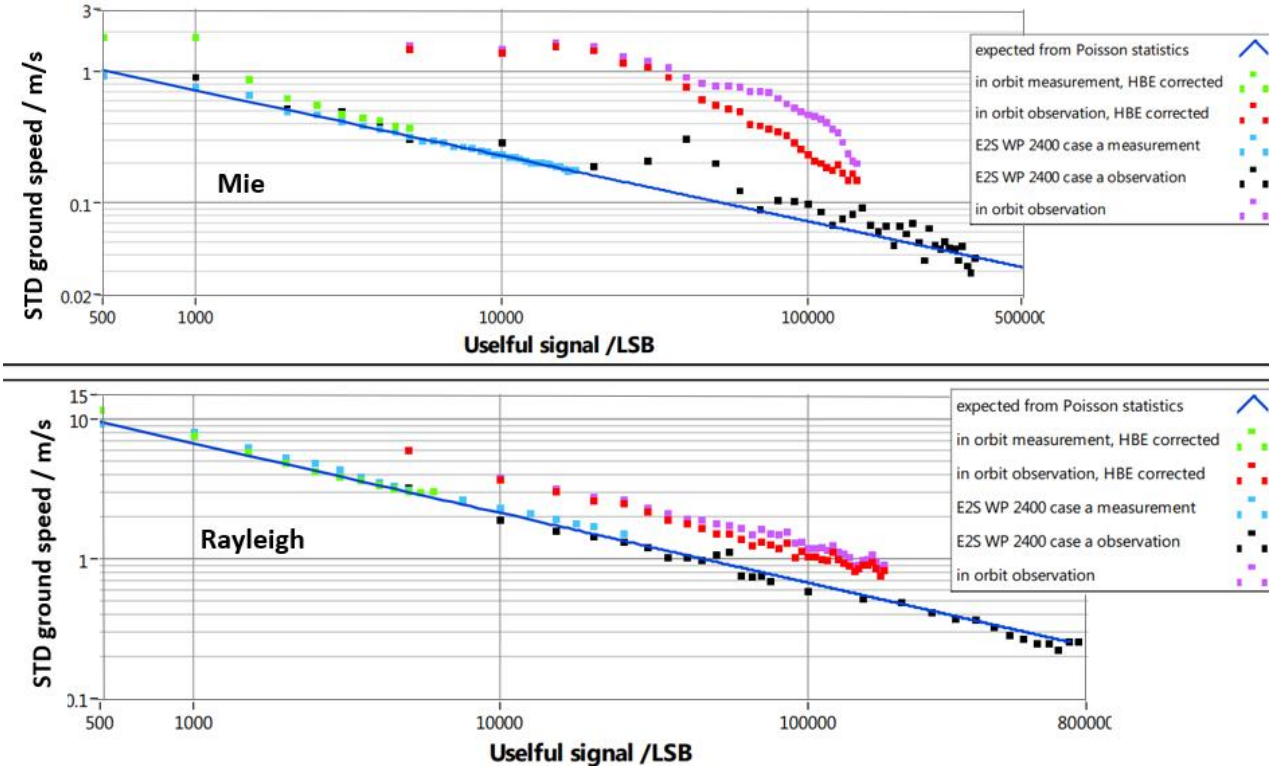

Figure 41: Standard deviation of "in-orbit" ground correction velocities at measurement and observation level from September 2018 until January 7th, 2019 (FM-A), compared to E2S simulations for the Mie (top) and Rayleigh channel (bottom). Ground returns from ice surface for the "in-orbit" data show useful signals larger than around 70000 LSB (at observation level).

3.7.3 Range-Dependent-Bias

Pre-launch investigations suggested that, in presence of a significant harmonic bias, the RDB should be determined over a small region of argument of latitudes with high albedo, preferably Antarctica. However, it turned out that the ground correction velocities changed over longer time scales for the same location. Therefore, considerable efforts were made to separate the (expectedly constant) range-dependent bias from the obviously variable harmonic bias according to Nikolaus et al. (2019). Three different approaches were applied to find evidence of a range-dependent bias, but none could provide sufficient significance:

1. Estimation of the RDB based on its harmonically varying component
2. Weekly determination of the RDB using a small range of argument-of-latitude
3. Calculation of the RDB after weekly HBE correction from a small range of argument-of-latitude

If existing, the RDB appears to be negligible or at least much smaller than the magnitude expected before launch (Nikolaus, 2016).

The investigations on the RDB were carried out at the beginning of the operational mission phase. Disregarding the M1 bias, it might still be of interest to re-assess the RDB with the latest baseline version. The improvements in the L1B processor should lead to less noisy, i.e. clearer results.

3.7.4 Lessons Learnt

- The ground correction velocities of Aeolus-1 derived from sea surface returns should not be used for the HBE / RDB detection. One reason is the low SNR and hence a low precision. Due to the low albedo of ocean a similarly insufficient performance is expected for Aeolus-2, despite its enhanced laser emit energy. However, based on its improved vertical resolution (~100 m) Aeolus-2 will be able to reduce the contamination of the ground return signal by the remaining atmospheric column above the surface. To profit from this effect, the vertical bin overlap (ACCD read-out during integration time) should be reduced significantly compared to Aeolus-1. Otherwise a summation of the ground return signal distributed over at least 2 bins would be required.
- The HBE as a function of latitude (argument-of-latitude) is not able to capture the variability of ground velocities caused by longitudinal influences (M1 temperature). Therefore, application of the HBE would introduce measurement artefacts along latitude bands, where it is not constrained by ground return measurements, and for example destroy the correlation between the uncorrected Rayleigh bias with the M1 temperature.
- Despite the predictions of higher useful signals and SNR (due to higher laser energy, better optics, smaller range-gates, etc.) for Aeolus-2, it remains to be shown, that Aeolus-2 can provide sufficiently precise ground velocity measurements that are suitable for bias correction (e.g. via Harmonic Bias Estimation) and can remove the dependence on the NWP model winds.
- The standard deviation of the ground correction velocities at observation level was found to be higher for real measurements compared to E2S simulations by a factor of 2 – 4 and ≈1.7 on the Mie and Rayleigh channel, respectively. This indicates that for Aeolus-2 a better on-ground characterization of the instrument is needed to be able to improve the end-to-end simulations. Improved comparisons to real measurements could then much more support potential troubleshooting during the operational mission.

3.8 Solar background

Karsten Schmidt and Oliver Lux, DLR

After each laser shot and the acquisition of the 24 atmospheric range gates, the acquisition of the atmospheric background radiation is started with a sufficiently long delay after the detection of the ground return. The background radiation can be assumed as a constant offset over frequency for the Mie and Rayleigh spectrometer measurements. It needs to be measured and corrected during the processing because it acts as a constant signal contribution to the acquired backscattered laser signals. Additional offsets to the signals, which need to be corrected for, arise within the detection chain from the electronic offset voltages (detection chain offset (DCO)).

3.8.1 DCO correction of the solar background signals

The operational L1B useful signals for solar background (SBG) were provided since the L1B processor version L1BP V7.08 in December 2019. Before that, a workaround was implemented by using L1A Mie and Rayleigh background measurement data. In order to compute the detection chain offset (DCO) for the Mie and Rayleigh detectors, the last two pixels 18 and 19 in the lowest row 24 on the ACCD for each measurement were used (2-pixels DCO; see Schmidt and Reitebuch (2024) for more details). This workaround was used throughout the mission to monitor the background radiation. After the availability of the operational SBG observations, comparisons with those of the workaround were performed. Additionally, a 4-pixels DCO correction to the L1A background measurements was also considered. It uses the pre-pixels (0,1) and the last two pixels (18,19) to compute the DCO.

Figure 42 shows a comparison of the operational L1B Mie and Rayleigh SBG observations (green lines) with those obtained by the 2- and 4-pixels DCO correction (blue and red lines, respectively) on 20/06/2022 during the primary SBG maximum in June. No large differences are seen. In this particular case, the mean Mie signal levels with the 2- and 4-pixels DCO correction, averaged over all observations, are about 2.2% smaller than that of the operational one. And the mean Rayleigh signal levels with the 2- and 4-pixels DCO correction are only about 0.1% larger than that of the operational one. The differences between the mean SBG signal levels with the 2- and 4-pixels DCO correction are even smaller (here about 0.03% for Mie and 0.005% for Rayleigh). A zoom in the signal minima reveals however larger differences. The Mie and Rayleigh SBG signal levels with the 2- and 4-pixels DCO correction are on the order of about 800 and 500 ACCD counts, respectively, while the operational L1B one varies around zero with a lot of negative values. About 20% of all L1B operational observations are negative on 20/06/2022. Similar situations were also found for other days (Schmidt and Reitebuch, 2024). Since the L1B SBG observations with a 2- and 4-pixels DCO correction were derived without a DCMZ correction, in contrast to the operational L1B one, the differences are due to the missing DCMZ correction.

3.8.2 Seasonal and orbital variations of the solar background levels

Figure 42 also reveals that the L1B Rayleigh SBG signals vary along the orbit. On 20/06/2022 during the primary SBG maximum, the orbital maxima were present in the Arctic while the minima were measured in the Antarctic. Vice versa, the maxima were given in the Antarctic and the minima were found in the Arctic in December during the secondary SBG maximum. The orbital variations are not only determined by the Earth orbit around the sun and the inclination of the Earth's rotational axis w.r.t. the ecliptic, but also by the changing sun irradiation with respect to Aeolus along the track, and by the changing Earth

albedo and clouds with respect to location and time. The sun irradiation on 20/06/2022, i.e. the sun elevation angle at the intersection of DEM and the LOS, is provided in the right panel of Figure 43

Figure 42 (red line). It is seen that the Rayleigh SBG signals (blue line) follow the sun elevation angle. The same holds also for the Mie SBG signals (Schmidt and Reitebuch, 2024). Furthermore, the ratio of the Rayleigh to Mie SBG observations exhibits the same orbital variations as the SBG signals themselves (left panel of Figure 43), and follows consequently the sun elevation angle, too.

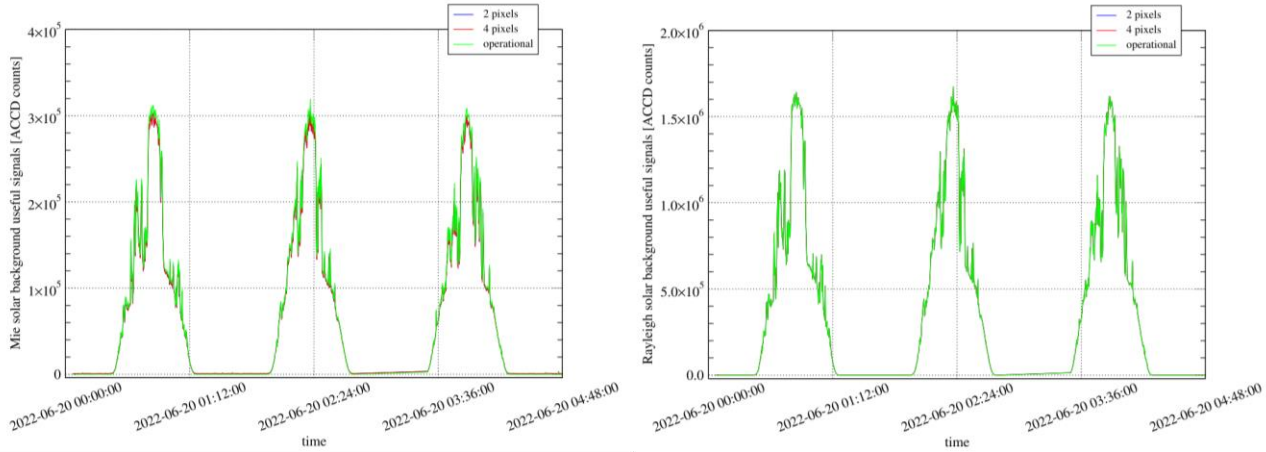

Figure 42: Left panel: Aeolus in orbit L1B Mie SBG useful signals on the observation level for the first three orbits on 20/06/2022, 00:04:17- 04:48:00 UTC (orbits 22154, 22155, and 22157) during the primary SBG maximum with a 2-pixels DCO correction (blue line), a 4-pixels DCO correction (red line), and the operational L1B SBG observations (green line). Right panel: Same as in the left panel but for Rayleigh.

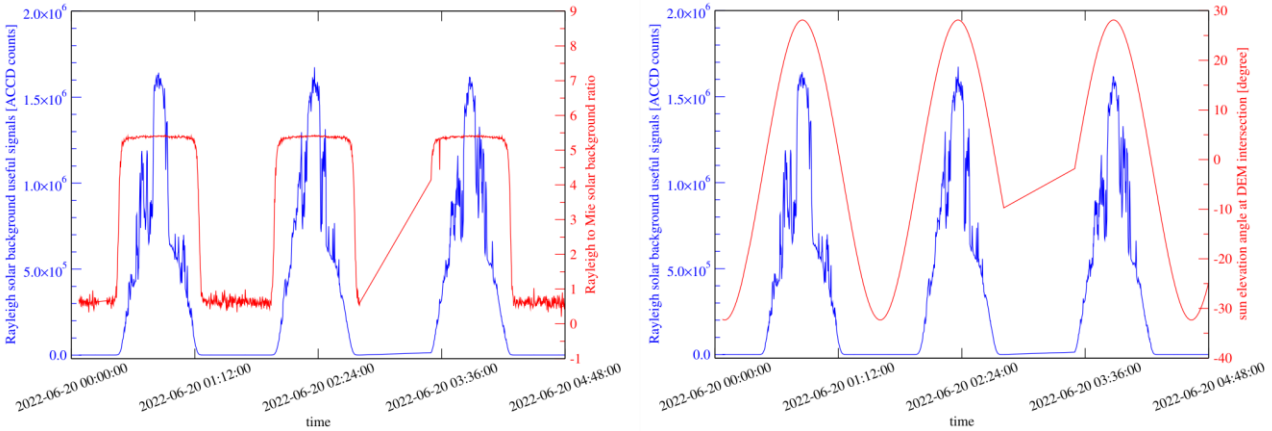

Figure 43: Left panel: Aeolus in orbit L1B Rayleigh SBG useful signals on the observation level for the first three orbits on 20/06/2022, 00:04:17- 04:48:00 UTC (orbits 22154, 22155, and 22157) during the primary SBG maximum with a 2-pixels DCO correction (blue line), and the corresponding ratio of the Rayleigh to Mie SBG useful signals on the observation level (red line). Right panel: Same as in the left panel, and the sun elevation angle at the intersection of DEM and the line-of-sight (red line).

The envelope of the orbital signal maxima exhibits an annual cycle (Figure 44). Maxima are obtained in June (primary, i.e. the largest SBG maximum) and December (secondary SBG maximum). The former arises in the Arctic, the latter in the Antarctic. Minima appear in October and in March when the orbital SBG maxima pass the equator. Note that the SBG signals versus the argument of latitude have been regularly monitored. The knowledge of this annual cycle could be exploited to perform special Aeolus operations and measurements requiring low SBG such as down under dark experiments (DUDEs). Mean L1B Rayleigh and Mie SBG useful signals on the observation level for a given orbit in the northern (NH) and southern hemispheres (SH) have been computed and checked for October 2020 to March 2022. In this way, the preferred dates when to switch the DUDE locations from NH to SH in March to minimize

the SBG contamination, and vice versa in October, have been determined, being the 3rd of March and the 9th of October (Schmidt and Reitebuch, 2024).

3.8.3 Changes in the operational settings

In Figure 44, a noticeable change of the signal behaviour is seen in April 2022. The subsequent overall signal level decrease was finally caused by two successive decreases of the background integration time. On 04/04/2022, starting with the orbit 20933, the number of pulses (P) per measurement and the number of measurements per observation (N) were increased and decreased, respectively from (P/N) = (37/15) to (114/5). The intention was mainly to improve the Rayleigh random wind error. However, this increase led to a saturation of the Rayleigh SBG pixels 4,5,6,13,14, and 15 due to the larger accumulation of background signals after every of the 114 laser shots per measurement, instead of formerly 37 only. This saturation, in turn, led to underestimated measured Rayleigh SBG signals. Note that there were only some few incidences of pixel saturation in the Mie channel so that a Mie SBG signal decrease was not observed. As a countermeasure, the background integration time was decreased from 180'000 TMC = 3750 µs to 60'000 TMC = 1250 µs on 11/04/2022 in both the Mie and Rayleigh channel. This led to a further Rayleigh SBG signal decrease and a corresponding Mie SBG signal decrease.

On 17/04/2022, pixel saturation started again, but mainly of the Rayleigh pixel 5 only, which was caused by the overall increasing background signals from the minimum in March towards the primary maximum in June. Therefore, the background integration time was further decreased from 1250 µs to 30'000 TMC = 625 µs on 22/04/2022, again applied to both channels. This led to a further signal decrease in both channels. The 625 µs background integration time was retained for the rest of the mission. In this way, pixel saturation could be avoided even in the SBG maxima in June 2022 and 2023. Note that background pixel saturation has been regularly monitored. Note furthermore that artificially large atmospheric Rayleigh useful signals were observed after the P/N setting change on 04/04/2022 and after 17/04/2022 which were caused by the saturated Rayleigh SBG pixels leading to erroneous background corrections of the atmospheric signals. The two subsequent decreases of the background integration time on 11/04 and 22/04/2022 corrected these artefacts.

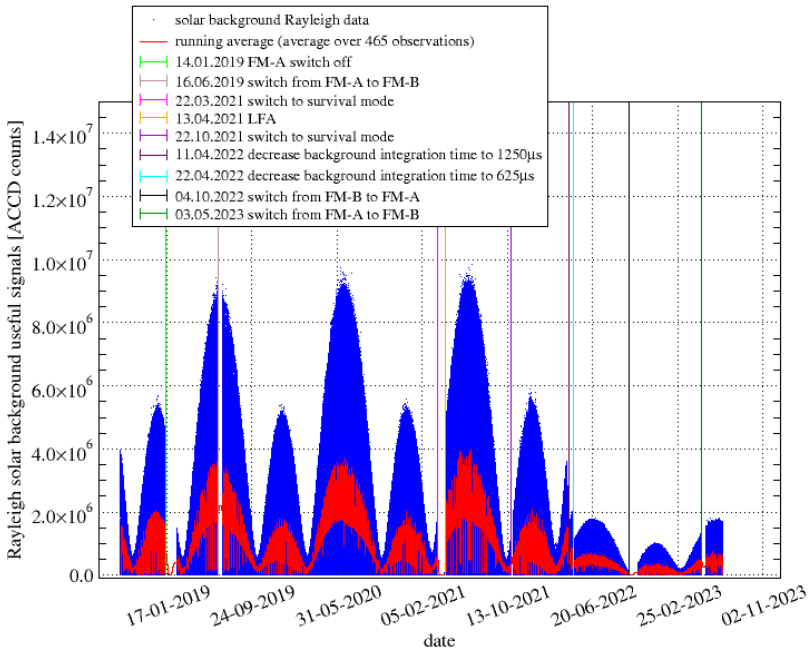

Figure 44: Aeolus in orbit L1B SBG useful signals on the observation level with a 2-pixels DCO correction in the Rayleigh channel from 03/09/2018 to 05/07/2023, comprising 24'487 orbits and 11'462'430 observations (blue line), and their running average, averaged over 465 observations (red line); on 11/04/2022 the SBG integration time was changed from 3750 µs to 1250 µs, and on 22/04/2022 to 625 µs, which explains the lower maxima in 2022 and 2023.

3.8.4 Differences between solar background signals on Mie and Rayleigh channel

It was seen that the L1B Rayleigh SBG observations are in general larger than the Mie SBG observations (y-axes in Figure 42), while their ratio was not constant along the orbit, but varied as the background signals and the sun elevation angle at the intersection of DEM and the line-of-sight did (Figure 43). The above-mentioned differences in the signal minima between the Rayleigh and Mie background signals with a 2- and 4-pixels DCO correction on one hand, and the operational L1B ones on the other hand, have also an influence on the ratio of the Rayleigh to Mie SBG observations. Compared to the former ratios with a DCO correction only, the ratio derived from the operational L1B data has a larger variance and also a lot of negative values (Schmidt and Reitebuch, 2024).

The plateau formed by the maxima of the Rayleigh to Mie SBG ratios was also not constant during the mission, but had increased gradually and slightly non-linearly (Figure 45). In this figure, the red line provides an estimate of the increase of the plateau values, ranging from about 4.82 on 03/09/2018 to about 5.48 on 05/07/2023. Note that the Rayleigh to Mie SBG ratio of the ALADIN Airborne Demonstrator (A2D) was also checked for several flights from 2016 to 2021. It ranged between 3.9 and 4.2. Investigations of the yearly mean L1B SBG observations have shown that the Rayleigh signal level has tendentially increased from 2019 to 2021 while the Mie signal level has tendentially decreased. This indicates that the Rayleigh channel is responsible for the observed increase of the Rayleigh to Mie SBG ratio. More detailed investigations of the L1A Rayleigh and Mie SBG useful signals on the measurement level per pixel in 01 – 12/12/2018 / 2019 / 2020 / 2021 / 2022 have confirmed this conclusion (Schmidt and Reitebuch, 2024).

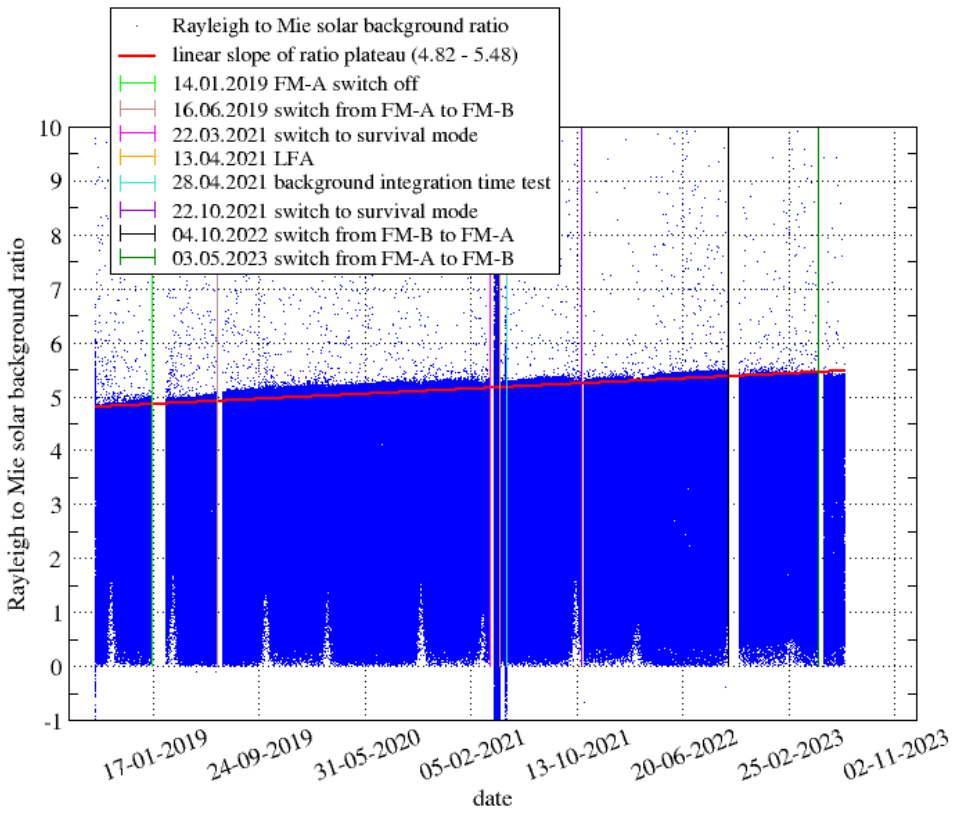

Figure 45: Ratio of the Aeolus in orbit L1B Rayleigh to Mie SBG useful signals on the observation level with a 2-pixels DCO correction from 03.09.2018 to 05.07.2023, comprising 11'437'308 observations. The maxima and minima have been truncated. The peak ratio is 1257.0 obtained on 03.04.2021, 19:00:20 UTC. The smallest ratio is −1053.0 obtained on 04.04.2021, 21:15:20 UTC. Both extrema occurred after the switch-on of ALADIN on 01.04.2021 and before the LFA on 13.04.2021.

Figure 45 shows periods of large positive and negative Rayleigh to Mie SBG ratios. In the beginning of the mission on 03/09/2018, a too short background integration time has led to too low and even negative Mie and Rayleigh SBG useful signals, resulting in such ratios. A too short background integration time was also the reason for the other occurrences of large positive and negative Rayleigh to Mie SBG ratios in the beginning of April 2021 after the switch of ALADIN from the measurement to the survival mode on 22/03/2021, and during the background integration time test from 28. to 29.04.2021 at the initial integration time of 101 TMC = 2.1 µs (Schmidt and Reitebuch, 2024). In the former case, an unexpected short background integration time also of 101 TMC (2.1 µs) was noticed on 01/04/2021 which was corrected during the LFA on 13/04/2021 by the usual one of 180'000 TMC (3750 µs).

3.8.5 Correction of the solar background integration time

When analyzing the detector anomalies, more specifically the non-uniformity of the memory zone efficiency (see section 3.3.3), it was noticed that the background integration time, reported in the L1A product from in-orbit settings, is slightly inaccurate. Based on solar background signals measured at different background integration times during a dedicated test on 14/05/2023 in the frame of the end-of-life activities (EOLA#27, section 3.6), a correction term was derived. The test results showed that the effective background integration time is (13.7 ± 0.8) µs longer than what is reported in the product, independent of the set value. This correction value was independently confirmed by analyzing the dependency between solar background levels and sun elevation angle. The reason for the discrepancy between reported and effective background integration time was found to be the specific image binning and flushing procedure of the ACCDs which is different for the atmospheric samples and the background samples.

The underestimation of the background integration time led to an overestimation of the solar background signals when normalizing to the integration time, and hence a subtraction of too high values during solar background correction. The error scaled with the integration times of the respective atmospheric range bins (due to the upscaling of the normalized solar background signals) and was largest toward the end of the mission after the background integration time was reduced from 3750 µs to 625 µs in April 2022, thereby increasing the relative error from $13.7/3750 \approx 0.4\%$ to $13.7/625 \approx 2.2\%$.

Lessons learnt for Aeolus Phase F:

- The computation of the current operational L1B SBG signals including DCO and DCMZ correction could principally result in negative SBG values per pixel. This issue is also known for atmospheric range bins especially for Mie pixels. Further investigations of the frequency of occurrence, its impact on higher level products and possible refinements (e.g. using zero for negative SBG values) should be investigated.
- Saturation of background and atmospheric pixels should be operationally checked including a flagging, warning, and the application of a quality control in the L1B processor, which was already implemented in B13 L1B processor versions. Correct flagging of SBG layers should be checked in further analysis.

3.9 Analysis of signal evolution and signal clipping at the field stop

Ines Nikolaus, Physics Solutions and Oliver Reitebuch, DLR

To find one of the possible root causes for the unexpectedly low and decreasing signal return of the Atmospheric Laser Doppler Instrument (ALADIN), we investigated the clipping at the field stop (FS) in the instrument's Rayleigh channel for laser beam monitoring (LBM, for internal path measurements) and instrument defocus characterization (IDC, for atmospheric returns), where full 2D spot images are available (see Figure 46).

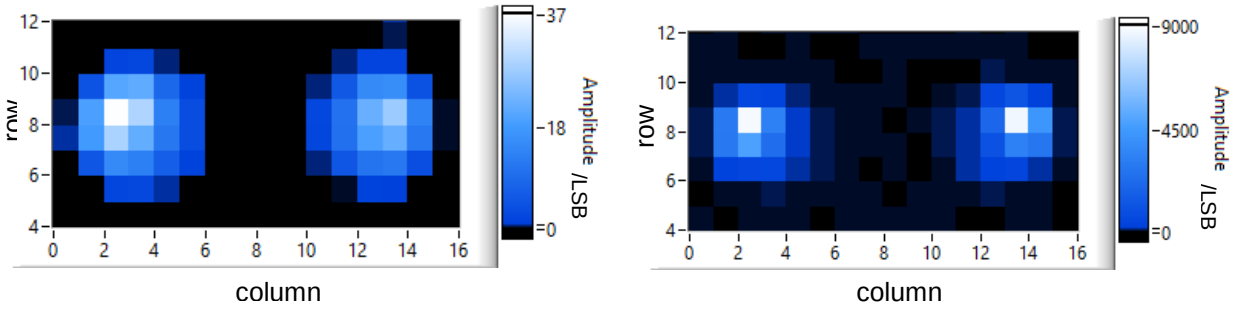

Figure 46: Example of an IDC image (left) and an LBM image (right), both on ACCD pixel subsets for vertical rows, counting starts from pixel 0 to 15 for rows and columns.

The expected design parameter of the instrument specifies a field of view of 18.1 µrad in the atmosphere, which corresponds to a diameter of the FS image of 3.75 pixel at the ACCD (Accumulation Charge Coupled device) detector plane. This assumption, however, does not explain the illumination of pixels in 2D images outside of the FS diameter from atmospheric as well as internal receive paths.

Initial model fits to ACCD images from atmospheric returns with location and size of the FS image and location and width of a Gaussian beam as model parameters indicate a significantly larger beam diameter. The model was then refined to an illuminated spot with trapezoidal illumination shape, suggesting a defocus or a FS with an inner and outer diameter structure rather than a circular hole, which is explained in Figure 47.

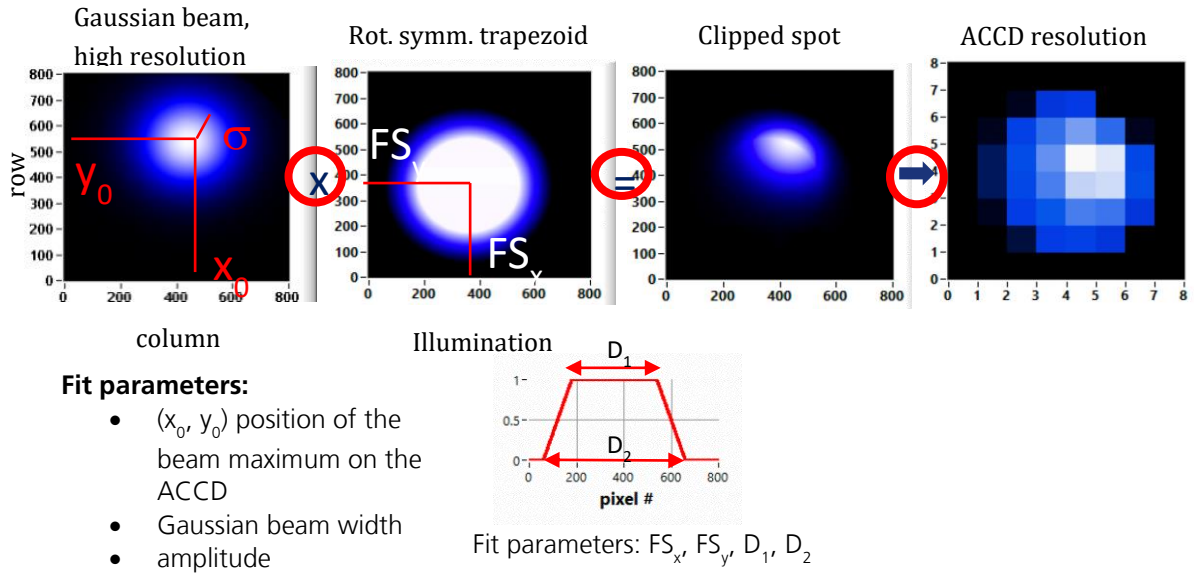

Fit parameters:

- (x_0, y_0) position of the beam maximum on the ACCD
- Gaussian beam width
- amplitude

Figure 47: Model: A Gaussian Beam (upper left) is clipped with an aperture with an internal diameter D1 and outer diameter D2 (2nd upper left), where the illumination within D1 is uniform and between D1 and D2 is linearly decreasing to zero (lower graph). This filed stop structure would result in a clipped beam (2nd upper graph from right), which results in a pixelated image on the ACCD (upper right).

This fit results in reasonable and consistent parameters values for the FS location and size, see Figure 48.

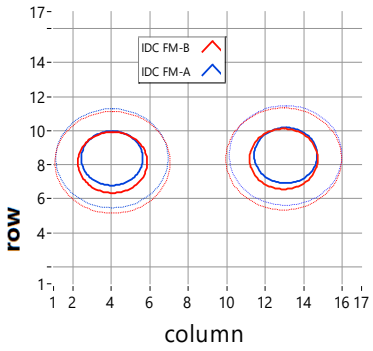

All values in pixel	FM-A		FM-B	
	direct	reflected	direct	reflected
Field stop center row	8.36 ± 0.09	8.50 ± 0.02	8.11 ± 0.07	8.31 ± 0.07
Field stop center column	4.08 ± 0.02	13.07 ± 0.03	4.09 ± 0.05	12.98 ± 0.07
Field stop diameter D_1	3.19 ± 0.05	3.27 ± 0.08	3.60 ± 0.06	3.55 ± 0.04
Field stop diameter D_2	5.82 ± 0.06	5.86 ± 0.08	5.98 ± 0.12	6.00 ± 0.12

Figure 48: Location and size of inner and outer FS diameters for direct and reflected Rayleigh channel and both lasers on the ACCD; values were derived from atmospheric path IDCs.

The determined beam parameters such as spot centre and width are nearly the same as the results of simple Gaussian fits used for other measurement modes such as Wind Measurement (WVM), and their temporal evolution is the same, as illustrated in Figure 49.

For the spot determination in WVM mode the Gaussian fit to the 1D WVM data does not take clipping into account and only fits mean ACCD pixel values, which explains the differences.

For IDC and LBM modes with 2D ACCD data it is also possible to calculate the spot movement in vertical (row) direction. It was found that the spot moved upwards by 0.2-0.3 pixel in both atmospheric and internal measurements for both channels. The spot movement in both channels is strongly correlated.

The resulting energy loss of the atmospheric signal as found in WVM measurements could be reproduced very well with this model. Both the total energy loss and the time evolution of the energy loss, however, cannot be explained by signal clipping at the FS alone, and additional signal losses in the clear aperture are being observed. Figure 50 shows the measured atmospheric and internal relative signal strength in comparison with the model's result as well as the decrease that is due to the clipping at the FS. The simulation also reveals, that there is a signal degradation because of clipping at the start of the measurement time, which is about 40% in the direct channel and 33% in the reflected channel for atmospheric returns and 5% / 12% for the internal channel (direct / reflected).

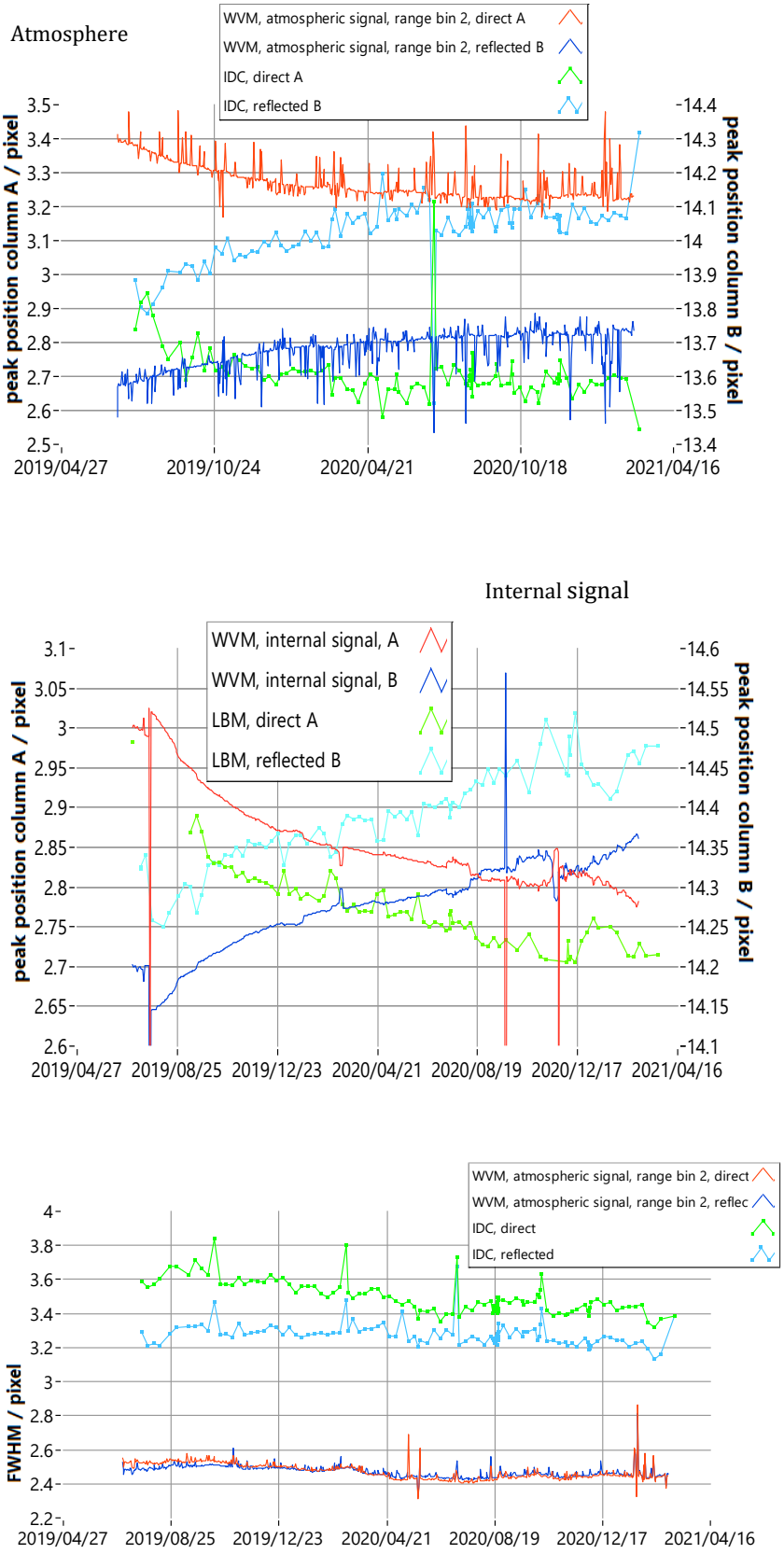

Figure 49: Temporal evolution of the beam's peak position in horizontal direction (uppermost graph for atmospheric signal, 2nd graph from above internal signal) and it's FWHM (lower two graphs for atmosphere and internal signal, respectively) in comparison with results of a fit of a 1D-signal in the 16 ACCD pixels from WVM mode without modelled clipping, for FM-B laser period from July 2019 to March 2021.

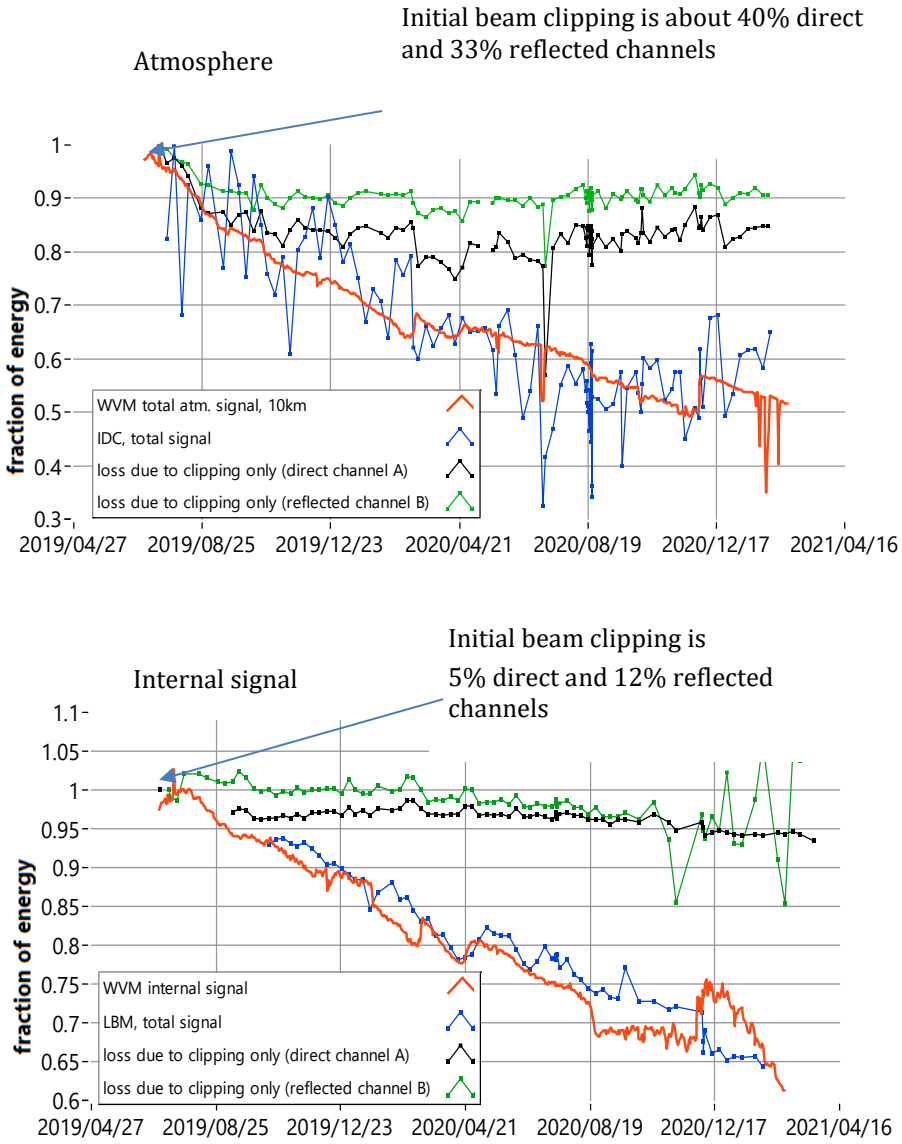

Figure 50: Comparison of energy loss from WVM and LBM measurements and energy loss due to clipping at the FS structure, above atmosphere, below internal channels, here for FM-B.

For FM-A, the (atmospheric) IDC measurements showed an irregular behaviour from October 2018 to December 2018. The energy (and maximum) of the beam increased by a factor of ≈ 5 (with the exception of 20/1/2018, where the energy was at the same level as in October 2018). This is shown in Figure 51. This increase could be traced back to the solar background change with time as IDC measurements were performed at the same orbit location each week, and the issue that no solar background measurement and correction is performed for IDC mode. Thus, IDC measurements are only representative of atmospheric laser returns, if they are performed in complete darkness. Energy and beam width are therefore not comparable with the atmospheric signal from WVM measurements, which showed an energy decrease of about 30% during the entire FM-A period from September 2018 to June 2019. The IDC measurements, however, revealed, that the beam is very well centred (see Figure 51, top graph), such that there is no energy loss because of decentring. Nevertheless, the beam is truncated at the field stop by about 40% (direct channel) and 30% (reflected channel) at FM-A start.

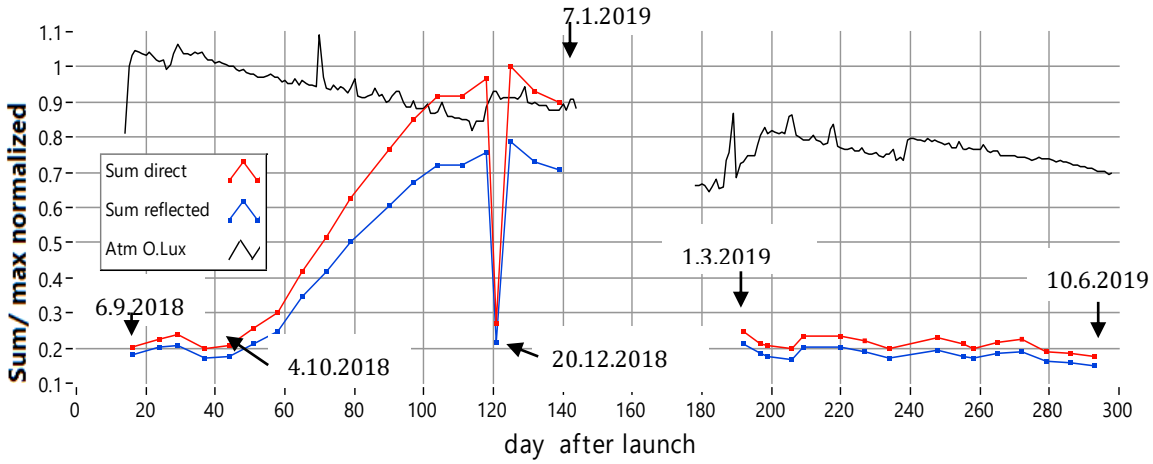

Figure 51: Energy from atmospheric returns (black line) in comparison to energy from IDC measurements (red and blue lines for direct and reflected channels, respectively), all curves normalized to 1.

For LBM (internal) measurements a comparison to apparent spot position and width from Gauss fit to internal WVM line data per BRC (mean value per day), and Gauss fits to ISR data is possible (Figure 52). The spot positions show the same trends (both spots move towards the field stop centre / ACCD centre) with a little difference of 0.05 pixel – the WVM results are in between ISR and LBM results. The 4σ-beam width found in LBM data is about 0.3 pixel lower for the direct channel than the apparent beam width from ISR / WVM line data. For the reflected channel it is near the WVM data before switch off in January 2019, after it is 0.1-0.05 pixel lower. The trends of the beam width are similar for the different products.

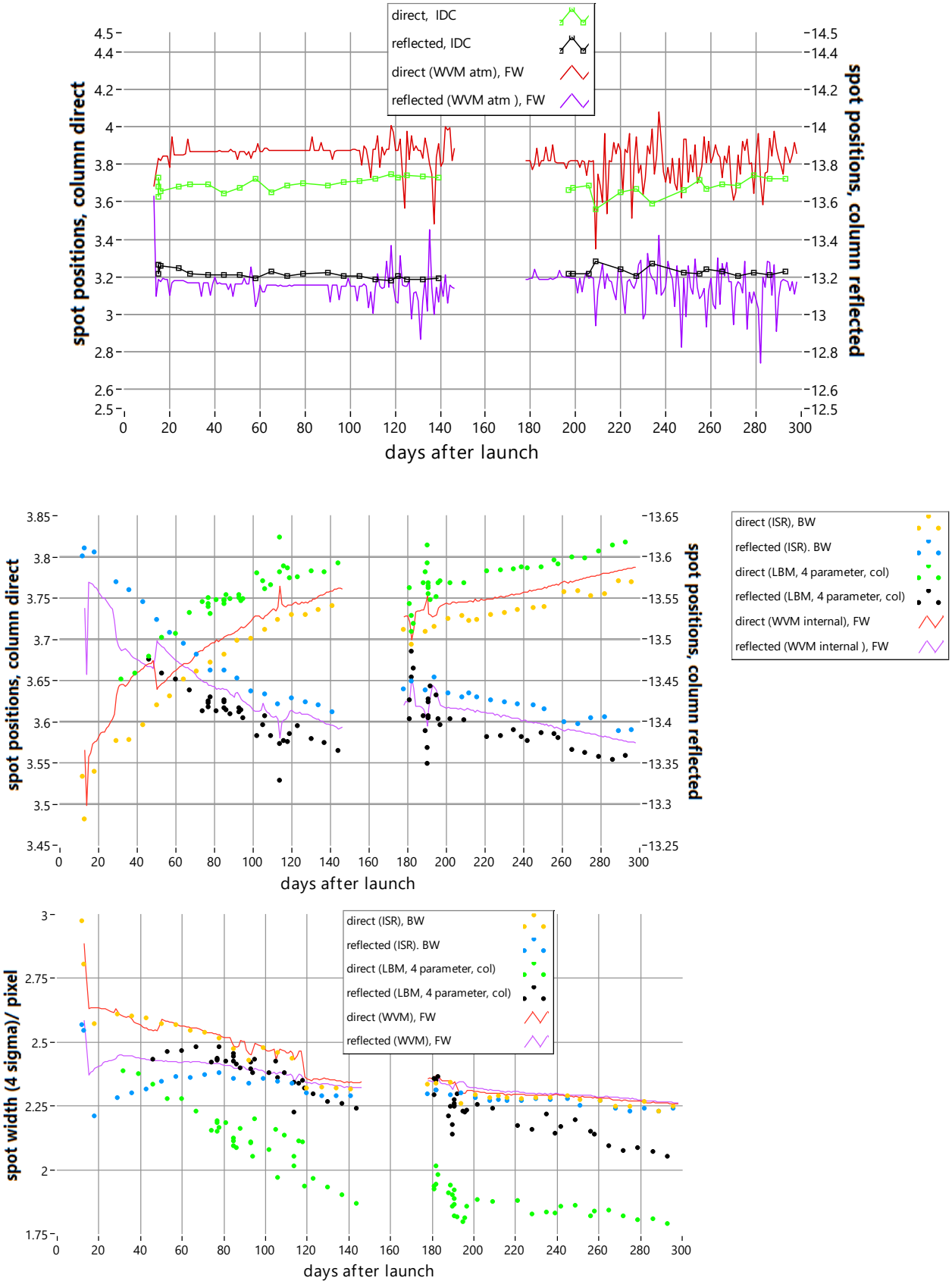

Figure 52: Temporal evolution of the atmospheric (upper graph) and internal beam's peak position (centre graph) in horizontal direction and the internal beam's FWHM (lower graph) from IDC / LBM measurements in comparison with results of a fit of a 1D-signal in the 16 ACCD pixels from WVM and ISR modes without modelled clipping, for FM-A laser period from September 2018 to June 2019.

The changes in the spot centre in vertical (row) direction are about 0.1 pixel for internal (LBM) measurements in both channels and 0.3 (direct) and 0.15 (reflected) for the atmospheric (IDC) measurements.

Figure 53 shows, that the energy decreases from the model fits to LBM data very well to the loss of the internal signal in WVM measurements. This confirms that for the internal path the measured internal signal at the Mie spectrometers is determined by the laser energy (see section 3.2.1), and no additional losses are observed in the clear aperture (as for the FM-B laser) and the signal decrease is not caused by additional clipping.

Further details of the clipping analysis are contained in several presentations (Nikolaus, 2021a-d) and a poster that was presented at the Aeolus 3rd Anniversary Conference in 2022 (Nikolaus and Reitebuch, 2022).

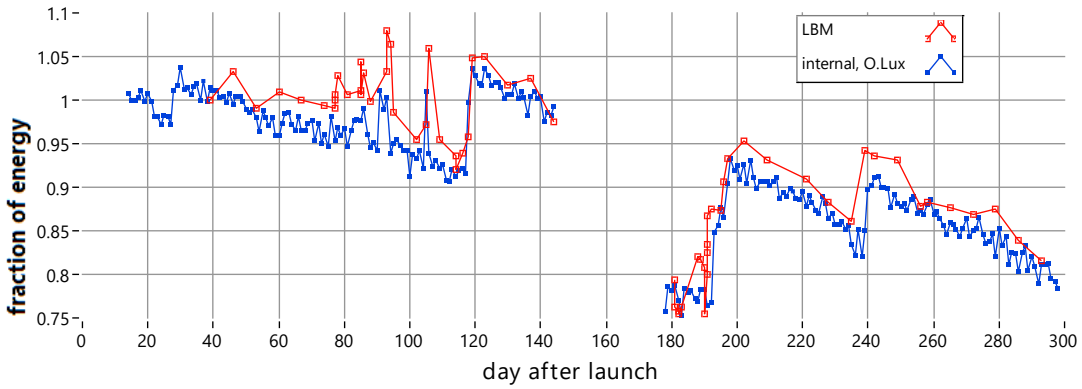

Figure 53: Comparison of energy loss from WVM measurements and energy decrease according to the fit to LBM measurements (internal signal) for FM-A laser period from September 2018 to June 2019.

3.10 Synthesis of the work performed in instrument performance

Frédéric Fabre, Les Myriades

3.10.1 Introduction

This section provides a synthesis of the work performed by Myriads Consulting for instrument performance. The collaboration between Myriads Consulting and DLR started beginning of 2020. At that time, the switch to the laser B was performed 7 months ago, in June 2019 and, despite correct operation of the instrument, the main issues were:

- An important signal loss from the initial operations after launch, about factor 2.5 on the Rayleigh channel,
- A start of decrease of the useful signal with the laser B
- An increased unknown bias

In the sections below, the main investigations are discussed, which were summarized in several documents.

3.10.2 Analysis of initial signal loss

The initial signal loss observed on the Rayleigh return impacted significantly the random error. For this reason, the analysis of the possible root causes was one of the first tasks performed. This is summarised in Fabre (2021a).

This analysis starts from the equation of the lidar link budget to identify systematically all potential contributors to the initial loss. A discussion about the likelihood of the causes was proposed in the document and led to conclude that the following causes are the most probable:

- Telescope aberrations
- Laser chopper mechanism synchronization anomaly
- Micro-vibrations
- Atmospheric turbulences

Later, a discussion with Airbus D&S led to identify the contamination on the primary mirror as a likely cause as well. Other causes were identified but with a lower probability.

Except the anomaly on the laser chopper synchronization, the most likely causes would increase the total field of view and then generate a clipping of signal on the instrument field stop. That is why an image synthesis (see section 3.10.4) was developed in order to estimate the actual clipping due to the far field properties measured on the Rayleigh receiver. This analysis did not allow to correlate the far field clipping with the instrument losses: in practice, the far field distribution remains grossly within the field stop. This would lead to remove the effects of the telescope aberrations, the micro-vibration effects and the impact of atmospheric turbulences. By the way, a new idea for the cause of the initial loss was discussed recently: the fact that the primary mirror is affected by spherical aberration, what is rather easy due to the aperture and resulting F-number of this mirror (F/0.9). In case spherical aberration is present in the mirror, the spot that is formed in the field stop is like a thin spot on top of a pedestal (the caustic). This is explained in Figure 54 below, the red circle being the field stop.

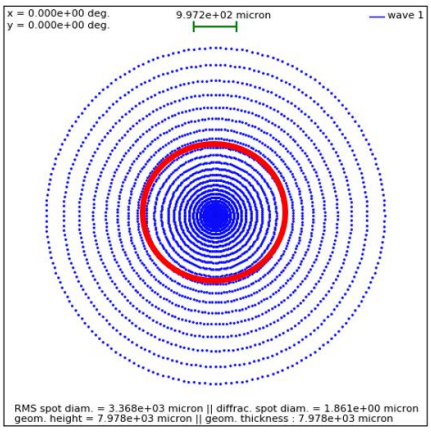

Figure 54: Illustration of a far field distribution generated by spherical aberration, seen through the field stop (red circle). The spot looks like a thin spot but the loss due to clipping is important.

In practice, Airbus D&S demonstrated that a loss of 50% can be achieved with the radial thermal gradients that were observed in the primary mirror. This cause is therefore confirmed as candidate to explain the initial losses. Other causes like an anomaly in the polarization management in the optical elements of the instrument TRO (transmit-receive optics), or the contamination of the primary mirror remain also highly probable. This could be a combination between all these causes.

3.10.3 Analysis of signal loss with laser B

Rather rapidly after the switch-on of the laser B, a decrease of the useful signal was observed. Like for the initial losses, a systematic analysis of the possible root causes was initiated and is detailed in Fabre (2020a). This analysis led to identify a possible gas release during the activation of the optical switch (flip flop mechanism) to go from the laser A to laser B (see Figure 55).

Other causes could be associated with the clipping in the far-field since the laser B presents a misalignment with regard to the receiver. Nevertheless, the image synthesis allowed to demonstrate that the clipping due to misalignment is not sufficient to explain the losses.

Later, the switch back to the laser A at the end of the Aeolus life demonstrated that the losses were nearly fully recovered, meaning that LIC (Laser-Induced Contamination) or LID (Laser-Induced Damage) is present in the optics that are specific to the laser B operations. Bulk absorption in one thick optical part is also identified.

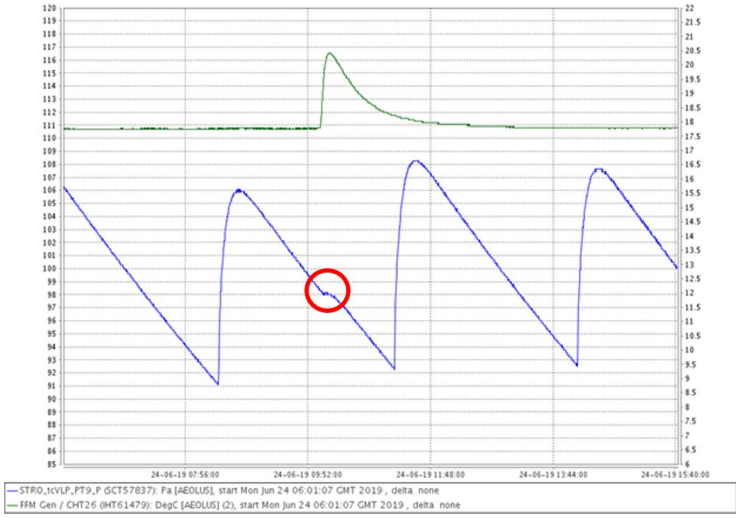

Figure 55: Pressure increase during the activation of the optical switch (red circle).

3.10.4 Image synthesis

All along the in-orbit life of Aeolus, the size and positions of the spots that are formed on the Rayleigh receiver were followed with care as they correspond to the far field pattern at the input the spectrometers. As a matter of fact, the far field pattern strongly acts on the receiver responses. Yet, the observation of the spots on the Rayleigh channel detector is made with low spatial resolution and behind a field stop which clips the spot. For these reasons, the spots that are seen on the detector are not necessarily the same as before the field stop. This led to perform an image synthesis in order to compare the real spot that is before the field stop and the apparent spot observed on the Rayleigh CCD. This image synthesis tool allowed the difference between the spot size and position of the apparent and the real spots to be computed. In addition, a module in the developed software allowed to compute the difference in spectral responses, for instance due to the spot differences on the internal calibration path and the atmospheric one. This analysis brought information about the effect of the beam clipping on the overall efficiency and led to propose several hypotheses about the initial losses and losses with the laser B. In addition, this analysis led to conclude that the signal jumps are due to a parasitic signal which is uniformly spread in the field stop. This analysis is presented in Fabre (2023b). Figure 56 shows the difference between the spot size and position (or far-field pattern at spectrometer input) with the laser A and with the laser B. The laser B spot images present a misalignment with regard to the centre of the field stop (red circle).

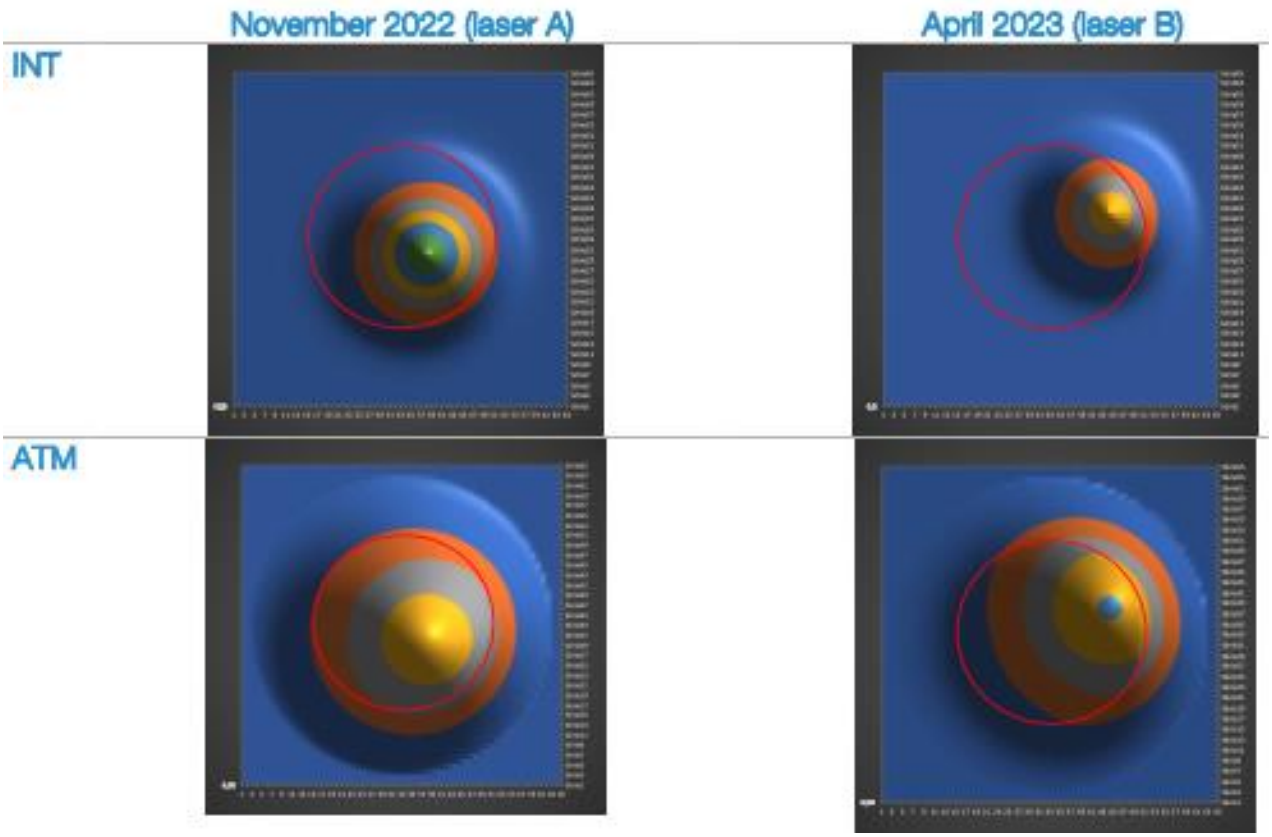

Figure 56: Far-field pattern at spectrometer input of the internal path (INT) and atmospheric path (ATM) beam for laser A and laser B. The laser B spot images present a misalignment with regard to the centre of the field stop (red circle).

3.10.5 Opportunity for orbit lowering

When the signal loss was observed with the laser B, an assessment was initiated about the interest in lowering the Aeolus orbit. As a matter of fact, a reduction of the orbit altitude by 10% is equivalent to an increase of the laser energy of 20%. This analysis was performed in three steps:

1. Trade-off between the different options to increase the useful signal with laser B (Fabre, 2021b)
2. Analysis of the show stoppers (Fabre, 2021c): what could prevent from lowering the orbit? The synchronization of the laser chopper mechanism was identified as the main potential issue.
3. Impact analysis (Fabre, 2021d): the impact on the performance, lifetime and robustness to space environment were analysed and led to conclude that the orbit lowering is feasible.
4. Conclusions and recommendations (Fabre, 2021e): even if the orbit lowering is feasible, caveats appeared during the study, like the fact that the orbit lowering would not allow to compensate the losses on the internal calibration path.

This study provided material to ESA for the decision about the lowering of the orbit. In the end, this was not implemented and the switch to the laser A was preferred, betting on the fact that the losses with laser B was due to LIC or LID in optics that are specific to this laser. And the bet was won.

3.10.6 Opportunity to switch to the laser A

Following the study about the orbit lowering, the switch to the laser A was identified as an interesting alternative although, if the LIC due to the flip-flop mechanism activation is the root cause of the signal loss with laser B, a new activation could even increase the attenuation. A dedicated study was led with different scenarios in order to predict the long-term gain of a possible switch to the laser A. In any configuration, an immediate interest was demonstrated for the switch to the laser A but long-term behaviour depends on the law used to extrapolate the signal loss with the laser B. In case a linear law is used for this extrapolation, there was a clear interest in switching to the laser A. In case an exponential negative law is used, the interest over long term is less obvious. This analysis was used to support a decision to switch to the laser A. This switch proved that losses observed with the laser B were due to attenuation on optics that are specific to the laser B (e.g. the flip flop mechanism optics). The study is reported in Fabre (2022b).

3.10.7 Analysis of parasitic signals

During the in-orbit operations of Aeolus, some spurious signals were observed, like the “signal jumps” (section 3.2.3). Several analyses were made to correlate these phenomena with other parameters, like the oxygen pressure, without clear success. Nevertheless, a detailed analysis of the signals during the “jump” phases allowed to identify that the jumps are due to a signal which is uniformly spread over the field stop, probably straylight. Several hypotheses were studied in Fabre (2020b) and Fabre (2022a) without real conclusion. The explanation came in the end from the end-of-life test, as explained in the next section.

3.10.8 Participation to the EOL test definition and analysis

In the frame of the Aeolus as an Earth Explorer mission, it was decided to perform some specific tests that may be critical for the satellite health at the end of the nominal mission. In order to better understand the role of the laser chopper mechanism in some anomalies like the initial losses or the jumps, it was decided to tune the synchronization of this chopper with regard to the laser emission. The result is that the signal and signal variability change versus this synchronization what could explain the jumps (section 3.2.3). Further, a hypothesis was made about spurious reflections on the rear side of the chopper blade, what could generate either parasitic signal back to the receivers or interference phenomena (only if the reflection on the blade generates depolarization). The latter hypothesis could explain the sensitivity of the "signal jumps" to the oxygen pressure in the receiver cavity. This is explained in Fabre (2023a) and Fabre (2023c).

The principle of the coupling with the chopper blade is given in Figure 61. The input signal is first forwarded to the Mie receiver, then to the Rayleigh receiver and a part of the signal is sent back to the chopper blade. This blade is closed during the acquisition of the internal calibration signal, so that a part of the signal is sent back to the receiver, leading to either straylight or interferences.

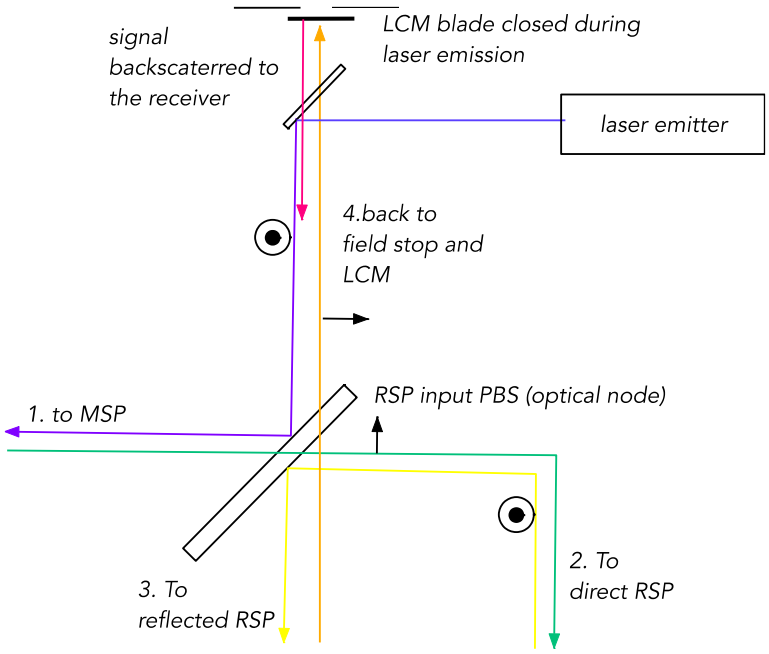

Figure 57: Optical path of nominal and parasitic laser beams that are propagating in the transmit-receive optics arrangement, potentially causing the internal path anomalies.

3.10.9 Lessons Learnt from performance synthesis:

- Playing some of the EOL tests earlier would have save time and money in analyses
- Detailed analyses from Airbus France (ADS-F) should have been made earlier. For instance, correlation of the thermal maps of the primary mirror, or links between thermal maps and bias. An additional budget for analyses, by industry, of the main anomalies would have been beneficial.
- Major progress was achieved during face-to-face meetings.

- There is sometimes a gap between engineers and scientists in terms of approach and understanding. How to ease mutual understanding? The DISC and institutes like DLR, which are in-between, have a major role for bridging this gap.

4 L1B, L2A, and L2B Algorithm and Processors

4.1 L1B algorithms

Oliver Reitebuch, DLR

4.1.1 Introduction and History

The Aeolus processing up to product level 1B (L1B) makes use of three processors: the L0 processor (converting the downlinked Annotated Instrument Source Packets (AISP) into L0 products), the L1A processor and the L1B processor. The study and development of the L1B Processor and the Aeolus End-to-End Simulator (E2S) started at DLR in cooperation with DoRIT already in 2004 within an ESA-ESTEC contract, which involved also Météo-France for the L2A processor. Already in the 1990's dedicated performance simulations and algorithm activities were conducted by DLR and others for preparation of the mission selection in 1999. This L1B/L2A processor development was performed in close collaboration with a similar activity for the L2B processor by ECMWF and KNMI. Both contracts were running until end of phase E1 (January 2019) and were merged into the Aeolus DISC activity. This long-standing and close cooperation of the algorithm teams and processor developers was one of the prerequisites for the swift availability of the first atmospheric signal and wind profiles within 2-4 weeks after Aeolus' launch, and the successful performance of the Aeolus mission. The decisions about the functionalities, algorithm implementation and trade-offs between L1 and L2 processing were made in close cooperation between these algorithm teams. Already the pre-launch version of the L1B operational processor had significantly more functionalities, output parameters, and refined algorithms as proposed by space industry (e.g. as described in the Master Algorithm Document), which is documented in the L1B Algorithm Theoretical Basis Document ATBD (DLR, 2018).

A significant difference between L1 to L2 processing is the usage of external data (e.g. atmospheric temperature, pressure), which is limited to the L2 processing stage. Thus, the L1 stage, relying solely on instrument and satellite data, does not contain any correction of the molecular line shape with respect to atmospheric temperature and pressure, which is needed for the correct derivation of the winds from the Rayleigh spectrometer. The grouping of measurements to a "clear-air" scene and a "cloudy" scene is only performed in the L2B processor, as the choice for the grouping might depend on the usage of the observations in a specific NWP model (e.g. global or regional model). Such groupings result in the L2B "Mie cloudy", "Rayleigh clear" and "Rayleigh cloudy" winds. In addition, the L1B winds or spectrometer responses are neither corrected for long-term drifts nor for errors based on orbital harmonics or orbital variations, the latter being correlated with the telescope primary mirror M1-temperatures. The respective biases are only corrected at L2B processing stage, as ECMWF model information is used in this step for the correlation analysis. Thus, it is not recommended to use the L1B Mie or Rayleigh winds for validation, assimilation in NWP models or scientific applications, as L1B winds are neither properly calibrated nor bias-corrected. Both the L2A and L2B processor do not use the derived L1B Mie or Rayleigh responses (or winds) as input. Instead they rely on the spectrally resolved Mie signal and Rayleigh filter A and B signal as well as on other L1B parameters such as the Signal-to-Noise Ratio SNR and the scattering ratio SR.

These trade-offs of functionalities between L1 and L2 processing are important for understanding the priorities for the L1 processing and its evolution after launch.

4.1.2 WIKI items and L1B evolution document

The development of L0, L1A and L1B algorithms and the evolution of the corresponding processor was tracked by respective WIKI items (one for L0, 5 for L1A, and 88 for L1B) on the DISC confluence site (DISC, 2024) and by the L1B evolution document from the processor developer DoRIT (DISC-DoRIT, 2023) with a total number of 94 items. With this approach the priorities for the implementation in the L1B processor were documented every 6 months for the next baseline update. The WIKI items, which describe issues, provide underlying analyses, figures, and recommendations for future work by the algorithm teams, in combination with the more formal process of transferring these into the operational processors via an evolution document under the responsibility of the processor development, is considered as a very useful approach for cooperation among different disciplines and partners.

4.1.3 Different ALADIN instrument modes and L1B processing

The ALADIN instrument was operated in wind velocity measurement (WVM) mode during the majority of its operation time. Besides the wind mode a number of other modes can be commanded mainly for the purpose of characterizing, monitoring or calibrating the instrument. All these modes must be processed differently by the L1B processor. The processing of these calibration and monitoring modes is only performed within the L1B processor. In contrast, both the L2A and L2B processor are limited to Aeolus measurements obtained during wind mode (WVM).

An overview of the different ALADIN instrument modes is provided in this chapter, because a significant part of the algorithm and processor evolution for the L1B level was dedicated to these modes other than WVM.

The other modes differ in:

- the line-of sight (LOS) pointing of the satellite (35° off nadir for WVM versus nadir pointing for Instrument Response Calibration (IRC) with MRC and RRC)
- the operation of the Accumulation Charge Coupled Device (ACCD) detector (lidar mode with range-bin information for WVM versus usage of the ACCD as camera in imaging mode for IDC, LBM and DCC)
- the operation of the laser at a fixed frequency (for WVM) or in a step-wise scan over a frequency range (e.g. during IRC, ISR, or IRONIC)
- the analysis of only the internal reference (e.g. ISR, LBM) or the atmospheric path (e.g. IDC, DUDE) or both paths.

A more detailed overview of the different instrument modes is provided in the L1B ATBD (DLR 2018). It is worth mentioning here that also the E2S is capable of simulating the different instrument modes for ALADIN (as defined pre-launch) in order to enable the testing of the complete processing chain for all instrument modes. Some of the introduced instrument modes were only defined and implemented after launch, such as DUDE or IRONIC. With regard to the DUDE processing (see section 4.11.3) a significant effort was made in the operational L1B processor.

The main objective of the different modes are summarized in the following Table 10:

Table 10: ALADIN instrument modes and objectives.

Mode	Name	Objective
WVM	Wind Velocity Measurement	Measurement of HLOS wind under 35° off-nadir angle
IRC MRC RRC	Instrument Response Calibration with Mie Response Calibration, Rayleigh Response Calibration	Measurement of non-linear dependency between spectrometer response and frequency Doppler shift for the MSP and RSP with nadir pointing, used for calibration of L1B winds and monitoring
IRONIC	Instrument Response OffNadIr Calibration	Measurement of non-linear dependency between spectrometer response and frequency Doppler shift for the MSP and RSP with off-nadir pointing, used for calibration of L1B winds and monitoring
ISR	Instrument Spectral Registration	Measurement of RSP filter A and B and MSP spectral transmission; used for monitoring and input to L2A/L2B aerosol/wind calibration
LBM	Laser Beam Monitoring	Measurement of laser beam profile on the MSP (near-field) and RSP (far-field) for monitoring purpose
IDC	Instrument Defocus Characterization	Measurement of MSP and RSP illumination on atmospheric path for monitoring instrument alignment, was initially planned as input for telescope focus adjustments
DCC	Dark Current Characterization	Characterization of dark currents in the detection chain in imaging zone during periods with no laser operation
DUDE	Down Under Dark Experiment	Regular measurement of dark current levels in memory zone for mitigating the effect of hot-pixels; used as input to L1B processor

Table 11 provides a short overview of the main operating parameters for the different modes and their occurrence during most part of the mission:

Table 11: ALADIN instrument modes - Operation conditions and occurrence of commanding, setting not applicable (n.a.) as laser is off.

Mode	LOS	ACCD	Frequency	Path	Occurrence
WVM	35°	lidar	fixed	ATM+INT	majority of time
MRC, RRC	0°	lidar	scan	ATM+INT	weekly
IRONIC	35°	lidar	scan	ATM+INT	on request
ISR	35°	lidar	scan	INT	weekly
LBM	35°	image	scan	INT	weekly
IDC	35°, 0°	image	fixed	ATM	on request
DCC	n.a.	image	n.a.	n.a.	during laser off
DUDE	35°	lidar	fixed	ATM	2-8 / day

Some of the ALADIN instrument modes, which were implemented pre-launch in the L1B processor, but which were not used in-orbit or only sporadically are not discussed here (e.g. Instrument Auto Test (IAT), Laser Chopper Phase (LCP) adjustment, or Laser Diode Temperature (LDT) adjustment). The following sections describe shortly the major algorithm refinements, modifications or newly implemented functionalities and new parameters for the L1A and L1B processors in phase E with a focus on discussing those items with impact on data quality; changes of the L0 processor are not discussed here. Details of the implementation of these changes in the operational L1A/B processor are discussed in section 4.11.3. The major changes for all processors are summarized in separate notes for each baseline update from DISC on ESA´s processor release webpage (https://earth.esa.int/eogateway/instruments/aladin/processor-releases)

4.1.4 Improvements of the L1A processors in phase E

Satellite velocity LOS calculation corrected for an on-board software error

The ALADIN laser and telescope LOS direction is perpendicular to the satellite ground speed, and an additional yaw-pitch steering of the satellite is applied to compensate for the frequency shift induced by the Earth rotation. Thus, the resulting satellite velocity component on the instrument LOS should be 0 m/s. In order to correct for any residual satellite velocity on the LOS (e.g. due to imperfect LOS pointing), this component is calculated within the L1A processor using ESA´s EO-CFI (Earth Observation Mission Customer Furnished Item) software (ESA, 2013) and corrected in the L1B and L2B processing. However, this reported satellite velocity component was wrongly calculated, which could finally be traced back to errors in parameters derived on-board the satellite and reported in the downlinked data stream. A workaround to correct for this on-board error was implemented in the on-ground L1A processor for B11.

Error in the longitude of the geolocation corrected

The geolocation parameters, such as altitude, latitude, longitude of the Aeolus measurements and observations are calculated in the L1A processor and used within all upper level products (L1B, L2A, L2B). The geolocation of each Aeolus measurement could be validated thanks to the ground-based cosmic ray observatory from Auger (see section 3.2.2, and The Pierre Auger Collaboration et al., 2024), which detected the geolocation, pointing angle and energy of each single laser shot emitted by Aeolus, when passing over the observatory site in Argentina. A constant offset between the geolocation reported in the Aeolus products and those measured on-ground was detected in the longitude direction of 0.0075°, which corresponds to 8 km at the equator. This geolocation error could finally be identified as an error in the usage of the EO-CFI sub-routines in the L1A processor. For their computation the relevant CFI routines use the time and an identifier stating if the time is UTC (Coordinated Universal Time), GPS (Global Position System), or TAI (International Atomic Time). In two places a wrong combination of time and identifier had been provided to the CFI routines, which led to a slightly wrong calculation of the longitude and latitude values. However, as the attitude angles of the platform, which are relevant for the wind retrieval, were not affected by the timing issue, there was no impact on the accuracy of the wind measurements. This error in the geolocation calculation was fixed in the L1A processor for B14.

New parameters included in the L1A and L1B product

A number of new parameters, which were considered to be useful for quality control (QC) or directly in the retrieval algorithms, have been added to the L1A and L1B product for different baselines. Examples are the gyro angles from the AOCS (Attitude and Orbit Control System), other AOCS status parameters

(moon blinding, star tracker, gyros, eclipse, sun elevation angle), and 15 additional temperatures from the primary mirror of the telescope (M1) for the purpose of L2B wind bias correction.

4.1.5 Improvements of the L1B processor in phase E

A number of improvements were implemented in the L1B processor for the calibration and monitoring modes (DCC, LBM, IDC), which are not described in this chapter. A significant change for the ISR mode processing was the implementation of a laser energy drift correction factor, described in more detail in section 4.11.3. The changes for the calibration modes MRC/RRC are described in more detail in section 4.6.1including the determination of an average, spectral Mie non-linearity function from a number of selected MRCs, which is then used as input for the Mie wind retrieval in the L1B processor.

The main processing steps and improvements of the L1B processor are described below:

Correction of Mie and Rayleigh signal offsets:

The Mie and Rayleigh signal levels for each range gate and each ACCD pixel contain several offsets, which are corrected in the L1B processing for each measurement and observation, before calculating the Mie and Rayleigh responses. These offsets are considered to be constant for each of the 16 signal pixels, but they vary for each range gate and are composed of the mean dark current, the solar background and a detection chain offset (DCO), the latter being added electronically before digitizing the signals. As the Mie response is calculated from the centroid of the fringe on the ACCD, a constant offset is not affecting the centroid but only the calculation of the scattering ratio (SR) and the signal-to-noise ratio (SNR) from the Mie channel. An error in the offset correction – even of only 1 digitizer count or 1 LSB (least significant bit) changes the Rayleigh response and wind, due to the low sensitivity in the order of $5*10^{-4}$ (response units) per MHz. Thus, an accurate determination of the offset-components is critical for avoiding Rayleigh wind biases. In addition, the offsets, which are measured separately, are composed of noise contributions, e.g. Poisson noise for the solar background measurement in a separate range gate, read-out noise for the dark-currents and electronic noise for the DCO.

Due to the low atmospheric signal levels of ALADIN after launch and the further decrease of atmospheric signal in the course of the mission, the SNR was not only dominated by signal Poisson noise as expected pre-launch but also by the other described noise terms. Thus, there was a need to study if these additional noise terms could be reduced. The DCO is measured for each read-out or measurement of the ACCD on four separate pre- and post-scan, virtual pixels, and is determined as a mean of either 2 or 4 of these pixels per range gate, which was introduced as option after launch.

A major improvement for the reduction of the noise in DCO correction was the calculation of an average DCO per orbit file (or more precisely for an instrument mode, if several modes are contained in an orbit file). It was verified that the mean of the DCO over one orbit is stable. This averaging could be achieved by introducing a pre-processing step in the L1B processor for Baseline 16, as the L1B processing is based on a sequential processing for each observation. As an orbit file contains in the order of 450 observations, this will reduce the DCO noise for each observation by a factor of $\sqrt{450}=21$. As the DCO correction is applied with the same DCO value to each pixel per observation and range gate, the resulting noise reduction to the Mie and Rayleigh response is significantly lower due to correlations in the noise term. Thus, the resulting influence on the Mie and Rayleigh winds is lower than anticipated from the pure noise reduction of the DCO value itself.

Corrections related to enhanced dark current levels due to hot-pixel

Another contributor to the offset on the signal levels is the dark current level from the memory zone of the ACCD. This level depends on the dark current rate (in electrons per s) und the time of the charges

in the memory zone, which is depending on the number of accumulated pulses P-1 (P being reduced by one as it takes one pulse for read-out). These dark current levels are determined in a specific mode resulting in an auxiliary file named DCMZ (Dark Current in Memory Zone), which is used as input to the L1B processor.

A few months after launch, strong Rayleigh wind biases of several m/s were seen in single range-gates, which could be traced back to enhanced dark current levels affecting these pixels – hereafter called hot-pixels (see section 3.3.1). A special instrument mode called DUDE (Down Under Dark Experiment) was introduced to characterize the behaviour of these hot pixels several times per day. The processing of these DUDE´s was implemented in L0, L1A and L1B processor level to provide AUX_DCMZ files, which are then used in the next orbits for correction of signal levels in the L1B processor (section 4.11.3). Changes in the HP levels are only corrected for subsequent orbits after a DUDE measurement, and only with constant corrections for each orbit file. Thus, changes of signal levels between DUDE´s (several hours) are not corrected in near-real-time NRT processing, and are only improved during reprocessing. Changes within one orbit cannot be corrected with this method, also not during reprocessing.

Several refinements of the DUDE processing were introduced including a check on complete darkness using the sun elevation angle (see section 4.11.3) or a check that the top-most bin is below the ground (as expected).

Corrections related to solar background and influence on SNR

The solar background is measured in a separate 25th range gate with long integration times of maximum 3750 µs. It is then used for correcting each Mie and Rayleigh measurement and observation by scaling the signal to the respective integration time of the range gate (multiples of 2.1 µs equivalent to 250 m altitude resolution under 35° off-nadir). As the solar background acts as a Poisson noise contributor to both the 24 atmospheric range gates and the separate and uncorrelated solar background range gate, the influence had to be refined in the processing of the Mie and Rayleigh SNR.

Saturated pixel handling

It was observed sporadically that, for a single measurement, single pixels on the Mie and Rayleigh ACCD contain the maximum value of 65535 LSB of the 16-bit digitizing process. This happened for the range-gates measuring solar background during periods of maximum solar radiation, in combination with a maximum solar background integration time of 3750 µs, and the commanded increase of the number of laser pulses P per measurement (see section 3.8.3). Another reason for saturated pixels could be the incidence of cosmic rays onto the detectors during transient events. Such measurements are flagged invalid and are not used for further accumulation to observations. This flagging of saturated pixels was applied to all instrument modes including DCMZ and imaging modes as of Baseline 13.

Retrieval of Mie and Rayleigh signal-to-noise ratio (SNR)

The main purpose of the Mie and Rayleigh SNR is the use for the classification in clear-air and cloudy scenes in the L1B/L2A/L2B processor and for the estimation of errors in the L2A/L2B processor.

The Mie SNR and Mie refined SNR are defined such that the Mie fringe from particulate backscatter is considered as "signal", whereas the noise term is composed of the Poisson noise of the Mie signal, the Rayleigh signal and the solar background on the MSP; the Poisson noise is then determined from the square root of the mean total signal level. Thus, the SNR as well as the scattering ratio (SR) computation requires the determination of the Rayleigh background offset on the MSP to separate the Mie from the Rayleigh signal contribution on the 16 pixels. This signal offset is determined for the Mie SNR and SR as the mean of the signal from the 4 pixels with lowest signal levels. This is a simplification especially in the case of a large Mie fringe with high SNR, as those 4 pixels at the edge of the useful spectral range (USR)

of the ACCD still contain Mie signal. Thus, a refined SNR and SR was already introduced pre-launch, where the offset is determined via the so-called Mie Core 2 algorithm, which uses a Lorentzian function on top of a constant offset as signal model. A significant improvement in the determination of the SNR and SR was achieved by introducing a Voigt function on top of a constant offset in the Mie Core 3 algorithm for Baseline 15.

It was recognized in the L2A processing that for deriving the product error estimates, a signal model needs to be applied for SNR calculation, where the total signal from the Mie fringe and the constant Rayleigh background is considered as signal contributor. This new definition was implemented in the Mie total SNR.

The Rayleigh SNR is derived from the filter A and B signals (sum of signal on pixel 1-8 for filter A, and 9-16 for filter B) assuming Poisson noise for the signal levels. Only after launch, due to the lower signal levels, it became clear that the Rayleigh SNR is not dominated solely by signal Poisson noise, but is also affected by noise of the solar background and its measurement, by the read-out noise per measurement and by the noise from the DCO correction. While the noise calculation from solar background for the Rayleigh SNR was revised for earlier baselines, the noise contributions from read-out noise and DCO were implemented for B16. This resulted in more realistic and lower Rayleigh SNR´s and increased the L2B Rayleigh wind error estimates, which are inversely proportional to the SNR. The implementation for the read-out and DCO noise contributors to the different Mie SNR´s is planned for B17.

Retrieval of Scattering Ratio (SR)

The SR defines the ratio of the total backscatter coefficients (molecular + particle) to the molecular backscatter coefficient $SR = (\beta_{mol} + \beta_{part})/\beta_{mol}$. It can be derived from the 16 signal pixels of the Mie spectrometer (MSP) with the assumption that the particle backscatter is proportional to the Mie fringe amplitude (or integral signal), whereas the molecular backscatter is proportional to the constant offset detected on the MSP. Two different methods were implemented in the pre-launch versions (as for the SNR), where the offset is either determined from the 4 pixels with the lowest signal or with the Mie Core 2 (Mie SR or Mie refined SR). It is recommended to use the refined SR, which is based on the Mie Core 2 and its better offset determination.

After launch, the values of the refined SR were compared to the SR determined from the backscatter coefficients of the L2A product (SCA: standard correction algorithm). It was concluded that also the refined SR shows some SR-dependent biases, which was corrected by application of a third-order polynomial as a function of the SR up to a maximum value (e.g. SR=5).

Other refinements of the SR after launch were the handling of negative offset values applying a workaround by setting them to the minimum value of 1 LSB.

As written below, only in 2022 to 2023 it became clear that the Lorentzian function used for the Mie Core 2 is not fully representative for the spectral line shape of a Mie signal. It was replaced by a Voigt function. Those 2 line-shape functions especially deviate in the wings of the spectrum, which is an important spectral region for the determination of the offset. Thus, for Baseline 15 the new Voigt function within the Mie Core 3 was used for determining the offset for the SR and SNR.

Detection of range bins with ground returns and ground-return velocity

The detection of ground range bins, which can contain the reflectance of land or ocean surfaces is a rather complex processing flow and relies on a series of checks using a Digital Elevation Model (DEM), the Mie and Rayleigh signal levels and other parameters. The ACCD of Aeolus provides only a relatively coarse vertical resolution with 250 m (best) and 500 m (during most of the mission). However, due to a temporal overlap of range gates, which corresponds to about 100 m (at the top and bottom), and a

coarse horizontal resolution of several km, resulting from the accumulation of a number of P laser pulse returns on the ACCD, the ground signal can be vertically spread over several range bins. These ground range bins also contain backscatter from atmospheric molecules and particles, which could move with the ground wind, resulting in biases on the ground-return velocity. In addition, the ground-returns had significantly lower signal levels than anticipated pre-launch, which made a clear detection only possible for land surfaces with higher albedo (e.g. deserts, snow and ice), but caused issues for low-albedo surfaces, such as vegetation or oceans.

Thus, the ground-bin detection algorithm was refined several times for the L1B processor including the checks on the DEM altitudes and the signal levels. After detecting the range bins with ground signal on measurement level, those are summed up to observations, and the respective Mie and Rayleigh responses and winds are determined. These are contained in the L1B product and also copied over to the auxiliary file for "zero-wind correction" (AUX_ZWC). The AUX_ZWC files were considered as input files for the harmonic bias estimator (HBE, see section 3.7.2), which was not used operationally due to the complexity of the temporal variation of the wind bias.

Retrieval of Mie response from fringe centroids on the MSP

The spectral line shape of the Mie fringe on the MSP was approximated as a Lorentzian function on top of a spectrally flat offset from the molecular Rayleigh-Brillouin line shape for the useful spectral range (USR) of the MSP. This Lorentzian line shape model was used for calculation of the centroid, amplitude, width, and offset in the so-called Mie Core 2 algorithm (DLR 2018) both in the L1B and L2B processor, where the centroid is further used for Mie response and Mie wind determination. Only in 2022 to 2023 it became clear through several independent investigations, that the actual line shape on the MSP is better approximated by a Voigt-function, which is probably due to non-perpendicular illumination of the MSP with a finite angle (see also section 3.4.1). A Voigt line shape was implemented into the new Mie Core 3 algorithm for the computation of the Rayleigh offset for Baseline 15 in order to improve SNR and SR computation. Work is on-going regarding the implementation of the Mie centroid computation into the Mie Core 3 for Baseline 17, aiming at an improvement of the Mie winds.

The main changes with relevance for wind quality from Baseline 11 (in operation since 8 October 2020) to Baseline 16 (in operation since 18 April 2023 and used for 4th reprocessing) for the L1A/L1B and L2B processors are listed in the Table below; this Table is limited to updates since B11, as products from earlier baselines are considered outdated.

Table 12: Changes in the L1A/L1B and L2B processors for Baseline 11 to Baseline 16 with improvements for the L2B wind product quality.

Baseline	L1A and L1B processor	L2B processor
B11	Satellite LOS velocity calculation corrected in order to compensate for an on-board software bug DCMZ correction values for the solar background range gate implemented Refinement of calculation of SNR and SR in case of negative offsets on the MSP	Different SNR thresholds for classification of Mie and Rayleigh winds implemented, replacing classification with noisier SR. Option to flag winds invalid for periods of degraded quality, e.g. instrument tests for users to automatically reject those data.
B12	Switch for use of internal reference response, due to anomalies in the internal path AOCS flags added, e.g. moon blinding, eclipse	Constant value for Rayleigh internal reference used due to anomalies Moon blinding flag used for QC of winds, which affects Tropical regions every 2nd week
B13	Detection of saturated pixels added (also for DCMZ files); QC of DCMZ improved by using sun elevation angle to avoid solar background during dark current measurements	New parameterization for Mie contamination correction of Rayleigh cloudy winds added Improvements of ground-detection, affecting low-level winds
B14	Correction of an error of the geolocation for the longitude error of 0.075° (eq. 8 km at equator)	AUX_TEL (M1-bias) correction improved by adding a harmonic bias component (affecting only months of March and October)
B15	Possibility to using improved MSP illumination function for Mie signal correction (EMSR (Effective Mie Spectrometer Spectral Response) instead of pre-launch TOBS (Tripod obscuration) array) Implementation of Voigt line shape fit for scattering ratio SR and SNR DCO handling via DCMZ correction	New threshold checks for gross errors on Rayleigh signal levels on measurement level before accumulation Climatology check on high winds, which will be flagged invalid
B16	Rayleigh SNR with read-out noise and DCO noise Orbital mean for DCO derived for noise-reduction Pixel map introduced for possibility to flag damaged pixels as invalid, which behave differently than the usual HP. EMSR array (laser dependent) implemented and used for Mie wind retrievals	More realistic and higher Rayleigh error estimates due to updated Rayleigh SNR in L1B Improved QC for Mie winds using residual error of fit => removes gross outliers for Mie Mie internal reference response can be used for Rayleigh winds

4.2 L1B scattering ratio and Voigt spectral line shape function for Mie

Ines Nikolaus, Physics Solutions and Oliver Reitebuch, DLR

It turned out, that the Lorentzian function, which was used as an approximate spectral model of the Fizeau transmission for the ALADIN Mie spectrometer, does not fit well enough to line shape of the measured atmospheric return signals. Especially when the signal amplitude is high, the fit to a Lorentzian function leads to unphysical negative offsets, which would represent a negative Rayleigh signal. In consequence, it is impossible to retrieve a valid scattering ratio and SNR from these fit results. To overcome this problem, it was suggested, that the Lorentzian response of the Fizeau may be broadened by a Gaussian function due to imperfections of the Fizeau plates and large off-axis illumination in combination with the divergent input beam. In this case, a Voigt function represents the Fizeau signal best.

Another result influenced the search of a best representation of the Fizeau spectral response: Within the L2A processor and its prototype by KNMI, the response of the Fizeau to a pure Rayleigh atmosphere was derived. This resulted in the EMSR (Effective Mie Spectral Response) correction of the ACCD signal (section 4.4.3). With this correction and strong ground returns from MRCs (Mie Response Calibrations), which mainly contain Mie contribution, we were able to show, that the Fizeau response for all different peak positions differ only by their offsets, i.e. by the different amount of Rayleigh signals from the atmospheric layer contribution above ground.

With this insight we were able to develop a response model for the Fizeau instrument. We used a pseudo Voigt function $V_p(x)$, given by the weighted sum of a Lorentzian L(x) and Gaussian function G(x):

$$V_p(x) = \eta \cdot L(x) + (1-\eta) \cdot G(x) \quad \text{mit} \quad 0 < \eta < 1$$

$$G(x) = \exp\left[-\ln(2) \cdot \left(\frac{x - x_0}{w}\right)^2\right]$$

$$L(x) = \frac{1}{1 + (\frac{x-x_0}{w})^2}$$

with peak position x_0, FWHM $2w$ and Lorentzian fraction η. We fitted the function $f(x) = A\, V_p(x) + o$ with amplitude A and offset o to the normalized ACCD signal of the Fizeau.

The resulting fit curves are shown in Figure 58 and the retrieved values for *FWHM* and η for the three different laser periods are summarized in Table 13.

It is shown that the FHWM of the two different FM-A periods is similar with around 1.8 pixel, while the FHWM for the FM-B period is significantly higher with 2.1 pixel (corresponding to around 210 MHz). Also, the fraction of the Lorentzian is lower for FM-B (34%) compared to FM-A (50%), thus resulting in a higher Gaussian contribution, which could arise from higher incidence angles on the MSP for the FM-B laser compared to FM-A.

With these parameters for the Mie line shape of the Fizeau instrument, and the peak position x_0 from a valid Mie Core 2 offset *o* and amplitude *A* of atmospheric returns can be retrieved by solving a set of two linear equations for amplitude *A* and offset *o* of the function

$$f(x) = AV_p(x) + o\,.$$

Since the contribution of the atmospheric Rayleigh signal in MRC ground signals is unknown, the offset may be a sum of an offset from a pure Mie signal o_{Mie} and the Rayleigh signal o_{Ray}.

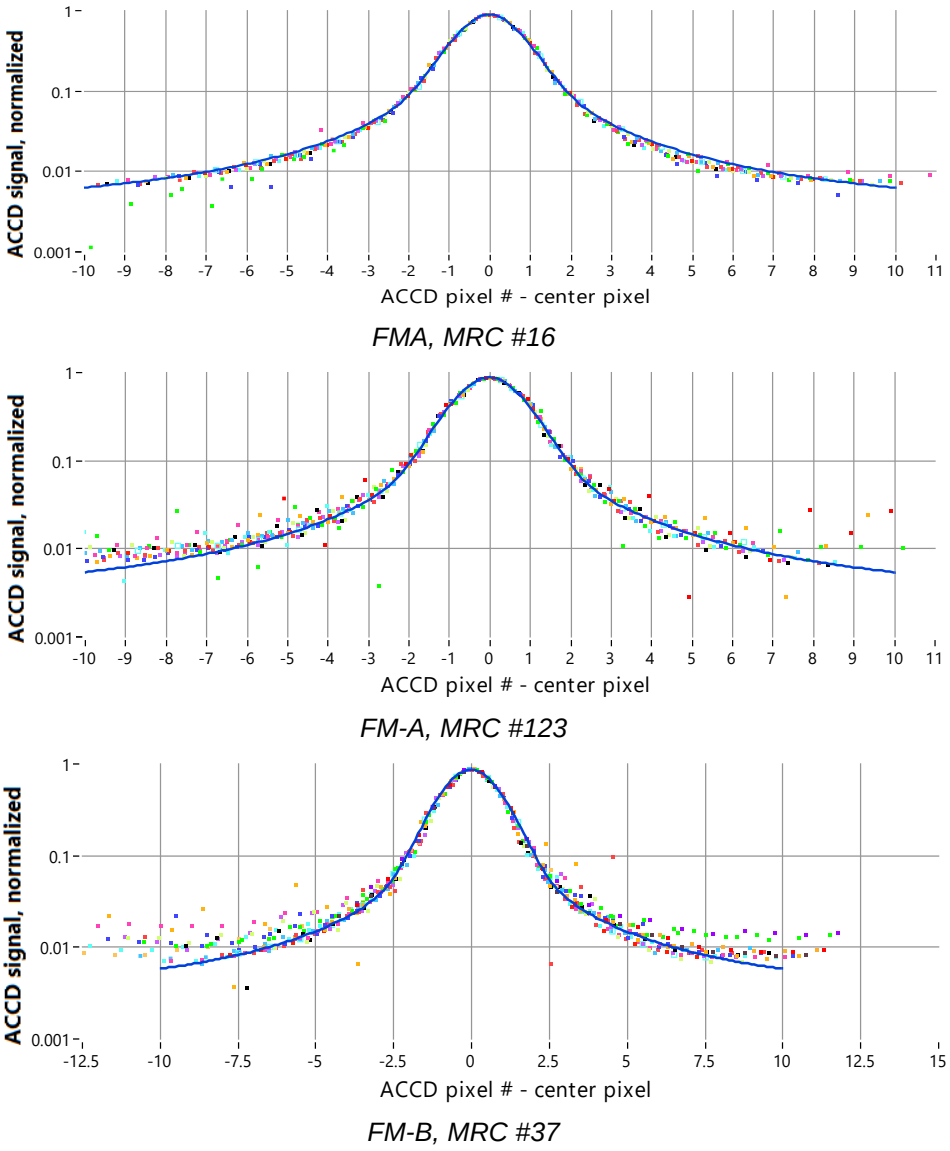

Figure 58: Fits (blue lines) of the ground returns of MRC signals (coloured dots), which were normalized to 1 and shifted to the same peak location, three different MRCs from different operation periods covering the FM-A and FM-B periods.

Table 13: Parameters of the Pseudo-Voigt function, representing a strong Mie signal.

	FM-A, 1st period	FM-B	FM-A, 2nd period
MRC used	# 16	#37	#123
FWHM	1.76 pixel	2.082 pixel	1.81 pixel
η	0.505	0.34	0.47

From amplitude *A* and Mie and Rayleigh offset contributions, a scattering ratio can be determined using the equation

$$SR = \alpha_{Voigt}\left[\frac{S_{Mie}A}{16(o - o_{Mie}A)}\right],$$

where S_{Mie} is the integral (in LSB) over the Voigt function for a pure Mie signal centred on the ACCD line with amplitude A = 1 within the MSP useful spectral range, and α_{Voigt} replaces the parameter $\alpha_{corbackscatterratio}$ in the definition of the refined scattering ratio from Mie Core 2 results. α_{Voigt} accounts for the efficiency ratio in detecting a Mie or a Rayleigh photon within the MSP useful spectral range covered by the 16 pixels of the ACCD. For FM-B with FWHM and η as given in Table 13 we get S_{Mie} = 2.659.

The unknown parameters o_{Mie} and α_{Voigt} have been determined from comparisons with the Level 2A product from AEL-PRO scattering ratios, which are determined with an independent retrieval using both the Mie and Rayleigh channel information, but also considering the atmospheric temperature and pressure profile (Dabas et al., 2008). They have been tuned such that a symmetrical distribution of scattering ratios from the L1B and L2A retrievals around the 1:1 line has been achieved for orbit 6139 (14.9.2019 initial FM-B period with high signal levels) on measurement level. We found o_{Mie} = 0.011 and α_{Voigt} = 0.7 and showed, that they are valid also for other orbits (16065, 1.6.2021 and 19162, 13.12.2021) and furthermore on observation level, see Figure 59 for orbit 16065 results

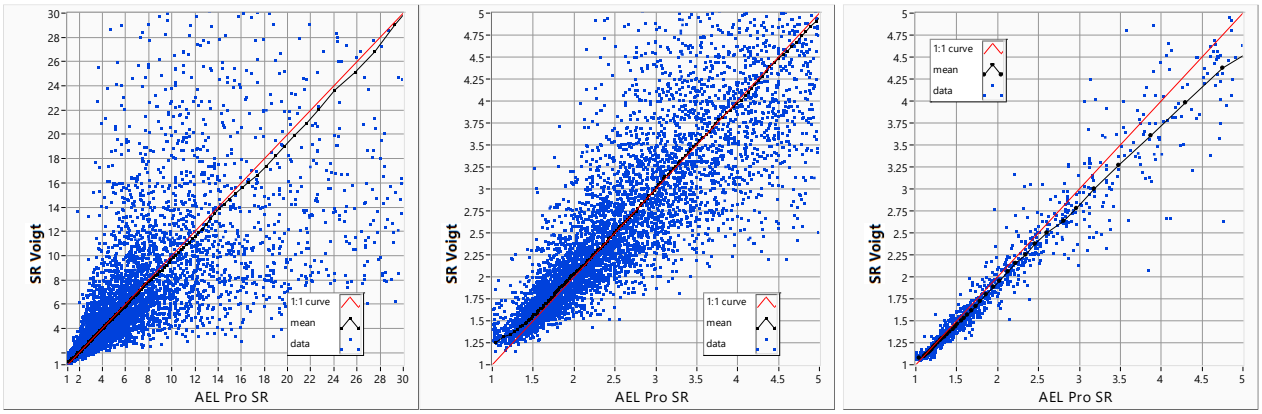

Figure 59: Scattering ratio from Voigt fit in comparison with the AEL-PRO scattering ratio for orbit 16065 (1.6.2021), left and centre graphs on measurement level, right graph on observation level, right and centre: only SR 1 to 5 are shown. The 1:1 line is shown in red. The black line is a mean of scattering ratios per interval and shows that on average the scattering ratios correspond to each other. Only scattering ratio data with valid Mie Core 2 results, Voigt SR > 1 and AEL-PRO SR > 1 have been used.

These results represent the scattering ratio much better than the previously used refined scattering ratio from Mie Core 2 results for the offset corrected by an emperically determined polynomial function derived also from a comparison of L1B to L2A scattering ratios.

Also a new SNR can be established using this knowlegde about the Mie signal shape:

$$SNR = \frac{1}{\sqrt{k_{Mie}}}\left(\frac{S_{Mie}A}{\sqrt{\sum_{j=1}^{16} LID(i,j,k)}}\right),$$

where k_{Mie} = 0.684 LSB/electron is the radiometric gain from the Mie detection chain. This equation gives very similar results as the refined SNR used before, but does not lead to negative SNR values.

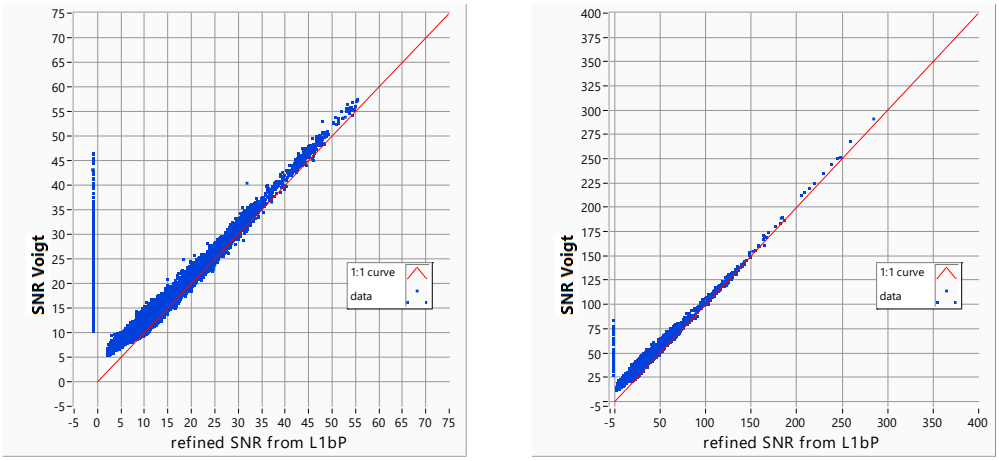

Figure 60: SNR from Voigt fit in comparison with the refined SNR from L1b product for orbit 16065 (1.6.2021), left on measurement level, right on observation level. The 1:1 line is shown in red. Both SNRs are very similar except for low scattering ratios, where the Voigt version leads to higher SNRs. Furthermore, the unphysical negative SNRs (vertical line at refined SNR = -1) do not occur for the Voigt SNR.

The limitation of the approach is, that we get only results, if the Mie Core 2 delivers a valid peak position. Furthermore, since in the denominator of the new SR definition a negative value may arise, we also get negative SRs here.

To get around the Mie Core 2 validity request we generalised the Voigt function fit, such that it includes also the determination of the peak position. This is only possible with a nonlinear optimiser. For this nonlinear optimization we minimize the negative Likelihood function (for Poisson distributed data *d*)

$$H(d,x,s) = -\log\left(P((d,x) \mid x_0, A, o)\right) = \sum_i \left(V_p(x_i,s) - d_i \log\left(V_p(x_i,s)\right)\right),$$

where

- x_i are the measurement points (ACCD pixel numbers),
- d_i are the data for each pixel (LSB),
- $P((d,x)|x_0, y = \ln(A), o)$ is the probability of the data d given the parameter vector $s = (x_0, y, o)$ = (peak position x_0, ln(amplitude), offset o). P should be maximized. Since P is positive, we minimize (- log P).
- The summation is over all 16 ACCD pixel.

In addition, a prior is taken into account for the optimization. The prior is an assumption on the probability distribution of the parameters x_0, y and o. Here we use a Gaussian probability distribution for the parameters.

This changes H to

$$H_1(d,s) = H(d,s) + p(s)$$

where p(s) is (for a Gaussian distributed parameter set s), as follows:

$$p(s) = \frac{1}{2}\sum_{i=1}^{3}\frac{(s_i - s_{start,i})(s_i - s_{start,i})}{s_{scale,i}^2}$$

with

$$s_{start} = (x_{0,COG}, \ln(\max(d_i)), \min(d_i)),$$

where $x_{0,COG}$ is the peak found from a centre of gravity search, and

$$s_{scale} = (\max(d_i)) - \min(d_i) = 15), \ln(\max(d_i)), \min(d_i)).$$

H_1 is minimal, if the derivatives wrt. the parameters are 0. The minimizer uses the algorithm RPROP [Martin Riedmiller and Heinrich Braun: Rprop - A Fast Adaptive Learning Algorithm. Proceedings of the International Symposium on Computer and Information Science VII, 1992] for orbit 16065 results.

With the peak centroid determined from the Voigt function the nonlinearity of the Mie response (in pixel units) compared to that of Mie Core 2 exhibits a less pronounced pixilation effect as shown in Figure 61 for the MRC #16, showing a better correspondence of the fit function to the measured Mie line shape.

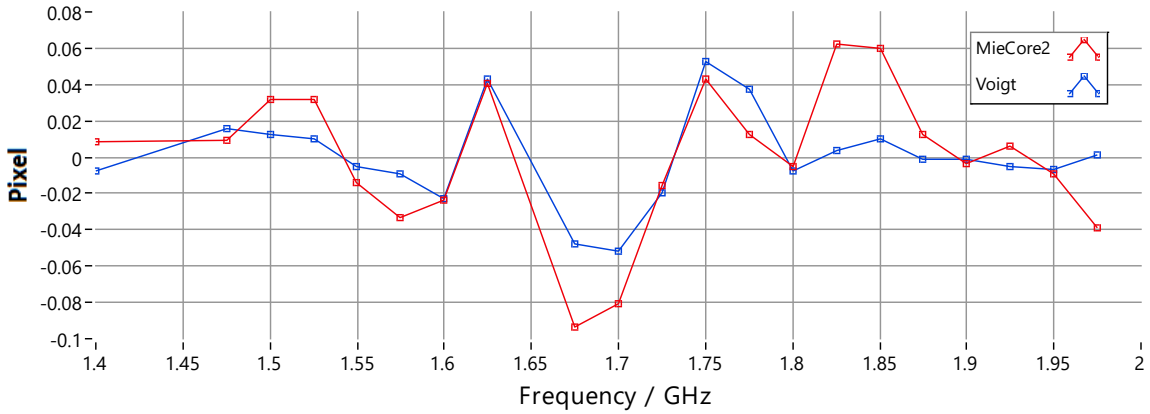

Figure 61: Nonlinearity of the MRC Mie response for MRC #16 (FM-A): Voigt fit in comparison with Mie Core 2. The peak dependent difference of linear fit and retrieved response (= nonlinearity) is smaller for the Voigt fit.

It turned out, that there is some vignetting of the ACCD not only in the atmospheric path (which leads to less illumination at the ACCD edges and is corrected with the EMSR), but also in the internal path. A correction factor for each pixel $EMSR_{int}(i)$ has been derived for each pixel *i* from internal MRC signals. The results compare well with the Fizeau illumination shape derived from ISRs (section 3.4) as shown in Figure 62, which show a strong difference for the FM-A (left) and FM-B (right) laser, which is due to the different laser beam profiles.

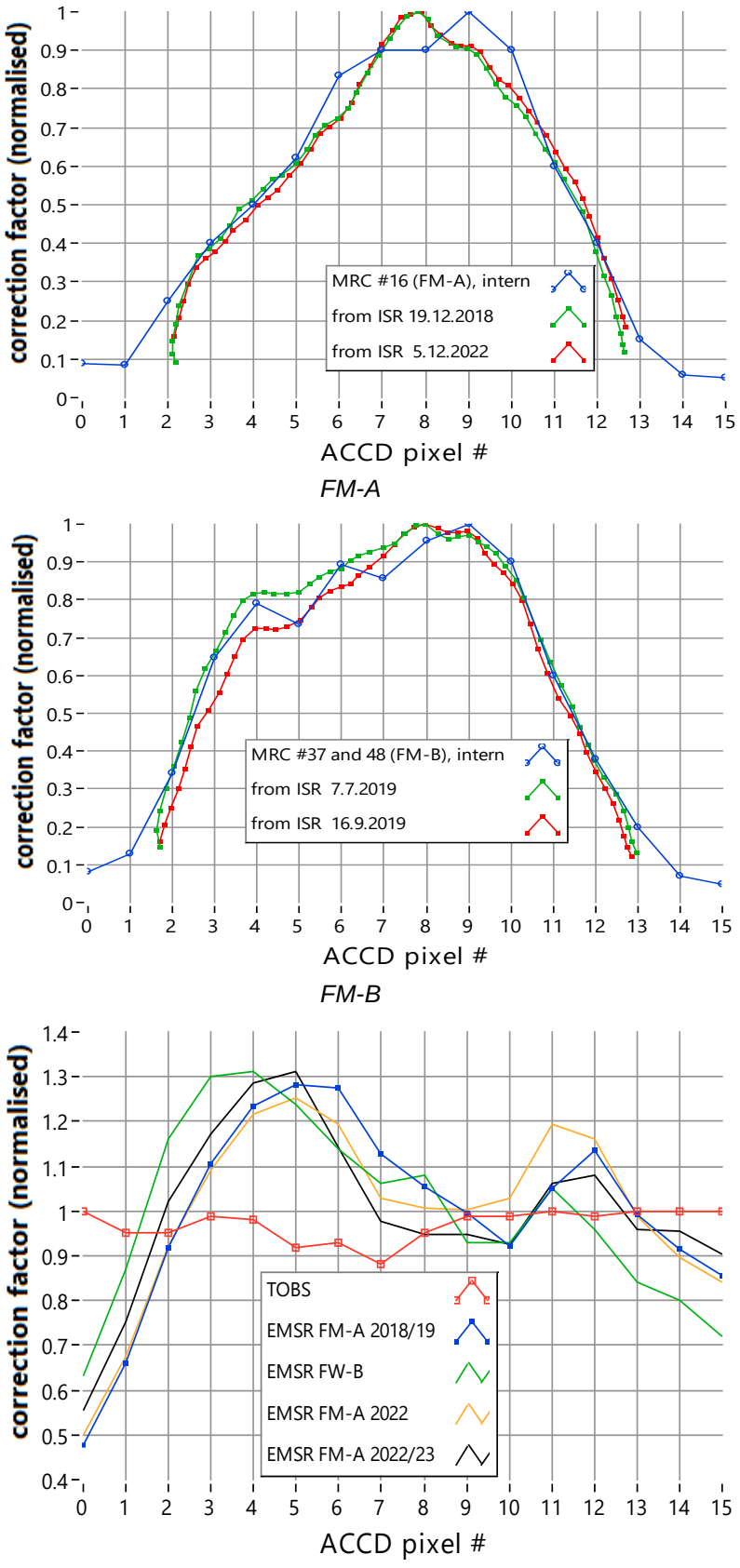

Figure 62: Top, middle: internal EMSR (blue lines) derived from two different MRCs) in comparison with the Fizeau illumination shape in ISRs for two nearby dates normalized to its maximum. Bottom: Atmospheric EMSR corrections for different periods in comparison with TOBS correction.

4.3 L2A algorithms: SCA and MLE

Dimitri Trapon, TROPOS and Alain Dabas, Météo-France

4.3.1 Introduction

This document is aimed at describing the Level-2A (L2A) prototype processor development covering Aeolus mission phase E from launch to latest operational by summer 2023. The L2A prototype was originally developed at Météo-France CNRS/CNRM until 31th December 2022, and then transferred to TROPOS. The prototype version was implemented in MATLAB, and the operational version being re-coded in C and implemented by DoRIT. Up to version 3.10, prototype and operational processors had a shift in version numbers (e.g. prototype with 3.09 implemented in operational version 3.10); after that both version numbers were aligned.

The present document focuses on the implementation and improvement of aerosol products related to the Standard Correct Algorithm (SCA) and Maximum Likelihood Estimation (MLE) as part of L2A prototype codes deliveries from versions 3.09 to 3.16 during Near Real Time (NRT) operations. The fine tuning of the radiometric correction and the quality monitoring of the L2A product using the main proxies are also highlighted.

4.3.2 L2A Algorithms SCA and MLE

The L2A prototype processor has been improved during the mission phase E at the light of the results obtained with real data and discussions with calibration and validation (Cal/Val) and external users. All the evolutions were listed and prioritized in (CNRM, 2022a). The major improvements were:

- The inclusion in the output product (L2A prototype processor (PP) version 3.09, activated within operational processor (OP) version 3.10 and Baseline 2A07) of the attenuated molecular and particulate backscatter profiles given at finer horizontal scale, i.e. the so-called Aeolus measurement aligned with ≈3km with initial laser configuration. These data were previously computed as intermediate results in the L2A but not included in the product. It corresponds to the cross-talk corrected signals, i.e. separated contributions from particles and molecules and denoted pure particulate Y_{ray} and molecular X_{ray} normalized by bin thickness and corrected by the squared satellite-to-target range with vertical Rayleigh scale.
- The inclusion in the output product (L2A PP version 3.12, activated within OP 3.12 and Baseline 2A12) of the extinction to backscatter ratio α_p / β_p, i.e. so-called lidar ratio. Data users expressed the wish to have access to lidar ratio which is more commonly used in atmospheric sciences for dominant aerosol typing than the backscatter to extinction ratio (BER) already provided in the L2A.
- The inclusion in the output product of a cloud mask based on Auxiliary Meteorological (AUX_MET) data. Tests have been conducted in the frame of the assimilation of L2A data in the ECMWF air quality model. The idea is to filter out the cloud-affected L2A data and measure the amount of data entering the assimilation cycle. A cloud-screening scheme using the total cloud backscatter derived from both liquid droplets and ice particles within AUX_MET has been evaluated (CNRM, 2020). The cloud mask is aligned with the Aeolus coarser horizontal scale, i.e. so-called observation (also referred as Basic Repeat Cycle (BRC)) and corresponding to ≈87km. It has been implemented within L2A PP version 3.13, activated within OP version 3.13 and Baseline 2A13.

- The refinement of the radiometric calibration coefficients K_{ray} and K_{mie}. In the first approach the coefficients were directly extracted from the L1B nadir pointing calibration mode (i.e. Instrument Response Calibration (IRC) acquisition) processed by the L2A. The coefficients K_{ray} and K_{mie} were then estimated from high altitudes clear sky signal using a scattering ratio threshold. A corrective factor was derived from signal prediction performed in aerosol-free conditions between 6km to 16km and averaged for all the observations. Single corrected values of K_{ray} and K_{mie} were then assigned to the whole orbit. This corrective scheme has been included in L2A PP version 3.10 (activated within OP version 3.10 and Baseline 2A08).

  Then a strong correlation with the temperatures of the telescope of the primary mirror M1 was observed (Figure 63). Calibration coefficients K_{ray} and K_{mie} have been recomputed using a multiple linear regression based on the temperatures in-orbit deviations (i.e. from 12 sensors distributed all over the telescope) and given this time per observation. The final scheme has been implemented in L2A PP version 3.11 (activated within OP version 3.11 and Baseline 2A11). More detailed can be found within the Algorithm Theoretical Baseline Document (ATBD, (CNRM, 2022b)).

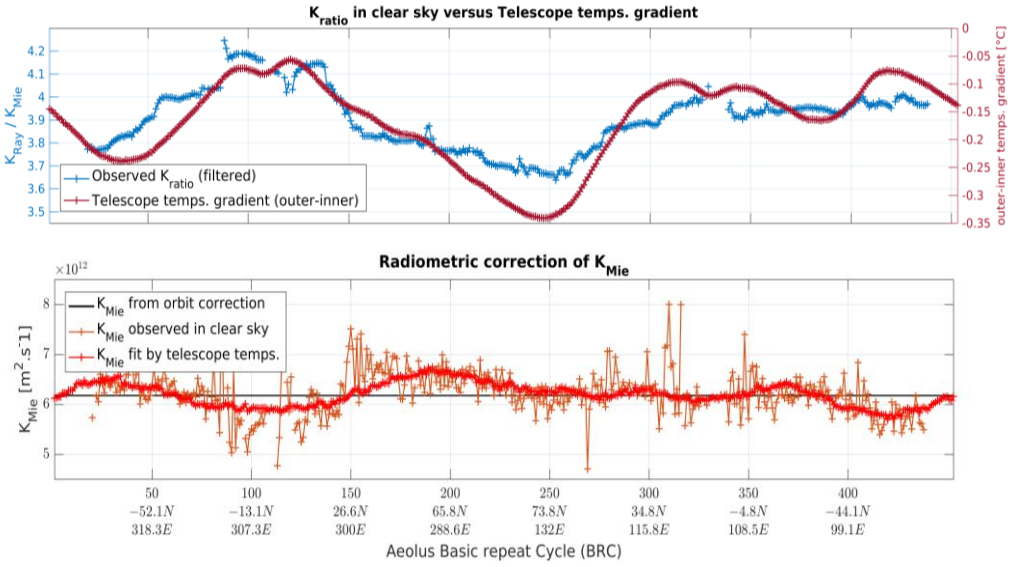

Figure 63: Correlation between temperatures gradient of the primary telescope (top, dark red line) and K_{ray} and K_{mie} ratio (i.e. Kratio, top blue line). Comparison of refined radiometric calibration coefficient K_{mie} from orbit averaged correction (bottom, black line) to fitted values per observation (bottom, light red line)

- Mid-bin products were designed in earlier versions of L2A PP to overcome the oscillating propagation of errors in the SCA extinction coefficient in the vertical. This approach consists in averaging retrievals of two consecutive vertical bins, providing products over a coarser vertical grid.
- A new algorithm based on an optimal estimation approach was introduced, the so-called Maximum Likelihood Estimation (MLE). This algorithm consists in finding the profiles of the optical parameters (i.e. backscatter coefficient for particles and lidar ratio) that achieve the best agreement with real signals. As such, this approach is similar to the SCA previously implemented as reference, but it allows to introduce additional constraints, e.g. the lidar ratio being bounded between 2 sr and 200 sr. Moreover, it assumes that extinction and backscatter are vertically collocated contrary to the SCA which is by concept a direct inversion of lidar equation. The MLE

was introduced in the L2A PP version 3.12 (activated within OP version 3.15 and Baseline 2A15). The method has been described in a publication (Ehlers et al., 2022).

- A grouping algorithm (i.e. signal accumulation over features with large enough Signal to Noise Ratio (SNR)) has been gradually improved and a heterogeneity index has been implemented in L2A PP version 3.12 (activated within OP version 3.12 and Baseline 2A12) to characterize the BRC homogeneity, high value indicating strong variability (CNRM, 2021a).
- Information at sub-BRC level with higher horizontal resolution were included. Despite the attenuated backscatter coefficients (being available on measurement scale), the SCA main output are given at coarser observation scale. The MLE improved stability to the noise was used to refine the horizontal resolution (CNRM, 2022c) and the aerosol retrievals were implemented at sub-BRC scale, i.e. accumulated measurements per sub-profile depending on settings for the number of accumulated laser pulses P per measurement and number of measurement N per observation. This MLEsub addition was finalized in the L2A PP version 3.15 (activated within OP version 3.16 and Baseline 2A16). See also Figure 64 and Figure 65.
- Quality check (QC) flags based on SNR and error estimates (i.e. variances) have been firstly designed for both SCA and SCA mid-bin algorithms. They have been gradually fine-tuned using in-orbit tests and data inter-comparisons with space-borne or ground-based lidar measurement (CNRM, 2021b). A QC flags updated was made in the L2A PP version 3.13 (activated within OP version 3.13 and Baseline 2A13), i.e. adjusting SNR thresholds and using absolute errors instead of relative errors. Following the implementation of the MLE and MLEsub algorithms corresponding QC flags were respectively introduced in the L2A PP versions 3.15 (activated within OP version 3.15 and Baseline 2A15) and 3.16 (activated within OP versions 3.16 and Baseline 2A16). Thresholds of SNR and error used for QC are described in the L2A user guide (TROPOS, 2023).

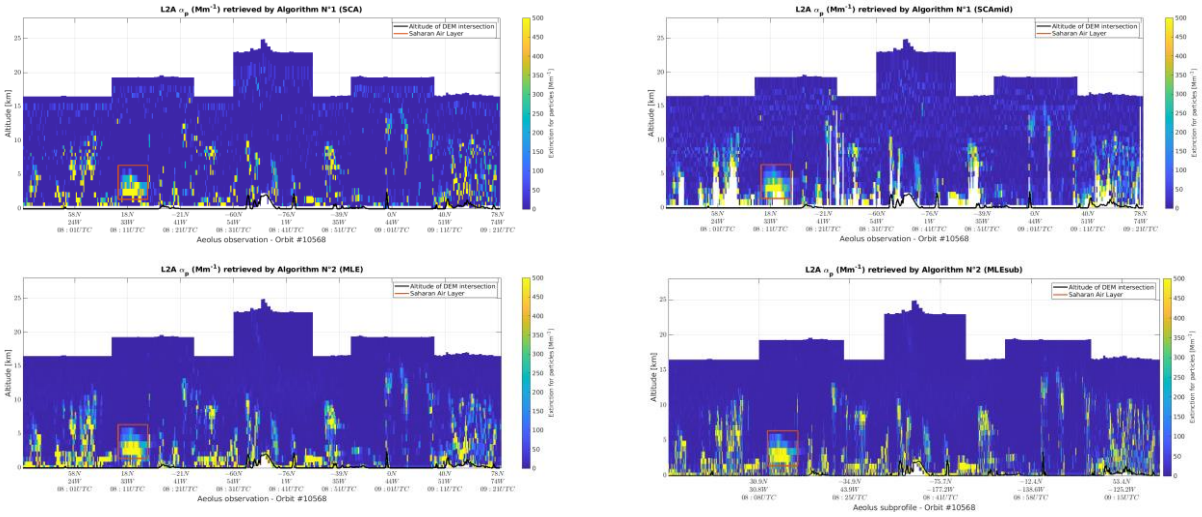

Figure 64: Extinction coefficient for particles retrieved by the main L2A algorithms (i.e. SCA, SCAmid, MLE and MLEsub) with June 2020 orbit crossing Saharan dust above the Atlantic Ocean.

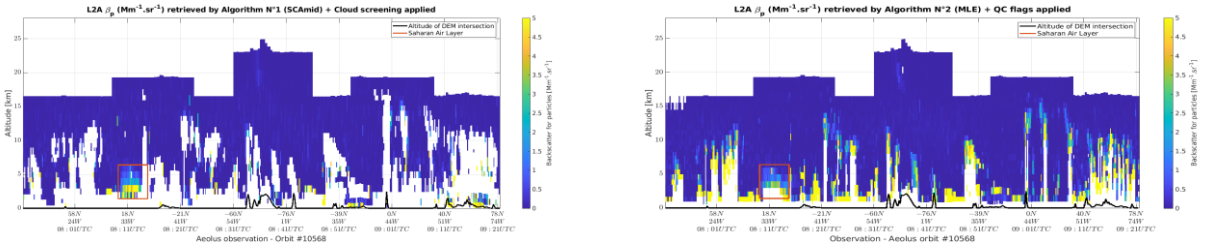

Figure 65: Cloud screened SCAmid (left) and QC flagged MLE (right) backscatter coefficient for particles with June 2020 orbit crossing Saharan dust above the Atlantic Ocean.

Eleven versions of the L2A PP have been delivered during phase E (latest one v3.17 dated October 2023). They were systematically accompanied with updated version of the following documents: Algorithm Theoretical Baseline Document (ATBD, (CNRM, 2022b)), L2A User Guide (CNRM, 2022d) and Software Release Note. A sustained support was given throughout the phase E to L2A Cal/Val users; the open issues and the code optimization being illustrated within dedicated discussions on DISC online confluence. A paper describing the SCA concept and highlighting the radiometric correction has been published (Flament et al., 2021). Figure 66 below shows the L2A prototype incremental implementations from the list above and their activation with operational processor and L2A baseline through NRT operations from July 2019 to April 2023. Laser switches and updates of settings for number of accumulated laser pulses per measurement and measurement per observation (i.e. N/P) are also illustrated. Note that this update of settings results in varying horizontal resolution for L2A products; one could then refer to the detailed Table 5 of the L2A User Guide (TROPOS, 2023).

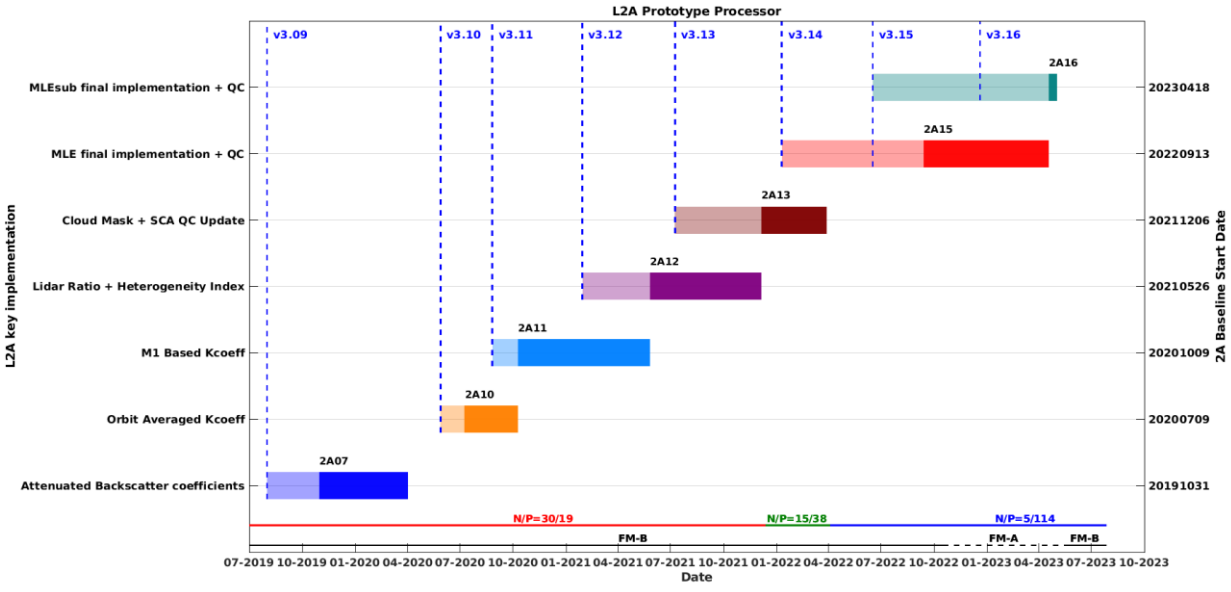

Figure 66: Temporal evolution of the L2A Prototype Processor including main implementations with final deliveries of the code and later activation within L2A baselines.

Some lessons learnt for future missions are summarized below:

- Robust housekeeping telemetry information such as primary telescope temperatures were valuable to correct the calibration coefficients using post launch in-orbit deviations.
- The QC should be easily readable by external team as the L2A product get maturing. To this end the nominal format (i.e. 8-bit unsigned integer that is the sum of the results of validity checks)

quickly appeared as not user-friendly, as the users have to split the integer into the results of the check themselves.

- The cloud screening is one of the most valuable information for assimilation of aerosols retrievals in models. As such it may be included in early version of aerosol product.
- Product heterogeneity such as varying vertical and horizontal scales should be described within a user guide as soon as possible following the beginning of the mission.
- The use of an Auxiliary parameter file (AUX_PAR_2A) made the sensitivity test for L2A code development easier as it allowed to quickly adjust the algorithms main parameters.

4.4 L2A algorithms: AEL-FM and AEL-PRO

Dave Donovan, Gerd-Jan van Zadelhoff, and Ping Wang, KNMI

4.4.1 Introduction

This Chapter describes two novel algorithms for cloud and aerosol property retrievals that have been implemented in the ALADIN operational processor. These two algorithms are known as AEL-FM and AEL-PRO. AEL-FM provides a high-resolution feature-mask based mainly on ALADIN crosstalk corrected particulate (Mie) profiles. AEL-PRO, which uses AEL-FM as an input (as well as attenuated backscatter profiles), provides profiles of particulate backscatter and extinction coefficients and the lidar-ratio. Both these algorithms are based on algorithms previously developed for application to the cloud/aerosol lidar on-board EarthCARE (ATLID) (Wehr et al., 2023)

Before AEL-FM and AEL-PRO could be successfully implemented, accurate pure-molecular and pure particulate profiles of the attenuated backscatter had to be retrieved. To this end, a procedure for producing crosstalk-free attenuated backscatter profiles using the Mie Spectrometer (MSP) data alone was implemented. Part of this procedure involves deducing and applying an Effective Mie Spectral Response (EMSR) correction to the MSP measurements.

In this Chapter, AEL-FM and A-PRO are described, and representative results presented and discussed. First, though, the procedure used to generate the pure Rayleigh and Mie attenuated backscatters that are used as inputs to AEL-FM and AEL-PRO is described.

4.4.2 Creation of crosstalk free Rayleigh and Mie attenuated backscatter profiles.

Neither the Mie spectrometer unit nor the Rayleigh spectrometer (RSP) unit detects light scattered purely by molecules or purely by particles. Instead, both units detect a mixture of the two with different weights. Thus, it is said that "crosstalk" exists in the system. In order to retrieve profiles corresponding to pure particulate and pure molecular scattering respectively, the appropriate set of crosstalk coefficients must be known (i.e. the respective fraction of each type of scattering detected by each channel).

The default manner used to produce estimates of the profiles of pure Mie and Rayleigh backscatter signals is to use both the total signals from the MSP and RSP. Using pre-computed crosstalk coefficients (which are a function of the Doppler shift) together with the MSP and RSP calibration coefficients, the observed total MSP and RSP signals are inverted to yield the pure Mie and Rayleigh signals. Using both the MSP and RSP signals is complicated by the fact that the RSP and MSP signals are generally not on the same vertical grid for all range-bins and the set of crosstalk coefficients depends on the Doppler shift. Moreover, the set of crosstalk coefficients is such that the error magnification associated with the default crosstalk correction procedure is large, i.e. the signal-to-noise ratio (SNR) associated with the

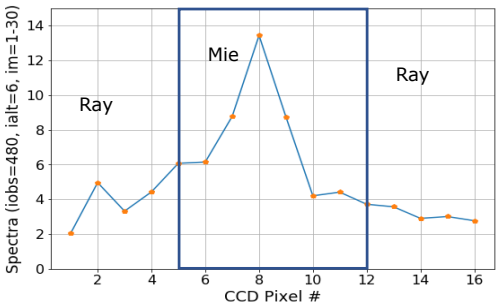

pure ATBs can be significantly higher than the SNRs associated with the uncorrected signals (see Appendix A of Donovan (2021)).

An alternative approach to estimating the pure Mie and Rayleigh attenuated backscatters can be realized by using the spectral data routinely delivered by the MSP. The idea is to form virtual Mie and Rayleigh channels by grouping appropriate ACCD pixels together. Referring to Figure 67, pixels 15 and 12-16 (the wing areas) are summed together to form the virtual Rayleigh channel and the central region pixels form the virtual Mie channel. Crosstalk between the virtual Mie and Rayleigh channels still exists, however, the associated set of crosstalk coefficients yields a favourable degree of error magnification. In addition, compared to using both the MSP and RSP data, only one calibration constant is present in the system.

Figure 67: Sample MSP spectra averaged over one observation period (30 measurements profiles) for a single range-gate. The `Ray' and `Mie' labels denote the pixels assigned to the virtual Mie and Rayleigh channels.

To determine the necessary crosstalk coefficients, an optical model of the Fizeau-based MSP was applied. The operation of the MSP is schematically depicted in Figure 68. Here the response to an input combined Mie and Rayleigh spectrum per ACCD pixel column is illustrated. The set of crosstalk coefficients are found by calculating the per-pixel relative response to pure Rayleigh and Mie inputs and then respectively summing these over the appropriate pixels comprising the virtual channels. The resulting set of coefficients are functions of the optical/physical parameters of the FSP as well as the input spectra. Rather than assume an analytical form for the MSP response function (e.g. Lorentzian, Airy or Voigt), an ab-initio calculation of the MSP response is performed (Novak et al, 2011). The calculation of the associated crosstalk coefficients as well as the Fizeau model used is described in Appendix-B of Donovan (2021).

Once the crosstalk coefficients are known, the total signal levels (after background and dark-count subtraction) in the virtual Mie and Rayleigh channels can be inverted to yield the pure Rayleigh and Mie signals. The crosstalk coefficients correspond to a zero Doppler shift and a uniform intensity distribution across the MSP. The process of accounting for the non-uniform spectral response across the MSP is described in the next section. Depending on the exact pixel boundaries chosen to define the Mie and Rayleigh virtual channels, the crosstalk coefficients are somewhat insensitive to Doppler shifts. Nevertheless, as a simple way to account for possible Doppler shifts, the centroid of the spectra is calculated and used to adjust the Mie and Rayleigh regions.

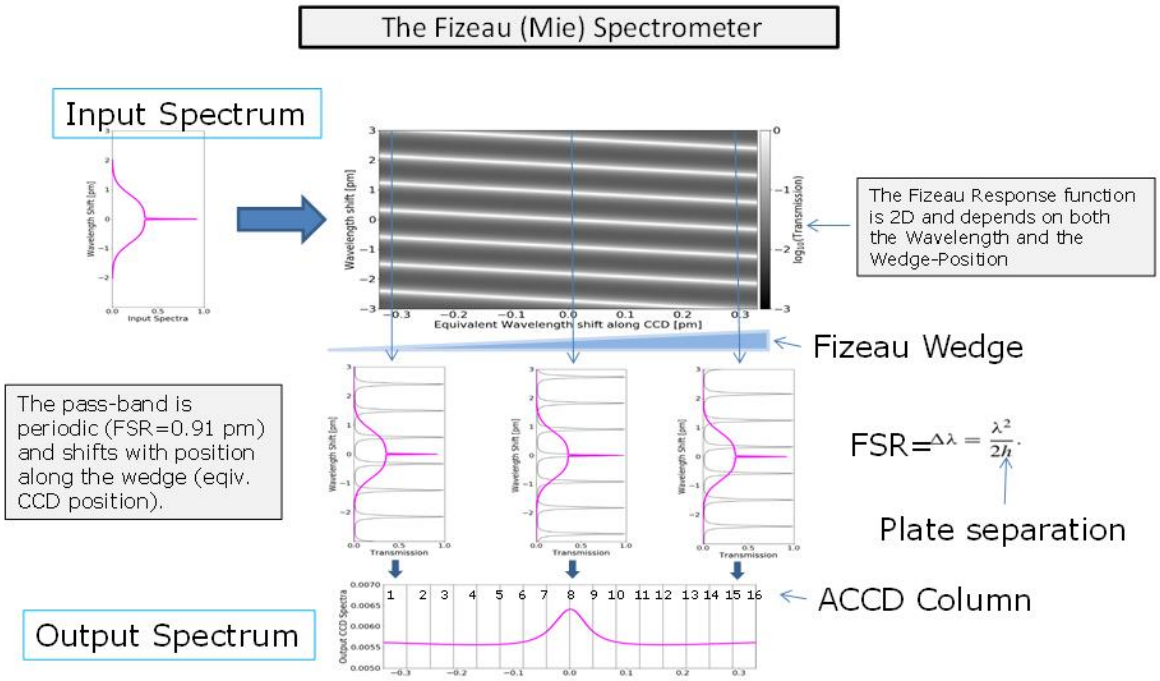

Figure 68: Schematic depiction of the optical transfer function of the MSP. The grey-scale image represents the spectral response for a single ACCD row (i.e., the image is 2-D in wavelength – wedge position space). The passband is a function of wedge position (which is here assumed to be the same for each ACCD row). The narrow Free-spectral-range (FSR) of the device is such that several FSRs must be taken into account to accurately calculate the response to an input Rayleigh spectrum signal.

4.4.3 Calculation of Effective Mie-spectrometer Spectral response (EMSR)

The Fizeau spectrometer spectral response depends on several factors, including the beam shape, and shadowing by the telescope tripod and secondary mirror. This response must be taken into account in order to produce accurate spectra. Information regarding the EMSR can be inferred by operating the ACCD array in imaging mode and shifting the laser frequency out of the useful spectral range so that Mie backscatter is out-of-band (this is the so-called Mie Outside of Useful Spectral Range or MOUSR method). This method can only be performed at infrequent intervals and requires a special operation mode. A method that uses clear-air returns was developed which has the advantage that it can be performed during the course of normal observations.

For clear-air regions the ideal response across the MSP output pixels should be close to being flat. The EMSR can then be deduced by comparing spectra measured in clear-sky conditions to the expected flat response. To identify clear-sky conditions the MSP spectra themselves are used. A rough estimate of the scattering ratio based on the ratio of the wings to a central spectral region is used along with distance from the tropopause. Typically, some of the most particle-free regions (when ice clouds are not present) in the atmosphere exist in the upper troposphere and in the stratosphere above the bulk of the stratospheric aerosol layer. The tropopause is diagnosed using the AUX_MET provided temperature profiles. The EMSR determination procedure is described in detail in Appendix-C of Donovan (2021).

Example EMSR functions are shown in Figure 69. Here it can be seen that a substantial non-uniformity is present. As the EMSR function is strongly depending on the illumination of the atmospheric path, it also strongly differs for the FM-A and FM-B laser periods.

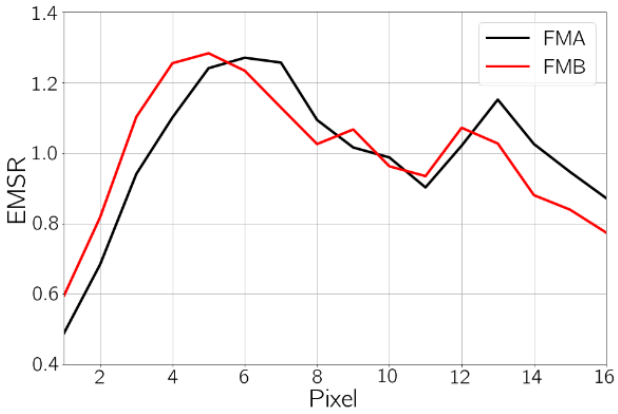

Figure 69: Normalized EMSRs derived using orbit 5221 (2019/07/18) FM-B and orbit 4347 (2019/05/24) FM-A.

4.4.4 MSP-Only ATB example

Example Mie and Rayleigh attenuated backscatter fields for one orbit are shown in Figure 70. For context, both the MSP-only derived fields and the fields retrieved using both the MSP together with the RSP are shown. The MSP+RSP ATBs are produced as part of the SCA retrieval (Flament et al., 2021). Here it can be seen that the MSP-only Mie ATBs appears to be more precise (i.e. less noisy) than their SCA counterparts while the MSP-only Rayleigh attenuated backscatter appears to share a similar level of precision with their SCA counterparts. This can be also seen in the example profiles shown in Figure 71. That the MSP-only crosstalk corrected ATBs have similar or even better levels of precision even though no photons collected by the RSP are used is a consequence of the fact that the set of cross-talk coefficients corresponding to the full MSP+RSP system is unfavourable when it comes to SNR inflation (see Appendix-A of Donovan (2021)). The crosstalk and calibration procedures associated with the MSP-only approach are also simpler and easier to characterize than the more complicated (and more uncertain) full MSP+RSP system.

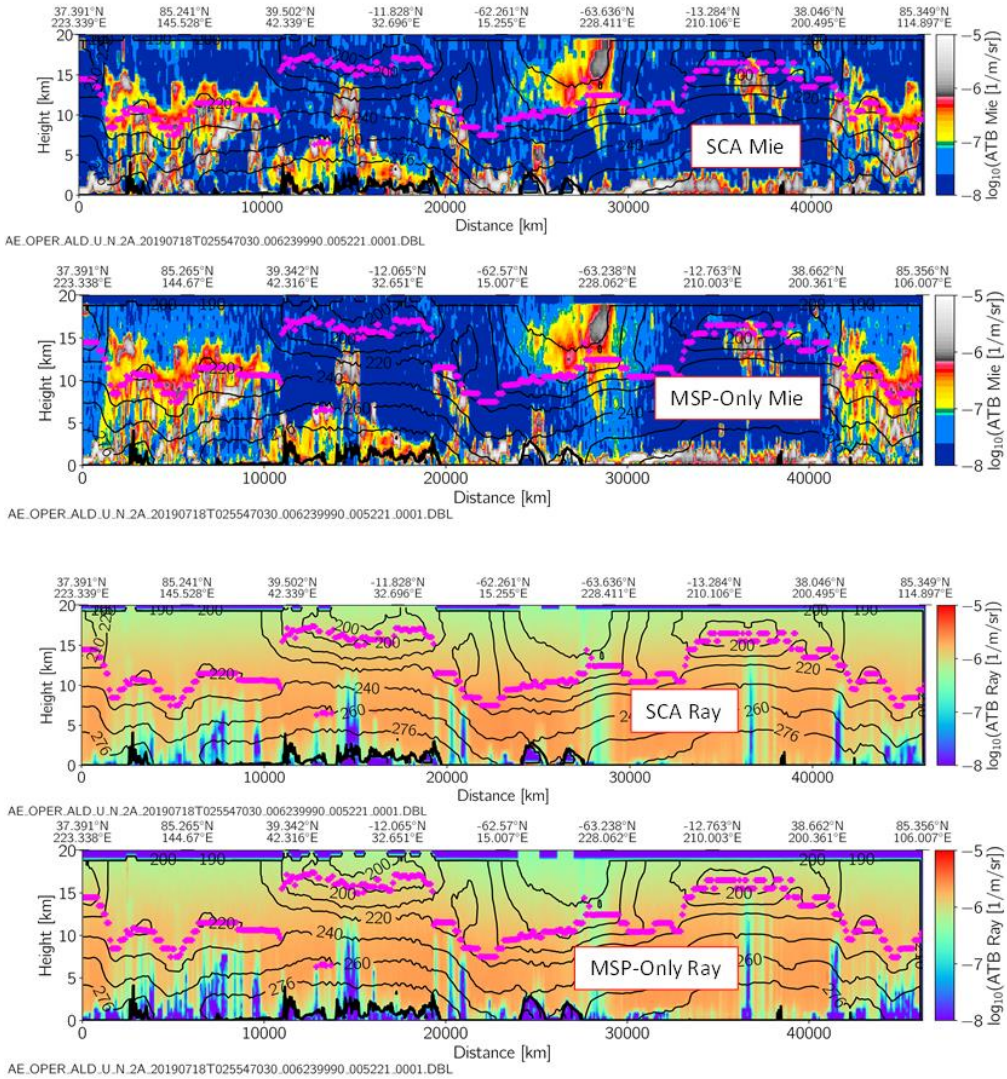

Figure 70: Attenuated backscatter fields for orbit number 5221 (20190718) produced using both the SCA method combining the RSP and MSP and the MSP only method described in this paper.

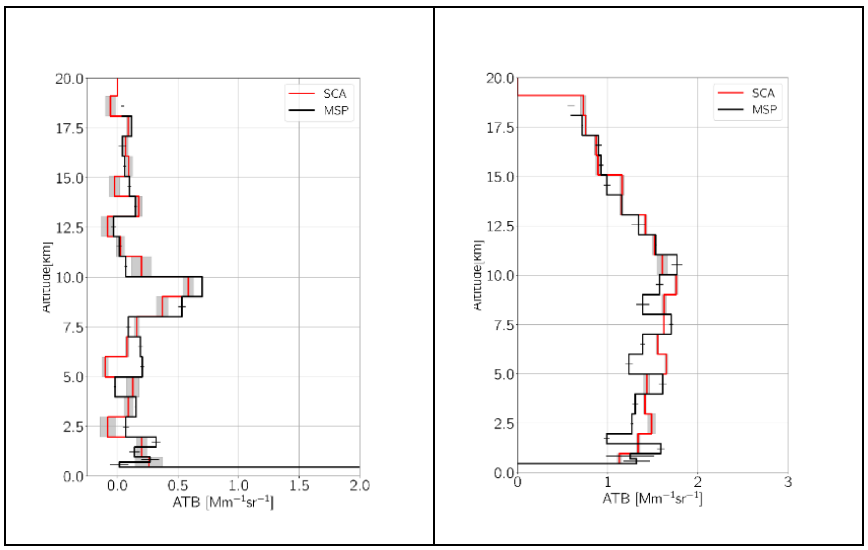

Figure 71: Profiles of Mie ATBs corresponding to averages from observations 51-54 (along-track from about 4521-4786 km) in Figure 70. The Grey shaded area represents the standard deviation of the SCA ATBs while the Black horizontal error bars represent the standard deviation of the MSP-only ATBs.

4.4.5 AEL-FM and AEL-PRO

AEL-FM and AEL-PRO are based on approaches originally developed for ATLID (the EarthCARE lidar). Like ALADIN, ATLID is a HSRL systems, however, unlike ALADIN (which is optimized for wind measurements) ATLID is optimized exclusively for cloud and aerosol observations. Both ALADIN and ATLID face similar challenges when it comes to the retrieval of aerosol and cloud properties. The most important challenge is the fact that the SNR ratios of the backscatter signals are low compared to e.g. those associated with terrestrial lidars. The low SNR of the atmospheric signals creates difficulties when using standard HSRL inversion methods. Along-track averaging can increase the SNR, however, the presence of clouds (and inhomogeneities in general) may lead to large biases in the retrievals. The cloud and aerosol algorithms that have been developed for ATLID that have focused on the challenge of making accurate retrievals of cloud and aerosol extinction and backscatter specifically addressing the low SNR nature of the lidar signals and the need for suitable binning of the data before averaging.

4.4.6 AEL-FM

AEL-FM provides an index that corresponds to the probability of a target being present and identifies clear-air as well as attenuated regions. The product is reported at the native resolution of the input ATBs (about 3 km horizontal resolution). The procedure combines a number of techniques applied to the Mie ATBs including a hybrid-median edge preserving filter (in order to identify ``strong'' returns) and iterative adaptive Gaussian smoothing (which is targeted towards weaker extended features). The pure Rayleigh profiles are also used, mainly to determine attenuated regions. AEL-PRO is closely based on A-PRO. Both A-FM and AEL-FM are described in more detail in van Zadelhoff et al. (2023). The AEL-FM results are used to as input to the AEL-PRO algorithm.

An example of the AEL-FM "feature mask" product is shown in Figure 72. Here a number of interesting features are seen to be present. High altitude clouds associated with tropopause heights above 16 km are seen to be present in the tropics. In the summer mid- and high-latitudes aerosol (forest file smoke) is present in the lower stratosphere and upper-troposphere. In the winter Antarctic stratosphere PSCs are seen to be present.

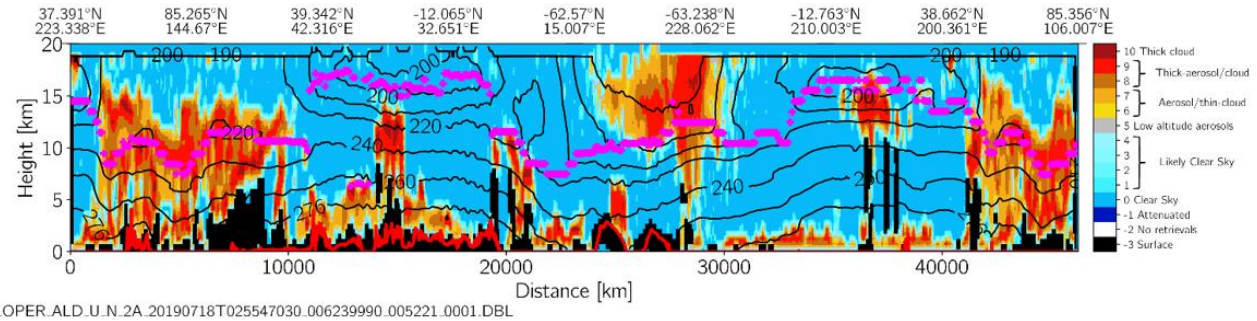

Figure 72: Example AEL-FM feature-mask index corresponding to the data shown in Figure 70. The magenta symbols mark the Tropopause level while the lower red line represents the surface elevation. The thin-black contours show the atmospheric temperature. The temperatures are taken from the AUX_MET data. The DEM is taken from the L1B product.

4.4.7 AEL-PRO

AEL-PRO is based mainly on the Extinction, Backscatter and Depolarization (EBD) component of the A-PRO ATLID processor (Donovan et al., 2024). However, since ALADIN does not measure the depolarization ratio of the backscatter light, the classification aspects of AEL-PRO are simplified with respect to A-PRO (which uses the depolarization ratio in its classification procedures). Like A-PRO, AEL-PRO uses a two-pass approach for processing both strong features (e.g. clouds) and weak features (e.g. aerosols). Unlike A-PRO (which uses a direct method to determine the weak feature extinction and backscatter fields) AEL-PRO uses the same optimal-estimation forward model approach applied to both passes but performed at different resolutions. Pass-1 of the algorithm is at a horizontal resolution of about 90 km and is applied to cloud-screened averaged ATBs while the Pass-2 is at the highest available resolution (about 3 km) and includes cloudy regions. A simple schematic of the AEL-PRO procedure is shown in Figure 73.

As is standard with any optimal estimation approach, the optimal solution (which balances the information in the signals against a priori knowledge of the parameters to be retrieved) is obtained by numerically minimizing an appropriate *cost-function*. The cost-function used in AEL-PRO is:

$$\chi^2 = [Y(x) - y]C^{-1}[Y(x) - y]^t + [x_r - x_a]{C_a}^{-1}[x_r - x_a]^t,$$

where **y** is the observation-vector composed of the observed ATBs, i.e.,

$y = \left(ATB_{Ray,1} \ldots\ldots ATB_{Ray,n_z}, ATB_{Mie,1} \ldots\ldots ATB_{Mie,n_z}\right)$ with n_z being the number of altitude gates.

Y is the forward-modelled observations which is a function of the state vector.

x is the state-vector:

$$\mathbf{x} = \log(\alpha_1 \ldots\ldots \alpha_{nz}, S_1 \ldots S_{nz}, Ra_1 \ldots\ldots Ra_{nz}, C_{lid})$$

and $\mathbf{x}_a$ is the a priori log state-vector

$$\mathbf{x}_a = \log(S_{a,1} \ldots S_{a,nz}, Ra_{a,1} \ldots\ldots Ra_{a,nz}, C_{lid,a}),$$

and $\mathbf{x}_r$ is the reduced state-vector (i.e. the state vector with the extinction terms missing, since no a priori constraints are placed on the extinction).

S is the lidar ratio, C_{lid} is the effective lidar calibration coefficient, and R_a is the effective particle size. $\mathbf{Y(x)}$ is the forward model, and $\mathbf{C}$ and $\mathbf{C_a}$ are the observation and a prior error covariance matrices. The particle sizes are used to account for multiple scattering effects, which for ALADIN, can be non-negligible for e.g. ice cloud particles (Donovan et al., 2023). The a-priori values and their associated uncertainties are based on a simple cloud/aerosol separation scheme which uses AEL-FM outputs, preliminary estimates of the backscatter as well as temperature and height with respect to the tropopause height. For regions classified as tropospheric aerosols, an a priori value of 50 Sr is used with an assumed 50% uncertainty.

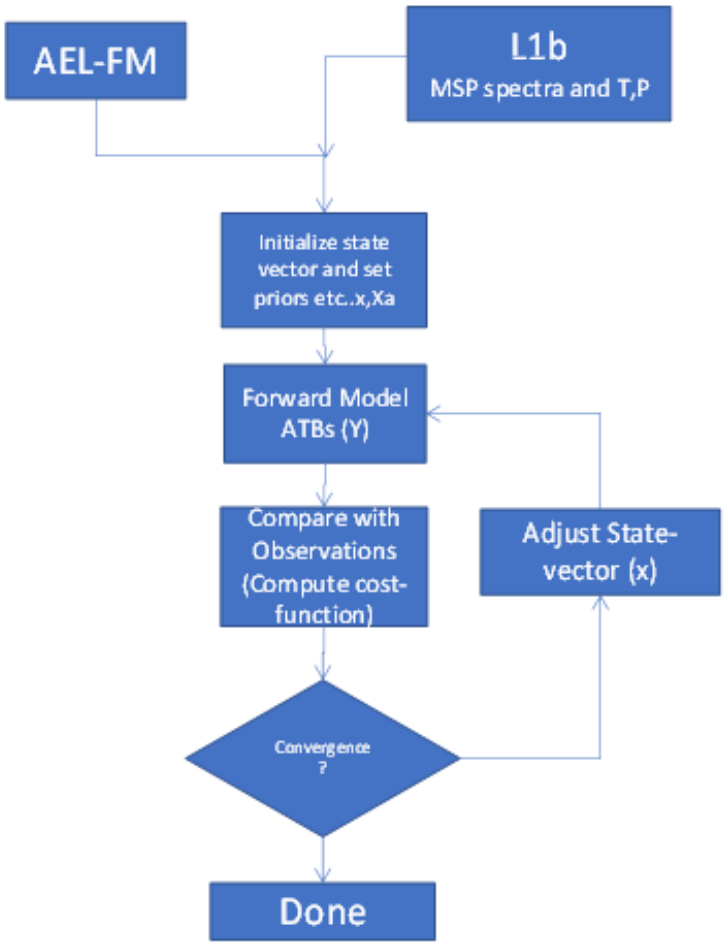

Figure 73: Schematic depiction of the AEL-PRO optimal estimation retrieval algorithm.

4.4.8 Example AEL-FM and AEL-PRO Results

Example extinction and lidar ratio retrievals corresponding to the same orbit as for Figure 70 and Figure 72. Both results from the SCA mid-bin algorithm (Donovan, 2021) and AEL-PRO results are shown in Figure 74. Here data where the estimated SNR is greater than 1 was aggregated to a resolution of 0.5 km (vertically) by 90 km (horizontally). There is a large degree of correspondence between the SCA and AEL-PRO results, however, the AEL-PRO results are more precise and sensitive, particularly with regards to the lidar-ratio retrievals. In particular, the SCA approach tends to only produce usable estimates of the lidar-ratio for extinction values above 0.05 km^{-1} while AEL-PRO supplied usable estimates of the lidar ratio for extinctions on the order of 0.002 km^{-1}.

The more precise nature of the AEL-PRO results can again be seen in Figure 75. Here the difference in precision (noise) is evident between the SCA and AEL-PRO results. This difference in precision is due to the combined effects of both more precise attenuated backscatter profiles estimates as discussed earlier and the regularization (or stabilization) effect afforded by the optimal estimation approach used by AEL-PRO. It can also be seen in Figure 75 that the resolution of the AEL-PRO products is finer than the SCA products at lower altitudes. This is a direct consequence of the need to create a merged grid to combine the MSP and RSP signals used by the SCA process. The AEL-PRO approach uses the MSP vertical grid which tends to have a finer resolution than the RSP vertical grid.

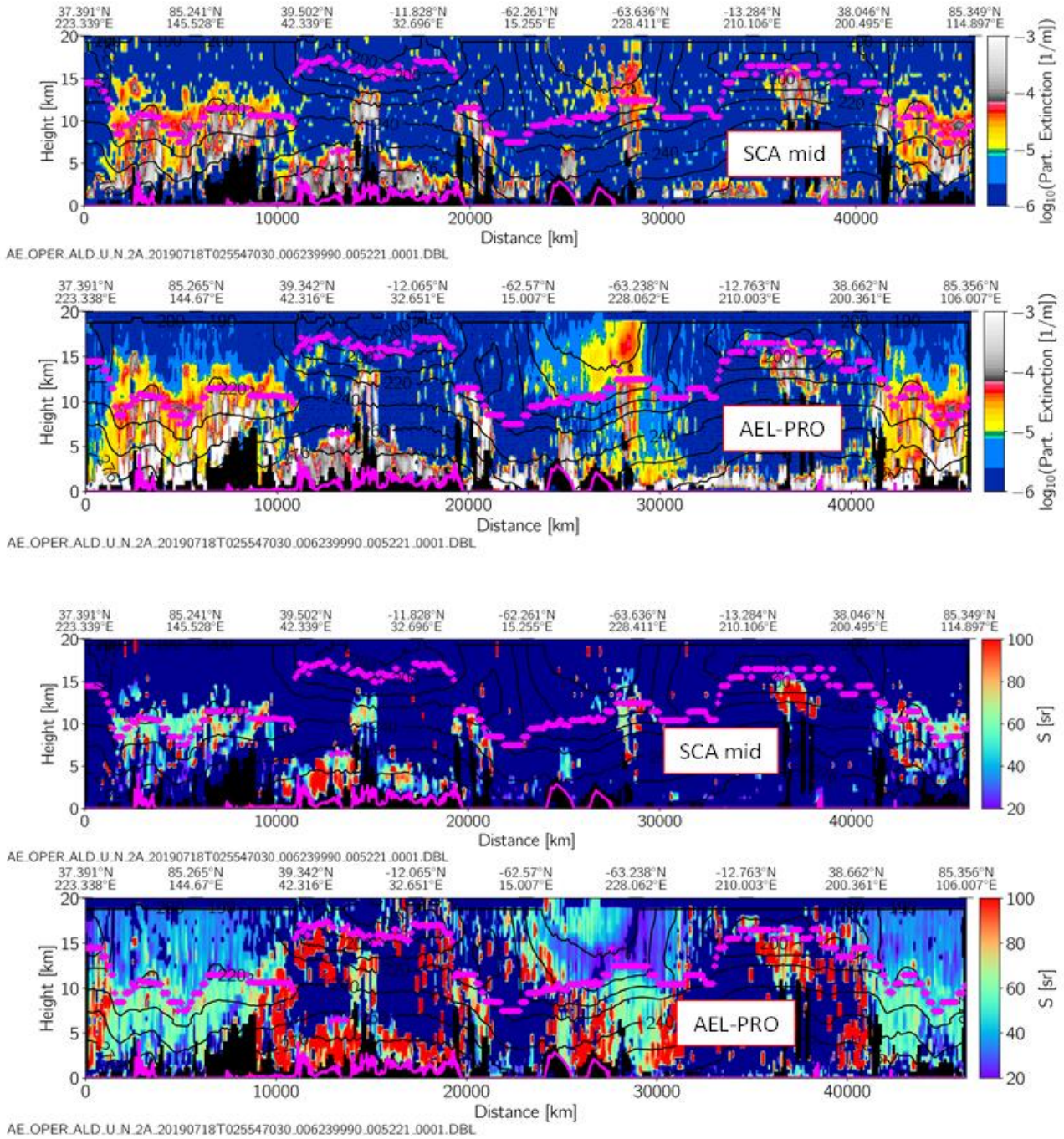

Figure 74: SCA and AEL-PRO (both Baseline 2A16) retrievals o particulate extinction and lidar-ratio for the same orbit as previously presented. The black areas correspond to attenuated or below surface altitudes. The lower magenta line represents the surface elevation, the back contour lines the temperature, and the magenta symbols the tropopause height.

AEL-PRO data is of sufficient accuracy and precision to support longer-term studies. An example of the type of studies possible using AEL-PRO data is shown in Figure 75. In Figure 76, a series of monthly averaged clear-sky profiles of aerosol extinction and lidar-ratio for an aerosol of the North-Atlantic Ocean east of Africa is shown. Aerosol scattering ratios above about 100 Sr are associated with desert-dust that is being transported from Africa. The yearly cycle of this transport is clearly visible in the time series.

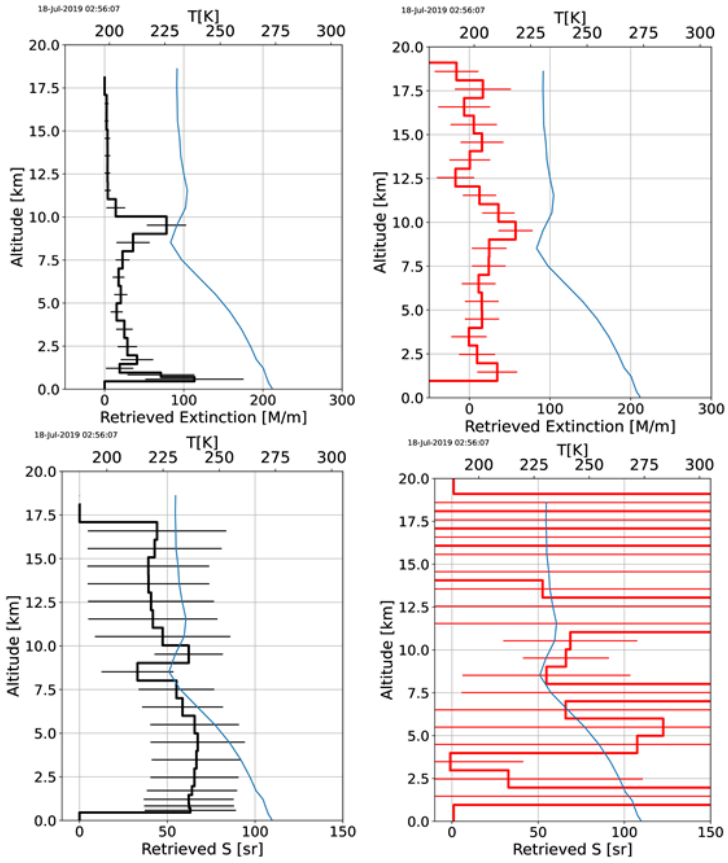

Figure 75: AEL-PRO (Black Left) and SCA Mid (Red Right) profiles of retrieved extinction and lidar-ratio for observation 51 (approx. 76ºN,201ºE) for the same orbit as presented earlier; the Blue line is the AUX_MET temperature profile (upper x-axis scale).

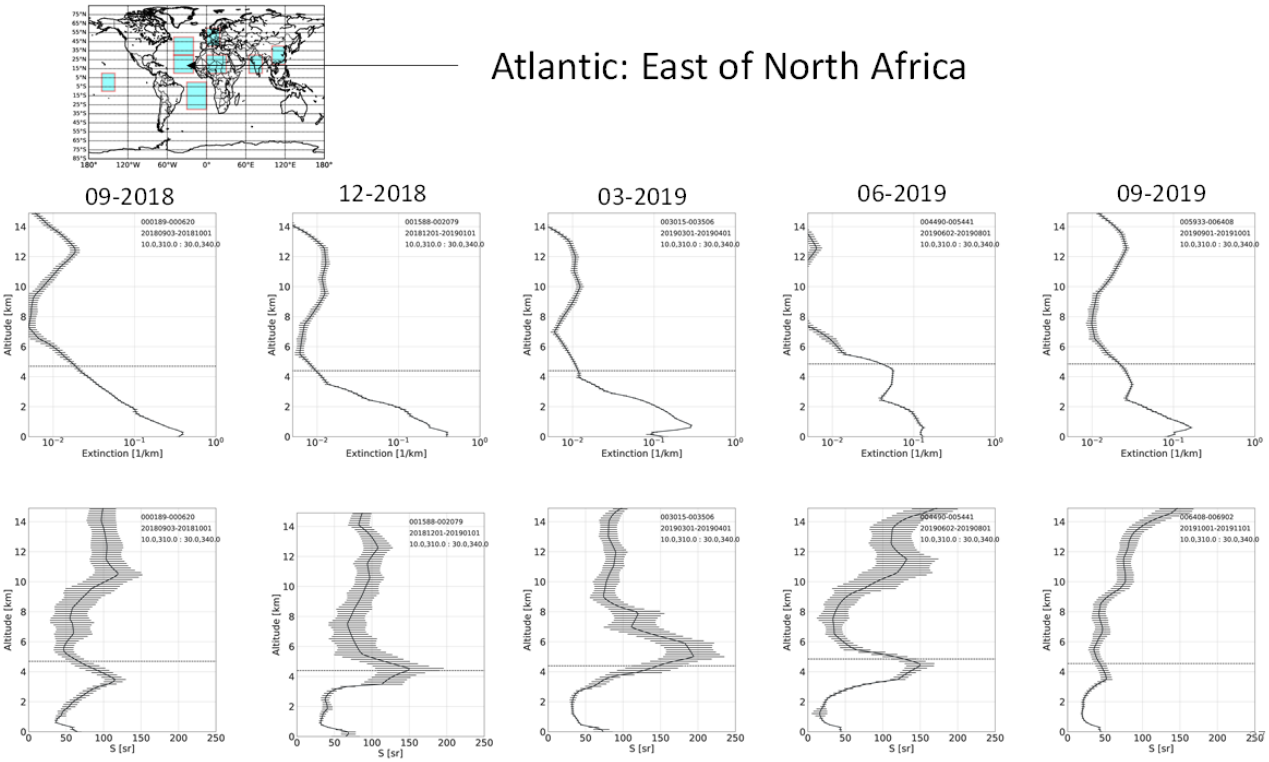

Figure 76: Average profiles of extinction and lidar ratio for the lat-lon area indicated in the figure for the labelled months. Here only clear-sky profiles have been used. The dotted horizontal line demarks the mean zero degrees Celsius level.

4.4.9 Summary and Lessons Learnt

The application of EarthCARE inspired approaches to ALADIN data has yielded benefits for both missions. Though A-FM and A-PRO had been developed using detailed realistic simulated ATLID data (Donovan et al, 2024), the successful application of A-FM and A-PRO methods to real data has boosted confidence in the fundamental approaches as well as building practical experience that will prove useful when actual ATLID observations will be available. From the ALADIN perspective, the work summarized in this chapter has yielded new insights into the impact of crosstalk on the precision and accuracy of the pure Mie and Rayleigh ATBs and has led to a successful alternative method for producing precise cross-talk corrected ATB profiles while correcting for the non-uniform spectral response of the MSP unit. Furthermore, AEL-FM and AEL-PRO have been successfully implemented into the operational Aeolus L2A processor and will yield a useful record of global aerosol extinction and lidar-ratio profiles. The evaluation of the AEL-FM and AEL-PRO processors is discussed further in section 5.2.2.

4.4.10 Lessons Learnt

The lessons learnt during the course of the work described in this Chapter are both of a scientific/technical nature and a broader qualitative nature. Starting with specific scientific or technical points.

1. Key methods being developed for ATLID aerosol cloud processing were successfully validated using real (and not just simulated) data. The interactions between AEL-FM/AEL-PRO and A-PRO/A-FM were indeed two-way. Improvements made to AEL-PRO/AEL-FM have found their way back into the A-FM/A-PRO codes.
2. A method to quantify the EMSR using operational data was implemented. This is relevant for Aeolus-2.
3. A robust method for creating accurate crosstalk free ATBs was developed that is simpler than the standard method. This may be of relevance for Aeolus-2.
4. The importance of considering the system crosstalk coefficients on the SNR of the crosstalk free attenuated backscatter signals was brought into focus. This is of relevance for Aeolus-2 which is planned to be more capable with respect to cloud and aerosol sensing.
5. The lack of a depolarization channel limits the available signal and greatly reduces the ability to conduct target typing (e.g. cloud phase and aerosol typing). This is relevant for Aeolus-2.

Regarding broader more qualitative issues:

1. For ALADIN it is easier to know where the photons are in spectral space than to accurately and precisely know how many of them there are! In other words, determining the Doppler shift is, in some ways, more forgiving with respect to issues such as background subtraction, crosstalk correction, and detector response non-uniformity. For example, if a robust peak in the MSP spectra is present, it would take a grossly incorrect EMSR characterization to significantly affect the determination of the peak location in spectral space. However, the accurate application of such corrections is essential for creating accurate crosstalk free ATBs which are necessary for determining high-quality quantitative aerosol and cloud properties. Furthermore, the ability to bias correct wind measurements using atmospheric forecast model data is a route not available for aerosol and cloud properties.
2. It was an advantage to have come into this project as “outsiders”, it let us be flexible and view issues connected with the aerosol/cloud retrievals with fresh eyes. Thus, useful checks and new

ideas were brought to the table e.g. realizing the importance of the EMSR correction and devising a means to deduce it.

4.5 L2A and L2B calibrations AUX_CAL, AUX_RBC

Benjamin Witschas, DLR and Alain Dabas, Météo-France / CNRM

In order to retrieve winds (L2B) and optical properties (L2A), particular calibrations have to be performed considering the spectral characteristics of the receiver (Fizeau and double-edge Fabry-Perot Interferometers (FPIs)), as well as the spectral characteristics of the backscattered light. This is done in the so-called Aeolus calibration suite, which provides AUX_CAL (L2A) and AUX_RBC (L2B) files for the respective processors as calibration input. During the DISC phase E2, a number of modifications were implemented in the calibration suite, mainly by CNRS/CNRM.

4.5.1 The Aeolus calibration suite

The general structure of the calibration suite is depicted in Figure 77 (see also (CNRM, 2019a)). The two initial steps 1 and 2 characterize the spectral transmissions of the two FPIs and the Fizeau interferometer based on ISR measurements (see also section 3.4 and (CNRM, 2019b)). Once the spectral characteristics of the interferometers are determined, steps 3a and 3b compute the calibration products needed in the L2B and L2A processors to retrieve winds and optical properties of aerosol and clouds, respectively (CNRM, 2019c,d).

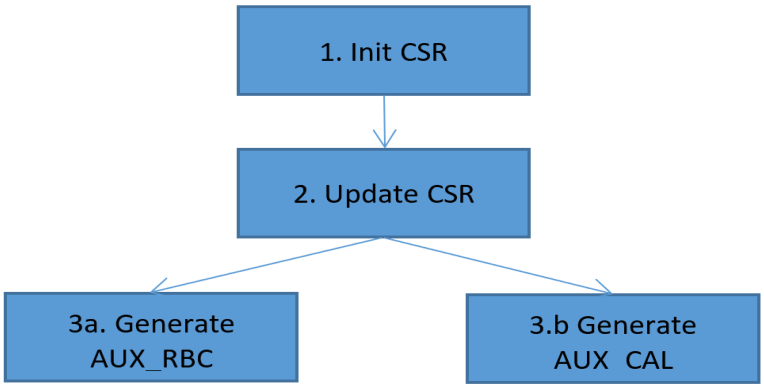

Figure 77: General structure of the Aeolus calibration suite.

All these components were developed in MATLAB and provided to the ACMF-C developers ABB with the accompanying documents (DPM, IODD, SUM, SRN) and test data. Originally, the idea was that the operational versions of the cal-suite components would be applied to Aeolus L1B calibration mode data automatically whenever these are available. In practice, though, the prototype codes were used throughout the mission to produce the calibration AUX_RBC and AUX_CAL files that were used operationally due to the following reasons:

- the calibration of Aeolus proved to be a difficult and tricky task, improvements had to be brought to correct for unexpected effects (like the impact of the temperature gradient at the surface of the M1 mirror of the telescope).
- the lidar proved to be stable once settled after new settings; so there is no need for regular (e.g. weekly updates) of the calibration files

Four versions of the calibration suite (4.1 in end 2018, 4.2 in mid-2019, 4.3 in end 2019 and 4.4 in mid-2020) were officially delivered. Further evolutions were coded in the prototype. Some of them were abandoned, as they proved unsuccessful (no improvement of the results). Others were used to produce operational calibration products as discussed below. Although tricky, a useful AUX_RBC was obtained

rapidly after launch, or FM-A / FM-B / FM-A switches and all new laser settings. The result is remarkable. It allowed useful measurement of winds in less than two weeks after launch.

4.5.2 Init and update CSR

The initial corrected spectral registration (CSR) contains the spectral transmissions $T_A(f)$, $T_B(f)$ and $T_{Fiz}(f)$ of the two FPIs A and B, and the Fizeau interferometer from the internal reference path (INT). It is based on a parametric fit of ISR data as it was discussed in Section 3.4. Although the CSR described the measured FPI transmission curves in great detail, it was realized that this is not necessarily true for the atmospheric path (ATM) on which the transmission curves cannot be measured accurately. The ATM path is described by a different illumination of the spectrometers with a different Field of View (FOV) and angle of incidence (AoI) which leads for instance to a frequency shift between INT and ATM FPI transmission as it is shown in Figure 78 based on an example of an IRC measurements performed on 19 August 2019. The black circles describe the INT Rayleigh response, whereas the orange circles indicate the ATM Rayleigh response. It is clearly obvious that both response curves are shifted in frequency. A line fit indicates a shift of -70.7 MHz. Since v4.4, this shift is corrected before the CSR is updated. Hence, the best-fit tilted top-hat function has in a much smaller width and tilt compared to the cases where the frequency shift was not corrected in advance. For comparison the INT Rayleigh response from the ISR measurement performed on the same day is shown by the blue line. It is in great accordance with the INT Rayleigh response from the RRC measurement. These modifications were added to v4.1 of the initial CSR generator.

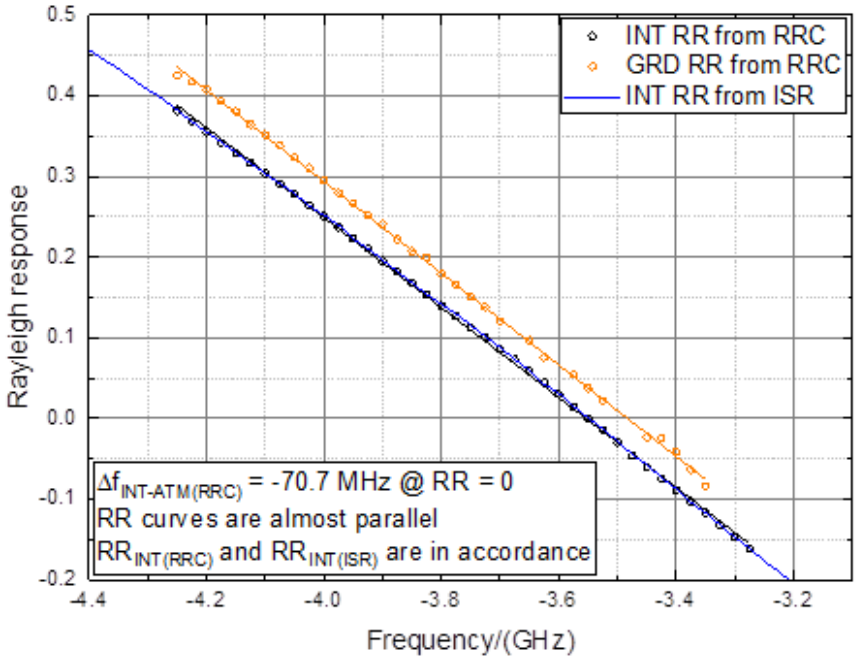

Figure 78: INT (black circles) and ATM (orange circles) Rayleigh responses obtained from RRC data from 19 August 2019. The blue line indicates e Rayleigh response obtained from ISR data from the same day.

The updating procedure of the CSR is the trickiest part of the calibration. It aims at estimating the impact of the different beam étendue in the INT and ATM paths. This impact is modelled by a simple convolution of the INT path FPI curves by a two-parameter, so-called tilted-top hat function. This model is a theoretical approximation. Its relevance to Aeolus has always been a question. On the one hand, it is generally questionable, if a tilted top-hat can represent the actual differences. On the other hand, a convolution can only increase the width of the FPI transmission curves, although it is not verified if the

ATM curves are really broader than the INT curves. Hence, for Aeolus 2, a careful characterization of the ATM path transmission on ground and in-orbit would be highly beneficial. Anyway, the AUX_RBC files generated with the updated CSR provided unbiased winds (after AUX_TEL correction for constant drifts and the M1-induced biases). Any optimization attempts of the theoretical model were tested without success.

The CSR updating code did not change much from versions 4.1 to 4.3. A significant improvement was brought in version 4.4 with the possibility to estimate on-line the frequency shift between the ATM ground and INT path Rayleigh responses (see also Figure 78). This new option did not prove to be very useful in practice because ground return Rayleigh responses are of poor quality with many invalid ground returns (due to clouds for instance or land surfaces with low albedo) and poor SNR for valid ones (due to initial signal loss and signal loss evolution).

Another CSR update was coded but not delivered to the ACMF, which made use of IRONIC data instead of IRC data to update the CSR. This was done when IRC acquisitions were stopped for several months in December 2021 due to anticipated technical issue and risk when rolling the satellite to nadir pointing. IRONIC data are similar to IRC, but they are acquired with a satellite pointing 35° off-nadir rather than nadir. As a result, the Doppler shift is not equal to zero anymore for ATM returns, which must be corrected by using the ECMWF model winds from the AUX_MET file.

4.5.3 Generate AUX_RBC

The AUX_RBC more or less remained the same during the DISC phase E. The AUX_RBC is a rather simple derivation from the CSR as it is sketched in Figure 79.

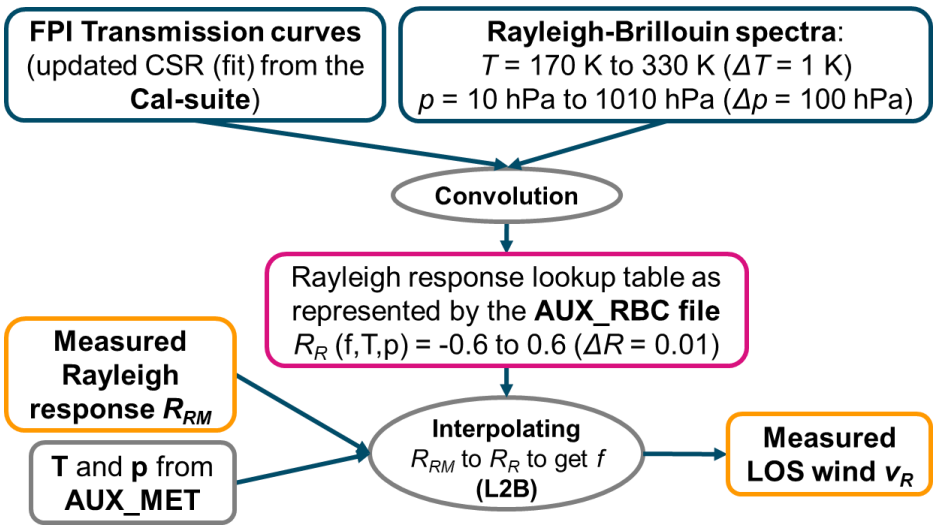

Figure 79: General structure of the AUX_RBC file generation and its use for the wind retrieval.

The FPI transmission curves resulting from the updated CSR are convolved with a set of Rayleigh-Brillouin spectra which are calculated by the analytical model of Witschas 2011 for temperatures varying from 170 K to 330 K (ΔT = 1 K), and pressures varying from 10 hPa to 1010 hPa (Δp = 100 hPa). The resulting look-up table contains the Rayleigh response depending on frequency for various temperatures and pressures and marks the content of the AUX_RBC file. When a certain response is measured by ALADIN, the temperature and pressure is used from the AUX_MET file, and afterwards, the actual frequency or rather wind speed can be determined by means of the AUX_RBC file via interpolation.

One major upgrade of the AUX_RBC file generation came with version 4.2 after the switch to FM-B. Before, the computation of Rayleigh responses from the CSR was done in an interval of frequency offsets centred around 0 GHz. However, the FM-B laser frequency during wind measurements was set to a value of $f_0 = -3.75$ GHz, far from 0 GHz, and the standard USR of about 1 GHz became too narrow to accommodate for the span of possible frequencies. An increased USR was used at first and solved the problem, but consequently led to a significantly larger AUX_RBC product with many useless data. The computation frequency interval in the AUX_RBC was then shifted to f_0, to solve that issue.

The ALADIN optimization activities, (in particular switches to FM-B from FM-A and back to FMA) led to studies on the optimal setting of the laser frequency relative to the cross-point and peak frequencies of the FPIs. Important results were found like why all Rayleigh response curves seem to cross at about one single point where the response presents the advantage of a minimal sensitivity to the temperature of the probed atmospheric volume (see also (CNRM, 2020a)).

The sensitivity of Rayleigh responses to the presence of particles in the probed atmospheric volume also led to interesting studies, as discussed in (CNRM, 2020b) and (CNRM, 2022). They had the two objectives: find a laser frequency operating point where this sensitivity is minimal (hoping it is not too far from the point that minimises the sensitivity to the atmospheric temperature), and provide an efficient correction tool up to the highest possible scattering ratio. Tests were conducted on an AUX_RBC file including a fourth dimension allowing the retrieval of winds in atmospheric volumes polluted with a high level of aerosols or clouds. The tests were not conclusive. The fourth-dimension option was abandoned.

4.5.4 Generate AUX_CAL

The generation of AUX_CAL has remained about the same during DISC phase E. The information contained in this product is a rather straightforward derivation of the AUX_CSR. It yields four calibration coefficients (or rather functions of frequency, temperature and pressure):

- C_1 as the relative contribution of molecular backscatter in the Rayleigh signals of the RSP, normalized to 1 for a pressure p = 1000 hPa, a temperature T = 300 K and a zero Doppler shift f = 0 MHz. C_1 usually varies between 0.8 and 1.4 depending on the respective T, p, and f.
- C_2 as the relative contribution of particulate backscatter in the Rayleigh signals of the RSP. C_2 usually varies between 0.4 and 1.8 depending on f.
- C_3 as the relative contribution of particulate backscatter in the Mie signals of the MSP. C_3 usually varies between 0.1 and 1.3 depending on f.
- C_4 as the relative contribution of molecular backscatter in the MSP, normalized to 1 for a pressure p = 1000 hPa, a temperature T = 300 K and a zero Doppler shift f = 0 MHz. C_4 usually varies between 1.0 and 10025 depending on the respective T, p, and f.

The product also contains estimations of the radiometric calibration coefficients K_{Ray} and K_{Mie} based on the signal levels recorded during an IRC acquisition with the satellite pointing to nadir. The monitoring of real signal levels during wind measurements (comparison of signal level predictions with real signal levels acquired in purely molecular atmospheric volumes at high altitudes) rapidly showed an underestimation of these coefficients by about 10% to 15%. The reason was found later: the calibration coefficients vary with the temperature gradient at the surface of the M1 mirror of the telescope. This gradient is different in nadir and off-nadir viewing geometries. The estimation of the calibration

coefficients K_{Ray} and K_{Mie} was then included in the L2A processor and derived explicitly for each orbit resp. L2A product file. The current version of the AUX_CAL generator still estimates K_{Ray} and K_{Mie}, but these values are not used by the L2A processor. Hence, the AUX_CAL generator could be simplified and would not need an IRC among the required input products (an AUX_CSR and an AUX_PAR_CL would suffice).

4.5.5 Summary, Conclusion and Lessons Learnt

- The first winds measured by Aeolus were available rapidly after launch. It took some time to understand the various sources of biases and correct for them, although a lot of work was done before launch. This demonstrates both, how important a sophisticated preparation is, but also that real data is needed to finally address all issues for the instrument calibration.
- Assimilation tests started in early 2019. There was a good hint of a positive impact on weather forecasts by the end of 2019. It led to the operational analysis of the data in 2020 (in January at ECMWF and June at Météo-France). Considering Aeolus as a demonstration mission, the time between launch and operational assimilation is remarkably short. This testifies the great expectation of many meteorological centres around the world. The impact on forecast skill was even higher than expected although the accuracy of wind measurements was below the specifications.
- The derivation of aerosol and cloud optical products by the L2A was a second priority for the mission. Significant progress was made during the phase E. The validation campaigns showed the products were reliable. This is true in particular for the backscatter coefficients. The high-spectral resolution capability of Aeolus was proven. On-going studies suggest the impact of the assimilation of L2A data on air-quality and weather forecasts is positive. These good results strengthen the option of a cross-polarization channel on Aeolus 2.
- The in-flight calibration of Aeolus proved to be a difficult task, which was not fully solved. The characterization of the Fizeau transmission and reflection, for instance, is still approximate when it is illuminated by the light backscattered by the atmosphere. This is probably the reason why the correction of Mie contamination on Rayleigh winds did not work as good as expected. The encountered difficulties led the DISC team to study more carefully the sensitivity of the receiver to various effects. The team learnt a lot. The expertise then gained by the team allowed to fine-tune the lidar after laser switches for instance and will certainly be of great value for Aeolus.
- The biggest challenge for the instrument calibration is, that the spectrometer transmission curves cannot accurately be measured on the atmospheric path.
- Studies about implementing an aerosol cross-talk correction in the AUX_RBC file as a fourth dimension were not conclusive and hence this option was abandoned. This should be investigated in further detail in the future, as such a correction would be even more crucial in case a Michelson interferometer is used for Aeolus 2.

4.6 NWP bias correction and L2B Optical Properties Code

Gert-Jan Marseille, KNMI

4.6.1 NWP based Mie non-linearity (Mie-NL) correction

During the operational phase of the Aeolus mission it became clear that the methodology for instrument calibration, developed before launch, were inadequate to yield good quality winds meeting the mission requirements. The anticipated alternative strategy to use NWP model winds for Aeolus instrument calibration and bias correction purposes was further developed. This idea is not new. The use of NWP model data has proven to be very useful for calibrating instruments (Stoffelen, 1999) and monitoring instrument performances, including those from satellites (Rennie and Isaksen, 2020). In addition, NWP model data has proven to be useful to detect instrumental imperfections and to develop schemes to correct for these imperfections by making use of NWP model data (e.g., applied to satellite radiance data; Eyre, 1992).

The apparent paradox of using NWP model data for instrument calibration or instrument bias correction schemes (Weiler et al., 2021) comes from the general notice that the model is always wrong[1] – and that is why we need observations to keep the model on track with the real atmosphere – but good on average (by design)[2]– and that is why we can use NWP model data over a long period for instrument calibration and instrument correction scheme purposes.

One of these calibration applications for Aeolus was developed for Mie channel winds in atmospheric conditions with clouds and/or strong aerosol, denoted Mie-cloudy winds. It was found that comparing Aeolus Mie winds against ECMWF model winds revealed systematic errors in retrieved Mie winds, which can be visualized as physically unrealistic structures ("wiggling") in the scatterplots for winds with amplitudes below 15 m/s, i.e., the bandwidth where most winds reside, see Figure 80.

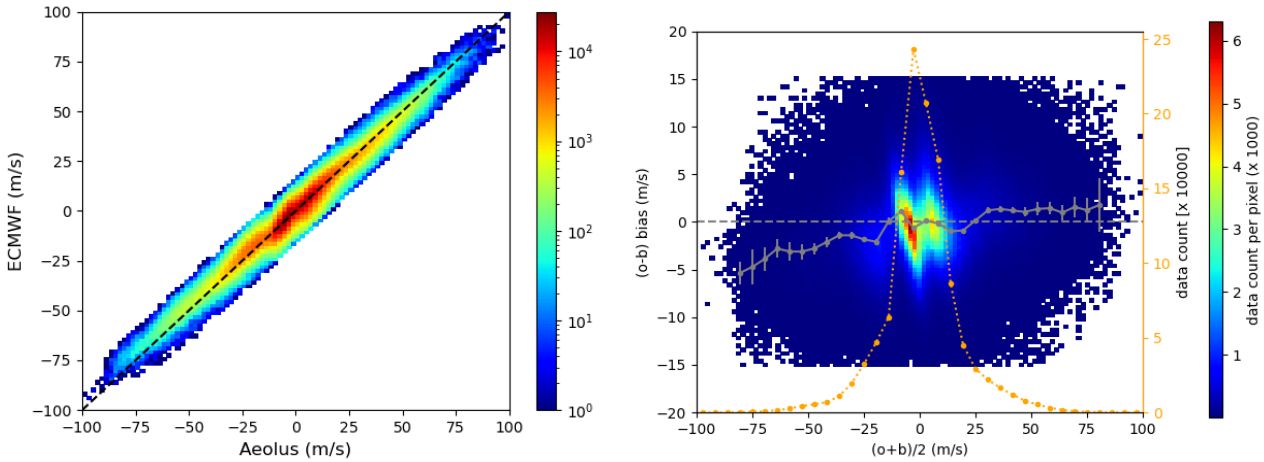

Figure 80. Left, density scatter plot of Aeolus Mie winds (denoted with 'o' in the right-hand-side plot) along the x-axis and the ECMWF model equivalent (denoted with 'b' in the right-hand-side plot) along the y-axis for the one-month period December 2019. The colour bar on the right denotes the number of observations. The black dashed line represents the diagonal. Right, Mie (o − b) density as a function of true wind speed represented by (o + b)/2.

[1] This statement is slightly exaggerated to emphasize the qualifications "wrong" and "good"; but in essence, at every time step, the model deviates from the true atmosphere and model uncertainties can be quite substantial (ensemble spread).

[2] NWP models are continuously tuned and monitored against observations with the aim to minimize model error biases

The systematic errors of retrieved Mie winds could be traced back to imperfections of the data in the calibration tables used for correcting for non-linear effects of the measured Mie response, in short denoted Mie-NL, i.e., the blue curve in Figure 81. These Mie-NL effects are fundamental to the Fizeau interferometer design and the corrections (blue curve) were based on Aeolus data gathered in calibration mode (where the laser was pointed downward at nadir) from surface returns over regions with high albedo, mainly the Poles.

As an alternative one can take NWP model winds at Aeolus locations, convert these to HLOS winds as measured by Aeolus and further convert these to the corresponding peak location on the Fizeau interferometer. The black crosses in Figure 81 are the result of differences between instrumental measured Mie peak locations and those derived from NWP model winds. Following the general notice mentioned above, a large sample, covering a long time period and all global regions, is needed to reduce the impact of potential model biases entering the NWP based calibration table (the black crosses).

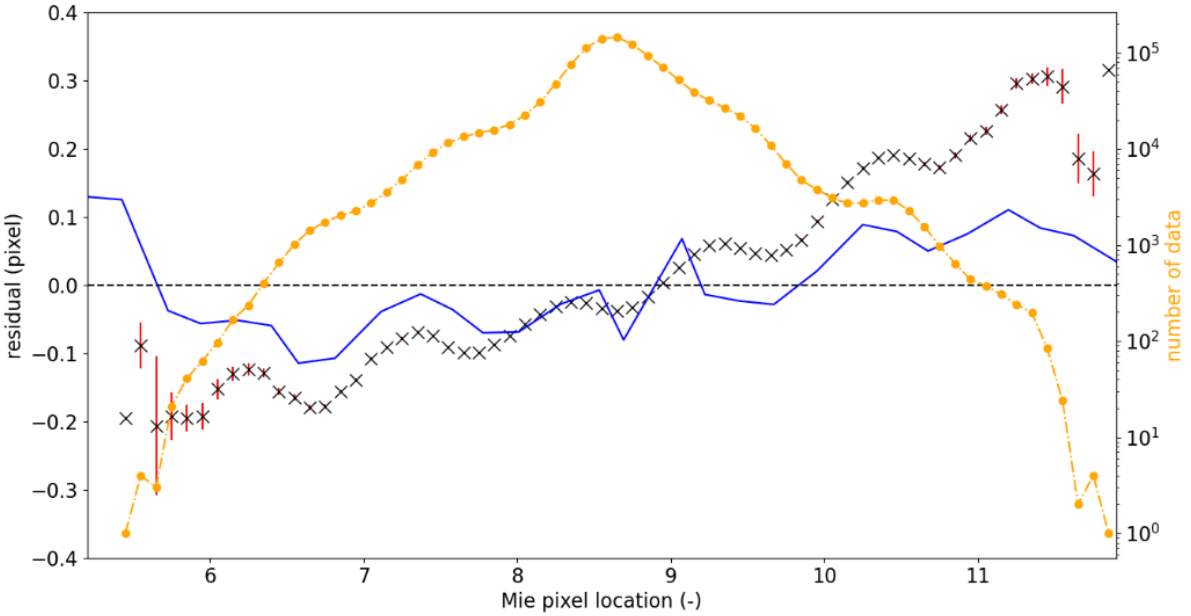

Figure 81. Mie spectral response nonlinearity (residual from linear fit) as a function of Mie pixel location as obtained from 16 September 2019 in orbit IRC#48, i.e., instrumental calibration (blue) and as obtained from NWP calibration (black crosses), which was derived from one month (December 2019) of Aeolus data. The orange dots denote the number of data available within the 0.1 sized pixel bins. The red error bar denotes the standard deviation of the values within the bin divided by the square root of the number of data in the bin to reflect the standard deviation of the mean value. The size of the error bar is negligible for most pixel bins.

Figure 82 is similar to Figure 80 and shows the statistics when using the Mie-NL calibration table based on the black crosses rather than the blue curve. Clearly, the wiggling feature apparent in Figure 80 has removed and in addition the density scatter in the left panel of Figure 82 is closer to the black dashed line for strong winds than in Figure 80. Also, the (o-b) random error has reduced by about 5% (not shown). More details are found in Marseille et al. (2022).

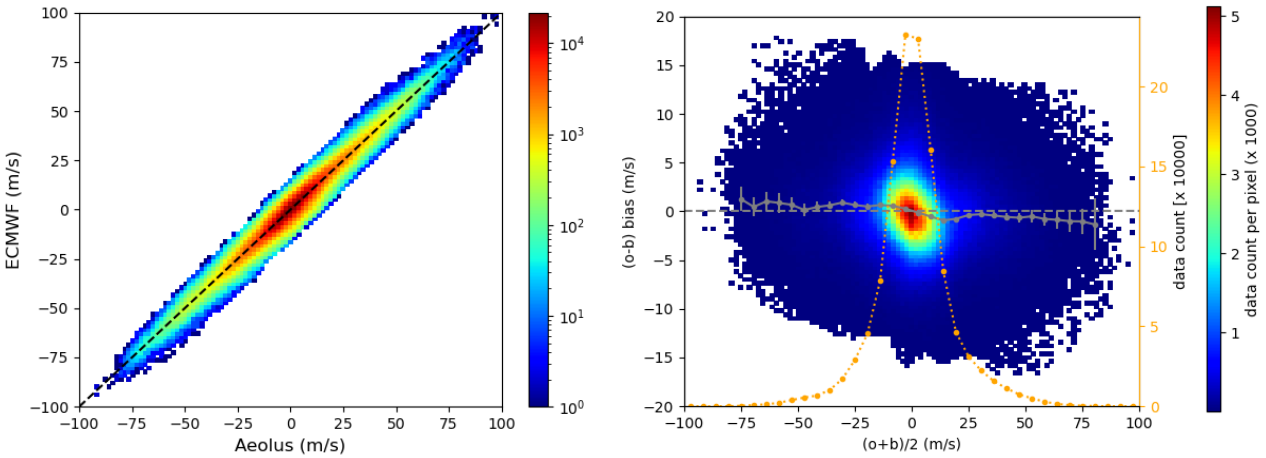

Figure 82. Same as Figure 80, but now correcting for Mie non-linearities based on NWP calibration, i.e., the black crosses in Figure 81.

Lessons learnt

- The above work was foreseen, but not explicitly planned within the original DISC Phase-E contract, because its priority was difficult to predict in the context of other possible anomalies. For completely new (Explorer) missions it is important to leave sufficient room within the contracts to explore different directions, either foreseen or not foreseen before the launch of the contract. We were happy to see that this has always been the case for Aeolus DISC;

  The bullets below mainly refer to the application of the Mie-NL calculation, described above, for reprocessing activities in phase F.

- The calculation of Mie-NL curves based on weekly periods is too short, mainly because the number of extreme winds over such short time period is too small which makes the Mie-NL calibration table values for the smallest and largest pixel values, i.e., smaller than 6 and above 11.5 in Figure 81, too uncertain;
- The solution for the above is to generate Mie-NL curves based on monthly data, as in Marseille et al. (2022), and apply the resulting curves to data of that particular month.
- This above approach enables also to better take into account the temporal (evolution) characteristics of the instrument;
- It is important to perform bias correction (AUX_TEL turned on) before estimating the Mie-NL curve, because Mie-NL is not meant to correct for these instrument-induced wind biases.

4.6.2 Aeolus Rayleigh-cloudy winds – the empirical correction scheme

The Aeolus level-2 processor (L2Bp) delivers three main products: Mie-cloudy winds (HLOS winds in cloudy and dense aerosol conditions retrieved from the Mie channel data), Rayleigh-clear winds (HLOS winds in clear air conditions (no clouds and or aerosol) retrieved from the Rayleigh channel data) and Rayleigh-cloudy winds (HLOS winds in cloudy and or dense aerosol conditions retrieved from the Rayleigh channel data). During the operational phase of the mission the first two products (Mie-cloudy and Rayleigh-clear) reached a level of maturity for operational use in NWP. In contrast, the quality of Rayleigh-cloudy winds has been insufficient for use in NWP during the complete operational phase of the mission, mainly because of biases which exceeded the mission requirement. It was found that the procedure, developed before launch, to correct for Mie contamination of Rayleigh channel data was inadequate.

An alternative approach has been developed based on the same principle as discussed for the Mie non-linearity correction in the previous section, namely by making use of NWP data to determine an empirical correction for Mie contamination of the molecular signal.

Starting from an NWP wind at the Aeolus location, one can convert to HLOS wind and further to LOS wind, Doppler shift (D) and Rayleigh Response (RR), given atmospheric pressure (P) and temperature (T) from the AUX_MET data and the AUX_RBC file which provides a 3D lookup table: RR(P,T,D). The AUX_RBC table has been used successfully for retrieving Rayleigh-clear winds but does not provide a measure that considers Mie contamination (or better Mie contribution) of the Rayleigh channel signal. The Mie contribution to the complete signal can be quantified through the scattering ratio (SR), which is estimated as part of the L1B processing and available to the L2Bp. The effect of Mie contribution is a delta, denoted ΔRR, on the Rayleigh Response compared to clean air conditions. Taking a large sample of differences between measured Rayleigh Responses in cloudy conditions, denoted RR_{meas}, and simulated Rayleigh Responses based on NWP data it was found, empirically, that ΔRR follows an exponential curve as a function of SR, see Figure 83. Besides a function of SR, ΔRR turned out to be a function of D as well, so ΔRR(SR,D), i.e., the parameters of the exponential function differ for different values of D.

Given this empirical relationship, the Doppler shifted frequency, D, for the Rayleigh-cloudy wind is obtained from solving the equation: RR_{meas} = RR(P,T,D) + ΔRR(SR,D), after linearizing the first term on the right-hand-side. More details are found in Marseille et al. (2023). With the new empirical correction method not only the bias has been removed, see Figure 84, but also the overall (o-b) random error is closer to a Gaussian distribution with an overall reduced scaled median absolute deviation (SMAD) by 5% (not shown).

An Observing System Experiment (OSE) over a 6-week period, ran by ECMWF, showed overall (slightly) positive impact by adding Aeolus Rayleigh-cloudy winds to the ECMWF observing system in addition to Aeolus Rayleigh-clear and Mie-cloudy winds, see slide 8 of (Rennie, 2023).

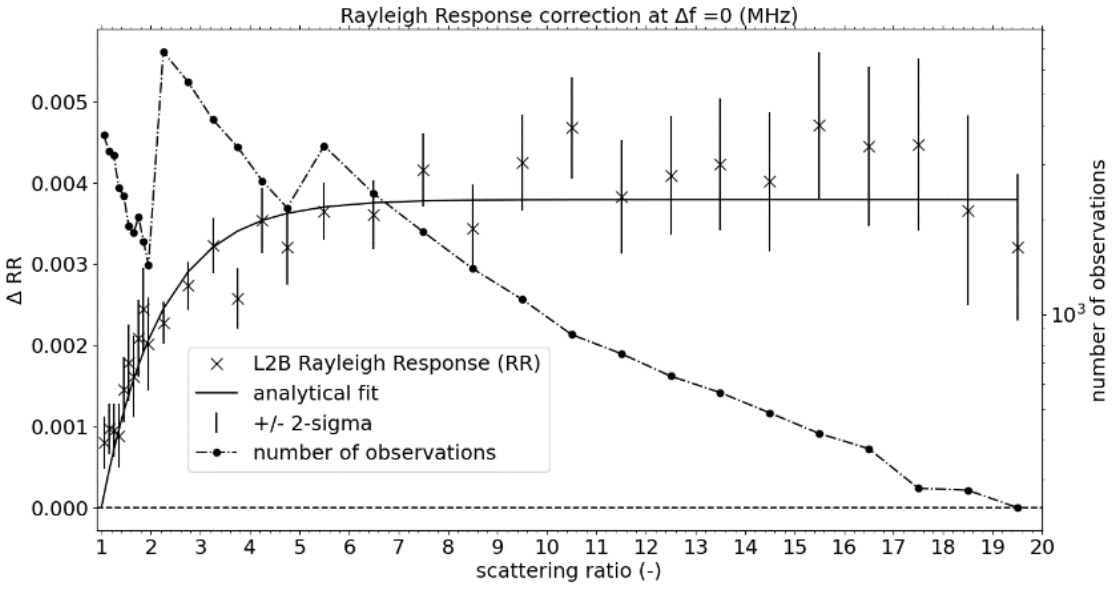

Figure 83: Rayleigh response increment, ΔRR, (crosses) as a function of scattering ratio (SR) for close to zero horizontal line-of-sight winds. One month of Aeolus data has been used: August 2019. The error bars denote plus/minus two times the standard deviation of the mean value. The dash-dotted line shows the number of observations available for each scattering ratio bin along the right-hand side y-axis which is on logarithmic scale

and ranges from 250 to 8000. The steps at SR values 2 and 5 are explained by a change of the resolution of the SR binning. The solid line is the result of a weighted exponential curve fit through the crosses.

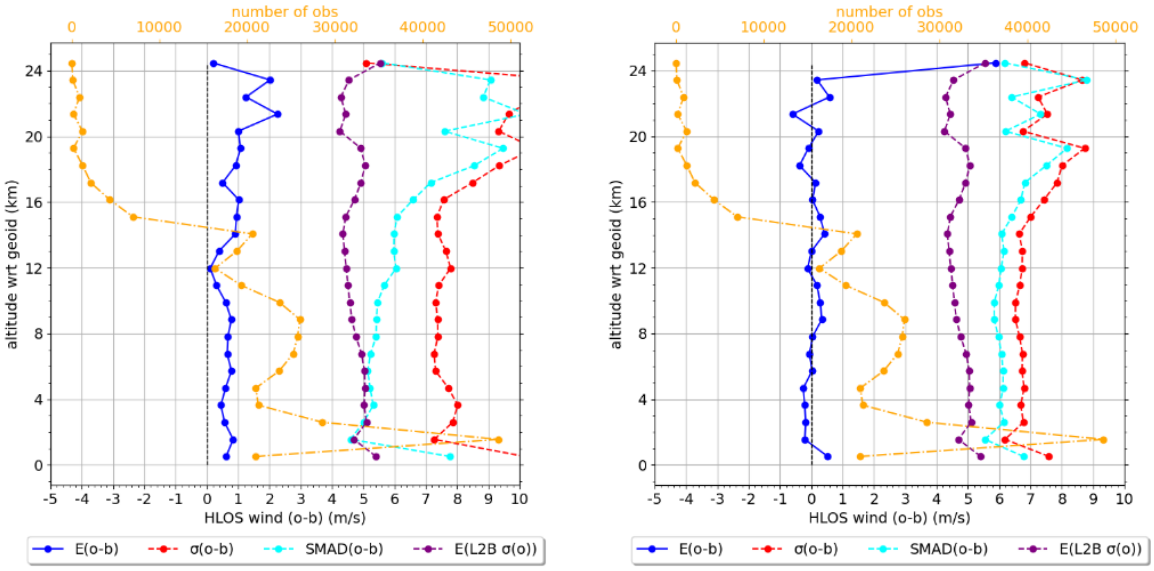

Figure 84: Rayleigh-cloudy (o-b) HLOS wind statistics versus altitude for the 1-month period August 2019, for the pre-launch implemented method (left) and with the new NWP based empirical correction method (right). The blue curve denotes the mean value (bias), the red and cyan curves represent the (o-b) random error, with red the standard deviation and cyan the scaled median absolute deviation (SMAD). The purple line denotes the observation error as estimated by the L2B processing and is based on the signal-to-noise ratio of the received Rayleigh signal on the detector. The orange curve denotes the number of observations used in the statistics.

Lessons learnt

- As for the Mie-NL calibration curves, discussed before, the above work was not planned within the original DISC contract, because it could not be foreseen;

The bullets below mainly refer to the application of empirical correction method described above for reprocessing activities) in phase F:

- The calculation of the parameters for the empirical correction of Mie contamination based on weekly periods is too short, mainly because the number of extreme winds over such short time period is too small which makes the fitting procedure less reliable;
- The solution for the above is to calculate the parameters of the empirical correction based on monthly data, as in Marseille et al. (2023), and apply the resulting curves to data of that particular month.
- This above approach enables also to better consider the temporal (evolution) characteristics of the instrument;
- It is important to perform bias correction (AUX_TEL turned on) before calculating the parameters of the empirical correction for Mie contamination, because the correction is not meant to correct for instrumental induced wind biases.

4.6.3 L2Bp Optical Properties Code (OPC)

In principle the L1B product provides sufficient input (scattering ratio, Mie signal SNR) for the classification of measurements in the L2Bp, before accumulation to observation level. These input parameters all rely on Mie channel data only.

The rational for having a backup plan for classification in the L2Bp, based on Rayleigh channel data only, was twofold. First, before launch various options for positioning the 24 Mie and Rayleigh bins within the profile were considered, which turned out that a perfect one-to-one collocation of Mie and Rayleigh bins was not optimal for wind retrieval since many Mie bins would be wasted in regions of known negligible cloud and aerosol occurrence at high altitude. Still, at some locations and for particular seasons high altitude particles would be observed (for instance polar stratospheric clouds) which should be detected in case of missing Mie bins at these altitudes. Second, in case of a failure of the Fizeau interferometer during the operational phase of the mission, we would have lost the ability to do signal classification as all measures relied on Mie channel data only.

The basics of the Rayleigh channel data-based feature detection, from OPC, is described in the L2B-ATBD, but was further developed during the beginning of the mission. An example is found in Figure 85 showing a typical case with a polar stratospheric cloud (close to the left-hand side border of the panels) measured by Aeolus on 1 June 2020, and which was well detected by the OPC algorithm.

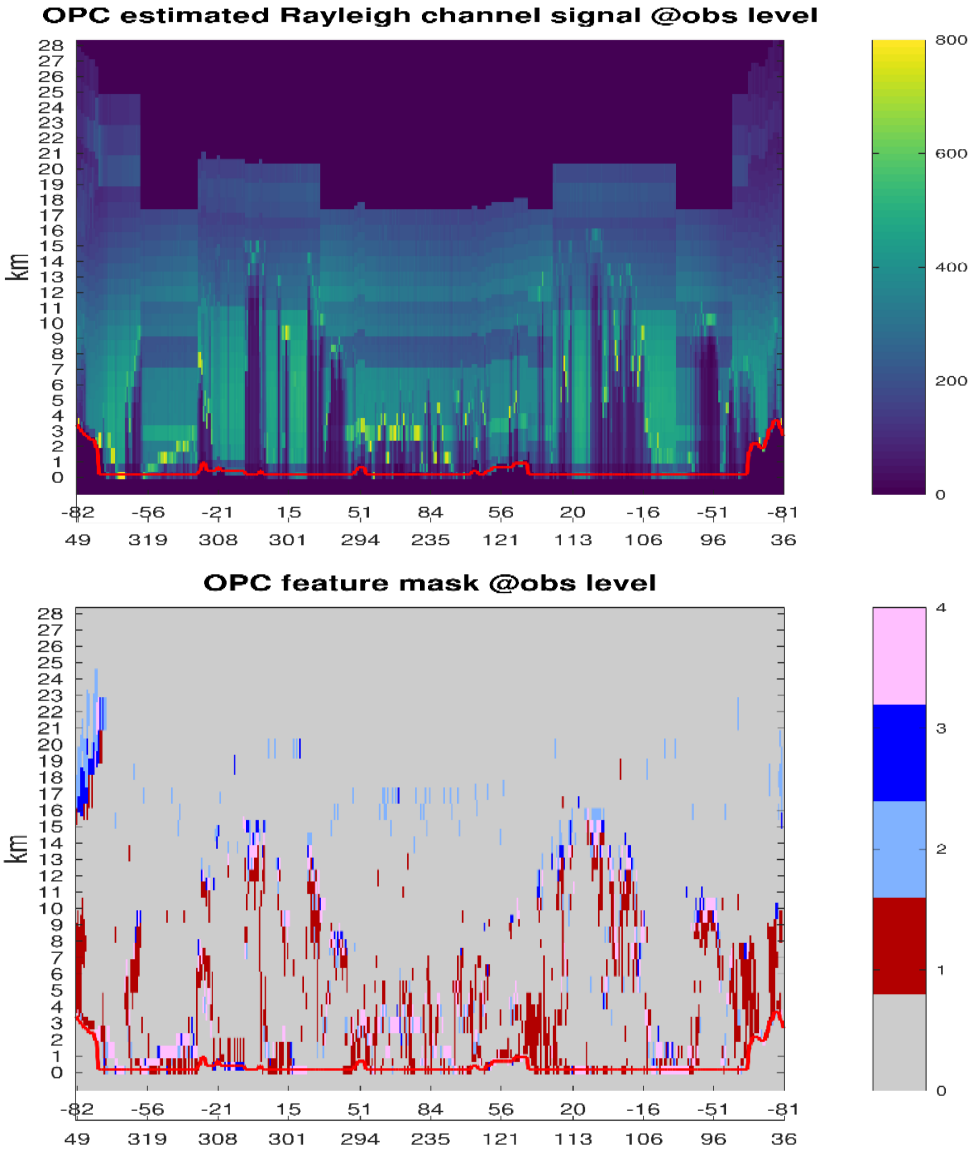

Figure 85: Typical example of a L2Bp OPC feature mask for 1 orbit from Aeolus data measured on 1 June 2020. The top panel shows the input Rayleigh channel signal (total number of photon counts in channels A and B). The bottom panel shows the resulting feature mask, i.e., cross-talk detected at measurement level from strong (cloud) returns (pink), cross-talk detected at observation level (light/dark blue) and particle layers detected not because

of cross-talk, but because of attenuated signal at lower altitudes (red). In the gray regions no particles were detected. The L1B input file used is named: AE_OPER_ALD_U_N_1B_20200601T212411035_005423999_010291_0001.

Besides a feature mask, OPC also provides estimates of particle optical properties such as the scattering ratio and lidar ratio. In 2021 an intercomparison study of the then available algorithms for feature detection and optical properties retrieval was conducted by Frithjof Ehlers (Young Graduate Trainee YGT at ESA). The algorithms involved in the study included: SCA (standard correction algorithm, default algorithm developed by Météo-France), MLE (Maximum Likelihood Estimation – algorithm developed by Frithjof Ehlers), AEL-PRO (EarthCARE based, adapted to Aeolus and developed at KNMI) and L2B-OPC (discussed here). The full presentation can be found on an [Aeolus Wiki page].

In the end, the L2BP OPC was (luckily) never needed during the operational phase of the mission but could still be integrated with the current L2A schemes, in particular AEL-FM, which fully relies on Mie channel data only, hence making no use of the information content in Rayleigh channel data.

Lessons learnt

- It is good to invest in methods, prior to satellite launch, that can act as plan B in case the original plan does not work out as expected. OPC is one example. Another example is the use of NWP model data for instrument performance monitoring which was, fortunately, already identified before Aeolus launch and turned out to be crucial for the success of the mission. NWP based bias correction and calibration schemes, developed during the operational phase of the mission, are good examples as well. Without these NWP based schemes the mission would have been much less successful.

4.7 L2B wind bias causes and correction

Oliver Reitebuch and Michael Rennie, ECMWF

4.7.1 Introduction

This chapter discusses the different causes of the systematic errors (biases) in the retrieved winds from the L2B product, which were unexpected and only encountered after launch. Different causes resulted in wind biases of different temporal behaviour and different magnitudes, which made it difficult to disentangle them in one approach. Basically, the bias causes of larger magnitude (e.g. several m/s) had to be identified and corrected before biases of magnitude below 1 m/s could be identified and corrected.

It was expected before launch and studied in detail that biases along the orbit with harmonic components (e.g. sinusoidal or higher harmonics) as a function of the orbital phase (argument of latitude) could be present. Thus, a harmonic bias estimator (HBE) was developed using the velocity of Rayleigh and Mie ground returns to determine the harmonic biases and allow for a correction in the L1B and L2B product. After launch those harmonic components were detected using ground returns. However, since also non-harmonic biases that could not be corrected with the HBE were present, the operational correction of the wind biases using the HBE as part of the operational ACMF (Aeolus Calibration and Monitoring Facility) was not activated during the complete Aeolus mission.

4.7.2 Combination of several systematic wind errors and causes

A very powerful method to detect biases in the L2B wind product was the comparison with the ECMWF model winds using monitoring tools and plots (see chapter 5.3) that had already been developed before launch. Here, mainly differences between Aeolus observations O and the ECMWF model background B, which are derived from short-range forecasts, were used in the so-called (O-B) departure statistics. Already within the commissioning phase E1, it was discovered that single range gates for Mie and Rayleigh winds showed a constant bias for a certain period (Figure 86, top left). Thanks to the strong expertise of the DISC ranging from NWP monitoring to detailed instrument knowledge, it was explored that those constant biases were caused by enhanced signal levels on single detector pixels (out of 16) of the affected range gate. Those enhanced signal levels could then be traced back to enhanced dark current signal levels for single pixels – called hot pixels (see chapter 3.3 and Weiler et al., 2021). A correction of these hot pixels was implemented using a special operation mode for the characterization of the dark current in the ACCD memory zone (so called DUDE (Down Under Dark Experiment)) which became operational on 14 June 2019.

After correction of the wind biases in single range gates in June 2019 and on-going investigations of the bias variation along the orbit for all observations of a wind profile, it became clear that also non-harmonic bias components were present (Figure 86, lower right), and that those biases are different for the ascending and descending orbits. This figure shows the Rayleigh bias (O-B) in m/s HLOS as a function of orbital phase (argument of latitude) for an orbit in August (blue) and November 2019 (orange). The locations of the North and South Pole (NP, SP) and Equator (Eq) together with the ascending (asc.) and descending (desc.) orbit are indicated. It is clearly visible from the averaged bias (orange and blue line) that the variation is more complex than could be represented by orbital harmonics, although the overall shape resembles a harmonic function. It was discovered by ECMWF in August-September 2019 that those bias variations along the orbit are correlated with the temperatures of the primary mirror M1 (Rennie et al., 2021), which will be discussed in more detail later in this chapter.

First, other bias components will be discussed, which are shown in Figure 86. Usually the atmospheric winds measured on a moving platform (e.g. satellite, aircraft) are derived from the difference between the Doppler frequency shift of the atmospheric winds and the shift induced by the moving platform onto the laser LOS. Although the ALADIN LOS is oriented perpendicular to the satellite motion on ground in order to nullify the induced Doppler frequency shift from the satellite ground speed, which is about 7.6 km/s, and the rotation of the Earth with a maximum of 465 m/s at the equator, which is compensated by a yaw-steering of the satellite. Nevertheless, remaining satellite-induced speeds on the ALADIN LOS on the order of 1 m/s were expected (e.g. due to mis-pointing, or slowly varying thermal mis-alignment) and corrected in the ground processing by using the satellite-induced speed on the LOS derived from the on-board satellite AOCS (Attitude and Orbit Control System). An example of this reported satellite LOS speed (blue dots), its harmonic fit (red line) and the corrected values (orange) is shown in Figure 86 (upper right). However, after checking the difference of the Aeolus winds to the ECMWF model, it was found that this single harmonic bias variation along the orbit was not present. Hence, the correction with the satellite-induced Doppler frequency shifts for the Mie and Rayleigh winds was de-activated in 2019. Further investigations revealed that the derived satellite LOS speed is wrong, which was caused by an on-board software error for the derivation of this parameter. A workaround in the L1A ground processing was implemented in baseline 11 (activated on 8 October 2020) to correct for this on-board error, but still no benefit from applying the correction could be found in the L2B wind O-B statistics.

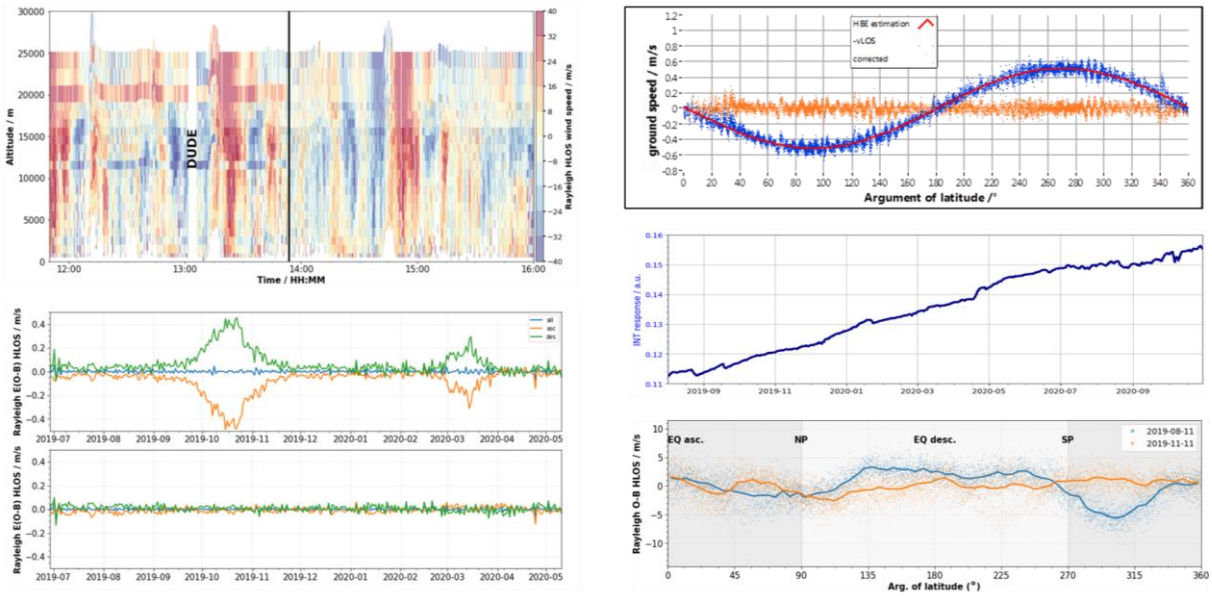

Figure 86: Summary of unexpected wind bias sources encountered after the Aeolus launch: hot-pixel-induced Rayleigh wind bias for selected range gates before and after correction with the DUDE (top left from Weiler et al. 2021); seasonal Rayleigh wind bias in March and October before and after correction (bottom left); satellite velocity LOS bias (top right); linear drift of Rayleigh internal reference response resulting in linear drift of the Rayleigh wind bias (middle right); Rayleigh bias as a function of orbital phase (arg. latitude) induced by temperature variations of the primary mirror M1.

Secondly a slow drift of a constant bias for both Rayleigh and Mie winds was observed. Those biases were different for Rayleigh and Mie winds and could exceed 10 m/s. In principle, such constant and slowly varying biases could be compensated by using a weekly response calibration performed in nadir pointing – so called IRC (Instrument Response Calibration, see chapter 3.5) or by using ground return velocities as zero-wind reference. It turned out that neither the IRC calibration nor the ground returns could correct for this slowly varying bias completely – so a residual constant bias remained. Thus, it was decided to add this constant component to the bias correction for the L2B together with the M1-

temperature-induced component and correct it with global, daily vertical averages over all altitudes, and averages along the orbit using the ECMWF model. The cause of this bias drift was mainly related to a drift in the internal reference for the Mie and Rayleigh channel, which was not only driven by laser frequency drifts but also affected by additional noise sources unique to the internal path (see also chapter 3.2). Usually, the measurements of the internal path of a Doppler wind lidar are used to correct the Doppler frequency shift for the outgoing laser frequency and its drifts. But the drifts of the internal path response (see Fig. Figure 86, middle right) could be related to drifts in the alignment of the spectrometers on the internal path with different alignment drifts on the atmospheric signal path. The figures show a response drift of the internal path for the Rayleigh channel from August 2019 to November 2020 of 0.04 Rayleigh response units corresponding to 80 MHz or 23 m/s HLOS (see also Figure 17).

Only after correction of the orbital bias variations correlated with the M1-temperatures, a remaining significant bias could be detected, but only for the months of October and March (Figure 86, bottom left). This figure depicts the Rayleigh bias from July 2019 to May 2020 for the orbital average (blue) and the average for the ascending (orange) and descending (green) path, showing a maximum bias of 0.4 m/s. It was found by an orbital analysis that this bias exhibits a harmonic behaviour as expected before launch, and was corrected by adding a harmonic component to the M1-bias correction. The lower figure illustrates that this bias can be completely corrected after this harmonic correction is applied. It is assumed that this bias was caused by a thermal effect present for these two months with the Aeolus satellite being in permanent twilight only during this period – it is an assumption, as no correlation of the bias with the temperature sensors on-board the satellite (e.g. close to the star tracker or ALADIN LOS) was found so far.

4.7.3 Geolocation error for longitude

Before discussing the M1-related wind bias in more detail, another unexpected bias in the geolocation (latitude, longitude, altitude) of all products (L1A, L1B, L2B) is presented in Figure 87.Geolocation errors could, in principle, also be visible as wind errors in case of horizontal and vertical wind gradients. An error of 0.075° in longitude was detected with the use of the ground-based Auger observatory for cosmic rays (Auger et al., 2024). This corresponds to a ground track error of 8 km at the equator (or 6.8 km at the geolocation of the Auger observatory) with the Aeolus ground track being too far to the West on descending orbits (orange dots compared to blue dots from Auger). This geolocation error could finally be traced back to an error in the L1A processor and the usage of ESA´s CFI (Customer Furnished Item) software tool for geolocation and LOS processing. It was corrected in the L1A processor version V7.12 as part of the baseline 14 (activated on 29 March 2022), showing a difference between Aeolus ground track (purple) and Auger (blue) of only 0.8 km after correction (inset in Figure 87), which is well within the mission requirements of 2 km for horizontal geolocation errors (95% confidence error definition).

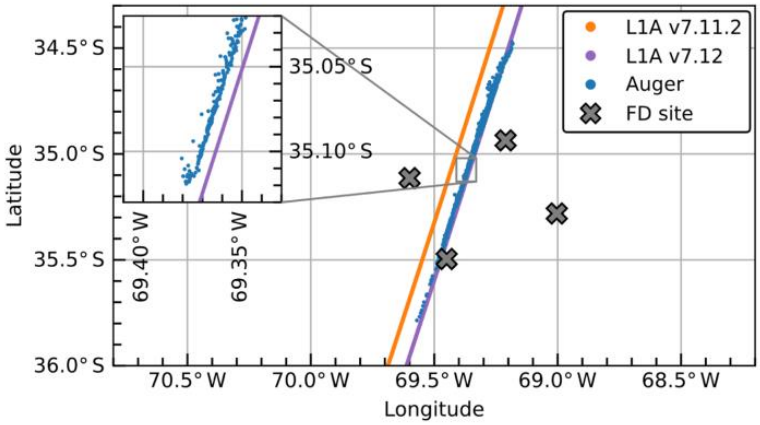

Figure 87: Comparison between the geolocation derived with different Aeolus data processor versions before (L1A v7.11.2, orange line) and after (L1A v7.12, purple line) the fix of the error and measurements by the Auger Observatory (blue dots) at 10 km altitude for the overpass on 17 July 2021. The offset amounts to 6.8 km between Auger and v7.11.2, and 0.8 km between Auger and v7.12 (Auger et al., 2024).

4.7.4 Wind bias caused by the primary mirror M1

Besides the hot-pixel-induced bias for single range gates, the other largest contributor to the wind bias (but also to the radiometric calibration for L2A products, see chapter 4.3) was showing a complex temporal behaviour. In contrast to a harmonic component with a dependency on the orbital phase (argument of latitude), which was expected before launch due to thermal distortions of the ALADIN instrument LOS, this bias additionally showed a strong dependency on both the argument of latitude and longitude. Thus, the bias was also varying over successive orbits, although it was soon recognized that these variations were not of random nature. Instead, the wind bias was found to be correlated with instrument parameters and showed a recurring pattern from week to week, i.e. it was nearly reproduced for successive repeat cycles of the satellite's geolocation. The amplitude of the Rayleigh-clear HLOS wind bias reached up to 8 m/s.

In August-September 2019, it was discovered at ECMWF (Rennie et al., 2021) that those wind biases were strongly correlated with the temperatures of the primary mirror (M1) of the ALADIN telescope, more specifically the M1 temperature gradients. In particular, there was a striking linear dependency of the bias as a function of the temperature difference from the outer part to the centre of the telescope (Figure 88). This finding paved not only the way for an instrument-based correction of this bias, but also revealed its root cause. The telescope temperatures and their gradients were affected by the top of atmosphere (TOA) radiation from Earth, both short- (reflected solar) and long-wave (infrared IR), and the mirror's thermal control mechanism, which aimed to stabilise its temperature at around 12°C. This heating and cooling of the primary mirror surface by the TOA radiation resulted in a thermal-mechanical deformation of the telescope mirror – although the M1 mirror was actively temperature controlled by several heating lines. This thermal-mechanical deformation led to a change in the optical focus within the instrument and an optical deformation of the illumination of the instrument spectrometers, which were both very sensitive to variations in the incidence angle and divergence of the illuminating beam. This resulted in changes of the spectrometer response and a resulting error in the retrieved winds. Since the M1 mirror temperature gradients varied seasonally, the bias showed seasonally varying magnitudes, peaking in the Northern Hemisphere summer. Biases for the Mie winds also showed some dependency on the M1 temperature gradients, but by a factor 10 smaller than the Rayleigh channel and with the opposite sign. The sensitivity for the Rayleigh winds was particularly large, at ~47 m/s HLOS wind per K change in M1 temperature gradient.

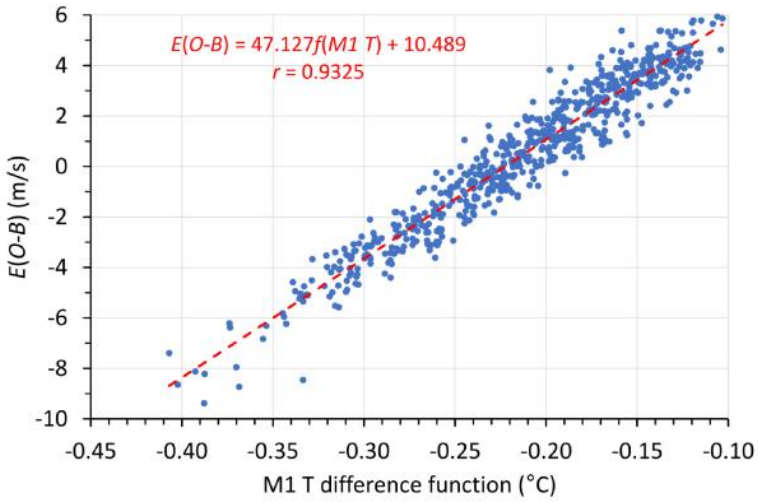

Figure 88: Aeolus L2B Rayleigh-clear HLOS wind bias *E*(*O–B*) (m·s^{-1}) as a function of a M1 mirror temperature function (in this example the mean outer temperatures minus mean centre temperatures) using all the data available on 8 August 2019. Each data point is derived from a 2 min sample mean, over all altitudes. The dashed line is the linear fit and the coefficients (gradient and intercept) are written in the chart, as is the Pearson correlation coefficient *r* (from Rennie et al., 2021).

More details about this correlation and its correction are discussed in the paper by Rennie et al. (2021), Weiler et al. (2021) and in the following figures. Figure 89 shows Hovmöller diagrams (latitude vs. time) of the mean M1 temperature (top), the radial temperature difference (outer minus centre T, middle), and the wind bias (O-B, bottom). The strong correlation of the patterns for the radial temperature gradient and the wind bias is seen in these plots, but also the strong seasonal variation of the bias patterns. The mean M1 temperatures from 11.7°C to 12.1°C, which was actively stabilized by heaters, shows a correlation with the TOA temperature with higher temperatures on the summer poles, which are illuminated by the sun (e.g. North Pole around +90° latitude in June-July 2019), and the colder M1-temperatures around the Inter Tropical Convergence Zone (ITCZ) with cold TOA temperatures from high clouds around the equator. A slight difference in the position of the temperature minimum (blue) is seen when comparing the plots for the ascending (left) and descending (right) orbital nodes due to the reaction times of the M1 mirror with its thermal inertia and reaction time of the active control loop after passing the ITCZ. The temperature gradients range from -0.32°C to -0.08°C, indicating that the centre part of the mirror is warmer than the outer part of the mirror. The temperature gradients as well as the wind biases are different for the ascending and descending nodes, demonstrating that the wind bias needs to be analysed separately for those orbit parts. In case one would analyse orbital means of the bias, those different biases for ascending and descending orbits could compensate or nullify each other. Although the changes in the radial temperature gradient were only on the order of a few 0.1°C, these changes resulted in a large variation of the Rayleigh wind bias of up to 8 m/s; the sensitivity of the Mie wind bias to this temperature gradient variations are a factor of about 10 lower (and not shown here).

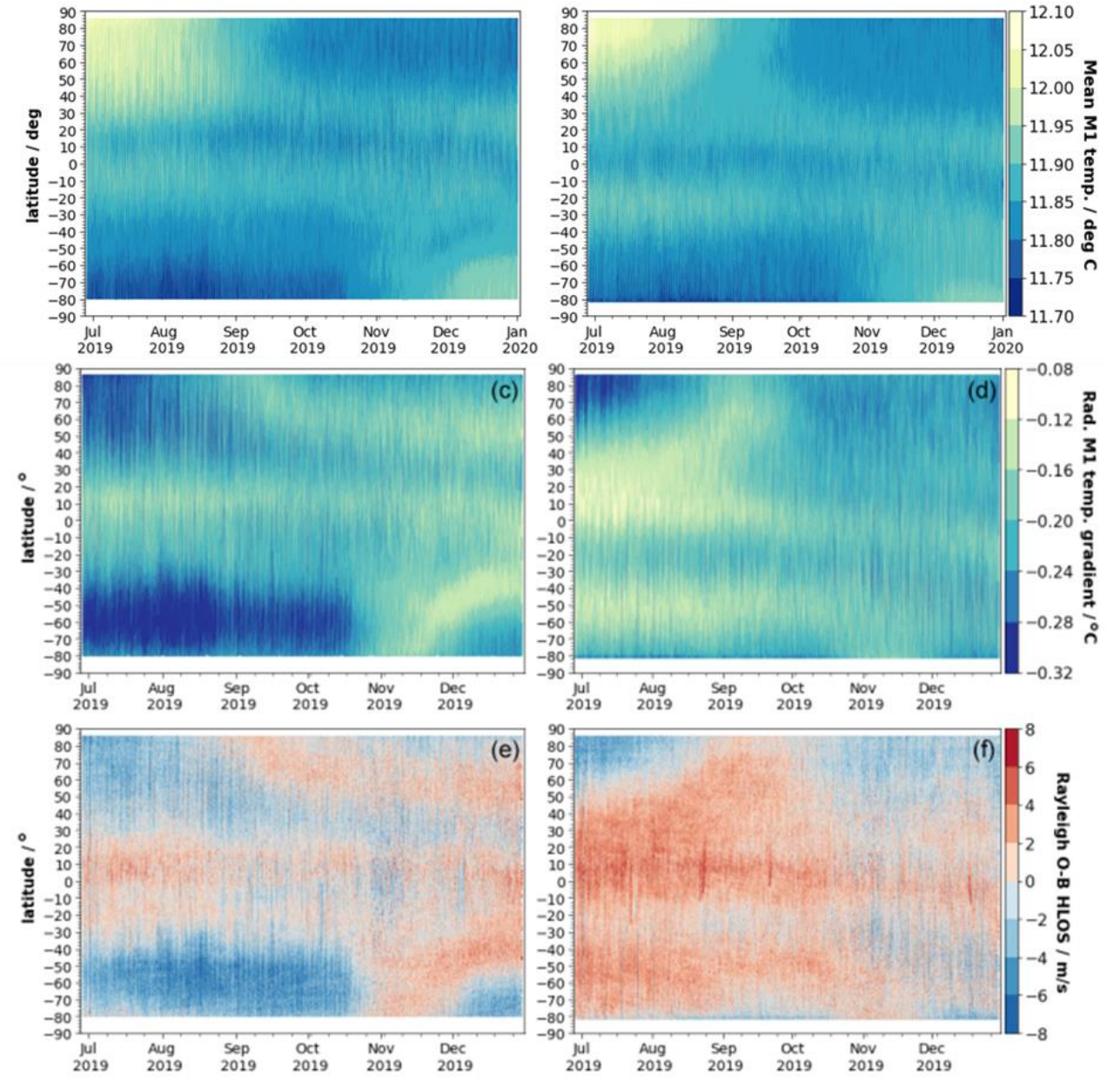

Figure 89: Hovmöller diagrams of the average over all M1 temperatures (a, b), the radial temperature gradient of the M1 telescope (c, d) and the Rayleigh clear *E.O - B/* HLOS values (e, f) from 28 June to 31 December 2019 split up into ascending (a, c, e) and descending (b, d, f) orbit phases (adapted from Weiler et al., 2021 with changes in figures a) and b).

The seasonal variation of the Rayleigh wind biases along the orbit and for different longitudes (colour-coded) is shown in Figure 90. Since the M1 mirror temperature gradients varied seasonally, the same was true for the bias magnitude, peaking in the Northern Hemisphere summer.

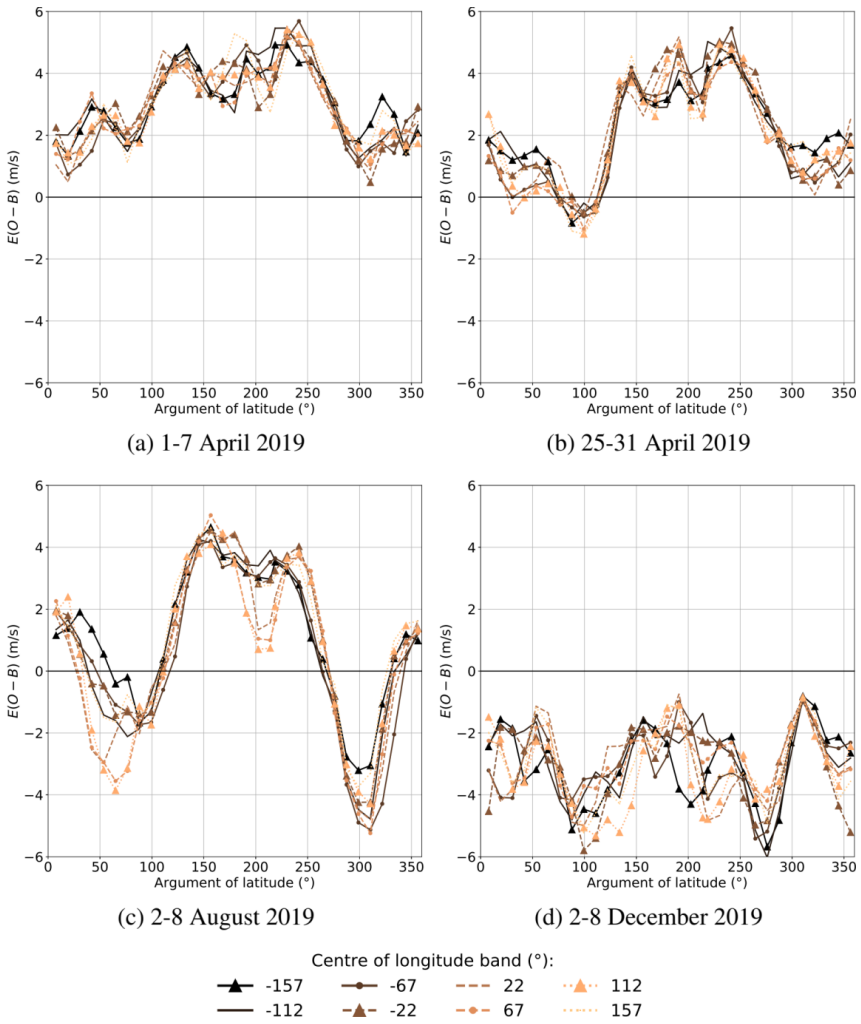

Figure 90: Rayleigh-clear bias ($E(O-B)$) without M1 temperature correction, binned by argument of latitude (orbit phase angle with the equator at 0°and 180°, the North and South Pole at 90° resp. 270°) and longitude for a) 1-7 April 2019 (FM-A) b) 25-31 April 2019 (FM-A) c) 2-8 August 2019 (FM-B) and d) 2-8 December 2019 (FM-B). There are 32 argument of latitude bins (11.25° wide) and eight longitude bins (45° wide). The argument of latitude and longitude bins are referenced by the value at the centre of the bin.

An operational correction was developed by the DISC and implemented as part of the L2B processing at ECMWF with baseline 09 in April 2020. It is based on a multiple-linear regression (MLR) model using the 15 temperature sensors of the M1 mirror, the uncorrected Aeolus Rayleigh and Mie observations (O) and the ECMWF model values (B) from a 24-hour period for all altitudes and geolocations of Aeolus observations to determine a set of 15 regression parameters β (Figure 91). Those regression parameters (as part of the so-called AUX_TEL file) are then used in the following 12 hours in combination with the actual M1 temperatures to correct each Rayleigh and Mie observations for this bias. It should be noted here, that the ECMWF model winds are only used to obtain the regression parameters β, but not for the actual correction. For the NRT correction the regression is performed using (O–B) values from the preceding 24-hour period, while for the re-processing of Aeolus products the regression can be performed using the same 24-h period for both regression and correction. This approach with using regression parameters with the AUX-TEL file is not only used for the M1-T induced bias, but also for the correction of the constant drifts and seasonal harmonic biases occurring in March and October mentioned above.

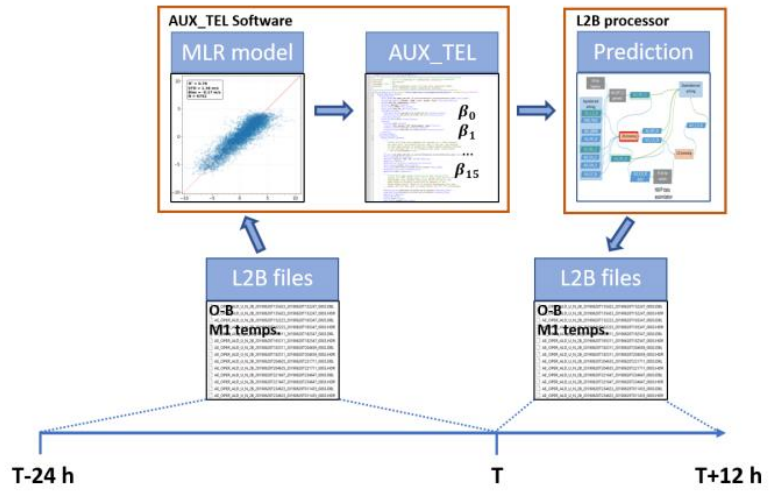

Figure 91: Flow chart of the operational M1 bias correction of the L2B wind results. In the AUX_TEL software, 24 h of past L2B data with the *E*(*O–B*) values as dependent and the 15 M1 temperatures as independent variables are used as input for the multiple linear regression (MLR) model. The model software produces an AUX_TEL file which contains the model coefficients $\beta_0 \cdots \beta_{15}$. Afterwards, the L2B processor uses the AUX_TEL files to make a prediction for the wind bias and to correct the wind results of the subsequent 12 h window. Then, the AUX_TEL file is updated in the same way. (from Weiler et al., 2021).

The quality of the bias correction is shown in Figure 92 for a period of 1 day, where the blue dots/line show the uncorrected Rayleigh wind bias varying with time (top) and along the orbit (bottom) within ±5 m/s HLOS. The wind bias after applying the bias correction is well below ±1 m/s HLOS (blue dots/lines).

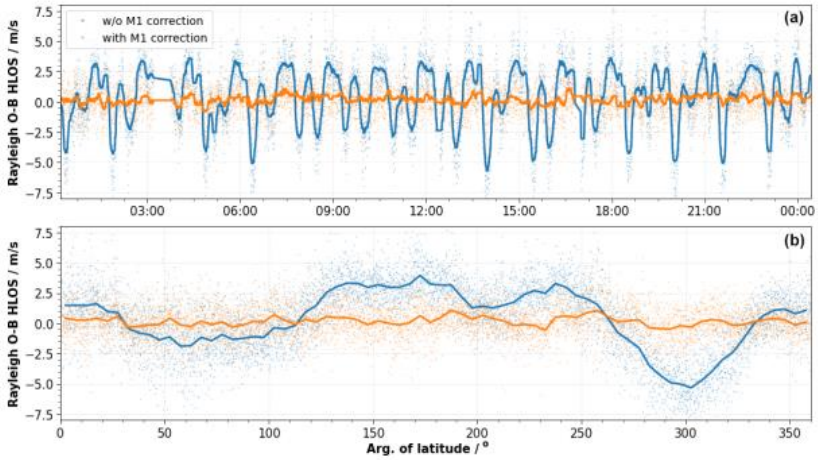

Figure 92: Rayleigh clear *E*(*O–B*) HLOS values as a function of time (a) and the argument of latitude (b) during 12 August 2019. The blue and the orange dots indicate the bias without and with M1 bias correction, respectively. The blue and the orange lines show temporal (5 min interval) and binned (5° bin size for the argument of latitude) averages of the *E*(*O–B*) values, respectively. The M1 bias correction coefficients are derived from data from 11 August 2019 (from Weiler et al., 2021).

An alternative M1-T bias correction method using the velocity of the Mie and Rayleigh ground returns instead of model wind information was also investigated (Weiler et al., 2021) and further refinements afterwards. In principle, a similar approach for the M1-T correlation to wind biases from (O–B) statistics can be established using ground returns instead of model backgrounds B. It could be demonstrated that the precision of this correction using ground returns is about 10-20% worse than using (O–B) statistics, which is a reasonably good performance. The largest issues so far with a ground-return-based correction is its strong variability in performance from day to day and its dependency on the atmospheric path signal levels and SNR. But the performance is also varying seasonally, which is mainly depending on the

availability of ground returns with high SNR from high albedo surfaces in the UV (ice, snow and to some extent desert) which is limited to few short sections along the orbit.

Most of the unexpected wind bias causes could be identified and corrected for NRT processing for Aeolus already within the first two years of the mission. Some known remaining biases are mainly related to an altitude-dependent Rayleigh wind bias (up to ±1 m/s), which is most probably related to the altitude-dependent atmospheric temperature profile in combination with an imperfect response calibration. Other bias causes are related to errors or imperfections in the corrections itself, e.g. response calibrations, Mie non-linearity correction, Rayleigh-cloudy winds (see chapter 4.6.2) and the dark current fluctuations on hot pixels between DUDE measurements. There are also sporadic biases affecting Mie and Rayleigh winds due to mis-pointing associated with moon-blinding of the star-tracker and the switch to inertial navigation system for short periods of affected orbits. This causes biases of up to 4 m/s (see also regular vertical stripes in the Tropics in Figure 89 (f) for descending orbits), however this is mitigated by flagging the L2B winds invalid during moon-blinding periods (and will use a combined moon-blinding and mean(O-B) check in B17 reprocessing to reduce wasting good data). Also, an expected bias due to Mie contamination with small scattering ratios is not applied so far for Rayleigh-clear winds, as it only adds additional noise to the observations probably arising from the noise in the scattering ratio determination. In addition, 2 Rayleigh hot pixels showed an anomalous behaviour starting in June and December 2022, most likely due to strong cosmic particle event with a permanent damage of these pixels and wind bias in the corresponding Rayleigh range gates #13 and #16 which cannot be corrected with the DUDE approach.

4.7.5 Lessons Learnt from product bias identification, investigation and correction

- "Expect the unexpected" especially for the instrument performance wrt. systematic errors; Try to be prepared for the unexpected and question all assumptions made before launch wrt. characteristic, cause and correction of systematic errors.
- Biases could occur only during some periods of the year due to different illumination of the satellite and the resulting thermal conditions (e.g. eclipse phases or satellite in permanent twilight). This makes an identification even more time-consuming as for other bias causes, as one usually would need to wait for another occurrence (e.g. separated by 1 year) for a confirmation of the bias.
- Horizontal and vertical geolocation errors could show up as errors in the retrieved parameters (e.g. wind or optical properties) in case of horizontal and vertical gradients of this parameter.
- NWP monitoring is mandatory to identify, characterize and potentially correct bias swiftly; validation campaigns with reference instruments are needed to support, confirm and refine the findings from NWP monitoring with higher accuracy and spatial resolution.
- Separate biases for ascending and descending orbits could occur. If this is the case, they could compensate or cancel each other, especially for parameters with positive/negative sign (e.g. LOS winds), but not limited to those. Thus, bias behaviour needs to be analysed separately for ascending and descending orbits.
- Biases of smaller magnitude can be identified, once biases of larger magnitude are corrected – so bias correction is a step-by-step approach; timing and duration is then also depending on the update cycle of the processor baselines. For Aeolus, it took about 1.5 years after launch to identify and correct for major bias sources (hot pixels, slow drifts, M1-T induced biases), thereby effectively extending the commissioning phase E1. It is unlikely to assume that unexpected bias causes could be identified and corrected during phase E1.

- In order to identify and correct for unknown biases of a mission, expertise is needed covering all aspects from a mission from instrumented related topics even for sub-units, such as detectors or telescopes, satellite related topics (AOCS, thermal behaviour), hands-on the complete chain of algorithm and processors from L1A, L1B to L2A, L2A, and observation monitoring with NWP models. This expertise should be combined in a DISC consortium involving several partners to cover these topics.

4.8 Aeolus Calibration and Monitoring Facility (ACMF) and Codadef

Arie Kuijt and Filippo Tagliacarne, S&T

4.8.1 Introduction

S&T has developed the Monitoring and Control part of the Aeolus Calibration and Monitoring Facility. with ABB. ACMF has a central role in the frame of Aeolus PDGS Surveillance Facility (APSF) configuration (Figure 93), being the entering point for most Auxiliary files needed for the data production.

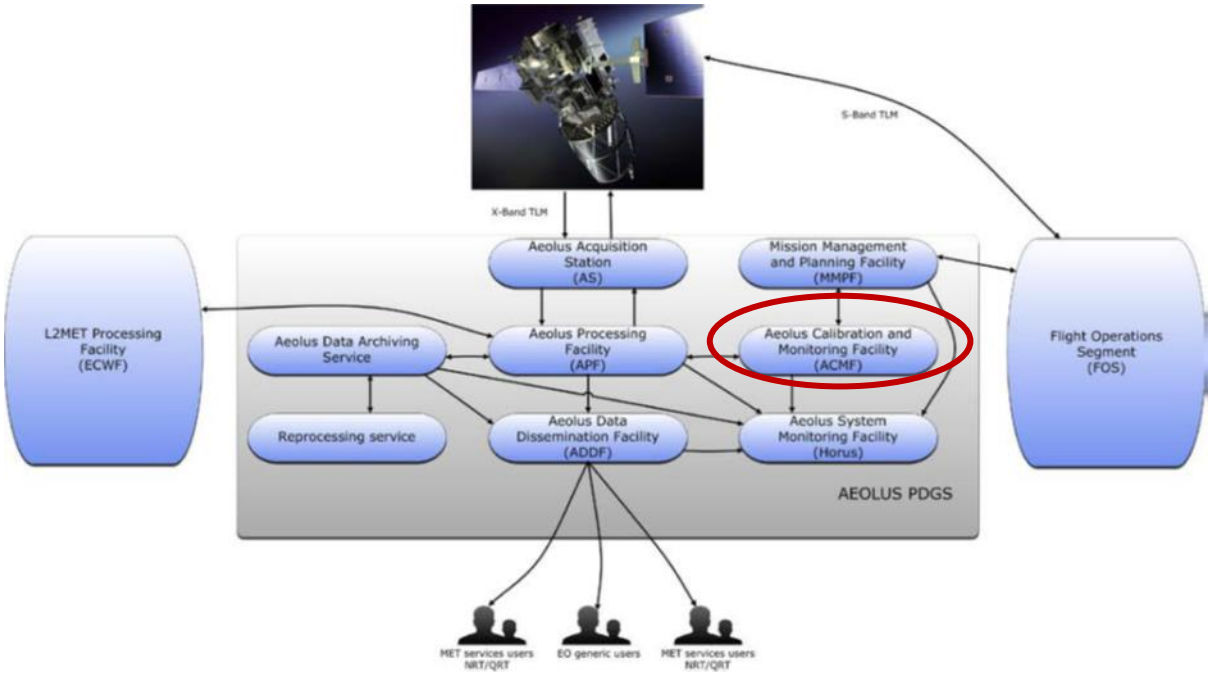

Figure 93: Aeolus ACMF (Red ellipse) within the Payload Data Ground Segment (PDGS).

4.8.2 ACMF

This facility is responsible for calibration and Quality Control (QC) of products in the Aeolus Ground Segment. It has been built on the S&T Software-framework for calibration and monitoring facilities. The framework uses QUADAS, STDB, TaskScheduler and Muninn (see Table 14) with QUADAS being the main element, although for Aeolus S&T already started to move away from that for the reporting (see Addition of Python Report Generator below). The framework uses the Aeolus specific configuration of the S&T APPROVE application (QCF) for basic quality control, and QUADAS for advanced calibration analysis, QC, and interactive analysis. APPROVE is an application on top of CODA that can perform format checks and internal consistency checks (including parameter range checks). It runs as a processor and produces an XML report with an overview of the warnings and errors. A Task scheduler component is used for overall system monitoring, control, and automatic execution of various QC tasks

The ACMF is responsible for the generation of calibration auxiliary files for the Aeolus PDGS and for providing a data analysis and monitoring environment. Furthermore, it provides important input to DISC activities and a dedicated team within the DISC directly interfaces with the ACMF, including product anomaly investigations performed interactively on an ACMF subsystem.

The ACMF roles with the Aeolus PDGS are composed of the following main tasks:

- Processing of in-flight calibration data and generation of updated processing auxiliary calibration data and delivery of those to the Aeolus PDGS, particularly to the Aeolus Processing Facility (APF) and L2/MetPF for subsequent processing.
- Computation of updated instrument control tables and their delivery to the Mission Management and Planning Facility (MMPF) for subsequent mission planning files update.
- Reprocessing of auxiliary calibration data and delivery of those to APF for reprocessing purposes.
- Long-term data analysis and data monitoring.
- First line Investigation of instrument anomalies (if based on Level 0/1A/1B products analysis).
- Delivery of activity reports to the Aeolus PDGS Surveillance Facility (APSF) for system monitoring

The ACMF is the component of the Aeolus PDGS that

- Generates all required auxiliary data for Aeolus processing,
- Delivers all auxiliary data for processing performed in the APF,
- Generates and delivers payload on-board settings resulting from in-flight characterization
- Monitors the quality of all Aeolus data products (systematically and interactively).

The ACMF consists of both hardware and software to perform these functions, and it interfaces to other components in the Aeolus PDGS by receiving and sending data products, reports, and other files through a network connection. The ACMF can perform various L0, L1 and L2 calibration and monitoring activities simultaneously. Examples of such activities are:

- Executing calibration algorithms, validating the resulting calibration output data, and disseminating these results to people and other facilities as Auxiliary Data Files.
- Analysing the data contents of a data product, storing analysis results, and producing a HTML-report about data quality.
- Extraction of data from an Aeolus data product for long term quality monitoring purposes (for example for monthly analysis of trends)
- Starting an interactive session for the user, such that the user can:
    - Read Aeolus data from data products or the ACMF databases.
    - Analyze the data, and plot or store the results.
    - Interactively “walk through” the data using plots.
    - Execute Quality Processing Algorithms (QPAs) which perform specific quality checks on data.
    - Generate reports containing results of quality monitoring.
- Providing an overview of all the activities that are currently going on.

ACMF consists of the subsystems/modules listed and described in Table 14, while Figure 100 shows the ACMF subsystems and interactions.

Table 14: ACMF subsystems/modules descriptions.

ACMF-A	The Data Analysis Subsystem (ACMF-A), performs interactive and systematic analysis on product screening and calibration outputs and on individual products. It is built on the QUADAS application for quality monitoring. ACMF-A is no longer used in Aeolus Phase E. Given the need of a tool more flexible than QUADAS to generate plots, tables and statistics and without dependency on IDL, S&T has created and provided the Python Report Generator.
ACMF-C	The Calibration Subsystem (ACMF-C) implements the Aeolus calibration algorithms as a series of processors and generates calibration auxiliary data files and on-board instrument and platform settings from input products and auxiliary data, which is provided by ABB.
ACMF-D	The Data Storage Subsystem (ACMF-D) stores extracted quality and performance parameters, auxiliary data, and configuration information. The ACMF-D mainly consists of a file archive on a file server, with supporting utilities for maintenance.
ACMF-M	The Configuration Management Subsystem (ACMF-M) is the driving engine of the ACMF. It can execute any of the other modules by data driven, time driven, user driven or event driven triggers. Without the ACMF-M no activity would take place unless a user would start it by hand. The ACMF-M disseminates calibration and processor configuration auxiliary data files, ensures consistency, and maintains traceability. In addition, it ensures that the configuration of the ACMF-C, P, D and A subsystems is consistent within the ACMF, and within the PDGS. Finally, it configures and manages inputs and outputs of the ACMF-C calibration processors and the L1B processor.
ACMF-P	The Product Screening Subsystem (ACMF-P), performs systematic product inspection integrated into the quality control environment, outside the core PDGS. It is implemented using the QUADAS application for quality monitoring.
QCF	Module integrated into the core PDGS performing rudimentary screening of products immediately after production by the processing facilities in the APF and ADAS. The QCF is also used internally in the ACMF (facility) to screen generated Auxiliary Data Files. QCF has two modi operandi (IPF processor and standalone executable) and performs three types of QC-checks on a product, that are at least partly defined in the AUX_PAR_QC parameter file: • A standard consistency check of the product and a read of all data. • A standard consistency check across data block and header files. • Configurable product specific tests by using tests defined in a Test Definition File.
Data access	The Data Access subsystem provides a single Application Programming Interface (API) to the other subsystems for reading data from Aeolus data products, as well as related data files. Data access is implemented using the CODA-library for data access.
QUADAS	QUADAS is an application built on IDL and additional C-functions, which provides UI functionality, Plot functionality, Reporting Functionality and Analysis functionality. The ACMF-P and ACMF-A are in fact QUADAS sessions that are started with a specific configuration. The QUADAS system is a high-performance quality analysis system that automates the routine analysis procedures and supports the in-depth manual investigation of the quality of the data products. Furthermore, the generic architecture of the QUADAS system allows for the easy incorporation of new quality control functionality, or adaptation of existing functionality.
Muninn	Muninn is a tool developed by S&T used to manage data products. This allows the user to archive products and retrieve them according any parameter set either (a) by default (such as names, validity date, etc.), (b) by the user. This tool is available both as a command line interface (CLI) or as a python Library making it very easy to incorporate in a workflow.

TaskScheduler	The task scheduler is a tool developed by S&T, which, in its basic form, allows a user to schedule tasks to be executed. These tasks can be anything, as the tool runs code in a shell environment. These tasks can either be executed at a specific time (time-driven task) e.g. every 10 minutes, or when data is available (data-driven task) e.g. when a product is present in folder X, use that file to execute the task. One such use for this data-driven task is to ingest a product in Muninn (see above) whenever a data product is available in a pickup directory. Muninn can them make the product available such that other tasks can be executed using the newly ingested product.
STDB	Storage of data in the Scientific Temporal Data Base (STDB) is performed through the ACMF-P screening function on the ACMF-OS (ACMF Operational Screening Facility, see below). Data to be stored by files that run through the ACMF-P can be configured. When screening or validating a file, the ACMF-P uses information in this configuration file to retrieve data. Furthermore, the ACMF-OS uses this configuration file for retrieving information for the daily report.

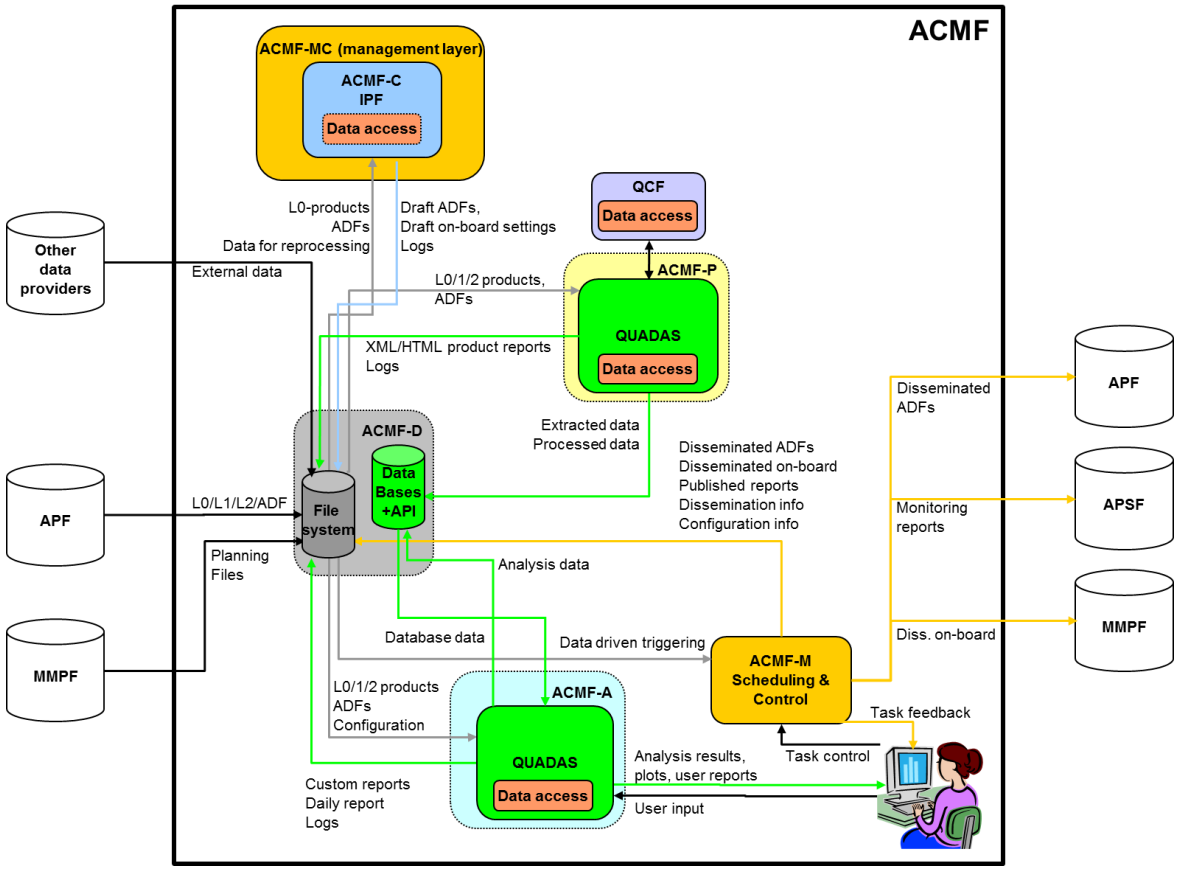

Figure 94: ACMF subsystems and interactions.

ACMF is implemented using three servers and a storage component (Figure 95).

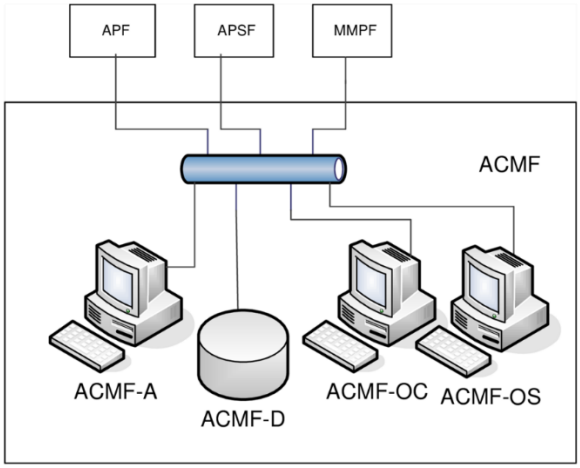

Figure 95: ACMF Server configuration.

ACMF elements include:

1. *The ACMF Operational Calibration Facility (ACMF-OC)*

   The ACMF-OC is the main control platform of the ACMF, and hosts a task-scheduler and Graphical User Interface for controlling all primary tasks.

   The ACMF-OC platform is a server platform that hosts the operational autonomous calibration part of the ACMF. This component controls processing, reprocessing and product generation. It consists of the calibration subsystem (ACMF-C + L1B processors), the configuration management subsystem (ACMF-M), the QCF as a standalone application for partial validation of produced ADFs.

1. *The ACMF Operational Screening Facility (ACMF-OS)*

   The ACMF-OS is an autonomous platform of the ACMF. It hosts a task-scheduler and Graphical User Interface for controlling screening tasks. In normal operation users do not require to monitor.

   The ACMF-OS platform is a server platform that hosts the operational screening functions of the ACMF. It consists of the ACMF-P subsystem in charge of inspecting products quality after production from the processing facility, the configuration management subsystem (ACMF-M) without the calibration part ACMF-MC, and the QCF as a standalone application that is used for part of the product screening.

2. *The ACMF Analysis Facility (ACMF-A) (- no longer used in Aeolus Phase E -)*

   The ACMF-A was used to further investigate data anomalies in terms of plots and statistics and is an analysis workstation which hosts the ACMF-A data analysis subsystem and is run interactively by the user. ACMF-A is no longer used in Aeolus Phase E.

   S&T has created the Python Report Generator to provide a more flexible tool to generate plots, tables and statistics.

4.8.3 Codadef

Codadef is an atmospheric toolbox aspect of CODA (Common Data Access toolbox) created by S&T, which describes data formats. Since the Aeolus data products are in a custom binary format, CODA is currently the primary software for accessing Aeolus data for all end users. The available data covers the following product levels: L0, L1A, L1B, L2A, L2B, L2C and all auxiliary products. Any format update will require work from S&T to allow end users to work with this update.

Codadef links:

- Aeolus Definitions for products and types: https://github.com/stcorp/codadef-aeolus
- Aeolus Release overview: https://github.com/stcorp/codadef-aeolus/releases
- CODA Documentation: https://stcorp.github.io/coda/doc/html/index.html

4.8.4 Maintenance activities performed during Aeolus Phase E

S&T has executed of the following maintenance activities on the ACMF:

- Evolutions, Maintenance (corrective, perfective), Anomaly investigation, resolution, validation, acceptance, and delivery, software Configuration Management.
- Creation of the Python Report Generator
  - The ACMF report generator relied on the commercial IDL package but its programming interface is too complex to maintain in comparison to Python.
  - The report generation tool (Figure 96) enables users to generate L1b reports, identical to these generated with the existing IDL code, for data analysis and inspection. Furthermore, a new daily and a weekly report were added. The outputs are in HTML, docx and PDF. The report generator functions independently from the existing ACMF modules.

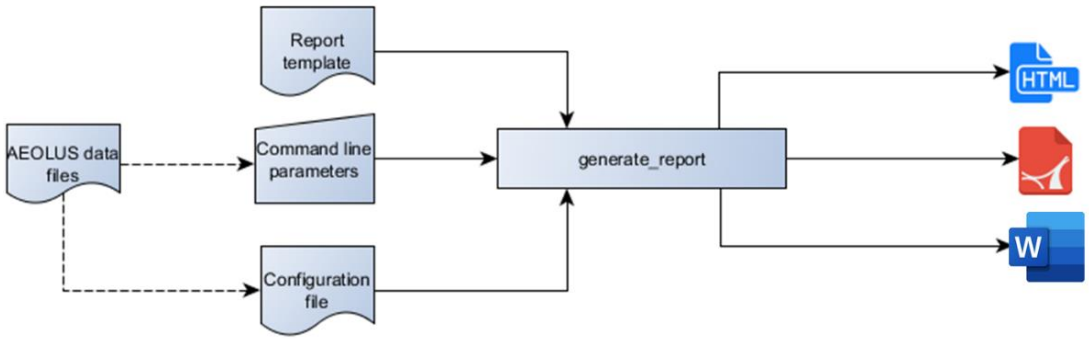

Figure 96: Diagram of the report generator module.

The first delivery in phase E was ACMF v 4.1.0. and QCF version 4.02. After that, deliveries were provided every 6 months totalling up to 8 full releases and 3 patch releases. The latest software and documentation versions delivered are:

- ACMF: 4.8.0
- QCF: 4.09 (patch version),
- ACMF-ST-processor-evolution-document: 1.3
- Software Release Note: 1.04
- Software Installation Manual: 1.02
- Test Plan: 1.04
- Test Report: 1.06

Three version releases and three path releases were delivered for the Python Report Generator. The latest software and documentation versions are:

- Python Report Generator: 1.02

- Software Release Note: 1.02
- Report Generator Validation Report: 1.1

Lessons learnt

- Users found QUADAS not flexible enough to generate plots, tables and statistics and due to its dependence on IDL. Within Aeolus Phase E, S&T has created the Python Report Generator for this purpose. In the meantime, S&T is working on a framework that replaces IDL with Python in all its applications.
- The entire testing procedure on S&T side could have been improved for ACMF software delivery. Testing is done manual now (start, monitor, check outcome), but automating these activities would improve continuous integration, repeatability, stability, and reporting.

4.9 ACMF Calibration Processors

Gaetan Perron, ABB Canada

4.9.1 Introduction

The goal of the project was the maintenance and evolution of the Aeolus Calibration and Monitoring Facility calibration processors (ACMF-C). The processor evolution started from ACMF-C version 4.03 delivered at the end of phase D on a previous contract. The calibration processors include the calibration suite from Météo-France and the HBE (Harmonic Bias Estimator) from DLR. ABB was in charge of the implementation into the operational calibration processors

Several ACMF-C versions 4.04 to 4.07 were delivered, accepted, and successfully integrated into the Aeolus payload data ground segment. Several test campaigns were performed in the ground segment operational environment. However, due to the unexpected behaviour of the ALADIN instrument, an automated calibration approach as foreseen with the ACMF-C had to be abandoned leading to a descope this activity.

4.9.2 The ACMF and ACMF-C interfaces and functionalities

The ACMF (see Figure 97) is part of the Aeolus Payload Data Ground Segment (PDGS). Through a file exchange interface, it is linked to the Aeolus Processing Facility (APF), the Aeolus PDGS Surveillance Facility (APSF) and the Mission Management and Planning Facility (MMPF).

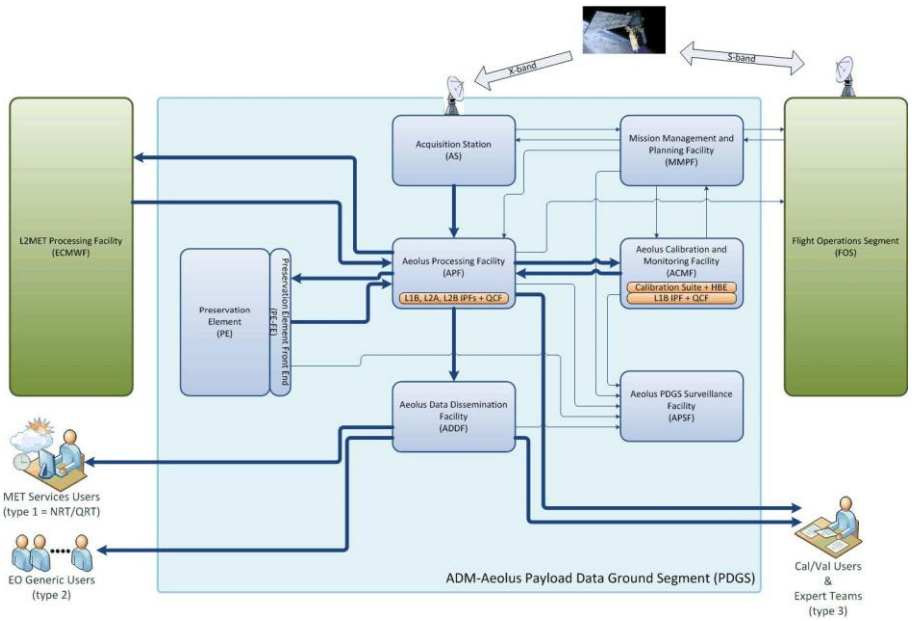

Figure 97: ACMF Overview within PDGS.

The ACMF supports the APF in Level 1B, Level 2A and Level 2B data production by means of instrument auxiliary calibration data generation, configuration management, as well as data dissemination and takes care of the automatic as well as on-demand data monitoring. Finally, it performs quality control and reports to the APSF all the information needed to identify potential anomalies in the PDGS workflow and data orchestration, actively participating in increasing the PDGS reliability. The ACMF offers an on demand data analysis environment able to access the full mission data archive. The facility is composed of two main subsystems associated to its high level functionalities: The calibration and the monitoring/analysis subsystems.

The ACMF-C calibration subsystem is in charge of the generation of the auxiliary calibration products and payload on-board parameters. It is compatible to the ESA Generic Instrument Processing Facility guidelines allowing an easy integration of processors. The subsystem provides routinely or on-demand sets of L1B calibration products as results of processing data from the associated satellite calibration operation mode.

The routine calibrations are the Instrument Defocus Characterization (AUX_IDC_1B), the Mie and Rayleigh Response Calibration (AUX_MRC_1B and AUX_ RRC_1B) and the Zero Wind Calibration (AUX_ZWC_1B). The on-demand calibrations are the Internal Spectral Registration (AUX_ISR_1B), the Dark Current Calibration (AUX_DCC_1B), the Dark Current in Memory Zone (AUX_DMCZ1B), the Instrument Auto Test (AUX_IAT_1B), the Off-line Wind Velocity (AUX_OWV_1B) and the Laser Beam Monitoring (AUX_LBM_1B).

Four additional processors part of ACMF-C generate calibration data products supporting the Level 1B, Level 2A and Level 2B processing: The HBE providing the Harmonic Bias Estimator coefficients wrt orbital phase (AUX_HBE_1B); The CSR providing the Corrected Rayleigh spectrometers Spectral Registration (AUX_CSR_1B and AUX_PRR_1B); The RBC providing the info needed for the Rayleigh-Brillouin Correction scheme (AUX_RBC_L2); The CAL providing the Calibration function and constants for the processing of the "optical" data from ALADIN signal (AUX_CAL_L2).

The subsystem has been designed to support both Near Real Time (NRT) and reprocessing scenarios at the same time, allowing a safe handling of the two processing flows and prioritizing the NRT data production over the reprocessing one. Moreover, it supports a proper baseline and processors versions handling.

4.9.3 Development of the ACMF-C

The development of the delivered ACMF-C versions is given below;

ACMF-C version 4.04

The changes integrated in the version 4.04 include the updated coda definition to Aeolus-20190408.codadef and changes associated with the Calibration Suite version 4.1. Namely:

- CSR modification of the reflection of the Fizeau in the atmospheric path and two CSRs are now output one for the internal path and one for the atmospheric path.
- RBC_L2 uses of the double CSRs and no need to fit the ISR to compute the Rayleigh response.

ACMF-C version 4.05

The changes integrated in the version 4.05 include the updated coda definition Aeolus-20200129.codadef, changes associated HBE DLR Matlab prototype 2019 version 3 and with the Calibration Suite version 4.2 (with patch 1 and 2). Namely:

- HBE modification of the record screening method with validity control, weighting method and fitting method.
- CSR addition of internal CSR fit parameters in the output product.
- RBC_L2 TA and TB are now resampled in the intervals centred about the middle frequency.
- CAL_L2 computation of calibration product in frequency intervals centred about the middle frequency. Filtering of height-bins entering the computation of Kray and Kmie to discard bins below clouds/aerosol layers.

ACMF-C version 4.06

The changes integrated in the version 4.06 include the updated coda definition Aeolus-20200529.codadef, changes associated HBE DLR Matlab prototype 2020 version 1 and with the Calibration Suite version 4.4 (with patch 1). Namely:

- HBE in case of duplicate observations, use the later one. Possibility to use different Fourier Series Order for the Mie and the Rayleigh channel. Create a log file. Correct Validity_Start information format in output file as per codadef. Correct Validity_Stop and Sensing_Stop information.
- CSR possibility to derive delta frequency variable from the ground returns, computation of the maximum slope and offset error allowed between predicted and observed RRC.
- RBC_L2 shifting of the frequency axis so that the cross-point in now at 0 for TA and TB.
- CAL_L2 addition of ISR centre frequency in output product.

ACMF-C version 4.07

The changes integrated in the version 4.07 include the updated coda definition Aeolus-20200731.codadef and changes associated HBE DLR Matlab prototype 2020 version 2. Namely:

- HBE add processor version in output file and log file. Calculation of the Chi^2 implemented for the usage of the of the Weighted Arithmetic Mean. Report weights user in the log file.

4.10 Chain of operational processors and Sandbox

Oliver Reitebuch and Isabell Krisch, DLR

The Aeolus chain of operational processors includes all processing levels starting with the Annotated Instrument Source Packets (AISP) downlinked from the satellite or generated by the Aeolus End-to-End Simulator (E2S) to the Levels L0-L1A-L1B-L2A-L2B; the Level L2 processor is not included here, as it is not a stand-alone Aeolus processor, but the product is generated at ECMWF from the NWP model output IFS (Integrated Forecast System). The different processors strongly depend on each other and the code development needs to be carefully coordinated. A simplified sketch of the chain of processors is shown in Figure 98 below:

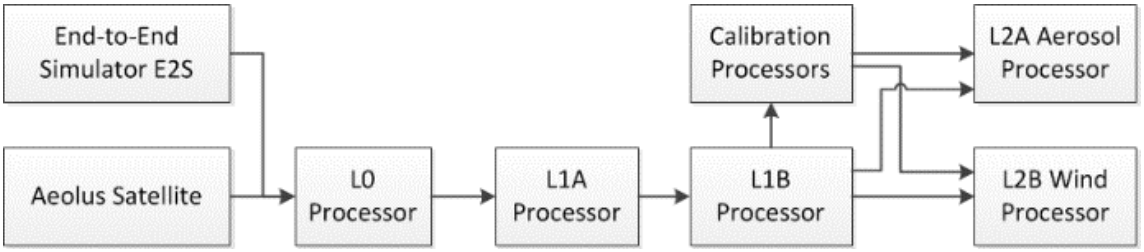

Figure 98: Aeolus chain of processors from the AISP data from the satellite or E2S to L0, L1, and L2 processor including the calibration processors running in the ACMF, the E2S, L0, L1A, L1B and L2A operational processors are under responsibility of D. Huber (DoRIT), the L2B operational processor by J. d Kloe (KNMI), the ACMF by S&T and ABB, and the processor and anomaly management by Serco.

The content of the different Aeolus data products is shown in Table 15 below:

Table 15: ALADIN data product content.

Product	Description
Level 0	Time-ordered source packet streams: measurement, housekeeping, platform, and AOCS (Attitude and Orbit Control System) data
Level 1A	Housekeeping source packet fully processed, AOCS source packets (geolocation) processed and assigned to measurement data, measurement data unprocessed.
Level 1B	Fully processed, calibrated and georeferenced measurement data including HLOS winds, viewing geometry, ground echo data and product confidence data (PCD)
Level 2A	Particle (aerosol/cloud) optical properties, as optical depth, extinction coefficient, co-polarized backscatter coefficient, lidar ratio and PCD.
Level 2B	L2B products represent corrected HLOS wind data and include calibrations using atmospheric pressure and temperature from ECMWF model, and bias corrections for winds (e.g. M1-T bias), measurements are grouped after a scene classification in Mie cloudy, Rayleigh clear and Rayleigh cloudy winds.
Level 2C	L2C products contains the L2B product and in addition two-component wind vector profiles on the location of the Aeolus ground track as obtained after the assimilation process of L2B products at ECMWF an NWP centre; thus, the L2C products mainly contain information from the NWP model

Throughout the Aeolus DISC in Phase E2, a staggered delivery schedule evolved, which takes these dependencies into account (see Figure 99). The first delivery in each round is a pre-delivery of the Aeolus end-to-end simulator (E2S). Output from this simulator is needed for the development of several prototype processors (PP). 4 weeks after the E2S pre-delivery, the HBE (Harmonic Bias Estimator) and CalSuite (Calibration Suite) prototype processors are delivered for implementation in the ACMF-C (Aeolus Calibration and Monitoring Facility - C) operational processor. Due to changes in the calibration concept and the wind bias correction without using the HBE, updates of the ACMF-C were only performed up to Baseline 12. Afterwards, this part of the operational processing chain was not further developed. 5 weeks after HBE and CalSuite PP delivery (or 9 weeks after the E2S pre-delivery), a first pre-delivery of the different L2A prototype processors takes place (SCA & MLE prototype, AEL-PRO & AEL-FM prototype), which is followed two weeks later by the final delivery of these prototypes. In between these two L2A PP deliveries, a pre-delivery of the L0/L1A/L1B processor takes place for first testing purpose and possibly adapting already the relevant format changes for product reading (e.g. with codadef files).

The final delivery of the L2A PPs includes updates related to changes in the L0/L1A/L1B processor (e.g. format changes of L1B products). These changes in the L1B products also need to be considered by the ACMF-C and L2B processors. The ACMF-C was delivered (up to B12) 5 weeks after the L0/L1A/L1B pre-delivery together with preliminary IODDs (Input Output Definition Documents) and example product for the L2A and L2B operational processors. These example products and IODDs were necessary to already start upgrading the ACMF-ST, QCF (Quality Control Facility within the ACMF) and codadef to the newest product formats. In this way, these processors can be delivered only one week after the final deliveries of the E2S, L0/L1A/L1B, L2A and L2B processors (7 weeks after the L0/L1A/L1B pre-delivery and 6 weeks after the L2A PP final delivery). The L0-L1A-L1B and the L2A operational processors were delivered from DoRIT to KNMI for integration and testing on the Sandbox together with the updated Auxiliary Files (AUX-Files). At the Sandbox the complete chain of processors up to L2B is tested.

Once all processors are available in their final version (after about 18 weeks), they are delivered to the DISC on-site team (DOS), where they are tested, compiled to executable files and packaged before they are handed on to PDGS. The validation and preparation of the processor software updates and baseline change at PDGS usually took 4-10 weeks.

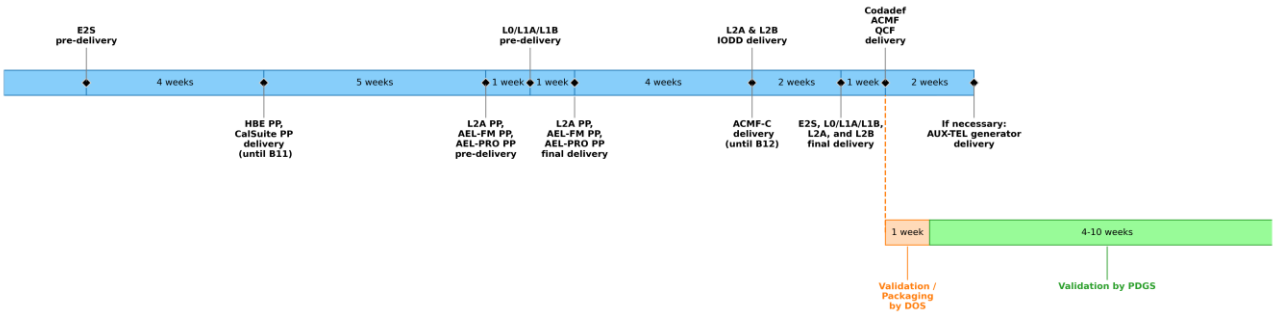

Figure 99: Aeolus DISC staggered delivery schedule.

This staggered delivery was performed every 6 months as long as the satellite was in orbit and lead to the following major processor releases and corresponding baseline changes since launch.

Table 16: Date of baseline updates for Aeolus processors by PDGS.

Baseline	Product release date
B01/02	3 September 2018
B03	16 May 2019
B04	14 June 2019
B05/06	28 June 2019
B07	31 October 2019
B08	02 April 2020
B09/10	20 April 2020
B11	8 October 2020
B12	26 May 2021
B13	6 December 2021
B14	29 March 2022
B15	13 September 2022
B16	18 April 2023

4.11 The operational L0-L1A-L1B Processors

Dorit Huber, DoRIT and Markus Meringer, DLR

4.11.1 Introduction

From August 2018 to March 2024, 13 major versions (V7.03 to V7.15) and in addition 8 patch versions of the L1B have been delivered; numerous code modifications, algorithm updates, new processing steps and product format changes have been implemented. This document can only briefly introduce the reader to the major changes. In the same time frame 10 major versions (V3.07 to V7.17; V7.09 skipped) and in addition 18 patch versions of the L2A have been delivered; here the major challenge was the re-coding of 3 additional prototypes delivered during phase E2.

In section 4.11.2 a short overview of the L1B processing chain and major tasks of the single chain elements are presented, before L1B code modifications are explained in section 4.11.3. Section 4.12 focusses on the integration of the 3 new prototype algorithms into the L2A operational code.

4.11.2 L1B processing chain

The L1B processor chain consists of three different steps, the L0, L1A, and L1B processing. Complexity of these steps increases gradually from L0 to L1B. A key factor in the processing is the instrument mode that is provided in the raw data product for each BRC; the instrument mode specifies the type of data that was recorded, wind mode, or one of the calibration types. The control flow of the three processing steps is built around the knowledge of the instrument mode.

L0 step

Input to the L0 processing is a raw data file which contains the telemetry source packets AISP down-linked from the satellite during one pass over the receiving ground station. This file may contain source packets from different system and instrument modes. At the beginning or end of a data file a BRC may not be complete. Sometimes raw data files will be concatenated at the ground station. Then, the resulting raw data file may contain duplicates of packets.

Thus, the first major task for the L0 step will delete all data of BRCs within a given time frame where a mandatory source packet (AOCS, housekeeping, and auxiliary data) is missing. Further, it will delete all duplicates.

In the second major task, all packets will be validated and sorted according to instrument mode. The validation is a sequence of error and consistency checks on Virtual Channel Data Unit (VCDU) error, Cyclic Redundancy Check (CRC) count, packet identification (ID) fields, consistency of sequence control fields, packet length, source packet data field header, and a check on source data. Packets are usually time sorted, and are reordered into time ordered segments of packets for the specific instrument modes.

L1A step

Input to the L1A step is the L0 product; the main purpose of the L1A step is the processing of the AOCS and housekeeping data and the separation of recorded data into different products according to the instrument mode. Thus, the Level 1A processor loops over the known instrument modes, processes the packets into annotation data sets and measurement data sets and writes the sets into instrument mode dependent L1A product files like AUX_IRC_1A, AUX_ISR_1A, or ALD_U_N_1A, the wind measurement data. Again, the instrument mode provided in the raw data and copied over to the L0 data drives the control flow.

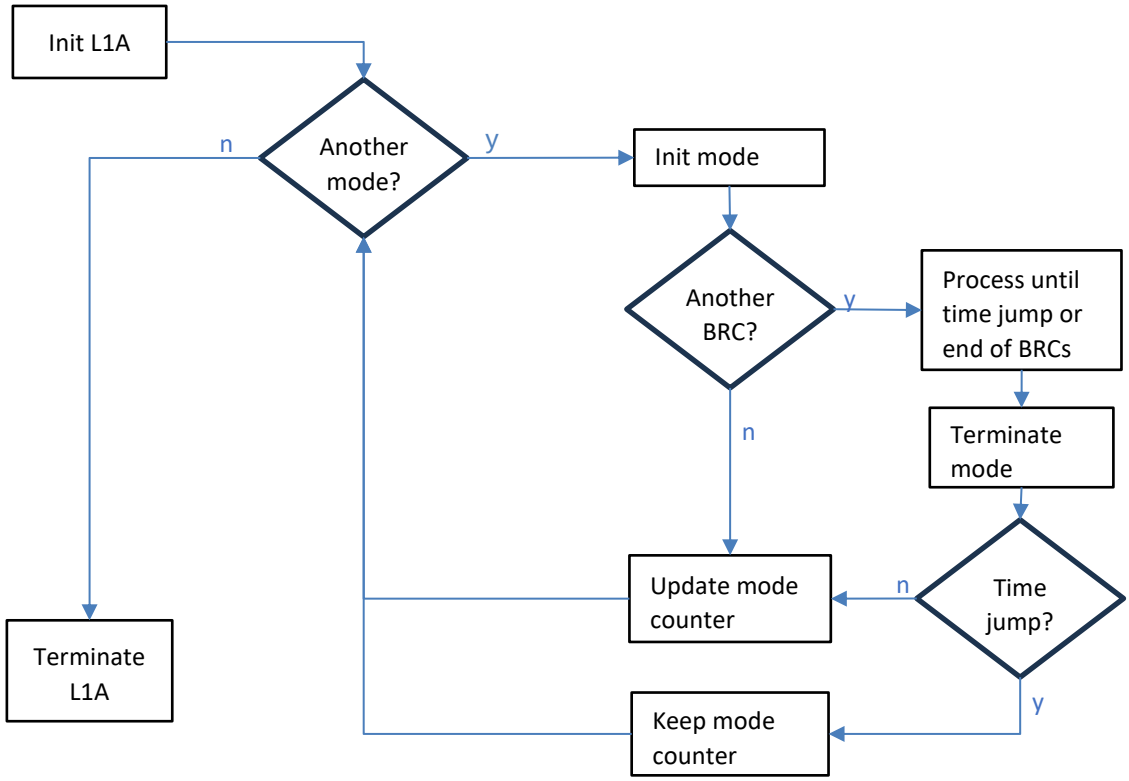

Figure 100: L1A processing scheme at launch.

Figure 2-1 shows a flow diagram of the L1A processing at the time of the launch of Aeolus. Changes to the L1A processing scheme during phase E2 are reported in section 4.11.3.

It may happen, that a second recording of the same calibration type data occurs within the segment of packets of a specific instrument mode found in the L0 product. In that case we detect this by a jump in the time stamps of the data packets and we must generate two L1A output products of the same type. The two products can be distinguished by the time stamps that are part of the product file name.

L1B step

Input to the L1B step are different L1A products; processing is again based on the instrument mode, but here this mode is extracted from the file type, i.e. the key words like ISR or IAT in the file name. Each file type is processed with its dedicated processor, that is instantiated on demand.

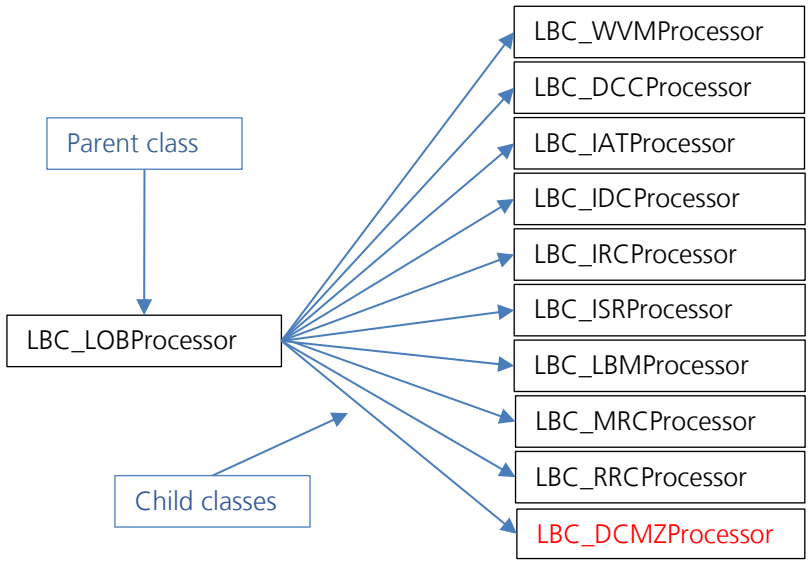

The parent class holds methods and data that are jointly used processing different instrument modes, whereas the child classes hold only the mode specific methods and data.

Each child class inherits the methods and data of the parent class.

At launch, the LBC_DCMZ Processor did not yet exist; we will come back to it at a later stage (see Section 3.14.1).

Figure 101: L1B structure of main processing classes.

4.11.3 Major L0/L1A/L1B code modifications

Major modifications described below were implemented in the L1B processor, but required also adaptions in the L1A processor. All processor modifications are described in detail in the Software release Notes (SRN), the Detailed Processing Model (DPM) and the output format changes in the Input/Output Data Definitions Interface Control Document (IODD).

Some of the modifications are clearly related to the processing of a specific mode. Others touch the processing of more than just one mode.

IDC processing improvements

In a first step processing of Mie data was added; mean Mie image pixel levels are retrieved in a similar manner as for the Rayleigh data and are written to the AUX_IDC product as new output parameters Mean_Mie_Image_Pixel_Level_Val. In a second step, DCO correction was added to the IDC processing, where the DCO correction may be performed in different ways, see 0 and SRN L1B V7.07.

Further information per input BRC was added to the IDC_1B product: 15 telescope temperatures, sun elevation angle, and latitude and longitude of DEM intersection; see SRN L1B V7.10.

MRC processing improvements

A weighted linear fit for the response calibration has been introduced using the accumulated useful signal as a weight; see SRN L1B V7.13.

RRC processing improvements

In the AUX_RRC_1B file of IRC #55 from Nov. 4th, 2019, all Calibration Validity Indicators are reported as FALSE (invalid) for the atmospheric (MEASUREMENT), the ground return (GROUND) and the internal reference (REFERENCE) response curve. Investigating this issue for the IRC data measured on 04. Nov. 2019 showed that the least squares fit of a polynomial to the ground response errors failed. More precise, the Cholesky Decomposition failed. Cholesky Decomposition is a mathematical method that is only applicable under certain assumptions, which were not met in this case. Thus, an alternative method has been implemented: the polynomial fit is calculated using a matrix representation and solving the linear equation system with Gaussian elimination. This method succeeds for the ground response error data of the IRC data measured on 04. Nov. 2019.

For robust retrieval of the polynomial fit data, the processing has been modified such that for reference pulse, atmospheric, and ground response error data, first the least squares fit is applied, and just in case this fit fails, the linear equation system is solved; see SRN L1B V7.09.

ISR processing improvements

The analysis of the Mie peak height from ISR measurements shows that the Mie peak height is frequency or rather laser energy depended. In the figure below, it can be seen that there is a linear trend (decreasing peak intensities) for higher frequencies.

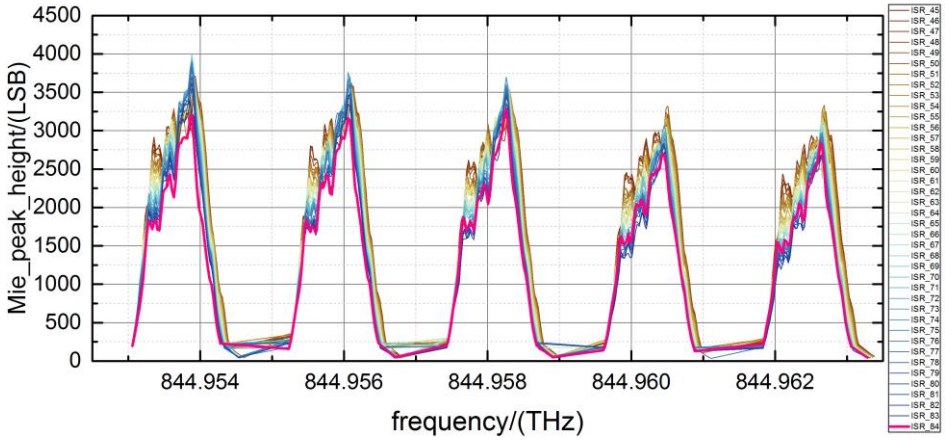

Figure 102: Mie peak heights for all ISR measurements performed with FM-B until 30. March 2020.

A non-perfect energy correction caused by the uncertain laser energy measurement of the photodiode was identified to be the reason for the varying Mie signal levels during ISR measurement. For the Rayleigh data an energy drift correction was already implemented before launch and it demonstrated that an energy drift correction is useful to avoid this frequency step dependent feature in the data, thus an energy drift correction was also implemented for the Mie.

In addition, different energy drift correction values for Rayleigh channel A & B have been defined and are used for the correction; see SRN L1B V7.09_1.

LBM processing improvements

The LBM processing provided data on Rayleigh and Mie average image, minimum pixel values for Rayleigh and Mie, column / row Rayleigh spot positions, binarized Mie image, and ellipse fit to binarized image.

Investigations undertaken by ESA and the DISC team have led to several processing modifications, see SRN L1B V7.10_1:

1. Energy drift correction for Rayleigh and Mie.
2. DCO correction for Rayleigh and Mie.
3. Additional output information per frequency step; among others frequency offset, validity, mean Rayleigh and Mie DCO per row.
4. Standard deviation for Rayleigh column / row spot positions.
5. Mie average image values per column.
6. Mie fluence values.

WVM processing improvements

1. AOCS status flags moon blinding, ground intervention, reconfiguration, eclipse status, GPS, and star tracker have been added to the measurement data set of the L1B wind product; see SRN L1B V7.10.
2. A new parameter for the Mie total SNR is retrieved on observation and measurement level for all height bins and has been added to the product confidence data set of the L1B wind product; see SRN L1B V7.11.
3. Mie non-linearities: The response curves, the non-linearities and the residuals of the first 21 Mie response calibrations had been analysed for the internal reference and the ground return. When plotting the non-linearities against their associated response, a very consistent arch-like shape became apparent. Furthermore, all residuals (after subtraction of a 5th order polynomial fit) showed the same kind of oscillation shape which is induced by the pixilation effect of the ACCD. But variations in the shape of the non-linearity and even more in the residual are mostly of random nature. Therefore, an "average shape" of all the available non-linearities constitutes a reasonable approximation of the actual physical shape of the Mie non-linearity. Data of this average shape was filled into new parameters for fitted non-linearities of the Mie internal reference path and atmospheric path that have been added to the AUX_PAR_1B file in the new section Fitted_Non_Linearities as well as the switch Use_Fitted_Non_Linearities. If the switch is set to TRUE, the raw Mie responses are corrected by using the fitted non-linearities provided in the AUX_PAR_1B file. If the switch is set to FALSE, the raw Mie responses are corrected by using the fitted non-linearities provided in the AUX_MRC_1B file; see SRN L1B V7.07.
4. Sat-LOS velocity correction: The satellite velocity on the LOS is an additional contributor on the measured Doppler frequency shift which needs to be subtracted to derive the atmospheric wind induced shift. The satellite velocity calculated with the ESA provided CFI routines showed a sinusoidal behaviour; a correction algorithm was developed and implemented into the L1A processing step; see SRN L1B V7.09.

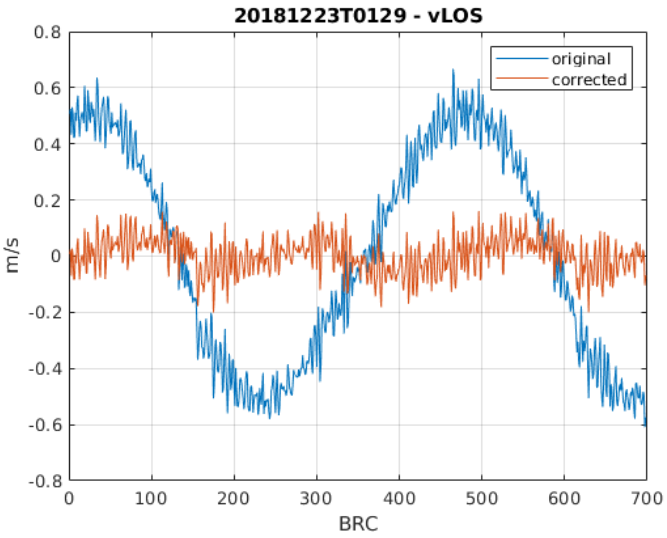

Figure 103: Satellite velocity vLOS before and after correction algorithm was implemented.

Cubic correction for refined SR retrieval

In the L1B the SR is derived based on Mie signal only, whereas the L2A derives an SR based on data from Mie and Rayleigh channel, which is more accurate. The precision of the derived values has a great impact on the L2B wind processing, e.g. separating scenes into clear and cloudy, and correcting Mie contamination for Rayleigh cloudy winds, see Šavli (2019a,b). An empirical cubic correction scheme was developed using L2A products; it has been implemented into the refined SR calculation of the L1B, see SRN L1B V7.07.

Two new parameters have been added to the AUX_PAR_1B file: Cubic_Correction_Lower_Application_Threshold and Cubic_Correction_Upper_Application_Threshold. The cubic correction of the refined SR is now only performed if the first guess value is above or equal to the lower threshold and below or equal to the upper threshold; see SRN L1B V7.09.

M1 telescope temperatures

A set of 15 telescope temperatures provided in the L0 product has been added to the L1A HK data set, and the L1B wind, MRC_1B, and RRC_1B products. Data is provided in different granularity, mean for an observation in L1A and L1B wind products, and mean over all values provided for a frequency step in MRC_1B and RRC_1B; see SRN L1B V7.08.

Gradient correction for imaging modes

Investigations of DCC data showed that a vertical gradient from top to bottom and a horizontal gradient from the right to the left part of the CCD can be observed for Rayleigh and Mie images. The vertical gradient is removed after DCO correction of the raw signal. However, the horizontal gradient in the signal map is still present. A new procedure for the correction of the vertical gradient was defined and implemented for the DCC, IDC, and LBM mode; see SRN L1B V7.13.

Saturated pixel handling

Handling of saturated pixels has been investigated for all lidar modes, investigation results and code modifications are described in detail in Huber (2020). A summary of major code modifications is listed below.

1. In WVM processing, the handling of measurements with corrupted data has been updated; measurements, where at least one atmospheric bin is affected are not processed by the ground detection algorithm. Thus, for these measurements no ground bin will be detected.
2. In MRC processing, the handling of measurements with corrupt data has been updated; measurements are additionally flagged invalid if one of the atmospheric layers shows corrupted data. A bug writing the parameter Mie_Measurement_Invalid has been detected and fixed. A new parameter Num_Input_Measurements has been added to the frequency step data statistics.
3. In RRC processing, the handling of measurements with corrupt data has been updated; measurements, where at least one atmospheric bin is affected are not processed by the ground detection algorithm. Thus, for these measurements no ground bin will be detected. Further, if an atmospheric bin is affected that is within the height range selected for atmospheric response calculation, the data of this bin is excluded from further processing.

Saturated pixel handling procedures have been defined also for imaging mode data, and have been implemented for the IDC, DCC, and LBM mode. For the imaging mode data, images with at least one saturated pixel are flagged invalid and excluded from further processing.

In addition, the saturated pixel handling procedure has also been defined and implemented for the DCMZ mode. Here a measurement is flagged invalid and excluded from further processing if either in the background row or in all atmospheric bins a saturated pixel occurs; see SRN L1B V7.11.

Rayleigh spot location and width

To derive the Rayleigh spot location and width for the atmospheric bins, the background bin, and the reference pulses of wind measurements and the Rayleigh Response Calibration measurements, an IDC like 1-dimensional retrieval for energetic centroid and the standard deviation have been added to the WVM and RRC processing. Values are provided in the WVM PCD of the L1B product on observation level, and per frequency step in the RRC product; see SRN L1B V7.09.

Ground detection

1. Shortly after launch it showed that an update of the ground detection algorithm was necessary; see SRN L1B V7.05. The list of early modifications includes:
   a) The DEM offset for each ground bin candidate and the DEM offset threshold check is calculated and applied as proposed in Weiler (2018): if the ground bin candidate is above the expected ground bin number, flag ground bin candidate invalid if the altitude of the lower edge of the ground bin candidate is greater than the sum of the altitude of DEM intersection and the maximum upper DEM offset. If the ground bin candidate is below the expected ground bin number, flag ground bin candidate invalid if the altitude of the upper edge of the ground bin candidate is less than the difference of the altitude of DEM intersection and the maximum lower DEM offset.
   b) A new air column thickness above DEM threshold check as recommended by the A2D team, see Weiler (2017) and DLR (2018), has been implemented: the air column thickness is calculated as the sum of differences of the upper edge of the ground bin candidate and the altitude of DEM intersection for all ground bin candidates equal to or higher above in atmosphere than the expected ground bin. Apply thickness above DEM threshold and flag all ground bin candidates invalid if threshold is not met.
   c) A new useful signal threshold check has been implemented as proposed in Huber (2019): the useful signal of remaining valid ground bin candidates is co-added and the useful signal threshold check is applied to this co-added useful signal. All ground bin candidates are flagged invalid if
      - the surface flag indicates a water surface and the sum of the useful signal is below the Mie water useful signal lower threshold or
      - the surface flag indicates a land surface and the sum of the useful signal is below the Mie land useful signal lower threshold.
   d) Selected Mie core algorithm is used on co-added useful signal as proposed in Huber (2019).
   e) After core algorithms being applied to co-added useful ground signal for Mie, threshold checks on the response shift, and on the retrieved FWHM (only if Mie Core 2 used) have been implemented.

2. A mismatch between DEM and altitude of detected ground returns during IRC mode has been found. The root cause for this error could not be identified; it is just known, that it is not in the software. But a workaround has been implemented that mitigates the impact of this error by adding special delay parameters for the IRC mode that are used in the processing now; see SRN L1B V7.15_1.

DCO processing and usage

DCO usage and processing is one of the issues that was under current review and update during phase E2. In the initial launch version, the DCO correction was performed

1. on internal reference pulses and on observation and measurement level on atmospheric Mie data for each row using the mean of the data found in pixels 19 & 20 of the ACCD for lidar modes.
2. on internal reference pulses and on observation and measurement level on atmospheric Rayleigh data for each row using the data found in pixel 20 of the ACCD for lidar modes.
3. and pixel 17 imaging mode data.

Several changes to the DCO correction have been implemented in the following order:

1. DCO correction of the Rayleigh lidar mode data using the mean of pixel 19 & 20; see SRN L1B V7.05.
2. DCO correction of Mie and Rayleigh imaging mode data using now the mean of pixel 17 & 18.
3. DCO information is also found in pixels 1 & 2 for lidar and for imaging mode. The code was updated to read from the AUX_PAR_1B file new parameters that allow to select which of the 4 pixels 1 & 2 and 19 & 20/17 & 18 should be used to calculate a mean DCO value per row for DCO correction; see SRN L1B V7.09_1.
4. For the atmospheric layers in lidar mode measurements, the DCO correction can be switched on/off using a new AUX_PAR_1B parameter. If this new flag is set to FALSE, the direct DCO correction is omitted in all lidar modes for the atmospheric bins. Instead, the DCO correction is performed implicitly via the DCMZ correction; DCMZ is also a lidar mode, so if DCMZ is not DCO corrected, then the DCMZ correction values hold a combination of DCO & DCMZ correction factor. Applying the DCMZ correction, DCO is then implicitly corrected; see SRN L1B V7.13_1.
5. A pre-processing step for the calculation of mode mean DCO values per row and for the background has been implemented. DCO values per row in all measurements of all BRCs of a certain mode available in the L1A product are selected according to modification 2. and are summed up and finally averaged and stored. Then the main processing loop over BRCs is started; see SRN L1B V7.14_3.
6. If the mode mean DCO calculation is used in the wind mode, a standard deviation for internal reference pulse DCO and atmospheric DCO values is calculated for the Mie and the Rayleigh. The mean DCO values and the standard deviation values have been added to the calibration & Characterization data set of the L1B product. In addition, for the modes ISR, IAT, DCMZ, MRC, and RRC, in case the mode mean DCO calculation is selected, standard deviation of the DCO values is calculated, and mean DCO and standard deviation values are reported in the products; see SRN L1B V7.15_1.

In summary, we can now select either implicit DCO correction (via DCMZ correction) or explicit DCO correction. For the explicit DCO correction, we can select either mode mean DCO calculation or direct DCO, i.e. immediately correcting each row with the DCO pixels selected.

DCMZ/DUDE processing and correction

DCMZ/DUDE processing and DCMZ correction are two separate steps. At first, the recorded calibration data needs to be processed up to L1B such that the calibration data is available in a dedicated AUX_DCMZ1B product. In a second step this calibration data is used in the L1B processing step of all other modes.

New DCMZ data recorded

Shortly after launch, the occurrence of hot pixels (section 3.3.1) led to the need to characterize the dark currents in memory zone (DCMZ) in lidar mode and a new type of calibration data was recorded: the DCMZ measurements. A new instrument mode was defined for the raw data, the sorting step in the L0 processor has been adjusted, and a new segment of DCMZ packets made available in the L0 product. In the L1A processor, the loop over known instrument modes was extended and a new 1A product (DCMZ1A) was written. For the L1B step a new dedicated processor LBC_DCMZProcessor was defined and coded (see Figure 101).

This extension of measurement mode processing in the L0-L1A-L1B chain was straight forward and simple to implement. At that stage the concept of instrument mode as a driver for the processing control has proven to be very flexible.

New DUDE data recorded

Yet another type of data was needed, the DUDE data. DUDE data is expected to be processed like DCMZ data. Unfortunately, the DUDE recordings do not have a separate instrument mode, like the DCMZ recordings, but are provided as "No Operation" (NOP mode) data in the instrument raw data. NOP is an instrument mode that is used for transition phases between two other modes. Data of this type is only processed up to L1A, as no dedicated processing of scientific data is defined.

The DUDE data are hidden in the standard NOP data and need to be extracted, so they can be processed up to L1B. Due to this, the concept of instrument mode-based data processing in the L0 and L1A step had to be abandoned.

The L0 step has no chance to detect DUDE packets within the NOP packets as it does not inspect the content of the data packets; thus, the L0 processor just generates a NOP mode segment in the L0 product with NOP and DUDE packets.

Usually, the NOP mode segment starts out with a couple of true NOP mode packets, and then DUDE packets occur. But we may also have DUDE packets right from the beginning of the segment. After the DUDE packets we have in general again a few NOP mode packets, but not always. We may also have two DUDE measurements separated in time within the NOP mode segment. Of course, we can have a couple of true NOP mode packets in between those two DUDE measurements, but not necessarily.

In addition, as mentioned earlier, in case of a time jump in a calibration mode, separate products are generated; this is not the case if we have the NOP mode. In that case, all NOP mode data is written to one single 1A product. Product writing is performed by the mode termination step. So, this case needed a special treatment as well leading to a decision point with three different ways forward in Figure 104: below.

To deal with this new situation a work around solution was implemented in the L1A processing step: two instances of the L1A processor are running in parallel, and control flow is jumping back and forth between the two instances.

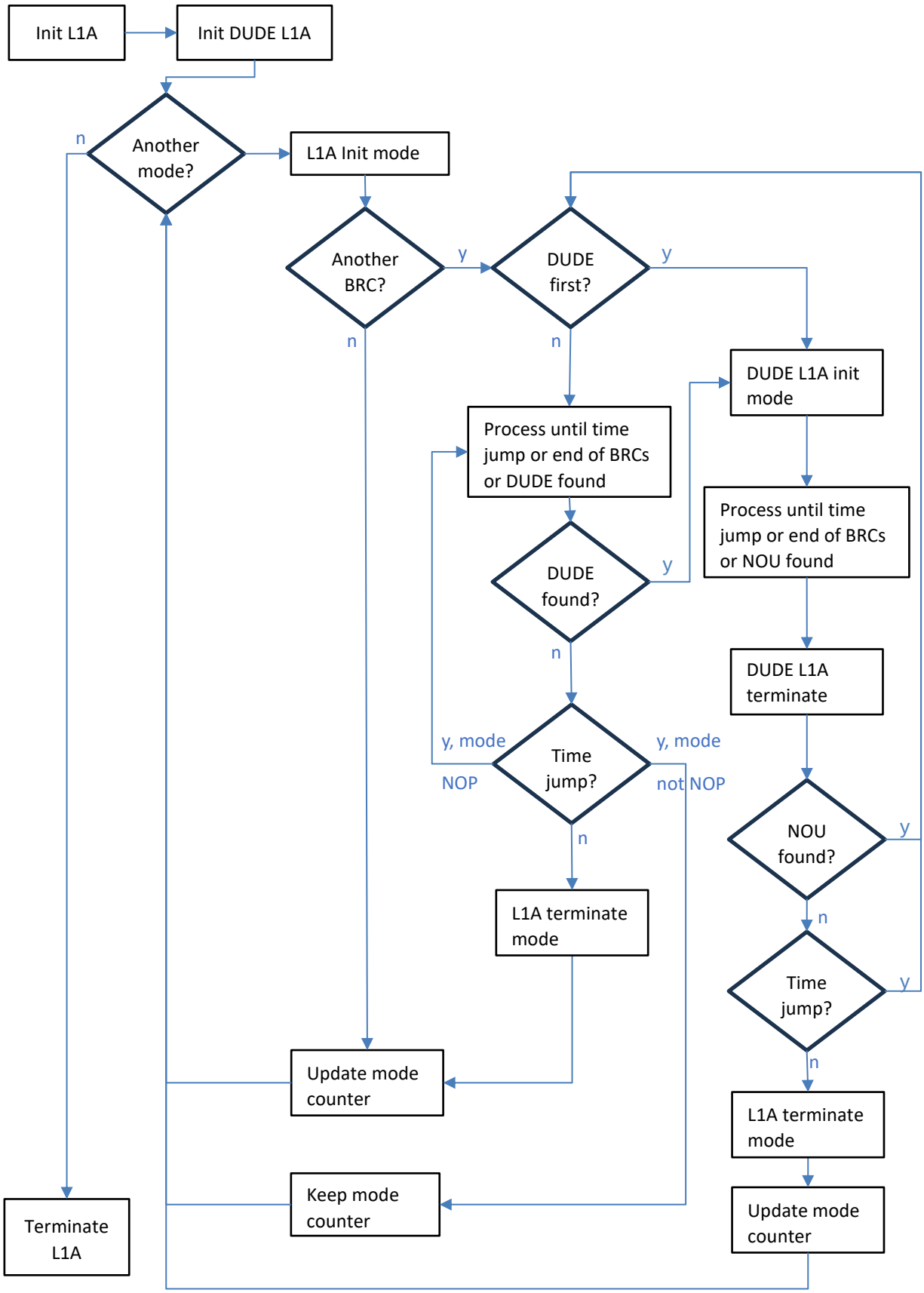

Figure 104: L1A processing scheme after insertion of DUDE data into NOP mode recordings.

DCMZ/DUDE data processing and data usage

DCMZ/DUDE data processing was one of the long-term issues constantly under improvement during phase E2. In the initial launch version, the calibration mode DCMZ did not exist at all, as this type of data was not yet recorded by the instrument.

Several modifications to the DCMZ/DUDE data processing were performed.

1. The initial version of an algorithm that processes new DCMZ/DUDE data up to AUX_DCMZ1B has been implemented based on the approach defined by ESA (Kanitz et al., 2019). The implementation involved several steps, see SRN L1B V7.06:
   a) Update of the L0 and L1A steps, as described above.
   b) Inclusion of a new LBC_DCMZProcessor, see Figure 101.
   c) Implementation of the DCMZ/DUDE data processing in the L1B step.
   d) Definition of a new AUX_DCMZ1B product file.
   e) Writing and reading of AUX_DCMZ1B product files.
   f) Adding and evaluating a new section of parameters for DCMZ/DUDE processing to the AUX_PAR_1B file.
   g) Implementation of a DCMZ correction scheme in the modes WVM, MRC, and RRC.
2. It was found that sometimes during DUDE data recording the top Rayleigh bin was polluted by atmospheric signal. Thus, additional checks have been implemented in the L1B DCMZ/DUDE processing to identify bins contaminated with atmospheric signal and eliminate them from further processing; see SRN L1B V7.08_2.
3. DCMZ/DUDE correction values are also derived for the background row as defined in DLR (2020), and WVM, MRC and RRC processing are updated such that the background row is DCMZ/DUDE corrected before it is used to perform the background correction; see SRN L1B V7.09_1.
4. The DCMZ/DUDE data processing was updated for pixels, where due to quality control no new value could be derived: the DCMZ/DUDE processing uses as input also an AUX_DCMZ1B file, the most recent that is available. In case a new value cannot be derived for a specific pixel, the value from the input AUX_DCMZ1B is copied over to the output AUX_DCMZ1B; see SRN L1B V7.09_1.
5. Instead of a median solar background threshold check used for the calculation of the background DCMZ/DUDE values, a new threshold check on the sun elevation angle has been implemented based on the investigation found in the corresponding wiki issue dL1B_DCMZ_006. As the background signal has a seasonal variation the threshold had to be updated several times. The sun elevation angle threshold is valid throughout the whole year; see SRN L1B V7.11_1.
6. A similar check on the sun elevation angle has been implemented for atmospheric layers DCMZ/DUDE calculation; see SRN L1B V7.14_3.
7. A new section DCMZ_Correction_Selections has been added to the AUX_PAR_1B file. This section holds parameters that allow a selection of pixels that should be DCMZ corrected. These new settings are evaluated and deselected pixels (setting of 0) are not DCMZ corrected in the lidar modes; see SRN L1B V7.14_3.

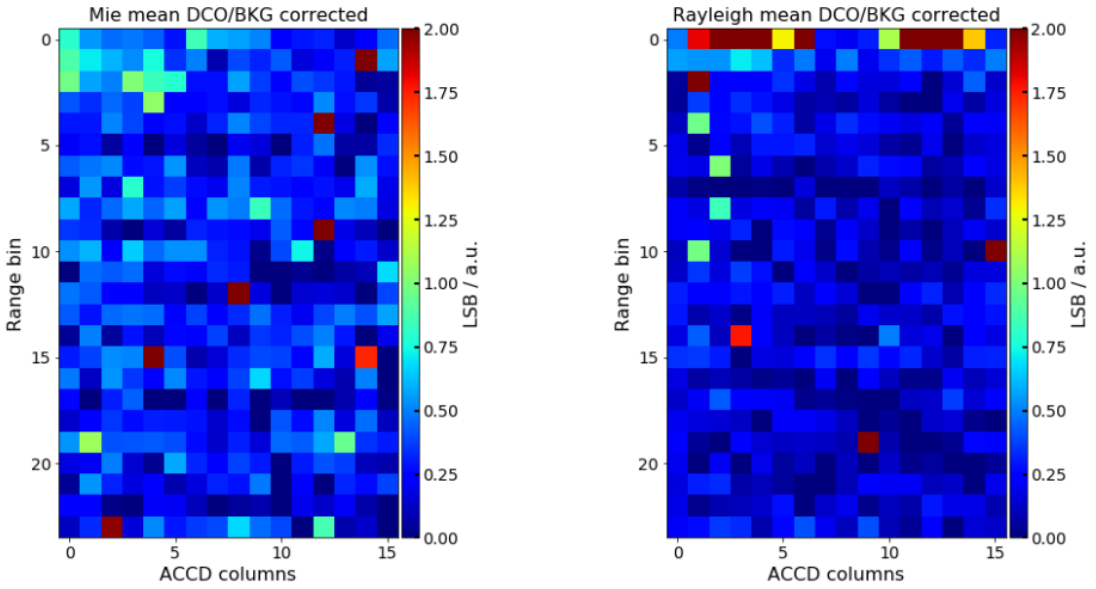

Figure 105: Example DUDE data that shows hot pixels and impact of atmospheric signal in the top most layers.

Mie Core algorithm and SR and SNR calculation

This is also a long-term issue; Mie core algorithms and the calculation of SR and SRN are currently still under modification. The list below shows the evolution of the processing so far:

1. The Mie Core 2 algorithm retrieves negative offset values for a significant amount of data, such that gaps in retrieved SNR/SR are visible. Those gaps lead to problems in the L2B processing. A work around solution was implemented: in case the retrieved offset is negative, a fixed offset of 1.0 is used for the refined SNR/SR calculation; see SRN L1B V7.09_1.
2. The calculation of a new parameter on total Mie SNR that includes the molecular contribution in the Mie channel has been implemented, see SRN L1B V7.11_1, and updated, see SRN L1B V7.12.
3. On the receive path light is obscured from the tripod holding the secondary mirror. This obscuration has a great impact on the atmospheric data seen on the Mie ACCD. The obscuration effect is corrected with an array called TOBS that holds correction factors for each column of the Mie ACCD. In a new approach the following correction was defined: an EMSR array provides column wise correction factors that not only correct for the tripod obscuration but in addition for the non-uniform illumination of the Fizeau; see SRN L1B V7.13_1. A mean EMSR array is derived from Rayleigh clear signals in the stratosphere of the Mie channel as part of the L2A processing.
4. Based on investigations described in Nikolaus (2023), a new method has been implemented as Mie Core 3 algorithm. It provides alternative output parameters amplitude and offset; see SRN L1B V7.13_1.
5. For the internal path, the tripod obscuration is of course not seen, but still the Fizeau illumination is not uniform due to the laser beam profile. An additional internal EMSR array is now input to the processing and can be used for the correction of the non-uniform illumination based on parameter selection; see SRN L1B V7.15_1.
6. A new Voigt fit routine replaced the former Mie Core 3 algorithm. The new Voigt fit provides not only amplitude and offset, but also a peak position. The output of this new Mie Core 3 is used for wind, SR, and SNR calculations if switches in the AUX_PAR_1B file are set accordingly; see SRN L1B V7.15_1.

AUX_PAR_1B updates

Last but not least, for all the changes described above and the minor ones not reported here, more than 100 new L1B processing control parameters have been added to the AUX_PAR_1B input file; the number of parameters increased from about 183 to 296.

4.11.4 Lessons Learnt from L1B development

Problems working with Word

The L1B IODD is a Word document with 332 pages, 435 tables, and 1695 references. Word is not able to handle a document of that size properly, especially the references cause a significant amount of extra work. When the document is exported to pdf format, references are screwed up: either reference is suddenly not known and needs to be inserted again, or in references to other tables suddenly the complete table is inserted as reference, etc. This regularly causes several passes through the document to clean the references before a proper conversion to pdf is possible.

Documents providing guidelines on the delivery process

DOS has provided guidelines for the software delivery process such as "Aeolus Software and Auxiliary Delivery ICD, AED-IC-SER-GEN-003" or "Aeolus DISC Phase E2 Final Report". These documents are highly appreciated as they clearly state how software delivery packages should be set up, who is responsible to deliver a specific entity, or communication chains. But these documents need to be ready before launch. An explorer mission with a short life time is a demanding undertaking also on the software developer's side. Any iteration of such documents and thus rules and workflows during the mission disrupt efficient functioning.

Change of servers and tools with the launch

In addition to the change of delivery processes and communication, there was also a change of servers and tools for anomaly management or open issues tracking. Any tools provided from ESA should be established well before the launch to decouple a ramp up phase on efficient tool usage from the first real measurement data processing.

Insufficient man power

There are many standards giving guidelines for good software development, like ECSS-E-ST-40C which is required to be applied. Especially proper software testing is a part that has been neglected; with two deliveries of L1B and L2A per year and the number of issues to be implemented the work load was so high that most of the time software updates have been tested simply by watching the single processing steps of the code piece under investigation in a debugger being executed on a specific example once.

Loose relationship of DPM and source code

Usually, the purpose of a DPM should be to detail the algorithms of the software and to list and describe the individual modules, classes and functions of the software. However, the Aeolus L1B DPM completely lacks even mentioning any classes and functions. On the other hand, the source code has only very few comments on classes and functions. E.g. descriptions of function arguments are in most cases completely missing. These deficiencies of the DPM and the source code complicate introduction of changes and extensions, as well as the general understanding of the source code. Some improvement was achieved by adding DPM equation numbers to the source code while extending scaffolding functionalities during late Phase D. A good tool for more systematic documentation of the source code would be Doxygen.

4.12 The operational L2A processor

Dorit Huber, DoRIT and Katja Reissig, IB Reissig

The operational L2A processors main input is the L1B product: data is further processed to derive clouds and aerosols optical properties. Up to launch it was based on one Matlab prototype, with a Mie channel algorithm (MCA) on BRC level and Rayleigh channel standard correct algorithm (SCA) applied to BRC and sub-BRC (grouping) data. The functionality of the operational L2A code matched this prototype in the launch version.

After launch, a complete new retrieval algorithm for the identification of different features from strong backscatter returns (e.g. clouds), weak returns (e.g. from aerosols), to aerosol-free regions was implemented (AEL-FM) in addition to the existing grouping algorithm as part of the SCA.

Further, two new retrieval methods for the derivation of aerosol-optical properties (backscatter, extinction coefficient) were implemented (MLE, AEL-PRO) in addition to the existing SCA and MCA algorithms, see van Zadelhoff et al. (2023). The MLE code was developed to reduce the noise in useful signals and cross talk corrected signals for both Rayleigh and Mie channels, see Ehlers et al. (2022), and its Python code was integrated into the Matlab prototype.

4.12.1 SCA improvement

The major improvement to the SCA algorithm was the introduction of estimation of calibration coefficients K_{ray} and K_{mie}. At launch, theoretically derived constant values for Kray and Kmie were used.

- In a first step a second option to derive these constants was added to the code, which derives Kray and Kmie from IRC measurements and applies an orbital correction using data of particle free bins, see SRN L2A V3.10.
- In a second step, a fit of K_{ray} and K_{mie} coefficients per observation by regression based on telescope temperatures was implemented, see SRN L2A V3.11.

4.12.2 Major challenges

It was a major challenge to re-code in addition three new prototypes in C/C++ and add their additional output to the L2A data product during the mission in short time.

AEL-FM is mainly coded in Fortran90, whereas AEL-PRO is a mixture of python and Fortran90 code. The Fortran90 parts of the AEL-PRO are just a copy of some of the Fortran90 code of the AEL-FM. XML files hold the processing parameters, which also had to be integrated into the L2A AUX_PAR_2A file. Fortran90 and python are two very different programming languages and they both bring their own difficulties while re-coding in C/C++.

For the Fortran90 part the main problem is the use of ‘goto’ statements that control the processing flow. This control flow must be transformed into object-oriented control of the processing flow. More than 26000 lines of Fortran90 code had to be re-coded.

For Python the main problem are the numerous mathematical packages that can be used. In C/C++ license free mathematical packages are often not available. Thus, a simple one-line Python statement may expand to a large amount of work in developing own code for a certain mathematical function, among them a function to calculate the pseudo-inverse of matrices, or a function which calculates the Jacobian of a given function. About 5000 lines of Python code had to be re-coded, excluding development of certain mathematical functions.

An additional challenge is also the integration of external libraries used by the Python prototypes:

1. The AEL-FM uses for the Fast Fourier Transform calculation the fftw3 library available from http://www.fftw.org/. Unfortunately, this library requires a license for commercial use. Thus, a discrete Fourier transformation algorithm had to be implemented.
2. The MLE uses the L-BFGS-B Fortran library available from http://users.iems.northwestern.edu/~nocedal/lbfgsb.html. Unfortunately, within Python the L-BFGS-B is hidden in a python wrapper interface. Thus, some effort had to be put into the tuning of parameters and settings after the integration of the Fortran library into the C++ code.

Finally, the cross verification of prototype and operational code results was a challenging undertaking. The complexity can be explained looking at the processor dependencies and the resulting staggered delivery of updated processors.

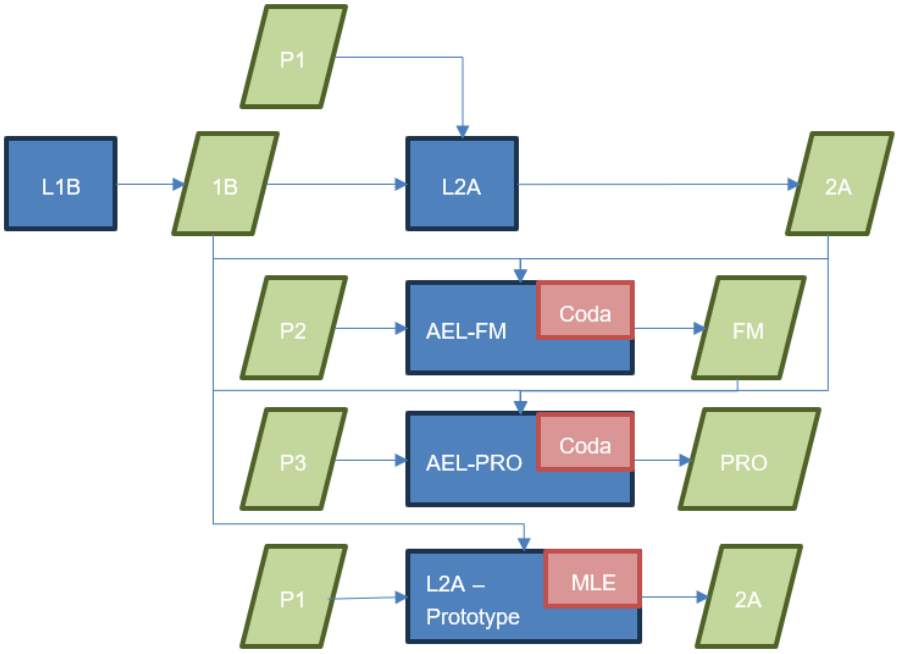

Figure 106: L1B - L2A processing scheme.

In Figure 106:, P1, P2, P3 are the three different parameter files in use; the operational L2A and the L2A prototype use the same file, whereas AEL-FM and AEL-PRO have their own parameter files with their own formats. Further, AEL-FM needs not only an L1B product, but also the L2A product, and AEL-PRO needs the L1B, the L2A, and the FM product. The operational L2A and the L2A prototype generate the same output format, but AEL-FM and AEL-PRO have their distinct output formats in netcdf.

Each processor update cycle started with an update and delivery of the L1B processor, then update and delivery of the L2A prototypes, and then the update of the operational L2A. The L2A prototype has its own Matlab reading routine for the L1B. Unfortunately, the AEL-FM and AEL-PRO use the external tool CODA, see https://atmospherictoolbox.org/coda/, to read the L1B and L2A products, but an update of the CODA tool came long after delivery of the next L2A operational was due.

To run the AEL-FM and AEL-PRO, the L1B and the L2A operational processors had to have an additional compile flag implemented, which allowed to write either the new product format or the previous product format. All parameter files had to be aligned, a single deviation was devastating all comparison results. The developer team of the L2A operational code had to generate all test data sets by themselves, and a series of unit tests was developed, that extracted data from the netcdf output of AEL-FM and AEL-PRO to compare results to the L2A operational data output.

4.13 The operational L2B processor and Chain of Processors (CoP)

Jos de Kloe, KNMI

4.13.1 The operational L2B processor

Introduction

The operational L2B processor (L2BP) implements the Aeolus NWP (Numerical Weather Prediction) assisted wind retrieval. Already during the definition phase of the mission (pre-launch) it was very clear that we would need to use operational NWP input data rather than climatological data, especially profiles of temperature and pressure, as input to obtain as good as possible Rayleigh wind retrieval results. For this reason, it was decided to have a clear division in processing levels. The L1B processor would include wind retrieval algorithms that did not need any NWP inputs, while the L2B processor would include algorithms and calibration results that used NWP inputs.

Another decision was to split the L2 processing in two stages, the L2A processing would retrieve optical properties profiles of the atmosphere, while the L2B processing would retrieve wind profiles. The initial idea was that the L2B processor would use the L2A optical properties as input for the classification procedure to allow use of different wind retrieval algorithms for clear and cloudy atmospheric conditions. Unfortunately, this classification algorithm for the L2A processor was not mature enough for production at the time of the launch of Aeolus. Also, it was clear, that the L2A products will be not processed in real-time to serve as input to the L2B processor. Therefore, quite some effort has been spent on L2B side to implement classification into clear and cloudy conditions.

We also defined the L2C product that contains all data from the L2B product, and some extra datasets holding the results of the data assimilation step of the Aeolus L2B winds in the ECMWF NWP model (see section 5.3). The L2C code is not further discussed in this section.

Requirements

From the start of the project the L2BP software was intended to be used in different locations with different computational platforms. A major target was the ECMWF NWP model. But also NWP models at other meteorological centres as well as individual scientists interested in using and/or adapting the retrieval algorithms should be able to use it. This had a clear influence on the requirements for the L2BP:

- It should be implemented in the Fortran 90 language. This was required since it was foreseen that the L2BP would be running as subroutine in the ECMWF IFS (Integrated Forecast System) which was also implemented in that language.
- The code should be able to run as a subroutine in an NWP model, but to be useful for individual scientists it should also be possible to run it as a standalone program, and it should be provided free of charge to interested scientists and NWP centres.
- The L2BP should process a L1B orbit file "fast". No actual number of minutes was defined, but to be useful for assimilation in NWP models, it should be able to process an orbit worth of data in just a few minutes (certainly less than 5 minutes).
- To facilitate use by many NWP centres and scientists it should be compatible with many linux and unix OS versions, and as many Fortran90 compilers as possible.
- Obviously, it should also run on the reference platform defined by ESA that was foreseen to be used for operational processing and reprocessing (which was RedHat v5 and later v6 and v7).

- Input and output products should use the Earth Explorer (EE) file format, i.e. a very specific binary format for large data sets, and xml format for smaller data sets, processor settings and header files.

In the end ECMWF changed their setup, and the L2BP was not used in subroutine mode after all, but as a standalone program, so parts providing this option have been removed again from the code, while some implementation decisions still reflect this requirement.

Implementation

The main requirements mentioned above had a number of consequences for the actual implementation of the processor. Using Fortran90 means that we needed a number of workarounds by calling C-code since not all needed functionality is available in Fortran90. In addition, the required EE file format is based on C datatypes, which are not all available in Fortran, so a significant effort of low-level byte handling has been implemented to make this possible and efficient.

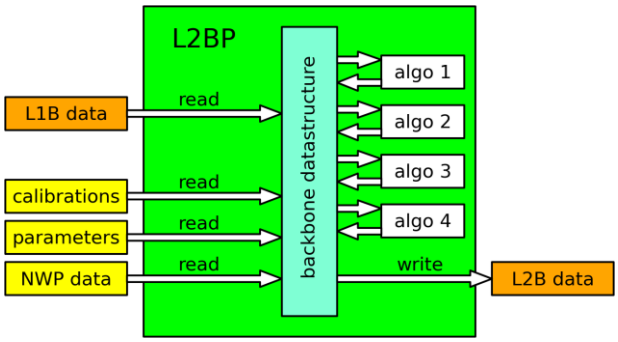

Figure 107: Layout of the L2B processor algorithms and data flow.

To aid the processor development ESA had provided a library called EO-CFI which included useful functions for orbit and pointing calculations, distance calculations, and xml file handling routines. Unfortunately, the library was only provided in compiled form, the source code could not be shared, and this was problematic for the L2BP implementation, since we were supporting unix operating-system environments for which no compiled EO-CFI version was provided. This was an essential requirement for the project since the ECMWF NWP model, and many other NWP models, are implemented and operated on unix machines. To fulfill our compatibility requirement, we therefore had to re-implement functionality that was provided in the EO-CFI library.

Some specific details of the L2BP implementation are worthwhile to mention here.

- We have chosen to use a central backbone data structure called working data (see Figure 107). This holds all input and output data of all algorithms that we use. This is very convenient, and since we use only a subset of data from most of the input files this is also more efficient for memory consumption than loading the full input data files into memory.
- We implemented file handling with very strict format checking. In particular, we systematically check all spare elements and all not-yet-used flag bits to be zero. This has proven to be a very powerful way to check for correctness of our file reading routines.
- The processor is not implemented to do parallel processing or multithreading. The run time for a single orbit file is not long enough to justify the effort to implement this (it typically takes between 30 and 60 seconds on a modern linux workstation). If speedup is required it is much easier to just run multiple copies of the L2BP next to each other on different working directories.

- It was decided to not split the development work in a prototype and an operational processor version. Just one codebase has been developed that was used for testing prototypes of algorithms as well as for operational processing. This has proven to be a convenient and efficient way to develop the L2BP.

Algorithms

This section briefly describes the important algorithms implemented in the L2BP. For more details see Tan et al. (2009) and Rennie et al. (2020).

- Input screening is a set of routines that checks incoming data using configurable thresholds. This ensures that unrealistic and unphysical results from the input files will raise a flag and mark the resulting wind invalid. Also, all flags of the incoming data are checked, so if data is flagged invalid in an incoming product then the resulting wind will be flagged invalid as well. This screening system is highly configurable, and each check can be switched on/off.
- Optical properties is a collection of routines that calculate inputs like scattering ratio, SNR and extinction. These values can be used as input for the relatively simple classification algorithm implemented in the L2BP. In addition, scattering ratio can be used to do the decontamination of the Rayleigh wind result, i.e. to correct for particles present in atmospheric layers that are mostly clear but not entirely. This is currently not used because instrument noise dominates the scattering ratio (SR) estimate, in particular for low SR values: 1<SR<1.5. ESA has decided to not use the L2A product as input for these values already in the early stage of the mission. It is not expected to come back to this decision in Phase F, but potentially for the Aeolus successor EPS-Aeolus.
- Classification decides on the highest resolution (measurement level) for each vertical range bin if the atmosphere inside the bin can be considered clear sky or not. This can be done using a threshold check on the scattering ratio, SNR or extinction. An alternative way for the Mie channel is to trust the fit result of the Mie spectrum. If a fit cannot be done, the signal levels are too low and the signal probably originates from clear sky or fully attenuated conditions.
- Horizontal measurement grouping is applied in a flexible way by the L2BP. The signal from a configurable number of measurements can be accumulated before entering the wind retrieval algorithms. The accumulation settings can be chosen independently for both channels (Šavli et al., 2019). Note that no vertical grouping has been implemented, mainly because of the rather coarse vertical resolution of Aeolus.
- Matchup provides a method to find the appropriate NWP temperature and pressure profile for a given measurement for the Rayleigh wind retrieval. It selects the data based on proximity in space and time, using thresholds as defined in the processor settings.
- Mie wind retrieval is based on the Mie Core 2 fitting procedure to the measured spectral peak, as is also implemented in the L1bP (Huber, 2023).
- Rayleigh wind retrieval is based on a pre-calculated look-up table which gives the Rayleigh spectral response value for different values of Doppler shift and atmospheric pressure and temperature. The atmospheric values are needed to account for the Rayleigh-Brillouin effect that causes a deformation of the shape of the spectral peak, depending on temperature and pressure (Loth et al., 2005; Šavli et al., 2023).

Note that we use NWP profiles as input since these are needed for the Rayleigh channel wind retrievals. But, in addition, it turned out to be very useful to also report the NWP reference wind values in the product. This makes product monitoring of observation minus background departures much easier (see section 5.3). It also allowed to develop several new NWP-based calibration schemes, that were not foreseen before launch (Marseille et al., 2022,2023; Weiler et al., 2021).

Testing

To have confidence in the correct functioning of the L2BP software in different conditions and on different platforms a range of tests has been implemented over the years on different levels. This includes very low-level unit tests, tests of separate algorithms, and tests of the fully integrated L2BP.

- Unit testing includes a large number of tests for individual functions, ranging from reading and writing single values of all relevant data types to and from a binary EE formatted file, to error handling, writing single log messages, interpolation functions, and much more.
- We have dedicated tests that compare the routines we needed from the EO-CFI library to our alternative implementation.
- Tests for a number of necessary scripts are provided, including the installation script.
- A number of science tests checking the full processor on different simplified (simulated) scenes as well as actual measured data are provided.
- A custom difftool was implemented to take care of numerical differences that occur between platforms and when using different compilers.
- Using the standard xmllint tool we perform xml schema checking for all xml file types that are needed by the processor.

All these tests have been combined in an automated test suite that can be run with a simple „make test“ command (561 test cases for the latest L2BP v3.95). Each test will run and generate specific output which is compared to reference output generated at the development platform, using the difftool to take numerical differences in to account.

We used this test suite for compatibility testing to show that the code is compatible to many linux and unix OS versions. We applied this to actual hardware that was available to us, and we also perform this testing in containers that allow tests on many different linux flavors and versions.

The effort to write compatible code has proven to be very useful. First, it enables to use the processor on many machines and with different compilers. Second and equally important is the fact that the code is tested and checked in different ways when using different compilers and machines. This has exposed many programming mistakes at an early stage and allowed fixing them long before they became harmful in operational use. It needs to be mentioned that except for ECMWF the L2BP has not been used operationally at other meteorological centres. However, it was at least used pre-operationally by Météo-France and NOAA.

In addition, some other types of tests have been performed:

- We have used the ESA provided Thin Layer Emulator (TLE) to test the interface that ESA PDGS (Payload Data Ground Segment) required for operational use on their side. This tool was provided as compiled executable so can only be used on one specific platform (32-bit linux)
- Fuzzy testing, i.e. providing random dummy data to test the robustness of the file reading routines, especially the xml reading code, has been applied.

4.13.2 Chaining of processors

Introduction

Early in the project there was a need to run tests in a scripted way. Not just for convenience, but because it was the only way to do it. The main reason to start implementing scripts was the very cumbersome graphical user interface provided by the E2S software for entering atmospheric data. Doing this manually by filling a form, as was the original design of the E2S GUI, was impossible when we needed to start using realistic atmospheric scenarios with many hundreds of profile definitions and many (order of magnitude 100) vertical layers. A script in python was written to replace the GUI and this has been the start of what has become the „Chain of Processors" (CoP) scripting environment (see Figure 108).

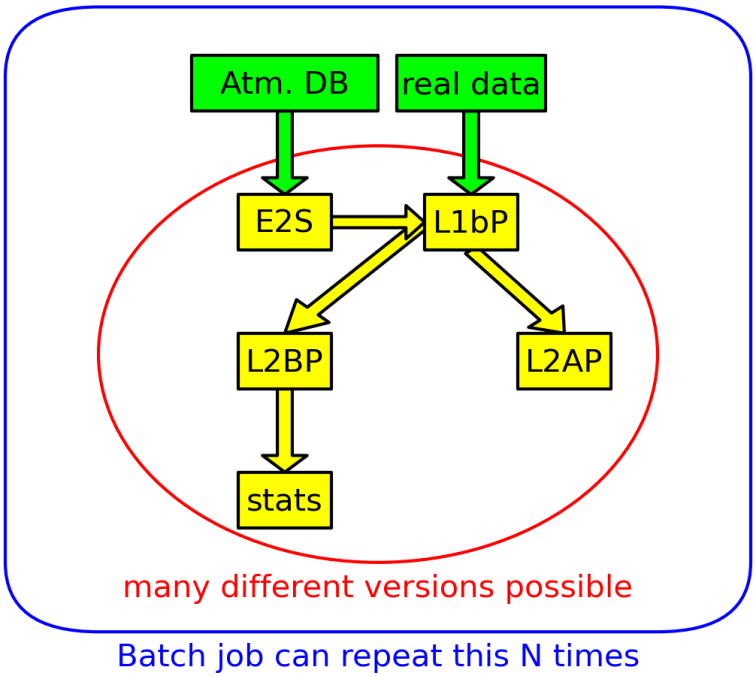

Figure 108: Overview of actions performed by the chain of processors system. It can start a simulation run based on the atmospheric database or a processing run based on real data. This can be repeated as batch job many times.

During the evolution of this system running of subsequent operational processors L1bP (split in L0, L1A, L1B steps), L2A and L2B was added, and in a next stage also some of the calibration processors[3] (prototype and operational versions) were added.

The script system creates for each processing step a working directory for the processor to use, and provides the needed input files in it. Then it runs the processor and verifies that the expected product file has been created. It can provide generated products of one processing stage as input for the next processing stage.

Although initially implemented before launch to be able to run test cases to aid processor development based on E2S simulations, it was trivial to adapt the system to use actual measured data after launch.

[3] The calibration processors that were added were the ones that operate on a single orbit, i.e. the GENCSR, GENRBC, GENCAL and UPDCSR processors (for each type both the operational version and the matlab prototype version was added). Calibration processors that need multiple orbit files as input, especially the HBE and TelSuite processors, could not easily been included since the CoP is very much single orbit based.

After this change the CoP has proven very valuable during the DISC project for several purposes:

- Testing of new processors before their actual delivery
- Testing of new AUX files (both parameter and calibration files) before delivery and deployment in the PDGS system.
- Testing of large sets of AUX files needed for reprocessing, before their actual delivery to ESA/PDGS (DISC-DLR, 2020,2021,2022).
- Experimental runs with large datasets to test new algorithms or alternative algorithm settings before deploying them.

Cloud system - the Sandbox

The CoP system was created on a local KNMI system, but during the DISC project we decided that it would be very useful for other team members to have access to its functionality. Hence, we have arranged a server on which the CoP system and relevant processors are pre-installed, and we provided at request the data needed for running experiments. It is usually referred to as „the sandbox".

This server is located "in the cloud" outside KNMI firewall restrictions and can be accessed by all DISC team members as needed.

Implementation

The CoP itself is written as a collection of python scripts, a language that has proven to be very suitable and flexible for this purpose. Actions performed by the CoP are:

- Conversion of KNMI atmospheric database (Marseille et al., 2011) to E2S input profiles and AUX_MET files
- Creating and filling a scenario folder as input for the E2S simulator.
- Creating and filling a working directory for each operational processor that is to be run.
- Providing a job-order file and filling it with the correct data to allow running the processor.
- Modifying xml input files, especially for the AUX_PAR settings file, if desired.
- Running scripts to provide accumulated O-B results of L2B products (data and figures)

Each CoP run starts with defining a test definition file that defines the processing steps to be done, the inputs to be used for each processor, and the possible modifications that are to be applied to some of the input files.

One test definition file can be included in another one, and this allows to group certain settings together in a convenient way. For example, a file can be created that defines all the input files for a given reprocessing round for all relevant processors.

A test definition can then be provided to a special run script that executes it. Since this run script is a command-line tool, it allows tests to be scripted in a larger script, to run a number of them in sequence. This has for example been used before launch to automatically generate a large number of simulation-based tests as documented in de Kloe et al. (2014,2017).

In addition, the CoP provides a possibility to define batch jobs, i.e., for a series of dates it can loop over a folder of input files and run a given test chain many times, once for each input file. The batch system has some options to allow it to resume its work after a crash to prevent doing the same processing twice in case a problem occurs in a long processing run.

Finally, some convenience scripts are provided to gather results and zip them, so they can easily be shared with other team members for further inspection.

The CoP provides several layers of configuration:

- Switches can be defined for each processor. These define possible options that can be set in the test definition file. A switch can for example define an option to modify a specific field in a given AUX_PAR settings file for a given processor. A switch can also define a folder to be used to find a specific input file for a given processor, or to define a selection criterion that should be used to decide which input file should be used, in case more than one file of the same file type is present in such an input folder.
- Processor definition files can be provided for each version of a given processor. These define where to find the executable file (usually provided as a zipped install folder, in PDGS terms also known as an "installation kit"). A processor definition also contains a list of all possible switches that can be used to configure it. Usually these switches are in a separate file and included in the files for different versions of the same processor.
- Chain definition files refer to a list of specific processor definition files. This allows to easily switch from one chain of specific processor versions to another different chain, on the same machine.
- Test definition files define a specific test to be run. It can hold any number of settings (as defined by the switches mentioned above) for all processors that are used in the chain.
- Batch definition files are used to set up a batch job. A batch job generates a (possibly large) number of test definition files, and launches the chain on each one. A batch definition file defines what settings should be used to generate these test definitions. It can also define start and stop datetime codes for the batch job, but these are more commonly provided as command-line arguments to the batch script.

Testing

The CoP system has a very limited automatic test system, which runs a series of dummy processors in sequence and checks if the expected outputs are generated. This was mainly due to lack of available time. The CoP has never been a formal delivery of the project, it is only a tool to generate needed deliveries.

Nevertheless, thanks to the fact that the CoP is used very frequently during the DISC project, and the generated outputs have been checked many times by other team members, we are very confident that the system works as intended.

4.13.3 Lessons learnt for L2B processor development and chain of processors

- It is essential for processor development and preparation of AUX files for (re)processing that the DISC team has access to a system that can evolve processing configurations. It is used to prepare new versions for the PDGS processing. The PDGS has no such evolving capability. The CoP is needed to run tests with experimental settings and pre-deliveries of processors that are not suitable yet for deployment on PDGS side.
- Such a system should be accessible from different locations and therefore a location "in the cloud" is the most convenient solution.
- Simulators and processors should never rely on a GUI for providing inputs. There should always be an automatically configurable interface to control the software through input files to allow including it in a scripted system.

1. If ESA provides a library to aid with the implementation of processors (like the EO-CFI library), then the source code should be provided as well. This will make it much easier to make the processors compatible to multiple computing platforms, and it would also make debugging of problems much easier.
2. It is very useful if ESA provides an emulator of the operational PDGS environment for processor testing during development, but also this tool should be compatible to different development environments, so preferably should be provided as source code, not as precompiled executable.
3. When defining custom binary files, some zero (or other well-defined) values should be inserted at a number of locations in the file (this is a form of canary checking). This allows for checking the file reading routines for correctness and provides an easy way to detect file corruption.
4. The effort to write compatible code has proven to be very useful. Not only it enables to use the processor on many machines and with different compilers. But equally important is the fact that the code is tested and checked in different ways when using different compilers and machines. This has exposed many programming mistakes early and allowed fixing them long before they became harmful in operational use. Therefore, it is recommended to apply compatible code writing and associated testing to all projects.
5. It is very useful to add a reference result (for the L2BP an NWP model reference wind) to the product. This makes monitoring much easier and allows easy investigation of different types of biases which may lead to improved (NWP-based) calibrations.
6. It is essential to take into account the fact that there will be numerical differences in the algorithm outputs when running on different computer platforms.
7. Thresholding decisions are made in many places in the code, and this can lead to different flagging, like in classifications or QC results. We found that it is worthwhile to tune the test cases as much as possible to prevent these thresholding decisions to differ.
8. It was critical for optimising the real L2B data quality to have the flexibility to control a large range of algorithm parameters in the AUX_PAR_2B.
9. Since EPS-Aeolus will probably use a much finer vertical binning, also a vertical grouping algorithm should be considered for processing this data.
10. There is no reason to move functionalities which are implemented in L1B and L2B to the other processor. Some examples:
11. Grouping should remain in the L2BP since this very much is a feature that is also relevant for scientific users of the L2BP. They should be able to adapt the signal accumulations to their intended use. And since the L2BP is provided to scientific users, this is the proper place to implement it.
12. Rayleigh wind retrieval depends on NWP data (temperature and pressure), therefore it has to be done in the L2BP
13. Mie wind retrieval depends on grouping and the resulting signal accumulation; therefore, it has to be done in the L2BP.
14. Bias corrections on signal level, for example the current hot-pixel correction, should be done in the L1bP, but wind bias corrections that depend on NWP data or are only applied after grouping, such as the Mie non-linearity correction or the M1 telescope temperature correction, should be done in the L2BP.

15. An important factor to keep in mind when considering moving functionalities from the L2A to the L2B processor is run time. Currently the L2AP has no runtime requirement, and as a consequence some of the algorithms take a lot of time. If the L2BP would have to wait for this input the wind results may come too late to be used as input for NWP models (especially the local area models that run every hour or every 3 hours).
16. Changing the functionalities and interfaces of the different Aeolus processor levels needs a careful trade-off involving all relevant parties, as the effort and consequences are large. Making such changes in an operational chain of processors requires a lot of time and testing.
17. The 6-months delivery schedule for processor updates, which we applied for Aeolus in the DISC project worked very well. Such a schedule is needed to ensure that even small modifications like small product file format changes to a given processor are handled well by processors upstream in the chain.
18. The L2BP team of 3 persons during the mission (Jos, Mike, and Gert-Jan), all working only part-time on the L2BP, clearly was too small. We could not implement all ideas that we had, and could not properly test all algorithms to get the best performance. For EPS-Aeolus the processor development teams should be larger,
19. It was critical to get the L2BP into a good state pre-launch to perform a large selection of chain-of-processor tests with realistically simulated, e.g. using ECMWF input data at highest available resolution, atmospheric scenarios. This led to many issues being discovered in the years before launch such that the first data produced in the Commissioning Phase was already of decent quality.

4.14 DISC on-site support for PDGS, LL and knowledge transfer

Massimo Cardaci and Giacomo Gostinicchi, serco

4.14.1 DOS Team and objectives

In the framework of the Aeolus DISC, the DISC On-site Support (DOS) Team was intended to be the main technical interface between DISC, ESA PDGS (Payload Data Ground Segment), and bridge logistically with ESA GMQ (Data Quality and Algorithms Management Office), as illustrated in Figure 109.

The team was responsible for WP 3000 "Anomaly and Configuration Management" and WP 6000 "ACMF analysis and processor release coordination". DOS team role was intended to work in strict liaison with ESA and PDGS and this was achieved by setting the DOS location in ESA-ESRIN premises. The DOS Team was in the position to provide direct support to the various external interfaces, by facilitating exchanges, requests, deliveries, questions and clarifications.

The DOS was initially composed of 2 people, who evolved over time because of the addition of new activities, but also following the natural reductions caused by changing necessity of the mission in its evolution. From the very beginning, despite a member of the team being designated as a key contact point, all tasks were shared within the team, following the approach to grant full support even in case one of not availability of part of the team. In this way, the DOS was active in every nominal working day with a full operative back-up person during all phase E.

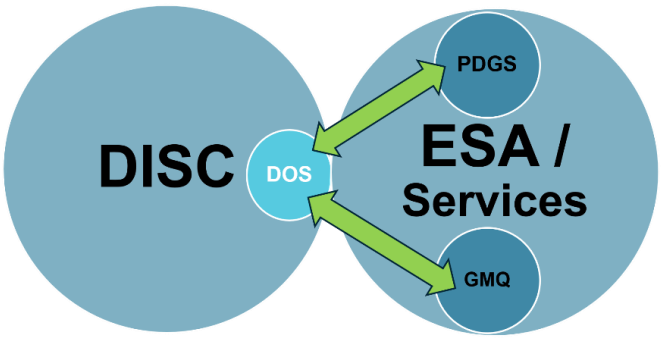

Figure 109: Schematic of the DOS team with the Aeolus DISC.

4.14.2 Key functions

The key role of bridging with external interfaces (PDGS primarily, but also with other ESRIN and ESA interfaces) allowed to smooth several tasks, frequently masking not visible the intrinsic complexities of dataflows crossing different contractual frames, procedures and technical solutions.

These were ranging from the PDGS infrastructure alignment to configuration management, from anomaly handling, to release management, up to purely administrative aspects linked to local policies (e.g. IT security) and procedures.

The detailed involvement of DOS Team in different areas was (Figure 110):

- Configuration management
- Release management
- Anomaly management
- Data Quality monitoring

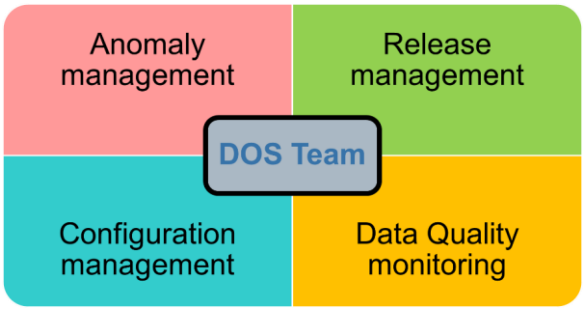

Figure 110: Tasks of the DOS team with the Aeolus DISC.

This has been possible only thanks to:

- The global view DOS acquired and maintained, to properly manage requests and exchanges.
- The access to several tools provided both by DISC and ESA, in particular:
- Configuration management tools (like Confluence and TellUS).
- Anomaly management tools (TellUS and Jira).
- Data Quality monitoring tools (e.g. screening reports, WebMUST, User Python Report Generator).
- The DOS good personal interaction with all teams (both on ESA and on DISC side), keeping always in mind roles and responsibilities, infrastructure setting, Configuration Items (CI), procedures and time schedules.
- The collaboration DOS found in all DISC teams.

4.14.3 DOS and Configuration Management

One of the first areas in which DOS has been involved is Configuration management. The collaboration between DOS and all teams put them in the position to gain a deep knowledge of the roles and responsibilities among the Aeolus mission and found an immediate application in their support to the Configuration Manager, with the aim to structure and detail processes. The core of the activity was to:

- identify the list of interfaces ("the who": teams and people involved),
- identify the CI list ("the what": items to be kept under configuration control),
- define a set of procedures to perform formal exchanges of CIs ("the how"),
- create repositories where CIs should be stored and could be retrieved by teams ("the where").

This close collaboration led to the generation of the Configuration Management Plan (CMP), a set of structured documents comprising:

- the Master document (describing the CMP and its usage): AED-MP-Serco-DCM-001--CMP_MP--v2_00--2022_09_07.pdf (v. 2.0, released on 07/09/2022);
- the Anomaly and Change Management document (reporting the procedure to follow in the management of anomalies discovered by PDGS and assigned to DISC and in the management of changes to be implemented in PDGS): AED-MP-Serco-DCM-002--CMP_ACMP--v2_1--2023_03_01.pdf (v. 2.1, released on 01/03/2023);
- the Interface Control Document (reporting roles and responsibilities and delivery procedures of processors and files): AED-MP-Serco-DCM-003--CMP_SADICD--v5_05--2023_03_01.pdf (v. 5.5, released on 01/03/2023);
- the Configuration Items (CI) List document: AED-MP-Serco-DCM-004--CMP_CIDD--v2_01--2023_03_01.pdf (v. 2.1, released on 01/03/2023).

This task in Configuration Management echoed in the Release Management area since procedures for delivery processes needed to be structured, detailed and finally put in place. Draft procedures have been reviewed by involved DISC teams and related stakeholders, to be as efficient as possible. Finally, when all teams gave their approval, procedures were put in place and circulated within DISC. This modus operandi allowed to start a very good collaboration between teams, so that such processes still find application. The involvement in the Configuration Management area, even if constant, decreased in time: thanks to the initial effort in identifying CIs, roles, responsibilities and in detailing procedures, the CM task in later stages was mainly to keep updated documents and interfaces, with at least a new CMP release per year. The central role of the DOS team in the Configuration Management made the team assume the role of Configuration Manager.

As point of contact, DOS Team has been directly involved in the CI Release Management, by bridging the input received from the Software Development and scientific teams (software and/or AUX files) and preparing it for release to PDGS. Below is shown the list of activities performed by DOS in the Release Management process for IPFs (Instrument Processor Facilities), following the delivery of the Operational code from the DISC developers:

- Inspection of the delivery and of related documentation;
- Compilation of the source code;
- Installation of the resulting binary on a dedicated Virtual Machine aligned in terms of configuration with PDGS, testing the correctness of the installation and of the underlying instructions;
- Generation of the Installation Kit accordingly to PDGS requirements, together with a file reporting the MD5 checksum to ensure the integrity of the download on PDGS side;
- Delivery of the Installation Kit package to PDGS for their Transfer to Operation (TTO); the original Source Code is delivered as well for Configuration Management purposes
- Support the PDGS for queries and issues optionally emerging during the TTO process.

Even releases of auxiliary files have been managed by DOS. Below is the corresponding list of Release management activities supported by DOS, following the delivery by DISC developers:

- Inspection of the auxiliary file and of the changes applied, using the EDFCF (External Data File Circulation Form) provided;
- Patching the file header to ensure the correct ingestion in PDGS system;
- Tracking all the changes applied in each file by updating the changelog maintained in the header of the file itself;
- Generation of the package for PDGS;
- Delivery to PDGS of the auxiliary file for being verified and then ingested in the operational platform;
- Once ingestion is completed (either in case of a success or failure), DOS generates an EDFIR (External Data File Ingestion Report), a form reporting all changes applied by DOS and the outcome of PDGS validation and ingestion process.
- In case of failure, the feedback is passed back to the DISC originating team and the process is restarted.

4.14.4 DOS and Anomaly Management

Thanks to its central role as node in the exchanges between DISC and ESA/External operational contracts, the DOS team has been involved in the Anomaly and Change Management. As single point of contact, DOS Team received at first credentials to access anomaly management system, adopted by ESA (TellUS). Anomalies identified by PDGS were assigned through TellUS to DOS, who was in charge to perform a first investigation and, in case, involve DISC members (according to the relevant roles and responsibilities) for providing a way forward in the solution of the anomaly. In the Ramp-Up phase, the concept was to grant access to TellUS to all relevant DISC members to allow a complete and shared visibility of anomalies. Unfortunately, this was not possible because of a TellUS licensing issue, so, in the end, it was established that TellUS Problems assigned to DOS team would have been rerouted through the Jira anomaly management tool used by DISC; DOS Team task was to keep aligned TellUS and Jira.

Along Aeolus phase E, DOS team managed operationally over 300 items, shared between anomalies and changes. Anomalies describe a malfunction observed in the operations (usually raised by PDGS); Changes identify all the deliveries performed by DOS to PDGS: they can be provided both as a fix to an anomaly (i.e. an IPF patch release) or as a software improvement (i.e. those provided within major deliveries).

The volumes of the events (both Problems and Change Requests) that DOS handled in all tools involved (Jira and TellUs) are summarized in Table 17 and a more detailed table in the Final Report Annex reports, grouped per Configuration Item and categorized by severity. Note that Anomalies and TellUS Problems are mirrored starting from 6th March 2020.

Table 17: Monitored anomalies and change requests per grouped item, where IPF (Instrument Processor Facility) contains all processors, more details are shown in the Annex of this report.

Row Labels	Blocking	Critical	Routine	Grand Total
AUX FILES	**10**	**18**	**97**	**125**
TellUS Change Request	10	18	95	123
TellUS Problem			2	2
IPF	**5**	**12**	**102**	**119**
Jira Anomaly		7	20	27
TellUS Change Request	5	5	50	60
TellUS Problem			32	32
OTHER			**1**	**1**
Jira Anomaly			1	1
QC TOOLS	**7**	**12**	**70**	**89**
Jira Anomaly		3	8	11
TellUS Change Request	6	8	40	54
TellUS Problem	1	1	22	24
Grand Total	**22**	**42**	**270**	**334**

To fulfill its tasks, DOS has been supported by several tools which the team could access. Anomaly tracking tools like TellUS and Jira, but also ARTS, which was mainly used in phase C, D, and E1, and progressively abandoned in phase. It allowed to keep track of anomalies and of the actions taken to solve or avoid them; also change management was performed thanks to TellUS system. Configuration management relied on TellUS for the ESA configuration, while DISC configuration management was maintained on Confluence. DOS monitored satellite status by accessing WebMUST tool where we retrieved information on ALADIN status as well. Data production and dissemination was mainly checked through the Aeolus Data Dissemination Facility (ADDF), but also thanks to Horus system (a tool used by PDGS to control the data production chain) at the beginning of phase E. Data quality monitoring was performed initially thanks to ACMF screening reports, and then through the User Python Report Generator; VirES allowed to perform more in-depth analysis on the data contents.

Other important items DOS used extensively are the virtual machines: the so called "DOS Generation Machine", provided by PDGS at the beginning of phase E as a machine compliant to the PDGS ones and which was used for the compilation, installation and test of the IPFs and finally for generating the Installation Kit for PDGS and the Linux VM (Virtual Machines) used by DOS for patching files and for performing investigations and inspections.

All such systems and tools helped greatly monitoring, releases, investigations, analysis and data quality related activities, but for completing some task, DOS team created its own tools, by using spreadsheets or by coding them (both in BASH at first and in Python 2.7 and Python 3.8 later). This allowed DOS to provide ad-hoc analysis (as for L2A K_{mie}/K_{ray} trend investigations), fulfill specific tasks (like the auxiliary file patching and the coverage analysis for reprocessing) and manage CIs under DOS responsibilities (as the AUX_PAR_QC file, for which DOS released a TN reporting all the changes applied to the file within Phase E: AED-SD-SER-AUX-073--AUX_PAR_QC_ChangesEvolution--v1.1--2024_02_05.pdf).

4.14.5 Internally produced tools

As part of DOS activities, there was the need to proceed with the automation of a few tasks that were increasing their complexity. The objective was to ensure an always correct implementation in case of long and repetitive tasks, and to decrease the time of completion. Over time these tools have evolved in complexity: they started as bash scripts and then evolved into full-fledged Phyton programs. The latest available versions at the time of writing are:

- file_patcher_py38_2.4.py:
  The script allows to patch Auxiliary files in the framework of ESA Aeolus Mission.
- EDFIRgen_v3.6.sh:
  The script is intended to be used by DOS Team to generate EDFIR reports for static auxiliary files or starting products patched and delivered by the DOS team; the script also handles the update of the AFD_Mapping spreadsheet with EDFCF-EDFIR correspondence.
- L2A_KrayKmie_py38_1.0.py:
  This script plots $K_{mie\ and}\ K_{ray}$ indices trends for all the products stored in a given folder.
- lut_parser_py38_v1.0.py:
  The script allows to parse the AUX_LUT_BL file to retrieve information on specific task table, baseline or the whole file.

4.14.6 DOS and Reprocessing

A good example of DOS involvement is the support provided to Aeolus Reprocessing. The team was involved from the early stages of the activity by inspecting the documentation and supporting the preparatory activities. During the release phases, DOS team received Instrument Processor Facilities (IPF) and auxiliary files to be provided to PDGS. According to the management of the releases, each delivery has been received, inspected and, according to the CI, different actions have been taken. In case of IPF, the source code has been compiled, installed and tested in the DOS Generation Machine, it has been generated the Installation Kit for PDGS and then it has been delivered to PDGS via TellUS.

Concerning the auxiliary data file package, DOS Team reviewed the package by inspecting each file according to the requirements provided by DISC teams, verified the correct selection and usage of each auxiliary data file according to PDGS infrastructure and selection rules. DOS team agreed with DISC members on file changes, necessary to grant the proper usage of the auxiliary files and implemented them in the DOS Linux VM. Once the package was coherent with requirements and the infrastructure, DOS Team released it officially to PDGS via TellUS. Every CI was kept under configuration control according to the guidelines provided in the CMP. Concerning Data Quality monitoring, the AUX_PAR_QC file reported the formalization of all the quality tests in place for all product and auxiliary file formats and versions. Such file could be generated and tuned by DOS Team, who supervised the whole process starting from the input collection from DISC (concerning tests - thresholds, product applications, format versions updates, etc.) up to changes implementation. Furthermore, according to the AUX_PAR_QC file configuration management, every change applied needed to be listed and provided both in the related Confluence page and in the file itself and DOS documented each change. Once every relevant CI was officially released to PDGS, DOS collaborated with PDGS on the reprocessing setup (by reviewing of the Look-Up Table, witnessing processor installation and ingestion of auxiliary files). When the reprocessing operations started, DOS team was involved in both Data Quality by monitoring the flow and providing ad hoc investigations, on Anomaly management, which has been always kept under control and on Release management by facilitating the exchanges between PDGS and DISC.

4.14.7 Key achievements and key challenges

- Operational data quality continuous monitoring
- Bridging smoothly DISC outcome with PDGS. This is the main task of DOS team, aiming at the harmonization of different systems, with different environments, configuration managements, which needed to interact.
- Bridging backwards PDGS with DISC. To ensure the cooperation of DISC and ESA, it was also necessary to understand, explain and bring internally to DISC the PDGS necessities for managing efficient and robust operations.
- Amongst the key procedures managed by DOS it is worth mentioning:
    - Evolution Documents: sharing these documents with ESA and PDGS improved the knowledge of the envisaged changes (improvement and fixes) and allowed PDGS to prepare on time configuration and infrastructure for upcoming changes. This facilitated mostly the validation process and made it possible for DISC to gather also PDGS input on the envisaged impacts, thus allowing a more robust implementation of new updates.

- Pre-deliveries: receiving in advance delivery-related draft documents and new format files, facilitated the entire delivery process by providing the developers with a first review performed by DOS (so still internal to DISC, but with the knowledge of PDGS configuration and requirements). This resulted in improved final deliveries, minimising the need for subsequent clarifications across the different teams at a later stage.

- Although resulting in a very efficient, friendly and constructive collaboration, the interactions with external teams, external to DOS within DISC and external to DISC, like PDGS, were a challenge to handle. The main difficulty was to facilitate the interactions between teams with different roles and configurations, with different work practices and needs, and not having the same "jargon".
- Ensure visibility of PDGS anomalies to DISC. DOS was the eye of DISC on PDGS anomalies. To make everything work properly they should be visible to all DISC members, while PDGS and ESA needed to receive updates on the investigation progress. DOS worked to grant full transparency on anomaly management, bridging also the different systems used to trace them.

4.14.8 Contribution to future missions and lessons learnt

The Need

- It is common experience that every new mission has an intrinsic difficulty to take advantage of the experience made by previous ones. There are several reasons beside this, many outside the possible control or contribution of a Supplier's consortium.
- This collides with the intrinsic nature of Earth Explorers, which should have as core objective to make experience and to propagate this experience so that it may be useful to future missions.
- The resulting impact of this difficulty is ranging from financial to technical, from planning to scientific aspects.

The opportunity

- Within Aeolus DISC, ESA approved the consortium's idea to pilot an experiment aiming to address the need to preserve the knowledge, focusing it from the ground towards future missions.
- The very good results achieved by Aeolus, joined with the significant complexities faced and successfully addressed, made this context the ideal candidate for this pilot.

The strategy

- To achieve the objective, some elements were considered in its actual implementation strategy:
- Select only topics that could be generalised enough to be "portable" to different instruments' domains.
- Ensure that the process to collate and document the information is agile and time-effective (i.e. not heavy).
- Consider the outcome as live-documents to progressively enrich, and not as just one-off snapshot static pictures taken at a certain point in time.
- Share them with future mission's interfaces to capture their feedback and interest, also as a further way of tuning them.
- Define a clear standard content structure, covering systematically four aspects (see picture below).

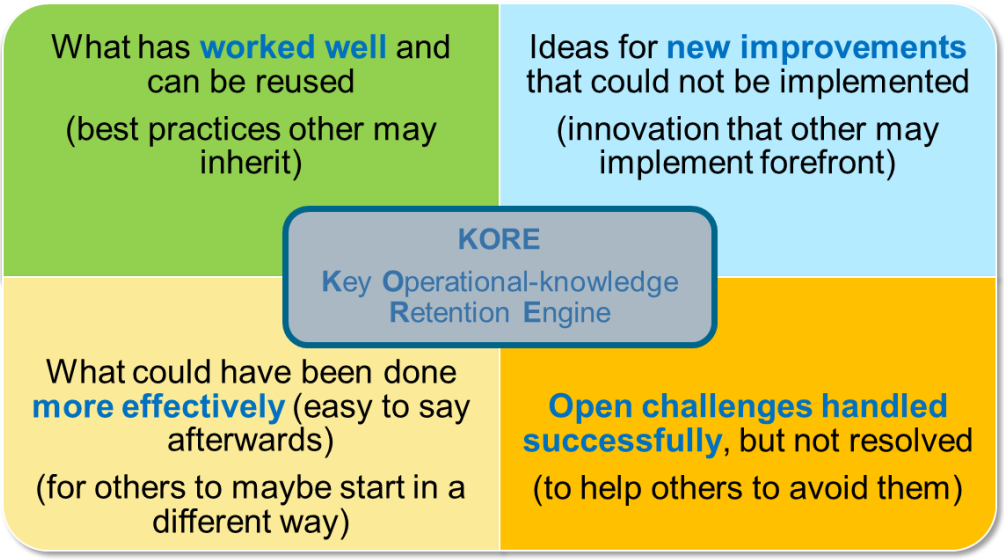

Figure 111: The Key Operational-knowledge Retention Engine (KORE).

Topics Addressed

- Following the defined strategy, some areas were identified.
- They cover Configuration Management, Anomaly and Change Management, Systematic Quality Control, Operational Software Verification, Outreach, LTDP (Long-Term Data Preservation), and QWG (Quality Working Group)

Overview of results

- An extensive replication of the complete results recorded in these documents would not be effective. So, in the next sections we aggregate them by type and focus only on major highlights:
- Key Best Practices emerged
- Key Challenges handled successfully (but improvements are recommended)
- An important element to add here is that the effectiveness of the exercise in terms of resource required (which was one of the key risks) was fully achieved, with impact on the involved people being actually very low, confirming the part of the pilot that proves the sustainability of exporting the model also to future missions.
- Last element to mention is that these KORE-TN documents were distributed to some future Earth Explorers ESA-SPPA (Sensor Performance, Products, and Algorithms) managers, receiving useful feedback and appreciation.

Key Best Practices emerged

- The following list is an excerpt of the most significant best practices emerged in Aeolus that could be reusable in future missions:
- Existence of a flexible collaborative platform (DISC internal sandbox)
- Processor Evolution documents, to trace software CI history
- Unique structured interface towards PDGS Operations
- Integrated layer covering Anomaly, Change and Configuration management
- Hierarchical and agile structure of the Configuration Management Plan

- Integrated Operational SW and AUX verification processes, leveraging the sandbox and a dedicated system bridging with the PDGS (build and filter)
- Dedicated Outreach service structure, joining scientific coordination and operational activities
- Distributing LTDP readiness and transition incrementally over the full Phase F

Key Challenges handled successfully (but improvements are recommended)

- The Aeolus mission had to handle several challenges through its life. All of them were managed in a very satisfactory way. Nevertheless, we learnt that doing things (frequently forefront) in a different way could have helped to make them better or smoother or with less pressure or less effort. As such these further improvements are a valuable asset for missions that are still in a stage in which these optimizations can be done:
- Bridging the different Anomaly Management tools (DISC operations, PDGS and tracking of prototypes anomalies) and Configuration Management tools (DISC operations, PDGS)
- Operational and Reprocessing activities overlapping
- Configuration Management of Prototypes wrt Operational SW
- PDGS operations and DISC verification platforms synchronization (DOS build VM and DISC sandbox)

5 L2A and L2B Product Monitoring, Cal/Val and Outreach

5.1 Reprocessing of Aeolus data products

Oliver Reitebuch, DLR

5.1.1 Introduction

The Aeolus algorithms and processors were continuously improved which resulted in operational processor and baseline updates about every half year in phase E. This resulted in improvements for the near-real-time NRT data products from the date of the deployment of the processor baselines at ESA´s Payload Data Ground Segment (PDGS). Thus, different baselines and resulting inhomogeneous product format and qualities were available for the NRT product during the mission lifetime. In order to improve the product quality from dates before the baseline update and also to provide data products over a longer period, which are processed with the same processor baseline and homogenous data format and quality, a reprocessing task started within the DISC in January 2020. In hindsight, it would have been preferred to already start with this reprocessing activity at the begin of the DISC activities in early 2019, e.g. with reprocessing of the commissioning phase E1 data products, but at that time other activities were of higher priority.

A number of DISC institutes and colleagues are involved in this activity including DLR, ECMWF, KNMI, Météo-France (until end 2022), TROPOS (from 2023 on) and Serco. In total more than 10 persons are involved with a significant amount of their allocated time (10% to 80%), which demonstrates the large effort needed for this activity. More than 1 year was needed for each reprocessing campaign, which mainly covered the different operating periods for the lasers, e.g. FM-A or FM-B as the product quality and the processor settings are largely depending on the laser.

5.1.2 Summary of four reprocessing campaigns

The activity for the first campaign started in January 2020 for the reprocessing of the early FM-B period from end June to end Dec 2019 using Baseline 10 of the processors including patches (L1BP 7.08.2, L2AP 3.10.1, L2BP 3.30.1, January 2020 delivery). The main activities are described in the TN for the 1st re-processing campaign (DISC-DLR, 2020a,b). This first re-processing campaign was finished with the delivery of the verification report by DISC (DISC-ECMWF, 2020) on 13 October 2020 and the public release of the re-processed data products on 14 October 2020 by PDGS.

The second re-processing campaign for the FM-B period covering June 2019 to October 2020 was using the Baseline 11 processor versions from the summer 2020 delivery (L1A/L1B 7.09.1, L2A 3.11.1 and L2B 3.40.2). The main activities started in November 2020 with the tasks as described in the TN for the 2nd re-processing campaign (DISC-DLR, 2021a,b). The data products from the second reprocessing campaign were publicly released on 11 October 2021 by PDGS and corresponding verification report was prepared (DISC-ECMWF, 2021).

The third reprocessing campaign covering the FM-A period from August 2018 to June 2019 was processed using the Baseline 14 processor versions which includes L1B 7.12, L2A 3.14.8 and L2B 3.70. as described in the corresponding TN (DISC-DLR, 2022). The verification report (DISC-ECMWF, 2023) was prepared by ECMWF as V1.0 (27 February 2023, and updated as V1.01 on 6 June 2023). The data products from the third reprocessing campaign were publicly released on 22 November 2021 by PDGS.

The fourth re-processing campaign will cover the full mission timeline using B16 processor versions (L1B 7.14.3, L2A 3.16.4, L2B 3.90) and is performed in 2 phases. First phase will cover the full FM-B period (June 2019 to September 2022) and is expected to be finished with a public release in spring 2024. The second phase will cover the different FM-A periods (August 2018-June 2019, and December 2022 to end April 2023) and is expected to be finished in spring 2025 and performed in cooperation with an external service to ESA as part of the DISC phase F1 activities.

The DISC verification reports for all reprocessing campaigns and a summary were made available on ESA´s eogateway website (https://earth.esa.int/eogateway/missions/aeolus/data). An overview of the time period, baseline and release data for the 4 reprocessing campaigns is provided in Figure 112.

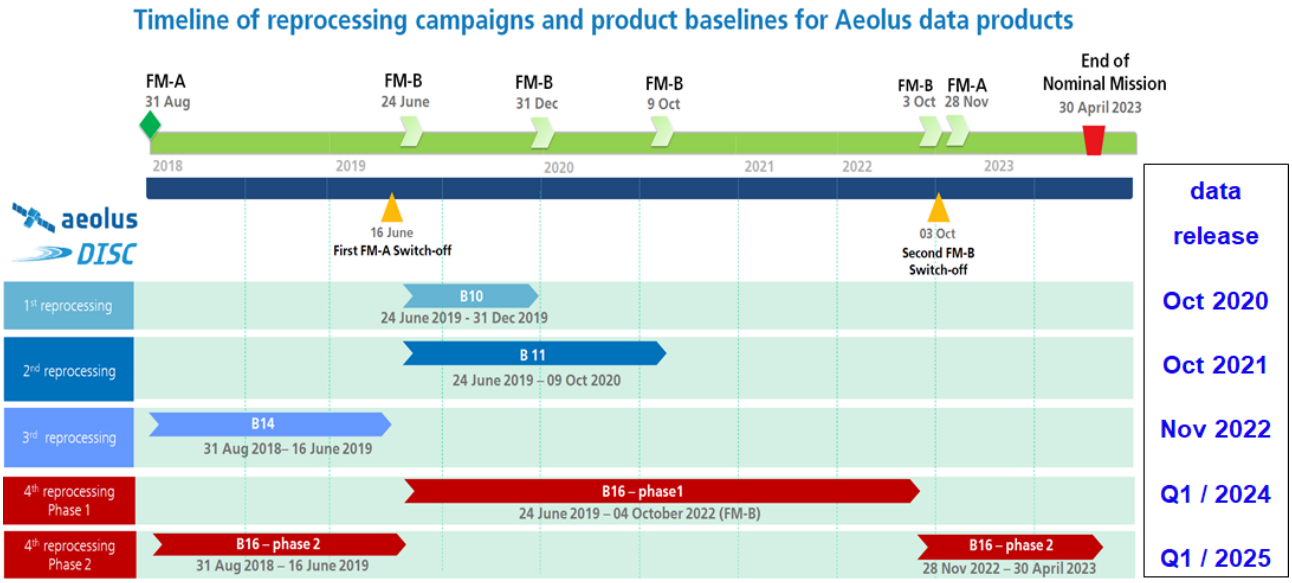

Figure 112: Timeline of the four reprocessing campaigns and product baselines (B10 to B16) for Aeolus data products covering different FM-A and FM-B laser operating periods; month/quarter of the public release of the data products by PDGS is indicated on the right.

The following major improvements for data product quality were implemented for the different reprocessing campaigns:

1st reprocessing covering period June to December 2019 (FM-B) with Baseline 10

- correction of hot pixels also in time periods between dark signal measurements (DUDE) for the L1B product
- M1-bias and drift correction of L2B winds with daily updates using ECMWF model correlation to M1 temperatures (M1-bias correction)
- use of orbital means for radiometric calibration (K_{ray}, K_{mie}) of L2A products (SCA) and improved quality control and flagging

2nd re-processing covering period June 2019 to October 2020 (FM-B) with Baseline 11

- filling of gap in L2B wind M1-bias correction from Jan-May 2020 and consistent processing for 15 months of data
- small improvements in L1B corrections for hot-pixels and M1-bias correction for L2B
- calibration of L2A product (SCA) with varying radiometric calibration (K_{ray}, K_{mie}) along the orbit

3rd re-processing covering period September 2018 to June 2019 (FM-A) with Baseline 14

- first time L1B hot-pixel correction for FM-A period
- first time L2B M1-bias correction for FM-A period
- first time orbital radiometric calibration for L2A product and
- first time that L2A products for AEL-PRO, -FM and MLE are available, although AEL-PRO, AEL-FM are still flagged invalid in B14

4th re-processing campaign covering June 2019 to Oct. 2022 (FM-B period) with Baseline 16

- first time consistent data set for full FM-B period
- wind bias correction improved for Mie winds (non-linearity) and Rayleigh cloudy winds
- more realistic L2B Rayleigh wind error estimates due to better L1B SNR estimates
- L2A aerosol products valid for AEL-PRO, -FM,
- L2 aerosol product with higher resolution product for MLE

5.1.3 Strategy and effort for reprocessing

The strategy and the different tasks for each reprocessing campaign evolved due to the experience of the previous campaigns, the challenge of incremental refinements or improvements for each campaign, and the updates in algorithms, processors and parameter file for each baseline update. The reprocessing mainly consists of an iterative loop of defining updates (e.g. in parameter AUX-Files), testing it on limited time periods on the chain-of-processors ("Sandbox") at KNMI, and validation of the results. This definition and testing of parameter updates would not have been possible without the availability of a DISC internal full chain of processors including L0, L1A, L1B, L2A, L2A processors and calibration processors in the so-called Sandbox at KNMI. This sandbox was already set-up before launch and further evolved during phase E. After delivery of the full set of auxiliary input files from DISC to PDGS, the reprocessing of the complete period is then performed on computers by PDGS (in parallel to the NRT production, which caused some constraints) before providing the products to the users on the Aeolus Data Dissemination Facility (ADDF). The data quality of the products was then assessed by the DISC and two data quality documents were prepared by the DISC and provided to the users by PDGS (summary of quality, verification report).

Each reprocessing campaign was structured into 18 different tasks/work packages with a strong interaction between these tasks and the different processors and product levels. Details for each reprocessing campaign and results are reported in TNs from the DISC (2020, 2021, 2022). 17 tasks are performed by the DISC, while one task of reprocessing the complete period was performed by PDGS with interaction to DISC for validation of products. The complexity and interaction of the different tasks is shown in the flow-chart below, with task split mainly along different product levels, corrections, reprocessing on the Sandbox or by PDGS and validation.

Not going into the details of each task, the major activities are discussed with the example of the latest 4th reprocessing campaign for the full FM-B period (June 2019 to October 2022) covering 28 months with a total of about 17400 product files per product level (usually a product file covers 1 orbit, some are covering more than 1 orbit). The 4th reprocessing campaign involves ESA-PDGS and all DISC partners with DLR, DoRIT, ECMWF, KNMI, TROPOS, serco with about 11 persons from DISC involved (by more than 10% to 80%) over a period of about 1 year. The main activities involve an iterative loop of preparation inputs, reprocessing and validation products structured in 16 tasks.

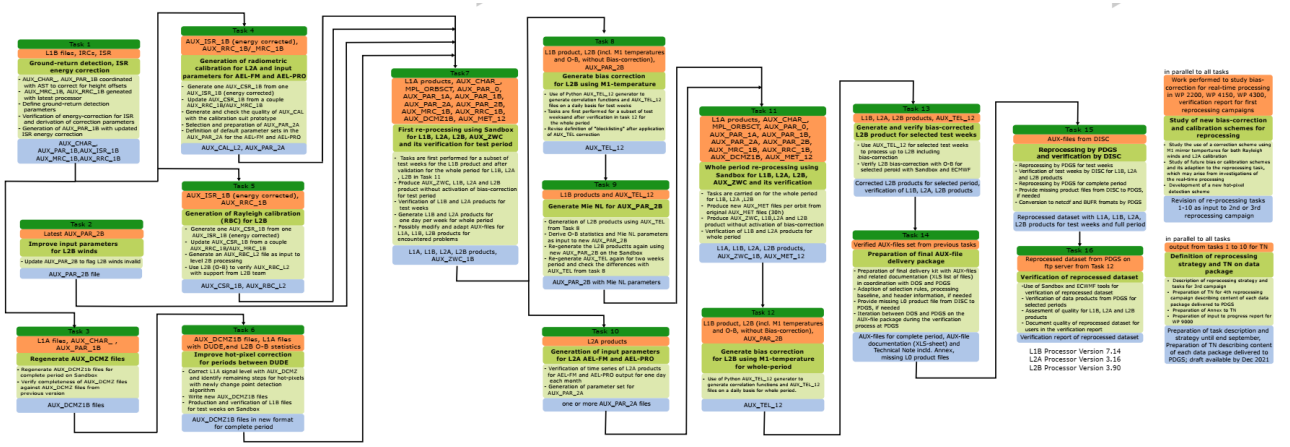

Figure 113: Flow chart of 18 tasks for the 4th reprocessing campaign of the full FM-B period as an example of the complexity of each campaign; the 2 tasks on the right are performed in parallel to the other 16 sequential tasks.

Most of the preparatory tasks and its validation are performed with dedicated software tools for this specific purpose, developed and improved by the different persons involved in this activity. Those tools are basically manual or semi-automated approaches for preparation of processor input files (AUX-files) and validation of products including visual inspection of daily to weekly plots. The full details of the activities for the 4th reprocessing campaign are reported in a DISC TN (DISC-DLR, 2023). Here the high-level tasks are shortly discussed:

- Hot-pixel correction on L1B level (AUX_DCMZ) for more than 4000 hot-pixel jumps during the FM-B period; this involves updates of the measured AUX_DCMZ files to the latest baseline format changes, detecting of hot-pixel steps using the L1A and L1B product, modifying measured AUX_DCMZ files for additional hot-pixel jumps or creating additional AUX_DCMZ files for periods in-between the DUDE measurements (4-8 times per day during FM-B period, due to the increasing number of hot-pixels). As the hot-pixel correction can only be performed with a single AUX_DCMZ files as input to the processing of one L1B product, the correction is performed on product file (orbit) level. Sub-orbital changes or jumps in the dark currents cannot be corrected with this method.
- Definition and testing of calibration inputs for L1B (AUX_MRC, RRC), L2A (AUX_CAL) and L2B (AUX_RBC): several calibration files for different periods to cover instrumental drifts during FM-B period were prepared; a remaining altitude-dependent wind bias is still observed in the data products (B16), which is related to the choice of the L2B calibrations; this needs to be improved for 5th reprocessing. It shows that the L2A and L2B calibration is still not fully consolidated and improvements are possible.
- L2B wind bias correction with daily updates of AUX_TEL files for correction of M1-Temperatur induced bias, drift and orbital harmonic.
- Derivation of Mie non-linearity correction using ECMWF model with 2 different sets of correction parameters to cover the FM-B period; This correction improves the Mie wind-speed dependent error. A validation showed that a monthly update of this correction is needed for the 5th reprocessing, as the instrument alignment is not stable enough.
- Derivation of correction parameters for Rayleigh cloudy winds with 3 different parameter files to cover the FM-B period. This correction for Mie contamination on the Rayleigh channel removes a large portion of the Rayleigh cloudy wind bias. Validation showed that a monthly update of this correction is needed for the 5th reprocessing due to instrument drifts.

- Definition of blocklisting (data invalid) periods for the L2B product using the ECMWF model as a reference to detect gross outliers due to e.g. instrument testing periods.
- Definition of processor parameter settings, which are contained in the files AUX_CHAR, AUX_PAR-1B, AUX_PAR-2A, AUX_PAR-2B; those AUX-files contain about 1500 (L1B), 500 (L2A), and 1000 (L2B) parameter values to control/adapt the processors; only a few percent of these parameters need to be adapted carefully and changes need to be tested thoroughly.
- First reprocessing of 8 test weeks covering FM-B period with DISC chain-of-processors ("Sandbox" at KNMI): 4 iterations with validation and updates of AUX-files were needed for this task.
- Reprocessing of full FM-B period on Sandbox up to Level 2B: three iterations were needed for L2B product.
- Preparation and verification of final package from DISC to ESA-PDGS with processors and AUX-Files: about 15 000 AUX-Files were prepared for FM-B period including 13 600 hot-pixel files (AUX_DCMZ), and 1200 L2B bias correction files (AUX_TEL); here a careful adaption of the validity times, selection rules and temporal coverage analysis is needed.

The effort for the reprocessing tasks were significantly larger than expected at the time of the DISC proposal preparation as well as the preparation of the CCN for reprocessing. Despite the relative low number of processors and output products (L1B, L2A, L2B), the reprocessing was a major activity within the DISC involving almost all consortium members. This significantly larger than expected effort is due to a number of reasons:

- Large number of parameters with significant changes for each baseline in the AUX_CHAR and AUX_PAR files for processor configuration, which were resulting both from algorithm refinements and improvements but also to cope with different instrument configurations and for mitigation of instrument anomalies.
- A significant effort was spent on characterizing and correcting for hot-pixels on the ACCD. A specific instrument mode (DUDE) was introduced some months after launch to measure dark currents, which were used for NRT correction on a regular basis per day. But the remaining hot-pixel jumps in periods between DUDE´s (several hours, several orbits) could only be corrected for reprocessing. Several persons at DLR were involved in this activity.
- The different illumination of the spectrometers for the FM-A and FM-B laser and the different operating points wrt. laser frequency and its position wrt. Rayleigh filter A and B crossing point and Mie useful spectral range (USR) caused the need for different calibrations for L2A product (AUX_CAL) and response calibration for L2B product (AUX_RBC). Actually, this issue could have been approached via a limited number of calibrations, but it turned out that the alignment itself was not stable over time. This resulted in the exploration of several calibration strategies (e.g. using IRONCS), which is not fully consolidated up to now.
- Instrument anomalies, instrument testing periods, instrument setting changes may result in a need for adaptation of calibrations and AUX_PAR settings.
- Instrument drifts on a daily basis together with a strong dependency of the alignment and the corresponding spectrometer responses with the primary mirror M1- temperatures causing the need for a daily update of the respective L2B wind correction via the AUX_TEL generator and file. As the AUX_TEL file content depends on both L2B calibration and inputs, it needs to be reprocessed for each day during reprocessing.

- A new concept to determine the Mie wind non-linearity was introduced by using the ECMWF model. The non-linearity was determined using off-line software tools and monthly datasets. As it turned out, that the instrument is not stable, the Mie wind non-linearity needs to be updated on a monthly basis.
- Introduction of parametric corrections for Rayleigh cloudy winds using ECMWF model; both the determination of the Mie non-linearities and the Rayleigh cloudy parameters need the reprocessing of the L2B product several times at the Sandbox with different parameter settings.
- Strong interdependency of the activities at least for the L1B-L2B chain including the wind-bias corrections.
- The envisaged automated calibration concept using the ACMF-C, which was setup before launch and included the harmonic bias estimator, had to be abandoned due to the unexpected instrument anomalies as hot-pixels and alignment drifts and orbital variations, which needed a more complex bias correction approach using the correlation between primary mirror M1-temperatures and the ECMWF model winds.

It is clear that such an effort for reprocessing was also caused by the fact, that several tools were only developed after launch (knowing the anomalies and drifts) and work mainly manual or semi-automated. This is certainly acceptable for an Explorer type mission, where many issues are solved during operation, but such a large effort is probably not a feasible approach for an operational mission as Aeolus-2.

5.2 L2A quality monitoring

Dimitri Trapon, TROPOS, and Ping Wang, KNMI

5.2.1 L2A quality monitoring for SCA and MLE

Near Real Time data monitoring

The quality of the operational data, i.e. measurement processed within NRT operations using operational version of the L2A prototype, was monitored in a total of more than 200 weekly quality reports (CNRM/TROPOS, 2019-2024) using the main proxies described below:

- The Rayleigh signal prediction in aerosol-free regions of the atmosphere for the range 6 to 16km altitudes. A weekly monitoring of the relative error of signal prediction (i.e. (observed signal – predicted signal) / predicted signal) was performed. The prediction being used to derive a corrective factor for the calibration coefficients within the L2A prototype processing itself, this allowed to assess any degradation of the performance.
- The calibration coefficients K_{ray} and K_{mie}: Orbit averaged values and fitted ones per observation with telescope temperatures were processed each week. This helped visualizing the evolution of the instrument performance, the K_{ray} and K_{mie} being linked to the signal levels on the Rayleigh and Mie channels in particle free regions and characterizing the radiometric efficiency of the receiver including corrections, e.g. for laser energy, range, range-bin thickness, atmospheric temperature and molecular extinction varying along the orbit. Figure 114 shows the evolution of K_{ray} and K_{mie} coefficients. This allows to assess the behaviour of the atmospheric path signal. A continuous decrease can be seen for laser FM-B until switch to laser FM-A on 17 October 2022, the signal level being back to nominal after 3 weeks. A slight increase is observed until second switch to FM-B by 17 May 2023, the signal being then back to the lowest magnitude.

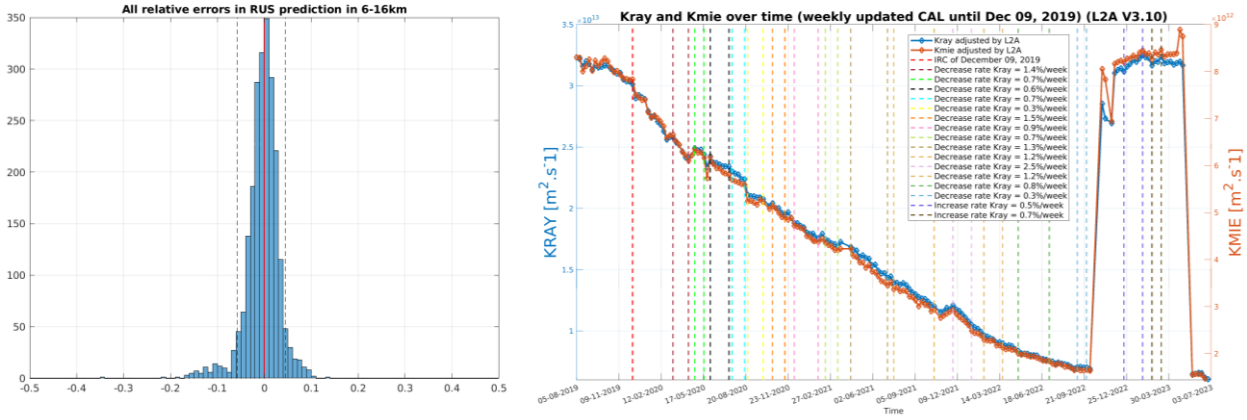

Figure 114: Relative errors ((observed-predicted)/predicted) for Rayleigh Useful Signal in 6-16 km altitude in particles-free regions of the atmosphere (left) for a whole orbit on 2023.04.24 and orbit averaged Kcoeff timeline by L2A Prototype Processor v3.10 (right) from August 2018 to July 2023.

- The crosstalk-corrected signals. The SCA makes use of the High Spectral Resolution capability of ALADIN. It uses both Rayleigh and Mie channels to perform so-called "crosstalk correction" to get separately attenuated molecular backscatter and attenuated particulate backscatter. This allows to retrieve particulate extinction and backscatter without any assumption on the lidar

ratio. Each week the pure molecular X_{ray} and particulate Y_{ray} signals were analysed using orbit of similar overpass.

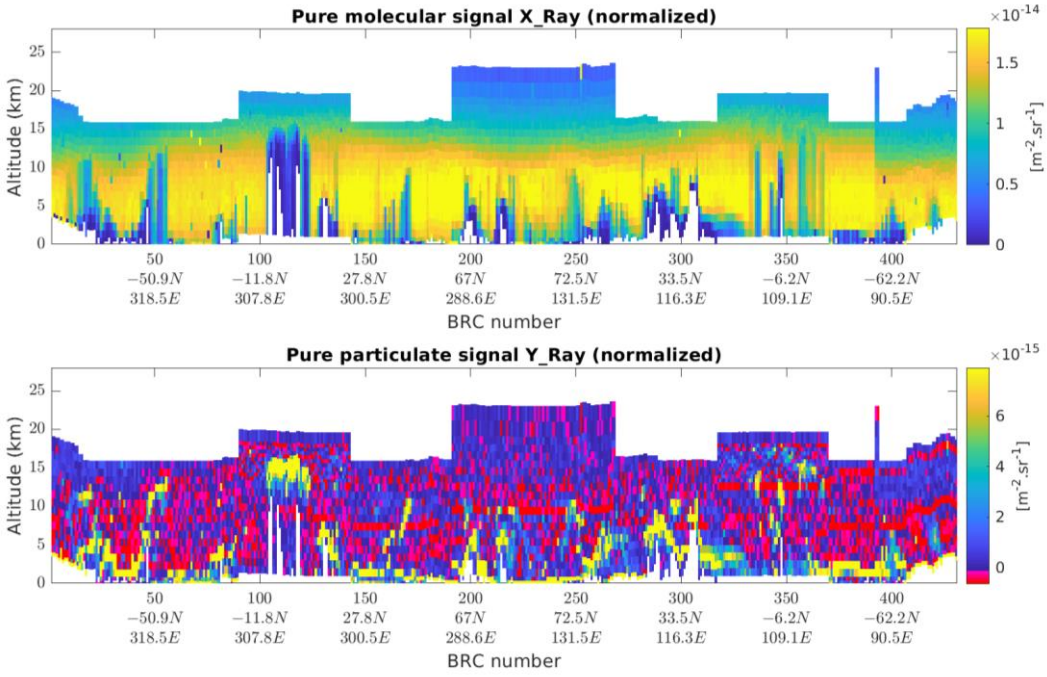

Figure 115: Crosstalk-corrected signals at observation scale normalized by bin thickness for second last Monday orbit on 2023.04.24. Negative values can be seen for pure particulate signal (bottom, light red) revealing non-perfect calibration.

- Comparison of predicted and observed pure molecular and particulate signals profiles. Profiles retrievals from ground to top range bin were selected each week to compare the pure signals. This allowed to show that the SCA slight overestimation of the observed pure molecular signal was reduced with the implementation of the new schemes of the radiometric correction.

Reprocessed dataset validation

Extended dataset of Aeolus observations can be processed with later version of the L2A operational code, the so-called reprocessing. The validation of the L2A output from SCA and MLE has been performed for four reprocessing during phase E using the following quality indices:

- Anomalous values of extinction and backscatter coefficients for particles were sorted in 3 categories (e.g. non-processed, negative, larger than 200 Mm^{-1} for extinction and 200 $Mm^{-1}sr^{-1}$ for backscatter) to easily point orbit discrepancies. Combined with a verification of bins flagged by QC these quality proxies have been used to easily point orbit discrepancies (see, e.g., Figure 116).
- Orbits with peaks in anomalous pixel fraction. A detailed analysis of orbits with unexpected scores and features was achieved when the Level-2A product showed limitations. It included truncated orbits due to special operations and localized ones with specific conditions, e.g. top most bin set in low altitudes or strong signal attenuation.
- Timeline of the calibration coefficients K_{ray} and K_{mie}. Both coefficients were analysed for all observation using the fitted values processed from the telescope temperatures regression.
- Absolute differences between reprocessed dataset. The reprocessing tasks were completed in two steps; first a processing was done DISC internally using the Sandbox. Then the Aeolus PDGS

processed the data which were publicly released. The quality of the PDGS dataset has been assessed by measuring the mean absolute differences with internal data either for calibration coefficients and main L2A products (e.g. extinction coefficients for particles, backscatter coefficient for particles, lidar ratio).

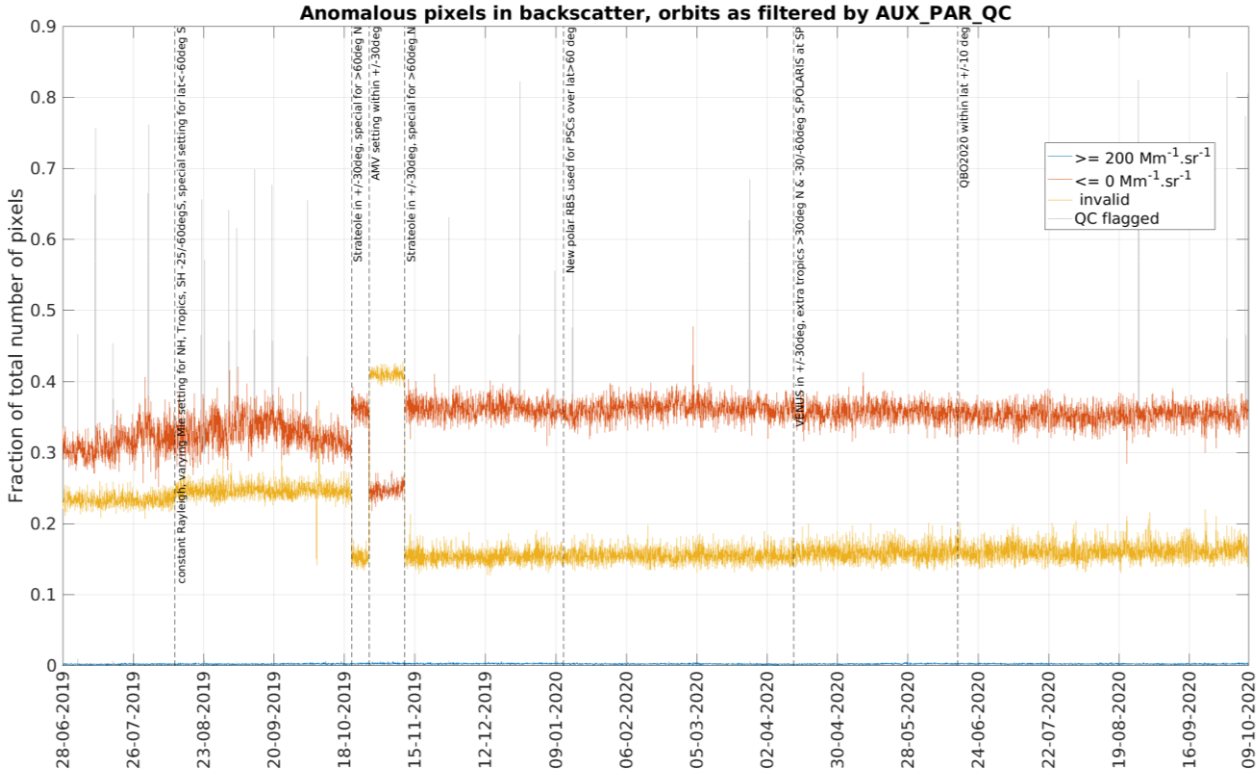

Figure 116: Anomalous pixels derived from SCA backscatter coefficient for particles for 2nd FM-B reprocessing campaign. Special operations and settings adjustment are indicated in vertical dotted lines.

Lessons learnt:

- Having a regular and detailed look at aerosol profiles per orbit allows to reveal aerosol layer of interest for ad-hoc analysis, e.g. Polar Stratospheric Clouds (PSCs) or wildfires smoke.
- Looking at in-orbits profiles from ground to top helps identifying deviations (e.g. hot pixels, spurious measurement linked to South Atlantic Anomaly (SAA) or attenuated signal) that may not always be revealed using statistics with extended dataset.
- Continuous monitoring of key performance proxies (e.g. calibration coefficients K_{ray} and K_{mie}) has provided further support to assess evolution of the atmospheric signal and the impact of special operations.
- Optimizing the laser configuration to get better SNR, e.g. adjustment of pulses accumulation and review of Range Bin Settings (RBS), may affect the performance indicator.
- The production of quick looks for L2A main product during NRT operations helps pointing the degraded orbit due to specific conditions.
- Planning validation campaign later in the mission (e.g. Tropical campaign ASKOS 2022) allowed to assess mature product validity. On-site participation of L2A developers was appreciated for data extraction and interpretation.

- The option for homogeneous horizontal resolution of sub-BRC level product (i.e. MLEsub algorithm) helps for reprocessing verification and may support application of extended dataset covering multiple periods (e.g. assimilation and validation campaign).

5.2.2 L2A quality monitoring for AEL-FM and AEL-PRO

The implementation of AEL-FM and AEL-PRO products was started in 2021, after the launch of Aeolus. The first public available AEL-FM, AEL-PRO products, which were flagged valid, were in the Baseline 16 release and the 4th reprocessing available for the FM-B period. The AEL-FM and AEL-PRO products in the L2A were verified with the prototype codes during the implementation in L2A processor from versions 3.14 to 3.17 (Wang et al., 2022a,b; 2023a). The products were also verified during the 3rd and 4th reprocessing (Wang et al., 2022c,d,e; 2023b,c,d). We found that the L2A and prototype products are almost identical for most orbits. Figure 117 and Figure 118 show an example of the verification of the prototype and L2A AEL-FM and AEL-PRO products for the L2A version 3.16.4. Figure 119 shows the Effective Mie Spectrometer Response (EMSR) derived from the MSP output for FM-A. The EMSR is different per detector pixel, which is expected. The EMSR value per detector pixel is quite stable in time, despite some outliers which could be due to hot pixels. The AEL-FM, AEL-PRO, and EMSR algorithms are described in the algorithm session of this report.

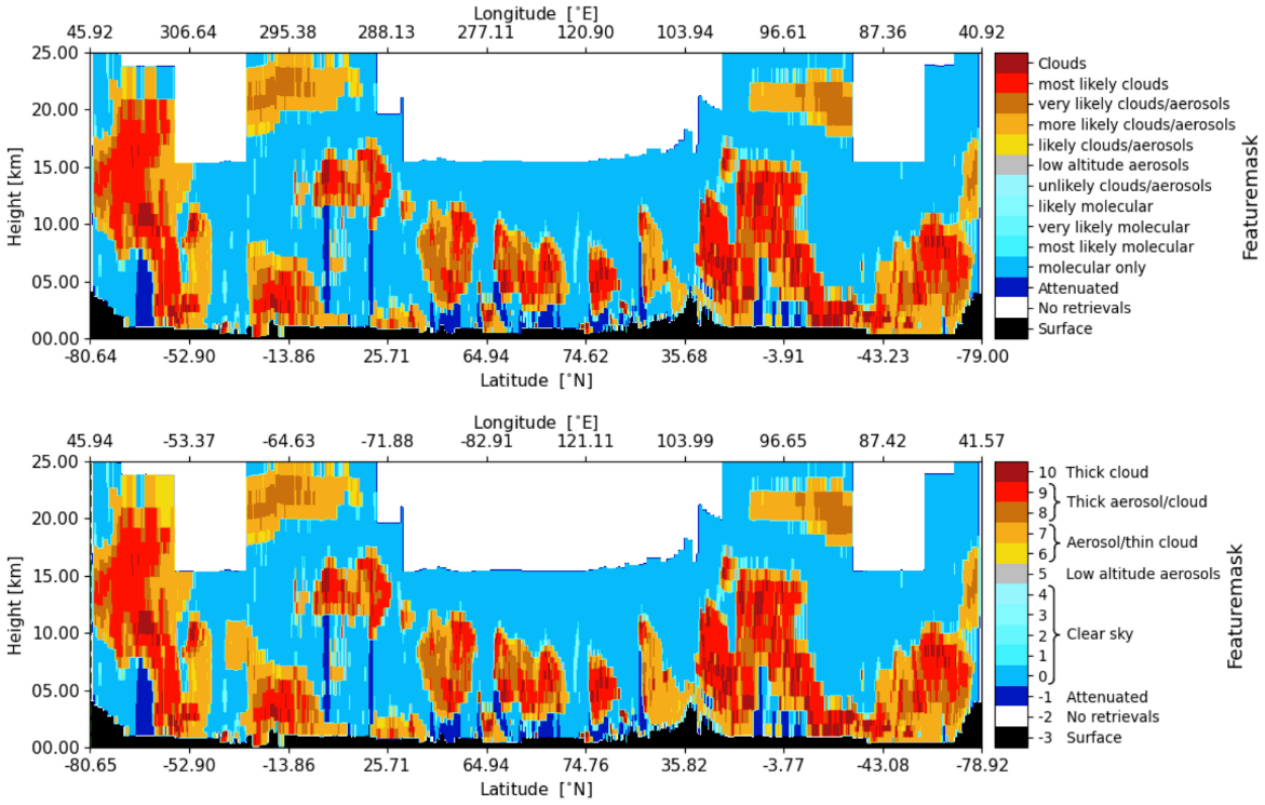

Figure 117: Comparison of the AEL-FM feature mask in L2A (upper image) with the prototype product (lower image) for orbit #23453 on 2022-09-09. L2A version 3.16.4.

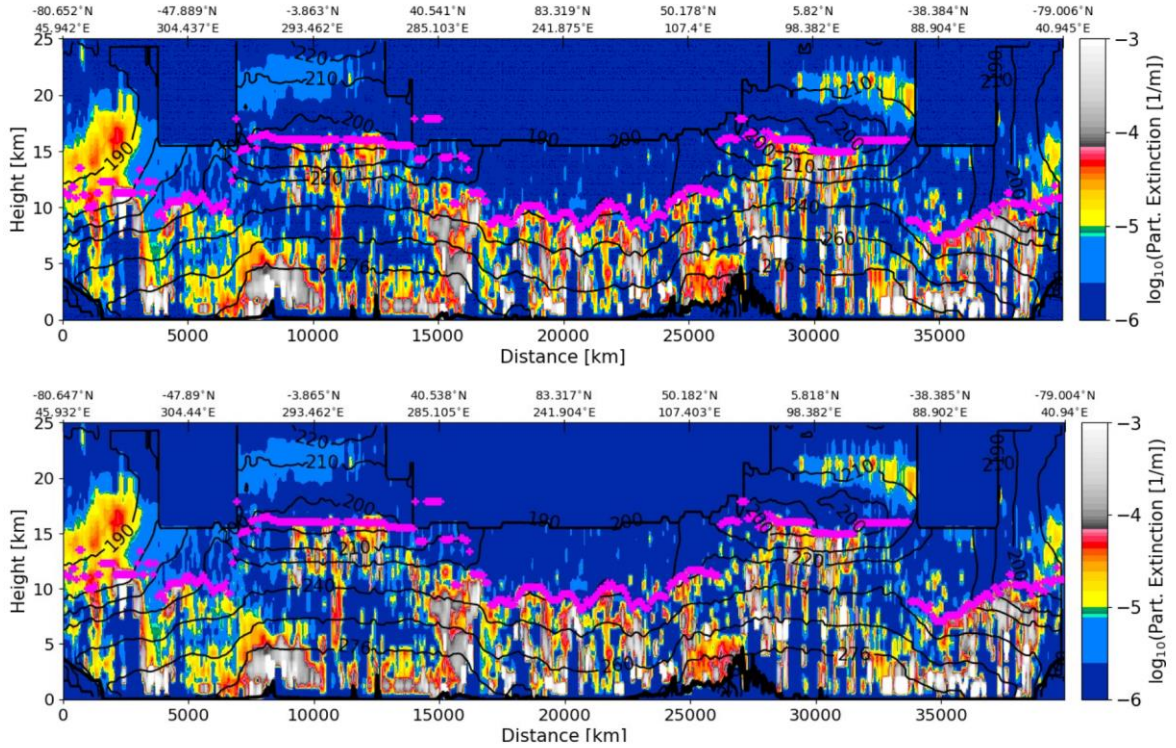

Figure 118: Comparison of AEL-PRO extinction coefficient profiles in L2A (upper image) and the prototype (lower image) for orbit 23453, 2022-09-09. L2A version 3.16.4.

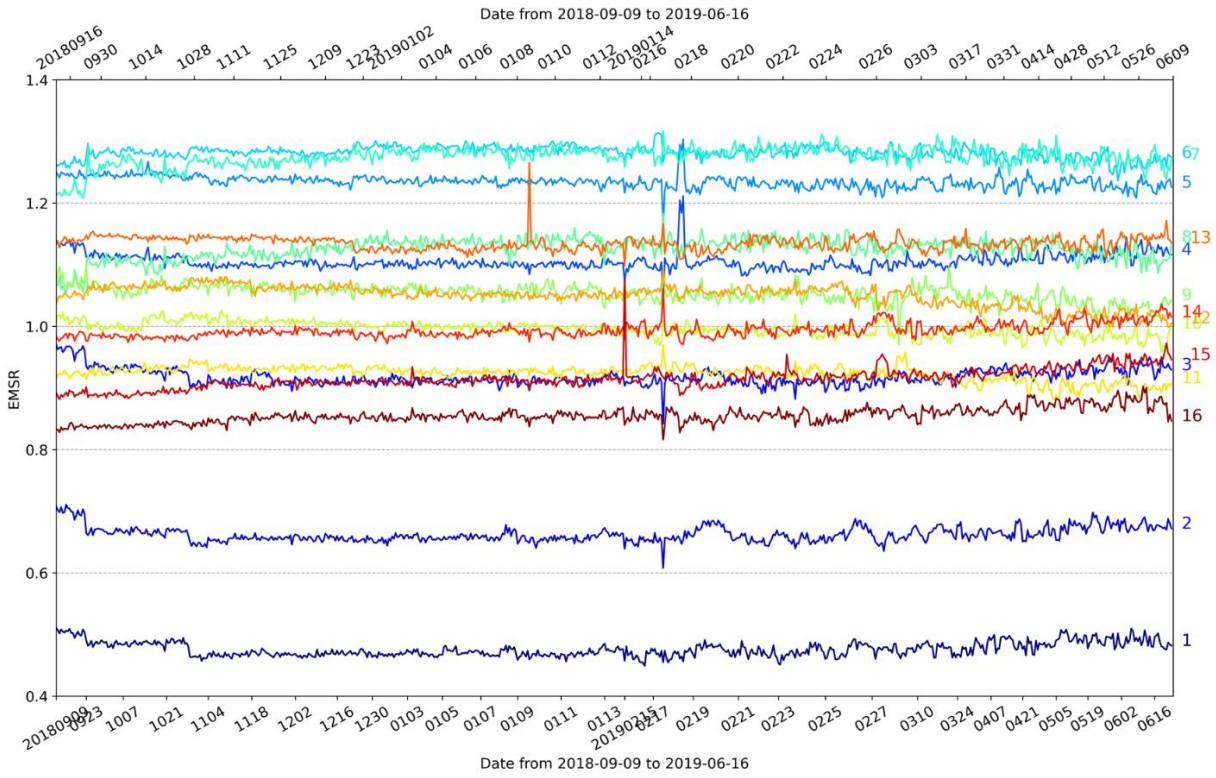

Figure 119: Time series of 16 EMSR values for each Mie pixel (colour-coded) from 2018-09-09 to 2019-06-16 (FM-A period). The data was taken from the L2A 3rd reprocessing data, Baseline 14.

The AEL-FM and AEL-PRO prototype products have been evaluated using the CALIPSO level 2 product (version 4.51, the latest version, https://www-calipso.larc.nasa.gov/). Figure 120 illustrates the comparison of Aeolus feature mask product with CALIPSO vertical feature mask for one orbit of data on 10 October 2018. We can see that Aeolus and CALIPSO measured similar aerosol and cloud patterns. CALIPSO detected dust aerosols and smoke aerosols. Aeolus detected similar features but no separation of the aerosols and clouds. The comparison of the extinction coefficient profiles between Aeolus (AEL-PRO) and CALIPSO is shown in Figure 121. The Aeolus and CALIPSO extinction profiles are comparable except that the Aeolus aerosol extinction coefficient profiles include some extinction coefficients from thin cirrus clouds above the aerosol plumes (at about 6 – 12 km altitude). Using the simple classification in the AEL-PRO product, most cloud contaminated extinction coefficients can be removed from the extinction coefficient profiles to get the aerosol extinction profiles. However, the separation of thin clouds and aerosols is rather difficult due to missing the cross polar channel in Aeolus. Similar results have been shown by Wang et al. (2022f, 2023e, 2024).

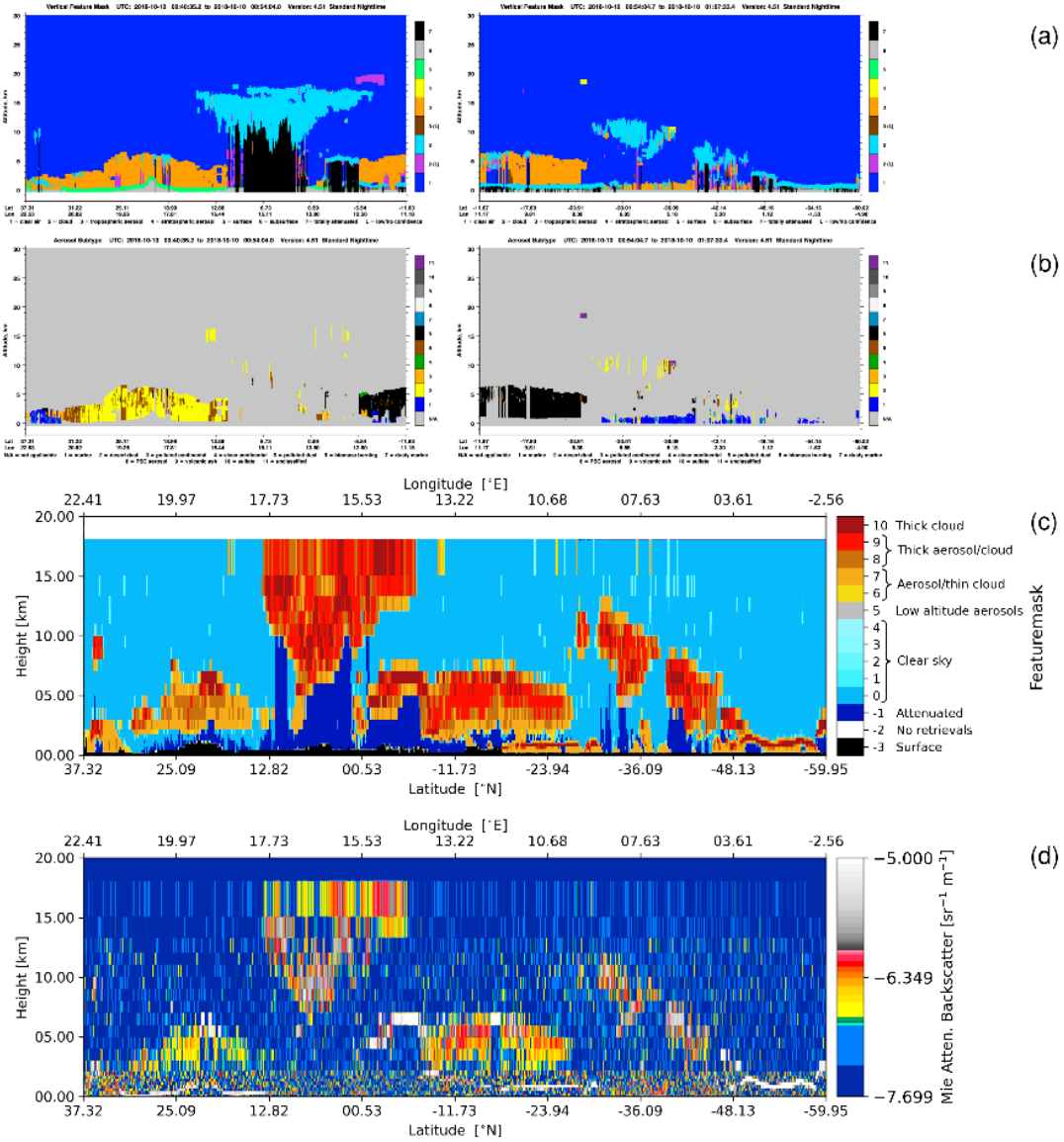

Figure 120: Comparison of Aeolus orbit 766 on 10 October 2018 and collocated CALIPSO orbit for feature masks, (a) CALIPSO feature mask, (b) CALIPSO aerosol subtypes, (c) Aeolus feature mask, (d) Aeolus Mie attenuated backscatter.

Summary and Conclusions:

- The feature mask algorithm should be the first algorithm in the processing chain. The signal to noise ratio of Aeolus is low, aerosol signals have to be averaged before applying the extinction profile retrieval. The feature masks are needed before the averaging of signals.
- Aeolus has no cross polar channel; therefore, no depolarization can be used to separate aerosols and clouds, also no aerosol types. The priori values of lidar ratio and effective area radius for aerosols and clouds are different in AEL-PRO, wrong priori values might be used for the mis-classified pixels, therefore the retrieved extinction coefficients and lidar ratio might have larger errors for these pixels. Aerosols and clouds have different climate effects. This is also a motivation to better distinguish aerosols and clouds.
- Due to the large vertical bin and horizontal pixel size, some bins may have mixed aerosol, cloud, and clear-sky. The retrieved products from these partly filled bins are less accurate than the fully aerosol or cloud bins.
- We derived the attenuated Mie backscatter and attenuated Rayleigh backscatter from the Mie spectrometer (Mie measurements) because the Mie and Rayleigh observations provided in the L1b were not good enough for the AEL-FM, AEL-PRO algorithms. For the Aeolus-2, we hope we can use Mie and Rayleigh signals directly from the L1b.

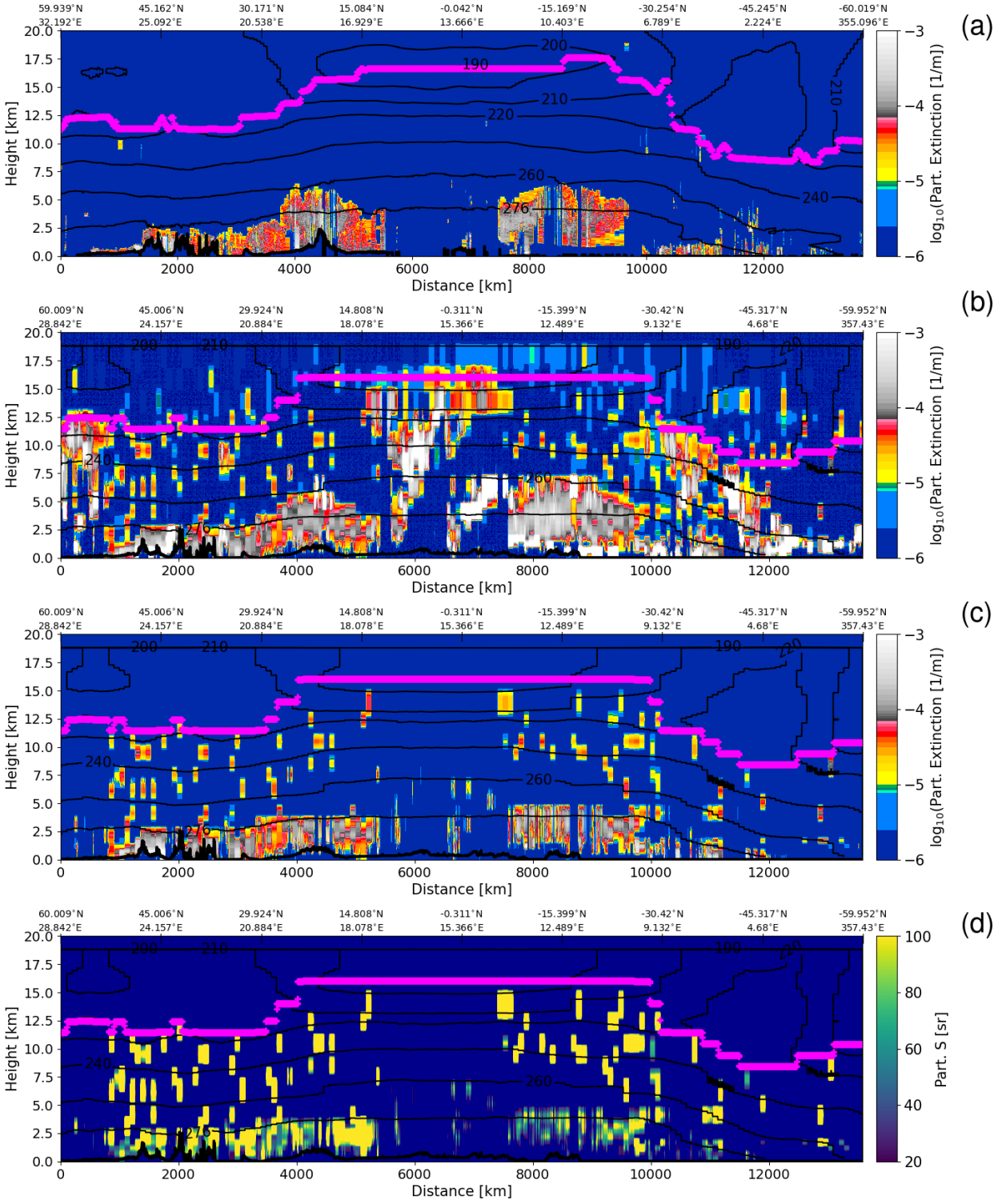

Figure 121: Comparison of Aeolus orbit 766 on 10 October 2018 with collocated CALIPSO extinction profiles, (a) CALIPSO tropospheric aerosol extinction profiles (L2 5 km aerosol profiles v4.51), (b) Aeolus extinction profiles for all measurements, (c) Aeolus extinction profiles for tropospheric aerosols, (d) Aeolus lidar ratios for tropospheric aerosols with extinction coefficients greater than 1.e-5 1/m. The black contour lines show the atmospheric temperatures. The magenta lines indicate the tropopause heights.

5.3 L2B quality monitoring using NWP model

Michael Rennie, ECMWF

5.3.1 Introduction

A state-of-the-art Numerical Weather Prediction (NWP) data assimilation system and forecast model, such as ECMWF's, is a powerful tool for monitoring and verifying a satellite-based meteorological observing system. To give an impression of the observations, a visualization of Aeolus Level-2B (L2B) HLOS (horizontal line-of-sight) wind data is shown in Figure 122.

The quality of the L2B wind data is assessed by comparing to the forward modelled HLOS wind from the ECMWF short-range forecasts (up to 12 hours, errors grow with forecast range). Statistics are calculated from observation minus background (or analysis) departures, from which estimates of observation systematic and random error statistics can be derived, given some knowledge of the background error statistics in HLOS wind space. The equations to obtain the error estimates are derived in the DISC NWP impact ESA Contract Report (Rennie and Isaksen, 2024). A great variety of tools have been developed for L2B data monitoring during the past years and only a small selection of the monitoring results has been covered in this summary for the Final Report.

5.3.2 Wind Monitoring

Daily updated, automatically produced statistics of L2B HLOS wind minus background (O-B) and observation minus analysis (O-A) were produced by ECMWF during the mission, on a publicly accessible ECMWF satellite monitoring webpage when Aeolus observations were available until end of April 2023. An example of the type of monitoring available during the mission is shown in Figure 123. A human interpretation of these statistics was provided in monthly reports, including insights into any relevant data events: the reports are still available on ESA's QRAS website. Quarterly reports were also produced, which were then included in the quarterly status reports from ESA.

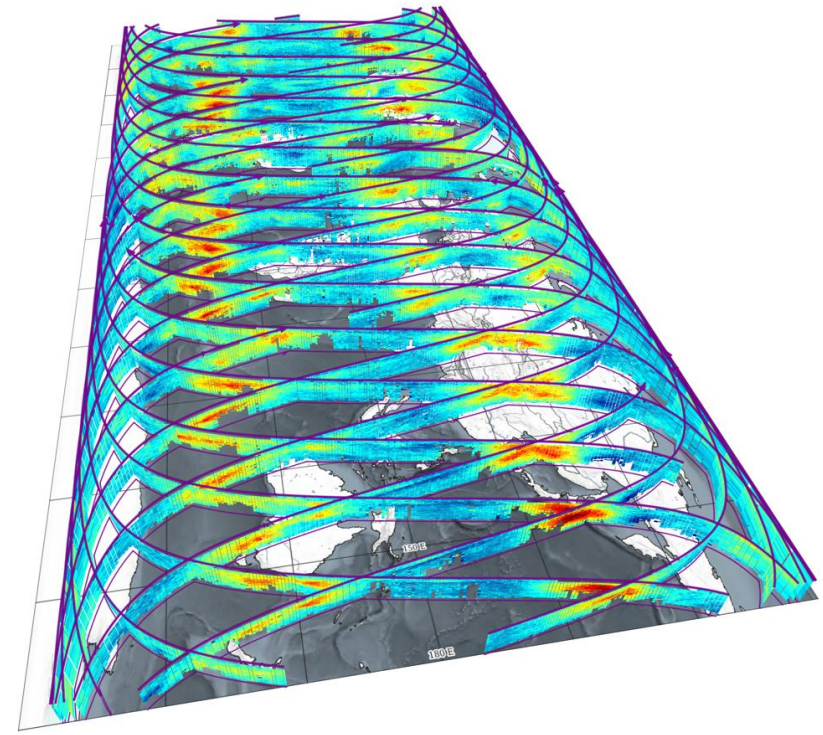

a)

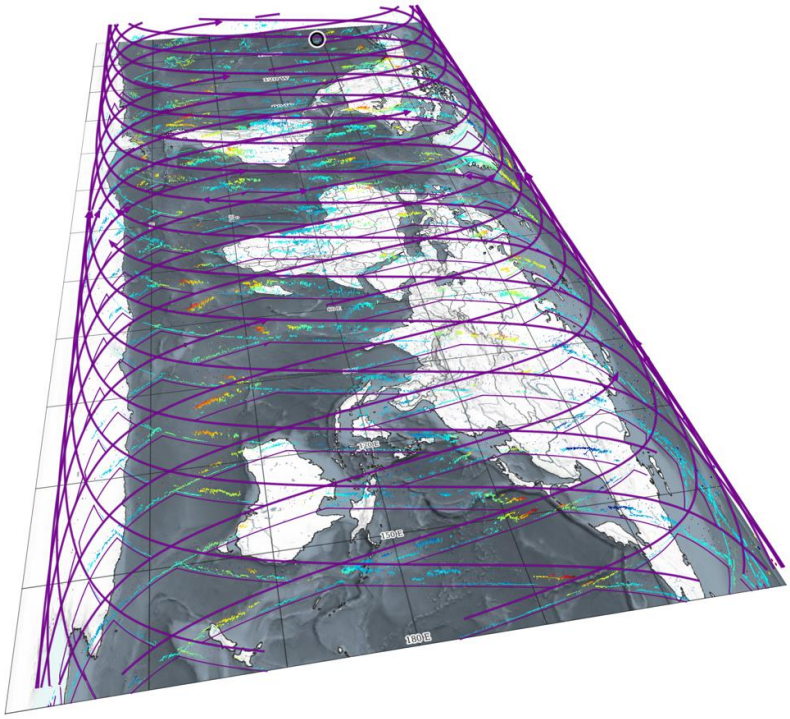

b)

Figure 122: A 3D map visualising one day's L2B HLOS wind data (15 November 2019) at B11 for a) Rayleigh-clear data and b) Mie-cloudy, from 0-20 km altitude. The HLOS wind has been altered such that descending orbits have positive (rather than negative) values for westerly jets (to match ascending orbits) to better highlight the strong jet streams e.g. in West Pacific. The colour scale represents the HLOS wind speed from -40 (dark blue, easterly for most of the orbit) to +80 m/s (red, westerly for most of the orbit). Created with the VirES tool (https://aeolus.services).

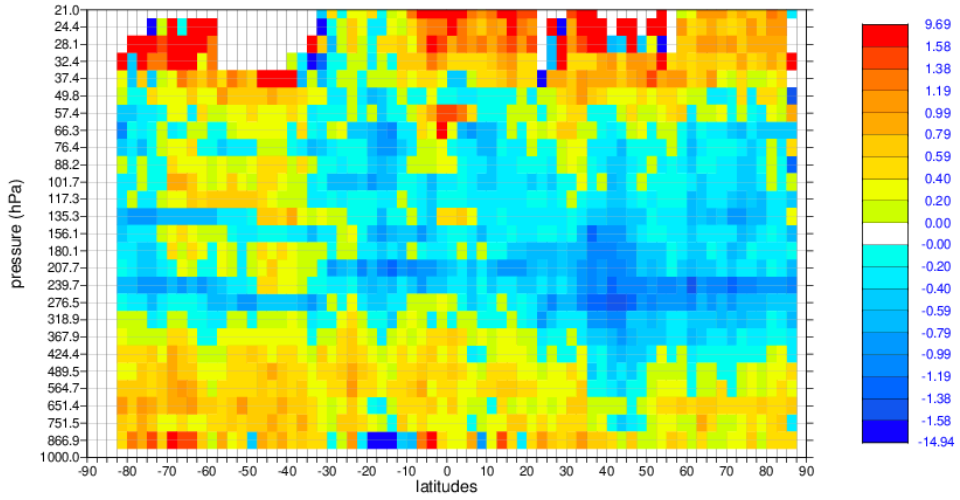

a)

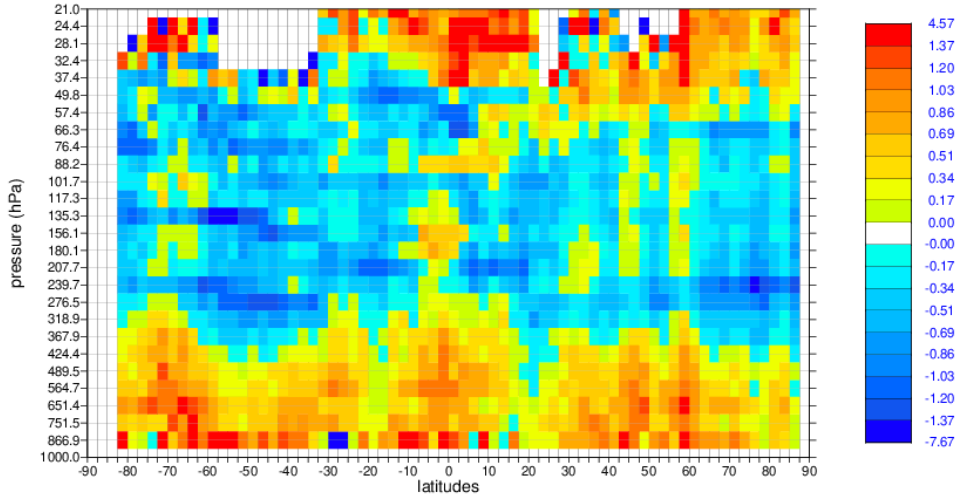

b)

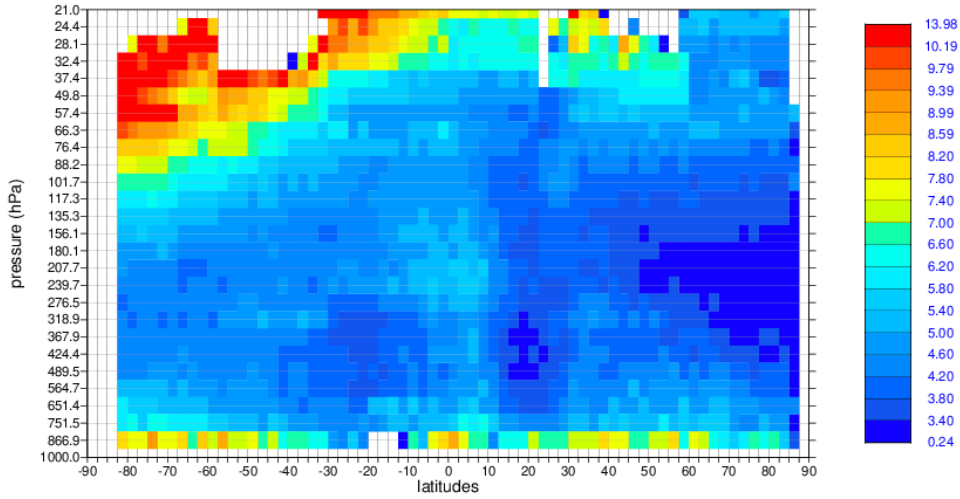

c)

Figure 123: Atmospheric pressure versus latitude dependence (zonal average) of the L2B Rayleigh-clear mean(O-B) i.e. bias for a) ascending and b) descending orbits. Panel c) is the standard deviation of (O-B) for ascending orbits. Unit: m/s. For the period: 1 December to 30 December 2022 i.e. with FM-A; from -90° (South Pole) to +90° (North Pole) latitude. 1000 hPa is approximately the surface as sea level, 500 hPa is ~4.5-6 km, 300 hPa is ~8-10 km and 100 hPa is ~15-17 km altitude.

Being a demonstration mission, Aeolus had its fair share of data quality issues. O-B departure statistics were very regularly relied on to provide information on data quality associated with such instrument problems. The statistics helped to first detect instrument problems e.g. hot-pixels (causing wind bias on specific range-bins), M1 temperature-dependent biases (causing large biases varying with geolocation and time), instrumental calibration issues (wind-speed dependent biases, altitude-varying biases), biases associated with instrument line-of-sight (LOS) mis-pointing due to moon-blinding, harmonic biases along the orbit for specific months, or biases caused by star-tracker switches, amongst others. The hot-pixel related biases on specific range-bins are evident in the 4th reprocessing DISC prototype L2B data product for FM-B data in 2022 (made worse due to low atmospheric path signals and an increasing number of hot-pixels), see Figure 124. The O-B monitoring was also employed during instrument test periods to assess performance e.g. laser settings adjustments, M1 mirror thermal control law testing and end-of-life tests.

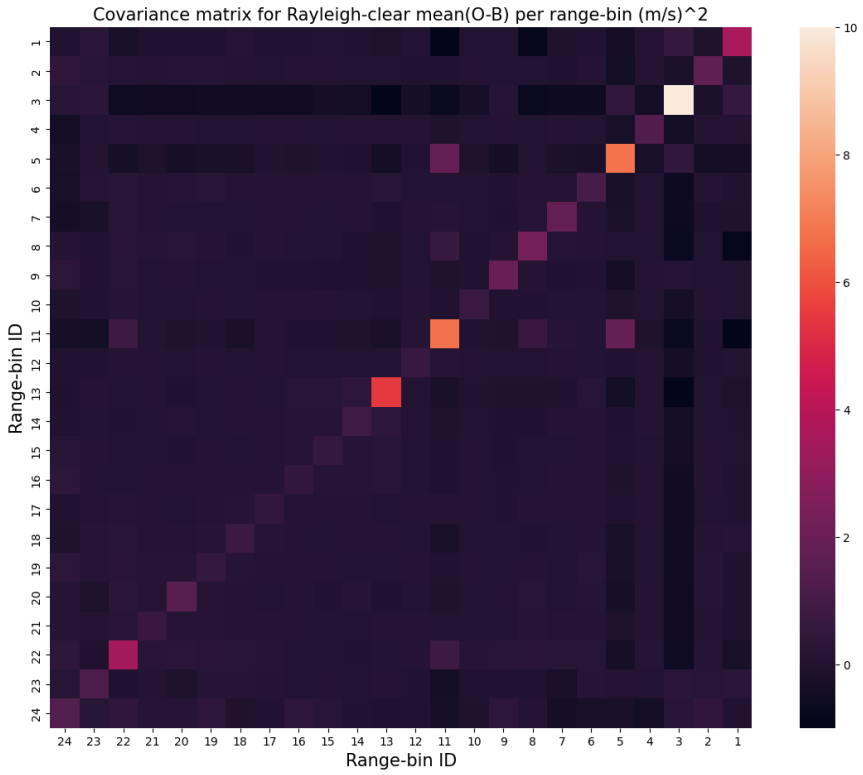

Figure 124: A covariance matrix for mean(O-B), i.e. wind bias, per range-bin constructed from mean(O-B) values per L2B file per range-bin, using FM-B data in 2022 i.e. January to October 2022 at B16 from the DISC's prototype 4th reprocessing. This highlights that range-bins 3, 5, 11, 13 and 22 had hot-pixel related bias issues that could not be adequately corrected.

The estimated L2B HLOS wind global average observation error statistics versus time are shown in the following paragraphs. Firstly, we show a time-series of the near-real time (NRT, PDGS-produced) data quality during the mission in Figure 125 and Figure 126, to represent what was seen at the time during the mission. These statistics are produced from the ECMWF operational long-window data assimilation (LWDA) statistics (apart from the first few months of the Commissioning Phase which used a research department (RD) experiment to fill the gap). Note that no QC based on L2Bp estimated error was applied in the time-series plots, due to it varying too much between processor baselines.

In 2018 and 2019 the NRT data HLOS wind global average bias (accuracy) drifted significantly with time (for periods longer than a few days), as is evident from the blue lines for both Rayleigh and Mie winds.

The observation bias is estimated as simply the mean(O-B), on the assumption that global average background bias is negligible (as confirmed by statistics of u-wind versus in situ wind observations, the blue error bars indicate the uncertainty on this assumption). In hindsight this was confirmed to be caused by instrumental drifts and the difficulty of obtaining high quality weekly calibrations (IRC) for automated updates, which would have compensated for such instrumental drifts. Global average Rayleigh-clear biases varied from being close to zero in some periods, to ±4 m/s in others due to the drifts. For example, for FM-B the global Rayleigh bias was drifting negatively at a large rate of around 1 m/s per month. The Mie-cloudy global average bias drifted during the Commissioning Phase (FM-A), but in contrast to the Rayleigh-clear, was more stable for early FM-B in 2019.

The random errors (precision, 1-σ) are shown by the magenta lines in Figure 125 and Figure 126. They are obtained by subtracting from the variance of O-B the background error estimated variance. The calculation assumes background error standard deviation of 2 m/s (the magenta error bar covers 1.5-2.5 m/s). Random error varied a lot for the Rayleigh-clear HLOS winds due to the strong sensitivity to atmospheric path signal levels (this is discussed further for the reprocessed data time-series). The bias stabilised in April 2020, due to the application of a bias correction scheme using the ECMWF model as a reference, as is explained in the next paragraph and Weiler et al. (2021). Biases did get worse again in May 2023 due to instrument testing during the end-of-life phase.

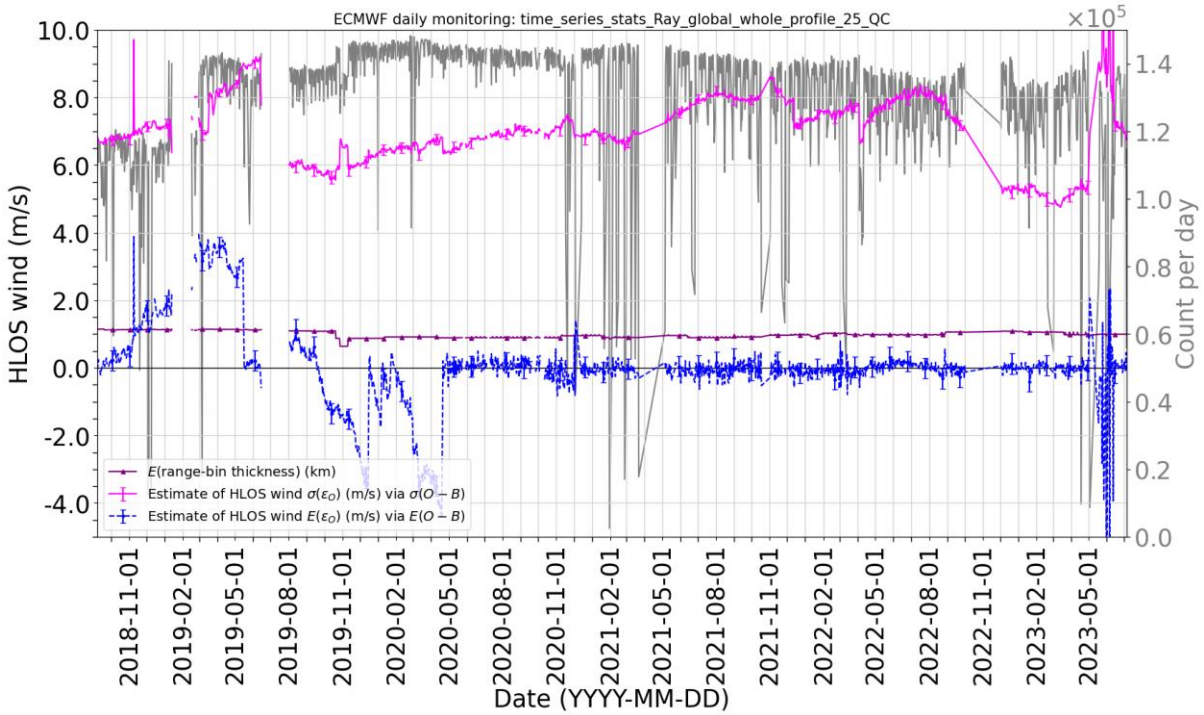

Figure 125: Time series of daily, global and all vertical-level *NRT dataset* L2B Rayleigh-clear O-B statistics, via operational monitoring from 7 September 2018 until 5 July 2023. The plot shows the estimated global average random error (magenta, $\sigma(\epsilon_O)$), systematic error (blue, $E(O-B)$), mean range-bin thickness (purple) and the data count per day in grey (on the right axis). Winds are rejected if flagged in valid or if $|O-B| > 25\ m/s$.

The NRT Mie-cloudy time-series in Figure 126, shows a remarkably stable random error, despite the processor baseline, instrument and also the average horizontal accumulation length (the additional green line) varying significantly with time for the NRT data. The mean horizontal accumulation was ~45 km during the commissioning phase and was reduced to ~10-20 km from 5 March 2019. The data counts passing QC (grey line) also varied considerably.

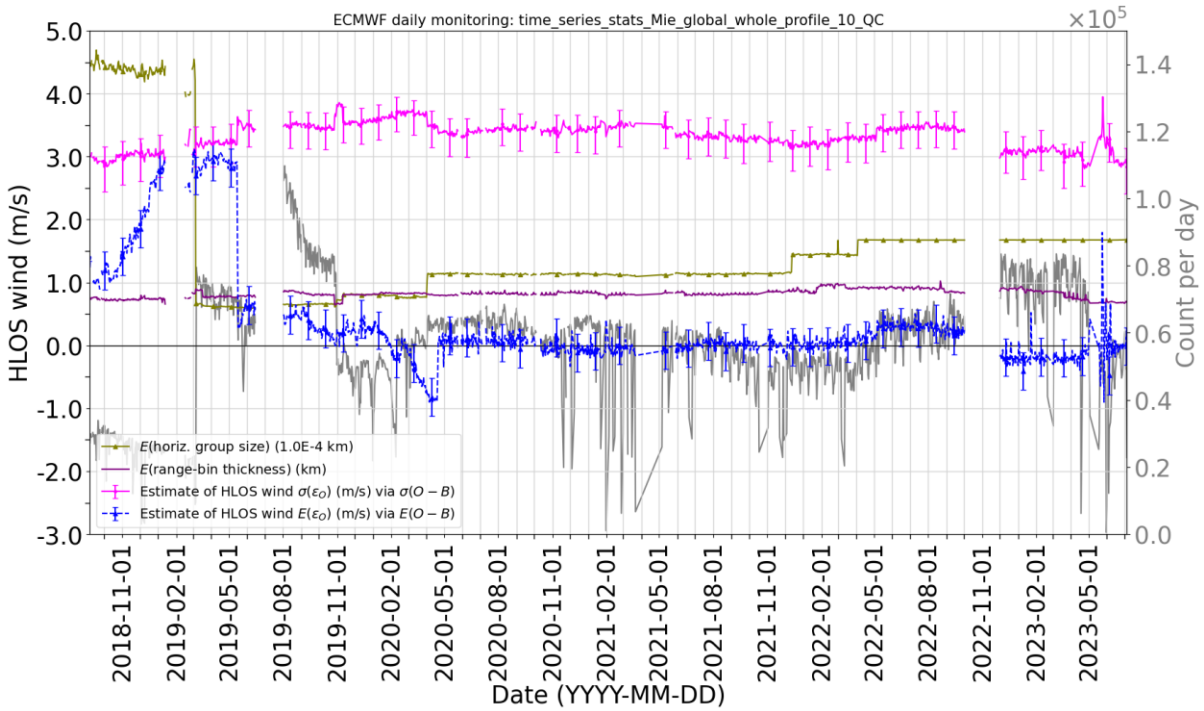

Figure 126: Daily time series of global and all vertical-level *NRT dataset* L2B Mie-cloudy O-B statistics, via operational monitoring from 7 September 2018 until 5 July 2023. The plot shows the estimated global average random error (magenta, $\sigma(\epsilon_O)$), systematic error (blue, $E(O-B)$), mean range-bin thickness (purple), mean horizontal-resolution of the L2B wind (green) and the data count per day in grey (on the right axis). Winds are rejected if flagged in valid or if $|O-B| > 10\,m/s$.

The quality of the L2B data has improved significantly during Phase E2 as the ground processing algorithms have improved. The time-series plots of Figure 127 and Figure 128 use reprocessed datasets when available i.e. the 3rd reprocessing (B14) covering the early FM-A period (September 2018 to June 2019), followed by the 2nd reprocessing (B11) covering the early FM-B period (June 2019 to October 2020), otherwise NRT produced data are used. Therefore, the biases are controlled during the early mission. The same QC decisions apply that were discussed for the NRT time-series.

The reprocessed data O-B statistics are calculated from the control (Aeolus not assimilated) of Observing System Experiments run at 18 km grid outer loop, whereas the NRT statistics are from the operational LWDA at 9 km grid outer loop (this does not seem to have a strong influence on the statistics). To improve the assessment of mission requirements, the statistics are partitioned into pressure ranges: 800-1100 hPa (surface to ~2 km) to roughly represent the planetary boundary layer (PBL); 100-800 hPa (~2 km to 16 km) to approximately represent the free troposphere; and less than 100 hPa to represent the lower stratosphere.

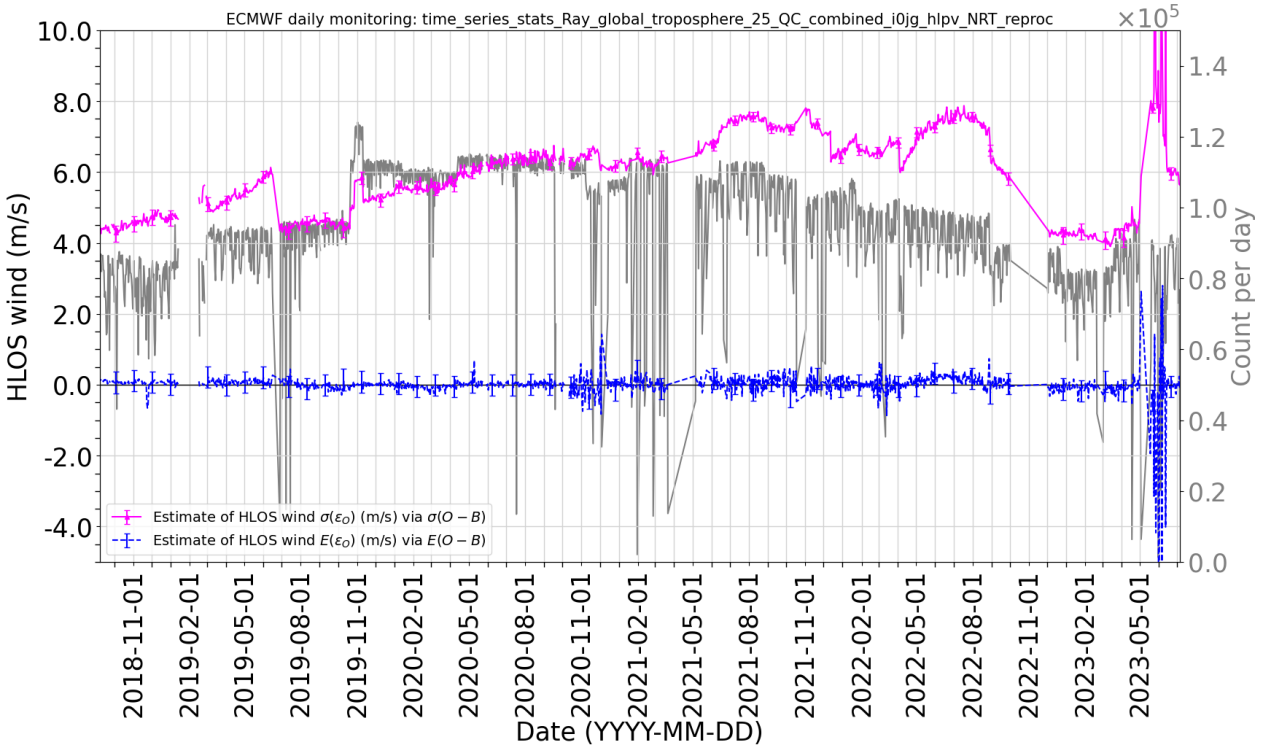

a) Free troposphere

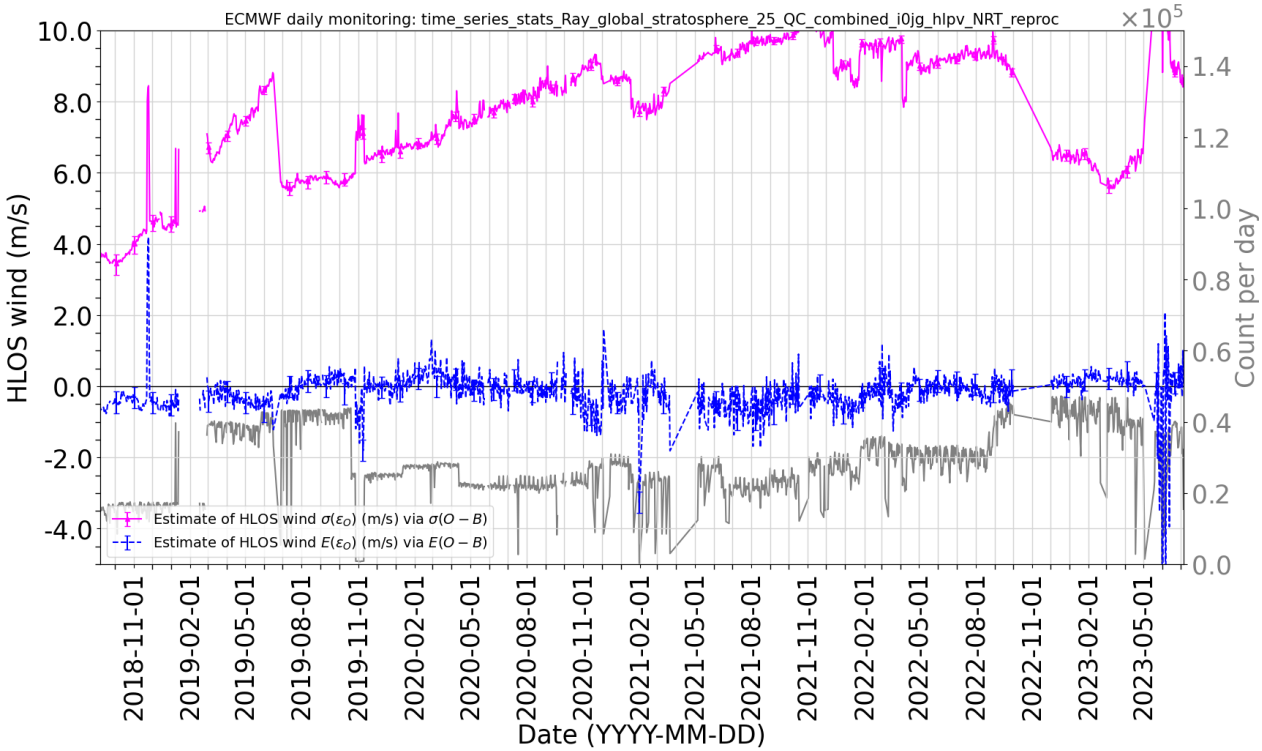

b) Lower stratosphere

Figure 127: Aeolus L2B Rayleigh-clear HLOS wind estimated global average random error (magenta, $\sigma(\epsilon_O)$) and systematic error (blue, $E(O-B)$) over the mission lifetime for a) Free troposphere (100-800 hPa) and b) Lower stratosphere (<100 hPa). The data count per day in grey (on the right axis). Winds are rejected if flagged invalid or if $|O-B| > 25\ m/s$.

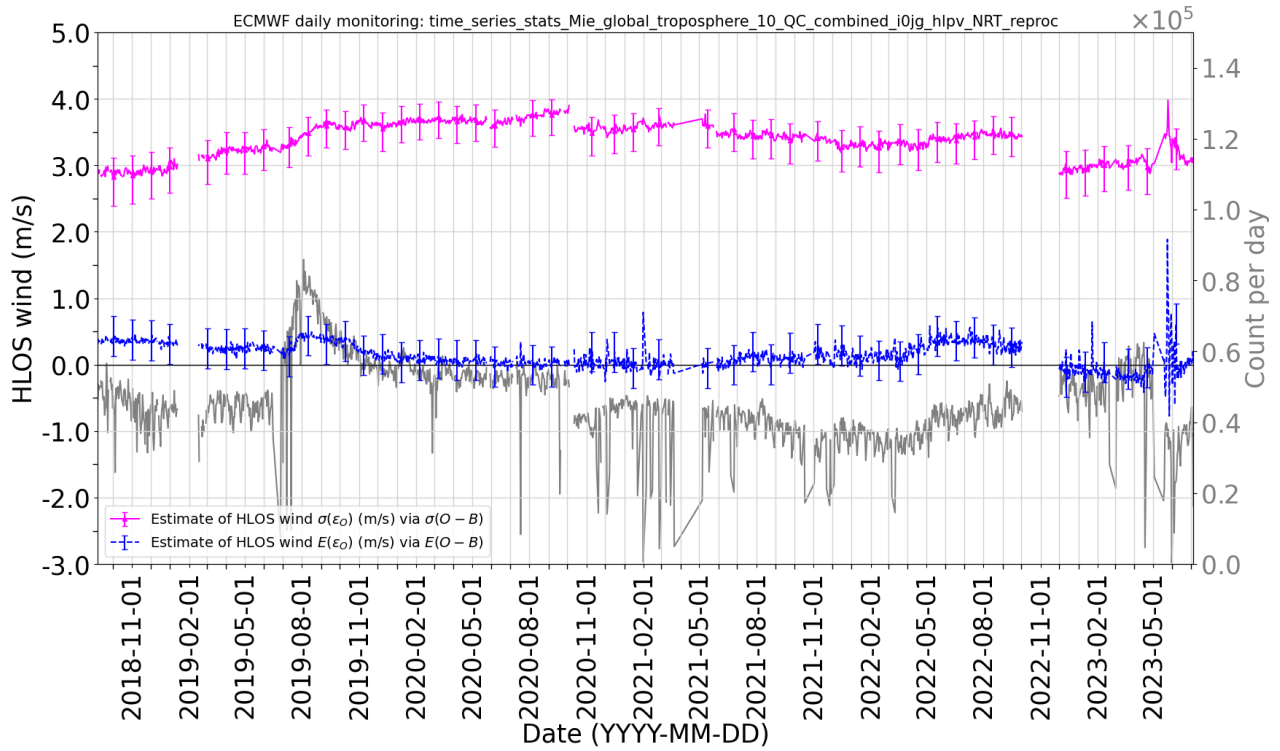

a) Free troposphere

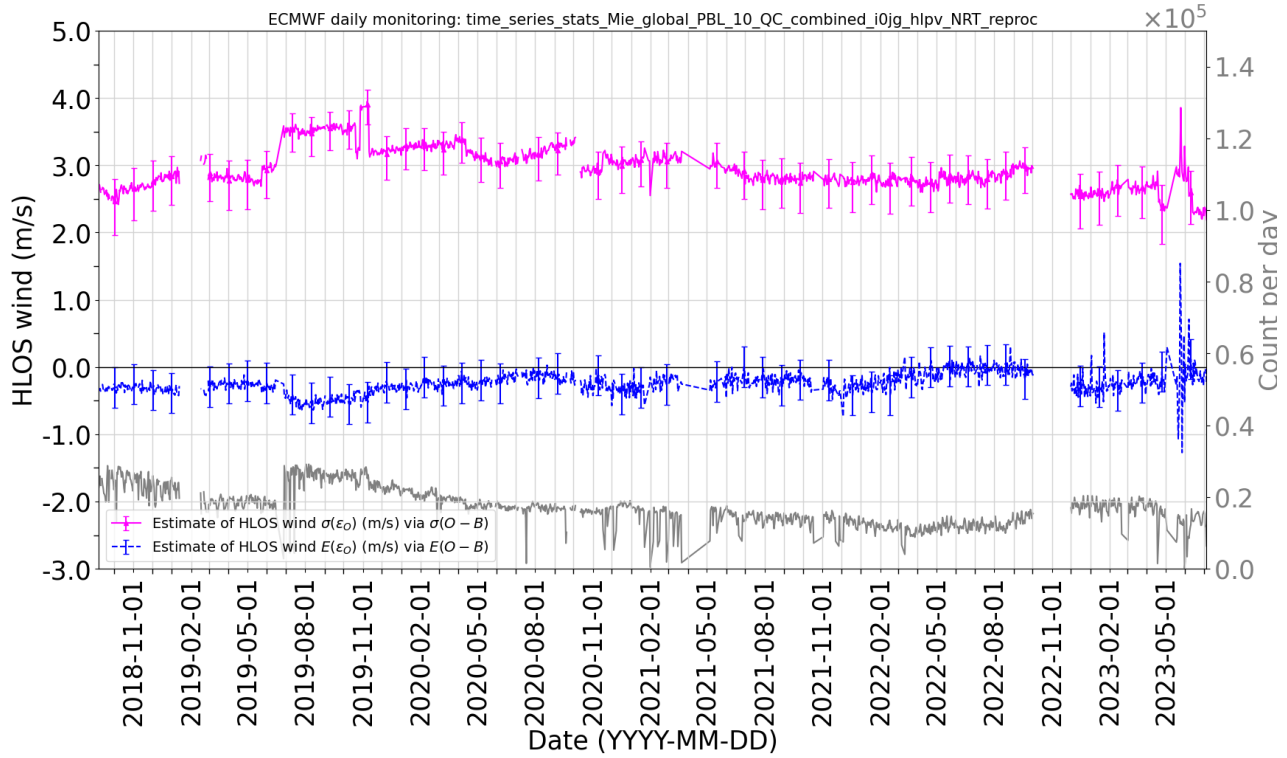

b) PBL

Figure 128: Aeolus L2B Mie-cloudy HLOS wind estimated global average random error (magenta, $\sigma(\epsilon_O)$) and systematic error (blue, $E(O-B)$) over the mission lifetime for a) Free troposphere (100-800 hPa) and b) Planetary Boundary Layer (800-1100 hPa). The data count per day in grey (on the right axis). Winds are rejected if flagged invalid or if $|O-B| > 10\ m/s$.

The more consistent data by reprocessing allows a fairer comparison of the statistics versus time compared to using only NRT data. The estimated precision (1-σ) of the Rayleigh-clear HLOS winds varied considerably with time, geolocation, season, processing software version and range-bin settings, ranging from 4-7.5 m/s in the troposphere and 3.5-10 m/s in the lower stratosphere. The Rayleigh-clear precision is strongly dependent on the received atmospheric path signal levels and hence varied with the outgoing laser pulse energy (affecting FM-A and FM-B laser periods) and the increasing transmission loss present on the FM-B optical path (see section 3.2.1). The trends in the L2B Rayleigh-clear HLOS wind random error estimates can be predicted rather well from the reported atmospheric path Rayleigh signal levels (mostly shot noise). The Mie-cloudy precision is more stable, ranging from 2.5-3.6 m/s in the troposphere and so it is less noisy than the typical Rayleigh-clear. Note that the average accumulation length for the Mie-cloudy winds varied between 12-17 km for the whole period when including the reprocessed data. However, the data counts for the Mie tend to decrease as the signal levels reduced, due to QC settings within the L2B processor (flagging winds invalid) and O-B based QC rejecting a larger fraction of the wind results. After M1 temperature-dependent bias correction (applied to all the data here), the systematic errors were typically within ±1 m/s (daily averages).

The ESA Aeolus mission requirements document (ESA, 2016) states a required precision of 2.5 m/s in the free troposphere and biases less than 0.7 m/s for the HLOS winds. These requirements were based on specific horizontal and vertical averaging scales and timescales for the metrics and a simplified atmosphere, making it difficult to precisely compare to error estimates for real Aeolus data with differing accumulations of measurement-scale data. However, given that the precision statistics estimated for real Aeolus Rayleigh data are considerably larger, then it is evident that the precision mission requirement was not met for the Rayleigh winds, and the systematic error requirement was only met thanks to the use of the ECMWF model as a reference for bias correction and for daily averages. The Mie-cloudy wind precision in the free troposphere is not too far from mission requirements, but the requirements on Mie winds in the PBL (1 m/s below 2 km) are not met.

An important contribution to the large Rayleigh-clear wind noise is the solar background, which was a more dominant random error source compared to pre-launch expectations given the low atmospheric path useful signal. The Rayleigh-clear random errors were significantly larger when Aeolus pointed into the sun-illuminated Earth e.g. see Figure 123c at southern polar latitudes and high altitudes in December 2022 (austral summer). Similarly, read-out noise and Detection Chain Offset correction noise were more dominant noise terms than expected due to the small atmospheric path signals, hence why reducing the number of readouts (N) per BRC (basic repeat cycle) helped to reduce the Rayleigh-clear noise in December 2021 and April 2022.

Finally, an example of Aeolus L2B HLOS wind O-B statistics at their best (in terms of atmospheric path signal levels and hence smallest random errors) from the 4th reprocessing campaign for 15 July 2019 is shown in Figure 129. The 4th reprocessing (still in production by ESA´s PDGS at the time of writing) has improved the Rayleigh-clear noise compared to the 2nd reprocessing. The Rayleigh-clear precision is near 3 m/s between 6-11 km altitude for this period, with accuracy typically less than 1 m/s and the linear correlation coefficient reached a record 0.97 (L2Bp estimated error QC was 12 m/s). The Mie-cloudy precision was typically 3-4 m/s, accuracy less than 0.5 m/s and linear correlation coefficient was 0.95 (some outliers remain, given the relatively relaxed L2Bp estimated error QC of 9.5 m/s).

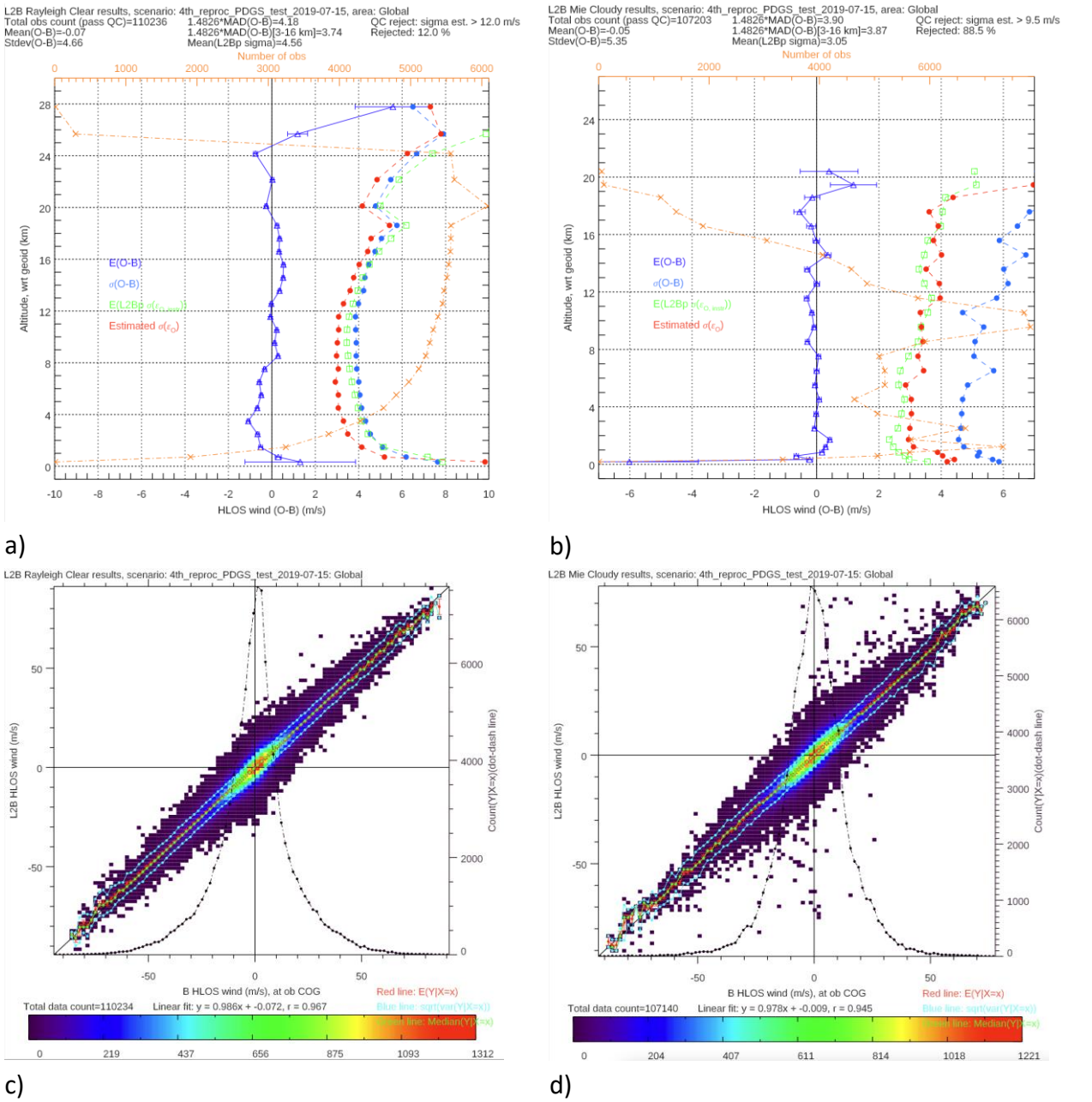

Figure 129: Error statistics of L2B HLOS winds for 13 orbits of data on 15 July 2019 using the 4th reprocessing (B16) dataset. a) Rayleigh-clear and b) Mie-cloudy HLOS winds, as a function of altitude. Dark blue triangles show $E(O-B)$ i.e. bias; red circles show $\sigma(\epsilon_O)$ i.e. estimated random error (by subtracting estimated background error); light blue circles show $\sigma(O-B)$; green squares show $E(\sigma(\epsilon_{O,instr}))$ i.e. the average L2B processor estimated instrument error, and orange crosses show the data count ("Number of obs" axis). QC of winds with L2B processor estimated error greater than 12 m/s for the Rayleigh-clear and 9.5 m/s for the Mie-cloudy was applied. 2D histograms of the L2B HLOS wind versus the ECMWF background HLOS wind are shown for c) Rayleigh-clear and d) Mie-cloudy data.

5.3.3 Improvements of the L2B wind product quality

The following are ground processing chain updates which are thought to have improved the NWP impact of Aeolus Level-2B HLOS winds:

- Increasing the number of Mie winds via reducing the L2Bp measurement grouping length-scale (improving horizontal resolution) to 10-20 km. This has been shown to lead to only a modest increase in random error (sufficient signal levels for cloud backscatter) but increases the number of Mie observations by a factor 2-3.

- The correction of the hot-pixel dark current offsets in the Level-1B processing step (since 14 June 2019), which massively reduced range-bin specific biases and avoids having to discard specific range-bins.
- Better classification of Rayleigh measurement-bins into clear and cloudy, thus reducing wastage of clear-air signal (important for low signal levels). This was done via tuning the classification thresholds; initially for L1B scattering ratio and then using the L1B Mie refined SNR for classification, which is less noisy, proved beneficial.
- Improved accounting for Mie backscatter signal on the Rayleigh channel, allowed for better quality Rayleigh-cloudy winds and hence more observations (an improvement in the way the Rayleigh-Brillouin calibration look-up table was used).
- Selecting more favourable vertical sampling (range-bin settings) for NWP impact; this was iterated on during the mission, following an ESA/DISC led advisory board. Highlights included higher altitude top range bins in polar winter to capture the polar vortex (and polar stratospheric clouds) and the Hunga-Tonga eruption plume Mie winds; higher vertical resolution to capture the shear in the tropical UTLS and in the polar-front jet stream.
- The bias correction of L2B Rayleigh-clear winds using the telescope's M1 temperature information. This led to a substantial improvement in the quality of the NRT L2B winds after 20 April 2020 and proved critical for more general uptake of the data for operational assimilation in NWP.
- More accurate Rayleigh HLOS wind instrument error estimates for large solar background conditions and the inclusion of read-out and detection chain offset noise; via corrections to the L1B processor Rayleigh SNR estimate.
- Switching off the use of the internal path Rayleigh response in the L2B processor due to anomalous step changes in the internal Rayleigh response; first noticed to cause bias jumps in December 2020.
- Use of NWP to help determine a more accurate Mie atmospheric path non-linearity correction and hence to improve the wind-speed dependent biases. The NWP derived non-linearity was applied to operational L2B winds on 1 July 2021; see Marseille et al. (2022).
- On 16 February 2023 the switch-on of the parameterised method for accounting for Mie contamination on the Rayleigh-cloudy winds via use of the L1B scattering ratio and using the ECMWF NWP model as a reference to derive the parameters; see Marseille et al. (2023).
- Not strictly a ground processing chain change; but modifying the N/P settings from N=30 to N=15 on 13 December 2021 and then N=5, P=114 on 4 April 2022, which led to a significant improvement in the random error for Rayleigh-clear winds (15% and 17% respectively), mitigating the FM-B signal decrease. Most of the improvement was due to reducing the read-out noise, an important noise source when the atmospheric path signal is low; however, the measurement-scale Mie SNR was less noisy with longer averaging, which also helps L2Bp clear/cloudy classification.
- Reducing the number of gross error Mie-cloudy wind results incorrectly flagged as valid by use of the "residual error" from the Mie-core fit for quality control; reducing reliance on L2Bp estimated error for QC of gross errors. This was possible with processor Baseline 16.

Some potential further improvements to NWP impact with future improvements in the ground processing chain:

- Improved Rayleigh calibration methods as a function of temperature, pressure, scattering ratio and M1 temperature gradient; possibly with the aid of NWP assisted calibration and analysis of IRONICs data. Should also lead to better quality Rayleigh-clear and Rayleigh-cloudy wind (although the parameterised method was implemented). A better understanding of the Rayleigh calibration would resolve the altitude varying (temperature dependent) bias (1 m/s) issues for Rayleigh-clear.
- Assessment of spatial observation error correlation and possible QC e.g. Mie-cloudy winds sometimes show dipole like error structures in the vertical.
- Improved quality control of anomalous measurement-bin useful signals (before accumulation) due to e.g. cosmic rays. Potentially using the median-filter QC method of DLR for airborne campaigns (Lux et al., 2022).

5.3.4 Lessons Learnt on L2B Product Monitoring at ECMWF

A recommendation for Aeolus-2 would be maintain strong links with NWP centres, such as ECMWF, to allow preparation of bespoke monitoring facilities well in advance of the launch, based on testing with end-to-end simulators, as was done with Aeolus. This led to the L2B processing being in a good state before the real data came along, and meant we had the monitoring tools in place to start assessing real Aeolus immediately with the first L1B and L2B data of the Commissioning Phase to detect issues that could later be resolved. This effectively maximised the time that Aeolus could be operationally assimilated in NWP. This is especially important due to the relatively short life of Doppler Wind Lidars (DWL) in space e.g. 5 years per satellite.

In terms of the instrument for Aeolus-2, we recommend measuring as much house-keeping data (e.g. temperatures) as possible in areas of the instrument which are likely to influence wind bias, based on the example of M1 thermistor readings being critical for the bias correction of Aeolus winds.

5.4 L2A quality monitoring using NWP model and L2A BUFR

William McLean, Karen Henry, Michael Rennie, and Angela Benedetti, ECMWF

5.4.1 Summary

The following chapter provides an overview of the monitoring of Aeolus Level-2A (L2A) particle backscatter retrievals in ECMWF's global data assimilation system configured in atmospheric composition mode (COMPO-IFS). This work was carried out at ECMWF as part of the Aeolus DISC consortium, with the work presented in this section mostly undertaken during the Aeolus Aerosol Assimilation in the DISC (A3D) work package, which ran from October 2021 to March 2023, and continued up until the end of the DISC phase E (McLean and Benedetti, 2023). The main goal of this work was to perform near-real time (NRT) monitoring of the Aeolus L2A particle backscatter product and compare to the model value calculated in COMPO-IFS.

Global and regional monitoring statistics are presented for the entire period of interest, in the form of vertical profiles of the first-guess departures, i.e. the difference between the Aeolus L2A particle backscatter coefficient and the model-calculated aerosol backscatter, averaged over different periods and across multiple regions. Results from varying the quality control parameters are also shown, which are necessary in order to maximise the impact of the data on the assimilation.

5.4.2 Introduction

Passive remote sensing relies on measuring the scattered solar radiation from the atmosphere, from which it is difficult to ascertain the vertical distribution of atmospheric constituents. Aerosol optical depth (AOD) values are retrieved from such measurements, which gives information on aerosol load in the atmosphere. Measurements from lidar, an active remote sensing technique equipped with its own radiation source, allows for the retrieval of aerosol extinction and backscatter as a function of altitude. These products can then be used in data assimilation to assess impact on air quality and NWP.

Beginning in the early 2000s, ECMWF's Integrated Forecast System (IFS) was extended to allow the simulation of reactive trace gases (Flemming et al., 2015; Huijnen et al., 2016), aerosols, (Morcrette et al., 2009; Rémy et al., 2019, 2022), and greenhouse gases (Agustí-Panareda et al., 2014), research that subsequently resulted in the formation of the Copernicus Atmosphere Monitoring Service (CAMS), a service implemented by ECMWF on behalf of the European Commission (Peuch et al., 2022).

This nascent capability to model atmospheric composition in the IFS enabled the inclusion of aerosol optical depth (Benedetti et al., 2009), reactive trace gases (Inness et al., 2015) and longer-lived greenhouse gas (Engelen et al., 2009; Massart et al., 2014) products retrieved from satellite measurements in the 4D-Var data assimilation system. All of these developments were carried out in collaboration with other European research institutions, including the national meteorological services of several member states of ECMWF.

The IFS in composition configuration, at the time of writing running operationally in cycle CY48R1, has a robust model for aerosols along with assimilation of several AOD products (MODIS, PMAp, and VIIRS products) into the 4D-Var data stream alongside the other air quality and meteorological products. However, as mentioned above, AOD does not provide a vertical distribution of aerosol, only the column-integrated total is known.

The Aeolus L2A atmospheric optical products contain both particle extinction and particle backscatter products, from several different retrieval algorithms. The particle backscatter product retrieved using the

SCA mid-bin algorithm (Flament et al., 2021) was transformed into the format required by the IFS, and ingested into the system allowing comparison with the model values.

The ECMWF model derives the lidar ratio, aerosol extinction coefficient, and aerosol backscatter coefficient for each height bin at the appropriate wavelength (355 nm for ALADIN) assuming cloud-free conditions, using the method from Ackerman (1998) and Huneeus and Boucher (2007). The model values are computed using Mie theory, assuming a spherical shape for each aerosol species, and therefore does not consider the effects of particle depolarization from non-spherical scatterers.

With the availability of any new satellite retrieval products, an operational weather and air quality forecasting centre such as ECMWF will spend a certain period monitoring the data in their data assimilation system. To monitor a product means to allow it into the system with zero weight in the assimilation (passive data use), so that it follows the same trajectory as any other product that is given a non-zero weight in the assimilation (active data use). This allows us to assess the quality of the new data product whilst disentangling the effects from assimilating the data. There are myriad reasons for monitoring a data product before adding it to the assimilation, including to check for consistency, and evaluate any problems that may arise due to the instrument, the data processing and retrieval pipeline, or with the handling of the product in the system itself. Careful study of any new product is required to calibrate the parameters assigned before and during the assimilation, including an evaluation of observation errors and quality control in pre-screening and during the analysis.

The rest of this chapter is structured as follows: Section 5.4.3 describes the methodology, that is, how the data were transformed into the format required by COMPO-IFS, and the procedure for comparing with the model-calculated values. Section 5.4.4 then presents the core results from the near-real time monitoring, showing comparisons of the particle backscatter as a function of time, geolocation, and altitude. Section 5.4.5 introduces the Aeolus L2A BUFR development for the ECMWF IFS, while section 5.4.6 finally provides a summary and outlook.

5.4.3 Methodology

The standard procedure for working with meteorological datasets is to use data encoded in Binary Universal FoRmat (BUFR). This is the ubiquitous standard amongst meteorological institutions across the globe. However, the need for a BUFRization of the Aeolus L2A retrieval products was not realised until after the mission launched, and use of the product could not wait until such developments were finalised. As a workaround, scripts were developed at ECMWF to take the data from the native Earth Explorer format and extract the required values. The Coda software, developed by S&T of the Netherlands as part of the DISC framework, was used to convert from the binary Earth Explorer format to ASCII. Following this, an in-house python script was used to take the Coda outputs and group the data into the files used in each of the two daily data assimilation windows used in the IFS (Vasiljevic et al., 2021).

Following the data grouping, the L2A particle backscatter product was read into the IFS along with the other meteorological and atmospheric composition data products. In the monitoring aspect of the work, the backscatter was included passively. The aerosol backscatter coefficient calculated in the IFS using the appropriate observation operator was then compared with the Aeolus particle backscatter product. The COMPO-IFS model backscatter is the "full" backscatter, and not just the co-polar component that Aeolus gives. Thus, in case of de-polarizing scenes (e.g. desert dust), the Aeolus co-polar backscatter is lower than the equivalent model backscatter value. As mentioned previously, the backscatter product we used in the near-real time monitoring was the SCA mid-bin retrieval, which is particle backscatter and not an aerosol-only product. A model-based cloud screening was implemented to reduce the

contributions from cloud, which only allowed the assimilation of data where the total cloud fraction was below 1%. Additionally, a filtering based on the threshold of the particle backscatter was used, rejecting any value lying outside the range $1x10^{-7}$ - $1x10^{-5}$ $(m\ sr)^{-1}$.

Prior to assimilation, a first-guess check is performed as part of the pre-analysis screening, which is used to reject observations for which the O - B departure is greater than a certain factor multiplied by the expected size, given the assigned observation error and the estimated background error, with the purpose of removing outliers (see Järvinen and Andersson, 1999), if:

$$O - B = y - H(x) > F\sqrt{\sigma_O^2 + \sigma_B^2}, \quad (1)$$

where σ_O and σ_B are the standard deviations of the observation and the background, respectively. During the near-real time monitoring and assimilation, the value of F was set to 7, with a value of F = 5 used more recently, which is in line with that used for the HLOS winds and other products assimilated in the ECMWF system.

5.4.4 Results and discussion

Figure 130 shows the average departure statistics for eight months of NRT monitoring, during January 01 – August 31, 2022. Also shown are the analysis departures, from the assimilation, which are discussed in the L2A NWP impact chapter. The statistics for all data (top plots; prior to screening) show a relatively large standard deviation and large O-B (bias). This is because the background (model without L2A assimilation) is produced from aerosol backscatter only, with no cloud contribution. The post-screening statistics (bottom plots) show a marked reduction in both standard deviation and O-B, with the largest values present in the planetary boundary layer. The number of observations in each layer is shown on the y-axis of the right-hand plots, with the atmospheric pressure also specified on each plot. The observation error in the NRT assimilation experiments was kept constant, at $1x10^{-7}$ $(m\ sr)^{-1}$.

Figure 131 shows maps of the mean first-guess departures (also called O-B, that is, the difference of the Aeolus L2A backscatter and the IFS model short-range forecast aerosol backscatter) for the month of September 2022. If the background forecast was unbiased, the mean O-B would represent the bias in the observations. The positively biased departures (red) occur in both figures, around the equatorial regions, and probably indicates cloud signal still present in the data post-screening. This can be explained by the ECMWF model not perfectly locating the convective cloud occurring in these regions of the atmosphere. The slightly negative biased departures (blue) over the Sahara and Arabian Peninsula could indicate that Aeolus backscatter is systematically too small in dusty regions due to not measuring the full backscatter, only cross-polar.

The left-hand plot in Figure 131 is from an experiment using a more relaxed first-guess check, with F=7 in Eq. (1), i.e. rejecting any data lying outside the 7-sigma range, and the right-hand figure is from an experiment using a more stringent first-guess check of 5 sigma (thus rejecting more Aeolus data, particularly positive biased data associated with clouds), the same as used in the CAMS AOD assimilation. Work is ongoing to implement a cloud screening method based on spatiotemporally-co-located cloud data from the CLAAS-3 product, the third edition of the Cloud property dataset using SEVIRI (Spinning Enhanced Visible and InfraRed Imager; see https://essd.copernicus.org/articles/15/5153/2023/essd-15-5153-2023-discussion.html).

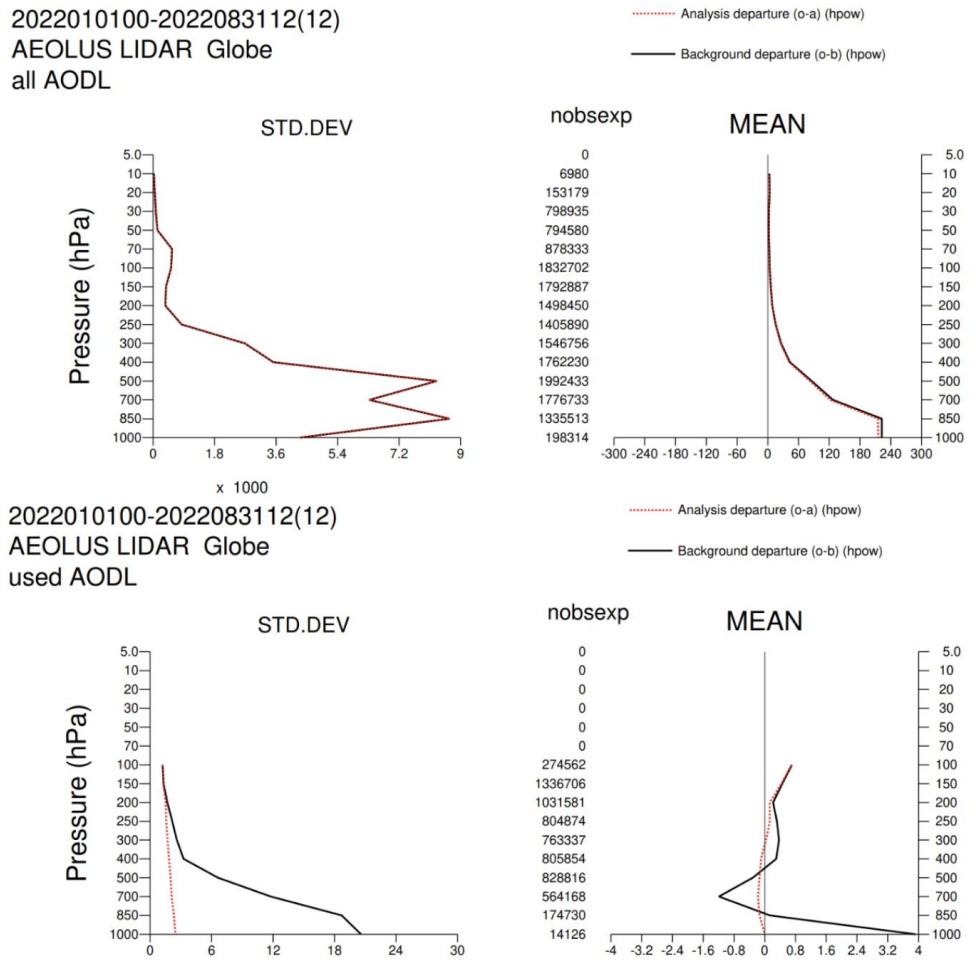

Figure 130: Global departure statistics for 01 January – 31 August 2022. The mean first-guess departures (O-B) are shown in black (red-dashed line shows the analysis departures, from assimilation) in the right-hand plots, with the standard deviation shown in the left-hand plots. Top plots are statistics for all data, and the bottom plots for data passing the pre-analysis cloud and altitude screening. Units are 10^{-7} $(m\ sr)^{-1}$, with atmospheric pressure indicated on each figure, and the number of observations in each layer is given on the y-axis of the right-hand plots.

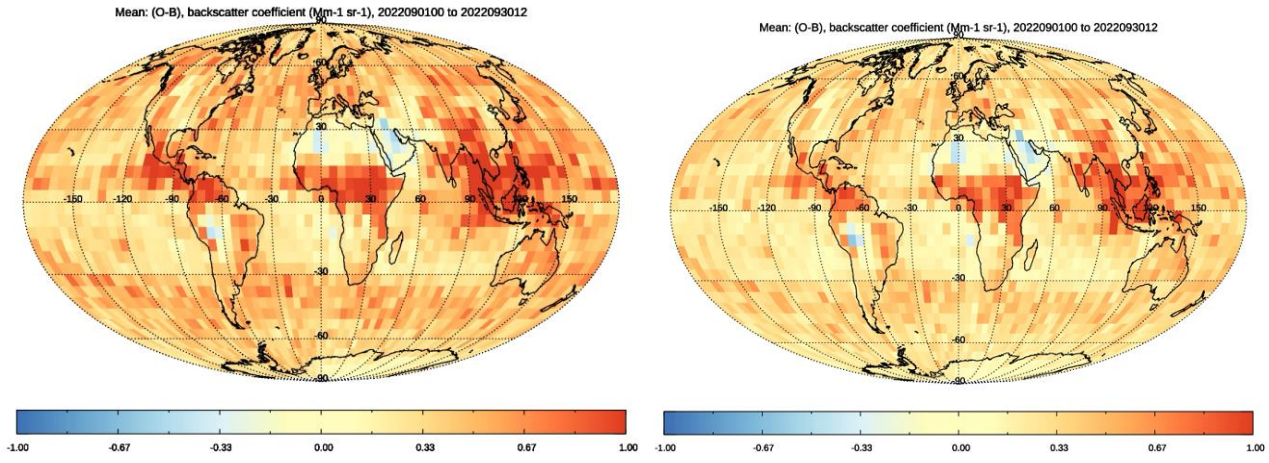

Figure 131: Mean first-guess departures (O-B) for September 2022, from two experiments assimilating the Aeolus L2A particle backscatter in the standard COMPO-IFS configuration in CY48R1. The right-hand figure is from an experiment with a stricter first-guess check, with the left-hand figure showing results from a more relaxed first-guess check. Units are $(Mm\ sr)^{-1}$, with the darker red and the blue areas indicating larger mean O-B values.

5.4.5 Aeolus L2A BUFR development for the ECMWF IFS

The L2A BUFR (Binary Universal ForRmat) work is in response to the need for BUFRization of the Aeolus L2A retrieval products. To assimilate observations into the ECMWF IFS system or other atmospheric composition or NWP forecast systems for operational use, observations need to be translated into the BUFR format, which is the World Meteorological Organization (WMO) format. At ECMWF the BUFR data is then translated into ODB (Observation DataBase) format. ODB is a proprietary database developed at ECMWF. This work required the following steps:

1. The development of a BUFR template, which is a group of WMO BUFR fields selected to represent the observations.
2. The development of a python program to translate the fields from the input file (which is in Earth Explorer format) into an output file in BUFR format.
3. Selection of the ODB fields and development of a bufr2odb program to translate the fields from BUFR to ODB format.
4. Development of a current branch of the ECMWF IFS (CY48R1) and supporting settings and code to enable the bufr2odb program to run within the IFS and support a 4-D Var data assimilation experiment.

BUFR templates and fields are strictly managed by the WMO, and this requires ongoing discussion on the validity and necessity of any new fields and templates. Assimilation of L2A aerosol observations into the IFS requires the particle backscatter and extinction values, their uncertainty, and their geolocation. For these reasons the final L2A BUFR template does not include many of the data parameters available in the Earth Explorer L2A files, but is focused rather on capturing the particle backscatter, extinction and uncertainty for 5 of the retrievals available in the L2A files. The 5 retrieval types selected were chosen for their applicability of use within the IFS system and are Standard Correct Algorithm (SCA), Standard Correct Algorithm mid-bin (SCA mid-bin), Maximum Likelihood Estimation (MLE), Maximum Likelihood Estimation sub resolution (MLE sub) and Optimal Estimation Profile (PRO). This retrieval has the acronym AEL-PRO within Aeolus IODD documentation, but the allocated WMO BUFR code is OE-PRO.

New WMO BUFR codes for L2A aerosol retrieval and AEL-PRO classification types were requested and approved. The L2A BUFR template must still be approved by the WMO, and this will be applied for in 2024. This requires submission of a few months of BUFR processed files, which are tested by other NWP sites, before approval is given. The technical details of the L2A BUFR can be found in the Technical Note AED-TN-ECMWF-L2A-089.

5.4.6 Summary and outlook

Monitoring of the SCA mid-bin L2A particle backscatter product was carried out at ECMWF as part of the Aeolus DISC activities, and after pre-processing was included in the IFS for near-real time monitoring of the product from January to August 2022. The differences between the Aeolus L2A particle backscatter and the IFS model aerosol backscatter were assessed, with first-guess departures showing the L2A backscatter placed the aerosol at different altitudes than in the model for several cases. A model-based cloud screening and a filtering based on the size of backscatter value was implemented, but this is not a perfect way to screen out cloud signals and isolate only the aerosol. Work ongoing at the time of writing includes assimilation of other L2A retrieval products, including the AEL-PRO particle backscatter, as well as a cloud screening based on cloud datasets constructed from geostationary satellite measurements over an extended period. A key achievement from the A3S, A3D, and follow-on activities under the auspices of the Aeolus DISC is that ECMWF have developed a framework to perform

near-real time data monitoring of any future satellite lidar particle backscatter products. ECMWF is therefore prepared for the future uptake of EarthCARE atmospheric aerosol products, and any future cloud and aerosol products from Aeolus follow-on missions.

5.5 Cal/Val Synthesis, user support and engagement

Sebastian Bley, TROPOS

5.5.1 Introduction

This document aims at providing an overview of the synthesis of Cal/Val results for the L2B wind and the L2A aerosol/cloud product, user support and the organization of the range bin setting working group. The report describes the activities covering the entire mission period from August 2018 until December 2023. Before SB joined TROPOS in March 2021 to perform the here described activities as part of the Aeolus DISC, he worked as research fellow for three years at ESA-ESRIN in Frascati, Italy where he was already strongly involved in the coordination of Cal/Val activities for Aeolus, including the development and management of the Cal/Val confluence and coordination of the range bin setting working group. During that time, the Cal/Val synthesis was performed at DLR. After March 2021, all these activities were bundled to one new work package within the Aeolus DISC performed at TROPOS.

While Cal/Val synthesis mainly focuses on validation activities from external validation teams, it also includes some findings made inside the DISC because of the strong collaboration between the DISC and Cal/Val teams, which led to joined studies. The main tool for exchange between the DISC and Cal/Val teams was the Aeolus Cal/Val confluence (https://www.aeolus.esa.int/confluence/index.action) which was maintained and coordinated by TROPOS within the DISC. Furthermore, the reply to user queries outside the Cal/Val confluence was covered by this activity. The strategy for proposing and updating new Range Bin Settings (RBS) via the range bin setting working group is also highlighted in this report.

5.5.2 Synthesis of Cal/Val results

Cal/Val synthesis is considered as bringing together main findings, results and issues from external validation teams in order to transfer them in a condensed way to the Aeolus DISC, particularly the product algorithm developers. Cal/Val teams who submitted Cal/Val proposals to ESA could participate in the official Aeolus Cal/Val programme, which implied that they were granted early access to the Aeolus products and that they were continuously informed about updates and findings through the Aeolus Cal/Val confluence platform (https://www.aeolus.esa.int/confluence/index.action). In order to share their results with the Aeolus DISC and ESA, they were asked to prepare half-yearly Cal/Val status reports. The main findings reported in these reports have been summarized in the Cal/Val synthesis reports v1-v6 (TROPOS, 2024).

The main objectives of these synthesis reports are to assess findings from external Cal/Val teams, extract recommendations for further algorithm studies to product developers within the DISC, to identify gaps in the validation and to provide guidance from the DISC to external Cal/Val teams. Cal/Val teams have substantially contributed to the quantification of biases and random errors of the wind product, but also of the aerosol and cloud products – for the whole mission lifetime. More than 60 papers have been published in Aeolus special issues in AMT (https://amt.copernicus.org/articles/special_issue1131.html) and QJRMS (https://rmets.onlinelibrary.wiley.com/doi/toc/10.1002/(ISSN)1477-870X.aeolus) between 2018 and 2023. The prerequisite for that was early access to the data and reliable validation tools and information channels between ESA, the Aeolus DISC mission experts and the Cal/Val community (e.g., about regular updates of the data quality). Regular exchange was further ensured through Aeolus Cal/Val and Science workshops as well as dedicated topical working meetings. The past five years of close interaction between Cal/Val teams and the DISC have led to several lessons learnt, as described in section 5.5.6.

Because it is out of the scope to present here the highlights from 29 individual Cal/Val teams, this report focuses on the assessment of the L2B and L2A products with statistical comparisons based on a sufficient larger number of observations.

5.5.3 Main findings from L2B wind product validation

The assessment of the L2B product quality relies mainly on the quantification of wind biases and random errors (scaled MAD, RMSE, STD) using collocated wind observations from super pressure balloons (Bley et al, 2022), radiosondes, ground-based Radar Wind Profilers (RWP) and Doppler Wind Lidars (DWL) complementing the quality assessment using ECMWF model winds.

Figure 132 shows a time series of wind bias and random error of the Aeolus HLOS Rayleigh clear wind speed using different reference datasets with different Aeolus product baseline versions.

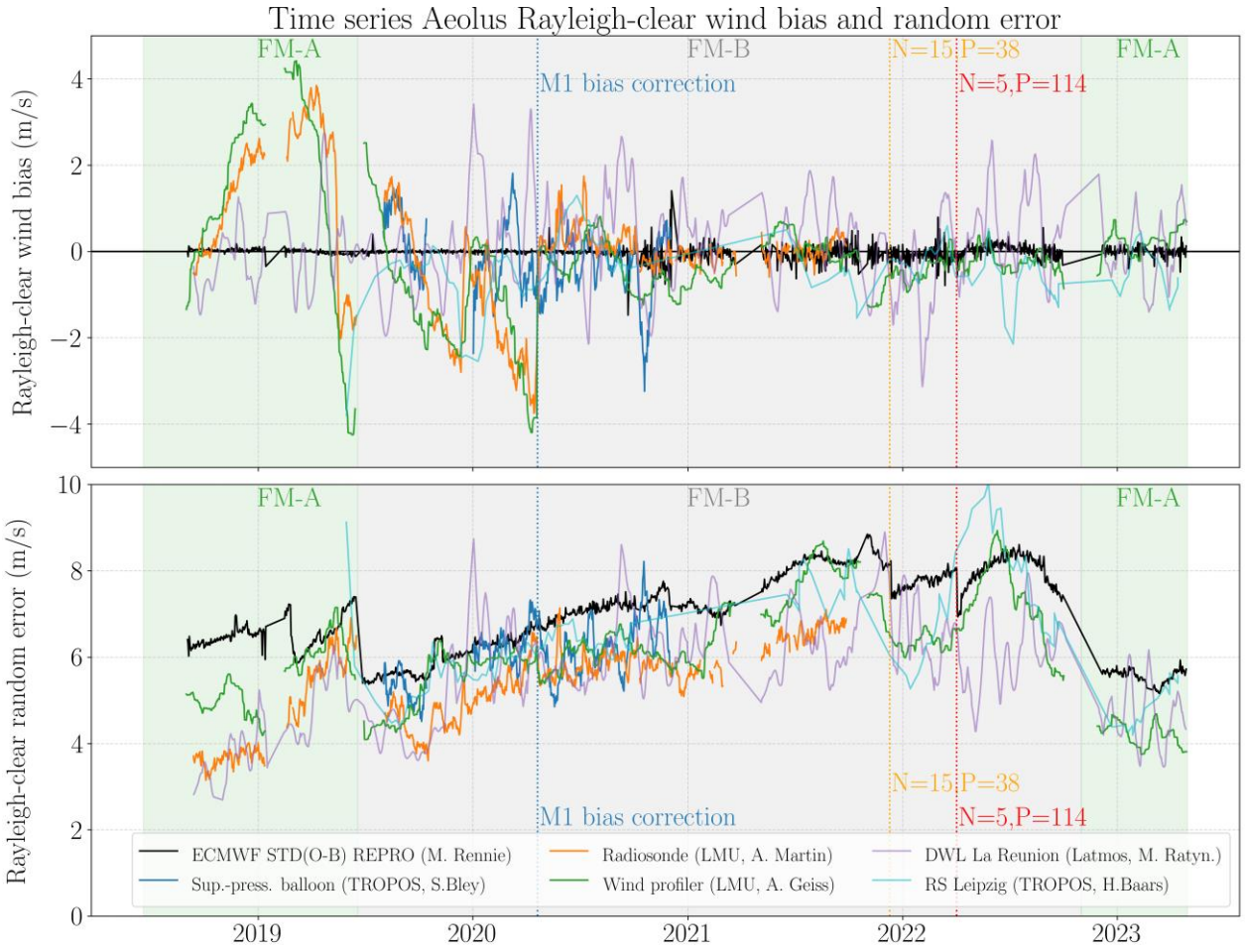

Figure 132: Time series of Aeolus HLOS Rayleigh clear wind bias (top) and random error (bottom) for the period from 3rd September 2018 until 28 April 2023. While most of the Cal/Val teams analyzed the Aeolus operational NRT data, ECMWF and Latmos used the reprocessed dataset for validation. This time series is not complete and only represents error statistics shared from Cal/Val teams. Laser FM-A and FM-B periods are indicated by background colours, the vertical dashed lines mark dates of major setting updates (e.g. M1 telescope bias correction, N/P settings).

The different statistics agree very well, particularly for the random errors. The fact that the ECMWF (M. Rennie, ECMWF), radiosonde (A. Martin, LMU) and wind profiler (A. Geiß, LMU) lines look smoother compared to the DWL at La Reunion (M. Ratynski, Latmos) and radiosonde at TROPOS (H. Baars, TROPOS) can be explained by the fact that the Cal/Val stations at La Reunion and TROPOS are single

stations compared to the networks or global model data from the others. This leads to differences in the frequency of collocated observations. Further deviations between the results of different teams can be also explained by the selection of different product baseline versions (operational NRT versus reprocessed), collocation criteria, QC and outlier filtering (z-score, threshold for absolute difference etc.). The ECMWF curve for the random error was derived using a more relaxed QC compared to the other statistics (reject data if abs(O-B)>25 m/s), this explains why the ECMWF STD(O-B) lies at the upper range of all references. Furthermore, different teams look into different regions of the world and different altitude regimes. Therefore, Figure 132 may serve as qualitative overview demonstrating consistency of the results and its temporal evolution rather than being a reference for drawing conclusions on the absolute differences.

The L2B wind product has been continuously improved and updated throughout the whole mission, 16 L2B processor versions have been generated from August 2018 until April 2023. Further, the laser has been switched from FM-A to FM-B in summer 2019, back to FM-A end of 2022 and after the end of the operational mission during the End-of-life tests back to FM-B in Mai 2023. Figure 133 gives an overview on the L2B processor evolution. The first L2B wind data was publicly released in May 2020, while Cal/Val teams had already early access to B02 in December 2018. After the reprocessed datasets from second and third reprocessing campaign became available, the teams were advised to only use B11 and newer, as B11 covers the time from the beginning of FM-B in summer 2019 until B12 was released and B14 covers the early FM-A period until switch to FM-B.

B10/B11 and B14 include data from the first and second reprocessing campaigns from June to December 2019 and from June 2019 to October 2020, respectively. Data from the third reprocessing campaign covering the first operations period of the ALADIN Flight Model A (FM-A) instrument during the period from 31 August 2018 to 16 June 2019 uses processor version 14 and was published in November 2022.

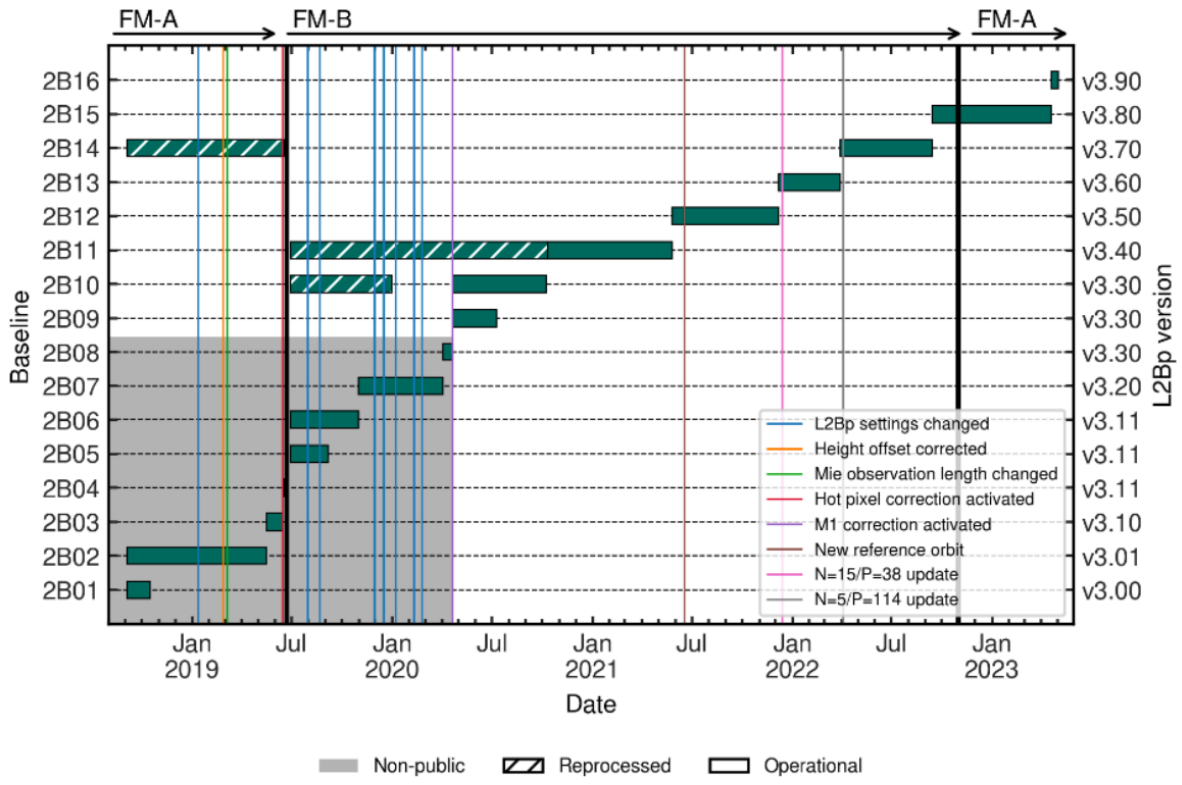

Figure 133: Temporal evolution of the L2B processor including the baseline versions, L2Bp versions, laser FM-A and FM-B periods, reprocessing campaigns and major setting adjustments, A. Geiß, LMU, 2023.

During the early mission phase from launch until April 2020, Cal/Val teams reported large wind biases which agrees with results from wind bias assessment against ECMWF model. The random errors started at relatively low levels (still above the mission requirement for the L2B product) and increased steadily until switch to FM-B. The main highlights of that early mission period were the implementation of the hot pixel and the M1 bias corrections. The large systematic errors in the L2B wind product could be significantly reduced to less than 1 m/s after implementation of the M1 bias correction scheme in May 2020. Several Cal/Val teams show a significant reduction of the wind product systematic error from Baseline 10 compared to previous results using Baseline 6.

However, due to the steadily decreasing atmospheric return signals, most teams report about slightly increasing random errors in the course of the mission lifetime. The random errors varied around 6 m/s in May 2020 and reached values above 8 m/s end of 2021. At this time, Baseline 13 was introduced together with an update of the N/P setting. Cal/Val teams reported an improvement of the Rayleigh-clear random error from around 8-9 m/s to around 5.5-7 m/s following the new N/P setting. This positive result triggered some more N/P tests to further improve the random errors of the wind products.

A new maximum of Rayleigh clear wind random errors could be observed from all validation activities, connected to the low atmospheric return signal towards the end of the FM-B lifetime and the high solar background. This led to the motivation to switch back to laser FM-A in December 2022. Cal/Val teams who assessed the quality of the wind products after this laser switch found very low random errors with values in the range of the start of the mission. ECMWF monitoring results agree well with those from collocated measurements from radiosonde (TROPOS), DWL (LATMOS) and RWP-Network (LMU).

Until the time of writing, already three reprocessed datasets have been released (DISC-ECMWF, 2020,2021,2023) and the fourth dataset is about to be published. The reprocessed dataset shows significantly reduced wind biases around ±1 m/s. The effect can be nicely demonstrated by the difference between the two statistics based on the reprocessed dataset (LATMOS and ECMWF) and the two lines reported by independent validation activities using the operational NRT data (LMU).

5.5.4 Main findings from L2A aerosol product validation

In contrast to the statistical validation of the L2B product, it is more challenging to summarize and quantify the main findings for the L2A product. This is mainly due to the fact that most of the Cal/Val teams have compared only single collocated profiles of backscatter, extinction and lidar ratio with independent lidar measurements, which makes it difficult to draw conclusions on bias and random errors. But also because several new variables including QC flags have been introduced in the frame of the mission, starting from the Standard Correct Algorithm (SCA), the Mie Channel Algorithm (MCA) and the Group product for the SCA. It was followed by the Maximum Likelihood Estimation (MLE) and its implementation on finer horizontal scale (i.e. so-called sub-BRC and corresponding to measurements accumulated per sub-profile). Finally, also the algorithms developed for the ATLID lidar on EarthCARE were adapted, prototyped and implemented in the Aeolus L2A product, namely the Feature Mask (AEL-FM) and the optical properties profiles (AEL-PRO).

All of the products require different QC handling and advanced knowledge on the L2A product structure. From the Cal/Val user perspective, guidance is very important about which product should be used for comparison against backscatter/extinction measurements from ground-based lidars. Therefore, the L2A user guide was created as complement to the L2A reference documents, which has been updated along with new baseline updates (CNRM, 2022).

Due to the continuous introduction of new parameters and QC flags, there has been a close exchange between the L2A developers in the DISC and the Cal/Val teams, to support their validation activities, but also to request specific validation aspects. Flagged scenes of interest including dominant particles (e.g. wildfires smoke or volcanic ash) have therefore been analysed in details revealing coherent mean values of L2A main products (e.g. extinction, backscatter, lidar ratio and scattering ratio), especially for layers below clear sky. This close interaction also led to a collection of joined key objectives for aerosol validation studies during the ASKOS and JATAC campaigns in summer 2021 and 2022 (e.g. Assessment of minimum detectable aerosol backscatter coefficient which led to a confluence discussion). The TROPOS Cal/Val team set up a permanent PollyXT/ACTRIS station at Mindelo, which allowed to perform a statistical analysis of the L2A particle backscatter. They observed an underestimation in the Saharan Air Layer (SAL), which they explained by the missing cross-polar component of the backscatter signal which leads in case of non-spherical particles to the loss of a certain amount of the signal. The EARLINET team collected 2313 collocated lidar profiles at 37 stations in Europe considering collocation criteria of 120 km and +-1.5 hours. After cloud screening, this number reduced to 556, and after further quality filtering following the single calculus chain, only 282 profiles remain for statistical analysis with the Aeolus L2A data. The results are in agreement with findings from TROPOS.

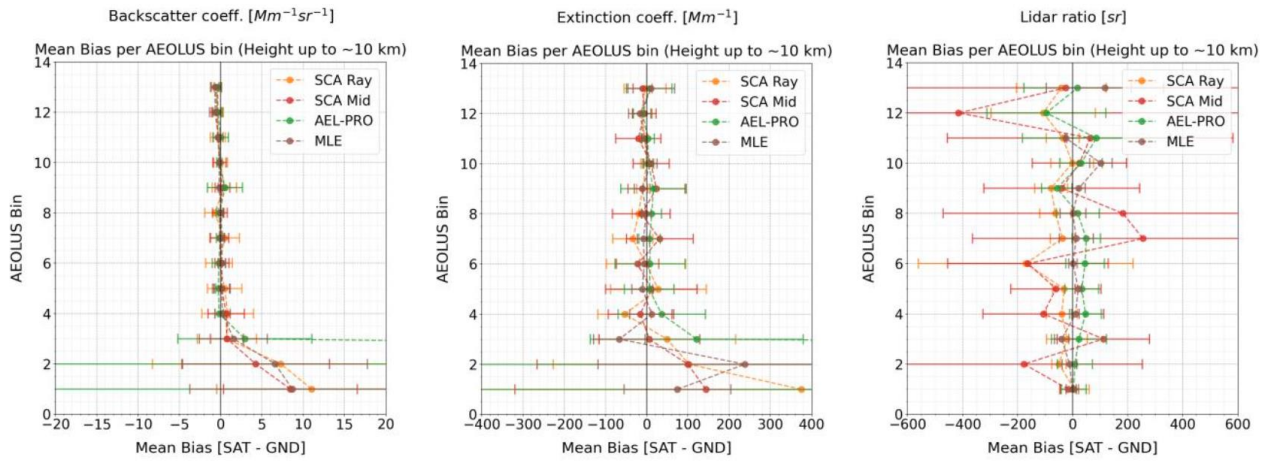

Figure 134: The mean bias along with its standard deviation for the backscatter coefficient (left), the extinction coefficient (middle) and the lidar ratio (right) per Aeolus bin. The biases have been calculated from the Aeolus profiles from the available algorithms (SCA, AEL-PRO, MLE) and the 14 collocated eVe profiles over Mindelo, using the eVe profiles as reference, ASKOS final report 2023.

The NOA/Raymetrics team acquired collocated profiles of backscatter, extinction and lidar ratio with the eVe reference lidar over Mindelo during the JATAC campaign in 2021 (ESA, 2021; Paschou et al., 2022). Figure 134 presents the mean bias for backscatter, extinction and lidar ratio from multiple L2A parameters (SCA, SCAmid, MLE and AEL-PRO) based on 14 collocated eVe measurements. In general, a very good agreement is found between all the four L2A parameters and the eVe observations above 2.5 km altitude, with the MLE profile being the less noisy of all and closer to the Aeolus-like lidar ratio retrieved from eVe. The discrepancy below 2.5 km can be most likely explained by the fact that for the comparison with the cloud screened eVe observations, Aeolus profiles where not cloud screened by the L2A product QC flags, which could have led to contamination by marine stratocumulus clouds that were not observed from eVe. This finding also highlights the challenge of the representativity of different measurements with different spatial scales. It also underlines the importance of suitable cloud screening on product level.

5.5.5 Strategy for the definition of range bin settings

Each Aeolus wind, backscatter and extinction profile consists of 24 vertical range bins with varying thicknesses between 250 m to 2 km, covering a total range from Earth surface up to 30 km. Multiple so-called Range Bin Settings (RBS) could be defined (in geographical boxes) at the same time for each orbit, for Rayleigh and Mie profiles separately (ESA, 2020).

The main reason to update RBS is to address particular scientific and Aeolus mission objectives. Some of the settings were changed seasonally, while others were long term and meant to support data assimilation by NWP centres. In the case of dedicated science objectives, validation campaigns or specific events such as volcanic eruptions or smoke, a limited spatial box could be defined. New RBS have been usually proposed by NWP centres, Aeolus Cal/Val teams, the Aeolus DISC or the Aeolus Science Advisory Group (SAG). For review and discussion of the RBS strategy, representatives from each of the groups met every six months in the RBS working group, organized by TROPOS as part of the tasks within the DISC project. Seven RBS working group meetings have been organized throughout the whole mission.

Figure 135 illustrates the geographical distribution of active global and regional range bins settings during Northern Hemispheric summer season 2020. During that time, the small limited area RBS campaign settings MARS and AUMATEX were active, MARS to support aerosol studies with Aeolus in the Mediterranean with high resolution range bins in the lower troposphere.

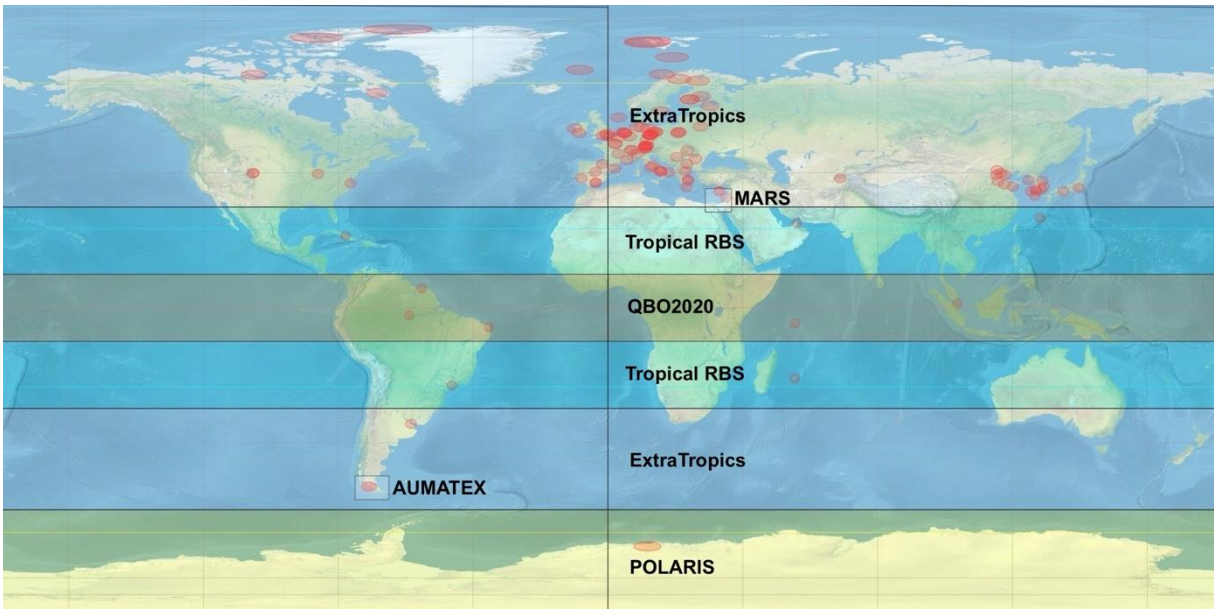

Figure 135: Distribution of global and regional range bin settings representative for summer 2020 with the regional campaign RBS boxes MARS (Mediterranean Aerosol Range bin Setting) and AUMATEX (AUstralian smoke Measurements Above the Troposphere EXperiment). Red circles show a selection of permanent, ground-based Cal/Val stations, active during that time.

One highlight was the QBO setting, introduced in June 2020 to allow high altitudes measurements up to 25 km in the tropics aiming to observe the disruption of the quasi-biennial oscillation (QBO). This setting was proposed by a Cal/Val team and led to an exciting dataset and several publications (Banyard et al., 2024; Ern et al., 2023). An example for a limited area RBS was the SATURN setting over the Cape Verde islands in support to the ASKOS and JATAC tropical campaigns. Another example for a very quick ad-hoc implementation was the Tonga RBS, introduced in January 2022 after the eruption of the Hunga Tonga volcano. This setting allowed to measure the ash plume up to 30 km, the highest setting in the whole Aeolus mission.

Figure 136 illustrates the vertical distribution of the 24 range bins for five RBS settings, MARS, Tropics, Extra-Tropics, QBO and the Tonga RBS setting. While MARS was aiming to have very high vertically resolved range bins in the boundary layer, the Tonga RBS aimed at reaching as high as possible with the drawback of having only 1.25-1.5 km vertical resolution. The other three settings in between were balanced to reach high while keeping high resolution at target regions (e.g. cloud top and wind shear region for the Tropics).

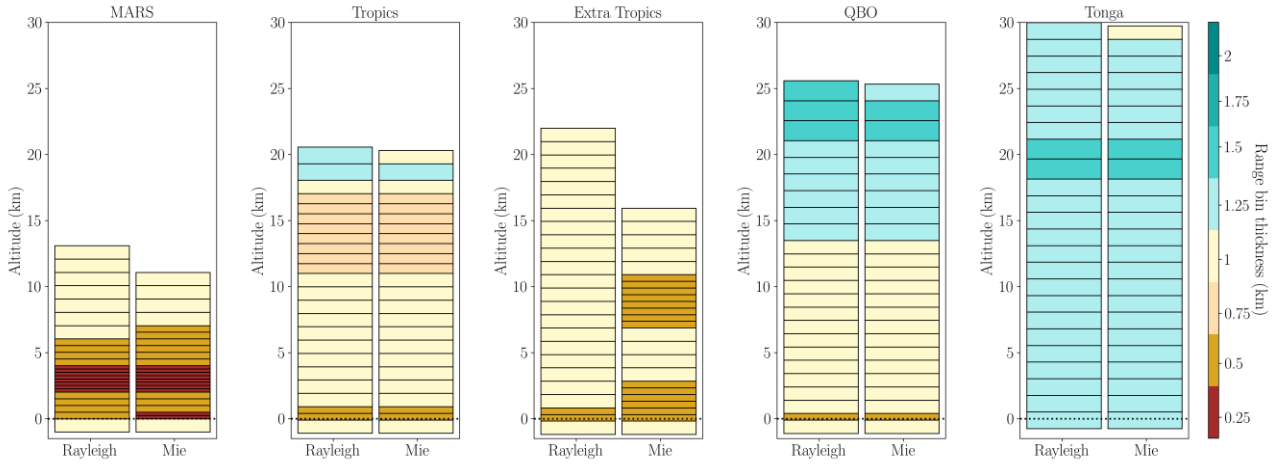

Figure 136: Example range bin settings covering different regions, time periods and vertical ranges between ground and 30 km. The varying vertical resolution ranges from 0.25 km to 2 km.

Along with dedicated campaigns, some RBS settings were defined not only for limited time periods but also for sometimes very small limited areas. These areas are indicated in Figure 137 on the left side, the time periods of their activation are shown on the right side.

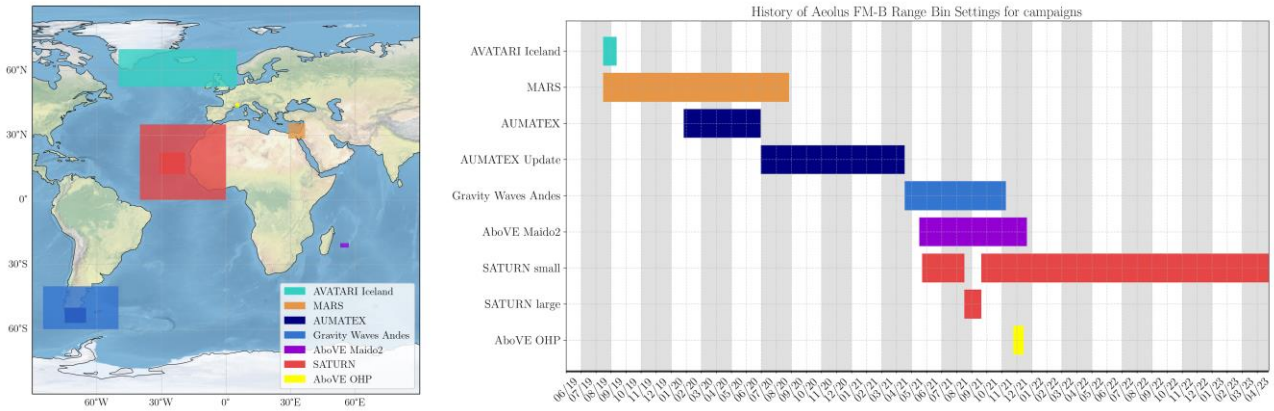

Figure 137: Geographical distribution of dedicated campaign RBS boxes (left) and the time period when they were active (right).

5.5.6 Lessons learnt from Aeolus Cal/Val

The Aeolus mission is considered as one of the most successful missions ever flown by ESA. This success could only be achieved through a strong collaboration between ESA, industry, NWP centres, Cal/Val and science teams and the Aeolus DISC. Cal/Val teams contributed by performing considerable validation activities using collocated measurements and reporting observed issues to the Aeolus DISC. In turn, the Aeolus DISC team provided validation needs, product guidelines and recommendations to the Cal/Val teams. This continuous exchange and interaction led to a number of lessons learnt which could be of interest for upcoming lidar and Earth explorer missions in space:

- **Early release of data products to Cal/Val teams**: Although several issues were known and not resolved at that point (e.g. hot pixels), the data products have been released to Cal/Val teams already 3 months after launch in the commissioning phase. This gave Cal/Val teams the opportunity to work with the data more than 1 year before public data release. ESA and DISC also profited from this early release as first validation results using external data could provide evidence to release data to the public in May 2020.
- **Provide regular updates regarding data products to Cal/Val teams**: Due to regular processor updates (so-called baseline versions usually every 6 months), it was important to inform users about the major changes (sometimes new variables, units, QC flags, resolution). Announcements of periods with special calibrations is important to avoid teams to measure, when the satellite was not in nominal measurement mode.
- **Flexibility in Range Bin Settings highly increased science impact:** Input from Cal/Val teams triggered scientific questions that could be addressed by adjustments of the vertical sampling (RBS) for special periods and geographical regions. This allowed to react ad-hoc on special events like the Hunga Tonga eruption. To discuss new RBS settings and propose them to ESA, a working group was created (Range Bin Setting Working Group). And overview of all RBS during the mission is provided on the ESA website (ESA (2020).
- **Communication platform (Cal/Val confluence) brings teams together:** The Cal/Val confluence platform was maintained by ESA and the Aeolus DISC to not only provide news, documents, baseline updates, instrument settings, timeline of planned calibration activities but also to discuss issues (open communication strategy allowed on confluence), provide preliminary results and to propose new settings. Until 2024, the Aeolus Cal/Val confluence counts 499 registered users.
- **Validation throughout the whole mission**: The product quality assessment by external Cal/Val teams using long-term collocated observations complemented the wind product monitoring at ECMWF. Also, beyond the mission, long-term validation of the reprocessed datasets is important together with dedicated scientific studies.
- **Joint validation campaigns using airborne instruments**: While several Cal/Val teams do validation for special geographical regions and often profile-to-profile comparisons, only aircrafts allow validation of multiple profiles along the satellite track, in remote areas and during special atmospheric conditions. 4 airborne campaigns were performed by DLR throughout the mission lifetime. In addition, major field campaigns with combination of several aircrafts and ground-based instrumentation, e.g. JATAC provide unique datasets for both validation and science.
- **Provide guidance to tools, e.g. for overpass prediction**: Not all users are familiar with the multiple tools, which significantly facilitate the work with Aeolus data, e.g. overpass tools, VirES, VRE (see section 5.6). Therefore, guidance is important what and how to make best use of it. For teams with only one ground-station, a table with overpass times for certain latitudes / longitudes was well received by the community.
- **Provide standards/recommendations for collocation criteria but also verification of them:** Certainly, standards for collocation (temporal/spatial) are important, but also the analysis needs common approaches for quality control of the data products, e.g. use of the error estimates in the products and handling of gross errors. Different altitude regions might require different collocation criteria.

- **Provide handbook for Cal/Val requirements**, as provided by Straume (2019), and implementation plan of external Cal/Val activities (Straume et al., 2019) before launch to ensure that teams are ready from the first day to perform collocated measurements (even before first data access is possible) > critical point for relatively short mission.
- **Organization of regular exchange meetings within certain topical sub groups (wind, aerosol, instrument, NWP):** This allows discussion in smaller groups between Cal/Val teams and ESA, DISC in form of 2-day working meeting every 6 months following the provision of the Cal/Val team reports and the synthesis of these reports.

A presentation about these lessons learnt from Aeolus Cal/Val has been given to the EarthCARE community at the ESA-JAXA Pre-Launch EarthCARE Science and Validation Workshop on 13-17 November 2023 in Frascati, Rome (Bley et al., 2023).

5.6 VirES Virtual Research Environment (VRE)

Isabell Krisch, DLR

VirES (Virtual Workspace for Earth Observation Scientists) for Aeolus (https://aeolus.services), a service provided by ESA, is a web-based client for the interactive analysis and visualization of Aeolus data. The service developed by the company EOX in cooperation with DLR was already operational when Aeolus was launched in August 2018 and was released to the Aeolus Cal/Val community in February 2019. It quickly became a well-established tool in the Aeolus community for data inspection and visualization. Since May 2020, with the public release of the Aeolus wind product; VirES is accessible via https://aeolus.services/.

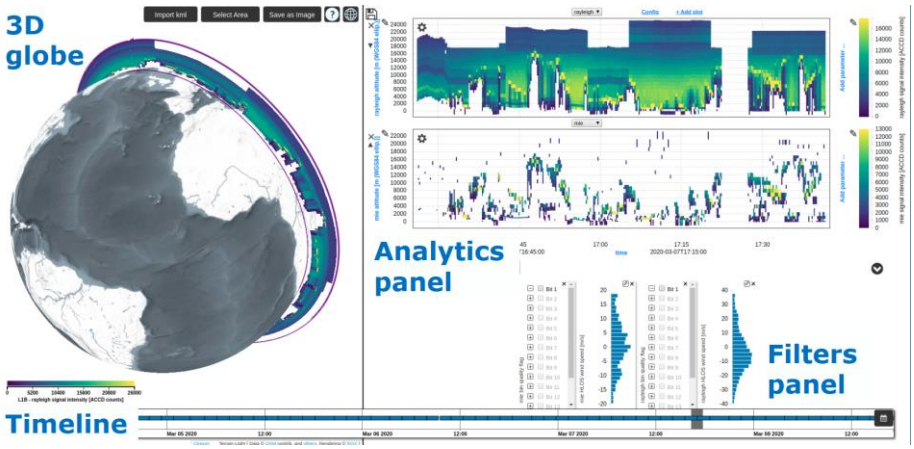

Figure 138: VirES for Aeolus service web client user interface (https://aeolus.services).

The VirES web client is built up of different panels that allow data filtering based on time and other product parameters as well as the visualization in an analytics or 3D globe view (see Figure 138). With the possibility to download data not only in the original Earth Explorer file format but also in the commonly used netCDF format, VirES was during Phase E2 the only possibility to obtain Aeolus data in this data format. This, together with its visualization capabilities, is a reason that makes this service very interesting for the Aeolus community and thus has become an essential tool for Aeolus data discovery.

However, due to a maximum possible time span for the selection of data products in the VirES web client, the analysis of long time series is limited. Furthermore, the web client does not offer the possibility to edit data or to fully customize visualizations as desired. A functionality to evaluate and visualize measurement comparisons, an important work in the validation of Aeolus observations, could not be implemented in the web client.

To overcome these deficiencies, an add-on to the existing VirES for Aeolus web-based application has been implemented as a virtual research environment (VRE) in 2021 (https://notebooks.aeolus.services). The implementation of the VirES VRE was done by the company EOX with the support of scientific expertise from the DISC team. Scientific experts from the DISC team were responsible for the definition of user requirements (Geiß, 2021) and to provide supporting documentation in the form of exemplary data analysis software.

The VirES VRE is a shared computing environment using JuypterLab, a web-based interactive development environment for Jupyter notebooks, code and data. Jupyter notebooks allow the combination of software code, computational output, explanatory text and multimedia resources in a single document. A notebook consisting of multiple “cells” can be executed in one shot or iteratively

cell by cell. With these functionalities and the large base of user-developers this free and open-source web tool has become very popular in data science, scientific computing, and machine learning.

The VirES VRE is set up in a customized JupyterHub distribution which provides an on-line execution environment in which a JuypterLab environment can be started and through which Jupyter notebooks can be created and executed. This allows to start the VirES VRE from anywhere with just a web browser.

Although the JupyterLab environment supports various programming languages, the main focus of the VirES VRE is Python as it is a widely used language in the scientific community and provides easy extendibility through package installation. The VirES VRE customization of the generic JupyterLab environment provides links to the VirES VRE on-line documentation and a library of tutorial notebooks.

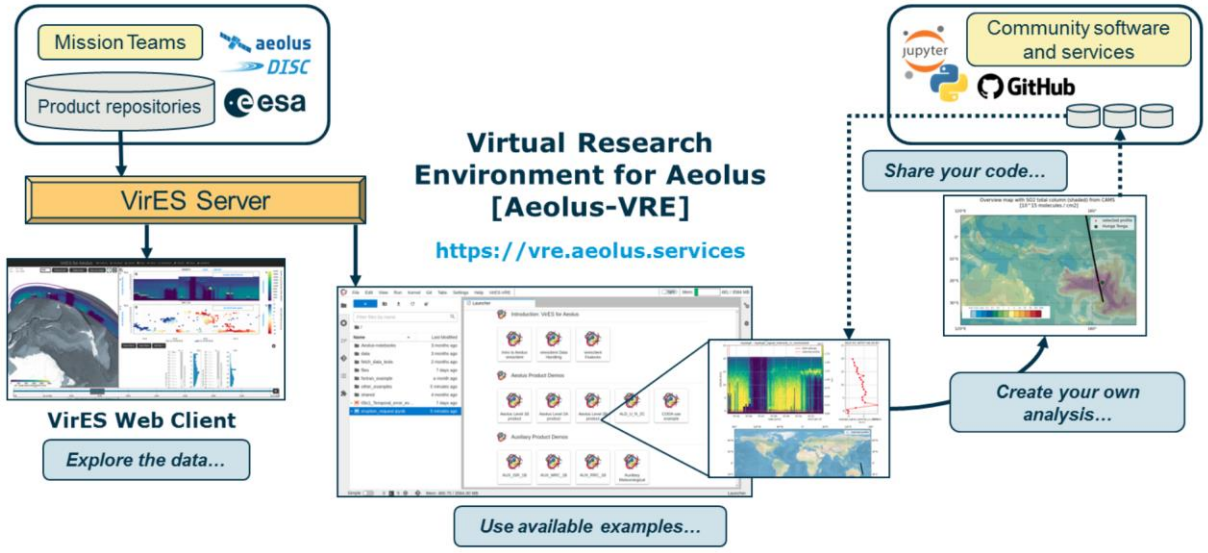

Figure 139: The Aeolus VirES VRE and web client. Figure from Santillan Pedrosa et al. 2022.

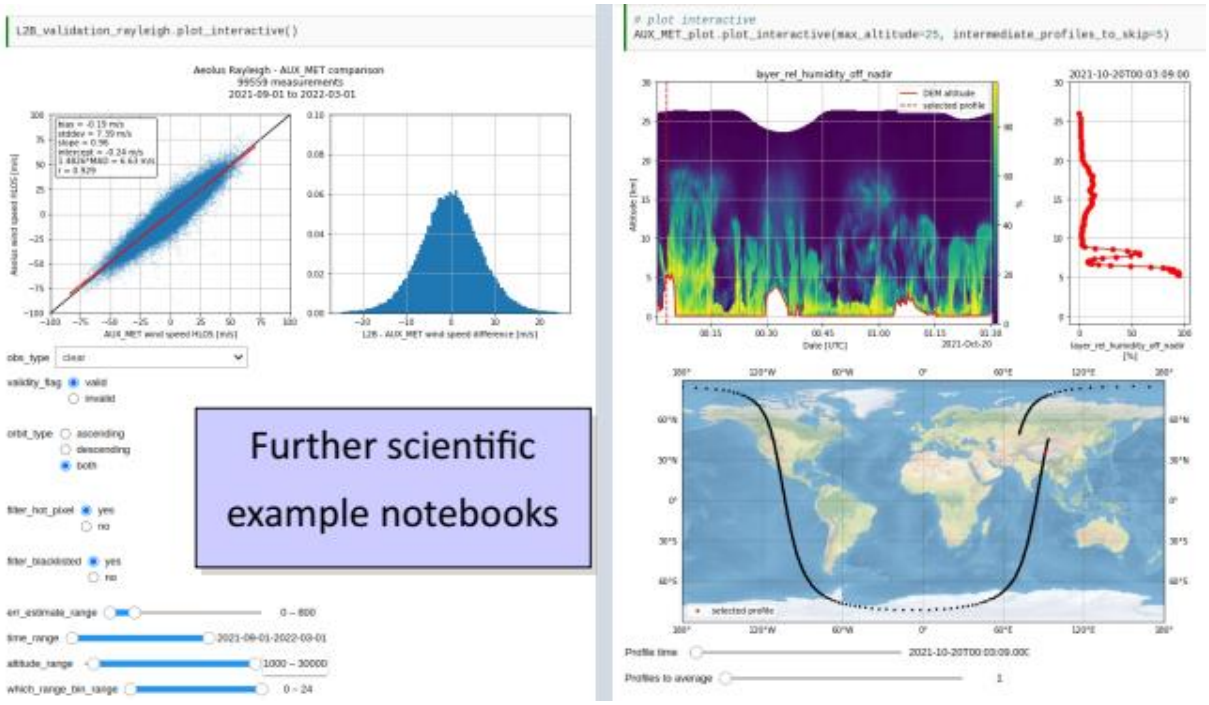

Figure 140: Scientific example notebooks available on the VirES VRE developed by the DISC team. Figure from Santillan Pedrosa et al. (2022).

5.7 Outreach

Ad Stoffelen, KNMI, and Paolo Sabbatini, serco

5.7.1 Introduction

The DISC Outreach includes many aspects and user engagement has been very successful. Prime, on the technical side, contacts with ESA and industry are necessary to understand the operation of Aeolus and the interaction of the UV laser beam with the earth's atmosphere and surface. Many of these communications are implicit and explicit elsewhere in this final report and the parties involved are part of the Aeolus mission. This outreach section of the final report is about the dissemination of Aeolus information to those not directly involved in the Aeolus mission, while constituting the most important user groups. The first part is about the targeted dissemination of information, while the second part is about the Web activities and monitoring of user statistics.

5.7.2 Contributions to science, operational users, and public domain

Contribution to science

Different international user groups associated with the different mission goals may be identified. First, many scientists are interested in the novel DWL (Doppler Wind Lidar) technology and to share experiences on Aeolus. A Copernicus inter-journal special issue (SI) was set up to contain manuscripts on measurement technique (AMT journal), atmospheric physics (ACP) and weather and climate dynamics (WCD). Up to today a total of 51 manuscripts has been accepted in this inter-journal Aeolus issue, while accumulation is ongoing. Many manuscripts on Cal./Val. are featured in here, both from within DISC, co-authored with DISC and with authors not in DISC from external Cal/Val teams. A second group of scientists is interested in the meteorological application of Aeolus, in particular as observing system and for Numerical Weather Prediction (NWP). A special collection (SC) was established with the Journal of the Royal Meteorological Society, featuring nine contributions. Main decisions concerning the SI and SC were taken in the Aeolus Science Advisory Group (SAG). Besides these special issues and collections, many other Aeolus contributions featured in the scholar domain. The global interest and association with the Aeolus mission is much broader and according to Google scholar 7,820 manuscripts appeared in total, featuring the "Aeolus mission". Several science contributions of broader and particular interest were featured in the ESA Aeolus mission web articles and subsequently spread in social media. Finally, Aeolus sessions and presentations in international lidar working groups, EGU, LPS, EUMETSAT conference and IEEE conferences were held, supporting the Aeolus mission science workshops.

Operational users

Given the short-designed mission length and the exploratory nature of the mission, producing a prolonged high-quality data flow of wind products appeared a priori rather challenging. Therefore, reaching the asset of a broad demonstration of Aeolus winds in Numerical Weather Prediction needed particular preparation and outreach. The WMO atmospheric wind community is well organized through the International Winds Working Group (IWWG) of the Coordination Group of Meteorological Satellites (CGMS) and their 15th meeting was facilitated by KNMI in 2021. In 2023 the 16th meeting was held in Quebec, Canada. Earlier on, Aeolus (DWL, or ADM-Aeolus) featured in all IWWG meetings since 1995 and the international winds community was hence well prepared for the mission. In addition, DWL missions have been called for in the international WMO workshops on NWP data assimilation in the past decades. Hence, the requirements for operational use of Aeolus winds were well expressed and a priori

accommodated to allow for operational use of the exploratory mission data. The overwhelming success of the world-wide global-impact demonstration of Aeolus winds in NWP would not have been possible without the noted outreach and preparation.

The ever-favourable recommendations of the WMO and CGMS plenary meetings were communicated by the Aeolus team to ESA and EUMETSAT directors, calling for an Aeolus follow-on mission (see Figure 141 with illustrating NWP impact results from Aeolus). These communications were well received, resulting in the design of the EPS-Aeolus mission by ESA and EUMETSAT. DISC members are also involved in preparations for the approval of the EPS-Aeolus mission, where communication of the expectations of NWP impact in the 2040-time frame to the EUMETSAT member states is fundamental.

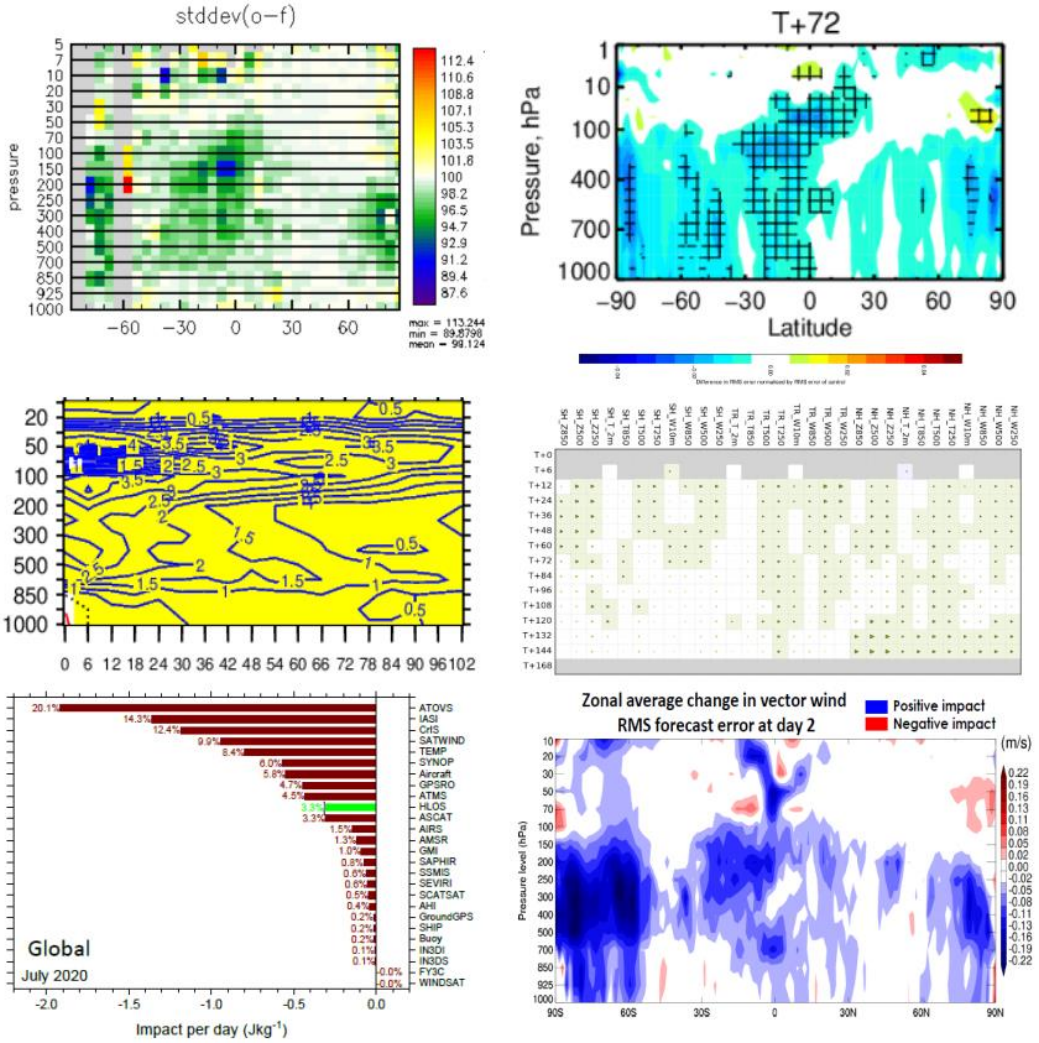

Figure 141: Examples of improvements of global NWP from different models when assimilating Aeolus HLOS winds, as shown at the 3rd Aeolus NWP Impact and L2B data quality Working Meeting, December 2021. Top left panel: Zonal average DWD 6-hour weather forecast fit to radiosondes show large improvement (up to 10%) after assimilation of Aeolus winds (Green and blue colours: forecast error reduction), Top right panel: Zonal average impact of Aeolus winds on ECMWF 3-day vector wind forecast error (normalized RMSE, ±5% colour-scale, blue colours indicate forecast error reduction, hashed areas 95% significant), Middle left panel: Normalized RMS(O-B) results from an Météo-France OSE assimilating Aeolus winds from July to October 2019 for the tropics. Blue isolines and yellow colour indicate areas with statistically significant positive impact. Middle right panel: UK Met Office forecast impact of including Aeolus Rayleigh-clear winds on scores for wind (W), geopotential height (Z) and temperature (T) in the regions SH, Tr and NH at 2 m, 850 mb, 500 mb and 150 mb level (horizontal) for forecast ranges from 0 to 168 hours (vertical), where triangles denote the size of the impact (green is positive). Lower right panel: Ranking of the FSOI impact of different observation types on the global model of NCMRWF for July 2020. Aeolus has the 3rd highest impact per observation on the NCMRWF model. Lower right panel: Impact of reprocessed (B10) Aeolus winds on the ECCC global model for August/September 2019. A large positive impact is seen in the tropics and polar regions.

Public domain

ESA outreach in the public domain was well supported within DISC and also successful. Several science contributions of broader and particular interest were featured in ESA Aeolus mission web articles and subsequently spread in social media. This included novel scientific findings, Aeolus NWP impact and specific contributions at conferences and workshops.

5.7.3 Web activities and user statistics

Web Portal Management

Ensuring the seamless operation and relevance of the Aeolus web portal is a pivotal aspect of the Aeolus DISC contract's activities. This responsibility encompasses a multifaceted approach, involving continuous updates and meticulous attention to detail. Collaborating closely with the AEOLUS DISC teams, the aim is to integrate the latest information pertinent to the mission. From the most recent overpass data and instrument status updates to timelines highlighting calibration interruptions and anomalies affecting product quality, each piece of information plays a crucial role in maintaining the portal's relevance. Adherence to the layout standards outlined by ESA's EOGateway is paramount, guaranteeing a user-friendly experience for all stakeholders. Moreover, securing necessary authorizations from ESA, excluding automatically generated content, is fundamental to the process, ensuring compliance and integrity throughout.

The **Aeolus Mission** webpage is visible at: https://earth.esa.int/eogateway/missions/aeolus

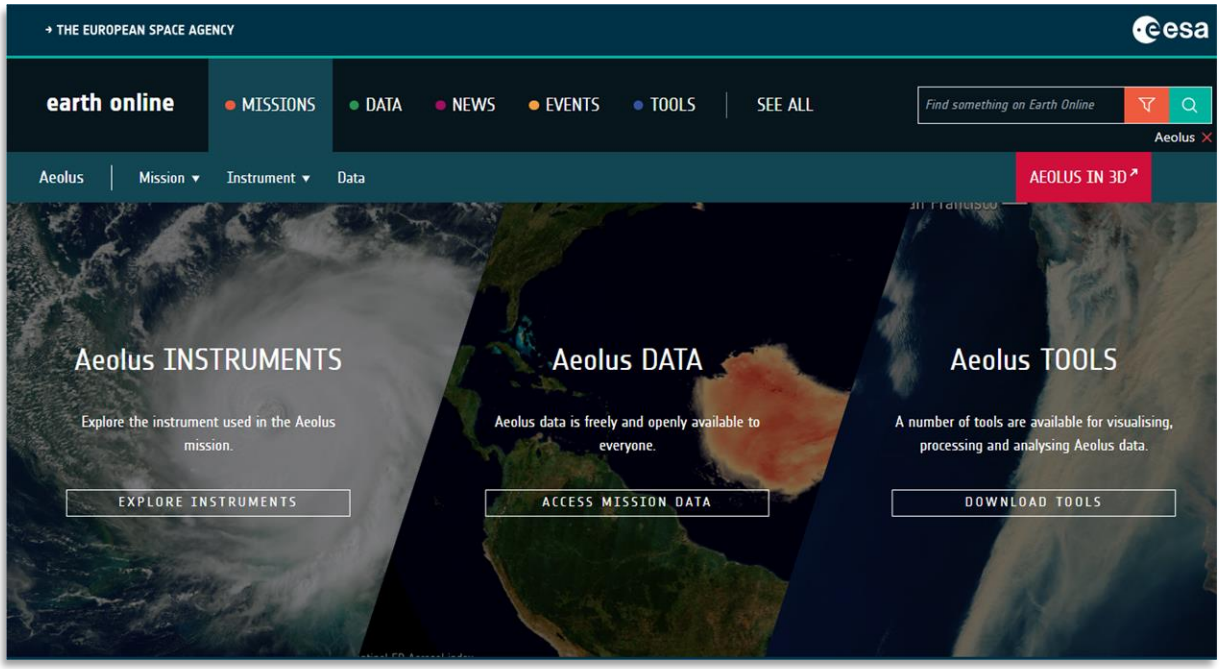

Figure 142: Aeolus mission webpage.

The **Aeolus DISC Activity** webpage is visible at: https://earth.esa.int/eogateway/activities/aeolus-disc

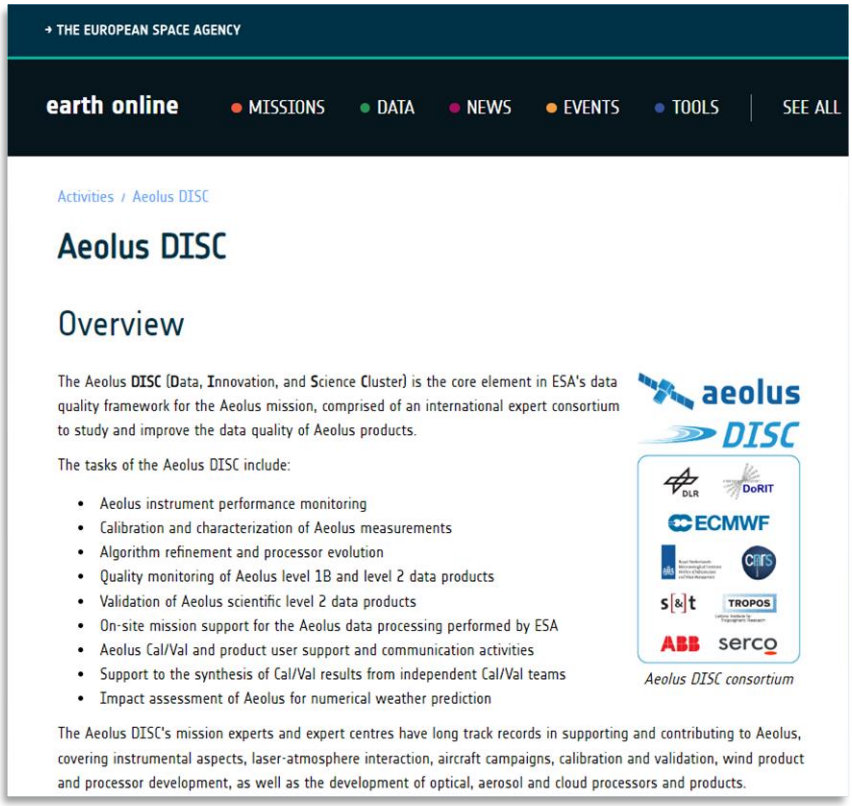

Figure 143: Aeolus DISC activity webpage.

The web update activities follow a content approval workflow described in the picture below:

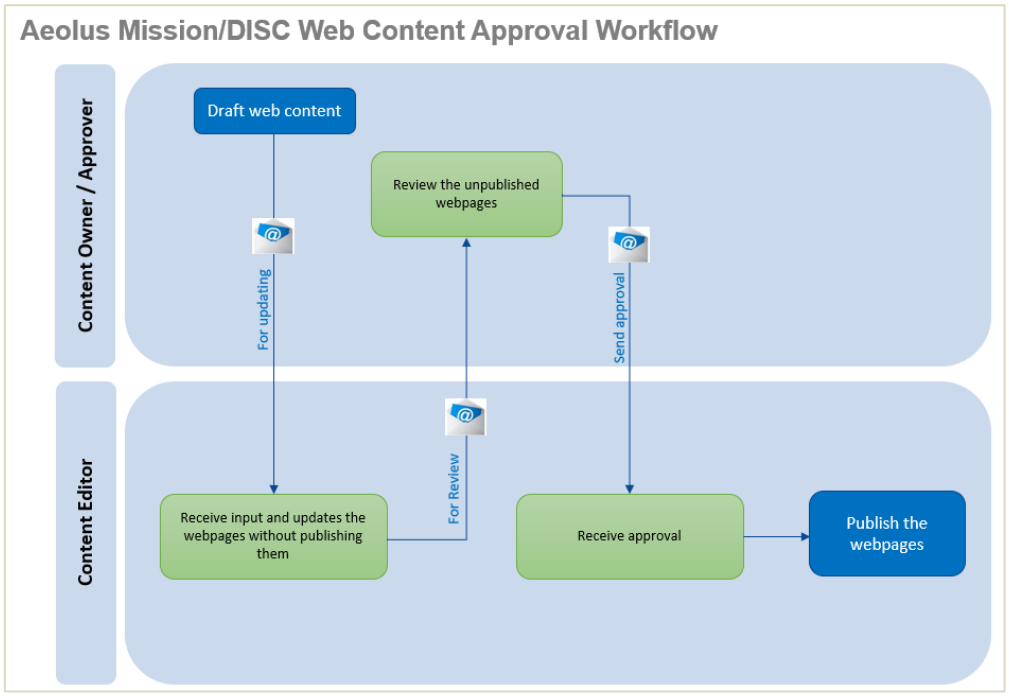

Figure 144: Approval workflow for the web update activities.

Direct Reporting and Data Analysis

Maintaining an efficient and transparent reporting line to the Data Quality Manager and other mission entities is imperative for the successful execution of Phase 2 tasks. This entails providing comprehensive statistics on Aeolus website usage and downloads of Quality Control (QC) and Anomalies reports from the QRAS (Quality Reports Advanced Search) portal. Statistics for Aeolus Mission and Aeolus-DISC (under "Activities" section) are provided on quarterly basis by SPPA (Sensor Performance, Products and Algorithms) Web Team. The collaboration with the QRAS Team is integral to this process, as it ensures accurate data collection and analysis, facilitating informed decision-making and strategic planning.

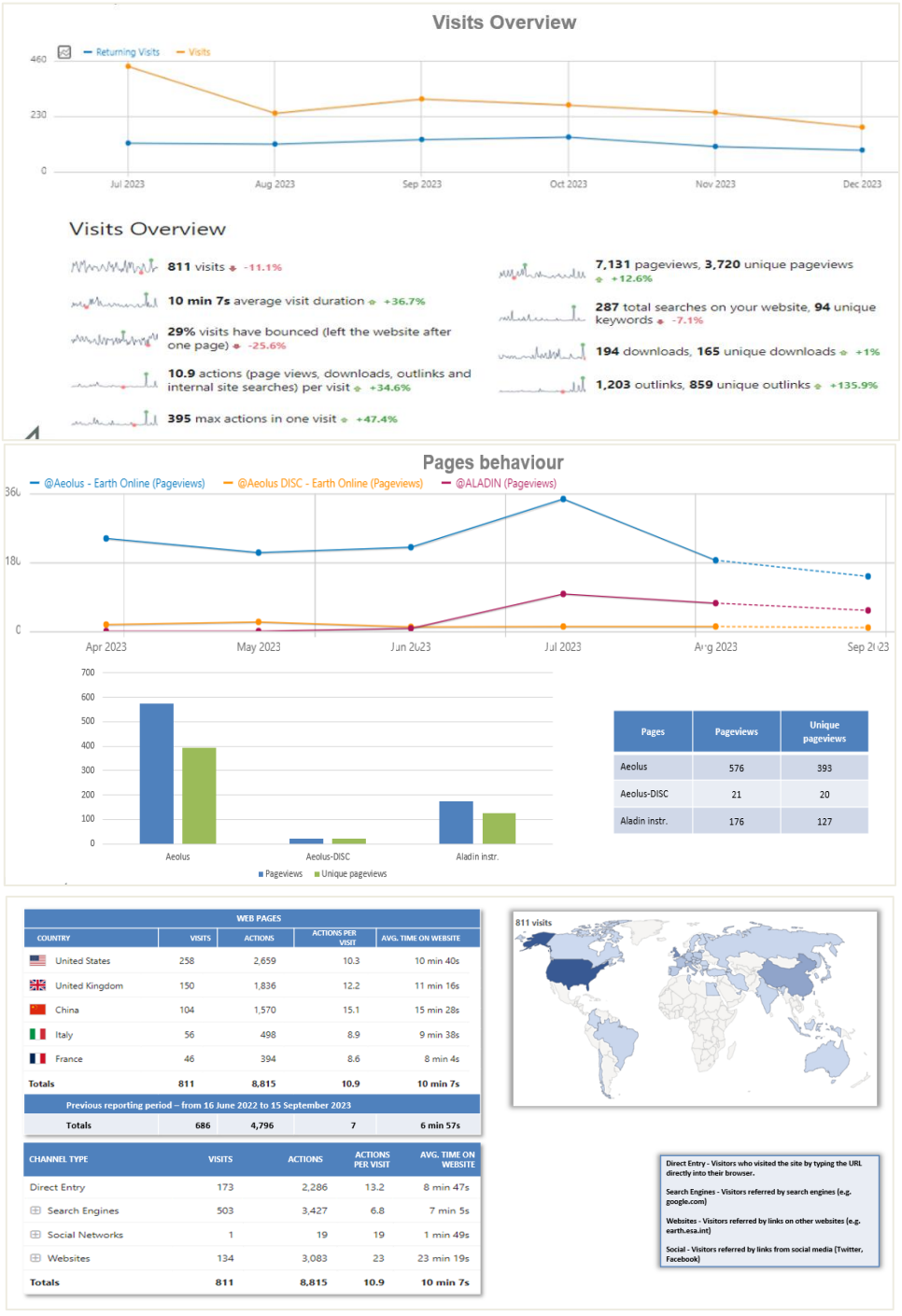

Figure 145: Exemplary statistics on Aeolus website usage and downloads of Quality Control and Anomalies reports from the Quality Reports Advanced Search portal.

Monthly Quality Control Reports Publication

The management of monthly quality control reports is streamlined through the utilization of the "core system" engine, automating the process for efficiency and accuracy. Following indexing and accessibility checks, all reports are uploaded to a dedicated server, ensuring seamless access for stakeholders.

The development of the QRAS tool is a crucial component of this process. Comprising three core systems, namely the Front-End, Back-End, and Engine, the tool offers advanced search and filtering capabilities to users. The Front-End, accessible via the internet, provides a user-friendly interface for accessing reports. Integrated seamlessly into the EOGateway pages, it maintains consistency in layout and URL for user convenience. Meanwhile, the Back-End portal, accessed through VPN, enables operators to manage the Front-End efficiently. The Engine component is responsible for the circulation of reports, facilitating daily uploads for live missions and bulk uploads for report reprocessing, along with updates to databases.

Ensuring meticulous attention to detail and adherence to established protocols, each Aeolus L2B Monthly Quality Control Report is meticulously named for accurate indexing in QRAS. This meticulous approach enhances ease of retrieval and accessibility for stakeholders.

Upon preparation, these reports are promptly published on the QRAS web portal, serving as a vital repository of information for all involved in the Aeolus mission. Furthermore, efforts are directed towards ensuring the seamless integration of Aeolus quality control reports into the EOGateway portal, enhancing user experience and maximizing the dissemination of critical information across platforms.

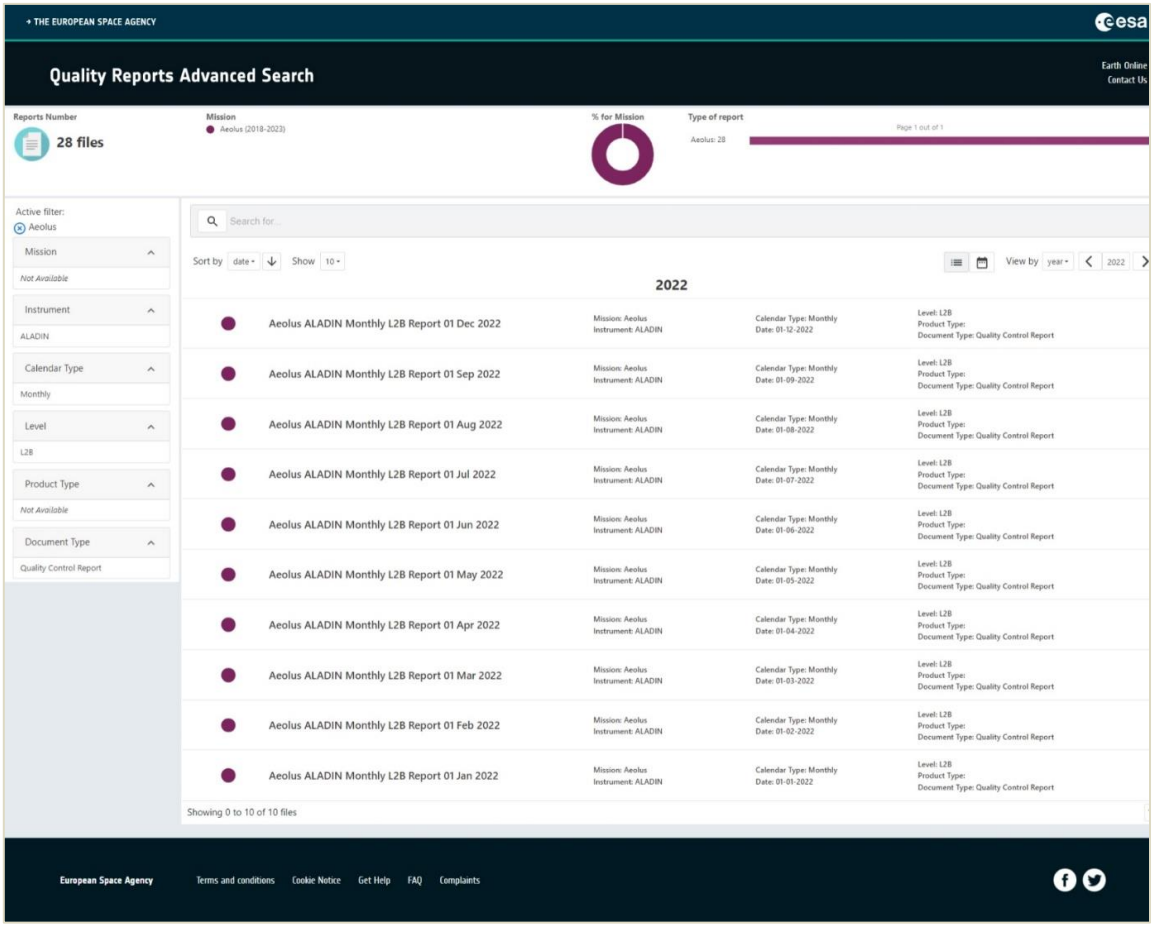

Figure 146: Exemplary search results for Aeolus L2B Monthly Quality Control Reports.

5.7.4 Lessons learnt from Outreach

The following aspects may need further attention for future missions:

- Identification of different global user groups according to mission objectives and an associated user information strategy and procedure;
- For Aeolus, although organized organically, the information flow to distinguished user groups has been efficient and successful, and no further formal procedures are necessary;
- Nevertheless, an a-priori generic description may be useful as a template in order to organize and control all aspects of outreach and communication to the different identified user groups.

6 NWP impact assessment

6.1 NWP impact assessment for wind at ECMWF

Michael Rennie, ECMWF

6.1.1 Impact from Observing System Experiments (OSE)

This chapter summarises the research as part of the DISC, between 2019-2023 on the data assimilation of Aeolus L2B HLOS winds and its impact assessment in ECMWF's global Numerical Weather Prediction (NWP) system. Further information can be found in: Rennie and Isaksen (2020), Rennie et al. (2021), Rennie et al. (2022) and the DISC NWP impact ESA Contract Report: Rennie and Isaksen (2024).

Despite the L2B HLOS wind random and systematic errors being larger than pre-launch expectations (see section 5.3), Aeolus has demonstrated a very useful positive impact in ECMWF's global NWP model (and for other NWP centres). The impact was assessed at ECMWF via the Observing System Experiment (OSE) and the Forecast Sensitivity Observation Impact (FSOI) methods. Given the positive impact, Aeolus was operationally assimilated at ECMWF from 9 January 2020 until 30 April 2023, which is not typically done for a relatively short, technology demonstration mission.

In OSEs, short- to medium-range forecasts with and without the observations being assessed are verified against a reference analysis atmospheric state. Such verification showed positive impact from Aeolus. The best impact was found for the early FM-B laser period (2nd reprocessing, B11) and FM-A 2018-2019 (3rd reprocessing, B14), for example see Figure 147. Positive impact was demonstrated in OSEs for most periods of the mission; however, the magnitude reduced to only a small positive impact for the Rayleigh-clear from the FM-B laser in 2021 and 2022 (tested with NRT-processed data so far), due to poor atmospheric path signals (as explained in the Instrument Performance and L2B monitoring sections).

At its best, Aeolus showed statistically significant positive impact on vector wind, temperature, geopotential and humidity forecasts in the tropical and polar troposphere and lower stratosphere, by ~2-3% for root mean square error at 2-day forecast range. The positive impact in tropospheric polar regions tended to neutrality by 4-day forecasts, whereas the positive impact in the tropics and midlatitudes persists for longer. At 100-50 hPa (15-20 km) in the tropics, the positive impact persists to 8–10-day forecasts, particularly for the FM-B period (the limit of forecast range in the OSEs), which is an unusually good impact for one satellite instrument.

This strong tropical impact agrees with pre-launch expectations, based on geostrophic adjustment theory: stating the increased importance of wind compared to mass information in the tropics due to the large Rossby radius of deformation. This was also demonstrated with *in situ* wind observations in Horányi et al. (2015a). Aeolus may be improving the representation of equatorial waves e.g. Kelvin waves, which could be a source of improved medium-range predictability e.g. Žagar et al. (2021). The largest tropical impact was in the east Pacific at 100 hPa (~16 km), around the tropical tropopause, with locally >5% improvements at 3-day forecast range, see Figure 148 – a region with the largest zonal wind background errors (Ensemble Data Assimilation (EDA) spread maps show this).

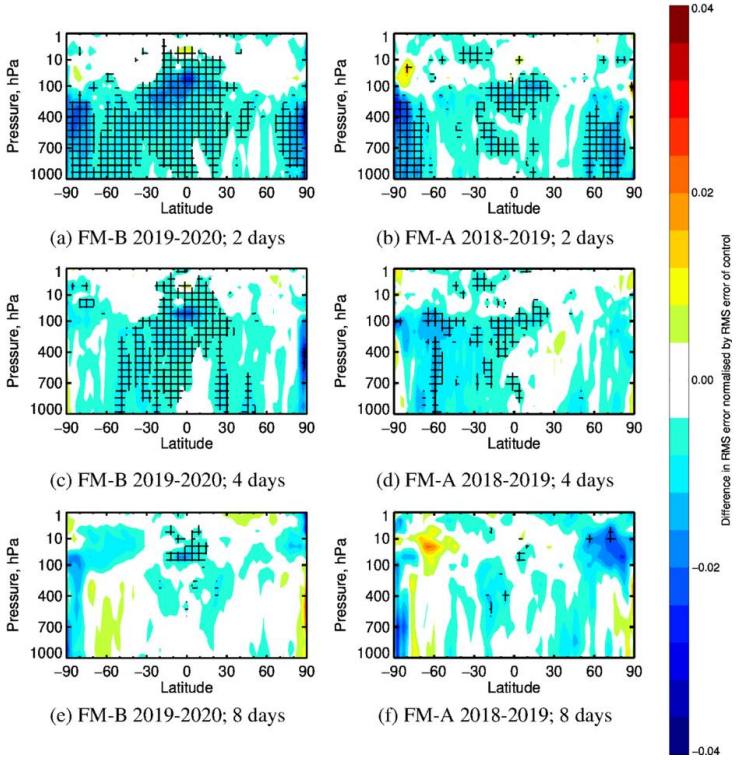

Figure 147: Zonal average normalised change in the RMS (root-mean-square) error of vector wind forecasts, verified with operational analyses, from assimilating Aeolus HLOS winds (Rayleigh-clear and Mie-cloudy) for the period 29 June 2019 to 9 October 2020 using the second reprocessed dataset (FM-B) for (a) 2-day forecasts, (c) 4-day forecasts and (e) 8-day forecasts, and similarly for the period 3 September 2018 to 16 June 2019, using the third reprocessing dataset (FM-A), for (b) 2-day forecasts, (d) 4-day forecasts, and (f) 8-day forecasts. Negative values indicate a reduction in error from assimilating Aeolus and positive values an increase in error. Cross-hatching indicates 95% confidence. Plots show from -90° (South Pole) to +90° (North Pole) latitude. 1000 hPa is approximately the surface as sea level, 500 hPa is ~4.5-6 km, 300 hPa is ~8-10 km and 100 hPa is ~15-17 km altitude.

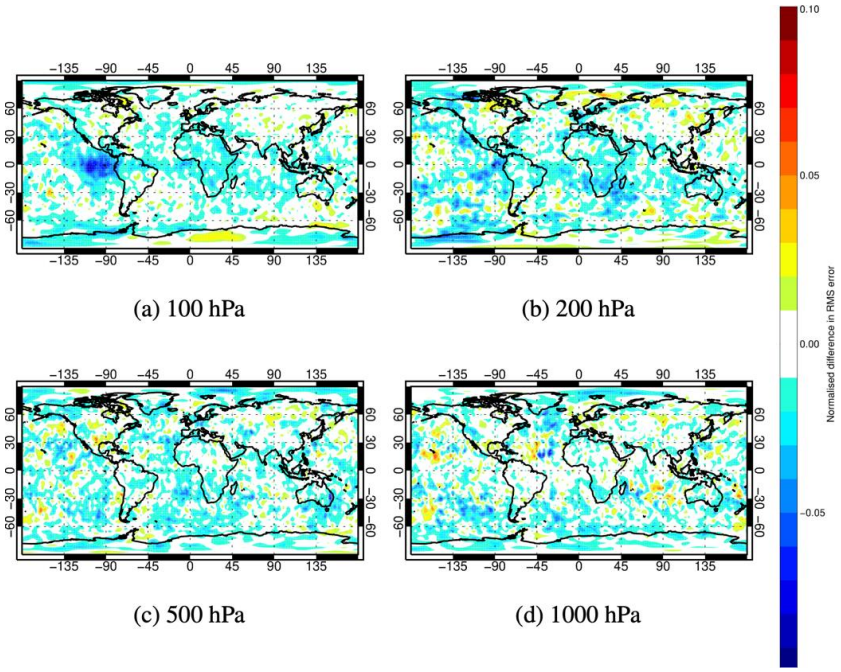

Figure 148: Maps of normalised change in the RMS (root-mean-square) error of vector wind forecasts, verified with operational analyses, from assimilating Aeolus (Rayleigh-clear and Mie-cloudy) at a forecast range of three days for the period 29 June 2019 to 9 October 2020 using the 2nd reprocessing. At pressure of (a) 100 hPa, (b) 200 hPa, (c) 500 hPa and (d) 1000 hPa. Negative values indicate a reduction in error from assimilating Aeolus and positive values an increase in error.

Aeolus impact improved using the 2nd reprocessing compared to the 1st reprocessing for early FM-B (July-December 2019) in the tropical lower troposphere, which justifies the efforts by the DISC to improve the ground processing algorithms.

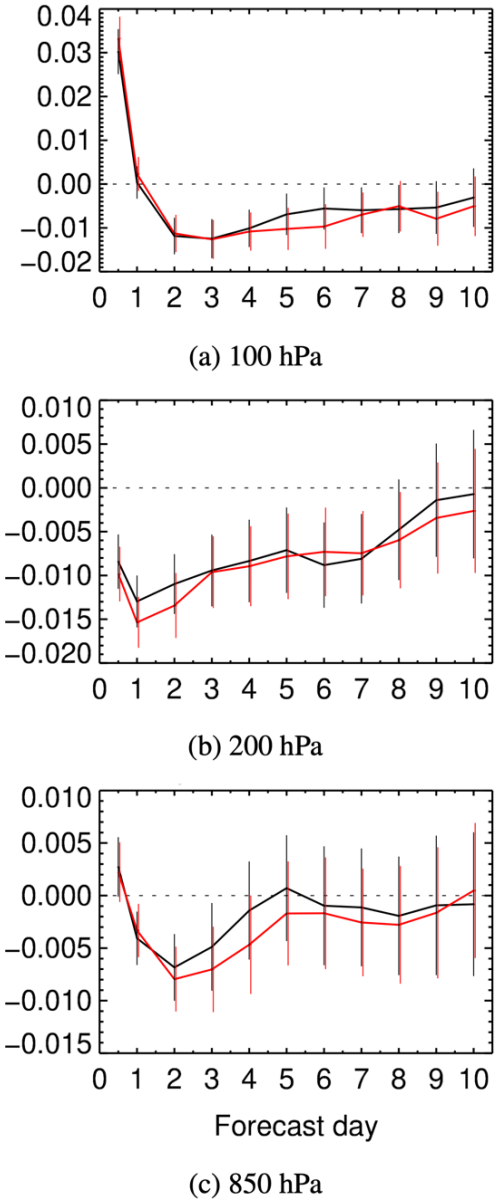

Figure 149: Normalised change in the RMS (root-mean-square) error of vector wind forecasts, verified with operational analyses, from assimilating Aeolus (Rayleigh-clear and Mie-cloudy) for the period 29 June 2019 to 31 December 2019 in the tropics at (a) 100 hPa, (b) 200 hPa and (c) 850 hPa. Black lines are the first reprocessing (B10), red lines are the second reprocessing (B11). Negative values indicate a reduction in error from assimilating Aeolus and positive values an increase in error. Since operational analyses are used for verification, the first day or so is untrustworthy.

Aeolus consistently improves the short-range forecast (and analysis) fit to other assimilated observation types sensitive to wind, temperature and water vapour e.g. see Figure 150, which is a reliable demonstration that Aeolus is improving the atmospheric state. The well vertically resolved radio occultation bending angles mostly provide temperature information and to a lesser extent water vapour. Aeolus has a maximum impact with respect GNSS (Global Navigation Satellite System) radio occultation data in the tropics at ~14-17 km, which is near the tropical tropopause, matching the good impacts in forecast verification against analysis. The improvement in the fit to *in situ* zonal wind observations (mostly radiosondes) in the Tropics peaks at 150 hPa, which is just below the tropical tropopause.

The fit to geostationary infrared water vapour channels is consistently improved – suggesting that Aeolus improves the advection of water vapour. The magnitude of improvement can be qualitatively compared to OSE denial experiments by Bormann et al. (2019). Aeolus' approximate 1-2% improvement in short-range forecast wind fit with respect to conventional wind data is similar in magnitude to that determined for GNSS radio occultation, infrared radiances and AMVs (Atmospheric Motion Vectors), observing systems at the time of those experiments, which can be considered a good result for a demonstration mission providing about 0.5% of the total number of observations assimilated.

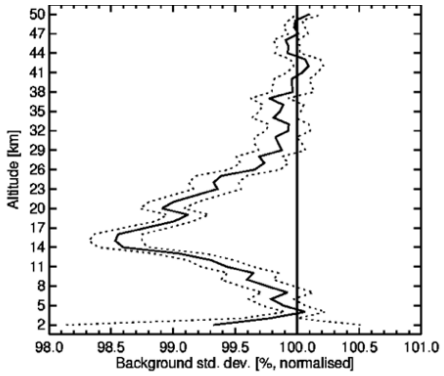

(a) Radio occultation; tropics

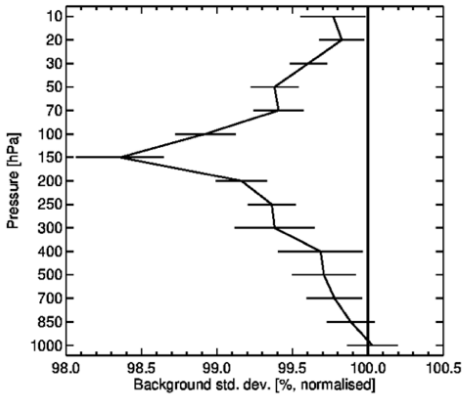

(b) Radiosonde and aircraft u-wind; tropics

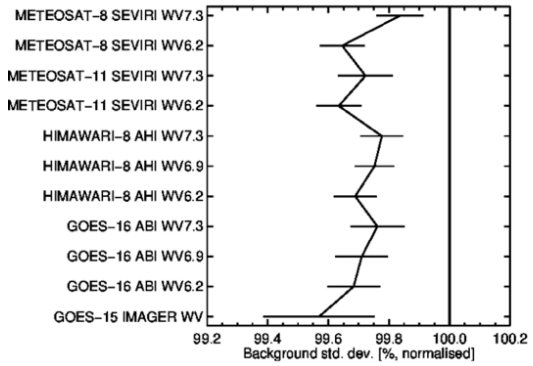

(c) Geostationary water vapour; global

Figure 150: The change in standard deviation of O-B departures resulting from assimilating Aeolus HLOS wind observations (Rayleigh-clear and Mie-cloudy), normalised so that the control is 100%. Values below 100% show an improved fit from assimilating Aeolus and above 100% show a degraded fit. The observation types are: a) GNSS radio occultation in the tropics, b) radiosonde and aircraft u-wind component in the tropics, and c) geostationary imagery water vapour channels. Horizontal bars show the 95% confidence range (Student's t-test). For the period 29 June 2019 to 9 October 2020 using the 2nd reprocessing.

The ECMWF global model average background (0-12 hour forecast) errors in HLOS wind space have a standard deviation typically of 1.5-2.5 m/s (via Desroziers' diagnostics with respect to radiosondes). Therefore, the Rayleigh-clear HLOS wind assigned errors in assimilation (1-σ > 4 m/s) are dominated by the instrument noise (mainly shot noise), rather than representativeness and forward model errors. The free troposphere Mie-cloudy noise estimates (1-σ ~ 3 m/s) are smaller, partly due to the strong backscatter from clouds. In weakly backscattering and attenuating aerosol loads e.g. desert dust, the Mie winds can have large instrument noise e.g. 6 m/s (L2B processor estimated errors).

Due to the typically smaller instrument noise, the Mie-cloudy assigned observation errors in data assimilation are more of a balanced combination of instrument and representativeness errors. The Mie-cloudy winds are thought to have larger representativeness errors than the Rayleigh-clear due to their smaller horizontal scales, uncertainties about where the cloud backscatter occurs within the range-bin in wind shear and the model's difficulties in representing winds in convective cloud regions. Mie-cloudy impact was improved by introducing a representativeness error term. This consisted of adding (in variance space) 2 m/s to the 1.25-scaled L2Bp estimated error; various options were tried and this gave the best impact and also agreed with expectations on standard deviation of O-B versus L2Bp estimated error.

With the caveat of relatively strong atmospheric path signal levels, the Rayleigh-clear provided a greater proportion of the positive impact than the Mie-cloudy, especially in the tropics. This is presumably due the Rayleigh's much greater spatial coverage compared to the Mie winds, helping to better capture the larger-scale flow. However, Mie winds tend to provide more positive impact in polar regions (to 3-day forecast range) – perhaps due to the more continuous spatial coverage in polar regions due to the orbit. However, it is somewhat surprising that winds are useful at high latitudes, when the abundant mass information should be more dominant. Running the Integrated Forecast System (IFS) 4D-Var outer loop and forecast model at higher resolution (18 km grid, rather than 28 km) increased the magnitude of Aeolus impact. The higher resolution model may allow wind data to be better exploited, since geostrophic adjustment theory predicts that winds are more important than mass observations at smaller horizontal scales. This perhaps suggests that Doppler wind lidar impact may increase even further with convection-resolving operational models (part of the ECMWF 10-year strategy).

6.1.2 Impact from short-range forecasts

The varying impact during the mission, as detected via OSEs, was also captured by the FSOI (Forecast Sensitivity to Observation Impact) metric (global dry energy norm), which assesses the short-range forecast impact (1 day); see Figure 151 showing the absolute FSOI time-series for Rayleigh-clear and Mie-cloudy (and the sum). The relative FSOI (fraction of the overall error reduction for a subset of data) was 5% in early FM-B reprocessed dataset in 2019 but reduced to 2% in mid-2022 due to poor signal levels. The Mie-cloudy impact exceeded the Rayleigh-clear from 2022, partly because the Mie-cloudy noise was less affected by signal loss in strong cloud backscatter conditions and partly due to improved use of the Mie data. The relative FSOI improved to 3-4% in late 2022/early 2023, with the switch back to the FM-A laser and improved signal levels. Other improvements in the observing system by 2023 e.g. a lot more GNSS radio occultation, may have influenced this relative FSOI as well.

At its peak in the early FM-B period, Aeolus' relative FSOI was similar in magnitude to a MetOp IASI instrument, and ranked amongst the highest FSOI per satellite instrument. Also, it had a similar impact to the radiosonde network. Aeolus has a strong impact per observation, as shown in Figure 152 (orange bars), by normalising the relative FSOI by the number of observations per instrument. The ongoing lack

of height-resolved global wind profile information in the Global Observing System could explain why the relatively noisy Aeolus data are important.

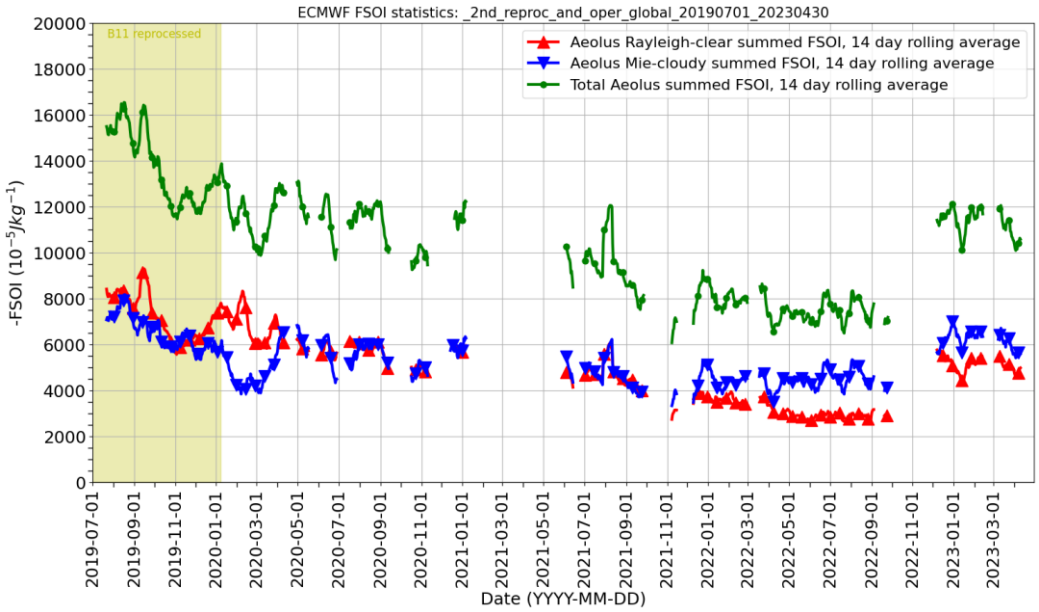

Figure 151: Time-series of global, daily summed FSOI for Aeolus HLOS winds, from 1 July 2019 to 30 April 2023. A two- week rolling average has been applied to reduce noise. The y-axis is the negative of the FSOI and therefore positive values represent positive impact. The second reprocessing FSOI is used before 9 January 2020 (light green background) and the operational FSOI thereafter. Gaps in the time-series are due to instrument testing periods or data outage, combined with the two-week averaging.

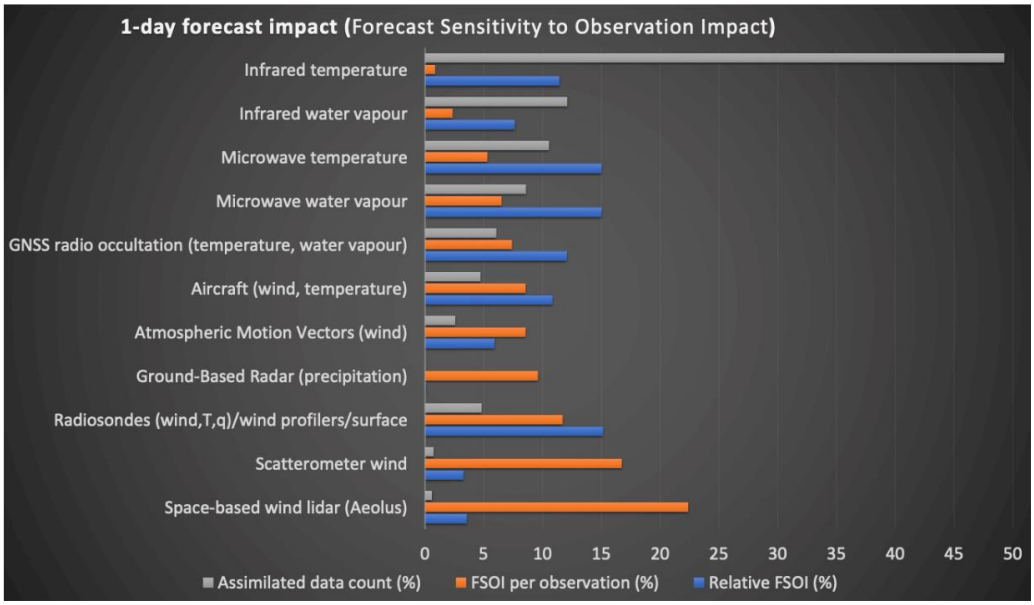

Figure 152: ECMWF operational FSOI statistics between 1 Dec 2022 and 19 February 2023, split into different observation types. The grey bars show the assimilated data count (got past IFS QC) for each instrument as a percentage of the total, the blue bars show the relative FSOI in percent and the orange bars show if the FSOI is normalised by the data count (scaling arbitrary). Note that Aeolus is the only satellite providing space-based wind lidar, whereas many satellites contribute to the other groups.

The short-range FSOI metric shows that the Mie-cloudy has a similar (global average) impact to the Rayleigh-clear, however the OSEs tend to show the Rayleigh-clear is more important. It may be that the Mie-cloudy better constrains the small atmospheric scales compared to the Rayleigh-clear due to its lower noise and better horizontal resolution. Small-scale forecast errors grow faster and saturate more

quickly than the larger-scale errors, therefore the Mie impact could saturate at shorter forecast ranges, e.g. polar impact, than the Rayleigh with its better large-scale coverage.

Aeolus modifies the analysis state in different periods with similar geographic patterns. The non-systematic changes u-wind (east-west component) are largest in convective areas at ~200-70 hPa (~13-18 km) which is where the wind random background forecast errors are largest. For example, Figure 153a shows the standard deviation of u-wind analysis differences at ~250 hPa (~11 km), with standard deviation up to ~3 m/s. The pattern of larger changes looks rather like a climatology of mesoscale convective systems. This may be due to the large rate of intrinsic chaotic error growth associated with convection. Systematic analysis changes are consistently relatively large in the tropical upper troposphere and lower stratosphere for zonal winds (peaking at 100-150 hPa), for example see Figure 153b showing ~130 hPa (~15 km) with mean differences up to 1.4 m/s – elsewhere the mean changes are small. The systematic changes may be caused by model biases e.g. lack of model vertical wind shear due to excessive parameterised vertical diffusion in the lower stratosphere and the known underactive Hadley cell circulation in the IFS.

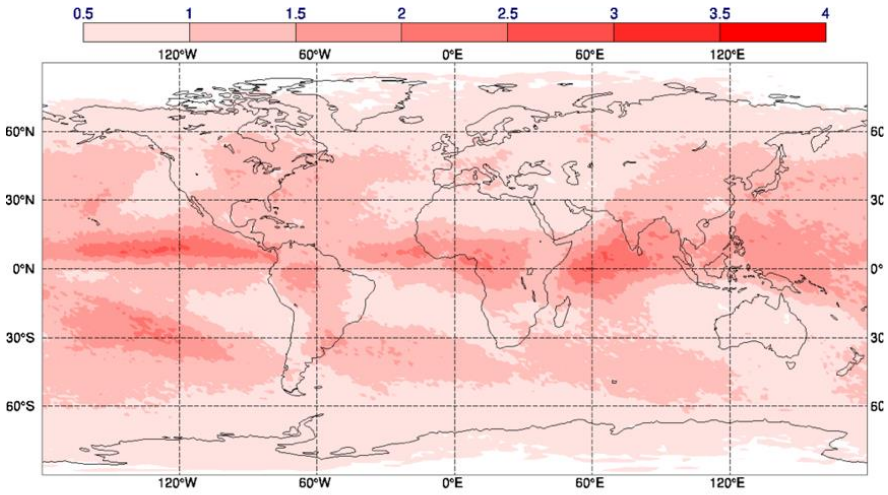

(a) Standard deviation of differences, altitude ≈ 11 km

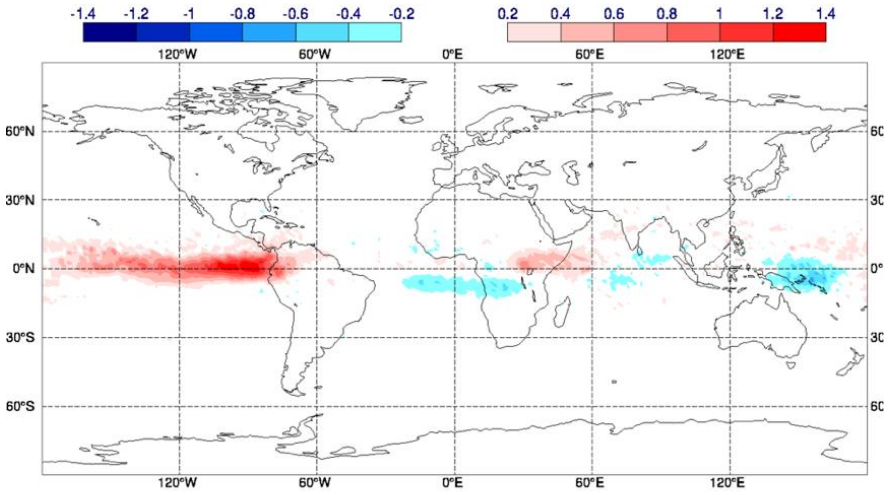

(b) Mean of differences, altitude ≈ 15 km

Figure 153: a) Standard deviation of the differences of u-wind component (m/s) at ~250 hPa (~11 km) between the analysis assimilating Aeolus (Rayleigh-clear and Mie-cloudy) and the control not assimilating Aeolus HLOS winds. b) Mean of the differences of u-wind component (m/s) at ~130 hPa (~15 km) between the analysis assimilating

Aeolus (Rayleigh-clear and Mie-cloudy) and the control not assimilating Aeolus HLOS winds. For the period 29 June to 31 December 2019 using the 4th reprocessing (B16).

Horányi et al. (2015b) showed that using real HLOS winds (calculated from conventional wind vector observations) with artificial biases that are a large fraction of the standard deviation of observation error, i.e. biases ~1-2 m/s, causes a considerable reduction in positive impact, and with sufficiently large bias an overall negative impact can result. Therefore, it was critical to correct biases in the data assimilation of Aeolus, or even better for them to be corrected by calibration procedures in the ground processing chain (preferably instrument-based calibrations). Indeed, the magnitude of Aeolus' positive impact was found to be strongly dependent on the implementation of an accurate bias correction of the HLOS winds derived using the ECMWF model as a reference (Weiler et al, 2021).

The positive NWP impact of the demonstration mission Aeolus suggests that a strong and consistent impact from the planned operational EUMETSAT follow-on mission (EPS-Aeolus) is likely. EPS-Aeolus aims for significantly improved precision HLOS winds and improved vertical resolution compared to Aeolus and operational robustness.

Potential improvements in Aeolus NWP impact via improved data assimilation methods:

- Better observation error modelling; improvements have already been achieved for the Mie-cloudy winds by accounting for a representativeness error (a simple model).
- Improvements in the forward modelling of HLOS wind e.g. vertical/horizontal averaging of model winds to match Aeolus range-bin resolution; inclusion of vertical wind and hydrometeor sedimentation component; geometric height as vertical coordinate.
- Assessment as to whether spatial thinning of observations is beneficial e.g. near the Poles, the data can be dense and some indications of over-fitting.
- Assimilation of Rayleigh-cloudy winds as the normal set-up (when biases are controlled in reprocessing).
- Further investigation/tuning of the first-guess check QC and variational QC (VarQC). Stricter QC has shown promising results in the third and fourth reprocessing OSEs.

6.1.3 Lessons Learnt from NWP impact assessment on winds.

Given ECMWF's readiness for Aeolus, quick progress was made during the Commissioning Phase in running OSEs and learning how to best use the data. This continued with major improvements during Phase E2, leading to record quick use of a new technology in operational assimilation at ECMWF. Therefore, we think it is important for maximising the exploitation of Aeolus-2 to give a lead NWP centre, e.g. ECMWF, enough time, and resources pre-launch to prepare and optimise the assimilation system. The work by ECMWF was crucial in providing advice to other NWP centres e.g. DWD, Met Office and Météo-France, for their own preparations pre-launch to exploit Aeolus to make progress in assimilation experiments during the Commissioning Phase as part of the Cal/Val teams.

6.2 NWP impact assessment for aerosol at ECMWF

William McLean, Karen Henry, Michael Rennie, and Angela Benedetti, ECMWF

6.2.1 Summary

The following chapter presents results pertaining to the impact from assimilation of Aeolus Level-2A particle backscatter in the ECMWF global data assimilation system, configured in atmospheric composition mode, i.e. running OSEs (Observing System Experiments). This work was undertaken at ECMWF as part of the Aeolus DISC consortium, with the work presented in this chapter mostly carried out during the Aeolus Aerosol Assimilation in the DISC (A3D) work package, running from October 2021 to March 2023, and continuing thereafter until the end of the DISC phase E.

The impact on the vertical profiling of aerosol backscatter is shown, along with the average regional impact in certain periods. Results from assimilation using a constant observation error and a variable observation error are shown, along with an analysis of changes to aspects of the quality control in the IFS. The model-AOD calculated from the L2A assimilation is also shown and compared with the control values, along with ground-based verification against AERONET stations. Also shown are comparisons with ground-based lidar measurements, using data from Mindelo, Capo Verde, provided by the PollyXT consortium.

6.2.2 Introduction and methodology

For a more detailed introduction and overview of the general methodology of transforming the Aeolus L2A data into the format required in the IFS, please see the chapter on L2A monitoring and BUFR development.

The assimilation of AOD products into the IFS provides information on aerosols at a global scale, such as sea salt, desert dust, and smoke, but does not give any information on the vertical distribution of these aerosols. However, the L2A particle backscatter retrievals provide information on the altitude of the aerosols and clouds present in an atmospheric column. An IFS model-based cloud screening, using the model trajectory at 40 km resolution, was used to filter out the contribution from cloud, but this is not a perfect method and some contribution from clouds will inevitably remain. Analysis from the monitoring (please see the chapter on L2A monitoring and BUFR development) does indeed indicate this.

Any new data product undergoes a rigorous period of testing and assessment to determine suitability for assimilation into the operational CAMS or NWP forecast at ECMWF. A significant part of this process is an evaluation of the observation errors, which directly correspond to the weight given in the assimilation, that is, a relatively large observation error translates to a lower weight in the 4D-Var assimilation, and vice-versa. The assimilation set up at ECMWF for ingesting the Aeolus L2A backscatter was established prior to the beginning of the A3D contract (Benedetti et al., 2020,2021), with a relatively small, constant error used to enable the impact of the assimilation to be clearly seen when comparing to a standard COMPO-IFS control run.

Following the pre-processing steps and ingestion to the IFS, the Aeolus L2A was "switched on" in the assimilation; that is, the blocklist was updated to include the L2A SCA mid-bin backscatter product along with all of the other NWP and atmospheric composition data products.

In the 4D-Var data assimilation used at ECMWF, all data products have a weight in the assimilation. These weights are defined through assignment of an observation error which consists of instrument error, representativeness error and forward model error, therefore it often varies spatiotemporally and

certainly does for Aeolus depending on the atmospheric path signal levels. In the NRT monitoring and assimilation experiments, the error was always set to the same constant value of $1x10^{-7}$ $(m\ sr)^{-1}$. The assimilation set up was still in a testing phase during this period, with the priority to ensure the L2A were proceeding to the minimization stage of the 4D-Var assimilation. As a result, the assimilation impact here is always artificially inflated, which is not a realistic case for a near-real time satellite product. However, successful demonstration of ECMWF's ability to assimilate such data products in near-real time has been achieved, with subsequent work on observation error diagnostics and IFS quality control further showing the capability to assimilate such products operationally, e.g. for the upcoming EarthCARE mission.

Following the conclusion of the NRT monitoring period, a more quantitative analysis of the observation error requirements was undertaken. This was aligned closely to the method used when initially testing the assimilation of the L2B HLOS winds product, where the impact of the observation error assignment is assessed through an evaluation of departure statistics. The method of Desroziers et al. (2005) was used to assess the observation error, which also considers the error on the background model. A tentative result from this study was that the native error on the retrieval product was too small, thus necessitating the inflation of this error by a factor of 3. This analysis is ongoing at the time of writing, and will also be applied to the other L2A retrieval products assimilated.

Evaluating the impact of assimilating the L2A particle backscatter on forecast skill was carried out by assessing the model-calculated aerosol optical depth (AOD) from including the L2A in the assimilation and comparing with a control run analogous to the CAMS-like product. Another way to assess the impact in the ECMWF system was to compare with other lidar measurements, such as the ground-based PollyXT lidar in Mindelo, Capo Verde. It is more difficult to determine if the L2A backscatter assimilation is improving aerosol forecasts in the IFS due to a lack of an accurate analysis state, unlike in the NWP OSEs for L2B winds; it is a much less well observed system.

The next section shows some key results from the near-real time assimilation, and initial results from modification of the quality control in COMPO-IFS. The analysis departures for the NRT period are shown as a function of time, along with ground-based verification of model AOD calculated with and without the L2A assimilation. Additionally, we show a comparison of our results with the ground-based PollyXT lidar from Mindelo, Capo Verde. As mentioned above, the near-real time monitoring was carried out using a configuration with constant error, and following the NRT data period an analysis of observation errors began. Assimilation of new retrieval products is also underway, including the AEL-PRO L2A product. A full discussion pertaining to the observation error analysis and assimilation of new retrieval products is omitted here for brevity, and will be included in a later publication.

6.2.3 Results and discussion

Figure 154 shows a time series of first guess and analysis departures for the NRT assimilation, along with the standard deviation for January 01 – August 31, 2022. These are the same statistics as for the vertical profiles shown in the L2A NRT monitoring chapter, using the same, constant, observation error of $1x10^{-7}$ $(m\ sr)^{-1}$. The first-guess departures (bias) and standard deviation of the bias pre-screening is relatively large, because the Aeolus SCA mid-bin L2A backscatter product is dominated by cloud signal, whereas the ECMWF background (model) value is from aerosol scattering only. The bias and the standard deviation are significantly reduced post-screening, though with cloud contamination likely still present, as Figure 115 in the L2A NRT monitoring chapter particularly corroborates when evaluating the departure statistics as a function of latitude and longitude. The analysis departures are close to zero, as expected for an artificially prescribed small observation error.

Figure 155 shows AOD values calculated in the IFS, for a denial, control, and L2A assimilation experiment, compared with ground-based AERONET sun photometer measurements from two stations in the Canary Islands for June 2020. This is a verification of the impact of the L2A assimilation compared to trusted ground-based observations. This coincided with the so-called "Godzilla" dust event with high AOD´s above 1, with Saharan dust advected west over the tropical Atlantic region, and therefore passing over the Canary Islands and Capo Verde. The near-real time (January-August 2022) assimilation consistently showed a positive bias in the model AOD calculated from including the Aeolus L2A in the assimilation. This is probably due to the positive bias in the data (see section 5.4.4) due to cloud contamination and overweighting the observation (unrealistically small error). This was the case throughout three different cycles of COMPO-IFS: CY47R1, CY47R3, and CY48R1. Therefore, any ostensible improvement to the AOD calculation should be considered with this in mind. However, in each case assimilation was carried out with the constant small value of observation error, and relaxed quality control parameters in the IFS. Thus far, from our testing, there is nothing to conclusively indicate that assimilation of the Aeolus L2A backscatter has a positive or negative impact.

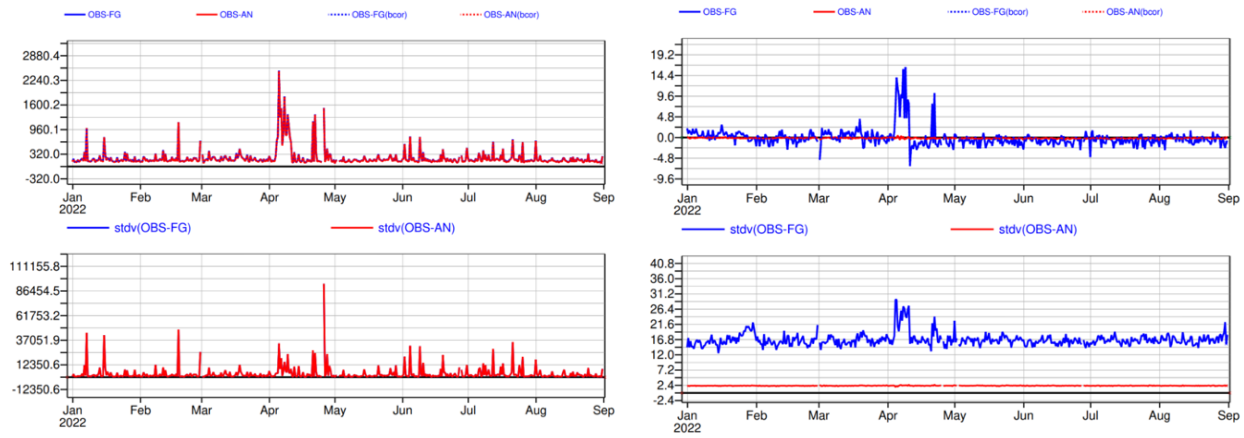

Figure 154: Time series of global first-guess departures (O-B) and analysis departures (O-A). Top plots show the mean first-guess and analysis departures in blue and red, respectively, with the corresponding standard deviation of each shown on the bottom plots. Left-hand plots show statistics for all data, with the right-hand plots showing the statistics for data passing the cloud screening. The units are 10^{-7} (m sr)$^{-1}$ for all plots.

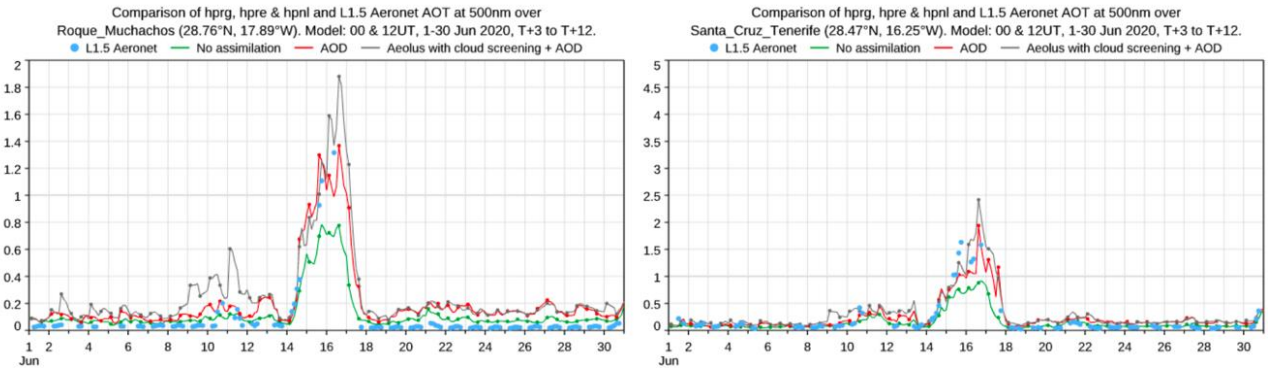

Figure 155: Verification of short-range AOD forecast impact for L2A assimilation. The grey line shows the AOD calculated from the L2A SCA mid-bin backscatter assimilation with a constant observation error; the red line shows the control with AOD assimilation and no L2A; green is the AOD from a denial experiment with no AOD or L2A assimilation. The discrete blue points are the AERONET values for AOD at 500 nm recorded for the respective stations: La Palma on the left and Tenerife on the right, both in the Canary Islands of Spain.

Figure 156 shows maps of the mean local analysis increment (A-B, in observation space) for two experiments: one with a more relaxed first-guess check (7-sigma rejection) and unscaled observation error, and one with a scaled (by a factor of 3) observation error (more realistic) and a stricter first guess check (strict in comparison to the one used in the prior NRT assimilation; the "stricter" check uses the same parameters as for the AOD product assimilation, a 5-sigma check. Please see the chapter on NRT monitoring for a more detailed explanation).

Darker red areas show where the L2A backscatter assimilation has systematically increased the aerosol backscatter compared to the short-range background forecasts, and darker blue areas show where the L2A is systematically reducing the backscatter, i.e. where Aeolus has caused a reduction in model aerosol backscatter. Systematic increments are a sign of bias in the observation or the model and are not desirable in variational assimilation. It is probably due to bias in the L2A observation i.e. too much convective cloud contamination causing positive increments and lack of cross-polar backscatter causing negative increments in dusty areas. Until bias are corrected and QC is improved it is unlikely that Aeolus L2A can provide a positive impact on aerosol forecasts.

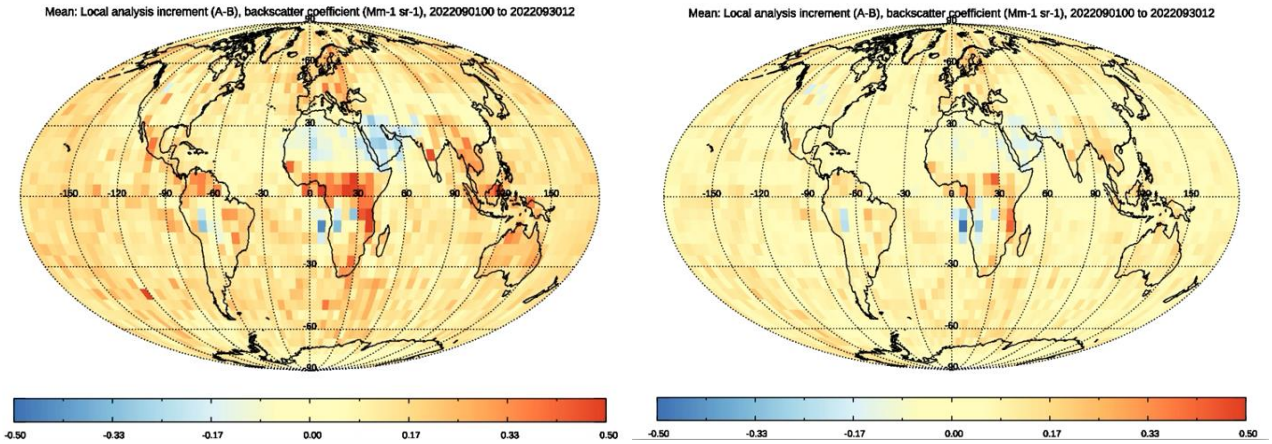

Figure 156: Mean local analysis increment (analysis minus background; i.e. how much the Aeolus L2A perturbs the original model value), for the month of September 2022. Left-hand figure shows this for the more relaxed (7-sigma) QC and unscaled native observation error, with the right-hand plot for an experiment with a stricter (5-sigma) first-guess check and a scaled (larger) observation error. Units are 10^{-7} $(m\ sr)^{-1}$.

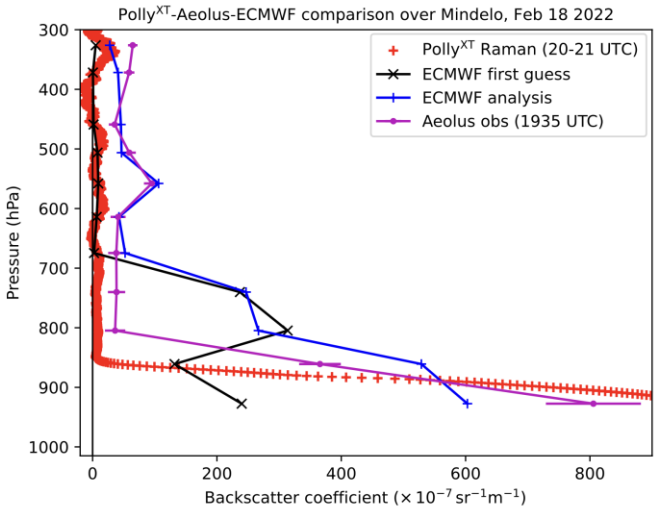

Figure 157: Comparison of L2A backscatter (purple), the ECMWF model from first guess (black) and analysis (blue), with the ground-based PollyXT lidar measurements (red) over Mindelo, Capo Verde. PollyXT observations were provided by TROPOS. Credit to Holger Baars and the Ground-based Remote Sensing Group (TROPOS; https://polly.tropos.de/) for providing ECMWF with these data.

Figure 157 shows a specific case comparison of the L2A SCA mid-bin particle backscatter product and the ECMWF models from first guess and analysis with the ground-based PollyXT lidar measurements over Mindelo, Capo Verde taken on February 18, 2022 between 20.00 - 21.00 UTC. Aeolus measurements are shown from an overpass at 19.35 UTC. The Aeolus L2A particle backscatter is positively biased when compared to the ground-based lidar profile for altitudes above 800 hPa, with the COMPO-IFS model from first guess corresponding closely to the PollyXT values at higher altitudes. The ECMWF first-guess model shows increased aerosol backscatter around 700 hPa and between 850-700 hPa compared to PollyXT. The COMPO-IFS model from analysis (i.e. from assimilating the L2A backscatter) is drawn towards the Aeolus backscatter; this is to be expected based on the inflated weight in the analysis resulting from the small observation error used in the assimilation.

6.2.4 Summary and outlook

OSEs with the SCA mid-bin L2A particle backscatter product have been carried out at ECMWF from January 2022 until the end of the mission in July 2023, in NRT and for several periods throughout the mission lifetime. Since then, OSEs have continued to be run at ECMWF, with the work after the satellite operational period focussing on an investigation into improving the assigned observation errors, as the use of a small constant error in the NRT assimilation is not representative of a real observing system. An improved treatment of the observation errors is necessary to help to try to maximise the impact of the L2A data assimilation, and to understand any biases in the observation or model AOD and particle backscatter.

Ongoing work to maximise the exploitation of the L2A product includes assimilation of reprocessed L2A data and comparing to older baselines. In addition to the SCA mid-bin retrieval product, assimilation of the other retrieval products: the AEL-PRO and the MLE product have commenced at ECMWF. Assimilation of the L2A particle extinction coefficient products is also planned, with a full testing of the COMPO-IFS aerosol extinction operator required. Improving the cloud screening is also necessary to try to reduce the positive biases from the SCA mid-bin product, and work is already underway to use a cloud product derived from geostationary satellite measurements. This work will continue through the DISC Phase F activities at ECMWF. The impact of changes to the errors, quality control, and cloud screening on the assimilation of the different retrieval products will continue to be assessed through O-B and O-A statistics, alongside verification with independently measured AOD and lidar particle backscatter data where available.

6.2.5 Lessons learnt from NWP impact assesses for aerosols

- To fully account for accurate aerosol scattering, depolarization measurements are necessary, thus if possible both co-polar and cross-polar components of the scattered radiation should be recorded by the instrument. Without this information, it is challenging to produce a true aerosol product. Obviously, Aeolus wasn't designed as an aerosol mission, but any mission conceived as having application to operational aerosol remote sensing must ensure this point is considered.
- Mismatches between the product and what the ECMWF model is currently capable of producing: attempting to remove the contribution from cloud signal was a necessary step when preparing the L2A SCA mid-bin backscatter product for assimilation, as the IFS-model for Aeolus backscatter only considered scattering from aerosols. A model-based cloud screening was used to reduce the contribution from cloud in the backscatter, but was not completely effective.
- The NRT monitoring of the L2A product at ECMWF began relatively near the end of the mission, with final preparations taking place whilst the mission was ongoing, and began 3 years after the

operational assimilation of the HLOS winds was implemented. Ideally, these preparations (analysis of errors, quality control and pre-screening requirements of data etc) would have been made prior to the satellite launch, such as for the assimilation of the winds, but again this likely stems from the fact that the atmospheric composition applications were funded later than the NWP wind activities. Despite the time limitations and the late start, a working BUFR template and a BUFR file program that produces IFS-ready products for 5 retrievals in the L2A aerosol product were produced, which are ready for future mission use.

6.3 NWP impact assessment for wind at Météo-France / CNRM

Alain Dabas, Jean-François Mahfouf and Vivien Pourret, Météó-France

6.3.1 Operation of L2B processor

Install and use of the L2B processor

A first installation and use of the stand-alone L2B processor of BUFR (Binary Universal Form for the Representation of meteorological data) files was done already in 2017. An Aeolus simulated test data set available from the ESA Aeolus was used to produce first BUFR files with the L2B processor and test NWP technical developments. In parallel, the NWP environment (including a specific Météo-France pre-processing software) was adapted to allow the assimilation of Aeolus HLOS winds. The L2B processor was used to produce BUFR files and apply a bias correction until ECMWF disseminated unbiased HLOS winds on EUMETCast (05/2020).

Temperature and pressure sensitivity of the L2B HLOS retrieval

One of the features of the L2B processor for the HLOS retrieval is the correction taking into account the quasi-real temperature and pressure fields (to be provided by an NWP model) needed to model the Rayleigh-Brillouin spectral line shape from molecular backscatter. This correction affects only the L2B Rayleigh HLOS winds. The temperature and pressure information are stored in AUX_MET files which are an input to L2Bp. One important question related to such correction was about the sensitivity of HLOS product by the specification of temperature and pressure fields. Differences in temperature between ARPEGE from Météo-France and IFS from ECMWF lead in 90 % of cases to HLOS wind differences smaller than $0.1\,ms^{-1}$ above ~2 km altitude. The differences significantly above are in average well described by the 1st order correction scheme available in L2Bp. In other words, to correct for pressure and temperature differences between NWP models, the L2B processor does not need to be rerun using specific AUX_MET files. The 1st order correction is sufficient. The study is depicted in CNRM (2020a) and in Šavli et al. (2021).

L1B scattering ratio verification and its impact on the L2B processing

The scattering ratio (SR) is an important quantity for the L2B HLOS retrieval, because it defines the amount of Mie contamination in the backscattered signal and thus directly affects the computation of the Rayleigh wind. The SR is used for the scene classification of Rayleigh clear or Mie/Rayleigh cloudy. The L2Bp uses the biased SR of the L1Bp, the so called "refined scattering ratio" which is provided at the measurement scale. Several methods, based on the comparison of the L1B refined scattering ratio and the scattering ratio provided by the L2A algorithms were tested. A cubic bias correction scheme was implemented in the L1B processor of version 7.07. Topics about the use of the Mie cross-talk correction were also discussed. The study is depicted in CNRM (2020a).

Development of a HLOS wind bias correction method

With significant systematic errors present in the Rayleigh-clear HLOS wind observations, that are known to be well correlated with the difference in the temperature measured across the Aeolus receiver mirror (M1), the activity on bias correction methods was crucial to be able to use the wind observations in NWP. An original methodology was developed to use observations optimally in the Météo-France ARPEGE Data Assimilation (DA) system. The model-independent method is based on the two specific properties of the Aeolus instrument. The first one is the similarity of the systematic errors of Rayleigh-clear and Rayleigh-cloud observations. The second one is the significantly smaller sensitivity on the Aeolus orbit phase variable systematic errors of the Mie-cloudy winds. The differences between the Rayleigh-cloudy and Mie-cloudy HLOS allow an estimation for the bias correction for the Rayleigh-clear

HLOS. This new methodology is described in CNRM (2020b). The methodology was tested against the first ECMWF operational bias correction technique. In terms of forecast scores, positive and similar results are depicted in CNRM (2020a).

The observation operator H

An attempt was tried to improve 'part' of the DA methodology by adapting optimally the HLOS wind observation operator H, respecting observation and model main characteristics, and understanding its limitations for global and limited area models. The L2B processor and its toolkit allowed us to investigate different H operator modifications. It was shown that improvement of H operator in DA is tricky as the model effective resolution (ARPEGE, IFS, etc.) and L2B Rayleigh HLOS on ~90 km accumulation are not that different. The model averaging used in H to reduce as much as possible representativeness errors, can quickly lead to a reduction of the model error variance linked to a loss of information larger than the noise reduction. It is likely that higher resolution models (AROME) could benefit more from such modifications (still under examination). This work was first presented at the Aeolus Cal/Val Workshop in 11/2020.

6.3.2 OSEs with ARPEGE (data quality and forecast scores)

FM-A Laser period

A first monitoring ARPEGE experiment was done soon after the launch and the availability of the first data (two periods: 15 Nov 2018 to 13 Jan 2019 and 16 Feb 2019 to 10 Mar 2019). The results allowed us to participate to the QC (Quality Control) definition (use of Rayleigh clear RC and Mie cloudy MC only, removal of hot pixels, observations with assigned observation errors above thresholds discarded, low level and small range-bin thickness data discarded, small accumulation length data discarded...) and to the first systematic error for Mie cloudy assessment.

About ~50 % of the data were rejected by the QC. The quality of the remaining data was estimated against the model background equivalent (methods used systematically for all OSEs) and also with co-located Mode-S (aircraft winds) data over France for the 9-10/2018 period. First observation random errors for MC and RC were assessed and found close to those assessed by ECMWF (~3.4 m/s for RC and ~2 m/s for MC). Even after QC, biases in RC data remained for ascending and descending orbits.

After the scaling of the prescribed error (S1, first attempt depending upon the distance to the ARPEGE numerical pole) in order to take into account representativeness errors, and, despite remaining ascending and descending orbit RC HLOS wind biases, we made a first assimilation experiment through an OSE (Observing System Experiment).

1st OSE: 9-10/2018 (real time dataset): encouraging results with first improved forecast scores (for wind and temperature in Tropics in the troposphere and in a lesser extent in Southern Hemisphere for all ranges until day-4) despite significant distinct biases for ascending and descending orbits for RC.

FM-B laser period

A new QC was defined and used to assimilate Aeolus data (60 % of rejected data) after the switch to the FM-B laser. Distinct biases for ascending and descending orbits for RC were still there. We developed an original method to debias RC HLOS winds. We compared our debiasing method with ECMWF.

The method designed at Météo-France (MF) follows the idea of very similar properties of the systematic errors of Rayleigh-cloudy and Mie-cloudy HLOS observations. As the Mie-cloudy HLOS systematic errors are very close to 0 m/s and the Rayleigh-cloudy and Rayleigh-clear HLOS systematic errors are comparable, the difference in the HLOS wind cloudy products gives a good estimate on the possible Rayleigh-clear HLOS systematic errors.

The other method is the one used at ECWMF before switching to the M1 temperature dependent bias correction. This method is essentially based on 7-day running means of the (O-B) statistics.

Globally, both methods were efficient to solve the ascending and descending orbit RC bias problem and led to a close assessment of observation errors: ~4.4 m/s for RC and ~2.8 m/s for MC over the 7-8/2019 period. Nevertheless, the Météo-France method presented some local latitude dependent biases linked to the structure of the Mie cloudy biases.

We used both methods to perform two OSEs over the 7-8/2019 with a new assessment S2 of the observation error scaling factors (depending upon latitude for RC and upon prescribed L2B error for MC).

Improved forecast scores were obtained for both OSEs:

- Tropics: for wind (up to 5 %) and in a lesser extent for temperature (up to 2 %), significant improvement from the mid troposphere to the Upper Troposphere Lower Stratosphere (UTLS, especially here) for all ranges until day-4. Improvement to a lesser extent (less than 1 %) for humidity in the whole troposphere for all ranges.
- Southern Hemisphere: improvement in the upper troposphere for wind and temperature for all ranges of ~1 % and to a lesser extent for humidity.
- Northern Hemisphere: small improvement, mainly for the temperature (1 % in the troposphere until day-2)
- Significant improvement over polar regions in the mid troposphere until day-3.

These previous results concerning FM-A and FM-B are depicted in details in CNRM (2020a).

Then, a set of different OSEs were undertaken for different purposes:

- **OSE during the Strateole 2 Tech campaign over the 12/2019-02/2020** period (real time dataset, scaling S2 and ECMWF running mean RC debiasing method). The fit of the ARPEGE model short-range forecasts to the STRATEOLE 2 stratospheric data is improved by assimilating Aeolus data. Results were presented at the Aeolus Cal/Val Workshop in 11/2020.
- **Pre-oper OSE over the 4-5/2020 period** (scaling S2, M1 temperature bias correction RC method, real time dataset). Observation errors: ~5.5 m/s for RC and ~3.2 m/s for MC. The Degree of Freedom for Signal (DFS) has been computed on a set of ARPEGE 4D-Var experiments by using perturbed observations over a 1-day period (10 April 2020): Aeolus data present only 0.42 % of all assimilated observations (10 % of wind observations); however, they contribute 2.3 % of the total DFS. The Forecast sensitivity to observations impact (FSOI) was also computed for Aeolus: it is ranked 10th in terms of more informative observation system, 3rd in terms of FSOI per obs (cf. Figure 158). The improvement in terms of forecast scores were the same to a lesser extent than the one obtained in 7-8/2019 OSE except with better results in the Northern Hemisphere where Aeolus data compensated for the lack of aircraft data due to the pandemic. The results that led to assimilate Aeolus winds operationally in the ARPEGE model are described in Pourret et al. (2022).

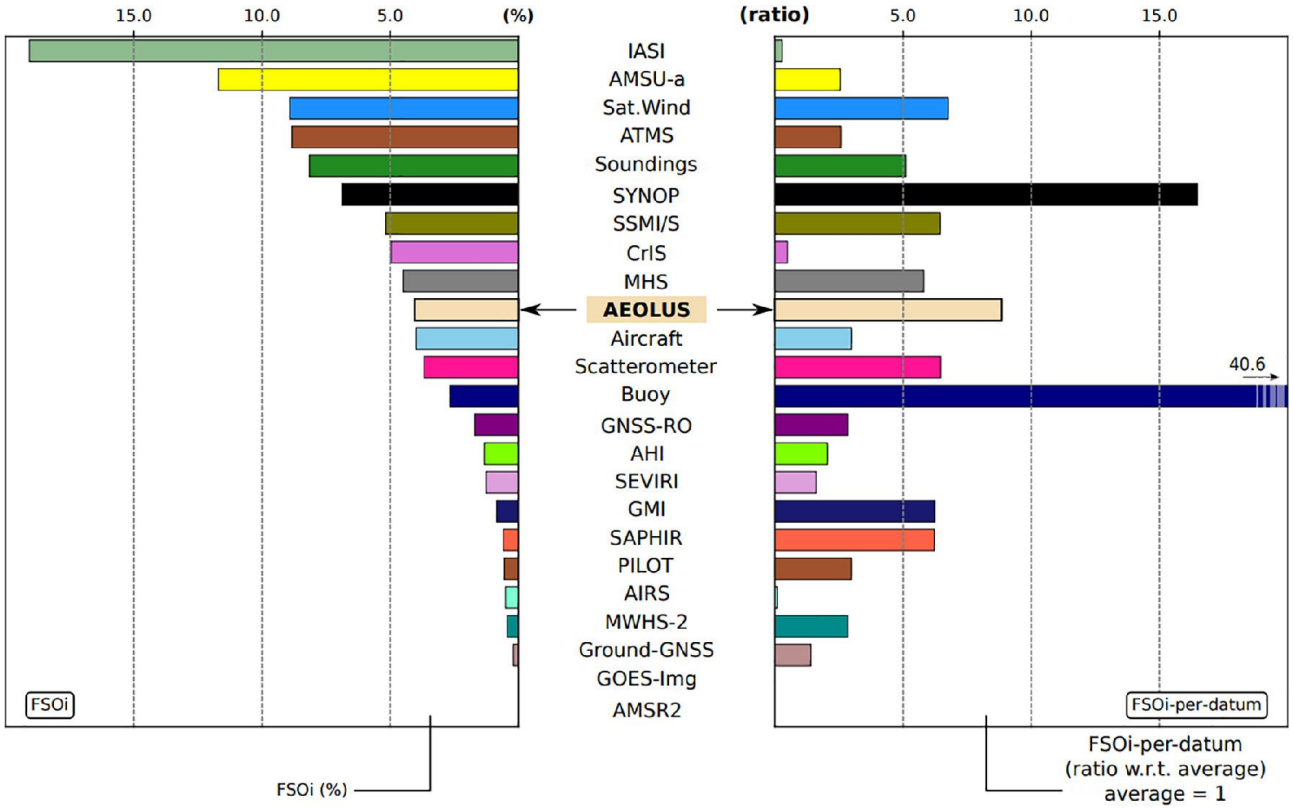

Figure 158: Relative FSOi (%) from 4D-Var ARPEGE assimilating Aeolus HLOSW, partitioned by observing systems and averaged over a 2-month period (April–May 2020, 204 cycles). FSOi is computed with order-3 formulae, dry norm and adjoint. A total relative impact by observation group ranked by contribution (left). A ratio between the mean impact per datum of the corresponding observing system and the mean impact per datum for all observations (right).

- **3 OSEs (RC+MC, MC and RC), 7-12/2019** (first reprocessed dataset of better quality than in real time, scaling S3 -see operation time line chapter- and M1 temperature bias correction RC method): results of the RC+MC OSE were similar to previous 7-8/2019 OSEs, but with larger positive impacts on forecast scores (0.5-1 %). Much larger positive impacts of RC on ARPEGE forecasts up to day-4 compared to the MC (limited to troposphere, poles and first ranges) were shown and presented to the Aeolus NWP Impact WORKSHOP in 12/2021. The impact of Aeolus data on forecasts of hurricanes during the North Atlantic season 2019 began. First slight positive impacts were shown and presented during the 10/2022 DISC progress review meeting.
- **OSEs over 9/2021 and 12/21-01/22 periods** (scaling S3 -see operation time line chapter-, M1 temperature bias correction RC method, real time dataset and Toy ARPEGE with coarser resolution) to assess improvements obtain with new N/P settings and anticipate the Aeolus end of mission. Results were presented during the Aeolus third anniversary conference (03-04/2022).

All the results from these different OSEs and the evolution of operational FSOI all along the Aeolus timeline were used to define forecasts scores and FSOI as a function of RC data quality to assess the expected forecast improvement moving from the Aeolus original to a future Aeolus-2 satellite mission. Results were presented during the 10/2022 DISC progress review meeting. As a minimum, if we follow the linear fits shown in Figure 159, we could expect improvements in the tropical UTLS of 3.3 % at 24 h, 3 % at 48 h, 2.25 % at 72 h and 1.7 % at 96 h for Aeolus-2.

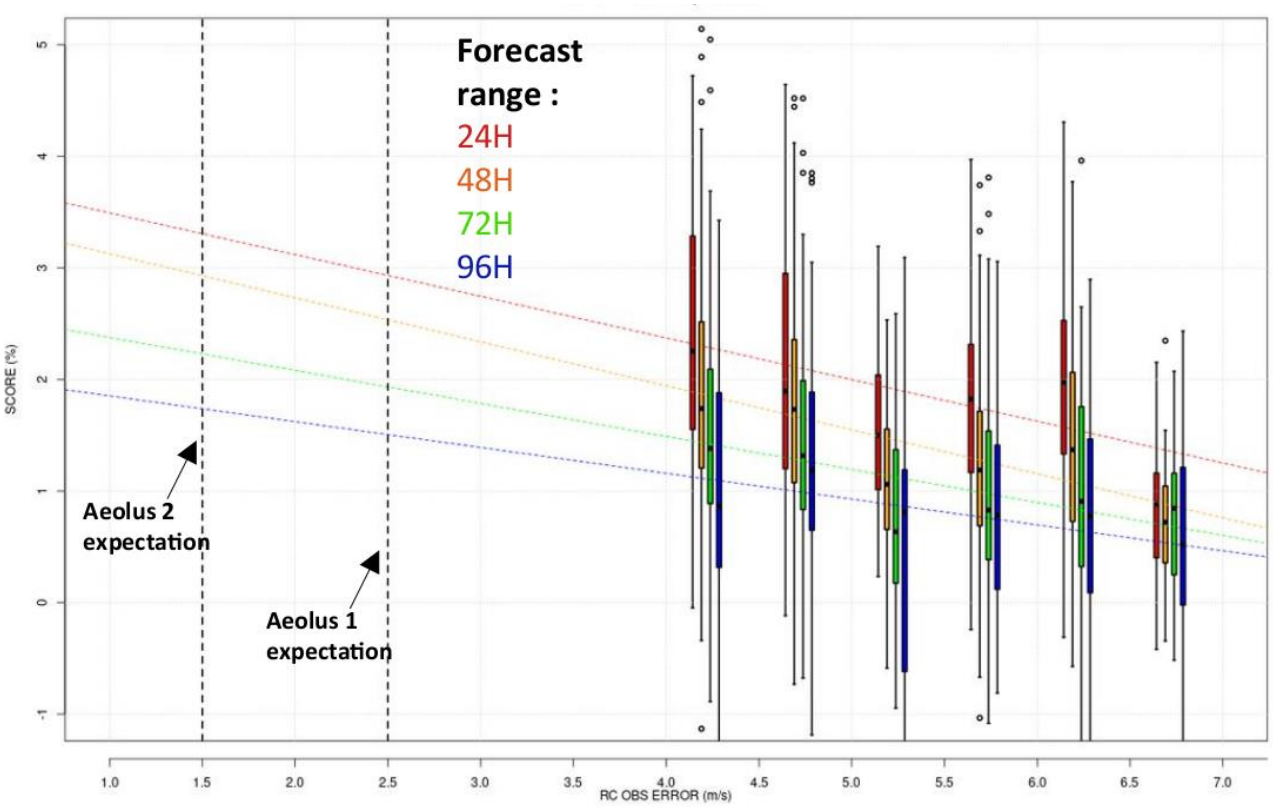

Figure 159: ALL OSEs tropical UTLS (250 hPa→10 hPa, -20°N/20°N) wind scores against IFS analysis by 0.5 m/s RC observation error class boxplots for 24 h, 48 h, 72 h and 96 h ranges and their linear fits.

6.3.3 Operation time line

December 2019: ECMWF dissemination of BUFR on EUMETCast entering in the MF operational observation database in real time.

- January 2020: operational monitoring (http://www.meteo.fr/special/minisites/monitoring/SATELLITE/LIDAR/lidar.html)
- June 2020: operational assimilation in ARPEGE (and ARPEGE Ensemble Data Assimilation System). Monitoring of RC and MC HLOS winds assimilated in ARPEGE are shown in Figure 160 and Figure 161. FSOI were systematically computed in operations with the 43t2 ARPEGE version from June 2020 to June 2022. We noticed a slow decrease of the positive total Aeolus relative impact (especially due to RC impacts) from 5% at the end of 2020 to 4% by mid-2022 for the total FSOi. During the 2-year period, Aeolus had one of the best positive impact in terms of FSOi per datum (top 3, after scatterometers and atmospheric motion vectors).
- June 2022: After the detection of a latitude dependent problem in the dataset that was used to develop S2, the observation error scaling was revised (S3: RC and MC scaling factor depending only on L2B prescribed observation errors computed over one year of operational statistics) for the new operational ARPEGE model (cf. (Pourret et al., 2022)).

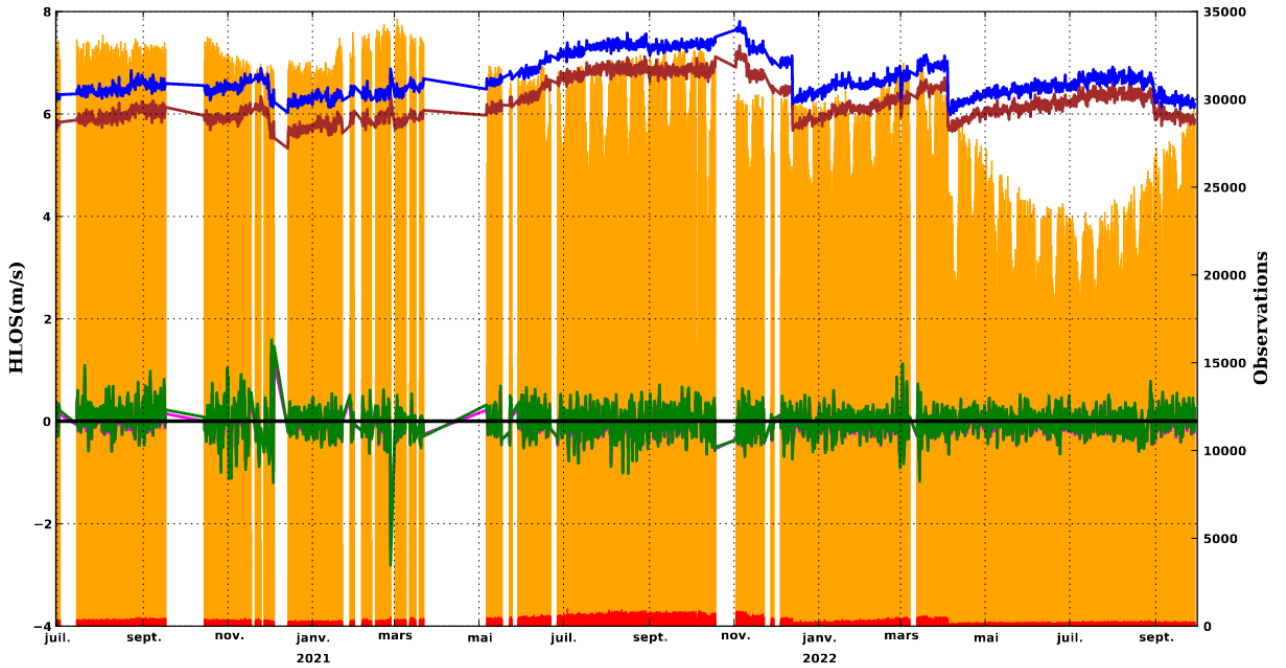

Figure 160: Evolution of STD(O-B) (blue), STD(O-A) (red), mean(O-B) (green), mean(O-A) (pink) and number of observations assimilated (orange) from June 2020 to October 2022. O stands for Observation of RC HLOS wind, B for Background and A for Analysis.

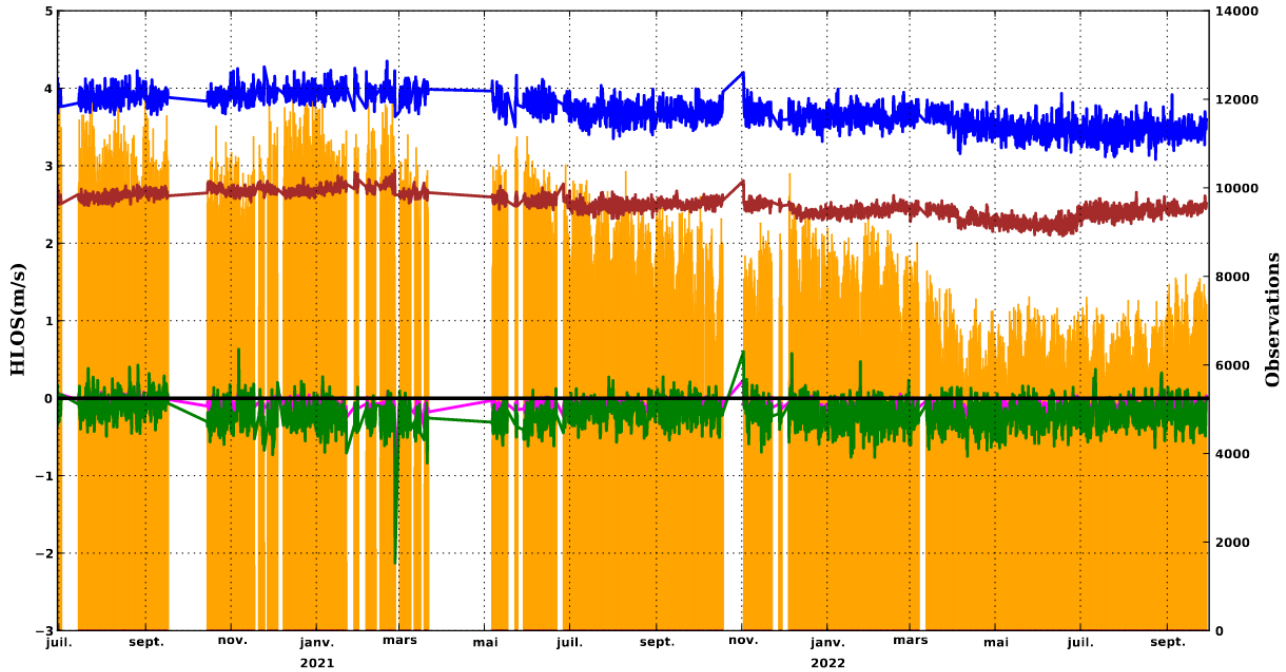

Figure 161: Evolution of STD(O-B) (blue), STD(O-A) (red), mean(O-B) (green), mean(O-A) (pink) and number of observations assimilated (orange) from June 2020 to October 2022. O stands for Observation of MC HLOS wind, B for Background and A for Analysis.

7 Lessons Learnt from the Aeolus DISC

Oliver Reitebuch, DLR

This chapter summarizes the Lessons Learnt (LL) from the Aeolus DISC activities with currently 67 recommendations and LL, which are considered to be relevant for the operational follow-on mission Aeolus-2 (LL-AE2), for upcoming lidar missions as EarthCARE (LL-EC), or future Earth Explorer (LL-EE) missions or more general LL (LL-GE). The detailed list of LL and very specific lessons learnt, which are only relevant for the future phase F activities of the DISC for Aeolus (e.g. algorithm updates, or recommendations for future analysis) are contained only in the specific sections of the Final Report.

The LL can be nicely structured according the sketch introduced in section 4.14.7, which shows the different approaches for defining LL and recommendations. As the different LL contain often several aspects from the Figure below, those are not explicitly highlighted:

- Processes that worked well and can be an example for other missions as best practice; often this part is overlooked as one considers these processes as normal work, and one only focusses on those topics, which could be improved.
- Processes that we would perform differently in hindsight, which includes also processes or documents, which should have been already prepared before launch and the DISC phase.
- Ideas for improvements that could not be implemented, but would be beneficial for upcoming missions.
- Open challenges, which could not be fully resolved or consolidated and are either followed up in phase F or for future missions

Figure 162: The Key Operational-knowledge Retention Engine (KORE) from section 4.14.7

The list presented in this chapter was further complemented for the revised version of the report after the Aeolus Lessons Learnt Workshop in May 2024. A more condensed version of the LL was provided for this workshop and the Aeolus Mission Report on LL, which is planned to be issued by ESA in July 2024. The LL are discussed in the order of the chapters of this Final Report – not in a specific order of priority. But we start with the main LL from the pre-DISC phase, which are considered as a prerequisite for a successful Aeolus mission and DISC.

7.1 Lessons Learnt from Aeolus pre-launch activities for DISC

As the DISC was established from teams already cooperating two decades on the Aeolus algorithm, processors and airborne demonstrator, it is clear that the Aeolus success and achievements builds on these pre-launch preparations. The swift availability of first atmospheric signal and winds from Aeolus only 2-4 weeks after launch are a remarkable achievement for an Earth Explorer mission and would not be possible without this long-standing cooperation and involvement of these experts.

Thus, a number of recommendations and LL need to reflect on these activities already before the launch.

1. The Aeolus processing chain was developed in close cooperation of L1 and L2 teams, defining the functionalities, products and interfaces among the different processors. This cooperation without a hibernation phase was a prerequisite to build-up and keep the expertise for the teams within the DISC. The chain-of processors (CoP) at KNMI´s Sandbox served successfully as a testing environment before launch including the end-to-end simulator (E2S), which was a prerequisite for processor and reprocessing activities within the DISC. The NWP monitoring tools were developed well before the launch by ECMWF, which made it possible to monitor the Aeolus L2B product from the first day after the instrument switch-on. Also having the responsibility of the L1 processing at an institute like DLR in cooperation with DoRIT (and not only at space industry with the mission prime) guaranteed a successful ground-processing development from Level 1 to Level 2. It is strongly recommended to setup a DISC like algorithm/processor team consortium also for Aeolus-2 (LL-AE2) and other Earth Explorer (LL-EE) well before launch (latest in phase B) in order to ensure a swift availability of high-quality data products after launch.
2. Another prerequisite for success of Aeolus and swift availability of products was the experience gained with the ALADIN airborne demonstrator (A2D) on real atmospheric scenes before launch for the algorithm development and testing. This was possible thanks to its high technological commonality with ALADIN. Also, the A2D mitigated the risk associated with the ALADIN development not having an end-to-end verification test including real atmospheric measurements (e.g. via a window with ALADIN in a clean room environment), as suggested initially by the Aeolus Mission Advisory Group MAG. In addition, only the A2D allowed to develop a deep understanding of the instrument calibration procedures, the operation of the instrument and the instrument performance. Without the A2D, the Aeolus DISC instrument performance monitoring (including calibrations) and analysis of anomalies could have not been performed on this high level. Also, the experience in the A2D operation (with more flexibility) allowed DISC to propose also dedicated new instrument modes, instrument test procedures and finally the definition of EOL activities. These aspects were vital for the fast commissioning of Aeolus and the quick solutions to unforeseen issues that rendered the mission successful over almost 5 years. Thus, the development of an airborne demonstrator is strongly recommended for Aeolus-2 and future Earth Explorer missions (LL-AE2, LL-EE), especially on the background that it will be rather a new evolution of ALADIN (Aeolus Next Generation) than a simple copy of Aeolus-1.
3. The availability of a s/w environment for testing the complete chain from outputs of the end-to-end Simulator (E2S) and the L0/L1A/L1B, L2A, L2B processors including calibration processors (e.g. prototype Cal-suite processor) is essential to have available already before launch for algorithm and processor development and testing by ESA-external teams (e.g. at KNMI), but also as a prerequisite for the more formal ground segment acceptance tests by ESA (LL-EE, LL-AE2). It was critical to get the L1 and L2 processors into a good state prior to launch to perform a large selection of chain-of-processor tests with realistically simulated, e.g. using ECMWF input data at highest available

resolution, atmospheric scenarios. This led to many issues being discovered in the years before launch such that the first data produced in the Commissioning Phase was already of decent quality.

4. A prerequisite for the pre-launch development of the operational ground processors was the availability of an End-to-End Simulator (E2S), which was used for different objectives. First, the E2S was providing data outputs with the same content and format as downlinked from the satellite science data stream with the X-Band (so called Annotated Instrument Source Packets AISP). This was used during the functional testing of the complete chain of processors starting from L0 to L1B, L2A and L2B for the processor developers, but also during formal ground-segment reviews by ESA´s PDGS. Second, the E2S was used to evaluate the performance of the ALADIN instrument wrt. random and systematic errors. This involved a representative simulation of the instrument, but also the Aeolus orbit and the modelling of the atmospheric and ground properties, which ranged from simplified homogenous scenes to heterogenous scenes, where the atmospheric profile parameters could be changed for every single laser pulse return. Thirdly, the E2S was used to optimize the retrieval algorithms, processors, settings, QC or bias correction tools for those biases, which were expected before launch. Thus, a powerful E2S tool, developed and maintained by scientific teams and fulfilling different objectives is mandatory for the development of robust processors during the development phase (LL-AE2, LL-EC, LL-EE). It should be noted here that the Aeolus E2S was not including an optical simulation (e.g. as CodeV or Zemax), thermal modelling of the instrument or satellite enabling a STOP (Structural-Thermal-Optical Performance) analysis. This is considered as a typical space industry activity.

7.2 Lessons Learnt from Management

5. The Aeolus DISC project was managed by a dedicated project manager in addition to the role of a scientific and technical coordinator. It is recommended to include a dedicated project manager role for such a large project including in the order of 10 partners with 20 to 40 persons involved. (LL-EC, LL-EE, LL-GE). The project management of the DISC and the project manager should be under the responsibility of the scientific institute leading the DISC, as a close cooperation with the scientific coordinator of the DISC is needed.
6. The Aeolus DISC consortium included the company serco for on-site support in ESRIN. It is recommended to include a dedicated team/partner from DISC on-site in ESRIN as personal interface to ESA´s ground segment and sensor quality group (LL-EC, LL-EE).
7. During the Aeolus DISC exploitation phase, a large number of performance indicators (PIs) was established, basically covering each work package. The number of PI´s were considered as too large in hindsight for an effective progress review. It is recommended to keep the number of PIs or key performance indicators (KPI´s) reasonable in order to assess the performance of the overall project. A number of 5 PI´s would have been sufficient for the Aeolus DISC phase E, and should be targeted for typical DISC activities (LL-EC, LL-EE, LL-GE).
8. A processor update cycle of every 6 months was achieved for the Aeolus DISC, which imposed rather strict time constraints and challenges for all DISC activities. For Aeolus an update cycle of every 6 months was considered necessary, due to the use of the data in operations at NWP centres. Certainly, this update cycle ensures fast availability of product improvements and ensures that even small modifications like small product file format changes to a given processor are handled well by processors upstream in the chain. On the cons side, this 6-months cycle limits the number of functionalities which can be implemented and the amount of testing performed for each update. Also, the frequent update of the processing baselines including the format changes were rather demanding and confusing for the Aeolus Cal/Val teams and scientific users. A careful trade-off needs

to be performed about the pros/cons for such a delivery schedule depending on the need of the mission (LL-AE2, LL-EC-, LL-EE), e.g. in phase F the DISC internal update cycle will be increased to 12 months, which could be a reasonable compromise also for future missions.

9. Proper processor release planning (especially the staggered delivery schedule) is absolutely necessary even for an instrument like Aeolus with quite a limited number of different processors. The time between the various steps should be assigned with margin and the plan should be communicated well in advance (at least 3 months before the first due date) (LL-EC, LL-EE).
10. The Aeolus DISC was managed during the COVID period (2019-2021) only with on-line meetings, which demonstrated its feasibility for most of the meeting types, e.g. meetings, which include mainly reporting. On the other hand, the limitations in discussing technical aspects among several groups were obvious during on-line meetings. Thus, it is proposed to establish at least yearly face-to-face working meetings on technical aspects, while progress reviews could be performed on-line (LL-GE).
11. The DISC expertise covered a majority of aspects from the Aeolus mission. This allowed to interface and to understand the needs for many different disciplines (engineering, science, operations) involved in the mission, including ESA-ESRIN, -ESOC, -ESTEC, space industry (ADS-UK, ADS-F, LND) via ESTEC Post-Launch Support Office PLSO, Cal/Val users, scientific users and NWP centres. Thus, it is recommended that a DISC setup should cover all relevant aspects of a mission with a broad range of expertise (LL-EC, LL-EE). The build-up of a strong collaboration with ESA, DISC, instrument prime at industry already before launch is the basis for an efficient and effective performance management. In hindsight, it would have been even more effective to already integrate the DISC teams in pre-launch testing activities (e.g. instrument tests, or TVAC tests) more strongly for the benefit of gaining experience on instrument data before launch on the DISC side, but also to have a different view on the analysis of instrument test data (LL-EE, LL-AE2).
12. The Aeolus DISC covered all relevant expertise for the instrument and the mission with the exception of the thermal engineering and detailed optical models of the instrument (e.g. within ZEMAX) Both fields were also not covered in the end-to-end simulator E2S. Thermal engineering expertise on DISC side would have been beneficial as many of the instrument performance parameters with slow and seasonal drifts are related to thermal parameters. It is recommended to build up a thermal expertise within the DISC teams already before launch, supported by optical models of the instruments in order to allow optical-thermal modelling on DISC side (LL-EC, LL-AE2, LL-EE).
13. The allocation of resources in the different tasks of a DISC needs to be highly flexible, adapted to the needs via prioritization management and re-assessed including the possibility of having sufficient resources available (e.g. in the order of 10%) for additional activities or changes of the tasks (LL-EC, LL-EE). This flexibility was achieved by a critical number of involved consortium team members in the DISC with broad expertise and certainly willingness on all sides for adaptation. Significantly more activities as originally foreseen had to be allocated to instrument performance monitoring and anomaly investigation, adapting algorithms and processors to the non-stable instrument operation including bias correction, and reprocessing. Certainly, these higher activities for some topics were performed on the cost of other activities, e.g. algorithm development and its refinement, which were originally planned with a higher effort, but then de-scoped or delayed. Other tasks were associated with lower effort than anticipated, as number of user requests or number of processor anomalies.
14. Related to this is the re-allocation or re-prioritization of resources, the following critical limitations were observed during the DISC phase:

a. The responsibility for both the operational L1B and L2A processor was with only 1 key person (DoRIT), which is considered as too risky in hindsight. The responsibility for both processors and its development should have been split among at least 2 developers, which would have been necessary already pre-launch for building up sufficient expertise. It is recommended to allocate at least one key person per processor for L1, L2A and L2B (LL-AE2, LL-EC, LL-EE) already in the pre-launch preparations.
b. On top of the different maintenance activities for the implemented algorithms in the L2A, it was decided to implement 3 new algorithms in the L2A, namely MLE, AEL-FM and AEL-PRO. Although certainly very beneficial from a technical and scientific aspect (and finally also successful) this caused significant more workload on the L2A processor (for a spin-off product) as originally foreseen. In hindsight, it was a critical decision to take new algorithms on-board during the operational mission wrt. workload on operational processor side. The timeliness of the decision was certainly also influenced by the aspect of experiencing synergies before the launch of EarthCARE. Certainly, this decision for the L2A had then also strong impact in workload on product verification and reprocessing. It is recommended to perform a more critical analysis and trade-off, when taking completely new retrieval algorithms on-board during the operational phase (LL-EC, LL-EE, LL-AE2).
c. The L2B algorithm and processor developers were significantly more involved in reprocessing activities (chain-of processor and testing) as originally foreseen, which limited the progress on the L2B algorithm and processor side, because the same key persons were involved in both activities. It is recommended to build-up a specific expertise for reprocessing and chain-of-processor development, independent from the processor developers (LL-AE2, LL-EC, LL-EE).

15. Setting up of a WIKI-based platform for discussion of different topics, for sharing information and documents was crucial for organizing the cooperation among a larger group. The Confluence tool provided sufficient flexibility for setting up a WIKI. Ideally all information, which is created and shared (e.g. via e-mails) is transferred to such a knowledge database. Setting up and maintaining a WIKI-based platform for communication and knowledge management is strongly recommended, preferably already pre-launch (LL-EC, LL-EE, LL-GE, LL-AE2).
16. The license situation wrt. operational software (or other items) should be clarified at the start of the DISC in the transition from phase E1 and E2 by ESA (LL-GE). Usually the license from the operational processing s/w have a long history from the development phase going back to early 2000´s for Aeolus. This clarification of licenses ensures consistency and clarity throughout the phase E2 and even beyond in phase F.

7.3 Lessons Learnt from Instrument Performance and Monitoring

Some of the below LL are related to the actual instrument performance as observed by ALADIN, and those are mainly relevant for considerations for Aeolus-2 or other lidar missions as EarthCARE. More details are found in the respective Chapter 3 of this Report. Some of the LL address only specific topics of the instrument performance, but are kept separately to allow better traceability.

17. Science data from the detector signals and wind performance need to be an integral part of the laser performance monitoring on top of the instrument house-keeping-data (LL-AE2, LL-EC). This has to be considered already during mission preparation and rehearsed during ground tests prior to launch.
18. Access for the DISC to the ESTEC MUST tool was essential for instrument monitoring as it allows on a daily basis a swift and easy access to all satellite and instrument related housekeeping telemetry

data including a plotting tool. MUST was used by different DISC partners (DLR, serco for on-site support, ECMWF) for monitoring. MUST also contained satellite and instrument parameters, which are not included in the science data packets downlinked with the X-Band, or were originally not included in the L1A and L1B product -an example here are the primary mirror M1 temperatures, which were included in later baseline versions in the products. Thus, access and usage of the ESTEC MUST monitoring tool is strongly recommended for future missions (LL-EC, LL-AE2, LL-EE).

19. The sensitivity of the laser energy and performance to the temperature and its gradients on the optical laser bench should be characterized on ground and validated during commissioning (LL-AE2). For Aeolus lasers once the temperature sensitivity was managed, the tunability of the lasers was crucial to optimize the send-receive co-alignment for improved atmospheric signal and wind error performance.
20. Providing and measuring more house-keeping data (e.g. temperatures) in areas of the instrument which are likely to influence instrument stability, alignment and wind bias is recommended; specifically, more telescope thermistor readings are critical (LL-AE2).
21. The instrument design should give value to embedded additional information or functionality of all components and sensors. e.g. the AHT-19 thermal sensor attached to the beam-dump in the TRO could have been designed as auxiliary energy monitor. For Aeolus-2, e.g. the cross-polar detector can provide additional or back-up co-alignment monitoring (LL-AE2).
22. Operation and commanding flexibility of the instrument are required for test designs. e.g. for Aeolus a mixed imaging/lidar operation mode for the two ACCDs would have been beneficial to study the atmospheric path stability in both axes and with additional ranging information (LL-AE2).
23. Detailed analyses from Airbus France (ADS-F) should have been made earlier in the mission. For instance, correlation of the thermal maps of the primary mirror, or links between thermal maps and bias. An additional budget for analyses, by industry, of the main anomalies would have been beneficial (LL-EE, LL-AE2).
24. The characterization of the instrument around its full operational conditions during tests on ground and in space during phase E1 is the basis for maintaining a robust performance without the need to explore outside the tested parameter-space (LL-EE, LL-AE2); an example of limited tests range on-ground was the ACCD operating temperature range, or testing different phase settings for the Laser Chopper Mechanism (LCM). A risk-minimized testability for performance relevant topics in space should be foreseen in the instrument and operational design (LL-AE2).
25. Performance of some of the end-of-life (EOL) tests either during commissioning phase or earlier in the nominal phase would have been beneficial (LL-AE2).
26. It is recommended to reserve fixed time slots (e.g. two slots of 1 week per year) for dedicated instrument calibrations or instrument performance measures and improvements (e.g. laser energy increase). These fixed time slots would allow users to adapt to missing or degraded data quality and to instrument teams for preparing these test periods in advance (LL-EE, LL-AE2). Also, the NWP users could be warned about invalid products during these periods in advance and block-listing of Aeolus data could be activated. In such periods, some of the EOL tests could have been foreseen.
27. The monitoring of the ALADIN instrument is based on regular calibration modes, like Instrument Spectral Registration (ISR, over a large frequency range of 11 GHz with resolution of 25 MHz to monitor precisely the interferometer characteristics, but also as an unexpected side aspect of the laser energy behaviour with frequency), and Laser Beam Monitoring (LBM for monitoring the laser

far-field and near-field image) both for the internal path. It is recommended to consider a weekly repetition cycle for these modes (LL-EC, LL-AE2).

28. The calibration of L2A aerosol products and L2B wind products is based on a combination of ISR, nadir-pointing Instrument Response Calibration IRC and off-nadir pointing IRONICS. The calibration approach could not be consolidated for all aspects during phase E, and further analysis is needed in phase F. But it is clear that also a precise characterization of the spectrometer transmission illuminated by the atmospheric path is needed, which can be achieved by IRC´s and IRONIC´s – for monitoring changes on the atmospheric path also weekly modes are needed (e.g. IRC). One proposed approach for calibration would be using a large number of sequentially performed IRONICS (e.g. 60) distributed over the globe to cover most atmospheric scenes, i.e. preferably a broad temperature range. This global sampling with IRONICs should be at least foreseen in the Aeolus-2 commissioning phase (LL-AE2). The stability of the Aeolus-2 instrument will determine how often these IRONICS need to be performed during nominal operation. Given the limited benefit of individual weekly IRONICs, due to limited sampling of meteorological conditions and instrument drift, then we would not recommend this weekly repetition of IRONIC´s for Aeolus-2. IRCs should still be considered for Aeolus-2, so the IRONIC derived calibration can be compared to the more traditional method (LL-AE2).
29. The largest challenge for the instrument calibration remains, that the spectrometer transmission curves cannot accurately be measured on the atmospheric path in-orbit. This is also complicated by the sequential implementation of the Fizeau interferometer and the two Fabry-Perot Interferometers (FPI´s), where the reflection of the Fizeau is imprinted on the Rayleigh channel FPI´s. This characterization of the atmospheric path is also a remaining challenge for the on-ground characterization, as only a narrow-bandwidth signal can be produced with a laser source, but not a fully representative, broadband molecular spectrum (LL-AE2).
30. The ground-return velocities were studied for bias correction of harmonic wind biases with the HBE and range-dependent biases (RDB) pre-launch. It could not be realized to use these ground-returns for Aeolus bias correction operationally, due to the lower than expected SNR, and resulting less geographical availability and higher random errors in combination with a more complex temporal behaviour of the wind bias. Nevertheless, it could be shown that also the information from ground-return velocities could be used for Aeolus wind bias correction – although with less accuracy and stability as using the ECMWF model as anchor. Nevertheless, it is recommended to continue the study of ground-returns for bias correction for Aeolus-2 (LL-AE2), as significantly higher SNR can be expected combined with a higher vertical resolution (100 m), which eases the ground detection and is less prone to biases induced by the atmosphere above the ground.
31. The measured signal levels of ground-returns over land and ice were significantly lower than expected from end-to-end simulations using global albedo maps derived from climatology for each month – even considering the initial loss observed on the atmospheric path. The use of albedo and reflectance in the UV from passive sensors should be correlated with in-orbit observations and revised for future performance simulations for Aeolus-2 (LL-AE2), e.g. considering the new lidar surface reflectance product (in phase F) or experience from ATLID on EarthCARE in nadir pointing.

7.4 Lessons Learnt from Algorithm and Processor Development

32. The L1B IODD (Input-Output-Data Description) is a Word document with 332 pages, 435 tables, and 1695 references (the other IODD´s were prepared with different tools, e.g. Excel for L2A or LaTeX for L2B). Word is not able to handle a document of that size properly, especially the references cause a significant amount of extra work. It is recommended to use other tools for generating IODD

documents, or even provide it via an online tool only (e.g. as available on https://stcorp.github.io/codadef-documentation/AEOLUS/index.html) (LL-GE, LL-AE2, LL-EE).

33. The DISC on-site team provided guidelines for the software delivery process such as "Aeolus Software and Auxiliary Delivery ICD, AED-IC-SER-GEN-003". These documents are highly appreciated as they clearly state how software delivery packages should be set up, who is responsible to deliver a specific entity, or communication chains. Also, there was a change of servers and tools for anomaly management or open issues tracking (e.g. from ARTS to TellUS and JIRA). It is recommended that such documents and tools for anomaly tracking are already available before launch (LL-GE, LL-EE)
34. The limited resources for operational software development in combination with the tight delivery schedule of 6 months resulted in compromising on standards for good software development, software documentation and software testing like outlined in the ECSS norms (e.g. ECSS-E-ST-40C which is required to be applied). It should be noted here, that certainly a significant number of s/w tests were performed on processor level and the chain of processors, which was sufficient for Aeolus indicated by the low number of anomalies and need for patch deliveries to correct for s/w bugs. It is clear for an Earth Explorer mission with a short lifetime resulting in a challenging delivery schedule, that compromises in the application of the ECSS norms need to be taken (LL-EC, LL-EE); on the other hand, it is anticipated that the approach for s/w testing will be different with Aeolus-2 as an operational mission and more resources need to be allocated on the software engineering side (LL-AE2).
35. Automation of s/w testing is an on-going topic in the development. While some of the processor testing was performed (semi-)automatically (e.g. CoP with test scripts and automated reporting) – some other parts were done manually, e.g. ACMF testing. It is recommended to consider automation of s/w testing already as in important task in pre-launch phases (LL-GE).
36. The s/w documentation for the different Aeolus processors is rather inhomogeneous ranging from DPM´s (Detailed Processing Models) for the L1B to more general ATBD´s for the L2A and L2B, which target a different audience. It is clear that the resources for s/w documentation was limited. As the s/w developers were already part of the Aeolus team since 2004, there was no need to have a detailed description of the s/w code available (e.g. with tools like Doxygen), which for example could be handed over to a third-party for implementation. Thus, there is certainly a significant effort involved, when new s/w developers come on-board for maintaining and refining existing codes. This is certainly a reasonable approach for an EE mission with limited lifetime (LL-EE), but will cause additional efforts when implemented for an operational mission (LL-AE2).
37. If ESA provides a library to aid with the implementation of processors (like the EO-CFI library), then the source code should be provided as well (LL-EE, LL-GE). This will facilitate the processors compatible to multiple computing platforms, and it would also make debugging of problems much easier.
38. It is very useful if ESA provides an emulator of the operational PDGS environment for processor testing during development, with this tool being compatible to different development environments, so preferably should be provided as source code, not as precompiled executable (LL-GE).
39. The concept of controlling the operational processors via auxiliary parameter files with a large number of parameters, which define algorithm settings or QC decisions, is considered as a successful approach (LL-EE, LL-GE). Certainly, those AUX_PAR files need to be part of the configuration management and a reasonable process needs to be defined for having the flexibility of updating

such parameter files, even in-between the 6-months deliveries and baseline updates (LL-EE, LL-GE, LL-AE2). It was also recognized that the use of auxiliary parameter files is certainly very beneficial for sensitivity tests of the algorithms implemented in the operational processor, even for experienced users of the processors within the DISC beyond the processor developers. In this context, it is recommenced to maintain a detailed and easily accessible history/tracking of the parameters contained in the AUX_PAR files including the justification of changes of their values (LL-GE).

40. Related to the above recommendations with AUX_PAR files is that simulators and processors should not rely on a GUI (Graphical User Interface) for providing inputs. There should always be an automatically configurable interface to control the software through input files to allow including it in a scripted system (LL-GE).
41. The effort to write compatible code for the L2B processor has proven to be very useful. It was specifically followed for the L2B processor during the pre-launch development, because of the requirement to run the L2BP at different NWP centres. Not only it enables the use the processor on many machines and with different compilers. But equally important is the fact that the code is tested and checked in different ways when using different compilers and machines. This has exposed many programming mistakes early and allowed fixing them long before they became harmful in operational use. Therefore, it is recommended to apply compatible code writing and associated testing to all projects and processing levels (LL-EE, LL-GE, LL-GE).
42. It is essential to consider the fact that there will be numerical differences in the algorithm outputs when running on different computer platforms (e.g. DISC internal Sandbox and then on the PDGS platforms) (LL-GE). Thresholding decisions are made in many places in the code, and this can lead to different flagging, like in classifications or QC results. We found that it is worthwhile to tune the test cases as much as possible to prevent these thresholding decisions to differ.
43. It is very useful to add a reference result (for the L2BP an NWP model reference wind) to the product (LL-AE2, LL-EE). This makes monitoring much easier and allows easy investigation of different types of biases which may lead to improved (NWP-based) calibrations.
44. The split of functionalities between Aeolus L1 and L2 processing was made in close cooperation between the algorithm teams before launch. Changing the functionalities and interfaces of the different Aeolus processor levels needs a careful trade-off involving all relevant parties, as the effort and consequences are large (LL-GE, LL-AE-2). Making such changes in an operational chain of processors requires a lot of time and testing. This pre-launch defined split between L1 and L2 has proven successful for Aeolus, and it is recommended to keep the main functionalities also for the future Aeolus-2 processing (LL-AE2) including:
    a. Horizontal grouping should remain in the L2BP since this very much is a feature that is also relevant for scientific and NWP users of the L2BP. They should be able to adapt the signal accumulations to their intended use.
    b. Since Aeolus-2 will probably use a much finer vertical binning, also a vertical grouping algorithm should be considered for processing this data in the L2BP.
    c. Rayleigh wind retrieval depends on NWP model data (temperature and pressure), therefore it has to be done in the L2BP.
    d. Mie wind retrieval depends on grouping and the resulting signal accumulation; therefore, it has to be done in the L2BP.
    e. Bias corrections on signal level, for example the current hot-pixel correction, should be done in the L1bP, but wind bias corrections that depend on NWP data, or corrections that are only

applied after grouping, such as the Mie non-linearity correction or the M1 telescope temperature correction, should be done in the L2BP (if necessary). Certainly, it is clear that the instrument design should minimize the bias contributors and mainly minimize a temporal evolution of the biases.

f. An important factor to keep in mind when considering moving functionalities from the L2A to the L2B processor is run time. Currently the L2AP has no runtime requirement, and as a consequence some of the algorithms take a lot of time. If the L2BP would have to wait for this input the wind results may come too late to be used as input for NWP models (especially the local area models that run every hour or every 3 hours).

45. It is essential for processor development and preparation of AUX files for (re)processing that the DISC team has access to a system that can evolve processing configurations. It is used to prepare new versions for the PDGS processing. The PDGS has no such evolving capability. The CoP is needed to run tests with experimental settings and pre-deliveries of processors that are not suitable yet for deployment on PDGS side. Such a system should be accessible from different locations and therefore a location "in the cloud" is the most convenient solution (LL-EC, LL-EE, LL-AE2).
46. The QC information for the different parameters and products is usually contained in QC flags using integer values with bit-wise coding of the QC information. This approach caused some difficulties for external users to fully anticipate and use this information. A more convenient format for the QC information would be preferred from a user perspective (LL-EE). In addition, when defining custom binary files (e.g. as for the EE format), some zero (or other well-defined) values should be inserted at a number of locations in the file (this is a form of canary checking) (LL-GE). This allows for checking the file reading routines for correctness and provides an easy way to detect file corruption. These points above result in a more common suggestion, that the Earth Explorer binary format is not very user-friendly and common and should be replaced by more common, self-explaining formats as netCDF (LL-EE, LL-GE).
47. "Expect the unexpected" especially for the instrument performance wrt. systematic errors; Try to be prepared for the unexpected and question all assumptions made before launch wrt. characteristic, cause and correction of systematic errors (LL-AE2, LL-EC, LL-EE).
48. Biases could occur only during some periods of the year due to different illumination of the satellite and the resulting thermal conditions (e.g. eclipse phases or satellite in permanent twilight). This makes an identification even more time-consuming as for other bias causes, as one usually would need to wait for another occurrence (e.g. separated by 1 year) for a confirmation of the bias (LL-AE2, LL-EC, LL-EE).
49. Horizontal and vertical geolocation errors could show up as errors in the retrieved parameters (e.g. wind or optical properties) in case of horizontal and vertical gradients of this parameter (LL-AE2, LL-EC, LL-EE, LL-GE).
50. NWP monitoring is mandatory to identify, characterize and potentially correct bias swiftly; validation campaigns with reference instruments are needed to support, confirm and refine the findings from NWP monitoring with higher accuracy and spatial resolution (LL-AE2, LL-EC, LL-EE).
51. Separate biases for ascending and descending orbits could occur. If this is the case, they could compensate or cancel each other, especially for parameters with positive/negative sign (e.g. LOS winds), but not limited to those. Thus, bias behaviour needs to be analysed separately for ascending and descending orbits (LL-AE2, LL-EC, LL-EE)

52. Biases of smaller magnitude can be identified, once biases of larger magnitude are corrected – so bias correction is a step-by-step approach; timing and duration is then also depending on the update cycle of the processor baselines. For Aeolus, it took about 1.5 years after launch to identify and correct for major bias sources (hot pixels, slow drifts, M1-T induced biases), thereby effectively extending the commissioning phase E1. It is unlikely to assume that unexpected bias causes could be identified and corrected during phase E1 (LL-AE2, LL-EC, LL-EE).
53. In order to identify and correct for unknown biases of a mission, expertise is needed covering all aspects from a mission from instrumented related topics even for sub-units, such as detectors or telescopes, satellite related topics (AOCS, thermal behaviour), hands-on the complete chain of algorithm and processors from L1A, L1B to L2A, L2A, and observation monitoring with NWP models. This expertise should be combined in a DISC consortium involving several partners to cover these topics. (LL-AE2, LL-EC, LL-EE, LL-GE).
54. Cloud-screening or classification in clear-scenes and cloudy-scenes is considered as a major challenge for passive remote sensing, but it turned out that this was also the case for an active mission as Aeolus – one of the main reasons was the accumulation of several pulse returns on the ACCD resulting in a horizontal resolution of a few km, which is considered coarse for the objective of cloud screening. The cloud screening and classification/grouping is relevant for the aerosol and the wind product, considering that a pure "aerosol" product should only be derived from measurements without clouds. The effort in cloud screening is also obvious for the assimilation of aerosol products in NWP models. This challenge of cloud-screening and grouping will remain for future lidar missions (LL-EC, LL-AE2), and it is recommended to provide measurements downlinked from the satellite with a higher resolution than Aeolus (e.g. on the 1 km scale).
55. The absence of a depolarization channel on Aeolus strongly limits the classification of different aerosol types and cloud phases, which is of major importance for using the aerosol product. Thus, an implementation of cross-polar channel is proposed for Aeolus-2 similar as implemented for ATLID on EarthCARE (LL-AE2).
56. The implementation of L2A algorithms being originally developed for ATLID on EarthCARE was certainly beneficial for Aeolus, but also the capability of testing the ATLID algorithms on real Aeolus data with its noise characteristics was beneficial for EarthCARE. It is recommended to continue the exploitation of synergies between Aeolus and EarthCARE (LL-EC) also for the benefit of future lidar missions (LL-EE, LL-AE2). Another aspect was that the ATLID algorithm developers came on-board only during the Aeolus operational mission. They had the advantage of having a "new look" as an "outsider" on the topics, which certainly had strong benefits for both sides, in the sense that useful checks and new ideas (e.g. derivation of the EMSR) were brought to the table. But it is also clear that such involvement is only possible with associated resources in order to be able to spend sufficient time on the project, which could not have been achieved by a very-time limited review process. It is recommended to exploit synergies for future lidar missions also by involving and exchanging expertise (LL-EC, LL-EE, LL-AE2). Certainly, also the EarthCARE mission will strongly benefit from the expertise gained by the involvement in the Aeolus mission and DISC. One might consider to involve also Aeolus DISC experts in future EarthCARE activities (LL-EC).
57. Studies about implementing an aerosol/cloud cross-talk correction in the AUX_RBC file as a fourth dimension (in addition to atmospheric temperature, pressure and laser frequency) were so far not conclusive and hence this option was abandoned. This should be investigated in further detail in the future, as such a correction would be even more crucial in case a Michelson interferometer is used for Aeolus 2 (LL-AE2).

58. This missing particle cross-talk correction caused a significant bias for the Rayleigh cloudy winds. A different approach using the ECMWF model for deriving a parametric model for cross-talk correction by means of measured scattering ratio was derived within the DISC phase E. Using the NWP model for calibration was also exploited for the non-linear response of the Mie spectrometer for correcting wind-speed dependent Mie wind biases in L2B. This work was not originally planned to be performed in the DISC phase, but the DISC set-up provided enough flexibility and sufficient room to explore also different directions. It is recommended for future Earth Explorer missions but also for Aeolus-2 to provide sufficient resources and flexibility for re-prioritization on topics, which only arise after launch (LL-EE, LL-AE2). This recommendation is also covered in the management part, and kept re-enforced here to provide an example for such flexibility.
59. Additional tools for automatically monitoring the data product quality in the ACMF were developed replacing the QUADAS tool (in IDL) by a report generator in Python due to the higher flexibility. It is recommended to develop flexible tools for automatic QC already pre-launch, which can be adapted after launch to the actual needs (LL-GE). It is important that a basic setup of product monitoring tools is already available pre-launch (e.g. as implemented for the L2B), in order to avoid tool development effort by several experts independently after launch.
60. The following key best practices were derived for the aspects of processor release management, which could serve as examples for future missions (LL-EE, LL-GE): existence of a flexible collaborative platform for processor development and testing (DISC internal sandbox); processor evolution documents, to trace software configuration item (CI) history; unique structured interface towards PDGS Operations with the DISC on-site (DOS) team; integrated layer covering anomaly, change and configuration management; hierarchical and agile structure of the configuration management plan, integrated operational s/w and AUX-file verification processes, leveraging the sandbox and a dedicated system bridging with the PDGS (build and filter); dedicated outreach service structure with joining scientific coordination and operational activities.
61. The following key challenges were handled successfully for processor and anomaly management but could be improved for future missions (LL-EE, LL-GE): Bridging the different anomaly management tools (DISC operations, PDGS and tracking of prototypes anomalies, e.g. see also specific recommendation on ARTS/Jira and TEllUS) and configuration management tools (DISC operations, PDGS); operational and reprocessing activities overlapping; configuration management of prototypes wrt operational s/w; PDGS operations and DISC verification platforms synchronization (DOS build virtual machine and DISC sandbox).

7.5 Lessons Learnt from Product Monitoring and NWP impact assessment

62. A recommendation for Aeolus-2 would be to maintain strong links with NWP centres, such as ECMWF, to allow preparation of monitoring facilities well in advance of the launch, based on testing with end-to-end simulators, as was done with Aeolus (LL-AE2). This led to the whole processing chain being in a good state before the real data came along, and meant we had the monitoring tools in place to start assessing real Aeolus data immediately with the start of the Commissioning Phase to detect issues that could later be resolved. This effectively maximised the time that Aeolus could be operationally assimilated in NWP.
63. Given ECMWF's readiness for Aeolus, quick progress was made during the Commissioning Phase in running OSEs (observing system simulation experiments) and learning how to best use the data. This continued with major improvements during Phase E2, leading to a record quick use of a new technology in operational assimilation at ECMWF. Therefore, we think it is important for maximising the exploitation of Aeolus-2 to give a lead NWP centre, e.g. ECMWF, enough time, and resources

pre-launch to prepare and optimise the assimilation system (LL-AE2). The work by ECMWF was crucial in providing advice to other NWP centres e.g. DWD, Met Office and Météo-France. This support by ECMWF to other NWP centres was crucial for their pre-launch preparations and exploitation of Aeolus observations (post-launch) to facility assimilation experiments at several NWP centres.

64. The following three recommendations are summarized with an (operational) assimilation of aerosol optical properties retrieval products from future aerosol lidar missions: To fully account for accurate aerosol scattering, depolarization measurements are necessary, thus both co-polar and cross-polar components of the scattered radiation should be recorded by the instrument (LL-AE2). Without this information, it is challenging to produce a true aerosol product.
65. Mismatches between the product and what the ECMWF model is currently capable of producing: attempting to remove the contribution from cloud signal was a necessary step when preparing the L2A SCA mid-bin backscatter product for assimilation, as the ECMWF model for Aeolus backscatter only considered scattering from aerosols. A model-based cloud screening was used to reduce the contribution from cloud in the backscatter, but was not completely effective. This reinforces the recommendation for an effective cloud screening (LL-EC, LL-EE, LL-AE2).
66. The NRT monitoring of the L2A product at ECMWF began relatively near the end of the mission, with final preparations taking place whilst the mission was ongoing, and began 3 years after the operational assimilation of the HLOS winds was implemented. Ideally, these preparations (analysis of errors, quality control and pre-screening requirements of data etc) would have been made prior to the satellite launch, such as for the assimilation of the wind (LL-EC, LL-EE, LL_AE2).

7.6 Lessons Learnt from Cal/Val, User Engagement and Outreach

Cal/Val teams contributed by performing considerable validation activities using collocated measurements and reporting observed issues to the Aeolus DISC. In turn, the Aeolus DISC team provided validation needs, product guidelines and recommendations to the Cal/Val teams. This continuous exchange and interaction led to a number of lessons learnt:

67. Early release of data products to Cal/Val teams (LL-EC, LL-EE, LL-AE2): Although several issues were known and not resolved at that point (e.g. hot pixels), the data products have been released to Cal/Val teams already 3 months after launch in the commissioning phase. This gave Cal/Val teams the opportunity to work with the data more than 1 year before public data release. ESA and DISC also profited from this early release as first validation results using external data could provide evidence to release data to the public in May 2020.
68. Provide regular updates regarding data products to Cal/Val teams (LL-EC, LL-EE, LL-AE2): Due to regular processor updates (so-called baseline versions usually every 6 months), it was important to inform users about the major changes (sometimes new variables, units, QC flags, resolution).
69. Announcements of periods with special calibrations is important to avoid teams to measure, when the satellite was not in nominal measurement mode (LL-EC, LL-EE, LL-AE2).
70. Flexibility in Range Bin Settings (RBS) highly increased science impact (LL-AE2): Input from Cal/Val teams triggered scientific questions that could be addressed by adjustments of the vertical sampling for special periods and geographical regions. This allowed to react ad-hoc on special events like the Hunga Tonga eruption. To discuss new RBS and propose them to ESA, a working group was created (Range Bin Setting Working Group).
71. Communication platform (Cal/Val confluence) brings teams together (LL-EC, LL-EE, LL-AE2): The Cal/Val confluence platform was maintained by ESA and the Aeolus DISC to not only provide news,

documents, baseline updates, instrument settings, timeline of planned calibration activities but also to discuss issues (open communication strategy allowed on confluence), provide preliminary results and to propose new settings. Until 2024, the Aeolus Cal/Val confluence counts 499 registered users.

72. Validation throughout the whole mission (LL-EC, LL-EE, LL-AE2) including continuation of validating reprocessed data products with new baselines in phase F: The product quality assessment by external Cal/Val teams using long-term collocated observations complemented the wind product monitoring at ECMWF. Also, beyond the mission, long-term validation of the reprocessed datasets is important together with dedicated scientific studies.
73. Joint validation campaigns using airborne instruments (LL-EC, LL-EE, LL-AE2): While several Cal/Val teams do validation for special geographical regions and often profile-to-profile comparisons, only aircrafts allow validation of multiple profiles along the satellite track, in remote areas and during special atmospheric conditions. 4 airborne campaigns were performed by DLR throughout the mission lifetime. In addition, major field campaigns with combination of several aircrafts and ground-based instrumentation, e.g. JATAC provide unique datasets for both validation and science.
74. Provide guidance to tools, e.g. for overpass prediction (LL-EC, LL-EE, LL-AE2): Not all users are familiar with the multiple tools, which significantly facilitate the work with Aeolus data (e.g. overpass tools, VirES). Therefore, guidance is important what to use and how to make best use of it. For teams with only one ground-station, a table with overpass times for certain latitudes / longitudes was well received by the community.
75. Provide standards/recommendations for collocation criteria but also verification of them (LL-EC, LL-EE, LL-AE2): Certainly, standards for collocation (temporal/spatial) are important, but also the analysis needs common approaches for quality control of the data products, e.g. use of the error estimates in the products and handling of gross errors. Different altitude regions might require different collocation criteria. These criteria should ensure comparability in the results from the different teams.
76. Provide handbook for Cal/Val requirements and implementation plan of external Cal/Val activities before launch to ensure that teams are ready from the first day to perform collocated measurements (even before first data access) → critical point for relatively short mission (LL-EC, LL-EE, LL-AE2).
77. Organization of regular exchange meetings in form of 2-day working meeting every 6 months following the provision of the Cal/Val team reports and the synthesis of these reports within certain topical sub groups (wind, aerosol, instrument, NWP) (LL-EC, LL-EE, LL-AE2). This allows discussion in smaller groups between Cal/Val teams and ESA / DISC.
78. The following LL are derived from the outreach activities (LL-EC, LL-EE, LL-GE, LL-AE2): Identification of different global user groups according to mission objectives and an associated user information strategy and procedure is crucial; an a-priori generic description may be useful as a template in order to organize and control all aspects of outreach and communication to the different identified user groups. Examples of these activities are the establishment of special issues in different journals or presentation of results at different conferences, which target different scientific user communities.
79. While some of the tools for the Aeolus user community were well prepared before launch (e.g. visualization tool VirES or codadef for reading the products), it would have been preferred to have analysis tools already available before launch for experienced users (LL-EC, LL-GE), like the VirES VRE should be available at the start of the mission and not throughout. Otherwise too many data users have already developed their own tools and will refrain from using the newly developed tools.

80. A closer cooperation with the Aeolus+ science activities, which were managed by ESRIN EO science division independently from the DISC, would have been beneficial for both the DISC activities, but also for achieving the objectives of the Aeolus+ activities. Several of the Aeolus+ science teams were newcomer to the Aeolus mission and need to understand the Aeolus data products for their specific scientific purpose. A stronger link and support of the Aeolus+ science teams would have required resources and a dedicated work package also on DISC side. It is recommended to establish a closer cooperation between science activities and the DISC for future missions (LL-EC, LL-EE).

The total of 80 LL discussed in this DISC Final Report are complemented by a large number of more instrument-related LL in the EOL Final Report from the DISC. Certainly, the most important LL is that the DISC played a critical and essential role for the success of the Aeolus mission and for reaching the Aeolus objectives. The question remains, how to best track and formalize the implementation of these LL into recommendations or even specifications for EarthCARE, Aeolus-2 and future Earth Explorer Missions.

APPENDIX

This page is left bank intentionally.

A LIST OF REFERENCES

The references are structured for each chapter and section with the identical numbering

1 Introduction and objectives of the Aeolus DISC

- Krisch, I., Reitebuch, O., von Bismarck, J., Parrinello, T., Rennie, M., Weiler, F., Huber, D., de Kloe, J., Dabas, A., Straume, A.-G., Abdalla, S., Aprile, S., Bley, S., Bracci, F., Bucci, S., Cardaci, M., Damman, W., Donovan, D., Ehlers, F., Fabre, F., Flament, T., Fischer, P., Isaksen, L., Jupin-Langlois, S., Gostinicchi, G., Kanitz, T., Lacour, A., De Laurentis, M., Lemmerz, C., Lux, O., Marksteiner, U., Marseille, G.-J., Masoumzadeh, N., Meringer, M., Niemeijer, S., Nikolaus, I., Perron, G., Pijnacker-Hordijk, B., Reissig, K., Savli, M., Schmidt, K., Stoffelen, A., Trapon, D., Vaughan, M., Veneziani, M., De Vincenti, C., and Witschas, B. (2021): *The Aeolus Data Innovation and Science Cluster,* International Geoscience and Remote Sensing Symposium (IGARSS), 759-762, Brussels, Belgium / Online, 11 – 13 July 2021.

2 DISC management approach

- ESA (2018): Statement of Work: Aeolus Data Innovation and Science Cluster (Aeolus DISC), ESA-EOPG-MOM-SOW-57, 20/08/2018.
- DLR (2023): Aeolus Data Innovation and Science Cluster (DISC) – Project Management Plan, AED-MP-DLR-GEN-005, v5.0, 22/11/2023.

3 Instrument Performance and Monitoring

- Lemmerz, C., Lux, O., and Reitebuch, O. (2018): Preparation of Tools for Phase E1 – Monitoring of ALADIN and Satellite Housekeeping Data, AE.TN.DLR.WP2300.HK, v1.0, 23/05/2018.
- Lemmerz, C., Lux, O., Weiler, F., and Reitebuch, O. (2019): Technical Note/Handover Report: Laser performance during IOCV, AE-TN-DLR-7300-1, v1.0, 25/04/2019.
- Lemmerz, C. and Lux, O. (2018 – 2023): Housekeeping and L1A data analysis reports, HK_E2_CL_OL_WM[001 to 254]_HK_data_analysis.pptx, 2018 – 2023.
- Lemmerz, C., Lux, O., Witschas, B., Rahm, S., Marksteiner, U., Geiß, A., Weiler, F., and Reitebuch, O. (2023a): Airborne Doppler wind LIDAR technology demonstration for Aeolus: from pre-launch campaigns to mission performance validation, Proc. SPIE 12777, 72–84.
- Lemmerz, C., Lux, O., Marksteiner, U., Witschas, B., and Reitebuch, O. (2023b): Aeolus End-of-Life (EOL) Tests – DISC Analysis Report, AED-TN-DLR-GEN-083, v1.0, 14/09/2023.

3.1 Laser performance

- Székely, G. S. and Henzelin, F. (2005): Design and qualification of the mechanisms for the ALADIN instrument, in: 11th European Space Mechanisms and Tribology Symposium (ESMATS), 85–90.
- Cosentino, A., D'Ottavi, A., Sapia, A., and Suetta, E. (2012): Spaceborne Lasers Development for ALADIN and ATLID Instruments, IEEE Int. Geosci. Remote. Sens. Symp., 5673–5676.
- Mondin, L. and Bravetti, P. (2017a): Aeolus high energy UV Laser wavelength measurement and frequency stability analysis, Proc. SPIE, 10563, 84, 105633B.
- Mondin, L., Era, F. F., Kheyrandish, H., Bolkhovitinov, A., Baselga Mateo, A., Hippler, M., Thibault, D., Schröder, H., Wernham, D., Ciapponi, A., Heese, C., Ivanov, T., van Papendrecht,

G., Riede, W., and Butenko, Y. (2017b): Caveats and pitfalls of high energy UV laser operation on ground, Proc. SPIE, 10562, 105621U.

- Lux, O., Wernham, D., Bravetti, P., McGoldrick, P., Lecrenier, O., Riede, W., D'Ottavi, A., Sanctis, V. de, Schillinger, M., Lochard, J., Marshall, J., Lemmerz, C., Weiler, F., Mondin, L., Ciapponi, A., Kanitz, T., Elfving, A., Parrinello, T., and Reitebuch, O. (2020): High-power and frequency-stable ultraviolet laser performance in space for the wind lidar on Aeolus, Opt. Lett., 45 (6), 1443–1446.
- Lux, O., Lemmerz, C., Weiler, F., Kanitz, T., Wernham, D., Rodrigues, G., Hyslop, A., Lecrenier, O., McGoldrick, P., Fabre, F., Bravetti, P., Parrinello, T., and Reitebuch, O. (2021): ALADIN laser frequency stability and its impact on the Aeolus wind error, Atmos. Meas. Tech., 14 (9), 6305–6333.
- Lux, O, Lemmerz, C., Reitebuch, O., Wernham, D., Kanitz, T., Bravetti, P., Schillinger, M., De Sanctis, V., Parrinello, T., and Fix, A. (2022): Solid-state lasers for earth observation by air- and satellite-borne lidar systems, XXIII International Symposium on High-power Laser Systems and Applications (HPLS&A), Prague, Czech Republic, 13 – 16/06/2022.

3.2 Internal reference and atmospheric path signals

- Székely, G. S. and Henzelin, F. (2005): Design and qualification of the mechanisms for the ALADIN instrument, in: 11th European Space Mechanisms and Tribology Symposium (ESMATS), 85–90.
- Schmidt, K., Reitebuch, O., Weiler, F., and Marksteiner, U. (2019): Radiometric Performance, ESA Handover Report AE-TN-DLR-7300-6, v1.1, 23/04/2019.
- Lux, O., Lemmerz, C., Weiler, F., Kanitz, T., Wernham, D., Rodrigues, G., Hyslop, A., Lecrenier, O., McGoldrick, P., Fabre, F., Bravetti, P., Parrinello, T., and Reitebuch, O. (2021): ALADIN laser frequency stability and its impact on the Aeolus wind error, Atmos. Meas. Tech., 14 (9), 6305–6333.
- Krisna, T.C., Bravetti, P., de Sanctis, V., Parrinello, T., and Wernham, D. (2022): Long Term Evolution of Laser Beam Monitoring (LBM) from Aeolus, Aeolus 3rd Anniversary Conference, Taormina, Italy, 28/03 – 01/04/2022.
- Schmidt, K., Lux, O., Reitebuch, O. (2022): Evolution of Aeolus Atmospheric and Solar Background Signals, Aeolus 3rd Anniversary Conference, Taormina, Italy, 28/03 – 01/04/2022.
- Lux, O., Lemmerz, C., Schmidt, K., Witschas, B., Weiler, F., Masoumzadeh, N., Marksteiner, U., Cito Filomarino, V., Krisch, I., and Reitebuch, O. (2023): ALADIN Instrument Monitoring and Investigation of Signal Anomalies, Aeolus Science Conference 2023, Rhodes Island, Greece, 22 – 26/05/2023.
- Schmidt, K., Lux, O., Lemmerz, C., and Reitebuch, O. (2023): Evolution of Aeolus Atmospheric and Solar Background Data, Aeolus Science Conference 2023, Rhodes Island, Greece, 22 – 26/05/2023.
- The Pierre Auger Collaboration, Lux, O., Krisch, I., Reitebuch, O., Huber, D., Wernham, D., and Parrinello, T. (2024): Ground observations of a space laser for the assessment of its in-orbit performance, Optica, 11 (2), 263–272.

3.3 ACCD hot pixels and other detector anomalies

- Janesick, J. R. (2001): Scientific Charge-coupled Devices, SPIE Press, ISBN 978-0-8194-3698-6.

- Widenhorn, R., Blouke, M. M., Weber, A., Rest, A., and Bodegom, E. (2002): Temperature dependence of dark current in a CCD, Proc. SPIE 4669, 193–201.
- Weiler, F., Kanitz, T., Wernham, D., Rennie, M., Huber, D., Schillinger, M., Saint-Pe, O., Bell, R., Parrinello, T., and Reitebuch, O. (2021): Characterization of dark current signal measurements of the ACCDs used on board the Aeolus satellite, Atmos. Meas. Tech., 14, 5153–5177.
- Masoumzadeh, N., Weiler, F., Krisch, I., and Reitebuch, O. (2022): Noise characterization of the ACCDs detectors onboard ESA's Wind Lidar Mission Aeolus, Aeolus 3rd Anniversary Conference, Taormina, Italy, 28/03 – 01/04/2022.
- Weiler, F., Masoumzadeh, N., and Reitebuch, O. (2022): Correction of hot pixel steps in Aeolus reprocessed data, Aeolus 3rd Anniversary Conference, Taormina, Italy, 28/03 – 01/04/2022.
- Reichert, R. (2023): Classification of Hot Pixels on Aeolus ACCD based on DUDE measurements, AED-TN-DLR-L1B-084, v1.1, 19/12/2023.

3.4 Characterization of the ALADIN spectrometers

- Witschas, B. (2019): Analysis of in-orbit measured Rayleigh spectrometer transmission curves, Handover Report – Technical Note, AE.HR.DLR.WP7300.SPACE.RSP, v1.0, 2019.
- Witschas, B. (2020a): Analysis of Rayleigh spectrometer transmission curves based on instrument spectral registration (ISR) measurements and investigation of instrumental drifts, AED-TN-DLR-L1B-030, v1.0, 2020.
- Witschas, B. (2020b) Analysis of Rayleigh spectrometer transmission curves based on instrument spectral registration (ISR) measurements and analysis of the first reprocessed data set, AED-TN-DLR-L1B-035, v1.0, 2020.
- Witschas, B., Lemmerz, C., Lux, O., Marksteiner, U., Reitebuch, O., Weiler, F., Fabre, F., Dabas, A., Flament, T., Huber, D., and Vaughan, M. (2022): Spectral performance analysis of the Aeolus Fabry–Pérot and Fizeau interferometers during the first years of operation, Atmos. Meas. Tech. 15, 1465–1489.
- Witschas, B., Vaughan, M., Lux, O., Lemmerz, C., Nikolaus, I., Reitebuch, O. (2023): Verification of different Fizeau fringe analysis algorithms based on airborne wind lidar data in support of ESA's Aeolus mission, Appl. Opt., 62, 7917-7930.

3.5 IRC and IRONICS

- Huber, D. and Marksteiner, U. (2021): IRONIC data measurements processing, AED-TN-DoRIT-L1B-049--IRONIC_Processing--v2_10--2021_11_04.pdf, v2.1, November 2021.
- Marksteiner, U., Lemmerz, C., Lux, O., Rahm, S., Schäfler, A., Witschas, B. and Reitebuch, O. (2018): Calibrations and Wind Observations of an Airborne Direct-Detection Wind LiDAR Supporting ESA's Aeolus Mission, Remote Sens., 10, 2056, https://doi.org/10.3390/rs10122056.
- Marksteiner, U., Lux, O., Reitebuch, O., de Kloe, J., Marseille, G.-J., and Rennie, M. (2023): Overview of Instrument Response Calibrations, Aeolus Science Conference 2023, Rhodes Island, Greece, 22 – 26/05/2023.
- Marseille, G.-J., de Kloe, J., Marksteiner, U., Reitebuch, O., Rennie, M., and de Haan, S. (2022): NWP calibration applied to Aeolus Mie channel winds, Q. J. R. Meteorol. Soc., 148, 1020 – 1034, https://doi.org/10.1002/qj.4244.

- Weiler, F., Rennie, M., Kanitz, T., Isaksen, L., Checa, E., de Kloe, J., Okunde, N. and Reitebuch, O. (2021): Correction of wind bias for the lidar on-board Aeolus using telescope temperatures. *Atmospheric Measurement Techniques*, 14, 7167–7185, https://doi.org/10.5194/amt-14-7167-2021
- Aeolus Level 1b Processor Detailed Processing Model (DPM), AED-SD-DoRIT-L1B-007, issue/revision 3/20, 06/10/2023.
- Aeolus Wiki page, dSYS_033 - Aeolus DISC - Confluence (esa.int) (https://csde.esa.int/confluence/display/AEOLUSDISC/dSYS_033).

3.6 End-of-life activities (EOLAs)

- Lemmerz, C., Lux, O., Marksteiner, U., Witschas, B., and Reitebuch, O. (2023b): Aeolus End-of-Life (EOL) Tests – DISC Analysis Report, AED-TN-DLR-GEN-083, final version in preparation for 06/2024.
- ESA (2024): Report of the Aeolus End-of-Life tests – merged report incl. ESA, industry and DISC analysis, final version in preparation for 06/2024.

3.7 Ground-returns, harmonic bias estimator and range-dependent bias

- Cito Filomarino, V., Weiler, F., Reitebuch, O., Masoumzadeh, N., Marksteiner, U. and Krisch, I. (2023a): Ground detection investigation to develop model independent bias correction, Aeolus Science Conference 2023, Rhodes Island, Greece, 22 – 26/05/2023.
- Huber, D. (2018): Quality Control Enhancement on Detected Ground Signal, AE-TN-DLR-L1B-023, 29/05/2018.
- Jupin-Langlois, S. and Perron, G., ACMF Detailed Processing Model, AED-DD-ABB-GS-0003, issue 4, rev. 4, 2021.
- Labzovskii, L.D., van Zadelhoff, G. J., Tilstra, L.G., de Kloe, J., Donovan, D.P., Stoffelen, A (2023): High sensitivity of Aeolus UV surface returns to surface reflectivity, Sci. Rep., 13, 17552.
- Marksteiner, U. (2013): Airborne wind lidar observations for the validation of the ADM-Aeolus instrument, PhD Thesis, Technical University of Munich.
- Marksteiner, U., Reitebuch, O. and Huber, D. (2018): Characterization and Verification of the Ground Echoes and its application to the Harmonic Bias Estimator, AE.TN.DLR.5200.1.280318, v1.2, 28/03/2018.
- Marksteiner, U. (2018), L1B_E1_UM_WM013_WebexMeeting_IRC.pptx, 21/11/2018.
- Marksteiner, U. (2019): Aeolus Instrument Response Calibrations, Radiometric Performance and Ground Detection During the IOCV Phase, AE-TN-DLR-7300-4_IRC, v1.1, 30/04/2019.
- Marksteiner, U., Nikolaus, I. and Reitebuch, O. (2020): Harmonic Bias Estimation from real ground speed observations, AED-TN-DLR-HBE-021, v1.0, 18/02/2020.
- Marksteiner, U., Lux, O., Reitebuch, O., de Kloe, J., Marseille, G.-J., and Rennie, M. (2023): Overview of Instrument Response Calibrations, Aeolus Science Conference 2023, Rhodes Island, Greece, 22 – 26/05/2023.
- Marseille, G.-J., de Kloe, J., Marksteiner, U., Reitebuch, O., Rennie, M., and de Haan, S. (2022): NWP calibration applied to Aeolus Mie channel winds, Q. J. R. Meteorol. Soc., 148, 1020 – 1034.
- Nikolaus, I. (2018): Preparation of Tools for RDB and HBE, AE-TN-DLR-L1B-2400, 15/05/2018.

- Nikolaus, F., Marksteiner, U., Weiler, F., and Reitebuch, O. (2019): Ground Return and RDB/HBE analysis, AE-TN-DLR-7300-5, 14/04/2019.
- Nikolaus, I. (2019): L1B_E2_IN_WM#3_DLR_2019_10_30_AnalysisReport_HBE, DISC Working Meeting #3, 30/10/2019.
- Nikolaus, I. (2020): L1B_E2_IN_WM#4_2020_04_02_AnalysisReport_HBE, DISC Working Meeting #4, 02/04/2020.
- Weiler, F. (2017): Bias correction using ground echoes for the Airborne Demonstrator of the wind lidar on the ADM-Aeolus mission, Master's Thesis, University of Innsbruck.
- Weiler, F. (2019): L1B_E2_FW_WM_046_Tuning of ground detection parameters.pptx, 09/07/2019.
- Weiler, F., Rennie, M., Kanitz, T., Isaksen, L., Checa, E., de Kloe, J., Okunde, N. and Reitebuch, O. (2021): Correction of wind bias for the lidar on board Aeolus using telescope temperatures, Atmos. Meas. Tech., 14, 7167–7185.
- Weiler, F. (2022): M1 bias correction based on ground returns, Working Meeting #7, 09/02/2022.

3.8 Solar background

- Schmidt, K. and Reitebuch, O. (2024): Background Radiation Measured by the ALADIN Instrument, AED-TN-DLR-L1B-088, v1.0, 09/01/2024 (under internal review).

3.9 Analysis of signal evolution and signal clipping at the field stop

- Nikolaus, I. (2021a): L1B_E2_IN_2021_03_09_RSP with clipping, 09/03/2021.
- Nikolaus, I. (2021b): L1B_E2_IN_2021_08_11_RSP with clipping-LBM Analysis, 11/08/2021.
- Nikolaus, I. (2021c): L1B_E2_IN_2021_08_25_RSP with clipping-TVAC and low energy LBM Analysis, 25/08/2021.
- Nikolaus, I. (2021d): L1B_E2_IN_2021_10_24_RSP with clipping_FM-A, 24/10/2021.
- Nikolaus, I. and Reitebuch, O. (2022): Looking for Aeolus/ALADIN signal losses: Modelling the clipping at the instrument's field stop, Aeolus 3rd Anniversary Conference, Taormina, Italy, 28/03 – 01/04/2022.

3.10 Synthesis of the work performed in instrument performance

- Fabre, F. (2020a): Synthesis of outcomes in root cause analysis for signal loss, AED-TN-MYR-GEN-037, issue 1.1, 23/08/2020.
- Fabre, F. (2020b): Root cause analysis on signal jumps on INT path, AED-TN-MYR-GEN-042, issue 1, 23/10/2020.
- Fabre, F. (2021a): Root cause analysis of the initial signal loss, AED-TN-MYR-GEN-046, issue 2, 22/02/2021.
- Fabre, F. (2021b): Aeolus orbit lowering - Phase 1: preliminary assessment, AED-TN-MYR-GEN-050, issue 2, 10/05/2021.
- Fabre, F. (2021c): Aeolus orbit lowering - Phase 2: show-stopper analysis, AED-TN-MYR-GEN-053, issue 2, 10/05/2021.
- Fabre, F. (2021d): Aeolus orbit lowering - Phase 3: impact analysis, AED-TN-MYR-GEN-055, issue 2.1.

- Fabre, F. (2021e): Aeolus orbit lowering - Phase 4: synthesis and recommendations, AED-TN-MYR-GEN-059, issue 2, 02/11/2021.
- Fabre, F. (2022a): Jumps and ghosts, AED-TN-MYR-GEN-063, issue 2, 24/01/2022.
- Fabre, F. (2022b): Benefits in switching to laser A, AED-TN-MYR-GEN-075, issue 2.1, 22/06/2022.
- Fabre, F. (2023a): Short note on test EoLA#12 - LCM synchronisation, AEO-MYR-TN-059, issue 1, 05/06/2023.
- Fabre, F. (2023b): Image synthesis for better understanding of in-orbit events, AED-TN-MYR-GEN-044, issue 7, 24/10/2023.
- Fabre, F. (2023c): First analysis of LCM synchronisation tests (EoLA#12), AEO-MYR-PRE-072, issue 1.

Additional documents were issued by Les Myriades Consulting, but are not reported here for the sake of synthesis.

4 L1B, L2A, and L2B Algorithm and Processors

4.1 L1B algorithms

- Reitebuch, O., D. Huber, I. Nikolaus (2018): ADM-Aeolus Algorithm Theoretical Basis Document ATBD Level1B Products, V 4.4, 20/04/2018.
- DISC-DoRIT (2023): E2S/L1bP open issues priority list, AED-TN-DoRIT-E2SL1B-001, V 1.10, 18/07/23.
- DISC (2024): L0, L1A, L1B WIKI items, https://csde.esa.int/confluence/display/AEOLUSDISC/Our+Discussions
- ESA (2013): Earth observation mission CFI software, v4.12, 2013, https://eop-cfi.esa.int/index.php/mission-cfisoftware/eocfi-software
- ESA (2024a): Aeolus processor release table with summaries, https://earth.esa.int/eogateway/instruments/aladin/processor-releases
- ESA (2024b): Aeolus reprocessing verification summaries and reports, https://earth.esa.int/eogateway/missions/aeolus/data
- The Pierre Auger Collaboration, Lux, O., Krisch, I., Reitebuch, O., Huber, D., Wernham, D., and Parrinello, T. (2024): Ground observations of a space laser for the assessment of its in-orbit performance, Optica, 11, 263–272.

4.2 L1B scattering ratio and Voigt spectral line shape function for Mie

- Dabas, A., Denneulin, M. L., Flamant, P., Loth, C., Garnier, A., and Dolfi-Bouteyre, A. (2008): Correcting winds measured with a Rayleigh Doppler lidar from pressure and temperature effects, Tellus A, 60, 206–215.
- Nikolaus, I. (2022): L1B_E2_IN_2022_07_27_New_SR and SNR, 27/07/2022.
- Nikolaus, I. (2023a): L1B_E2_IN_2023_03_16_Voigt fit for atm and internal signals, 16/03/2023.
- Nikolaus, I. (2023b): L1B_E2_IN_2023_04_03_New_SR for FM-A new period, 03/04/2023.
- Nikolaus, I. (2023c): L1B_E2_IN_2023_07_05_Verification SR with Voigt fit, 05/07/2023.

- Witschas, B., Vaughan, M., Lux, O., Lemmerz, C., Nikolaus, I., and Reitebuch, O. (2023): Verification of different Fizeau fringe analysis algorithms based on airborne wind lidar data in support of ESA's Aeolus mission, Appl. Opt., 62, 7917 – 7930.

4.3 L2A algorithms: SCA and MLE

- CNRM (2020): A3S activities: L2A cloud screening from Auxiliary Meteorological Data, AED-TN-CNRM-L2A-052, 07/09/2020.
- CNRM (2021a): Updated Mie SNR in L2A V3.12, AED-TN-CNRM-L2A-047, v1.0, 22/02/2021.
- CNRM (2021b): L2A v3.12 –SNR based QC flags tuning: Application on smoke layer tracked from Californian wildfires, AED-TN-CNRM-L2A-048, 04/03/2021.
- CNRM (2022a): L2A open issues priority lists. AE-TN-CNRM-L2A-002, v1.6, 20/09/2022.
- CNRM (2022b): L2A Algorithm Theoretical Baseline Document. AED-SD-CNRM-L2A-030, v6.0, 17/06/2022.
- CNRM (2022c): Providing a L2A product with a sub-BRC horizontal resolution, AED-TN-CNRM-L2A-065.
- CNRM (2022d): L2A User Guide. AED-TN-CNRM-L2A-036, v2.1, 17/06/2022.
- Ehlers, F., Flament, T., Dabas, A., Trapon, D., Lacour, A., Baars, H., and Straume-Lindner, A. G. (2022): Optimization of Aeolus Optical Properties Products by Maximum-Likelihood Estimation, Atmos. Meas. Tech., 15, 185–203.
- Flament, T., Trapon, D., Lacour, A., Dabas, A., Ehlers, F., and Huber, D. (2021): Aeolus L2A Aerosol Optical Properties Product: Standard Correct Algorithm and Mie Correct Algorithm, Atmos. Meas. Tech., 14, 7851–7871.

4.4 L2A algorithms: AEL-FM and AEL-PRO

- Donovan, D.P. (2021): Creation of Crosstalk corrected Attenuated backscatter Signals from the Aeolus Mie Spectrometer Unit (MST-ATBs ATBD), AED-SD-KNMI-L2A-046, v1.1, 08/07/2021.
- Donovan, D. P., Kollias, P., Velázquez Blázquez, A., and van Zadelhoff, G.-J. (2023): The generation of Earth-CARE L1 test data sets using atmospheric model data sets, Atmos. Meas. Tech., 16, 5327–5356.
- Donovan, D. P., van Zadelhoff, G.-J., and Wang, P. (2024): The EarthCARE lidar cloud and aerosol profile processor (A-PRO): the A-AER, A-EBD, A-TC and A-ICE products, EGUsphere, preprint.
- Flament, T., Trapon, D., Lacour, A., Dabas, A., Ehlers, F., and Huber, D. (2021): Aeolus L2A Aerosol Optical Properties Product: Standard Correct Algorithm and Mie Correct Algorithm, Atmos. Meas. Tech., 14, 7851–7871.
- Novak, O., Falconer, I.S., Sanginés, R., Lattemann, M., Tarrant, R.N., McKenzie, D.R., and Bilek, M.M.M. (2011): Fizeau interferometer system for fast high-resolution studies of spectral line shapes, Rev. Sci. Ins., 82, 023105.
- van Zadelhoff, G.-J., Donovan, D. P., and Wang, P. (2023): Detection of aerosol and cloud features for the EarthCARE atmospheric lidar (ATLID): the ATLID FeatureMask (A-FM) product, Atmos. Meas. Tech., 16, 3631–3651.
- Wehr, T., Kubota, T., Tzeremes, G., Wallace, K., Nakatsuka, H., Ohno, Y., Koopman, R., Rusli, S., Kikuchi, M., Eisinger, M., Tanaka, T., Taga, M., Deghaye, P., Tomita, E., and Bernaerts, D. (2023): The EarthCARE mission – science and system overview, Atmos. Meas. Tech., 16, 3581–3608.

4.5 L2A and L2B calibrations AUX-CAL, AUX-RBC

- CNRM (2019a): Generation/update of L2 calibration data at ACMF. AE-TN-MFG-L2P-CAL-002, v4.3, 19/12/2019.
- CNRM (2019b): Generation and update of AUX_CSR. AED-TN-MFG-L2P-CAL-003, v4.2, 26/07/2019.
- CNRM (2019c): Generation of the RBC Auxiliary file: Detailed Processing Model. AE-TN-MFG-GS-0001, v4.2, 26/07/2019.
- CNRM (2019d): Generation of AUX_CAL Detailed Processing Model Input / Output Data Definition. AE-TN-MFG-L2P-CAL-004, v4.3, 19/12/2019.
- CNRM (2020a): RRC cross point study. AE-TN-CNRM-CAL-043, v1.0, 20/10/2020.
- CNRM (2020b): Conditions for minimizing the impact of particles on Rayleigh winds, 11/11/2020.
- CNRM (2022): Sensitivity of the Rayleigh response to the scattering ratio, 13/03/2022.

4.6 NWP bias correction and L2B Optical Properties Code

- Eyre, J.R. (1992): A bias correction scheme for simulated TOVS brightness temperatures. Technical Memorandum 176, Reading, UK: ECMWF.
- Marseille, G.-J., de Kloe, J., Marksteiner, U., Reitebuch, O., Rennie, M., and de Haan, S. (2022): NWP calibration applied to Aeolus Mie channel winds, Q. J. R. Meteorol. Soc., 148, 1020–1034.
- Marseille, G.-J., de Kloe, J., Dabas, A., Flament, T., and Rennie, M. (2023): Aeolus Rayleigh-channel winds in cloudy conditions, Q. J. R. Meteorol. Soc., 149, 3270–3289.
- Rennie, M. and Isaksen, L. (2020): The NWP impact of Aeolus, level-2B winds at ECMWF. Technical Memorandum 864, Reading, UK: ECMWF.
- Michael Rennie (2023): A Consolidated Assessment of the Impact of Aeolus Winds in NWP at ECMWF, Aeolus Science Conference 2023, Rhodes Island, Greece, 22 – 26/05/2023.
- Stoffelen, A. (1999): A Simple Method for Calibration of a Scatterometer over the Ocean. J. Atmos. Oceanic Technol., 16, 275–282.
- Weiler, F., Rennie, M., Kanitz, T., Isaksen, L., Checa, E., de Kloe, J., Okunde, N. and Reitebuch, O. (2021): Correction of wind bias for the lidar on board Aeolus using telescope temperatures. Atmos. Meas. Tech., 14, 7167–7185.
- Aeolus Wiki page, dL2A_017 - Aeolus DISC - Confluence (esa.int) (https://csde.esa.int/confluence/pages/viewpage.action?spaceKey=AEOLUSDISC&title=dL2A_017).

4.7 L2B bias correction

- Weiler, F., Kanitz, T., Wernham, D., Rennie, M., Huber, D., Schillinger, M., Saint-Pe, O., Bell, R., Parrinello, T., and Reitebuch, O. (2021a): Characterization of dark current signal measurements of the ACCDs used on board the Aeolus satellite, Atmos. Meas. Tech., 14, 5153–5177.
- Weiler, F., Rennie, M., Kanitz, T., Isaksen, L., Checa, E., de Kloe, J., Okunde, N. and Reitebuch, O. (2021b): Correction of wind bias for the lidar on board Aeolus using telescope temperatures. Atmos. Meas. Tech., 14, 7167–7185.

- Rennie, M. P., Isaksen, L., Weiler, F., de Kloe, J., Kanitz, T., and Reitebuch, O. (2021): The impact of Aeolus wind retrievals on ECMWF global weather forecasts, Q. J. R. Meteorol. Soc., 147, 3555–3586.

4.8 Aeolus Calibration and Monitoring Facility (ACMF) and Codadef

4.9 ACMF Calibration Processors

4.10 Chain of operational processors and Sandbox

4.11 The operational L0-L1A-L1B Processors

- DLR (2018): Final Report WindVal II: Wind Validation II for Aeolus, FR.DLR.WindVal_II.020318, v1.0, 02/03/2018.
- DLR (2020): L1B_E2_WM078_IK_SB_DCMZ_Analysis.
- Huber, D. (2020): DL1B_IRC_008 Investigations & Findings, AED-TN-DoRIT-L1B-027, v1.0, 29/04/2020.
- Huber, D. (2019): Quality Control Enhancement on Detected Ground Signal, AE-TN-DLR-L1B-023.
- Kanitz, T., Weiler, F., and Reitebuch, O. (2019): The dark side of Aeolus during the IOCV phase, AE-TN-ESA-SY-094 / AE-TN-DLR-7300-2, issue 1.1, 16/04/2019.
- Nikolaus, I. (2023): L1B_E2_IN_2023_03_16_Voigt fit for atm and internal signals, 16/03/2023
- Šavli, M. (2019a): Validation of the scattering ratio for the improvement of the L2B HLOS retrieval – additional results, sr_sensitivity_results_maticsavli_march2019_v02_mschanges.pdf
- Šavli, M. (2019b): Validation of L1B scattering ratio, discacceptancereview_06062019_maticsavli.pdf
- Weiler, F. (2017): Bias correction using ground echoes for the Airborne Demonstrator of the wind lidar on the ADM-Aeolus mission, Master's Thesis, University of Innsbruck.
- Weiler, F. (2018): L1B_E1_FW_WM005_ZWC_analysis_presentation_26_09.pptx.

4.12 The operational L2A processor

- Ehlers, F., Flament, T., Dabas, A., Trapon, D., Lacour, A., Baars, H., and Straume-Lindner, A. G. (2022): Optimization of Aeolus Optical Properties Products by Maximum-Likelihood Estimation, Atmos. Meas. Tech., 15, 185–203.
- van Zadelhoff, G.-J., Donovan, D. P., and Wang, P. (2023): Detection of aerosol and cloud features for the EarthCARE atmospheric lidar (ATLID): the ATLID FeatureMask (A-FM) product, Atmos. Meas. Tech., 16, 3631–3651.

4.13 The operational L2B processor and Chain of Processors (CoP)

- de Kloe, J., Stoffelen, A., Marseille, G.-J., Dabas, A., and Huber, D. (2014): Test cases for the L2B processor, AE-TN-KNMI-GS-0031a, v1.2, 19/12/2014.
- de Kloe, J., Stoffelen, A., Marseille, G.-J., Dabas, A., and Huber, D. (2017): Test results for the L2B processor, AE-TN-KNMI-GS-0031b, v1.5, 05/10/2017.
- Huber, D. (2023): Aeolus Level 1b Processor Detailed Processing Model, AED-SD-DoRIT-L1B-007, v3.20, 06/10/2023.
- Loth, C., Flamant, P.H., Dabas, A. et al. (2005): Impact of Line Shape on Aeolus-ADM Doppler Estimates, Final report, November 2005.

- Marseille, G. J., Houchi, K., de Kloe, J., and Stoffelen, A. (2011): The definition of an atmospheric database for Aeolus, Atmos. Meas. Tech., 4, 67–88.
- Marseille, G.-J., de Kloe, J., Marksteiner, U., Reitebuch, O., Rennie, M., and de Haan, S. (2022): NWP calibration applied to Aeolus Mie channel winds, Q. J. R. Meteorol. Soc., 148, 1020–1034.
- Marseille, G.-J., de Kloe, J., Dabas, A., Flament, T., and Rennie, M. (2023): Aeolus Rayleigh-channel winds in cloudy conditions, Q. J. R. Meteorol. Soc., 149, 3270–3289.
- Rennie, M., Tan, D., Andersson, E., Poli, P., Dabas, A., de Kloe, J., Marseille, G.-J., and Stoffelen, A. (2020): Aeolus Level-2B Algorithm Theoretical Basis Document, AED-SD-ECMWF-L2B-038, v3.40, 16/07/2020.
- Šavli, M., de Kloe, J., Marseille, G.-J., Rennie, M., Žagar, N., and Wedi, N. (2019): The prospects for increasing the horizontal resolution of the Aeolus horizontal line-of-sight wind profiles, Q. J. R. Meteorol. Soc., 145, 3499–3515.
- Šavli, M., Pourret, V., Payan, C., and Mahfouf, J.-F. (2021): Sensitivity of Aeolus HLOS winds to temperature and pressure specification in the L2B processor, Atmos. Meas. Tech., 14, 4721–4736.
- Tan, D.G.H., Andersson, E., de Kloe, J., Marseille, G.-J., Stoffelen, A., Poli, P., Denneulin, M.-L., Dabas, A., Huber, D., Reitebuch, O., Flamant, P., Le Rille, O. and Nett, H. (2008): The ADM-Aeolus wind retrieval algorithms. Tellus A, 60, 191-205.
- Weiler, F., Rennie, M., Kanitz, T., Isaksen, L., Checa, E., de Kloe, J., Okunde, N. and Reitebuch, O. (2021): Correction of wind bias for the lidar on board Aeolus using telescope temperatures. Atmos. Meas. Tech., 14, 7167–7185.
- DISC-DLR (2020): First Reprocessing campaign for FM-B covering the time period 2019-06 to 2019-12, AED-TN-DLR-REPRO-028, v1.1, 03/08/2020.
- DISC-DLR (2021): Second Reprocessing campaign for FM-B covering the time period 2019-06 to 2020-10, AED-TN-DLR-GEN-041, v1.1, 23/02/2021.
- DISC-DLR (2022): Third Reprocessing campaign for FM-A covering the time period 2018-08 to 2019-06, AED-TN-DLR-GEN-061, v2.0, 30/09/2022.

4.14 DISC on-site support for PDGS, LL and knowledge transfer

The following technical notes from serco are not explicitly referenced in the text:

- AED-TN-Serco-GEN-066 KORE-TN Document template (v1.20)
- AED-TN-Serco-GEN-067 Configuration Management KORE-TN (v1.40)
- AED-TN-Serco-GEN-068 Anomaly and Change Management KORE-TN (v1.20)
- AED-TN-Serco-GEN-069 Systematic Quality Control KORE-TN (v1.00)
- AED-TN-Serco-GEN-070 Operational Software Verification KORE-TN (v1.10)
- AED-TN-Serco-GEN-071 Outreach KORE-TN) (v1.00)
- AED-TN-Serco-GEN-090 Being efficiently ready for LTDP KORE-TN (v0.50 – under finalization)
- AED-TN-Serco-GEN-091 QWG KORE TN (v0.50 – under finalization)

5 L2A and L2B Product Monitoring, Cal/Val and Outreach

5.1 Reprocessing of Aeolus data products

- DISC (2020): Summary of Quality of Aeolus Data Products from 1st Reprocessing Campaign covering June to December 2019, v1.0, 08/10/2020.

- DISC (2021): Summary of Quality of Aeolus Data Products from 2nd Reprocessing Campaign covering June 2019 to October 2020, Status, v1.1, 11/11/2021.
- DISC (2022): Summary of Quality of Aeolus Data Products from 3rd Reprocessing Campaign covering September 2018 to June 2019, v1.0, 28/11/2022.
- DISC-ECMWF (2020): Verification report of first Reprocessing campaign for FM-B covering the time period 2019-06 to 2019-12, AED-TN-ECMWF-GEN-040, v1.0, 13/10/2020.
- DISC-ECMWF (2021): Verification report of the second reprocessing campaign for FM-B from 24 June 2019 till 9 October 2020, AED-TN-ECMWF-GEN-060, v1.1., 10/12/2021.
- DISC-ECMWF (2023): Verification report of the third reprocessing campaign for first FM-A period from September 2018 till June 2019, AED-TN-ECMWF-GEN-080, v1.01, 06/06/2023.

The following reports are only available internally:

- DISC-DLR (2020a): First Reprocessing campaign for FM-B covering the time period 2019-06 to 2019-12, AED-TN-DLR-REPRO-028, v1.1, 03/08/2020.
- DISC-DLR (2020b): Annex to first reprocessing campaign for FM-B covering the time period 2019-06 to 2019-12, AED-TN-DLR-REPRO-028, V1.1., 11/06/2020.
- DISC-DLR (2021a): Second Reprocessing campaign for FM-B covering the time period 2019-06 to 2020-10, AED-TN-DLR-GEN-041, v1.1, 23/02/2021.
- DISC-DLR (2021b): Annex to second reprocessing campaign for FM-B covering the time period 2019-06 to 2020-10, AED-TN-DLR-GEN-041, v1.2, 03/03/2021.
- DISC-DLR (2022): Third Reprocessing campaign for FM-A covering the time period 2018-08 to 2019-06, AED-TN-DLR-GEN-061, v2.0, 30/09/2022.
- DISC-DLR (2023): Fourth Reprocessing campaign for the full mission time period from August 2018 to end of mission, AED-TN-DLR-GEN-081, v1.0, 01/03/2023.

5.2 L2A quality monitoring

- CNRM/TROPOS (2019-2024): L2A aerosol and cloud data product quality statement, https://www.aeolus.esa.int/confluence/display/CALVAL/Weekly+Quality+Reports
- Wang, P., van Zadelhoff, G.-J., and Donovan, D.P. (2022a): Evaluation of L2A 3.13.6 AEL-FM operational product, FM-B_verification_L2A3.13.6_AEL_FM_20220222_KNMI.pptx, DISC aerosol working meeting, 22/02/2022.
- Wang, P., van Zadelhoff, G.-J., and Donovan, D.P. (2022b): Evaluation of AEL-FM in FM-A reprocessing, FM-A_reprocessing_verification_L2A13.6_AEL_FM_20220210_KNMI.pptx, DISC meeting report, 10/02/2022.
- Wang, P., van Zadelhoff, G.-J., and Donovan, D.P. (2022c): Evaluation of L2A 3.14 AEL-FM reprocessed product, FM-A_verification_L2A3.14.2_AEL_FM_20220309_KNMI.pptx, DISC working meeting, 09/03/2022.
- Wang, P., van Zadelhoff, G.-J., and Donovan, D.P. (2022d): Evaluation of L2A B14 AEL-FM fully reprocessed product, FM-A_verification_L2A3.14.6_AEL_FM_full_reprocessing_20220613 _KNMI.pptx, DISC working meeting, 13/06/2022.
- Wang, P., van Zadelhoff, G.-J., and Donovan, D.P. (2022e): Evaluation of AEL-FM in L2A B14 v3.14.8 in OPS REPO, FM-A_verification_L2A3.14.8_AEL_FM_OPS_REPO_20220729_ KNMI.pptx, DISC meeting, 29/07/2022.

- Wang, P., van Zadelhoff, G.-J., Donovan, D.P., de Kloe, J., and Huber, D. (2022f): Evaluations of Aeolus aerosol products derived using modified ATLID algorithms, Aeolus 3rd Anniversary Conference, Taormina, Italy, 28/03 – 01/04/2022.
- Wang, P., van Zadelhoff, and G.-J., Donovan, D.P. (2023a): Evaluation of AEL-FM AEL-PRO in L2A B16, DISC working meeting, Zugspitze, Germany, 15 – 17/03/2023.
- Wang, P., van Zadelhoff, G.-J., and Donovan, D.P. (2023b): Verification of reprocessing v4 test weeks L2A AEL-FM, AEL-PRO B16, verification_reprocess4_test_weeks_B16_L2A_wangp_20230704.pptx, DISC meeting, 04/07/2023.
- Wang, P., van Zadelhoff, G.-J., and Donovan, D.P. (2023c): Verification of reprocessing v4 L2A B16 v3.16.4 AEL-FM, verification_reprocess4_B16_L2A_3.16.4_20231024_KNMI_updated_PDGS_20231106.pptx, DISC meeting 24/10/2023.
- Wang, P., van Zadelhoff, G.-J., and Donovan, D.P. (2023d): Verification of reprocessing v4 PDGS test weeks L2A AEL-FM, AEL-PRO B16, verification_reprocess4_test_weeks_B16_L2A_PDGS_wangp_20231117.pptx, DISC report, 17/11/2023.
- Wang, P., Donovan, D.P., and van Zadelhoff, G.-J. (2023e): Comparison of Aeolus aerosol products derived using modified ATLID algorithms with Calipso L2 aerosol product, Aeolus Science Conference 2023, Rhodes Island, Greece, 22 – 26/05/2023.
- Wang, P., Donovan, D.P., van Zadelhoff, G.-J., de Kloe, J., Huber, D., and Reissig, K. (2024): Evaluation of Aeolus feature mask and particle extinction profile products using CALIPSO data, submitted to AMTD in March 2024.

5.3 L2B quality monitoring using NWP model

- ESA (2016): ADM-Aeolus Mission Requirements Document, ESA EOP-SM/2047, https://earth.esa.int/eogateway/documents/20142/1564626/Aeolus-Mission-Requirements.pdf
- Lux, O., Witschas, B., Geiß, A., Lemmerz, C., Weiler, F., Marksteiner, U., Rahm, S., Schäfler, A., and Reitebuch, O. (2022): Quality control and error assessment of the Aeolus L2B wind results from the Joint Aeolus Tropical Atlantic Campaign, Atmos. Meas. Tech., 15, 6467–6488.
- Marseille, G.-J., de Kloe, J., Marksteiner, U., Reitebuch, O., Rennie, M., and de Haan, S. (2022): NWP calibration applied to Aeolus Mie channel winds, Q. J. R. Meteorol. Soc., 148, 1020–1034.
- Marseille, G.-J., de Kloe, J., Dabas, A., Flament, T., and Rennie, M. (2023): Aeolus Rayleigh-channel winds in cloudy conditions, Q. J. R. Meteorol. Soc., 149, 3270–3289.
- Rennie, M. and Isaksen, L. (2024): The NWP impact of Aeolus Level-2B winds at ECMWF, ESA Contract Report, February 2024, https://dx.doi.org/10.21957/d4ea1c09d4.
- Weiler, F., Rennie, M., Kanitz, T., Isaksen, L., Checa, E., de Kloe, J., Okunde, N. and Reitebuch, O. (2021): Correction of wind bias for the lidar on board Aeolus using telescope temperatures. Atmos. Meas. Tech., 14, 7167–7185.

5.4 L2A quality monitoring using NWP model and L2A BUFR

- Ackermann, J. (1998), The extinction-to-backscatter ratio of tropospheric aerosol: A numerical study, J. Atmos. Ocean. Technol.,15, 1043–1050.
- Agustí-Panareda, A., Massart, S., Chevallier, F., Boussetta, S., Balsamo, G., Beljaars, A., Ciais, P., Deutscher, N.M., Engelen, R., Jones, L., Kivi, R., Paris, J.-D., Peuch, V.-H., Sherlock, V.,

Vermeulen, A.T., Wennberg, P.O., and Wunch, D. (2014): Forecasting global atmospheric CO2, Atmos. Chem. Phys., 14, 11959–11983.

- Benedetti, A., Morcrette, J.-J., Boucher, O., Dethof, A., Engelen, R. J., Fisher, M., Flentje, H., Huneeus, N., Jones, L., Kaiser, J. W., Kinne, S., Mangold, A., Razinger, M., Simmons, A. J., and Suttie, M. (2009): Aerosol analysis and forecast in the European Centre for Medium-Range Weather Forecasts Integrated Forecast System: 2. Data assimilation, J. Geophys. Res., 114.
- Engelen, R. J., Serrar, S., and Chevallier, F. (2009): Four-dimensional data assimilation of atmospheric CO 2 using AIRS observations, J. Geophys. Res., 114.
- Flament, T., Trapon, D., Lacour, A., Dabas, A., Ehlers, F., and Huber, D. (2021): Aeolus L2A Aerosol Optical Properties Product: Standard Correct Algorithm and Mie Correct Algorithm, Atmos. Meas. Tech., 14, 7851–7871.
- Flemming, J., Huijnen, V., Arteta, J., Bechtold, P., Beljaars, A., Blechschmidt, A.-M., Diamantakis, M., Engelen, R.J., Gaudel, A., Inness, A., Jones, L., Josse, B., Katragkou, E., Marecal, V., Peuch, V.-H., Richter, A., Schultz, M.G., Stein, O., and Tsikerdekis, A. (2015): Tropospheric chemistry in the integrated forecasting system of ECMWF, Geosci. Model Dev., 8, 975–1003.
- Huijnen, V., Flemming, J., Chabrillat, S., Errera, Q., Christophe, Y., Blechschmidt, A.-M., Richter, A., and Eskes, H. (2016): C-IFS-CB05-BASCOE: Stratospheric chemistry in the integrated forecasting system of ECMWF, Geoscientific Model Development, 9, 3071–3091.
- Huneeus, N. and Boucher, O. (2007): One-dimensional variational retrieval of aerosol extinction coefficient from synthetic LIDAR and radiometric measurements, J. Geophys. Res., 112.
- Inness, A., Blechschmidt, A.-M., Bouarar, I., Chabrillat, S., Crepulja, M., Engelen, R. J., Eskes, H., Flemming, J., Gaudel, A., Hendrick, F., Huijnen, V., Jones, L., Kapsomenakis, J., Katragkou, E., Keppens, A., Langerock, B., de Mazière, M., Melas, D., Parrington, M., Peuch, V. H., Razinger, M., Richter, A., Schultz, M. G., Suttie, M., Thouret, V., Vrekoussis, M., Wagner, A., and Zerefos, C. (2015): Data assimilation of satellite-retrieved ozone, carbon monoxide and nitrogen dioxide with ECMWF's Composition-IFS, Atmos. Chem. Phys., 15, 5275–5303.
- Järvinen, H., and Andersson, E. (1999): Variational quality control, Q. J. R. Meteorol. Soc., 125, 697-722.
- Massart, S., Agusti-Panareda, A., Aben, I., Butz, A., Chevallier, F., Crevoisier, C., Engelen, R., Frankenberg, C., and Hasekamp, O. (2014): Assimilation of atmospheric methane products into the MACC-II system: from SCIAMACHY to TANSO and IASI, Atmos. Chem. Phys., 14, 6139–6158.
- McLean, W. and Benedetti, A. (2023): Technical note on Aeolus Aerosol Assimilation in the DISC (A3D), AED-TN-ECMWF-NWP-076, v1.0, 31/03/2023.
- Morcrette, J.-J., Boucher, O., Jones, L., Salmond, D., Bechtold, P., Beljaars, A., Benedetti, A., Bonet, A., Kaiser, J., Razinger, M. et al. (2009): Aerosol analysis and forecast in the European Centre for Medium-Range Weather Forecasts Integrated Forecast System: Forward modelling, Journal of Geophysical Research: Atmospheres, 114, D6).
- Peuch, V.-H., Engelen, R., Rixen, M., Dee, D., Flemming, J., Suttie, M., Ades, M., Agustí-Panareda, A., Ananasso, C., Andersson, E., Armstrong, D., Barré, J., Bousserez, N., Dominguez, J. J., Garrigues, S., Inness, A., Jones, L., Kipling, Z., Letertre-Danczak, J., Parrington, M., Razinger, M., Ribas, R., Vermoote, S., Yang, X., Simmons, A., Garcés de Marcilla, J., and Thépaut, J.-N.

(2022): The Copernicus Atmosphere Monitoring Service: From Research to Operations, Bull. Amer. Meteor. Soc., 103, E2650-E2668.

- Rémy, S., Kipling, Z., Flemming, J., Boucher, O., Nabat, P., Michou, M., Bozzo, A., Ades, M., Huijnen, V., Benedetti, A., Engelen, R., Peuch, V.-H., and Morcrette, J.-J. (2019): Description and evaluation of the tropospheric aerosol scheme in the European Centre for Medium-Range Weather Forecasts (ECMWF) Integrated Forecasting System (IFS-AER, cycle 45r1), Geoscientific Model Development, 12, 4627–4659.
- Rémy, S., Kipling, Z., Huijnen, V., Flemming, J., Nabat, P., Michou, M., Ades, M., Engelen, R., and Peuch, V.-H. (2022): Description and evaluation of the tropospheric aerosol scheme in the Integrated Forecasting System (IFS-AER, cycle 47r1) of ECMWF, Geoscientific Model Development, 15, 4881–4912.
- Vasiljevic et al. (2021): Aeolus/EarthCARE Aerosol Assimilation Study CCN 1, WP-2 Technical Note: Definition of a BUFR converter and template for Aeolus L2A data, ESA contract report, *available on request from ECMWF*.

5.5 Cal/Val Synthesis, user support and engagement

- Banyard, T.P., Wright, C. J., Osprey, S. M., Hindley, N.P., Halloran, G., Coy, L., Newman, P. A., Butchart, N., Bramberger, M., and Alexander, M.J. (2024): Aeolus wind lidar observations of the 2019/2020 quasi-biennial oscillation disruption with comparison to radiosondes and reanalysis, Atmos. Chem. Phys., 24, 2465–2490.
- Bley, S., Rennie, M., Žagar, N., Pinol Sole, M., Straume, A.G., Antifaev, J., Candido, S., Carver, R., Fehr, T., von Bismarck, J., Hünerbein, A. and Deneke, H. (2022): Validation of the Aeolus L2B Rayleigh winds and ECMWF short-range forecasts in the upper troposphere and lower stratosphere using Loon super pressure balloon observations, Q. J. R. Meteorol. Soc., 148, 3852–3868.
- Bley, S., Reitebuch, O., von Bismarck, J., Straume, A.G., Baars, H., Fehr, T., and Trapon, D. (2023): Lessons learnt from Aeolus Cal/Val, ESA-JAXA Pre-Launch EarthCARE Science and Validation Workshop, Frascati, Italy, 13 – 17/11/2023.
- CNRM (2022): L2A User Guide. AED-TN-CNRM-L2A-036, v2.1, 17/06/2022.
- DISC-ECMWF (2020): Verification report of first Reprocessing campaign for FM-B covering the time period 2019-06 to 2019-12, AED-TN-ECMWF-GEN-040, v1.0, 13/10/2020.
- DISC-ECMWF (2021): Verification report of the second reprocessing campaign for FM-B from 24 June 2019 till 9 October 2020, AED-TN-ECMWF-GEN-060, v1.1., 10/12/2021.
- DISC-ECMWF (2023): Verification report of the third reprocessing campaign for first FM-A period from September 2018 till June 2019, AED-TN-ECMWF-GEN-080, v1.01, 06/06/2023.
- Ern, M., Diallo, M. A., Khordakova, D., Krisch, I., Preusse, P., Reitebuch, O., Ungermann, J., and Riese, M. (2023): The quasi-biennial oscillation (QBO) and global-scale tropical waves in Aeolus wind observations, radiosonde data, and reanalyses, Atmos. Chem. Phys., 23, 9549–9583.
- ESA (2020): A Guide to Aeolus Range Bin Settings, https://earth.esa.int/eogateway/news/a-guide-to-aeolus-range-bin-settings.
- ESA (2021): ASKOS campaign validated Aeolus data (eVe reference): https://earth.esa.int/eogateway/news/jatac-askos-the-campaign-validating-aeolus-data-from-the-ground.

- Paschou, P., Siomos, N., Tsekeri, A., Louridas, A., Georgoussis, G., Freudenthaler, V., Binietoglou, I., Tsaknakis, G., Tavernarakis, A., Evangelatos, C., von Bismarck, J., Kanitz, T., Meleti, C., Marinou, E., and Amiridis, V. (2022): The eVe reference polarisation lidar system for the calibration and validation of the Aeolus L2A product, Atmos. Meas. Tech., 15, 2299–2323.
- Straume, A.G. (2019): Aeolus Scientific Calibration and Validation Requirements, AE-RS-ESA-GS-005, issue 3, revision 2, 07/11/2019.
- Straume, A.G., Schuettemeyer, D., von Bismarck, J., Kanitz, T. and Fehr, T. (2019): Aeolus Scientific Calibration and Validation Implementation Plan, EOP-SM/2945/AGS-ags, issue 1, revision 2, 15/11/2019.
- TROPOS (2024): Aeolus Cal/Val synthesis report, v6.1, January 2024.

5.6 VirES Virtual Research Environment (VRE)

- Geiß, A. (2021): User requirements for the VirES Virtual Research Environment (VRE), AED-TN-LMU-GEN-057, v1.0, 30/07/2021.
- Santillan Pedrosa, D., Geiß, A., Pačes, M., Krisch, I., Weiler, F., Rommanazzo, M., and Troina, G. (2022): VirES for Aeolus – Virtual Research Environment (VRE), ESA LPS 2022, 66135.

5.7 Outreach

6 NWP impact assessment

6.1 NWP impact assessment for wind at ECMWF

- Horányi, A., Cardinali, C., Rennie, M. and Isaksen, L. (2015a): The assimilation of horizontal line-of-sight wind information into the ECMWF data assimilation and forecasting system. Part I: The assessment of wind impact. Q.J.R. Meteorol. Soc., 141, 1223–1232.
- Horányi, A., Cardinali, C., Rennie, M. and Isaksen, L. (2015b), The assimilation of horizontal line-of-sight wind information into the ECMWF data assimilation and forecasting system. Part II: The impact of degraded wind observations. Q.J.R. Meteorol. Soc., 141, 1233–1243.
- Marseille, G.-J., de Kloe, J., Marksteiner, U., Reitebuch, O., Rennie, M., and de Haan, S. (2022): NWP calibration applied to Aeolus Mie channel winds, Q. J. R. Meteorol. Soc., 148, 1020–1034.
- Marseille, G.-J., de Kloe, J., Dabas, A., Flament, T., and Rennie, M. (2023): Aeolus Rayleigh-channel winds in cloudy conditions, Q. J. R. Meteorol. Soc., 149, 3270–3289.
- Rennie, M. and Isaksen, L. (2020): The NWP impact of Aeolus, level-2B winds at ECMWF. Technical Memorandum 864, Reading, UK: ECMWF.
- Rennie, M. P., Isaksen, L., Weiler, F., de Kloe, J., Kanitz, T., and Reitebuch, O. (2021): The impact of Aeolus wind retrievals on ECMWF global weather forecasts, Q. J. R. Meteorol. Soc., 147, 3555–3586.
- Rennie, M., Healy, S., Abdalla, S., McLean, W., and Henry, K. (2022): Aeolus positive impact on forecasts with the second reprocessed dataset, 2022. ECMWF newsletter, 173, 14–20.
- Rennie, M. (2022): Aeolus L2B horizontal HLOS wind product monthly quality report for January 2022, available from: https://ftp-qras.earth.esa.int/aeolus/aladin/monthly/l2b/2023/aeolus--aladin--monthly--20230101--l2b.pdf, (monthly reports available from Aug 2020 to April 2023).
- Rennie, M., and Isaksen, L. (2024): The NWP impact of Aeolus Level-2B winds at ECMWF, ESA Contract Report, February 2024, https://dx.doi.org/10.21957/d4ea1c09d4.

- Weiler, F., Rennie, M., Kanitz, T., Isaksen, L., Checa, E., de Kloe, J., Okunde, N. and Reitebuch, O. (2021): Correction of wind bias for the lidar on board Aeolus using telescope temperatures. Atmos. Meas. Tech., 14, 7167–7185.
- Žagar, N., Rennie, M., and Isaksen, L. (2021): Uncertainties in Kelvin Waves in ECMWF Analyses and Forecasts: Insights from Aeolus Observing System Experiments, Geophys. Res. Lett., 48.

6.2 NWP impact assessment for aerosol at ECMWF

- Benedetti et al. (2020): Aeolus/EarthCARE Aerosol Assimilation Study CCN, WP-1 Technical Note: Upgrade of the ECMWF CAMS assimilation system, refinement and further testing of the data pre-processing cloud clearing approach before assimilation, ESA contract report, *available on request from ECMWF*.
- Benedetti et al. (2021): Aeolus/EarthCARE Aerosol Assimilation Study CCN, WP-3 Technical Note, ESA contract report, *available on request from ECMWF*.
- Desroziers, G., Berre, L., Chapnik, B., and Poli, P. (2005): Diagnosis of observation, background and analysis-error statistics in observation space, Q. J. R. Meteorol. Soc., 131, 3385–3396.

6.3 NWP impact assessment for wind at Météo-France / CNRM

- CNRM (2020a): Assessment of the impact of AEOLUS HLOS winds in the numerical weather prediction at Météo-France. AE-TN-CNRM-NWPL-031, v1.0, 29/05/2020.
- CNRM (2020b): The alternative bias correction methodology for the Rayleigh-clear HLOS winds. AE-TN-CNRM-NWP-026, v1.0, 26/02/2020.
- Pourret, V., Šavli, M., Mahfouf, J.-F., Raspaud, D., Doerenbecher, A., Bénichou, H., and Payan, C. (2022): Operational assimilation of Aeolus winds in the Météo-France global NWP model ARPEGE, Q. J. R. Meteorol. Soc., 148, 2652–2671.
- Šavli, M., Pourret, V., Payan, C., and Mahfouf, J.-F. (2021): Sensitivity of Aeolus HLOS winds to temperature and pressure specification in the L2B processor, Atmos. Meas. Tech., 14, 4721–4736.

B LIST OF ACRONYMS AND ABBREVIATIONS

4D-Var	Four-dimensional variational data assimilation
A2D	ALADIN Airborne Demonstrator
A3D	Aeolus Aerosol Assimilation in the DISC
A3S	Aeolus Aerosol Assimilation Study
ABB	Asea Brown Boveri
AboVE-Maido2	Aeolus Validation Experiment at high-altitude Maido observatory at the French La Reunion Island (Aeolus Range Bin Setting)
AboVE-OHP	Aeolus Validation Experiment at high-altitude observatory at the Haute Provence validation station (Aeolus Range Bin Setting)
ACCD	Accumulation Charge Coupled Device
ACMF	Aeolus Calibration and Monitoring Facility
ACMF-A	ACMF Data Analysis Subsystem / Facility (no longer used in Phase E)
ACMF-C	ACMF Calibration Subsytem
ACMF-D	ACMF Data Storage Subsystem
ACMF-M	ACMF Configuration Management Subsystem
ACMF-OC	ACMF Operational Calibration Facility
ACMF-OS	ACMF Operational Screening Facility
ACMF-P	ACMF Product Screening Subsystem
ACMF-ST	Components of the ACMF maintained by S&T
ACP	Atmospheric Chemistry and Physics Journal
ACTRIS	Aerosol, Clouds and Trace Gases Research Infrastructure
ADAM	A surface reflectance DAtabase for ESA's earth observation Missions
ADDF	Aeolus Data Dissemination Facility
ADM	Atmospheric Dynamics Mission
AEL-FM	Aeolus L2A Feature Mask Processor
AEL-PRO	Aeolus L2A OE-based Extinction and Lidar-ratio Profile Processor (WMO BUFR code is OE-PRO)
AERONET	Aerosol Robotic Network
A-FM	ATLID Feature Mask Processor
AHT	Accurate Housekeeping Thermistors
Airbus D&S / ADS	Airbus Defence & Space
AISP	Annotated Instrument Source Packets
ALADIN	Atmospheric LAser Doppler INstrument
ALD_U_N_1A/1B/2A/2B	Aladin L1A, L1B, L2A, or L2B product
AMP	(Power) Amplifier
AMT	Atmospheric Measurement Techniques (journal)
AMV	Atmospheric Motion Vector
AOCS	Attitude and Orbit Control System
AOD	Aerosol Optical Depth
AoI	Angle of Incidence
APF	Aeolus Processing Facility
A-PRO	ATLID OE-based Extinction and Lidar-ratio Profile Processor
APSF	Aeolus PDGS Surveillance Facility
ARB	Acceptance Review Board
AROME	Application of Research to Operations at MEsoscale, a small-scale numerical prediction model operational at Météo-France

ARPEGE	Action de Recherche Petite Echelle Grande Echelle, a global numerical weather prediction model operational at Météo-France
ARTS	Anomaly Report Tracking System
ASAG	Aeolus Science and Advisory Group
ASKOS	Ground-based measurement campaign at Cabo Verde Islands for the calibration and validation of the aerosol/cloud product from Aeolus and the preparation of the terrain for EarthCARE cal/val activities
ATB	Attenuated Backscatter
ATBD	Algorithm Theoretical Background Document
ATLID	ATmospheric LIDar (Lidar of the EarthCare Mission)
ATM	Atmosphere / atmospheric (path)
AUMATEX	Australian smoke Measurements Above the Troposphere Experiment (Aeolus Range Bin Setting)
AUX	Auxiliary
AUX_CAL	Auxiliary File with Calibration Data
AUX_CHAR	Auxiliary File Containing the Satellite Characterisation
AUX_CSR	Auxiliary File with the Corrected Spectral Registration
AUX_DCC	Auxiliary File with Dark Current Calibration Data
AUX_DCMZ	Auxiliary File with Dark Current in Memory Zone Calibration Data
AUX_HBE	Auxiliary File with Harmonic Bias Estimator Coefficients
AUX_IAT	Auxiliary File with Instrument Auto Test Data
AUX_IDC	Auxiliary File with Instrument Defocus Characterization
AUX_IRC	Auxiliary File with Instrument Response Calibration
AUX_ISR	Auxiliary File with Instrument Spectral Registration
AUX_LBM	Auxiliary File with Laser Beam Monitoring Data
AUX_LUT_BL	Auxiliary File with Baseline Lookup Table
AUX_MET	Auxiliary File with Meteorological Content
AUX_MRC	Auxiliary File with Mie Response Calibration
AUX_OWV	Auxiliary File with Off-line Wind Velocity Data
AUX_PAR_1B/2A/2B	Auxiliary File Defining Processing Parameters for 1B, 2A, or 2B Processing
AUX_PAR_CL	Auxiliary File Defining Processing Parameters for the CalSuite
AUX_PAR_QC	Auxiliary File Defining Quality Control Parameters
AUX_PRR	Auxiliary File with Predicted Rayleigh Response
AUX_RBC	Auxiliary File with Rayleigh-Brillouin Correction Factors
AUX_RRC	Auxiliary File with Rayleigh Response Calibration
AUX_TEL	Auxiliary File with Telescope Temperature Correction Coefficients
AUX_ZWC	Auxiliary File with Zero-Wind Correction Coefficients
B01 - B18	Processor Baseline
BIER	Broader InstrumEnt Response calibration
BRC	Basic Repeat Cycle (one Aeolus observation corresponding to ≈87km)
BS	Beam Splitter
BUFR	Binary Universal Form for the Representation of Meteorological Data
CAL	Calibration
Cal/Val	Calibration and Validation
CALIOP	Cloud-Aerosol Lidar with Orthogonal Polarization
CALIPSO	Cloud Aerosol Lidar and Infrared Pathfinder Satellite Observations
CalSuite	Calibration Suite Prototype Processor

CAMS	Copernicus Atmosphere Monitoring Service
CCD	Charge-Coupled Device
CCN	Contract Change Notice
CFI	Custumer Furnished Item
CGMS	Coordination Group of Meteorological Satellites
Ch.	Chapter
CI	Configuration Item
CIC	Clock-Induced Charge
CIDL	Configuration Items Data List
CLAAS-3	Third Edition of the Cloud Property Dataset using SEVIRI (Spinning Enhanced Visible and InfraRed Imager)
CM	Configuration Management
CMP	Configuration Management Plan
CNRM	Centre National de Recherches Météorologiques
CNRS	Centre National de Recherches Scientifique
CODA	Common Data Access Toolbox
CODADEF	Common Data Access Definition File
COMPO-IFS	ECMWF's Global Data Assimilation System Configured in Atmospheric Composition Mode
CoP	Chain of Processors
CP	Cold Plate *or* Cross Point
CRC	Cyclic Redundancy Check
CSNVRUS	Clear Sky Normalised Valid Rayleigh Useful Signals
CSR	Corrected Spectral Registration
CTI	Charge Transfer Inefficiency
D	Doppler Shift
DA	Data Assimilation
DAMPS	Data Archival, Management and Processing Services
DC	Dark Current
DCC	Dark Current Characterisation
DCMZ	Dark Current in Memory Zone
DCO	Detection Chain Offset
DEM	Digital Elevation Model
DFS	Degree of Freedom for Signal
DISC	Data Innovation and Science Cluster
DLR	Deutsches Zentrum für Luft- und Raumfahrt (German Aerospace Center)
DN	Digitizer Numbers
DoRIT	Company DoRIT on Research Information Technology
DOS	DISC On-Site Team
DPM	Detailed Processing Manual
DSNU	Dark Signal Non-Uniformity
dt	Delay Time
DUDE	Down Under Dark Experiment
DWD	German Weather Service (Deutscher Wetterdienst)
DWL	Doppler Wind Lidar
E2S	End-to-End Simulator
EARLINET	European Aerosol Research Lidar Network

EarthCARE	Cloud, Aerosol and Radiation Earth Explorer Mission
EBD	Extinction, Backscatter and Depolarization component
ECCC	Environment and Climate Change Canada Climate Model
ECMWF	European Centre for Medium-Range Weather Forecast
ECMWF RD	ECMWF Research Department
ECSS	European Cooperation for Space Standardisation
EDA	Ensemble Data Assimilation
EDCF	Energy Drift Correction Factor
EDFCF	External Data File Circulation Form
EDFIR	External Data File Ingestion Report
EE	Earth Explorer
EGU	European Geoscience Union
EMSR	Effective Mie Spectral Response
EO	Earth Observation
EO-CFI	Earth Observation Mission Customer Furnished Item Software
EOL	End-of-Life
EOLA	End-of-Life Activity
EOX	A Geospatial Engineering and Service Company Based in Austria
EPS	EUMETSAT Polar System
ERR	Exploitation Readiness Review
ESA	European Space Agency
ESA GMQ	Data Quality and Algorithms Management Office
ESA-ESOC	ESA's European Space Operation Centre
ESA-ESRIN	ESA's Centre for Earth Observation (European Space Research Institute)
ESA-ESTEC	ESA's European Space Research and Technology Centre
EUMETCast	EUMETSAT's Primary Dissemination Mechanism for the Near Real-Time Delivery of Satellite Data and Products
EUMETSAT	European Organisation for the Exploitation of Meteorological Satellites
eVe	Enhancement and Validation of ESA products, a Depolarization Lidar System Developed by Raymetrics S.A
FDIR	Failure Detection Isolation and Recovery
FFM	Flip-Flop Mechanism
FM-A/B	Flight Model A/B
FOV	Field of View
FPI	Fabry-Perot interferometer
FS	Field Stop
FSOI	Forecast Sensitivity Observation Impact
FSR	Free Spectral Range
FWHM	Full Width at Half Maximum
GCV	Ground Correction Velocity
GNSS	Global Navigation Satellite System
GPS	Global Position System
GUI	Graphical User Interface
H&S	Health and Safety
HBE	Harmonic Bias Estimator
Hi-DCC	DCC Measurement with Acquisition Window High Above Atmosphere
HK	Housekeeping

HLOS	Horizontal Line-of-Sight
HP	Hot Pixel
HR	Highly Reflective Mirror
HSRL	High Spectral Resolution Lidar
HWP	Half-Wave Plate
IAT	Instrument Auto Test
IB Reissig	Ingenieur-Büro Reissig
ICD	Interface Control Document
ID	Packet Identification
IDC	Instrument Defocus Characterisation
IEEE	Institute of Electrical and Electronics Engineers
IF	Interference Filter
IFP	Instrument Full Performance
IFS	Intergrated Forecasting System
INT	Internal (path)
IOCV	In-Orbit Commissioning and Validation
IODD	Input/Output Data Description
IPF	Instrument Processor Facilities
IR	Infra-Red
IRC	Instrument Response Calibration
IRONIC	Instrument Response OffNadIr Calibration
ISR	Instrument Spectral Registration
IT	Information Technology
IWWG	International Winds Working Group
JATAC	Joint Aeolus Tropical Atlantic Campaign
JAXA	Japanese Aerospace Exploration Agency
Jira	A Software developed by Atlassian that allows bug tracking, issue tracking and agile project management
JupyterHub	A cloud-based or on-premises service that lets users access computational environments and resources without installation or maintenance tasks
JupyterLab	A web-based interactive development environment for notebooks, code, and data
KDE	Kernel Density Estimation
KNMI	Koninklijk Nederlands Meteorologisch Instituut (Royal Netherlands Meteorological Institute)
KO	Kick-off
KORE	Key Operational-knowledge Retention Engine
KPI	Key Performance Indicator
L0	Level 0 Product / Processor
L1A / L1AP	Level 1A Product / Processor
L1B / L1BP	Level 1B Product / Processor
L2A / L2AP	Level 2A Product / Processor
L2B / L2BP	Level 2B Product / Processor
L2C	Level 2C Product
L2MetPF	The Aeolus Level 2 processing facility, hosted by ECMWF, responsible for the generations of the Level 2B and Level 2C products.
LATMOS	Laboratoire Atmosphères, Observations Spatiales

LBC	Level 1B Processor Control Main
LBM	Laser Beam Monitoring
LBWU	Laser Burst Warm-Up
LCM	Laser Chopper Mechanism
LCP	Laser Chopper Phase
LDT	Laser Diode Temperature
LFA	Laser Frequency Adjustment
LIC	Laser-Induced Contamination
LID	Laser-Induced Damage *or* Lidar Mode Data
LL	Lessons Learnt
LL-AE2	Lessons Learnt Relevant for the Operational Follow-on Mission Aeolus-2
LL-EC	Lessons Learnt Relevant for Other Upcoming Lidar Missions as EarthCARE
LL-EE	Lessons Learnt Relevant for Future Earth Explorer Missions
LL-GE	Lessons Learnt Relevant for Missions in General
LMU	Ludwig-Maximilians-Universität München
LND	Leonardo S.p.A.
LOS	Line-of-Sight
LPS	Living Planet Symposium
LSB	Least Significant Bit
LSR	Land Surface Return
LT	Light Trap
LTDP	Long Term Data Preservation
LWDA	Long-Window Data Assimilation
M1	Telescope Primary Mirror
MAD	Median Absolute Deviation
MAG	Mission Advisory Group
MARS	Mediterranean Aerosol Range Bin Setting
MC	Mie Cloudy
MCA	Mie Channel Algorithm
meas / MEAS	Measurement
MetOp IASI	Infrared Atmospheric Sounding Interferometer (IASI) onboard the Meteorological Operational Satellite (MetOP)
MF	Météo-France
MLE	Maximum Likelihood Estimation Algorithm
MMPF	Mission Management and Planning Facility
MO	Master Oscillator
MODIS	Moderate Resolution Imaging Spectroradiometer
MoM	Minutes of Meeting
MOUSR	Mie Outside of Useful Spectral Range
MPL_ORBSCT	Mission Planning Orbit Scenario File
MRC	Mie Response Calibration
MSP	Mie Spectrometer
Muninn	Tool to manage data products (developed by S&T)
MUST	Mission Utility & Support Tools
MZE	Memory Zone Efficiency
N	The Number of Measurements / Read-outs per Observation / BRC

N/P	The Number of Measurements per Observation / BRC (N) and Number of Pulses (P) per Measurement
NCMRWF	National Centre For Medium Range Weather Forecasting (India)
netCDF	Network Common Data Format
NH	Northern Hemisphere
NL	Non-Linearity
NOA	National Observatory of Athens
NOAA	National Oceanic and Atmospheric Administration
NOP	No Operation
NRT	Near Real Time
NWP	Numerical Weather Prediction
O-A	Observation Minus Analysis
O-B	Observation Minus Background
OBA	Optical Bench Assembly
obs / OBS	Observation
ODB	Observation DataBase (file format used at ECMWF)
OLA	Optical Lidar Associates
OP	Operational Processor
OPC	Optical Properties Code
OS	Operating System
OSE	Observing System Experiment
P / p	Number of Pulses *or* pressure
P/N	See N/P
PAO	Pierre Auger Observatory
PBL	Planetary Boundary Layer
PBS	Polarizing Beam Splitter
PCD	Product Confidence Data
PD	Photodiode
PDGS	Payload Data Ground Segment
PDSC	Preserved Data Set Content
PI	Performance Indicator
PLSO	Post-Launch Support Office
PMAp	Polar Multi-Sensor Aerosol Optical Properties Product
PMP	Project Management Plan
POLARIS	POLAR Instrument Setting (range bin setting)
PollyXT	Portable, Remote-Controlled Multiwavelength-Polarization-Raman Lidars Next Generation
PP	Prototype Processor
PR	Performance Review Meeting
PreAMP	Pre-Amplifier
Px.	Pixel
QBO	Quasi-Biennial Oscillation
QC	Quality Control
QCF	Quality Control Facility
QJRMS	Quarterly Journal of the Royal Meteorological Society
QPA	Quality Processing Algorithm
QRAS	Quality Reports Advanced Search tool

QUADAS	QUAlity Data Analysis System providing UI functionality, plot functionality, reporting functionality and analysis functionality for the ACMF
QWG	Quality Working Group
QWP	Quarter-Wave Plate
RBC	Rayleigh-Brillouin Correction
RBS	Range Bin Settings
RC	Rayleigh Clear
RCT	Rayleigh Cover Temperature
RDB	Range Dependent Bias
RMS / rms	Root Mean Square
RMSE	Root Mean Square Error
RR	Rayleigh Response
RRC	Rayleigh Response Calibration
RSP	Rayleigh Spectrometer
RSR	Refined Scattering Ratio
RTS	Random Telegraph Signal
RWP	Radar Wind Profilers
s [&] t / S&T	Science & Technology B.V.
SAA	South Atlantic Anomaly
SAG	Science Advisory Group
SAL	Saharan Air Layer
Sat-LOS	Satellite Velocity on the LOS
SATURN	Range Bin Setting for the Tropical Campaign in summer 2021
SBG	Solar Background
SC	Special Collection
SCA	Rayleigh Channel Standard Correct Algorithm
SH	Southern Hemisphere
SMAD	Scaled Median Absolute Deviation
SNR	Signal-to-Noise Ratio
SoW	Statement of Work
SPPA	Sensor Performance, Products, and Algorithms
SPR	Software Problem Report
SR	Scattering Ratio
SRN	Software Release Note
STD	Standard Deviation
STDB	Scientific Temporal Data Base
STRATEOLE 2	A French-US project using CNES superpressure balloons drifting around the globe to study the climate processes in the Tropical Tropopause Layer and the lower stratosphere
STRO	Sealed Transmit-Receive Optics
SUM	Software User Manual
SW *or* s/w	Software
T	Temperature
TAI	International Atomic Time
TellUS	Issue Tracking Tool for Software Development Management
TLE	Thin Layer Emulator
TMC	Period of Master Clock

TN	Technical Note
TOBS	Tripod Obscuration
TOC	Table of Content
TRO	Transmit–Receive Optics
TROPOS	Leibniz Institute for Tropospheric Research
TTO	Transfer to Operation
TVac	Thermal Vacuum
USR	Useful Spectral Range (part of the frequency range that is imaged onto the 16 pixels of the Mie ACCD of about 1.6 GHz)
UTC	Coordinated Universal Time
UTLS	Upper Troposphere Lower Stratosphere
UV	Ultra-Violet
VarQC	Variational Quality Control
VCDU	Virtual Channel Data Unit
VIIRS	Visible Infrared Imaging Radiometer Suite
VirES	Virtual Workspace for Earth Observation Scientists
VM	Virtual Machine
VRE	Virtual Research Environment (for VirES)
WBS	Work Breakdown Structure
WCD	Weather and Climate Dynamics Journal
WM	Working Meeting
WMO	World Meteorological Organisation
WO	Work Order
WP	Work Package
WPD	Work Package Description
WVM	Wind Velocity Measurement
YGT	Young Graduate Trainee

C LIST OF PROCESSOR ANOMALIES AND CHANGE REQUESTS

The following list of Configuration Item anomalies and change requests, which was tracked by Jira and TellUS was compiled by Serco:

Configuration Item	Severity			Total
	Blocking	Critical	Routine	
Common		**2**	**18**	**20**
Jira Anomaly		2	8	10
TellUS Problem			10	10
ACMF	**3**	**5**	**18**	**26**
Jira Anomaly		1	1	2
TellUS Change Request	2	4	10	16
TellUS Problem	1		7	8
ACMF L1B			**3**	**3**
Jira Anomaly			3	3
ACMF-C	**1**	**1**	**6**	**8**
TellUS Change Request	1	1	4	6
TellUS Problem			2	2
ACMFOC			**3**	**3**
TellUS Problem			3	3
AUX_CAL_L2	**1**		**5**	**6**
TellUS Change Request	1		4	5
TellUS Problem			1	1
AUX_CHAR__	**1**		**5**	**6**
TellUS Change Request	1		5	6
AUX_CLM_L2			**1**	**1**
TellUS Change Request			1	1
AUX_LUT_BL		**1**		**1**
TellUS Change Request		1		1
AUX_MRC_1B	**2**		**5**	**7**
TellUS Change Request	2		5	7
AUX_PAR _CL		**1**	**1**	**2**
TellUS Change Request		1	1	2
AUX_PAR_0_			**3**	**3**
TellUS Change Request			3	3
AUX_PAR_1A	**1**		**4**	**5**
TellUS Change Request	1		4	5
AUX_PAR_1B		**5**	**25**	**30**
TellUS Change Request		5	25	30
AUX_PAR_2A		**2**	**11**	**13**
TellUS Change Request		2	11	13
AUX_PAR_CS	**1**		**2**	**3**
TellUS Change Request	1		2	3
AUX_PAR_HB			**3**	**3**

Configuration Item	Severity			Total
	Blocking	Critical	Routine	
TellUS Change Request			3	3
AUX_PAR_QC	**3**	**4**	**11**	**18**
TellUS Change Request	3	4	10	17
TellUS Problem			1	1
AUX_PAR_RB	**1**	**1**	**2**	**4**
TellUS Change Request	1	1	2	4
AUX_RBC_L2		**1**	**2**	**3**
TellUS Change Request		1	2	3
AUX_RRC_1B		**2**	**4**	**6**
TellUS Change Request		2	4	6
CALIBRATION PROCESSING			**3**	**3**
TellUS Problem			3	3
CODADEF			**1**	**1**
Jira Anomaly			1	1
L1A			**1**	**1**
Jira Anomaly			1	1
L1B	**3**	**4**	**35**	**42**
Jira Anomaly		3	3	6
TellUS Change Request	3	1	16	20
TellUS Problem			16	16
L2A	**1**	**4**	**40**	**45**
Jira Anomaly		3	8	11
TellUS Change Request	1	1	25	27
TellUS Problem			7	7
L2A QCF			**1**	**1**
Jira Anomaly			1	1
L2B	**1**	**3**	**12**	**16**
Jira Anomaly			1	1
TellUS Change Request	1	3	9	13
TellUS Problem			2	2
QCF	**3**	**4**	**20**	**27**
TellUS Change Request	3	3	19	25
TellUS Problem		1	1	2
REPORT GENERATOR		**1**	**12**	**13**
Jira Anomaly		1	2	3
TellUS Change Request			7	7
TellUS Problem			3	3
STARTING PRODUCTS		**1**	**13**	**14**
TellUS Change Request		1	13	14
Total	**22**	**42**	**270**	**334**

D LIST OF MEETINGS

Meeting	Phase	Date	#days	Location	Description
WM	RUP	19/02/2019	1	DLR	Working meeting on wind products #1
KO	RUP	20/02/2019	1	DLR	Project kick-off
PM1	RUP	07/05/2019	1	Online	Ramp-up Progress Meeting following IOCR
WM	RUP	06/06/2019	1	ESRIN	Working meeting on wind products #2
AR	RUP	06-07/06/2019	2	ESRIN	DISC Acceptance Review/ Operation Readiness Review
WM	OP	29/10/2019	1	DLR	Working meeting on aerosol products #1
WM	OP	30/10/2019	1	DLR	Working meeting on wind products #3
PM2	OP	22/11/2019	1	KNMI	Progress Meeting 2
WM	OP	02&08/04/2020	2	Online	Working meeting on wind products #4
WM	OP	17/04/2020	1	Online	Working meeting on aerosol products #2
Pre-ERR	OP	30/04/2020	1	Online	Preparation of Exploitation Readiness Review
ERR	OP	24-25/09/2020	2	Online	Exploitation Readiness Review
WM	EP	27/10, 10/11, 18/11/2020	3	Online	Working meeting on wind products #5
WM	EP	26/11/2020	1	Online	Working meeting on aerosol products #3
WM	EP	26/03/2021	1	Online	Working meeting on aerosol products #4
PR1	EP	30/03/2021	1	Online	Performance Review Meeting 1
WM	EP	31/03 & 26/04/2020	2	Online	Working meeting on wind products #6
PR2	EP	28/10/2021	1	Online	Performance Review Meeting 2
WM	EP	09-10/02/2022	2	Online	Working meeting on wind products #7
WM	EP	22/02/2022	1	Online	Working meeting on aerosol products #5
PR3	EP	03/03/2022	1	Online	Performance Review Meeting 3
PR4	EP	12-13/10/2022	1	CNRS	Performance Review Meeting 4
PR5	EP	14/03/2023	1	DLR	Performance Review Meeting 5
WM	EP	15-17/03/2023	3	Schnee-fernerhaus	Working meeting on wind products #8 and working meeting on aerosol products #6
PR6	EP	18/10/2023	1	Online	Performance Review Meeting 6
FR	EP	13-15/03/2024	3	ESRIN	Final Review

In addition, regular online meetings with the whole DISC team took place on the following dates (including special topical discussion meetings):

02-Jan-2019, 09-Jan-2019, 16-Jan-2019, 23-Jan-2019, 30-Jan-2019, 06-Feb-2019, 13-Feb-2019, 27-Feb-2019, 06-Mar-2019, 13-Mar-2019, 04-Apr-2019, 10-Apr-2019, 17-Apr-2019, 24-Apr-2019, 15-May-2019, 29-May-2019, 12-Jun-2019, 19-Jun-2019, 26-Jun-2019, 03-Jul-2019, 10-Jul-2019, 17-Jul-2019, 24-Jul-2019, 31-Jul-2019, 07-Aug-2019, 21-Aug-2019, 04-Sep-2019, 18-Sep-2019, 02-Oct-2019, 16-Oct-2019, 23-Oct-2019, 06-Nov-2019, 27-Nov-2019, 11-Dec-2019, 08-Jan-2020, 15-Jan-2020, 05-Feb-2020, 19-Feb-2020, 04-Mar-2020, 18-Mar-2020, 01-Apr-2020, 15-Apr-2020, 29-Apr-2020, 13-May-2020, 27-May-2020, 03-Jun-2020, 10-Jun-2020, 24-Jun-2020, 08-Jul-2020, 15-Jul-2020, 21-Jul-2020, 22-Jul-2020, 05-Aug-2020, 19-Aug-2020, 02-Sep-2020, 16-Sep-2020, 30-Sep-2020, 14-Oct-2020, 28-Oct-2020, 11-Nov-2020, 25-Nov-2020, 09-Dec-2020, 10-Dec-2020, 16-Dec-2020, 13-Jan-2021, 27-Jan-2021, 03-Feb-2021, 10-Feb-2021, 24-Feb-2021, 10-Mar-2021, 17-Mar-2021, 07-Apr-2021, 21-Apr-2021, 05-May-2021, 12-May-2021, 19-May-2021, 09-Jun-2021, 23-Jun-2021, 07-Jul-2021, 21-Jul-2021, 27-Jul-2021, 02-Aug-2021, 04-Aug-2021, 18-Aug-2021, 01-Sep-2021, 15-Sep-2021, 29-Sep-2021, 13-Oct-2021, 27-Oct-2021, 10-Nov-2021, 24-Nov-2021, 08-Dec-2021, 22-Dec-2021, 05-Jan-2022, 12-Jan-2022, 26-Jan-2022, 09-Feb-2022, 23-Feb-2022, 09-Mar-2022, 23-Mar-2022, 06-Apr-2022, 20-Apr-2022, 04-May-2022, 18-May-2022, 01-Jun-2022, 15-Jun-2022, 29-Jun-2022, 13-Jul-2022, 27-Jul-2022, 10-Aug-2022, 24-Aug-2022, 07-Sep-2022, 21-Sep-2022, 05-Oct-2022, 19-Oct-2022, 02-Nov-2022, 16-Nov-2022, 30-Nov-2022, 14-Dec-2022, 11-Jan-2023, 25-Jan-2023, 08-Feb-2023, 22-Feb-2023, 08-Mar-2023, 05-Apr-2023, 19-Apr-2023, 10-May-2023, 31-May-2023, 14-Jun-2023, 05-Jul-2023, 02-Aug-2023, 06- Sep-2023, 04-Oct-2023, 02-Nov-2023, 06-Dec-2023, 10-Jan-2024, 07-Feb-2024, 06-Mar-2024

Management meetings between DLR management and ESA were performed on the following dates:

20-Feb-2019, 18-Apr-2019, 07-Jun-2019, 28-Nov-2019, 20-Apr-2020, 10-Jun-2020, 19-Aug-2020, 02-Dec-2020, 14-Dec-2020, 02-Feb-2021, 16-Apr-2021, 25-Jun-2021, 11-Aug-2021, 19-Aug-2021, 07-Dec-2021, 16-Mar-2022, 26-Apr-2022, 04-Jul-2022, 01-Dec-2022, 10-Mar-2023, 13-Jun-2023, 04-Aug-2023, 09-Oct-2023, 08-Nov-2023.

E LIST OF CONFERENCES WITH AEOLUS CONTRIBUTIONS FROM THE DISC

Conference	Date	Location
Aeolus Cal/Val and Science Workshop 2019 (**)	26-29 Mar 2019	Frascati
ESA Living Planet Symposium 2019 (*)	13-17 May 2019	Milan
2019 Joint Satellite Conference	28 Sep – 4 Oct 2019	Boston
Aeolus NWP impact working meeting (**)	12 Sep 2019	Darmstadt
EGU General Assembly 2020 (*)	4-8 May 2020	Online
Aeolus NWP impact working meeting (**)	17 Jun 2020	Online
Aeolus L2A working meeting (**)	30 Jun 2020	Online
Aeolus Cal/Val and Science Workshop 2020 (**)	2-6 Nov 2020	Online
European Lidar Conference 2020	18-20 Nov 2020	Online
AGU fall meeting 2020	1-17 Dec 2020	Online
7th WMO Workshop on the Impact of Various Observing Systems on NWP	30 Nov – 3 Dec 2020	Online
AMS101; 101st Annual Meeting	10-15 Jan 2021	Online
15th Int. Winds Working Group Workshop(*)	12-16 Apr 2021	Online
EGU General Assembly 2021 (*)	19-30 Apr 2021	Online
Coordination Group for Meteorological Satellites CGMS-49	19-21 May 2021	Online
IEEE IGARSS 2021 (*)	11-16 Jul 2021	Brussels / Online
EUMETSAT Meteorological Satellite Conference	20-24 Sep 2021	Online
European Lidar Conference 2021	16-18 Nov 2021	Granada
ESA ATMOS Conference 2021 (*)	22-26 Nov 2021	Online
Aeolus NWP impact and L2B data quality meeting (**)	1 & 3 Dec 2021	Online
Aeolus L2A working meeting (**)	16 Dec 2021	Online
Aeolus 3rd Anniversary Conference (**)	28 Mar – 01 Apr 2022	Taormina
16th Int. Winds Working Group Workshop (*)	8-12 May 2023	Montreal
ESA Living Planet Symposium 2022 (*)	23-27 May 2022	Bonn
XXIII International Symposium on High-power Laser Systems and Applications	13-16 Jun 2022	Prague
Coordination Group for Meteorological Satellites CGMS-50	15-17 Jun 2022	Geneva
21st Coherent Laser Radar Conference	26 Jun – 01 Jul 2022	Online
EUMETSAT Scientific Workshop Towards an Operational Doppler Wind Lidar Programme (**)	8-9 Sep 2022	Darmstadt
EUMETSAT Meteorological Satellite Conference	19-23 Sep 2022	Brussels
International Conference on Space Optics	3-7 Oct 2022	Dubrovnik
2nd Climate Observation Conference	17-19 Oct 2022	Darmstadt
EGU General Assembly 2023 (*)	23-28 Apr 2023	Vienna / Online
Aeolus Science Conference 2023 (**)	22-26 May 2023	Rhodes Island
EUMETSAT Meteorological Satellite Conference	11-15 Sep 2023	Malmö
EarthCARE Science and Validation Workshop	13-17 Nov 2023	Frascati

(*) Dedicated session for Aeolus related content

(**) Special conference / workshop only for Aeolus related content

F LIST OF DISC PARTICIPANTS PER WORK PACKAGE

The list of participants starts with the work package manager(s).

WP 100: O. Reitebuch (DLR), U. Marksteiner (DLR), F. Weiler (DLR), B. Witschas (DLR), C. Lemmerz (DLR), O. Lux (DLR), K. Schmidt (DLR), I. Nikolaus (Physics Solutions), M. Vaughan (OLA), M. Rennie (ECMWF)

WP 200: U. Marksteiner (DLR), F. Weiler (DLR), B. Witschas (DLR), C. Lemmerz (DLR), O. Lux (DLR), D. Huber (DoRIT), F. Bracci (DLR)

WP 300: O. Reitebuch (DLR), U. Marksteiner (DLR), F. Weiler (DLR), B. Witschas (DLR), C. Lemmerz (DLR), O. Lux (DLR), K. Schmidt (DLR), I. Nikolaus (Physics Solutions), Huber (DoRIT), M. Rennie (ECMWF)

WP 400: O. Reitebuch (DLR), U. Marksteiner (DLR), F. Weiler (DLR), I. Krisch (DLR)

WP 1000: D. Huber (DoRIT), M. Meringer (DLR), K. Reissig (IB Reissig), F. Bracci (DLR)

WP 1100: J. de Kloe (KNMI), M. Rennie (ECMWF)

WP 1200: A. Dabas (CNRS), D. Trapon (CNRS/TROPOS), T. Flament (CNRS), H. Stieglitz (CNRS), A. Lacour (CNRS)

WP 1300: B. Witschas (DLR)

WP 2000: D. Huber (DoRIT), M. Meringer (DLR), K. Reissig (IB Reissig), F. Bracci (DLR)

WP 2100: M. Rennie (ECMWF), J. de Kloe (KNMI), G.-J. Marseille (KNMI), D. Donovan (KNMI), D. Hemminga (KNMI)

WP 2200: A. Dabas (CNRS), D. Trapon (CNRS/TROPOS), T. Flament (CNRS), H. Stieglitz (CNRS), A. Lacour (CNRS)

WP 2300: J. de Kloe (KNMI)

WP 2400: D. Huber (DoRIT), K. Reissig (IB Reissig)

WP 2450: G.-J. van Zadelhoff (KNMI), P. Wang (KNMI)

WP 2500: D. Huber (DoRIT), K. Reissig (IB Reissig)

WP 2550: D. Donovan (KNMI), P. Wang (KNMI)

WP 3000: F. Bracci (DLR), G. Gostinicchi (Serco), M. Meringer (DLR), D. Huber (DoRIT), K. Reissig (IB Reissig), J. de Kloe (KNMI), M. Rennie (ECMWF), A. Dabas (CNRS), D. Trapon (CNRS/TROPOS), T. Flament (CNRS), H. Stieglitz (CNRS), A. Lacour (CNRS), L. Di Ciolo (Serco), Simone Bucchi (Serco)

WP 3100: D. Huber (DoRIT), M. Meringer (DLR), K. Reissig (IB Reissig), F. Bracci (DLR)

WP 3200: J. de Kloe (KNMI), M. Rennie (ECMWF)

WP 3300: A. Dabas (CNRS), D. Trapon (CNRS/TROPOS), T. Flament (CNRS), H. Stieglitz (CNRS), A. Lacour (CNRS), S. Bley (TROPOS)

WP 3400: J. de Kloe (KNMI), G.-J. Marseille (KNMI), D. Huber (DoRIT), M. Rennie (ECMWF)

WP 3500: J. de Kloe (KNMI), G.-J. Marseille (KNMI)

WP 3600: O. Reitebuch (DLR), S. Abdalla (ECMWF), M. Rennie (ECMWF), N. Masoumzadeh (DLR), F. Weiler (DLR), U. Marksteiner (DLR), J. de Kloe (KNMI), T. Flament (CNRS), D. Trapon (CNRS/TROPOS), A. Lacour (CNRS), V. Cito Filomarino (DLR), S. Knobloch (DLR), R. Reichert (DLR), A. Das (DLR)

WP 4000: O. Reitebuch (DLR), U. Marksteiner (DLR), F. Weiler (DLR), B. Witschas (DLR), J. de Kloe (KNMI)

WP 4050: S. Bley (TROPOS), D. Trapon (TROPOS)

WP 4100: U. Marksteiner (DLR), F. Weiler (DLR), O. Reitebuch (DLR), C. Lemmerz (DLR), O. Lux (DLR), B. Witschas (DLR), I. Krisch (DLR), F. Bracci (DLR), F. Fabre (Les Myriades), K. Schmidt (DLR), V. Cito Filomarino (DLR)

WP 4150: U. Marksteiner (DLR), F. Weiler (DLR), O. Reitebuch (DLR), B. Witschas (DLR), C. Lemmerz (DLR), O. Lux (DLR), K. Schmidt (DLR), F. Bracci (DLR), I. Nikolaus (Physics Solutions), M. Vaughan (OLA), F. Fabre (Les Myriades), N. Masoumzadeh (DLR), I. Krisch (DLR), V. Cito Filomarino (DLR)

WP 4155: O. Reitebuch (DLR), L. Labzovskii (DLR)

WP 4200: A. Dabas (CNRS), D. Trapon (CNRS/TROPOS), T. Flament (CNRS), H. Stieglitz (CNRS), A. Lacour (CNRS), S. Bley (TROPOS)

WP 4300: M. Rennie (ECMWF), J. de Kloe (KNMI), G.-J. Marseille (KNMI), D. Donovan (KNMI), D. Hemminga (KNMI)

WP 4350: G.-J. Marseille (KNMI), D. Donovan (KNMI), D. Hemminga (KNMI)

WP 4400: M. Veneziani (S&T), J. Smeets (S&T), S. Niemeier (S&T), B. Pijnacker Hordijk (S&T), W. Damman (S&T), F. Vonk (S&T)

WP 4500: F. Weiler (DLR), U. Marksteiner (DLR), O. Reitebuch (DLR), T. Flament (CNRS), D. Trapon (CNRS), J. de Kloe (KNMI), M. Rennie (ECMWF), A. Lacour (CNRS)

WP 4600: O. Reitebuch (DLR), A. Dabas (CNRS), A. Stoffelen (KNMI), M. Rennie (ECMWF), L. Isaksen (ECMWF), J.-F. Mahfouf (CNRS)

WP 4700: A. Stoffelen (KNMI), J. de Kloe (KNMI), G.-J. Marseille (KNMI), A. Dabas (CNRS), T. Flament (CNRS), H. Stieglitz (CNRS), D. Trapon (CNRS), A. Lacour (CNRS), V. Pourret (CNRS)

WP 4750: C. de Vincenti (Serco), P. Sabbatini (Serco)

WP 4800: I. Krisch (DLR), A. Geiss (LMU), F. Weiler (DLR)

WP 5000: M. Rennie (ECMWF), L. Isaksen (ECMWF), G.-J. Marseille (KNMI), J. de Kloe (KNMI)

WP 5100: A. Benedetti (ECMWF), W. McLean (ECMWF), K. Henry (ECMWF), Julie Letertre-Danczak (ECMWF)

WP 5500: M. Rennie (ECMWF), L. Isaksen (ECMWF), G.-J. Marseille (KNMI)

WP 5550: J.-F. Mahfouf (CNRS), V. Pourret (CNRS), C. Pavan (CNRS), M. Savli (CNRS), I. Seck (CNRS)

WP 5600: A. Benedetti (ECMWF), W. McLean (ECMWF), Julie Letertre-Danczak (ECMWF)

WP 6000: S. Bucci (Serco), G. Gostinicchi (Serco), L. Di Ciolo (Serco), M. Galli (Serco)

WP 7000: M. Veneziani (S&T), Arie Kuijt (S&T), S. Niemeier (S&T), J. Smeets (S&T), B. Pijnacker Hordijk (S&T), F. Tagliacarne (S&T)

WP 7100: M. Veneziani (S&T), Arie Kuijt (S&T), S. Niemeier (S&T), J. Smeets (S&T), B. Pijnacker Hordijk (S&T), W. Damman (S&T), F. Tagliacarne (S&T)

WP 7200: M. Veneziani (S&T), Arie Kuijt (S&T), S. Niemeier (S&T), J. Smeets (S&T), B. Pijnacker Hordijk (S&T), W. Damman (S&T), F. Tagliacarne (S&T)

WP 7300: M. Veneziani (S&T), Arie Kuijt (S&T), S. Niemeier (S&T), J. Smeets (S&T), B. Pijnacker Hordijk (S&T), W. Damman (S&T), F. Tagliacarne (S&T)

WP 7500: G. Perron (ABB), P. Berube (ABB), S. Jupin-Langlois (SJL)

WP 7600: G. Perron (ABB), P. Berube (ABB), S. Jupin-Langlois (SJL)

WP 7700: G. Perron (ABB), P. Berube (ABB), S. Jupin-Langlois (SJL)

WP 8000: J. de Kloe (KNMI)

WP 9000: I. Krisch (DLR), O. Reitebuch (DLR), P. Derkes (DLR), R. Thiess (DLR), C. Lemmerz (DLR), O. Lux (DLR), U. Marksteiner (DLR), F. Weiler (DLR), B. Witschas (DLR), N. Masoumzadeh (DLR), V. Cito Filomarino (DLR), S. Knobloch (DLR), K. Schmidt (DLR), M. Meringer (DLR)

WP 9100: D. Huber (DoRIT)

WP 9200: A. Dabas (CNRS), T. Flament (CNRS), H. Stieglitz (CNRS), A. Lacour (CNRS), D. Trapon (CNRS), J.-F. Mahfouf (CNRS), V. Pourret (CNRS)

WP 9300: A. Stoffelen (KNMI), N. A. Krijgsman (KNMI), P. Wittenberg (KNMI), J. de Kloe (KNMI)

WP 9400: M. Rennie (ECMWF)

WP 9500: M. Veneziani (S&T), Arie Kuijt (S&T), S. Niemeier (S&T), J. Smeets (S&T), B. Pijnacker Hordijk (S&T), W. Damman (S&T), F. Tagliacarne (S&T)

WP 9600: G. Perron (ABB), P. Berube (ABB), S. Jupin-Langlois (SJL)

WP 9700: S. Bley (TROPOS), D. Trapon (TROPOS)

WP 9900: M. Cardaci (Serco)

G LIST OF DOCUMENTS IN DISC RESPONSIBILITY

Cnt	Type	CI	DocRef Code	Prev. Ref. Code	Document Title	File Name of newest version
Management Plans						
1	MP	DCM	AED-MP-Serco-DCM-001	AED-MP-SER-GEN-001	Configuration Management Plan - Master Document	AED-MP-Serco-DCM-001--CMP_MP--v2_01--2024_02_16.pdf
2	MP	DCM	AED-MP-Serco-DCM-002	AED-MP-SER-GEN-002	Configuration Management Plan - Anomaly and Change Management	AED-MP-Serco-DCM-002--CMP_ACMP--v2_02--2024-02-16.pdf
3	MP	DCM	AED-MP-Serco-DCM-003	AED-IC-SER-GEN-003	Configuration Management Plan - Software and Auxiliary Delivery Interface Control Document	AED-MP-Serco-DCM-003--CMP_SADICD--v5_06--2024-02-16.pdf
4	MP	DCM	AED-MP-Serco-DCM-004	AED-MP-DLR-GEN-004 AED-MP-DLR-DCM-004	Configuration Management Plan - Configuration Items, Definitions and Dependencies	AED-MP-Serco-DCM-004--CMP_CIDD--v2_02--2024-02-16.pdf
5	MP	GEN	AED-MP-DLR-GEN-005		Project Management Plan	AED-MP-DLR-GEN-005--Project-Management-Plan--V5_00--2023_11_22.pdf
6	MP	GEN	AED-MP-DLR-GEN-006	AED-CVP-DLR-001	Calibration and Validation Cal/Val Plan	AED-MP-DLR-GEN-006--CVP--V1_10--2020_08_17.pdf
7	MP	L1B	AED-MP-DLR-L1B-007	AED-QMP-L1B-DLR-001	L1B Data QC and Monitoring Plan	AED-MP-DLR-L1B-007--QMP--v2_00--2020_08_20.pdf
8	MP	L2A	AED-MP-CNRM-CSL2A-007	AED-QMP-CAL-L2A-CNRM-001	Calibration Suite and L2A QC/Monitoring Plan	AED-MP-CNRM-CSL2A-007--QC_Monitoring_Plan--v2_0--2020_08_24.pdf
9	MP	L2B	AED-MP-ECMWF-L2B-009	AED-QMP-L2B-ECMWF-001	L2B QC/Monitoring Plan	AED-MP-ECMWF-L2B-008--QMP--v1_3--2020_08_25.pdf
10	MP	GEN	AED-MP-DLR-GEN-010		Exploitation Phase Performance Plan	AED-MP-DLR-GEN-010--Exploitation-Phase-Performance-Plan--v1_00--2020_10_16.pdf
Change Proposals						
11	WO	GEN	AED-WO-DLR-GEN-001		Proposal for Aeolus DISC WO#1: Reprocessing	AED-WO-DLR-GEN-001--Reprocessing--v1_10--2019_11_27.pdf
12	WO	GEN	AED-WO-DLR-GEN-002		Proposal for Aeolus DISC WO#2: Python Report Generator	AED-WO-DLR-GEN-002--Python-Report-Generator--v1_10--2020_03_26.pdf
13	WO	GEN	AED-WO-DLR-GEN-003		Proposal for Aeolus DISC WO#3: ALADIN Expert Support	AED-WO-DLR-GEN-003--ALADIN-Expert-Support--v1_00--2020_02_26.pdf

14	WO	GEN	AED-WO-DLR-GEN-004		Proposal for Aeolus DISC WO#4: L2A	AED-WO-DLR-GEN-004--ATLID_L2A_proposal--v1_00--2020_11_04.pdf
15	WO	GEN	AED-WO-DLR-GEN-005		Proposal for Aeolus DISC WO#5: Additional ACMF maintenance	AED-WO-DLR-GEN-005--ACMF-evolution_DISC-proposal--v1_00--2020-08-17.pdf
16	WO	GEN	AED-WO-DLR-GEN-006		Proposal for Aeolus DISC: Analysis of Aeolus orbit lowering and other options	AED-WO-DLR-GEN-006--orbit_lowering_proposal--v1_00--2020_11_12.pdf
17	WO	GEN	AED-WO-DLR-GEN-007		Proposal for Aeolus DISC: Scientific support for VirES VRE development	AED-WO-DLR-GEN-007--Vires-VRE--v1_00--2021-02-19.pdf
18	WO	GEN	AED-WO-DLR-GEN-008		Proposal for Aeolus DISC: Additional Cal/Val Activities	AED-WO-DLR-GEN-008--Cal-Val--v1.0--2021_04_12.pdf
19	WO	GEN	AED-WO-DLR-GEN-009		Proposal for Aeolus Aerosol Assimilation in the DISC (A3D)	AED-WO-DLR-GEN-009--A3D--V1_00--2021_05_19_for-ftp.pdf
20	WO	GEN	AED-WO-DLR-GEN-010		Proposal for Aeolus DISC extension to 2022	AED-WO-DLR-GEN-010--extension--V1_00--2021_08_27_for_ftp.pdf
21	WO	GEN	AED-WO-DLR-GEN-011		Proposal for the use of FFTW software in Aeolus L2A processor	AED-WO-DLR-GEN-011--FFTW--V1.1--2022_01_25_for-ftp.pdf
26	WO	GEN	AED-WO-DLR-GEN-012		Proposal for Aeolus DISC extension to 2023	AED-WO-DLR-GEN-012--3033880_DLR-Proposal_Aeolus_DISC_Extension_2023--v1.0_2022_09_26.pdf
27	WO	GEN	AED-WO-DLR-GEN-013		Proposal for Aeolus Science Conference Support and Codadef Maintenance	AED-WO-DLR-GEN-013--3036417_Aeolus_DISC_WO9_DLR-Proposal--conference_support_and_codadef--v1.0--04_05_2023.pdf
28	WO	GEN	AED-WO-DLR-GEN-014		Proposal for Aeolus DISC extension to March 2024	AED-WO-DLR-GEN-014--extension-2024--v1.0--2023_12_07_for_DISC.pdf
Progress Reports						
29	PR	GEN	AED-PR-DLR-GEN-001	AED-PR-DLR-001	Ramp-Up Progress Report in preparation of Progress Meeting #1 on 07/05/2019	AED-PR-DLR-GEN-001--v1_10--2019-04-25.pdf
30	PR	GEN	AED-PR-DLR-GEN-002	AED-PR-DLR-002	Ramp-Up Report in preparation of ARR on 06/06/2019	AED-PR-DLR-GEN-002--V1_00--2019-05-29.pdf
31	PR	GEN	AED-PR-DLR-GEN-003	AED-PR-DLR-003	Progress Report #3 in preparation of Progress Meeting #2 on 22/11/2019	AED-PR-DLR-003_V1_00--2019-11-12.pdf
32	PR	GEN	AED-PR-DLR-GEN-004		Progress Report #4 in preparation of Pre-ERR Meeting on 30/04/2020	AED-PR-DLR-GEN-004--Pre_ERR--V1_00--2020_04_17.pdf

33	PR	GEN	AED-PR-DLR-GEN-005		Progress Report #5 in preparation of ERR Meeting	AED-PR-DLR-GEN-005--ERR--V1_01--2020_09_18.pdf
34	PR	GEN	AED-PR-DLR-GEN-006		Progress Report #6 in preparation of Performance Review Meeting #1	AED-PR-DLR-GEN-006--PR1--V1_00--2021_03_16.pdf
35	PR	GEN	AED-PR-DLR-GEN-007		Progress Report #7 in preparation of Performance Review Meeting #2	AED-PR-DLR-GEN-007--PR2--v1.00--2021_10_11.pdf
36	PR	GEN	AED-PR-DLR-GEN-008		Progress Report #8 in preparation of Performance Review Meeting #3	AED-PR-DLR-GEN-008--PR3--v1.00--2022_02_18.pdf
37	PR	GEN	AED-PR-DLR-GEN-009		Progress Report #9 in preparation of Performance Review Meeting #4	AED-PR-DLR-GEN-009--PR4--v1.01--2022_10_05.pdf
38	PR	GEN	AED-PR-DLR-GEN-010		Progress Report #10 in preparation of Performance Review Meeting #5	AED-PR-DLR-GEN-010--PR5--v1.00--2023_03_01.pdf
39	PR	GEN	AED-PR-DLR-GEN-011		Progress Report #11 in preparation of Performance Review Meeting #6	AED-PR-DLR-GEN-011--PR6--V1_00--2023_10_04.pdf
40	PR	GEN	AED-PR-DLR-GEN-012		Progress Report #12 in preparation of Final Review Meeting	AED-PR-DLR-GEN-012--FRM--V1_00--2024_02_28.pdf
41	PR	GEN	AED-PR-DLR-GEN-013		Aeolus DISC Phase E2 Final Report	
Technical Notes						
42	TN	E2SL 1B	AED-TN-DoRIT-E2SL1B-001		E2S/L1B open issues priority list	AED-TN-DoRIT-E2SL1B-001--Processor_Evolution-V1_10--2023_07_18--noTrack.pdf
43	TN	L2A	AED-TN-TROPOS-L2A-002	AED-TN-CNRM-L2A-002	L2A open issues priority list	AED-TN-TROPOS-L2A-002_V1.8.pdf
44	TN	L2B	AED-TN-KNMI-L2B-003		L2B evolution document	AED-TN-KNMI-L2B-003--Processor_Evolution--v2.1--2023_04_28.pdf
47	TN	ACMFC	AED-TN-ABB-ACMFC-004		ACMF-C evolution document	AED-TN-ABB-ACMFC-004--Evolution_Document--v2_0--2020_09_10.pdf
48	TN	ACMFST	AED-TN-ST-ACMFST-005		ACMF-ST processor evolution document	AED-TN-ST-ACMFST-005-v1.3-20220331-ACMF-ST-processor-evolution-document.pdf
49	TN	SNDBX	AED-TN-KNMI-SNDBX-006		Sandbox evolution document	AED-TN-KNMI-SNDBX-006--sandbox_evolution_docu

						ment--v0_01--2020-02-17.pdf
50	TN	L2A	AED-TN-KNMI-L2A-007		AEL-FM & AEL-PRO open issues priority list	AED-TN-KNMI-L2A-007--Processor_Evolution--v1_7--2023_07_19_tracked_changes.pdf
51	TN	L2A	AED-TN-DoRIT-L2A-008		Operational L2A open issues priority list	AED-TN-DoRIT-L2A-008--Processor_Evolution--v1_4--2023_07_25--noTrack.pdf
52	TN	L1B	AED-TN-DoRIT-L1B-010	AED-TN-DoRIT-L1B-001	L1bP AUX_PAR_1B Updates	AED-TN-DoRIT-L1B-010--PAR1B_Updates--v1_09--2022_03_23.pdf
53	TN	L2B	AED-TN-KNMI-L2B-020		L2B Classification Settings	
54	TN	HBE	AED-TN-DLR-HBE-021		Harmonic Bias Estimation from real ground speed observations	AED-TN-DLR-HBE-021--AeolusGroundReturns--v1_00--2020-02-18.pdf
55	TN	L1B	AED-TN-DLR-L1B-022		Radiometric Performance of the ALADIN Instrument	AED-TN-DLR-L1B-022--RadiometricPerformance--v1_01--2020-03-02.pdf
56	TN	GEN	AED-TN-DLR-GEN-023		Cal/Val Synthesis	AED-TN-DLR-GEN-023--Cal_Val_Synthesis--V6.1--2024-01-30.docx
57		L1B	AED-TN-DLR-L1B-024		L1B algorithm consolidation	AED-TN-DLR-L1B-024--AlgorithmConsolidation--v1_00--2020-03-24.pdf
58	TN	NWP	AED-TN-ECMWF-NWP-025		The NWP impact of Aeolus Level-2B winds at ECMWF	AED-TN-ECMWF-NWP-025--20230809_v7.0.pdf
59	TN	NWP	AED-TN-CNRM-NWP-026		Bias correction Météo France	AED-TN-CNRM-NWP-026--bias-correction--v1_00--2020-02-26.pdf
60	TN	L1B	AED-TN-DoRIT-L1B-027		DL1B_IRC_008 Investigations & Findings	AED-TN-DoRIT-L1B-027--DL1B_IRC_008_Investigation--v1_00--2020_04_29.pdf
61	TN	GEN	AED-TN-DLR-GEN-028		First Reprocessing campaign for FM-B covering the time period 2019-06 to 2019-12	AED-TN-DLR-REPRO-028--FRC_FMB--v1.1--2020_08_03.pdf
62	TN	L1B	AED-TN-DoRIT-L1B-029		PF1B_016 Investigation Results	AED-TN-DoRIT-L1B-029--PF1B_016_Investigation--v1_01--2020_04_27.pdf
63	TN	L1B	AED-TN-DLR-L1B-030		Analysis of Rayleigh spectrometer transmission curves based on instrument sprectral registration (ISR) measurements and investigation of instrumental drifts	AED-TN-DLR-L1B-030--ISR_analyses--v1_00--2020-05-25.pdf

64	TN	NWP	AED-TN-CNRM-NWP-031		NWP impact assessment with ARPEGE	AED-TN-CNRM-NWP-031--ARPEGE-impact--v1_00--2020-05-29.pdf
65	TN	L2A	AED-TN-CNRM-L2A-032		Aeolus Level 2a Prototype: Evolution at end of Exploitation phase 1	AED-TN-CNRM-L2A-032--L2A_ERR_Consolidation--v1_00--2020-05-28.pdf
66	TN	GEN	AED-TN-MYR-GEN-033		ALADIN performance analysis report – Number 1	AED-TN-MYR-GEN-033--ALADIN_performance--v1_00--20200602.pdf
67	TN	NWP	AED-TN-KNMI-NWP-034		NWP Calibration (WP 4350)	
68	TN	L1B	AED-TN-DLR-L1B-035		Analysis of Rayleigh spectrometer transmission curves based on instrument spectral registration (ISR) measurements and analysis of the rst reprocessed data set	AED-TN-DLR-L1B-035--ARSTC_ISR--v1_00--2020_08_14.pdf
69	TN	L2A	AED-TN-TROPOS-L2A-036	AED-TN-CNRM-L2A-036	L2A user guide	AED-TN-TROPOS-L2A-036--V2_3--2023_10_13.pdf
70	TN	GEN	AED-TN-MYR-GEN-037		Aeolus - Laser B: Synthesis of outcomes in root cause analysis for signal loss	AED-TN-MYR-GEN-037--Signal_loss--V1_1--20200823.pdf
71	TN	GEN	AED-TN-Serco-GEN-038	AED-TN-SER-GEN-010	Instrument Calibration Status and Recommendations	AED-TN-Serco-GEN-038--Instrument_Calibration_Status_and_Recommendation--v1_2--2020_08_31.pdf
72	TN	GEN	AED-TN-MYR-GEN-039		Evaluation of angle of incidence on spectrometers	AED-TN-MYR-GEN-039--AoI--V1_2--20201030.pdf
73	TN	GEN	AED-TN-ECMWF-GEN-040		Verification report for first Reprocessing campaign for FM-B covering the time period 2019-06 to 2019-12	AED-TN-ECMWF-GEN-040--1st_reprocessing_verification_report--v1_00--2020_10_13.pdf
74	TN	GEN	AED-TN-DLR-GEN-041		Second Reprocessing campaign for FM-B covering the time period 2019-06 to 2020-10	AED-TN-DLR-GEN-041--SRC_FMB--v1.1--2021_02_23.pdf
75	TN	GEN	AED-TN-MYR-GEN-042		Root cause analysis for signal jumps on INT path	AED-TN-MYR-GEN-042--Signal_jumps--V1_0--20201023.pdf
76	TN	CAL	AED-TN-CNRM-CAL-043		RRC cross point study	AED-TN-CNRM-CAL-043--RRC-cross-point-study--v1_00--2020_10_28.pdf
77	TN	GEN	AED-TN-MYR-GEN-044		Image synthesis for better understanding of the in-orbit events	AED-TN-MYR-GEN-044--Image_Synthesis--V7_0--20231024.pdf

78	TN	GEN	AED-TN-MYR-GEN-045		Short note about receiver behaviour	AED-TN-MYR-GEN-045--receiver-behaviour--V2_0--20210813.pdf
79	TN	GEN	AED-TN-MYR-GEN-046		Root cause analysis for initial signal loss	AED-TN-MYR-GEN-046--Initial-Signal-Loss--V2_0--20210222.pdf
80	TN	L2A	AED-TN-CNRM-L2A-047		Updated Mie SNR in L2A V3.12	AED-TN-CNRM-L2A-047--SNR_Mie_update--V1_0--2021_02_22.pdf
81	TN	L2A	AED-TN-CNRM-L2A-048		SNR based QC flags tuning	AED-TN-CNRM-L2A-048--SNR_based_QC_flags_tuning--v1_0--2021_03_04.pdf
82	TN	L1B	AED-TN-DoRIT-L1B-049		IRONIC Data Measurements Processing	AED-TN-DoRIT-L1B-049--IRONIC_Processing--v2_10--2021_11_04.pdf
83	TN	GEN	AED-TN-MYR-GEN-050		Aeolus orbit lowering - Phase 1: preliminary assessment	AED-TN-MYR-GEN-050--orbit-lowering-phase-1--V2_0--2021_05_10.pdf
84	TN	L1A	AED-TN-DoRIT-L1A-051		Investigation results dL1A_005: Outliers observed in DCO and SBKG measurements	AED-TN-DoRIT-L1A-051--dL1A_005_Investigation--v1_00--2021_03_24.pdf
85	TN	L2A	AED-TN-CNRM-L2A-052		Cloud screening based on derived backscatter from AUX_MET data	AED-TN-CNRM-L2A-052-Cloud_screening_using_AUX_MET--v1_0--2020_09_07.pdf
86	TN	GEN	AED-TN-MYR-GEN-053		Aeolus Orbit lowering - Phase 2: show-stopper analysis	AED-TN-MYR-GEN-053--orbit-lowering-phase-2--V2_0--2021_05_10.pdf
87	TN	GEN	AED-TN-DoRIT-GEN-054		Aeolus lower orbit simulation and processing with E2S-L1B chain	AED-TN-DoRIT-GEN-054--Lower_Orbit_E2S_L1B--v1_01--2021_05_03.pdf
88	TN	GEN	AED-TN-MYR-GEN-055		Aeolus orbit lowering - Phase 3: impact analysis	under NDA - not available here
89	TN	L2A	AED-TN-CNRM-L2A-056		Analysis of the L2A Group product	AED-TN-CNRM-L2A-056--Group_analysis--V1_0--20210719.pdf
90	TN	GEN	AED-TN-LMU-GEN-057		User requirements for the VirES Virtual Research Environment (VRE)	AED-TN-LMU-GEN-057--VirES-VRE-URD--v1_0--2021_07_30.pdf
91	TN	GEN	AED-TN-MYR-GEN-058		Correlation of the optical efficiency on the INT path and consequences	AED-TN-MYR-GEN-058--INT correlation--V1_0--20210823.pdf
92	TN	GEN	AED-TN-MYR-GEN-059		Aeolus orbit lowering - Phase 4: synthesis and recommendations	AED-TN-MYR-GEN-059--orbit-lowering-phase-4--V2_0--2021102.pdf
93	TN	GEN	AED-TN-ECMWF-GEN-060		Verification report for second Reprocessing campaign for FM-B covering the time period 2019-06 to 2020-10	AED-TN-ECMWF-GEN-060-2nd_reprocessing_verification_report--V1.1--2021_12_10.pdf
94	TN	GEN	AED-TN-DLR-GEN-061		Third Reprocessing campaign: FM-A covering	AED-TN-DLR-GEN-061--SRC_FMA--v2.0_20220930.pdf

					the time period 2018 to 2019-06	
95	TN	L1A	AED-TN-DoRIT-L1A-062		Investigation results dL1A_004: Beam propagation with refractive index using EO-CFI	AED-TN-DoRIT-L1A-062--dL1A_004_Investigation--v1_01--2021_11_12.pdf
96	TN	GEN	AED-TN-MYR-GEN-063		Jumps and ghosts	AED-TN-MYR-GEN-063--Jumps--V2--20220124.pdf
97	TN	L1B	AED-TN-L1B-GEN-064		Detecting hot pixel induced steps in Aeolus atmospheric signals	AED-TN-L1B-GEN-064--DetectingHotPixelSteps--v1.0.pdf
98	TN	L2A	AED-TN-CNRM-L2A-065		Providing a L2A product with a sub-BRC horizontal resolution	AED-TN-CNRM-L2A-065--L2A_Sub-BRC--V1_0--2022_02_03.pdf
99	TN	GEN	AED-TN-Serco-GEN-066		KORE-TN Document template	
100	TN	GEN	AED-TN-Serco-GEN-067		Configuration Management KORE-TN	AED-TN-Serco-GEN-067-KORE-TN-ConfigurationMangement--v1_40.pdf
101	TN	GEN	AED-TN-Serco-GEN-068		Anomaly and Change Management KORE-TN	AED-TN-Serco-GEN-068-KORE-TN-AnomalyAndChangeManagement--v1_20--2022_09_26.pdf
102	TN	GEN	AED-TN-Serco-GEN-069		Systematic Quality Control KORE-TN	
103	TN	GEN	AED-TN-Serco-GEN-070		Operational Software Verification KORE-TN	
104	TN	GEN	AED-TN-Serco-GEN-071		Outreach KORE-TN	
105	TN	GEN	AED-TN-Serco-GEN-072		Processes, Roles and Effort KORE-TN	
106	TN	L2B	AED-TN-TROPOS-L2B-073		L2B Mie cloudy winds and AMVs	AED-TN-TROPOS-L2B-073--Mie_cloudy_assessment_v1_2022_03_15.pdf
107	TN	L2A	AED-TN-KNMI-L2A-074		AEL-FM / AEL-PRO quality assessment report for B13 NRT data	AED-TN-KNMI-L2A-074--L2A-FM-PRO-B13-NRT-assessment--v1--2022-04-22.pdf
108	TN	GEN	AED-TN-MYR-GEN-075		Benefits in switching to laser A	AED-TN-MYR-GEN-075--FM_A_switch--V2_1--2022_06_22.pdf
109	TN	L2A	AED-TN-ECMWF-NWP-076		Technical note on Aeolus Aerosol Assimilation in the DISC (A3D)	AED-TN-ECMWF-NWP-076--aerosol-assimilation--V1_0--2023_03_31.pdf

110	TN	GEN	AED-TN-MYR-GEN-077		Processing inter-calibration	AED-TN-MYR-GEN-077--Processing_intercalibration--V1--2022_10_21.pdf
111	TN	E2S	AED-TN-DoRIT-E2S-078		Mie Geomterical Factor Usage in E2S Simulations	AED-TN-DoRIT-E2S-078--Internal_Ref_Geometrical_Factor--v1_00--2022_11_25.pdf
112	TN	GEN	AED-TN-MYR-GEN-079		Effect of correlated and non-correlated noises on the Rayleigh channel random error	AED-TN-MYR-GEN-079--Correlated_Noise--V2-2023-01-18.pdf
113	TN	GEN	AED-TN-ECMWF-GEN-080		Verification report for third reprocessing campaign for FM-A covering the time period 2018 to 2019-06	AED-TN-ECMWF-GEN-080-3rd_reprocessing_verification_report--V1.01.pdf
114	TN	GEN	AED-TN-DLR-GEN-081		Fourth Reprocessing campaign for the full mission time period from August 2018 to end of mission	AED-TN-DLR-GEN-081--RC-4th-2023_03_01.pdf
115	TN	GEN	AED-TN-MYR-GEN-082		Analysis of the Aeolus performance achieved after come back to laser A	AED-TN-MYR-GEN-082--FMA_switch-V2_2023_08_29.pdf
116	TN	GEN	AED-TN-DLR-GEN-083		Aeolus EOL Test Analysis	AED-TN-DLR-GEN-083--EOL-test-analysis--V1_2023_09_14.pdf
117	TN	L1B	AED-TN-DLR-L1B-084		Hot Pixel investigations	AED-TN-DLR-L1B-084--Hot_Pixel--V1_1_2023-12-19.pdf
118	TN	L1B	AED-TN-DoRIT-L1B-085		Refined SR wedge investigation	AED-TN-DoRIT-L1B-085--dL1B_016_SR_Wedge_Investigation--v1_00--2023_07_26.pdf
119	TN	GEN	AED-TN-OLA-GEN-086		Towards an Optimum Fizeau Spectrometer for Doppler Wind Lidar at 0.355µm	AED-TN-OLA-GEN-086--Optimum_Fizeau_Spectrometer--v5_01--2023_08_20.pdf
120	TN	GEN	AED-TN-ECMWF-GEN-087		Verification report for fourth reprocessing campaign for FM-B	
121	TN	L1B	AED-TN-DLR-L1B-088		Solar background	
122	TN	L2A	AED-TN-ECMWF-L2A-089		L2A BUFR conversion	
123	TN	GEN	AED-TN-Serco-GEN-090		Being efficiently ready for LTDP KORE-TN	
124	TN	GEN	AED-TN-Serco-GEN-091		QWG KORE TN	
Software Documentation						

125	SD	E2S	AED-SD-DoRIT-E2S-001	522890	E2S Software Release Note	AED-SD-DoRIT-E2S-001--SRN--v4_09--2023-01-31.pdf
126	SD	E2S	AED-SD-DoRIT-E2S-002	522250	E2S Software User Manual	AED-SD-DoRIT-E2S-002--SUM--v2_15--2022_11_15.pdf
127	SD	E2S	AED-SD-DoRIT-E2S-003	521801	E2S Detailed Processing Model	AED-SD-DoRIT-E2S-003--DPM--v4_05--2022_11_15.pdf
128	SD	E2S	AED-SD-DoRIT-E2S-004	521791	E2S Acceptance Procedures	AED-SD-DoRIT-E2S-004--SATP--v1_11--2020_05_15.pdf
129	SD	E2S	AED-SD-DoRIT-E2S-005	521389	E2S Architectural Design Document	AED-SD-DoRIT-E2S-005--ADD--v3_09--2020_05_15.pdf
130	SD	L1B	AED-SD-DoRIT-L1B-006	521666	L1B Input Output Definition Document	AED-SD-DoRIT-L1B-006--IODD--v4_18--2023_01_31.pdf
131	SD	L1B	AED-SD-DoRIT-L1B-007	521800	L1B Detailed Processing Model	AED-SD-DoRIT-L1B-007--DPM--v3_18--2023_01_31.pdf
132	SD	L1B	AED-SD-DoRIT-L1B-008	522888	L1B Software User Manual	AED-SD-DoRIT-L1B-008--SUM--v2_12--2022_12_09.pdf
133	SD	L1B	AED-SD-DoRIT-L1B-009	523330	L1B Software Release Note	AED-SD-DoRIT-L1B-009--SRN--v7_14--2023_01_31.pdf
134	SD	L1B	AED-SD-DoRIT-L1B-010	AED-TN-DoRIT-L1B-001	L1B AUX_PAR_1B updates	AED-TN-DoRIT-L1B-010--PAR1B_Updates--v1_08--2021_08_31.pdf
135	SD	E2SL1BL2A	AED-SD-DoRIT-E2SL1BL2A-010	AED-PL-DoRIT-E2SL1B-001	E2S/L1B/L2A Test Validation Plan	AED-SD-DoRIT-E2SL1BL2A-010--TVP--v1_03--2020_06_12.pdf
136	SD	E2SL1B	AED-SD-DoRIT-E2SL1B-011	521387	E2S/L1B Software Requirement Specification	AED-SD-DoRIT-E2SL1B-011--SRS--v1_09--2020_05_15.pdf
137	SD	L1B	AED-SD-DoRIT-L1B-012	521388	L1B Architectural Design Document	AED-SD-DoRIT-L1B-012--ADD--v3_06--2020_06_12.pdf
138	SD	L1B	AED-SD-DoRIT-L1B-013	521390	L1B External Interface Control Document	AED-SD-DoRIT-L1B-013--EICD--v1_11--2020_06_12.pdf
139	SD	L1B	AED-SD-DoRIT-L1B-014	521792	L1B Acceptance Procedures	AED-SD-DoRIT-L1B-014--PATP--v1_06--2020_06_12.pdf
140	SD	E2SL1B	AED-SD-DoRIT-E2SL1B-015	521793	E2S/L1B Verification Control Document	AED-SD-DoRIT-E2SL1B-015--VCP--v1_09--2020_05_15.pdf
141	SD	E2SL1B	AED-SD-DoRIT-E2SL1B-016	ADM-PL-52-1589	E2S/L1B Acceptance Test Plan	AED-SD-DoRIT-E2SL1B-016--ATP--v1_05--2020_05_15.pdf
142	SD	L1B	AED-SD-DoRIT-L1B-017	AE-TN-ESA-GS-100	The E2S Satellite Characterization and L1B AUX_CHAR input files	AED-SD-DoRIT-L1B-017--ESC_LAIF--v1_01--2020_06_12.pdf

143	SD	E2S	AED-SD-DoRIT-E2S-018	ADM-RP-DLR-E2S-001	E2S Validation Report Part 1	AED-SD-DoRIT-E2S-018--FAT_Results--v4_09--2022_11_15.pdf
144	SD	E2S	AED-SD-DoRIT-E2S-019	ADM-RP-DLR-E2S-001	E2S Validation Report Part 2	AED-SD-DoRIT-E2S-019--ETEST_Results--v4_09--2022_11_15.pdf
145	SD	L2A	AED-SD-DoRIT-L2A-020	AE-MA-DLR-L2A-002	L2A Auxiliary Data Editor Software User Manual	AED-SD-DoRIT-L2A-020--ADE_SUM--v1_03--20120_07_31.pdf
146	SD	L2A	AED-SD-DoRIT-L2A-021	AE-IF-DLR-L2A-001	L2A External Interface Control Document	AED-SD-DoRIT-L2A-021--EICD--v2_05--2020_07_31.pdf
147	SD	L2A	AED-SD-DoRIT-L2A-022	AE-DD-DLR-L2A-001	L2A Processor Design Document	AED-SD-DoRIT-L2A-022--PDD--v2_06--2020_07_31.pdf
148	SD	L2A	AED-SD-DoRIT-L2A-023	AE-RS-DLR-L2A-001	L2A Software Requirements Document	AED-SD-DoRIT-L2A-023--SRD--v2_03--2020_07_31.pdf
149	SD	L2A	AED-SD-DoRIT-L2A-024	AE-PL-DLR-L2A-001	L2A Software Validation&Verification Plan	AED-SD-DoRIT-L2A-024--SVVP--v2_03--2020_07_31.pdf
150	SD	L2A	AED-SD-DoRIT-L2A-025	AE-IF-DLR-L2A-004	L2A Input Output Definition Document	AED-SD-DoRIT-L2A-025--IODD--v3_16--2023_01_31.pdf
151	SD	L2A	AED-SD-DoRIT-L2A-026	AE-MA-DLR-L12-003	L2A Data Visualization Software User Manual	AED-SD-DoRIT-L2A-026--DV_SUM--v1_04--2020_07_31.pdf
152	SD	L2A	AED-SD-DoRIT-L2A-027	AE-MA-DLR-L2A-001	L2A Software User Manual	AED-SD-DoRIT-L2A-027-SUM--v2_17--2021_04_21.pdf
153	SD	L2A	AED-SD-DoRIT-L2A-028	AE-RN-DLR-L2A-001	L2A Software Release Notes	AED-SD-DoRIT-L2A-028--SRN--v3_16_1--2023_03_24.pdf
154	SD	L2A	AED-SD-DoRIT-L2A-029	AE-PL-DLR-L2A-999	L2A Software Life-Cycle Document References	AED-SD-DoRIT-L2A-029-SLCDR--v1_14--2023_01_31.pdf
155	SD	L2A	AED-SD-CNRM-L2A-030	AE-TN-IPSL-GS-001	ADM-Aeolus L2A Algorithm Theoretical Baseline Document - Particle spin-off products	AED-SD-CNRM-L2A-030--ATBD--v5_09-2021_12_20.pdf
156	SD	L2B	AED-SD-ECMWF-L2B-031	AE-IF-ECMWF-L2BP-002	L2B External Interface Control Document	AED-SD-ECMWF-L2B-031--EICD--v2_00--2018_08_09.pdf
157	SD	L2B	AED-SD-ECMWF-L2B-032	AE-RS-ECMWF-L2BP-001	L2B Software Requirements Document	AED-SD-ECMWF-L2B-032--SRD--v2_03--2020_07_31.pdf
158	SD	L2B	AED-SD-ECMWF-L2B-033	AE-TN-ECMWF-L2BP_0073	L2B BUFR Description	AED-SD-ECMWF-L2B-033--BD--v1_00--2015_11_23.pdf
159	SD	L2B	AED-SD-ECMWF-L2B-034	AE-DD-ECMWF-L2BP-001	L2B Processor Design Document	AED-SD-ECMWF-L2B-034--DD--v1_02--2018_02_21.pdf
160	SD	L2B	AED-SD-KNMI-L2B-035	AE-TN-KNMI-BUFR-001	L2B Bufr Converter Software User Manual	AED-SD-KNMI-L2B-035--BC_SUM--v1_03--2021_07_31.pdf

161	SD	L2B	AED-SD-KNMI-L2B-036	AE_PL_KNMI_L2BP_001	L2B Software Validation&Verification Plan	AED-SD-KNMI-L2B-036--SVVP--v2_03--2020_07_31.pdf
162	SD	L2B	AED-SD-ECMWF-L2B-037	AE_IF_ECMWF_L2BP_001	L2B Input Output Definition Document	AED-SD-ECMWF-L2B-037--IODD--v3_90--2023_01_31.pdf
163	SD	L2B	AED-SD-ECMWF-L2B-038	AE_TN_ECMWF_L2BP_0023	L2B Algorithm Theoretical Basis Document	AED-SD-ECMWF-L2B-038--ATBD--v3_40--2020_07_16.pdf
164	SD	L2B	AED-SD-ECMWF-L2B-039	AE-MA-ECMWF-L2BP-001	L2B Software User Manual	AED-SD-ECMWF-L2B-039--SUM--v2_05--2023_01_31.pdf
165	SD	L2B	AED-SD-ECMWF-L2B-040	AE-RN-ECMWF-L2BP-001	L2B Software Release Notes	AED-SD-ECMWF-L2B-040--SRN--v3_90--2023_01_31.pdf
166	SD	L1B	AED-SD-DoRIT-L1B-041	ADM-RP-DLR-L1B-002	L1B Validation Report Part 1	AED-SD-DoRIT-L1B-041--FAT_Results--v7_09--2020_06_12.pdf
167	SD	L1B	AED-SD-DoRIT-L1B-042	AED-RP-DoRIT-L1B-004	L1B Runtime Performance Overview	AED-SD-DoRIT-L1B-042--Runtime_Performance--v7_09--2020_06_12.pdf
168	SD	L1B	AED-SD-DLR-L1B-043	AED-TN-DoRIT-L1B-001	L1bP AUX_PAR_1B Updates	duplicate of AED-TN-DoRIT-L1B-010?
169	SD	L1B	AED-SD-DLR-L1B-044	AE-RP-DLR-L1B-001	ADM-Aeolus Algorithm Theoretical Basis Document - Level1B Products	AED-SD-DLR-L1B-044--ATBD--v4_04–2018_04_20.pdf
170	SD	L1B/L2A	AED-SD-DoRIT-L1BL2A-045		L1bP and L2A final report on processor modifications during phase E2	AED-SD-DoRIT-L1BL2A-045--Final_Report_Phase_E2--v1_10--2024_01_26.pdf
171	SD	L2A	AED-SD-KNMI-L2A-046	MSP-ATBs_V1.1_SWV_1	Creation of Crosstalk corrected Attenuated backscatter Signals from the Aeolus Mie Spectrometer Unit (MST-ATBs ATBD)	MSP-ATBs_V1.1_SWV_1.pdf
172	SD	CS_PP	AED-SD-CNRM-CS_PP-050	AED-TN-MFG-GS-0001	Generation of the RBC Auxiliary file - Detailed Processing Model	AED-SD-CNRM-CS_PP-050--RBC_DPM_ATBD--v4_04--2020_04_30.pdf
173	SD	CS_PP	AED-SD-CNRM-CS_PP-051	AED-TN-MFG-GS-0003	ADM-Aeolus Rayleigh-Brillouin Correction Look-up Table Generator. Input / Output Data Definitions, Interface Control Document	AED-SD-CNRM-CS_PP-051--RBC_IODD_ICD--v4_04--2020_04_30.pdf
174	SD	CS_PP	AED-SD-CNRM-CS_PP-052	AED-TN-MFG-L2P-CAL-003	Generation and update of AUX_CSR	AED-SD-CNRM-CS_PP-052--CSR_IODD_DPM--v4_04--2020_04_30.pdf
175	SD	CS_PP	AED-SD-CNRM-CS_PP-053	AE-TN-MFG-L2P-CAL-004	Generation of AUX_CAL Detailed Processing Model Input / Output Data Definition	AED-SD-CNRM-CS_PP-053--CAL_IODD_DPM_ATBD--v4_04--2020_04_30.pdf

176	SD	CS_PP	AED-SD-CNRM-CS_PP-054	AE-TN-MFG-L2P-CAL-002	Generation / update of L2 calibration data at ACMF	AED-SD-CNRM-CS_PP-054--CAL_ICD--v4_04--2020_04_30.pdf
177	SD	CS_PP	AED-SD-CNRM-CS_PP-055	AED-TP-CAL-L2A-CNRM-001	Calibration suite and L2A Test Plan	AED-SD-CNRM-CS_PP-055--CS_L2A_TP--v1_01--2019_04_29.pdf
178	SD	CS_PP	AED-SD-CNRM-CS_PP-056	AED-TR-CNRM-CAL-001	Calibration suite Test Report	AED-SD-CNRM-CS_PP-056--CS_TR--v1_01--2020_04_30.pdf
179	SD	CS_PP	AED-SD-CNRM-CS_PP-057	AED-TN-MFG-L2P-CAL-006	Calibration Suite: Software Release Note	AED-SD-CNRM-CS_PP-057--SRN--v4_04--2020_04_30.pdf
180	SD	ACMF_C	AED-SD-ABB-ACMF_C-060	AED-DD-ABB-GS-0003	ACMF Detailed Processing Model	AED-SD-ABB-ACMF_C-060--DPM–v4_04–2021_11_30.pdf
181	SD	ACMF_C	AED-SD-ABB-ACMF_C-061	AE-MA-ABB-GS-0002	ACMF-C Acceptance Test Procedure	AED-SD-ABB-ACMF_C-061--ATP–v1_03–2021_01_22.pdf
182	SD	ACMF_C	AED-SD-ABB-ACMF_C-062	AE-MA-ABB-GS-0001	ACMF-C Software Transfer Document	AED-SD-ABB-ACMF_C-062--STC--v4_04–2021_01_22.pdf
183	SD	ACMF	AED-SD-SnT-ACMF-065	AE-TN-STC-GS-0013	ACMF-OC/OS/A software release note	AED-SD-SnT-ACMF-065--SRN--v1_03--2022_08_05.pdf
184	SD	ACMF	AED-SD-SnT-ACMF-066	AE-MA-STC-GS-0002	ACMF User Manual	AED-SD-SnT-ACMF-066--SUM--v3_00--2018_05_29.pdf
185	SD	ACMF	AED-SD-SnT-ACMF-067	ST-DLR-DISCA-NOT-002	ACMF-ST Installation manual	AED-SD-SnT-ACMF-067--SIM_ST--v1_01--2021_08_06.pdf
186	SD	ACMF	AED-SD-SnT-ACMF-068	ST-DLR-DISCA-ATP-001	ACMF-ST Test Plan	AED-SD-SnT-ACMF-068--TP_ST--v1_04--2022_08_05.pdf
187	SD	ACMF	AED-SD-SnT-ACMF-069	ST-DLR-DISCA-ATR-001	ACMF-ST Test Report	AED-SD-SnT-ACMF-069--TR_ST--v1_05--2022_08_05.pdf
188	SD	L2A_PP	AED-SD-TROPOS-L2A_PP-070	AED-SD-CNRM-L2A_PP-070	L2A Prototype Processor Software Release note	AED-SD-TROPOS-L2A_PP-070--SRN_v3_17--v1_00--2023_10_13.pdf
189	SD	L2A_PP	AED-SD-KNMI-L2A_PP-071		AEL-FM Prototype Processor Software Release note	
190	SD	L2A_PP	AED-SD-KNMI-L2A_PP-072		AEL-PRO Prototype Processor Software Release note	
191	SD	AUX	AED-SD-SER-AUX-073		AEOLUS AUX_PAR_QC Changes and Evolutions	AED-SD-SER-AUX-073--AUX_PAR_QC_ChangesEvolution--v1.1--2024_02_05.pdf